This work is protected by copyright and other intellectual property rights and duplication or sale of all or part is not permitted, except that material may be duplicated by you for research, private study, criticism/review or educational purposes. Electronic or print copies are for your own personal, non-commercial use and shall not be passed to any other individual. No quotation may be published without proper acknowledgement. For any other use, or to quote extensively from the work, permission must be obtained from the copyright holder/s.

Identifying and characterising young, nearby, low-mass members of stellar moving groups

Alexander Slater Binks

Doctor of Philosophy

School of Physical and Geographical Sciences, University of Keele.

October 2015

For my family

Abstract

Since the early 1990s, several groups of comoving, coeval stars younger than 100 Myr and within 100 pc have been revealed. Studying and identifying members in these 'Nearby Young Moving Groups' (MGs) is vital because they provide: well characterised samples to test pre-main sequence evolution; ideal targets for direct imaging of exoplanets, discs and brown dwarfs; observational evidence for the birthsites of stars in the Solar neighbourhood.

Spectroscopy is used to perform tests of membership for 24 M-dwarf candidates of both the Beta Pictoris MG (BPMG) and AB Doradus MG, confirming 8 and 6 new members, respectively. Measurements of lithium provide a precise age for BPMG, using the 'Lithium Depletion Boundary' (LDB) technique. This represents the most accurate age yet determined for this important MG and is about double what has been commonly assumed in the literature from other methods.

A kinematically unbiased sample of 146 X-ray emitting FGK stars in the Northern hemisphere with short rotation periods chosen from the SuperWASP All-Sky Survey were spectroscopically investigated to assess their ages and kinematics. The search identified 26 stars younger than 200 Myr based on their photospheric lithium. Whilst most of these were not associated with any MG, seven are comoving with the sparse (mostly Southern) Octans-Near MG.

Infrared photometry is used to identify debris discs amongst M-dwarfs in MGs and their debris disc fractions are compared as a function of mass and age. Eight per cent of the sample younger than 40 Myr were identified as debris disc objects, although some may have remained undetected because the sensitivity limits for detecting debris discs around M-dwarfs is lower than for higher-mass stars. No debris discs were observed in MGs older than 40 Myr, suggesting the timescale for disc removal is more rapid than for higher-mass stars.

Acknowledgements

As I'm sat here in the corner of my local pub on a quiet Sunday, in the village where I grew up for most of my life I've finally had time to stop and ask myself two questions about my career as a Ph.D. student: Firstly, "has it changed me in any way?" Secondly, "was it worth it?" The answer to both of these is invariably **yes**!

I would have never imagined when I began my undergraduate physics course at Exeter in 2007 on the verge of giving it all in that seven years later I'd be giving a talk in Flagstaff, Arizona in an auditorium full to the brim with professional astronomers! For every time I've sat at my desk rueing the endless menial data entry tasks, I cannot forget the places I have been, but, more importantly, the amazing people I have met over the last few years.

Although it was many years ago, I can't forget to thank the staff and students in the physics department at Exeter for giving me the encouragement and willpower to carry on in the subject and for sharing countless hazy nights spent in the Cavern on a Wednesday. Without them I'd have never pushed myself to carry on.

When I first asked Nathan Mayne at Exeter what Rob Jeffries was like, his response was "he's an incredible guy, but he'll get his pound of flesh out of you!" Nathan, you were correct. I'd be totally lost without Rob's supervision over the last few years, and it's only towards the end of this process that I've come to appreciate his tenacity and professionalism. I can only hope a fraction of his work ethic has rubbed off on me. Working with him also means I have developed a fondness of 80s rock and experienced gatecrashing a private family party on New Years Eve in La Palma.

Whilst on my observing runs in La Palma (I've been lucky enough to go on three) the observing staff at the Nordic Optical Telescope and the Isaac Newton Telescope have been superb at ensuring the best possible conditions for a night's observation. Travelling around the island has been unforgettable and I really hope to be back there someday.

The staff at Keele have facilitated all of my needs to study astronomy and have always been on hand to provide help. It has been a pleasure working with my fellow Ph.D. students and I'll miss our (extended) Friday lunchtimes at the KPA. They have always been there to provide technical support, and more importantly, boost morale. Keele is simply unique. Nothing compares to an afternoon with friends on the lawns of Keele Hall (or indeed the inevitable night). I am a country-sider at heart and I have felt completely at home at Keele and the surrounding area over the last three years. Gabi and Alex – there's a drink on me for accommodating me over the last few months.

It's hard to thank my parents enough. I don't think I'll ever understand the support and encouragement they have invested in me, but I am eternally grateful. I'm incredibly blessed to have a family that has always been there. Overwhelming to put into text if I'm honest. Christian, you're not just a brother, you're a best mate. *'Minha gata, obrigado pelo seu amor'.*

Overall, it has been an incredible ride. I wouldn't dream of changing it.

Alex, October 2014

Contents

List of Figures

List of Tables

1 Introduction: the ages of young stars in Moving Groups

How old is that star? Whilst being the fundamental parameter in understanding stellar evolution, age is also arguably the most difficult property to measure. As summarised in Barnes (2009), from an observational perspective, a desirable situation would be one in which a stellar property is highly age sensitive, easily measurable, insensitive to other parameters (e.g., mass, luminosity, temperature), calibratable against stars of known age (i.e., objects in clusters), easily invertible (the age-dependent parameter is single-valued, leading to a single age), able to provide errors and is consistent for all coeval objects. No techniques are available which satisfy all of these criteria, however, several stellar properties are known to be highly age-sensitive on the pre-main sequence (PMS). Ideally, one would find that ages based on a number of techniques are consistent and can therefore be used to strengthen the precision (and possibly accuracy). Precise and accurate ages are vital to improve current knowledge of PMS evolution. Several methods are now commonplace in obtaining empirical ages, most of which have been calibrated with clusters of known age and will be discussed in this chapter.

Since the early 1990s, several groups of young[1], comoving stars have been identified within about 100 pc of the Sun (for a detailed description of these see Zuckerman & Song 2004; Torres et al. 2008; Malo et al. 2013, or chapter 2 in this thesis). Termed 'nearby young moving groups' (herein MGs), several hundreds of stars have been identified in a dozen MGs which required a large observational effort. Samples of low-mass (throughout this thesis 'low-mass' refers to stars with spectral-types F, G, K and M) members of MGs are the focus of this thesis.

Members of MGs are comoving and coeval. One identifies new MGs and members of existing MGs by ensuring their constituents are relatively compact and have similar kinematics, chemical composition (see, for example, Barenfeld et al. 2013; McCarthy &

[1] throughout this thesis, 'young' refers to ages equal to, or younger than members in the Pleiades at ~ 125 Myr.

Wilhelm 2014), but perhaps most importantly, age. The motivations to obtain accurate ages for MGs and their members are two-fold: firstly to provide an age calibration to study evolutionary processes, and secondly as a means of *identifying* new members of MGs. Because determining ages for PMS stars plays such an important role throughout this thesis, the first chapter focuses on the methods used in estimating the ages of young stars, both individually and as part of clusters. The techniques may be split into three separate sections, as prescribed in Soderblom (2010) and Soderblom et al. (2014): semi-fundamental (§1.2), model-dependent (§1.3) and empirical (§1.4). A full description of MGs and discussion of their origins is provided in chapter 2.

1.1 The pre-main sequence evolution of low-mass stars

Low-mass PMS stars form from molecular clouds comprised of interstellar dust and gas which have coalesced under gravity. As a molecular cloud collapses due to gravitational instability, the density of the cloud core increases, leading to higher central temperatures, and the formation of a stable 'protostar' at the centre. The central, hottest region of the protostar quickly becomes opaque to its own infrared (IR) radiation. Material that gently drifts inwards onto the structure can freely radiate in the IR, however, this is smothered by successive layers of incoming matter, which effectively traps the outward radiation.

With increasing temperature and density, for a cloud of radius on the order of several $R_{\odot}$, the core soon reaches temperatures $\geq 10^5$ K; high enough to collisionally ionise most of the hydrogen (Stahler & Palla 2005). Almost all of the light observed from protostars is a result of the accretion luminosity – the radiation released as material impacts onto the protostellar surface. Gas that approaches the surface of the protostar does so at supersonic velocity, causing the cloud to collapse in an inside-out manner. At this point the star is said to be in its *main accretion phase*.

Protostars are deeply embedded within their surrounding gas and dust clouds,

therefore whilst they undergo contraction, large dust absorption coefficients reduce the photon energies and suppress the peak fluxes towards IR wavelengths. As evolutionary processes rarefy and disperse the cloud material, radiation becomes no longer buried within the opaque dust cloud, and for the first time light is able to freely emanate from the surface, which defines a stellar *birthline*. The initial collapse is expected to last no longer than 0.1 Myr (Evans et al. 2009).

Due to conservation of angular momentum, the cloud cannot simply collapse radially. The infalling material from the surrounding envelope is slowed in the direction perpendicular to the rotation axis, causing a increase in density along this axis and the formation of a disc (Yorke, Bodenheimer & Laughlin 1993). The cloud becomes thinner along the axis of rotation and light from the star may escape through cone-shaped voids which are formed at the poles. The disc acts to remove angular momentum from the protostar and transports disc material towards it through viscous interactions. During this phase, the protostar is expected to acquire a significant fraction of its total mass. If angular momentum was not removed from the protostar, the build up of mass would result in angular velocities large enough to inhibit further core collapse.

On timescales of ~ 0.5 Myr, the natal envelope disperses and a protoplanetary disc comprised of gas and small dust particles remains. The gas content of the protoplanetary disc disperses after several Myr (see §1.4.4 and Lada 2000 for the mechanisms of disc dispersal). Dust grains can coagulate via oligarchic growth, forming km-sized planetesimal objects. At this stage, accretion onto the star has almost completely ceased. After 10 Myr a young star may be left with an optically thin, gas-deprived "debris disc".

Observationally, the relationships between the envelope, star and disc can be classified by the slope of their spectral energy distributions (SEDs), as introduced by Lada (1987). In this framework, three classes of young stellar object (YSO) were proposed, labelled as class I, II and III in order of their evolutionary sequence based on the spectral index $\alpha = \frac{d \log \lambda F_\lambda}{d \log \lambda}$, where λ is the wavelength and F_λ is the observed flux density, measured over the wavelength range $2.2 - 20.0\,\mu$m. In chapter 6, α is used to characterise class I/II/III sources based on IR photometry. André, Ward-Thompson &

Barsony (1993) later extended the classification scheme to include the very young class 0 objects. Age estimates are based on number counts of class I/II/III objects combined with an estimate of the disc dispersal times. These ultimately rely on the age scale for young clusters and assessments of disc lifetimes, both of which are subsequently discussed in this chapter (see §1.4.4). Figure 1.1 is a diagram illustrating the major wavelength components of SEDs for classes 0 to III.

•Class 0 – These objects are deeply embedded within their surrounding circumstellar environment and have yet to contract to temperatures high enough to radiate in the optical to mid-IR range. As such, these sources are undetectable at wavelengths $< 10\,\mu$m and the majority of the light observed in the protostellar phase is at longer wavelengths, usually peaking in the sub-mm range (see Figure 1.1). During this phase the object has yet to form a stable central protostar or discernable protoplanetary disc. André, Ward-Thompson & Barsony (2000) listed three criteria for class 0 objects: (1) Indirect evidence for a central YSO; (2) Extended sub-mm continuum emission due to the presence of a spheroidal circumstellar dust envelope and (3) High ratio of sub-mm to bolometric luminosity, suggesting that the envelope mass exceeds the central stellar mass. The class 0 phase is expected to last no longer than 0.1 Myr (Evans et al. 2009).

•Class I – As the natal envelope beings to clear, the protostar and its accreting protoplanetary disc become visible in the mid- and far-IR. Class I sources have $\alpha > 0.3$ (Wilking, Lada & Young 1989), and are still embedded in their natal clouds. The peak emission lies in the far-IR ($\sim 100\,\mu$m), however a significant amount of flux is present at near- and mid-IR wavelengths (Figure 1.1). The shorter wavelengths are indicative of the rise in core temperature, whereas the longer wavelength source is likely to be a result of accreting gas from the surrounding disc and envelope. The youngest of these sources emit the bulk of their energy around $0.1 - 10$ mm. The duration of this phase is about 0.5 Myr (Evans et al. 2009). Class I sources observed in the $1 - 2$ Myr Taurus-Auriga cloud (e.g., Barsony & Kenyon 1992; Greene et al. 1994; Kenyon & Hartmann 1995) suggest that star formation in this cloud has been continuous for at least 1 Myr.

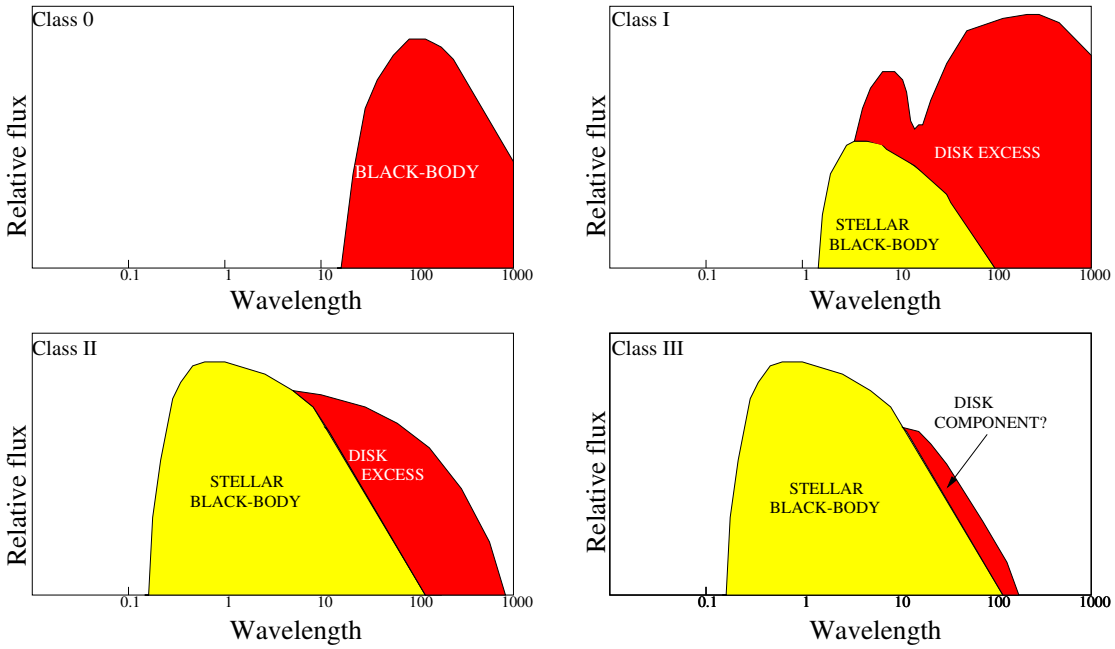

Figure 1.1: A sequence of SEDs displaying the evolution of a Solar-type star on the PMS. The wavelength scale is in μm and the relative flux is on a logarithmic scale. Initially a forming protostar with a cold-core ($T_{\rm eff} \sim 20 - 30\,{\rm K}$) peaks in emission in the sub-mm (class 0). SEDs that emit strongly in the IR, peaking in the far-IR are indicative of protostars (class I) with strong accretion luminosity as material is accreted from the surrounding envelope. As the surrounding material takes the form of an optically thick disc around the protostar, the peak emission moves towards mid- and near-IR (class II). Whether the disc is passive (reradiating photons from the parent star) or active (heating maintained through on-going accretion) governs the shape of the class II SED. As material in the surrounding disc disperses, the excess IR radiation reduces and the disc becomes optically thin (class III).

•Class II – As the star evolves towards class II, the circumstellar gas in the envelope dissipates via accretion processes and dispersal of bipolar jets forming a protoplanetary disc containing small grains. The peak of the flux density moves towards the optical and near-IR (as seen in Figure 1.1). Objects in this class are defined by $-0.3 > \alpha > -1.6$ (an intermediate class of 'flat-spectrum' objects are defined between $\alpha = -0.3$ and $\alpha = 0.3$, Greene et al. 1994). T-Tauri stars are formed during the class II phase. Strong Hα emission lines and substantial IR or ultra-violet excesses are indicative of large amounts of ongoing accretion. The lack of an optically thick envelope and the presence of a protoplanetary disc in which the surrounding gas has coagulated to form small dust particles indicates the major difference between class II and earlier phases. Class II sources are relatively common in star forming regions, where they typically outnumber class I objects by a factor of 10 (Lada 2000) and are therefore expected to have lifetimes ~ 10 times longer.

•Class III – This class of object describes stars that have almost fully cleared their surrounding disc. The flux is almost all from photospheric emission, and very little IR-excess from the remnant disc is present. Spectral indices for this class are $\alpha < -1.6$ and are indicative of optically-thin debris discs.

The lifetimes of the class I and II phases are a fraction of a Myr and a few Myr, respectively (Feigelson & Montmerle 1999). The Kelvin-Helmholtz timescale is maybe 10 Myr, but is highly mass dependent. The first two timescales are dependent on measurements of the disc dispersal times and hence on the absolute age scale assigned to young PMS stars. The majority of the objects studied throughout this thesis are class III sources, with a small number categorised as class II.

The time taken for stars of spectral-type F, G and K to move from the birthline to the zero age main sequence, $t_{\rm ZAMS}$, is expected to last from ~ 10 Myr to several hundred Myr, respectively as it takes longer for lower mass stars to reach temperatures high enough to initiate hydrogen fusion (see Table 1.1 and §1.3.1). The continued contraction increases the core temperature of the star, which in turn causes thermal and nuclear changes to the structure. During this time the surface temperature remains fairly constant, whilst the contraction reduces luminosity. Young stars that are convective on the PMS descend near-vertical Hayashi tracks on a Hertzsprung-Russell diagram (HRD, Figure 1.2). The ignition of deuterium slows the contraction by increasing the internal pressure. For low-mass stars, deuterium burning at temperatures of $t_D \sim 10^6\,{\rm K}$ (Bally & Reipurth 2006) can stall contraction for as long as several Myr. Only when hydrogen is ignited does the contraction cease and the star becomes hydrodynamically stable. This marks the age at which the star can finally be labelled as a main sequence object. Figure 1.2 displays evolutionary tracks from Siess, Dufour & Forestini (2000) for several low-mass objects from the stellar birthline to the ZAMS. Table 1.1 shows the stellar properties at the birthline, the timescale for deuterium to undergo full depletion and the time taken for an object to traverse from the birthline onto the main sequence for the mass range 0.1 to $3.0\,M_\odot$.

Mass ($M_\odot$)	Radius ($R_\odot$)	$\log L_*$ ($L_\odot$)	$\log T_{\rm eff}$ (K)	t_D (yr)	$t_{\rm ZAMS}$ (yr)
0.1	2.49	−0.28	3.49	1.5×10^6	3.7×10^8
0.2	2.52	−0.01	3.52	8.5×10^5	2.4×10^8
0.4	2.70	+0.27	3.56	3.0×10^5	1.1×10^8
0.8	4.32	+0.78	3.61	2.7×10^4	5.2×10^7
1.0	4.92	+0.85	3.63	6.9×10^3	3.2×10^7
1.5	5.09	+0.89	3.65	0	1.2×10^7
2.0	4.94	+0.90	3.67	0	8.4×10^6
3.0	5.66	+0.94	3.70	0	2.0×10^6

Table 1.1: Table from Stahler & Palla (2005). The radius, luminosity and surface temperatures for stars on the theoretical birthline in the mass range between 0.1 and $3.0\,M_\odot$. The period of active deuterium burning on the PMS is t_D and $t_{\rm ZAMS}$ is the time taken to reach the ZAMS from the birthline.

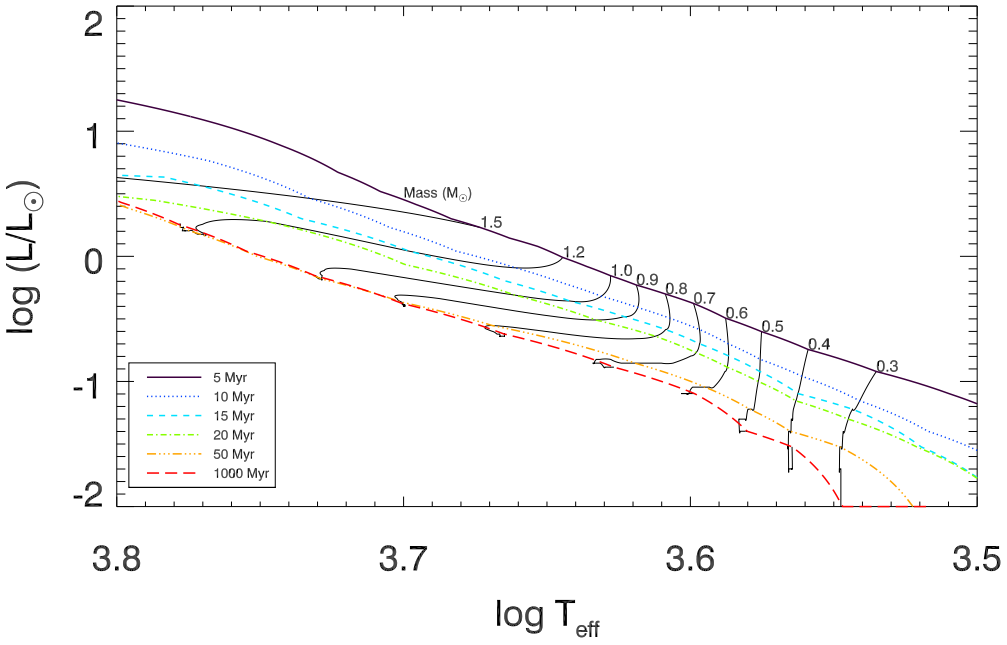

Figure 1.2: HRD generated from the Siess, Dufour & Forestini (2000) evolutionary models. The mass tracks are from 0.3 to 1.5 $M_{\odot}$. A 1.0 $M_{\odot}$ object should have reached the ZAMS at 50 Myr, whereas a 0.3 $M_{\odot}$ object requires several hundreds of Myr to arrive on the main sequence. A 1.5 $M_{\odot}$ star evolves along the PMS along a track of almost constant luminosity (a Henyey track), whilst objects $< 0.5\,M_{\odot}$ descend tracks of near-constant temperature (a Hayashi track).

1.2 Semi-fundamental ages

Fundamental ages are *direct* measurements and require no calibration because their input physics are completely understood. In reality there is only one star for which a fundamental age can be measured: the Sun. By applying radiometric dating techniques to meteorites in the laboratory, the minimum Solar system age has been measured at 4.5695 ± 0.0002 billion years (Baker et al. 2005). The techniques for age-dating all other stars are of much lower precision.

Semi-fundamental ages rely on assumptions about the input physics, but ones

which are straightforward, well understood and reasonable. Two highly effective semi-fundamental techniques to measure ages for young groups are the lithium depletion boundary method and the kinematic trace-back method. The techniques and methods for both of these are discussed, with focus towards their applicability for estimating the ages of MG members.

1.2.1 The lithium depletion boundary method

At temperatures of $\sim 3 \times 10^6$ K Li atoms are destroyed in p, α reactions[2]:

$$^7_3\mathrm{Li} + \mathrm{p} \longrightarrow {}^4_2\mathrm{He} + {}^4_2\mathrm{He} \tag{1.1}$$

As PMS stars evolve, they contract towards the ZAMS, increasing their core temperatures. Li burning will eventually occur in the cores of stars, provided they are more massive than $0.065\,M_\odot$[3].

Fully convective stars reach burning temperatures on a mass-dependent timescale. Once this temperature has been reached, the full Li content is rapidly exhausted due to the extremely efficient convective mixing processes which transport material from the surface to hotter regions where Li is burned and brought back to the surface, diluting the photospheric abundance. Bildsten et al. (1997) calculate that a fully convective $0.5\,M_\odot$ object ($T_{\rm eff} \approx 3500$ K) will begin to burn Li at a core temperature of 3.04×10^6 K, with small differences in ignition temperatures for fully convective objects of different mass. The Li-depletion rate in fully convective stars is extremely sensitive to changes in the core temperature ($\propto T_C^{20}$, Bildsten et al. 1997; Ushomirsky et al. 1998) and thus very rapid once it reaches this temperature.

[2]Li-6 is destroyed much more readily at temperatures close to 2×10^6 K via the reaction: $^6\mathrm{Li} + \mathrm{p} \longrightarrow {}^3\mathrm{He} + {}^4\mathrm{He}$. In this thesis ^{6}Li is not taken into account as this contribution is negligible in comparison with ^{7}Li. The relative abundance A(Li) is normalised using $\mathrm{A(Li)} = 12 + \log \frac{\mathrm{N(Li)}}{\mathrm{N(H)}}$.

[3]If an object of Solar composition is less massive than $0.075\,M_\odot$ then the core will never reach temperatures high enough to fuse hydrogen and the object is classed as a 'brown-dwarf' (Burrows et al. 2001). Brown-dwarfs lighter than $0.065\,M_\odot$ never reach Li burning temperatures, as their contraction is halted by degeneracy pressure at temperatures too low to burn Li (Basri 1997).

In a coeval group of young stars, the rapid destruction of Li sets up a sharp, age-dependent boundary between low luminosity stars that retain their protostellar Li and objects at a slightly higher luminosity that have burned the vast majority of their Li. The luminosity at the transition between non-depleted and fully depleted objects is called the 'lithium depletion boundary' (LDB), originally pioneered by Rebolo, Martin & Magazzu (1993) and further developed by Basri, Marcy & Graham (1996). In principle, the technique is a precise and potentially very accurate way of estimating the age of the stellar group. The main observational challenge is to locate the LDB on a colour-magnitude diagram (CMD) and the level of age precision obtained is largely based on the size of the colour-magnitude space which occupies the LDB. Ideally, one would hope to observe a number of targets either side of the LDB to strengthen the choice in location. The technique is considered semi-fundamental, as it relies on well understood physics, and is insensitive to variations in assumed opacity, convective efficiency, rotation and equation of state (Burke, Pinsonneault & Sills 2004). However, the technique does require a distance measurement to convert from apparent to absolute magnitude and this can affect precision.

To obtain the LDB luminosity, a conversion from absolute magnitude in one photometry band to a bolometric magnitude is required. Bolometric magnitudes and luminosities are calculated from the appropriate bolometric correction for the photometric band used:

$$M_{\rm bol} = m_x - 5\log\frac{d}{10{\rm pc}} + BC_x \tag{1.2}$$

$$\log\frac{L}{L_\odot} = \frac{M_{\rm bol,\odot} - M_{\rm bol}}{2.5}, \tag{1.3}$$

where $M_{\rm bol}$ is the bolometric magnitude, and m_x and BC_x are the apparent magnitude and the applied bolometric correction in the required photometry band, respectively. $M_{\rm bol,\odot}$ is the Solar bolometric magnitude (= 4.755, Mamajek 2012).

The LDB technique is effective for coeval groups between 20 and 200 Myr, which

encompass the ages of most MG members. At ages older than 200 Myr, the age dependence becomes increasingly insensitive, such that small uncertainties in the LDB location result in large age errors. At ages > 200 Myr, the LDB will have shifted to luminosities approaching the brown dwarf limit, requiring unfeasibly long integration times even on large telescopes. The left panel of Figure 1.3 suggests that the age dependence ($\tau_{\rm LDB}$) of the luminosity at the LDB ($L_{\rm LDB}$) is roughly $\tau_{\rm LDB} \propto L_{\rm LDB}^{-1/2}$ for $\tau_{\rm LDB} < 100$ Myr, and gradually becomes shallower towards a $\tau_{\rm LDB} \propto L_{\rm LDB}^{-1}$ dependence beyond 100 Myr. At ages younger than 20 Myr, the initial conditions such as deuterium burning, and the definition of an initial stellar birth time need to be accounted for. There is also model sensitivity to the mixing length at these younger ages because the treatment of superadiabaticity becomes important in lower density envelopes (Baraffe et al. 2002). For very young clusters < 5 Myr, inherent ages spreads from star to star are problematic. A careful treatment of both theoretical and observational uncertainties can provide age precisions of ~ 10 per cent for clusters in the range $20 - 200$ Myr (Jeffries & Naylor 2001; Burke, Pinsonneault & Sills 2004).

Figure 1.3 shows 6 different 'flavours' of evolutionary model indicating the luminosity/age and $T_{\rm eff}$/age at 99 per cent Li depletion. The model insensitivity is clear from the left plot; between 20 and 100 Myr the luminosities at 99 per cent Li-depletion are consistent to within 0.1 dex for all models. However, comparing $T_{\rm eff}$ and age at 99 per cent does *not* provide the same model insensitivity (Jeffries 2006). At $T_{\rm eff} = 3000$ K models vary in age between 50 and 100 Myr. Uncertainties in $T_{\rm eff}$ can be as large as 200 K, particularly for mid M-dwarfs (see §1.3.1). Taking the Chabrier & Baraffe (1997) isochrones as an example, a 0.1 dex error in luminosity between 20 and 100 Myr corresponds to age errors < 20 per cent, whereas a 200 K error in $T_{\rm eff}$ results in age errors of at least 50 per cent! The presence of molecular lines and the gravity and metallicity dependency of stellar atmospheres with $T_{\rm eff} < 3500$ K are increasingly difficult to model, evidenced by the variation from model-to-model in the right-hand plot of Figure 1.3. The lesson from Figure 1.3 is that the *luminosity* at which 99 per cent depletion occurs is model insensitive and strongly age-dependent, whereas the surface temperature at 99 per cent depletion depends on the choice of model and is much less age-dependent.

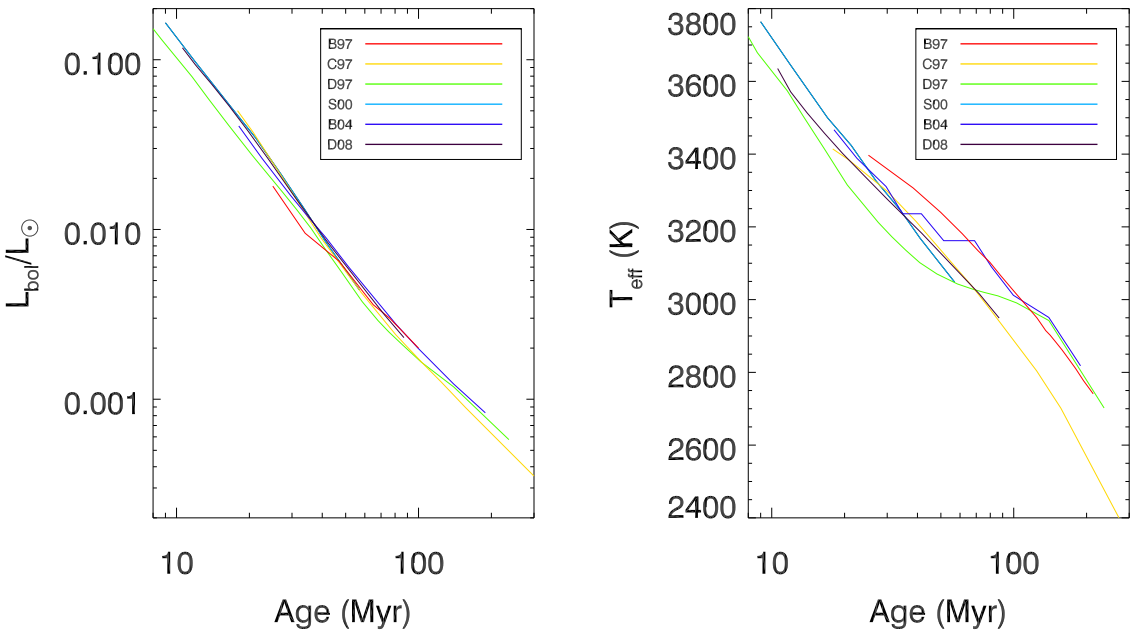

Figure 1.3: Six separate evolutionary models indicating (left) the luminosity and (right) the temperature for 99 per cent Li depletion. The models are more consistent using the LDB luminosity in comparison with the LDB surface temperature. The models are from B97 = Burrows et al. 1997; C97 = Chabrier & Baraffe 1997; D97 = D'Antona & Mazzitelli 1997; S00 = Siess, Dufour & Forestini 2000 (Z=0.02), B04 = Burke, Pinsonneault & Sills 2004 and D08 = Dotter et al. 2008.

It is predicted that a 20 Myr group should have a LDB at a mass of $\sim 0.3\,M_{\odot}$ (spectral-type M4, e.g., the β Pictoris MG, herein BPMG, Binks & Jeffries 2014; NGC 1960, Jeffries et al. 2013), whereas an older cluster at 125 Myr is expected to have an LDB mass around $0.1\,M_{\odot}$ (spectral-type M6.5, e.g., the Pleiades, Stauffer, Schultz & Kirkpatrick 1998). In practice, locating the LDB of a cluster requires moderately high resolution ($R = \lambda/\Delta\lambda \geq 3000$) optical spectroscopy to measure the 6708Å Li feature in groups of very low-mass, faint M-dwarfs. A further challenge lies in confirming that these low-mass objects are indeed bonafide members of the cluster. In general, candidates are qualified as cluster members on the basis of combined kinematic and youth indicators. A detailed procedure outlining how LDB ages are measured in practice is presented in chapter 4.

Presently there are 10 young associations with measured LDB ages ranging between 21 Myr (BPMG, Binks & Jeffries 2014 – see chapter 4) and 132 Myr (Blanco 1, Cargile, James & Jeffries 2010). The LDB ages and bolometric magnitudes for the 10 groups are detailed in Table 1.2. The LDB can potentially be measured for any young cluster, with the main limiting factor being the faint magnitudes of targets in distant clusters. For example, the LDB location in the 22 Myr cluster NGC 1960 is at spectral-type M4.5. Targets close to this boundary at a distance of 1164^{+11}_{-26} pc (Bell et al. 2013) have $I \sim 19\,(V \sim 22)$, approaching the limiting magnitudes of even the largest ground-based telescopes.

The analysis in Burke, Pinsonneault & Sills (2004) did not consider all possible problems in the models – e.g., magnetic suppression of convection (Feiden & Chaboyer 2014) or starspots (Opitz & Gallardo 2011; Jackson & Jeffries 2014, see Figure 1.4), both of which act to increase the LDB ages from the unspotted scenario. The presence of starspots would serve to lower the effective temperatures, by as much as 10 per cent for M-dwarfs close to the LDB (see the polytropic model presented in Jackson & Jeffries 2014). As a result of the virial theorem, the radius increases, reducing the luminosity. The calculated age at which the LDB occurs would be shifted to higher ages – which depending on the fractional spot coverage, may be as much as 15 per cent. The analysis in Jackson & Jeffries (2014) uses a polytropic model to calculate

Cluster	$I_{\rm LDB}$ (mag)	$M_{\rm bol}$ (mag)	LDB Age (1) (Myr)	LDB Age (2) (Myr)	Ref	MS Age (1) (Myr)	MS Age (2) (Myr)	Ref
BPMG		8.28 ± 0.54	21 ± 4	$20.3 \pm 3.4 \pm 1.7$	a			m
		8.48 ± 0.20	26 ± 3		b			m
NGC 1960	18.95 ± 0.30	8.57 ± 0.33	22 ± 4	$23.2 \pm 3.3 \pm 1.9$	c	< 20	$26.3^{+3.2}_{-5.2}$	n
IC 4665	16.64 ± 0.10	8.78 ± 0.34	28 ± 5	$25.4 \pm 3.8 \pm 1.9$	d	36 ± 5	41 ± 12	o
NGC 2547	17.54 ± 0.14	9.58 ± 0.20	35 ± 3	$35.4 \pm 3.3 \pm 2.2$	e		48^{+14}_{-21}	p
Tuc-Hor		9.89 ± 0.10	41 ± 2	$39.1 \pm 3.3 \pm 2.4$	f			m
IC 2602	15.64 ± 0.08	9.88 ± 0.17	46^{+6}_{-5}	$40.0 \pm 3.7 \pm 2.5$	g	36 ± 5	44^{+18}_{-16}	p
IC 2391	16.21 ± 0.07	10.31 ± 0.16	50 ± 5	$48.6 \pm 4.3 \pm 3.0$	h	36 ± 5	45 ± 5	q
α Per	17.70 ± 0.15	11.27 ± 0.21	90 ± 10	$80 \pm 11 \pm 4$	i	51 ± 7	80	r
Pleiades	17.86 ± 0.10	12.01 ± 0.16	125 ± 8	$126 \pm 16 \pm 4$	j	78 ± 9	120	r
Blanco 1	18.78 ± 0.24	12.01 ± 0.29	132 ± 24	$126 \pm 23 \pm 4$	k		115 ± 16	k
		11.80 ± 0.19	114^{+9}_{-10}		l			k

Table 1.2: LDB properties for the 10 groups with a measured LDB age. Data mainly extracted from table 1 in Soderblom et al. (2014). Columns 2, 3 and 4 are from the original source publication. Column 5 is the LDB age using the data from the source publication, the bolometric correction in Pecaut, Mamajek & Bubar (2012), a 0.1 magnitude calibration error in color and magnitude and the Chabrier & Baraffe (1997) evolutionary models. Column 6 gives an upper main sequence age using the models in Mermilliod (1981) with no convective overshoot, column 7 is the same as column 6 but for moderate overshoot. References: (a) Binks & Jeffries (2014); (b) Malo et al. (2014); (c) Jeffries et al. (2013); (d) Manzi et al. (2008); (e) Jeffries & Oliveira (2005); (f) Kraus et al. (2014); (g) Dobbie, Lodieu & Sharp (2010); (h) Barrado y Navascués, Stauffer & Jayawardhana (2004); (i) Stauffer et al. (1999); (j) Stauffer, Schultz & Kirkpatrick (1998); (k) Cargile, James & Jeffries (2010); (l) Juarez et al. (2014); (m) No UMS age; (n) Bell et al. (2013); (o) Cargile & James (2010); (p) Naylor et al. (2009); (q) derived by E. Mamajek using data from Hauck & Mermilliod (1998) and isochrones from Bertelli et al. (2009); (r) Ventura et al. (1998).

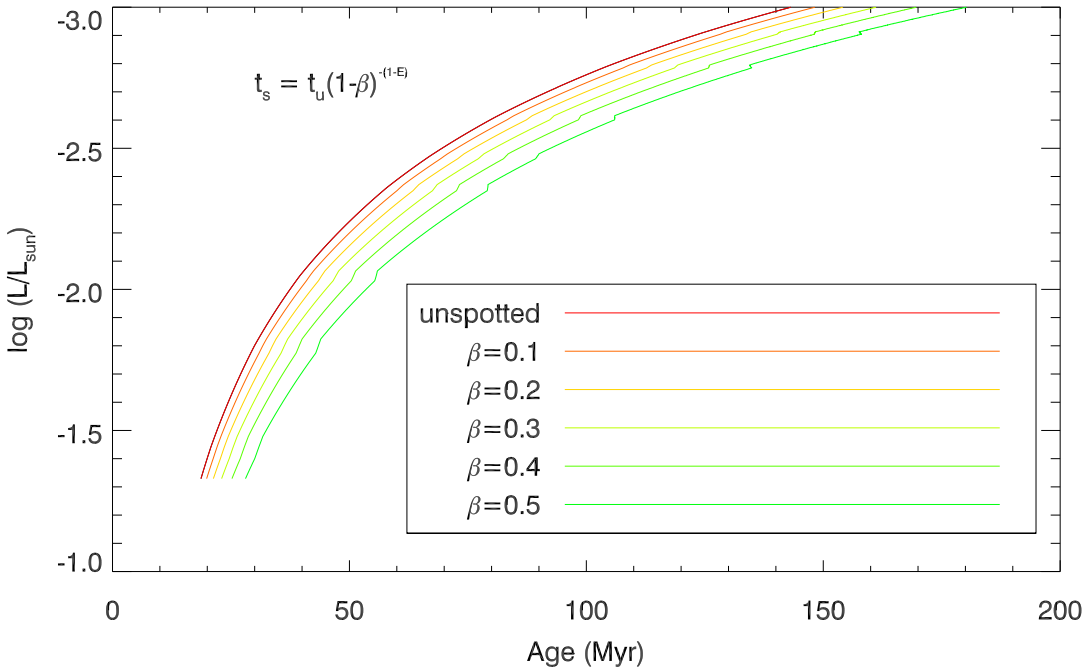

Figure 1.4: The effect of starspot coverage on the LDB age based on the polytropic model in Jackson & Jeffries (2014). Young M-dwarfs are expected to generate a significant amount of starspot coverage via their internal magnetic dynamos (Jackson & Jeffries 2013) and the models demonstrate that larger percentages of starspot coverage result in increased LDB ages. Generally it appears that a coverage of 30 percent of the photosphere by dark spots results in an apparent age increase of 15 per cent. Evolutionary models are from Chabrier & Baraffe (1997).

the effect of surface spot coverage on the LDB age. The LDB ages are expected to increase by a factor of $\tau_{\rm u}(1-\beta)^{-({\rm E}-1)}$, where $\tau_{\rm s}$ is the revised 'spotted' LDB age, $\tau_{\rm u}$ is the original unspotted age, β is the fraction of the stellar surface covered by black spots and E is defined by the gradient $-\frac{\partial \log \tau_{\rm u}}{\partial \log L_{\rm u}}$ where $L_{\rm u}$ is the luminosity at the LDB for the unspotted model. Spots affect all evolutionary models in a similar way, so the "baseline" model dependency still holds (see Figure 1.3). The models of Jackson & Jeffries (2014) are provided in Figure 1.4 for 5 different spotted scenarios and one unspotted scenario.

Young M-dwarfs are expected to have reasonably large surface magnetic fields and Malo et al. (2014) use the Dartmouth evolutionary models with an empirically constrained surface magnetic field of 2.5 kG (Feiden & Chaboyer 2013) to re-evalute the LDB age of BPMG at 26 Myr (compared to the 21 Myr 'non-magnetic' age measured by Binks & Jeffries 2014). An analysis of both of these ages is carried out in §4.3.2 and the revised age is consistent with the predictions in Opitz & Gallardo (2011) and Jackson & Jeffries (2014).

LDB ages in clusters can be used in comparison with ages derived from fitting higher mass stars in the HRD or any other empirical method for that matter. LDB ages can serve as a test, or even calibration, to the amount of core convective overshoot required in stellar models – a process which is expected to have a strong impact on the evolution of higher mass stars (Maeder 1976; Schaller et al. 1992). The main sequence turn-off (MSTO) ages of the Pleiades and α-Per clusters with no convective overshoot are significantly younger than their LDB ages. Stauffer et al. (1998; 1999) noted that their ages could be brought into agreement by incorporating a moderate amount of core overshoot (see Stauffer, Schultz & Kirkpatrick 1998 for details). Table 1.2 summarizes the LDB ages for the 10 reported groups, and compares them to ages derived from MSTO (see §1.3.2). There is agreement between the LDB and MSTO, particularly for the older clusters.

1.2.2 Kinematic ages

If a coeval ensemble of stars occupied a small spatial volume in its past then ages for unbound, expanding, coeval stellar associations can be inferred by integrating the orbits of stars backwards in time to identify: (1) A time at which the association occupied a spatial minimum ('trace-back ages', see for example Fernández, Figueras & Torra 2008). (2) The rate of expansion in the group as a function of position, where the age is calculated as the inverse of the velocity-position gradient ('expansion ages', e.g., Brown, Dekker & de Zeeuw 1997). (3) The average time of minimum separation between pairs of stars in a group ('flyby ages', see Makarov 2007). As each of these

techniques is largely free from modelling uncertainties (albeit requiring a reasonable Galactic potential), UVW velocity data[4] and a parallax are all that are required to provide a kinematic age.

Soderblom (2010) discusses the major advantages and disadvantages of kinematic ages. The major strengths of the technique are: (1) No modelling of stellar interiors are required and few starting assumptions necessary, apart from the group occupying a spatial minimum at birth. (2) It can be applied to objects of any mass. (3) It potentially provides age constraints for young stellar groups that lack a reliable age from alternative techniques, for example, at ages younger than 20 Myr where the LDB method is less useful. The limitations of kinematic ages are: (1) As the method is only applied to stellar groups, individual objects with no association to coeval clusters (i.e., field stars) cannot be considered. (2) Only young (< 20 Myr) groups can provide reliable ages, as the errors in X, Y and Z coordinates quickly become larger than the volume occupied by the group. (3) Precise parallaxes are required. In the absence of parallaxes, early attempts to derive expansion ages relied on proper motion data (Blaauw 1952; 1978). However, even if group members had perfectly parallel proper motion vectors, any non-zero motion relative to the line of sight may cause a virtual expansion (or contraction). Brown, Dekker & de Zeeuw (1997) demonstrate that it is not possible to derive expansion ages based on proper motions alone.

Observational data for star-formation over scales of 0.1 to 10^3 pc (Elmegreen & Efremov 1996) provides a characteristic timescale for star-formation across a length scale l of $\tau_{\rm SF} \sim l_{\rm pc}^{1/2}$, where $\tau_{\rm SF}$ is in Myr. Soderblom et al. (2014) suggest that uncertainties in kinematic ages can be inferred by considering the mean adopted age for a group member $\overline{\tau}$ and the size of the star-forming region l. The fractional age uncertainty for an individual group member is then expressed as:

$$\epsilon = \frac{\tau_{\rm SF}}{\overline{\tau}} \sim \tau_{\rm Myr}^{-1} l_{\rm pc}^{1/2} \tag{1.4}$$

[4]The UVW coordinate system describe the Galactic velocities of stellar objects where U is in the direction of the Galactic centre, V is in the Galactic rotation plane and W points towards the Galactic North pole. XYZ are the positional coordinates, in the same directions as UVW, respectively.

This a fundamental limitation of the technique, assuming all the stars were born in a small volume at the same time.

The launch of the Hipparcos satellite (Perryman et al. 1997) resulted in a major advance in precision astrometry. Parallax measurements precise to 10 per cent became available for 10^5 bright, nearby stars, reigniting interest in kinematically based ages, especially as a number of MGs were discovered shortly after the main Hipparcos data release. Several members of these MGs were bright and close enough to have precise kinematics measured by Hipparcos (Perryman et al. 1997; van Leeuwen 2007).

Constituents of the BPMG provide a useful example of the potential risks in assigning kinematic ages to stellar groups. A number of studies have calculated a kinematic age of $11 - 12$ Myr, consistent with the isochronal age of 12^{+8}_{-4} Myr reported in Zuckerman et al. (2001). Using kinematic data for the 19 BPMG stellar systems provided in Zuckerman et al. (2001) and a realistic Galactic potential, Ortega et al. (2002) report a minimum separation for BPMG members of ~ 24 pc around 11.5 Myr ago (where the group appears to be 1/3 of today's size). However, this analysis does not specify whether the authors are referring to the mean separation between members, or the whole bulk of the group itself. Figure 1.5, from Song, Zuckerman & Bessell (2003), shows the present X and Y positions of BPMG members and also 12 Myr ago where the group's volume is claimed to be at a minimum. According to Song, Zuckerman & Bessell (2003), the size of the group along the X coordinate 12 Myr ago was ~ 50 pc, whereas it is currently ~ 100 pc. A useful rule of thumb is that $1\,\mathrm{km\,s^{-1}}$ is approximately 1 pc per Myr. If uncertainties in U, V and W are assumed to be $2\,\mathrm{km\,s^{-1}}$, then 12 Myr ago, this would lead to an overall position uncertainty of ≈ 24 pc for each member. This is similar to the 1σ dispersion at 12 Myr, so the real extent of the group 12 Myr ago could be much larger, which critically questions the validity of a group of stars occupying a spatial minimum at this time. If the age given in Ortega et al. (2002) is used, then it is unlikely to be robust, as the result is sensitive to interlopers. Torres et al. (2006) claim that there is evidence for expansion in the BPMG, estimating a linear expansion in the U coordinate of $0.053\,\mathrm{km\,s^{-1}\,pc^{-1}}(X) - 11\,\mathrm{km\,s^{-1}}$ and an expansion age of 18 Myr, although no errors are provided.

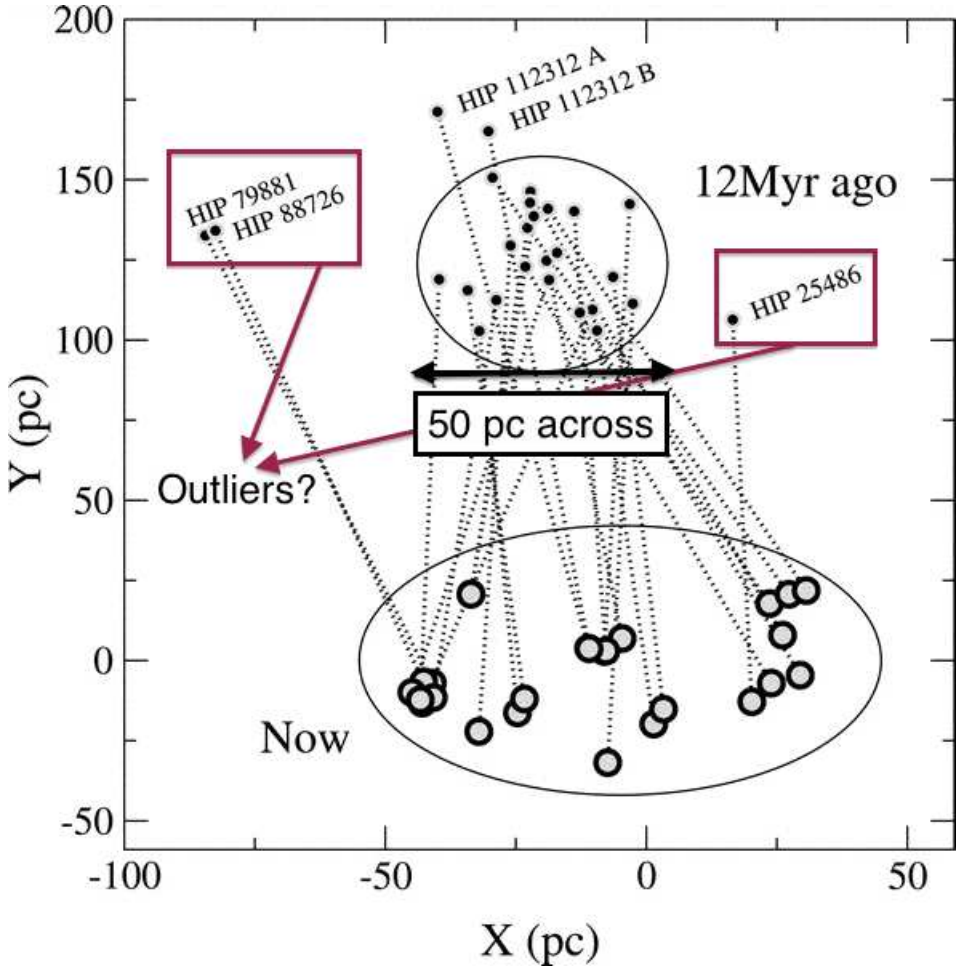

Figure 1.5: Figure from Song, Zuckerman & Bessell (2003). The orbital motions of known BPMG members are back-integrated to a period ~ 12 Myr ago where the members occupy a region of 50 pc in X and Y. Song, Zuckerman & Bessell (2003) use the back-integrated 12 pc separation of the HIP 112312 AB binary pair as an estimate of the uncertainty in position, as these two objects should occupy the same location.

If 12 Myr ago the size of BPMG was genuinely 50 pc, then Equation 1.4 provides fractional age errors of at least 60 per cent. The HIP 112312 AB binary pair in Figure 1.5 has a separation of $\sim$ 12 pc around 12 Myr ago. As there should be no separation between the pair at birth, Song, Zuckerman & Bessell (2003) suggest that this could be indicative of the positional error.

Makarov (2007) traced back the orbits of 14 BPMG members to identify the time of closest encounters between pairs of stars, finding the average time of nearest approach to be 22 ± 12 Myr (the 'fly-by' age). More recently, Mamajek & Bell (2014) reanalysed the Hipparcos data for the sample of BPMG members present in Zuckerman & Song (2004) and fail to recover any significant spatial minimum around 12 Myr. Whilst they report marginal evidence for expansion (but only significant to $\sim 2\sigma$), a epicyclic trace-back model shows that the dispersion in the Y and Z positions in the past are, in fact, much larger than the current dispersion. They find that the BPMG was actually *larger* 12 Myr ago.

Based on these discussions, it is uncertain if *any* realistic kinematic trace-back age has been derived for an MG. In §2.4 the kinematic ages of 4 other MGs are discussed (TW Hya, AB Doradus MG, η Cha and ϵ Cha). Given the potential for kinematic trace-backs to provide not only accurate ages but also a location of the birthsites of young associations, the astrometry of the forthcoming Gaia mission in 2016 is duly anticipated. Gaia is expected to measure astrometry of $\sim$ 1 billion stars down to 20^{th} magnitude, of which the majority of known MG members will be included (see §7.5).

1.3 Model-dependent methods

Model-dependent methods require more assumptions than semi-fundamental techniques. Nevertheless, provided an observable changes systematically and consistently for the full duration of the PMS, it can be utilised as an age indicator. During the PMS, the luminosity and temperature of a star change with time. The most commonly used model-dependent method is to plot isochrones for objects in a HRD or a CMD.

The cores of higher mass stars reach hydrogen burning temperatures quicker than lower mass and a fraction of these objects will have reached the ZAMS. Measuring the point at which this occurs provides a *turn-on* age. A smaller fraction of higher-mass stars will have evolved off the main sequence, the terminal age main sequence (TAMS). The luminosity at which this departure from the main sequence occurs provides a main sequence *turn-off* age. The small movement between the ZAMS and the TAMS can give a *main sequence* age (Naylor et al. 2009; Bell et al. 2013). Additional model-dependent age indicators based on surface gravities and projected radii (from $v \sin i$ measurements) may also signpost youth, however are generally less precise.

1.3.1 Isochronal fits and placing stars on the pre-main sequence

Figure 1.2 (on page 8) is a HRD with evolutionary tracks from the Siess, Dufour & Forestini (2000) models for stellar masses between 0.3 and 1.5 $M_\odot$ with isochrones at ages 5, 10, 15, 20, 50, 100 and 1000 Myr. §1.1 describes a basic outline of PMS evolution. Both the luminosity and the temperature of a star change with age during PMS contraction, and the rate at which these change depends on the mass. Ages for individual PMS stars and groups of stars are estimated by modelling the evolution of the luminosity and surface temperature as a star descends onto the main sequence. The luminosities of low-mass stars are expected to decrease as $t^{-2/3}$ (Hartmann et al. 1998), so two stars of the same mass, differing by a factor of 10 in age should have luminosity differences of $\Delta \log(L/L_\odot) \sim 2/3$. This is generally the behaviour observed in Figure 1.2. Objects up to a few $M_\odot$ will trace out an evolutionary track on the HRD from the birthline to the ZAMS, which can be modelled to estimate ages – a technique originally pioneered by Sandage (1962) and further developed by Demarque & Larson (1964), Kippenhahn (1967) and Iben (1967). Although this can work for individual stars, assuming that all stars in a MG or cluster have the same age, then they should all lie on one isochrone and the appropriate isochrone might be identified with more precision.

Accurate ages based on this method require a full appreciation of the physics that governs the radial profiles of the density and equation of state of a star as it undergoes contraction over time. How the luminosity and surface temperature of stars change as they contract onto the main sequence is dependent on the opacity, equation of state, atmospheres, energy transfer and convection (Gray 1992; Böhm-Vitense 1992). Low-mass objects evolve more slowly onto the ZAMS, and the spacing between isochrones is larger than higher-mass stars at a given mass and age (this can be seen in Figure 1.2 by comparing a $0.3\,M_{\odot}$ evolutionary track with a $1.2\,M_{\odot}$ track). However, the atmospheres of low-mass stars are more difficult to model. Although the atmospheres of high-mass stars are much easier to simulate, there are usually very few objects earlier than spectral-type A in relatively sparse MGs (as would be expected from the initial mass function, Salpeter 1955; Kroupa 2002). This often prohibits a statistically robust age.

1.3.1.1 Isochronal modelling

Three major difficulties in predicting the luminosity and surface temperature as a function of time are:

1) Treatment of atmospheres - Processes occuring in the photospheres of stars, at small optical depths largely determine the opacity levels. An incorrect treatment of stellar atmosphere will drastically affect the calculated fluxes and surface temperatures. Metallicities can also significantly alter opacity values (Gray 1992) and atmospheric modelling becomes increasingly difficult at lower surface temperatures, as an increasing number of molecular absorption lines require consideration (Bozhinova, Helling & Stark 2013), particularly for M-dwarfs. The optical spectra of M-dwarfs are dominated by molecular absorption bands from metal oxide species such as titanium oxide (TiO), vanadium oxide (VO), and hydrides such as CaH and H_2O (Rajpurohit et al. 2014). Correct modelling of stellar atmospheres is essential in order to obtain correct values for surface temperature, metallicity and age. Models such as NextGen (Hauschildt, Allard & Baron 1999), BT-Settl (Allard 2014) and AMES dusty/COND (Baraffe et al. 2003) have all been developed with a focus towards modelling low-mass stars and brown

dwarfs.

2) Surface convective zone depths - Convective instability will occur if the radiative temperature gradient ($\nabla_{\rm rad}$) is greater than the adiabatic temperature gradient ($\nabla_{\rm ad}$, Schwarzschild 1906). This can be the case if either $\nabla_{\rm rad}$ becomes large or $\nabla_{\rm ad}$ becomes small. Therefore correct treatment of radiative flux, temperature, opacity and pressure are needed to fully describe the radiative temperature gradient. Adiabatic gradients require an accurate measurement of the ratio of specific heat capacities, which change due to processes within the star that absorb energy without changing temperature (i.e., ionisation). In practice, the radii predicted by stellar models are fixed by the choice of the mixing length parameter α (which is the ratio of the distance over which the convective cell dissolves and releases its energy to the pressure scale height, Böhm-Vitense 1958), usually calibrated to the Sun. Altering the value of α by $\pm$ 0.5 affects the heat transfer efficiency, which can inflate or deflate the radius. Quantitatively, this can affect surface temperatures by as much as $\pm$ 300 K (Siess 2001). In fully convective stars ($M < 0.35\,M_{\odot}$) treatment of convective zone depths is unimportant for these objects, as no radiative zones exist. However, at very young ages, the correct modelling of superadiabaticity is required to calculate the radius.

3) Convective core overshoot - In the mixing length theory (Böhm-Vitense 1958; 1992), convection in the outer envelope will circulate material through layers between the photosphere and the base of the surface convective zone (SCZ). The material transported downwards to the base of the envelope can penetrate into the radiative region, increasing the size of the SCZ, more so than a classical treatment of convection would predict. This affects the heat transfer rate and the temperature of the stellar interior (and the main sequence lifetime). The level to which this occurs depends largely on the size of the temperature gradient at the SCZ base. In fully convective stars, however, core overshoot is not an issue as there are no radiative regions present.

There are a variety of models that generate isochrones (D'Antona & Mazzitelli 1997; Baraffe et al. 1998; Siess, Dufour & Forestini 2000; Yi, Kim & Demarque 2003; Demarque et al. 2004; Dotter et al. 2008; Tognelli, Prada Moroni & Degl'Innocenti 2011; Georgy et al. 2014 – see Hillenbrand, Bauermeister & White 2008 for a description

of the 'flavours' of evolutionary models). All the aforementioned models provide radii, surface temperature and luminosities for stars in a given mass range as a function of time as they undergo PMS contraction. In the context of young stars, one must also account for additional physics pertinent to the early stages of evolution. The isochronal models of Baraffe et al. (1998) and Siess, Dufour & Forestini (2000) are plotted on a HRD and M_K versus $V-K$ CMD in Figure 1.6. At 2 Myr the two models at 4500 K (spectral-type K5) have differences in luminosity of about 0.2 dex but by 50 Myr they are separated by only 0.05 dex. At 2 and 10 Myr, the CMD isochrones at $V-K \approx 4$ (spectral-type M0) appear to differ by as much as 0.75 mag in M_K and still differ by ~ 0.5 mag at ages of 1 Gyr.

Processes such as the initial conditions on arrival at the birthline, deuterium burning, accretion and accretion outbursts, rotation and magnetic fields may all act to some level to alter the luminosity and surface temperature (Hartmann et al. 1998; Palla & Stahler 1999; Tout, Livio & Bonnell 1999; Baraffe et al. 2002; Baraffe, Chabrier & Gallardo 2009; Baraffe, Vorobyov & Chabrier 2012; Feiden & Chaboyer 2013). Baraffe & Chabrier (2010) find that episodic accretion can produce objects with significantly higher central temperatures than the non-accreting counterparts with the same mass and age. Rotation affects the star by shifting the PMS tracks to lower surface temperatures and luminosities as the star readjusts to the structural changes. Siess (2001) suggested that a reasonable level of rotation contributes to uncertainties of $\Delta T_{\rm eff} \sim 100-200$ K and $\Delta L = 0.1 L_{\odot}$. Almost all young, nearby PMS stars have a Solar-like chemical composition ($Z = 0.02$, Spina et al. 2014). Stars with higher values of Z have more metal atoms, hence larger opacity values. This causes more radiative absorption and lower luminosities and surface temperatures. At $0.7\,M_{\odot}$, an error of $\Delta Z \sim 0.02$ could cause uncertainties of as much as $\Delta T_{\rm eff} \sim 100$ K, but with little change to the luminosity. Magnetic fields or significant spot coverage suppress the energy flow out of the star. This can significantly change the luminosity and radius, which consequently alters $T_{\rm eff}$ (Spruit & Weiss 1986; Chabrier, Gallardo & Baraffe 2007; Feiden & Chaboyer 2012). Measurements of close, magnetically active, eclipsing binary systems have found that $T_{\rm eff}$ may be decreased by 10 per cent or more. Fully

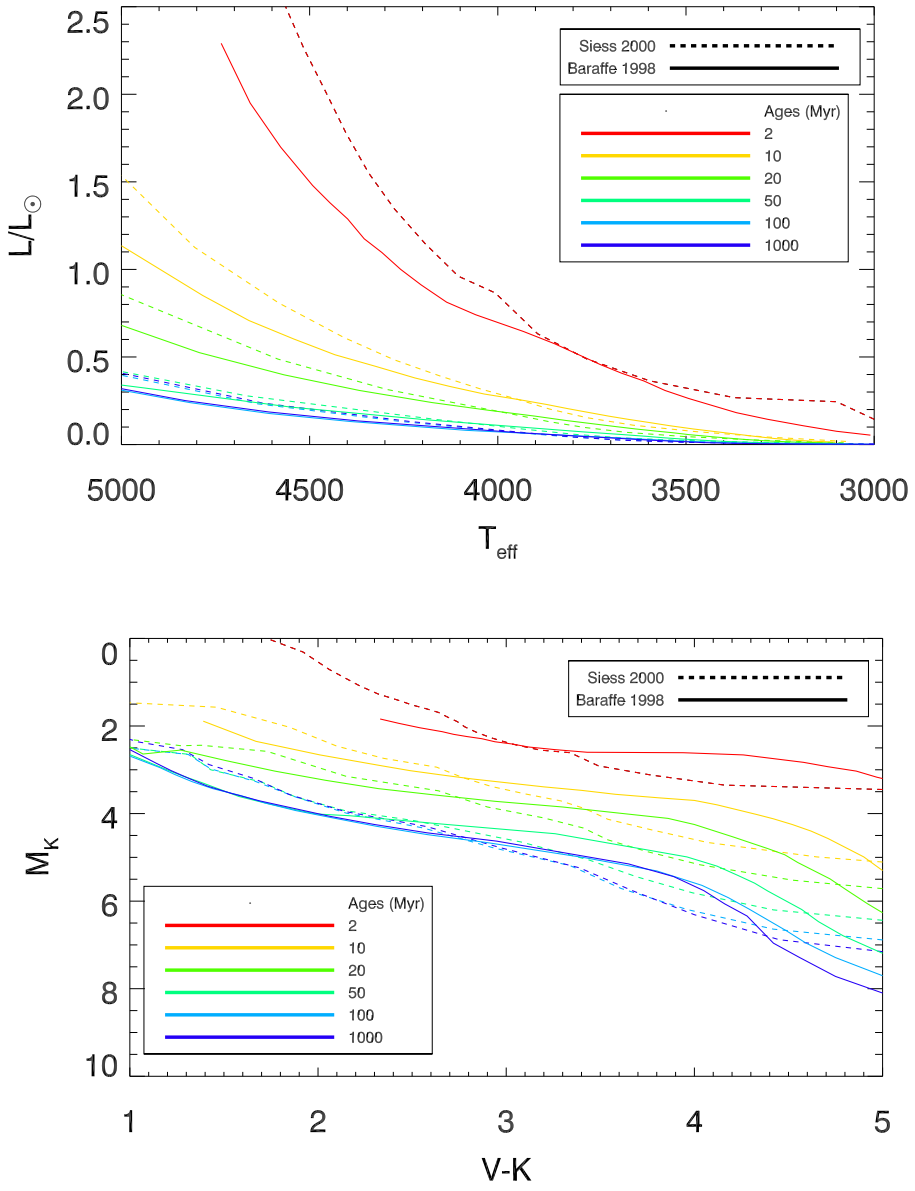

Figure 1.6: A HRD (top) and M_K versus $V-K$ CMD (bottom) based on the models of Baraffe et al. 1998 (solid) and Siess, Dufour & Forestini 2000 (dotted). The CMD produced from the Siess, Dufour & Forestini (2000) models are generated by interpolating the luminosity and effective temperature using the conversion tables in Kenyon & Hartmann (1995). V and K magnitudes in Baraffe et al. (1998) are calculated directly from theoretical isochrones.

convective PMS stars may be more affected by changes in magnetic field (Jackson, Jeffries & Maxted 2009; MacDonald & Mullan 2013), although there have been no definitive investigations of how magnetic activity or spot coverage affects the position on a HRD.

Age discrepancies between various theory groups increase towards younger ages and lower mass. Hillenbrand, Bauermeister & White (2008) note that model-to-model variations lead to log-age variances (from the birthline to the ZAMS) of $< 0.1 - 0.3$ dex at spectral-type G2, but this increases to $0.25 - 0.6$ dex at K6 (see figure 3 in Hillenbrand, Bauermeister & White 2008). The authors comment that the treatment of convection and the choice of model opacities dominate the discrepancies between predicted and measured luminosities and temperatures for *all* ages.

1.3.1.2 Observational issues

Even if the different theoretical models provided a consistent and accurate chronometer using the isochrone method, limitations would still exist due to observational uncertainties. It is crucial that if the theory is to be transformed into the observational plane that it must be done so that both the data and the observations are placed in the same photometric system. Similarly, should one wish to work in the theoretical plane, careful treatment in converting colours (or spectral-types) and magnitudes to luminosity and temperature is required.

The precision in converting a photometric colour or spectral-type to an effective temperature is presently only good to $50 - 100$ K (Clem et al. 2004; Ramírez & Meléndez 2005; Casagrande et al. 2014). However, as can be seen in Figure 1.1, at $0.5\,M_{\odot}$, an uncertainty of 100 K only alters ages on the PMS by ~ 0.1 dex, as the stars are descending Hayashi tracks and are far more sensitive to luminosity than $T_{\rm eff}$. Surface temperatures are also affected by stellar variability and molecular lines dominate the atmospheres of low-mass PMS stars, making a temperature measurement less straightforward. If the objects were located on the main sequence, it would be relatively easy to convert a colour to an effective temperature using relationships from,

for example Kenyon & Hartmann (1995), Alonso, Arribas & Martinez-Roger (1996) or Casagrande et al. (2010). However, the colour-temperature relationships inferred from these main sequence samples are not necessarily scaled with younger stars, and are more uncertain at very cool temperatures ($T_{\rm eff} < 3500\,{\rm K}$), therefore alternative colour scales have been generated (Luhman 1999; Lawson, Lyo & Bessell 2009; Da Rio, Gouliermis & Gennaro 2010; Scandariato et al. 2012; Pecaut & Mamajek 2013). These PMS colour offsets are not necessarily systematic offsets from the main sequence and an intrinsic uncertainty is present in colour-temperature transformations. In addition to the colour transforms, one must apply appropriate bolometric corrections for PMS objects which become increasingly difficult for lower-mass objects on the PMS.

Although extinction is often an issue for young objects, most objects studied in this thesis are within 100 pc, therefore the effects of reddening are not considered. Many young stars generate excess flux through means of either (or both): accretion luminosity, which is at its strongest in the UV (but can extend far into the optical range) and disc emission, which peaks in the mid- to near-IR, but is present at wavelengths as short as the mid-optical. Actively accreting discs can have photometric variabilities of as much as ~ 30 per cent (Semkov 2011). Stellar surface inhomogeneities such as coronal flares and starspots can produce variabilities of up to a few tenths in magnitude in young, rapid rotators (Messina et al. 2010). Well measured luminosities require good parallaxes and a suitable bolometric correction. For some MG members, parallaxes are available for the brightest, nearest objects (Riedel 2012). An unresolved equal mass binary system may overestimate luminosity by as much as 100 per cent.

How useful is the isochrone method for objects observed in this thesis? The constituents of MGs have ages between 10 and 100 Myr. For stars later than spectral-type F, this provides a useful opportunity to plot PMS isochrones. Isochronal ages have been reported for MGs younger than 10 Myr (e.g., TWA, Ducourant et al. 2014; ϵ and η Cha, Fang et al. 2013) to Pleiades-like ages (e.g., ABDMG, Barenfeld et al. 2013). In several circumstances, however, the isochronal ages do not agree with alternative age indicators (for example, the LDB age of BPMG in chapter 4). Section 2.4 provides an overview of previously determined isochronal MG ages. The isochronal method could

potentially provide a precise age, but its usefulness is restricted mainly by the position in the HRD. A distance is needed to put objects onto either a CMD or a HRD. Looking at a set of isochrones one can see that PMS fitting is useful for individual stars over a mass-dependent age range. However, if a group of stars is assumed to be coeval then significant gains can be made in precision, though not necessarily in accuracy.

1.3.2 Main sequence turn-on/turn-off ages

If there are a suitable number of high-mass stars in a coeval group, one would be able to use isochrones to identify both the main sequence and the turn-on/turn-off age. A strong advantage of using the main sequence turn-off (MSTO) is that high-mass stars have fewer molecular lines. Spectra of B- and A-type stars have strong hydrogen Balmer lines and helium lines, which may cause fewer complications when considering opacities than for the lower-mass stars. The major challenges for the placement of the upper main sequence are the correct treatment of convective overshoot, rotation and mass-loss in the models. Rapid rotation in high-mass stars induces mixing, which mildly inhibits the hydrogen burning in the core, and causes longer MS lifetimes (Girardi, Eggenberger & Miglio 2011; Yang et al. 2013). A larger amount of rotationally-induced mixing also causes a reduction in luminosity during the early main sequence (Ekström et al. 2012), however, the overall position of the isochrones vary little. Mass-loss also appears to have little effect on main sequence ages, as it tends to move an object along the same isochrone (Naylor et al. 2009). Rotational effects strongly modify the isochrones and can reduce turn-off ages by as much as 30 per cent (Ekström et al. 2012).

The model dependency for the main sequence fitting is small, but becomes much stronger for the MSTO. On the other hand, precision is hard to obtain because the position of isochrones in the HRD changes only slowly with time. To model these slow changes on the main sequence, well calibrated photometric data are required, or a very good conversion for models onto the observational plane. The diminishing number of objects at higher masses renders the technique susceptible to extinction, interlopers and binarity. Lyra et al. (2006) found an agreement between the PMS and main sequence

ages for four clusters between $10 - 150$ Myr. Earlier work sometimes found agreement, sometimes disagreement between MS and PMS ages, cluster but little homogeneous work was available. Naylor et al. (2009) found that a homogeneously determined set of MS ages were $1.5 - 2$ times the PMS ages for many clusters found in the literature. Bell et al. (2013) were able to reconcile these differences by tuning the PMS bolometric corrections using the Pleiades sequence as a calibrator. Recently, the coincidence of MS, PMS and a semi-fundamental LDB age for NGC 1960 at 25 Myr lends some confidence that a uniform age scale for PMS stars has been derived (Jeffries 2014).

1.3.3 Surface gravity diagnostics

The surface gravity $g = GM/R^2$. Between ages of 1 and 100 Myr, stars of the same temperature may vary in $\log g$ by as much as 1 dex (Dotter et al. 2008). Differences in surface gravity will affect both the shape of spectral lines and the observed colours, which can be used in combination with evolutionary models to infer a model-dependent age. However, the colours of stars with $T_{\rm eff}$ warmer than 3000 K are not affected much by surface gravity and these modest colour changes must be distiguished from reddening effects. In general, differences in $\log g$ are easier to observe towards lower masses (Schlieder et al. 2012).

Spectroscopic measurements of $\log g$ may be more useful. Observing the effect of surface gravity on spectral lines is distance independent. The most gravity sensitive are the alkali lines which are found at red-optical and mid-IR wavelengths; these include the most-used Na I doublets at 8190Å and 2.21 μm (Takagi et al. 2011) and the K I doublet at 7700Å and 1.25 μm (Slesnick, Hillenbrand & Carpenter 2004). Low-gravity M-dwarfs (and cooler) often display a distinct triangular shape in their H-band spectra (Lucas et al. 2001; Allers et al. 2007). This H-band shape is capable of separating young stars from old stars but not of giving a precise age estimate. The Na I 8190Å doublet has assumed an important role in the surface gravities of MG members and is capable of placing MGs in *rank* order (Mentuch et al. 2008; Lawson, Lyo & Bessell 2009; Schlieder et al. 2012; Murphy, Lawson & Bessell 2013).

At bluer wavelengths, gravity-sensitive lines are more capable of probing to earlier spectral-types. Prisinzano et al. (2012) used the Ca I at 6100Å to measure surface gravities for members of NGC 6530, finding that Ca I was the most gravity sensitive for late-G and K stars.

1.3.4 Projected stellar radii

Young, low-mass stars often display high levels of chromospheric and coronal activity, indicative of rapid rotation (Kraft 1967; Noyes et al. 1984; Montesinos et al. 2001; Mamajek & Hillenbrand 2008). Objects with short rotation periods are often observed to have rotationally modulated starspots and rotation periods, $P_{\rm rot}$ can be estimated by photometrically monitoring this surface activity (Messina et al. 2010). The projected equatorial velocity, $v \sin i$ (where v is the equatorial velocity and i is the inclination of the spin-axis to the line of sight) can be measured using high-resolution spectroscopy to compare line widths with a set of artifically broadened template stars. For a more detailed description of the spectroscopic techniques involved in $v \sin i$ measurements, see §3.3.2. The projected radius of star is $(R/R_{\odot}) \sin i = 0.02(P_{\rm rot}/{\rm day})(v \sin i/{\rm km\,s^{-1}})$. Due to the $\sin i$ ambiguity, this formula provides the minimum radius of a star. As PMS stars contract, their radii can be compared to isochrones of R versus $T_{\rm eff}$, providing a model dependent upper-limit to the age. This makes it a potentially useful technique for age dating objects on the PMS.

A measurement of both $P_{\rm rot}$ and $v \sin i$ requires no knowledge of distance and is insensitive to extinction. Binarity is not a complicating issue, providing one object is several magnitudes brighter than the other. However, the technique implicity relies on the correct modelling of isochrones in the R versus $T_{\rm eff}$ plane and a large amount of time-series photometry are needed to measure a period. Magnetic activity is expected to inflate the radii of low-mass stars (López-Morales 2007; Jackson, Jeffries & Maxted 2009; Jackson & Jeffries 2014) and models are required to accurately replicate this. An accurate $T_{\rm eff}$ and spectra with sufficient resolution to measure $v \sin i$ are required for the analysis. It is possible to work with luminosity as a function of radius, however

this requires accurate parallaxes. If the spin-axis orientation in a large sample of stars is assumed to be random then the technique can be used to statistically determine the average radius of a star in the sample (Jackson & Jeffries 2013).

The rotation periods of 11 BPMG members are presented in Holloway et al. (2005), where they find an average period of 4 days in the sample. Lawson & Crause (2005) measure the rotation periods of TWA members, identifying a bimodal distribution between TWA $1-13$ (median $= 4.7$ days) and TWA $14-19$ (median $= 0.7$ days). The RACE-OC project (Messina et al. 2010) report 134 rotation periods in 6 MGs, aged between $\sim 8-100$ Myr. Figure 12 in Messina et al. (2010) suggests that that the MG members spin-up from $P = 7$ days at 1 Myr to < 1 day at 70 Myr. In chapter 5, a sample of object chosen with $P < 5$ days are used as a criterion in the initial search mechanism for PMS stars.

1.4 Empirical methods

An empirical age is inferred based on how an age-related property of a star (or group of stars) compares to the same property in clusters of "known" age. All empirical techniques rely on accurate and precise age-calibrated data in well-studied fiducial clusters. Any inaccuracies in these cluster ages lead to systematic errors, regardless of how well the age-dependent variable has been measured. It should be possible, however, to at least use empirical calibrations to *rank* ages in comparison to data in clusters. To this end, empirical methods are "secondary" age indicators, although they may be utilised to support age estimations based on alternative techniques.

1.4.1 Rotation and activity

The rotational history of a star and its instantaneous spin rate directly modify processes such as magnetic activity, surface abundances, mass-loss rates and overall structure (Kawaler 1988; Barnes 2003). Solar-mass stars start on the birthline with rotation

periods between 1 to 10 days and spin-up as they undergo contraction on the PMS. Figure 1.7 shows that at ages of $50 - 100\,\mathrm{Myr}$, some objects can have periods as short as 0.4 days. Disc locking causes their angular speeds to be constant and operates well before the ZAMS. Once discs have dissipated their angular speeds then decelerate as they lose angular momentum via processes such as rotational braking due to magnetized winds (Schatzman 1962) and star-disc interactions (during early PMS, Bouvier 2007).

Measurements of stellar rotation are carried out using two techniques: spectroscopy and photometry. The spectroscopic method involves comparing the width of gravity-insensitive absorption lines in a stellar spectrum to those in slowly-rotating stars of similar spectral-type to measure $v \sin i$ (Weise et al. 2010, see also §3.3.2). If the luminosity and effective temperature of the star are known, the radius is obtained using the Stefan-Boltzmann law, resulting in a maximum rotation period of $P_{\mathrm{rot}} = R/v \sin i$. Photometrically, one observes the modulation of surface inhomogeneities such as starspots or chromospheric plages (Norton et al. 2007; Messina et al. 2011). The amplitudes can be as large as 0.1 mag – easily detectable using ground-based photometry. Starspots represent regions of intense local concentrations of magnetic flux, which in turn reduce the surrounding surface temperature. The surface layers of convective PMS stars are especially prone to large coverage of starspots and their rotation periods can be measured with precision by observing long cadence time-series photometry of the variable photometric flux.

Following the earlier work of Kraft (1967), Skumanich (1972) collated the mean $v \sin i$ of Solar-type stars in the Hyades and the Pleiades together with the Sun and obtained a relationship of $v \propto t^{-1/2}$. Durney & Latour (1977) later showed this was the expected outcome when considering braking due to magnetic winds, an idea originally proposed by Schatzman (1962). Although conceptually satisfying, $v \sin i$ measurements in subsequent decades have revealed a large velocity dispersion for objects on the ZAMS at $\sim 100\,\mathrm{Myr}$. A classic example of such a wide range in $v \sin i$ is provided by Stauffer et al. (1987), reporting stars with rotation rates from less than $10\,\mathrm{km\,s^{-1}}$ to speeds greater than $150\,\mathrm{km\,s^{-1}}$ in the α-Per and Pleiades clusters at ages of $80 - 125\,\mathrm{Myr}$. The Skumanich relationship does not account for mass dependency, and non-Solar-type

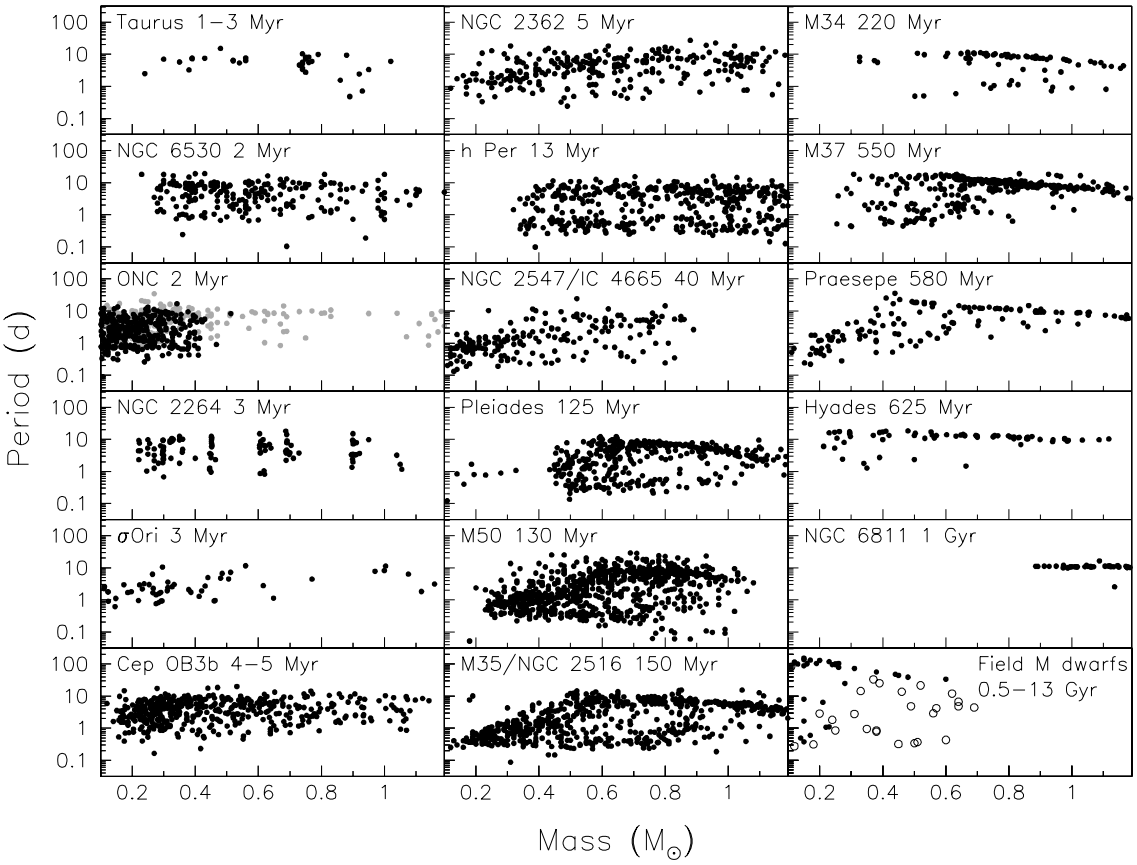

Figure 1.7: Figure from Bouvier et al. (2014). Rotation periods as a function of age for 17 open clusters between 1 Myr to 1 Gyr and for field stars older than ~ 0.5 Gyr. It is evident that for all objects $< 1\,M_{\odot}$ in clusters younger than 600 Myr there is no single-valued rotation period and there appears to be a bimodal period distribution in h Per, Pleiades and M 35.

stars may not follow the same trend. Whilst the $t^{-1/2}$ proportionality may be revealing some of the underlying physics for Solar-type objects, the rotational evolution of stars clearly requires much more complexity than a simple treatment of magnetic braking on the main sequence. The Skumanich relationship is calibrated for objects on the main sequence and requires a constant moment of inertia to produce the $t^{-1/2}$ relationship. This is not applicable for stars undergoing contraction on the PMS.

If the Skumanich law were extrapolated backwards to a 1 Myr PMS G-type object, rotational velocities around $200\,\mathrm{km\,s^{-1}}$ would be expected; not far from the Keplerian break-up speed (Bouvier 2013). However, the first $v \sin i$ measurements in PMS stars revealed that they rarely exceeded $25\,\mathrm{km\,s^{-1}}$. Gallet & Bouvier (2013) have compiled rotation periods for Solar-type objects in several PMS open clusters and demonstrate that a scatter of around 1.5 to 2.5 dex exists in clusters younger than 200 Myr (see Figure 1.8). There is no clear trend in the median rotation period for the first 100 Myr, causing rotation-based age estimates to be indeterminate.

As stars reach the ZAMS a bimodal distribution becomes apparent amongst fast and slow rotators. In clusters older than the Hyades (625 Myr) all FGK stars have converged towards one clear, single sequence in the period-colour plane. Motivated by a substantial increase in the measurements of rotation periods in young open clusters and the detection of bimodality in rotation periods, Barnes (2003; 2007) examined stars of different mass and age to provide a colour-dependent form of the Skumanich law, an empirical tool now referred to as 'Gyrochronology'. It is assumed in the Gyrochronology framework that a given star will begin its main sequence rotational evolution with some initial period on the ZAMS. These will be found on either the fast (C-) or slow (I-) sequence. Stars initially on the C-sequence will eventually traverse onto the I-sequence. The motion of the bifurcation point between the sequences suggests that the time taken to traverse onto the I-sequence, which moves redwards with age, is zero for F-type stars, increasing towards 300 Myr for early M-dwarfs. Figure 1.9 displays the periods and $B - V$ colours used to generate the gyrochrones in Barnes (2003).

Irrespective of the underlying physics of PMS rotation (Denissenkov et al. 2010; Barnes & Kim 2010; Brown 2014), the phenomenon of an I-sequence can be used

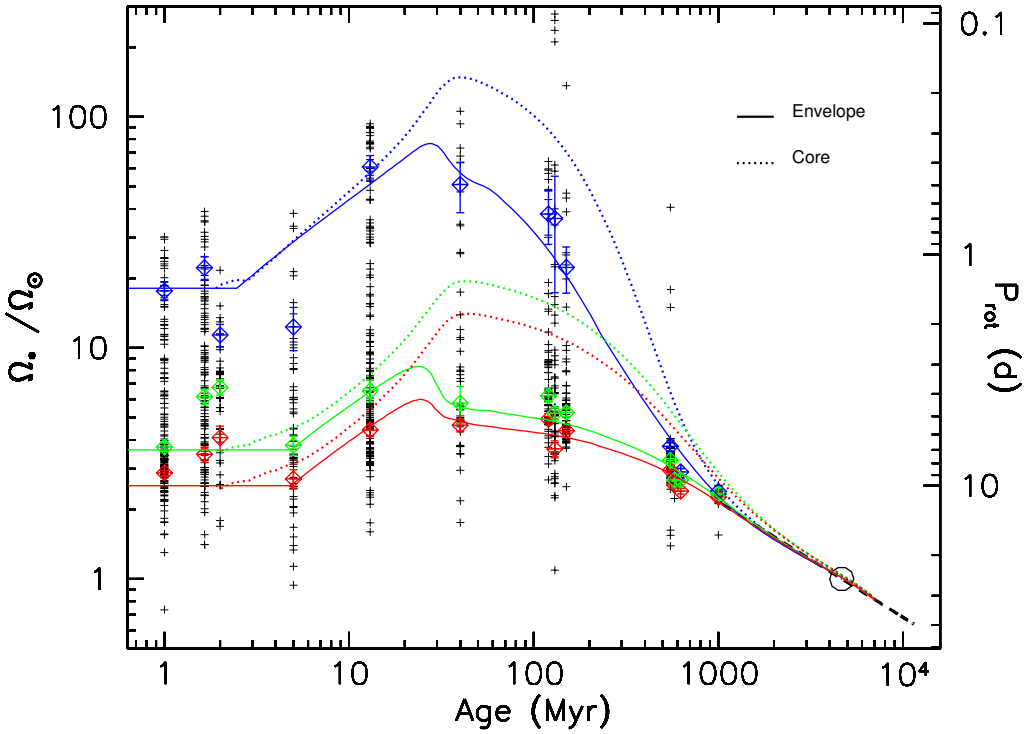

Figure 1.8: Figure from Gallet & Bouvier (2013). The dashed and solid lines are models representing the angular velocity of the radiative core and the convective envelope. These are calculated as a function of time for fast (blue), median (green), and slow (red) rotator models. The blue, red, and green diamonds represent the 90$^{\text{th}}$ percentile, the 25$^{\text{th}}$ percentile, and the median rotation period for Solar-type star in a given star forming region or young open cluster. The present-day angular velocity of the Sun is represented by the open circle and the dashed black line between $10^3 - 10^4$ Myr illustrates the $t^{-1/2}$ Skumanich relationship. For clusters up to 100 Myr there is a spread of $\sim$ 1.5 dex in angular velocities, converging towards a single sequence for older clusters beyond a few 100 Myr.

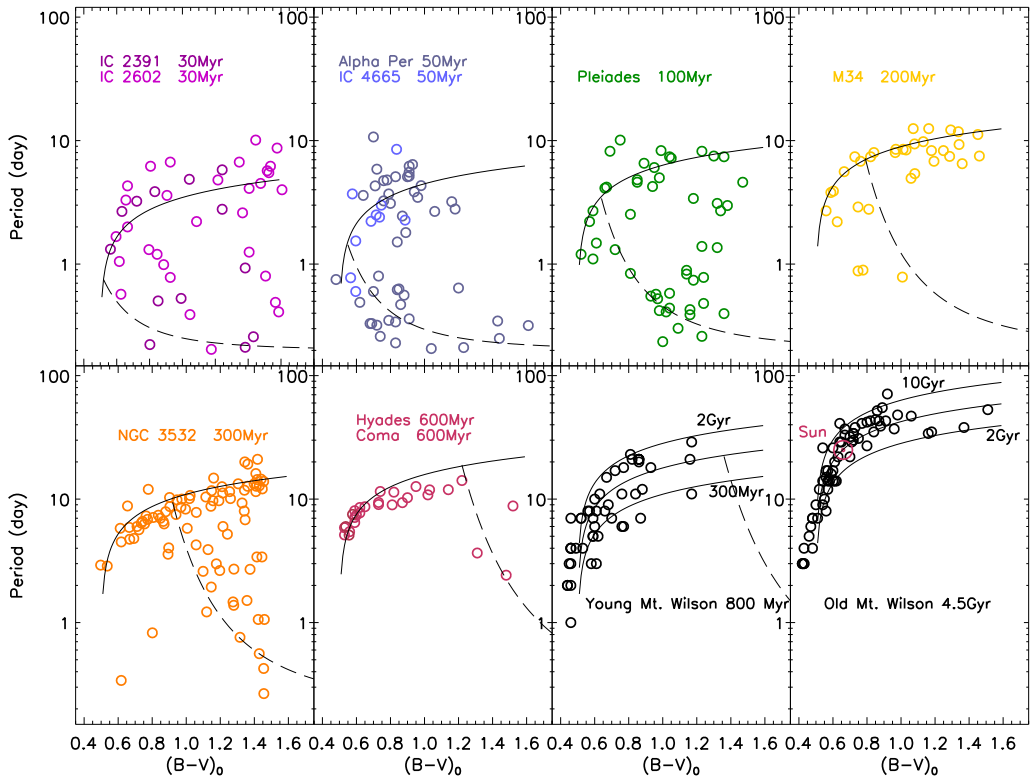

Figure 1.9: Rotation periods and de-reddened $B - V$ colours for a sample of 8 open clusters. Solid lines are the radiative 'I' sequence and the dotted lines are the convective 'C' sequence, generated using the functional forms provided in Barnes (2003; 2007). Each panel shows an increasing number of stars moving from the C-sequence to the I-sequence with age. Beyond ages of the Hyades (625 Myr) almost no stars are observed on the C-sequence. Figure from Barnes (2003).

to estimate stellar ages. The technique has been calibrated so far for objects in the spectral ranges of mid-F to early-M. The basic procedure is to separate the time and the colour dependency. The functional form to generate rotation periods for the I-sequence, calculated in Barnes (2007) is:

$$P_I(B-V,t) = f(B-V)g(t), \tag{1.5}$$

$$f(B-V) = a[(B-V)-b]^c \quad g(t) = t^n \tag{1.6}$$

The function f is chosen to match the shape of the I-sequence in young clusters, n is ~ 0.5 (as would be expected from the Skumanich relationship) and t is the age (in Myr). Several calibrated relationships of this type have been presented in the literature (see table 1 in Epstein & Pinsonneault 2014 for a compilation of the previously calibrated values for a, b, c and n); f is found from fitting one (or several) clusters in the P versus $B-V$ plane, whilst n is determined by matching the Solar rotation rate. Values for n vary between 0.52 and 0.57 and there are also significant differences in the form of f (Barnes 2007; Mamajek & Hillenbrand 2008; Meibom, Mathieu & Stassun 2009; Collier Cameron et al. 2009).

The C sequence (from Barnes 2003) is characterised as an exponential decay with colour:

$$P_C(B-V,t) = 0.2e^{t/100[B-V+0.1-(t/1000)]^3} \tag{1.7}$$

Gyrochronology is used in §5.6.1 to identify a sub-sample of several hundred potentially-young, nearby, low-mass stars.

1.4.2 Magnetic activity as an age indicator

If rotational velocities or periods are unavailable, an alternative is to identify rotationally-induced magnetic activity. It is well known that magnetic activity increases with rotation rate (Skumanich 1972; Noyes et al. 1984). Spectral features indicative of magnetic

activity are mainly from coronal X-ray emission from highly ionised gas at $1 - 10$ million K and from chromospheric activity. Both methods are potentially *distance independent*.

1.4.2.1 Coronal activity

In low-mass PMS stars, X-rays are produced by hot coronal gas, which is likely to be heated by particles accelerated in reconnection events. X-ray observations of many PMS objects reveal the presence of highly-ionised plasma in coronae with temperatures of $1 - 10$ million K. The level of coronal emission present is usually measured through the X-ray to bolometric flux ratio and is observed to diminish with age. Coronal activity is related to rotation ($L_X \propto (v \sin i)^2$, Pallavicini et al. 1981; Pizzolato et al. 2003; Wright et al. 2011) and therefore as stars spin down, they also become less active. Detailed studies of the time-dependence of X-ray activity are available in the reviews of Randich (2000), Ribas et al. (2005) and Güdel (2007).

Figure 1.10 shows the empirical trend between X-ray luminosity and age, which relies on a distance determination (X-ray flux is distance independent). There is a clear overall decrease in X-ray luminosity with age, however, this is shallow for the first few hundred Myr. At high rotation rates X-ray activity appears to saturate at $L_X/L_{\rm bol} = 10^{-3}$. The saturation rotation rate is about 3 days for G-type stars, perhaps growing to 6 days in early M-dwarfs (Pizzolato et al. 2003). Scatter is also present for all ages but appears to be largest in very young clusters, where the dispersion in L_X is at least a factor of ten. Such a spread in L_X cannot be attributable to observational uncertainties. Jeffries (2014) note that this spread is largely due to a spread in rotation, although other effects are present in SFRs. Some authors have suggested the dispersion in L_X (or $L_X/L_{\rm bol}$) is partially attributable to the presence of circumstellar material, or from photometric variability (e.g., starspots, flaring, etc. Wolk et al. 2005; Flaccomio, Micela & Sciortino 2012). This has been shown not to be the case for early ZAMS clusters (see Simon & Patten 1998) where there is little variability and very little circumstellar material should be present.

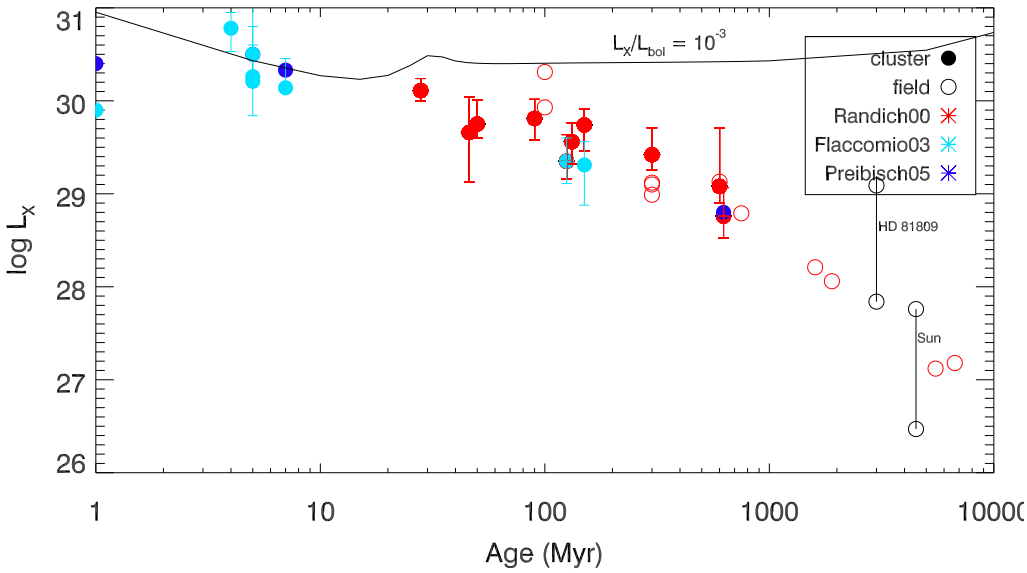

Figure 1.10: X-ray activity as a function of age for $0.5 - 1.2\,M_{\odot}$ objects. Cluster ages are from the LDB, or CMD/HRD isochrones if an LDB age is not available. The black line represents the measured $L_X/L_{\rm bol} = 10^{-3}$ (from the Siess, Dufour & Forestini 2000 models) which is the observed saturation threshold for X-ray activity. Open circles are field stars and filled circles are the median cluster values for L_X. The error bars denote the interquartile range in L_X. Red objects represent cluster data collated from Randich (2000), light-blue from Flaccomio, Micela & Sciortino (2003) and dark-blue from Preibisch & Feigelson (2005). The field objects are from table 3 in Güdel (2007) (note that these are single observations and do not indicate the X-ray variability of individual field stars). Long period observation of the Sun (Peres et al. 2000) and HD 81809 (Favata et al. 2004) reveal factors of ten in variability.

At older ages, a significant number of stars in a cluster will have spun-down to a level where they no longer in the saturation regime, whereas a number of faster rotators will remain saturated. At ages > 1 Gyr, the vast majority of stars have moved onto the I-sequence and their periods are characterised by a Skumanich-like relationship (see §1.4.1). Low-mass stars generally remain rapidly rotating for several hundreds of Myr, and M-dwarfs can remain saturated much longer than Solar-types. Generally speaking, coronal activity as an age indicator in these stars is only useful for Solar-type stars beyond 100 Myr, and M-dwarfs at ages > 1 Gyr (e.g., Preibisch & Feigelson 2005). Older stars have much greater X-ray variability, and observations of X-ray activity over several years for the Sun (Peres et al. 2000) and HD 81809 (Favata et al. 2004) reveal variations of factors of ten (see Figure 1.10). This makes using X-rays to estimate precise ages difficult both at young and old ages. In §5.3 X-ray luminosities are used as an initial empirical youth indicator for a sample of 146 rapidly-rotating stars.

1.4.2.2 Chromospheric activity

The most frequently utilised spectroscopic indicator of chromospheric activity is the Mount Wilson $R'_{\rm HK}$ index, a measure of the flux in the emission reversals in the cores of the Ca II H and K lines normalised to the bolometric flux. Observations have revealed that the strength of chromospheric activity, generated through the stellar magnetic dynamo, scales with rotational velocity (Kraft 1967; Noyes et al. 1984; Montesinos et al. 2001; Mamajek & Hillenbrand 2008). Stellar activity is routinely seen to decay with age and there are several flavours of $R'_{\rm HK}$-age relations in the literature (e.g., Barry, Cromwell & Hege 1987; Soderblom, Duncan & Johnson 1991; Lachaume et al. 1999). Mamajek & Hillenbrand (2008) observe chromospheric activity in Solar-type stars in several open clusters ranging from 5 Myr (Upper Sco) to ~ 8 Gyr (NGC 188) and provide an updated activity-age relation, as plotted in Figure 1.11. The data used for the old open clusters M 67 (4 Gyr) and NGC 188 provide useful estimates on the precision of the best-fit age to the open clusters.

Whilst Figure 1.11 clearly demonstrates an inverse relation between age and

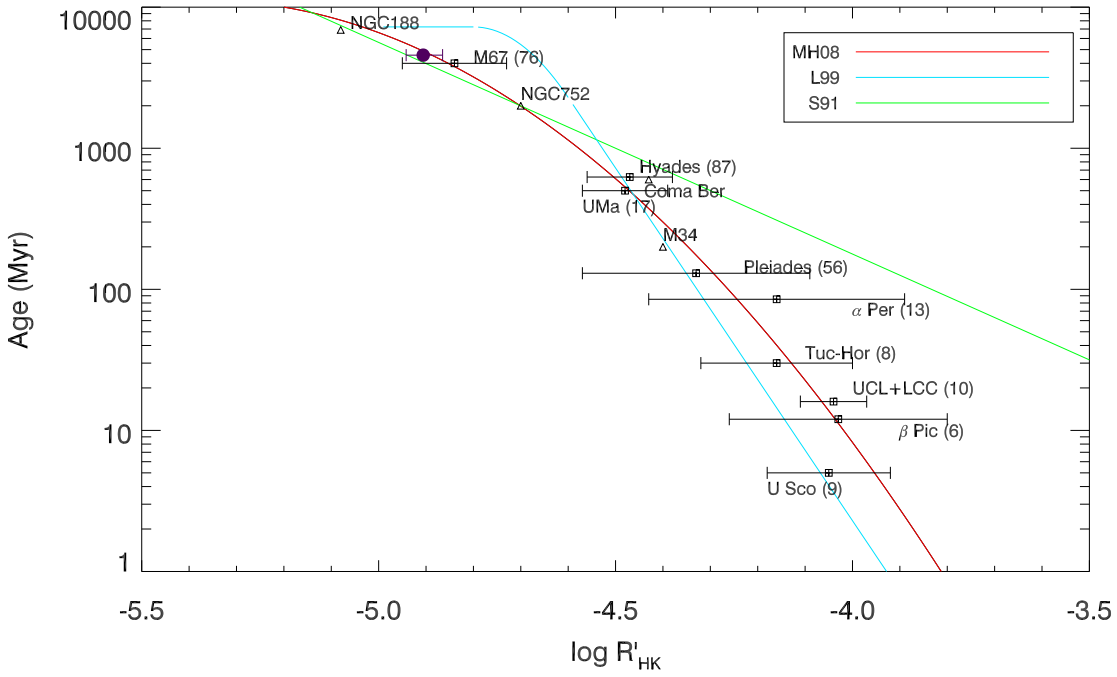

Figure 1.11: The chromospheric log $R'_{\rm HK}$ activity-age relationship for several open clusters. Data (and cluster ages) are from Mamajek & Hillenbrand (2008). The solid purple circle represents the Solar activity and the 1σ range. Green, blue and red solid lines are the empirical fits provided in Soderblom, Duncan & Johnson (1991), Lachaume et al. (1999) and Mamajek & Hillenbrand (2008), respectively. Error bars represent the rms scatter in measurements within each cluster and the number in brackets is the number of stars used for each association. Clusters younger than the Pleiades have a large scatter in log $R'_{\rm HK}$, due to the large scatter in rotation periods.

activity, the age dependency becomes increasingly shallow at younger ages. By 100 Myr (and younger) the technique is very difficult to apply as the overlap between different-age clusters and the dispersion in $R'_{\rm HK}$ for an individual cluster overpowers any genuine trend in $R'_{\rm HK}$ and age. Between Upper Sco (5 Myr) and the Pleiades (125 Myr) the mean values for $R'_{\rm HK}$ only differ by 0.2 dex. The large dispersion in $R'_{\rm HK}$ is likely caused by the magnetic dynamos of PMS objects, which are yet to be fully understood. Mamajek & Hillenbrand (2008) conclude that for Solar-mass stars older than a few hundred Myr, a carefully measured $R'_{\rm HK}$ potentially yields a value of log age to within $\pm$0.2 dex (or 60 per cent). For reasons yet to be established it is also observed that the dispersion in empirically determined ages based on binary systems is lower than that in the single star sequence. Finally, these relations are for *Solar-type* stars. An activity-age relationship for K-dwarfs and cooler is much less well defined.

1.4.2.3 Hα emission/absorption

Whilst Ca II H & K lines are indicative of the presence of strong internal stellar magnetic dynamos, this is also manifested in the strength of the Hα line at 6563Å. M-dwarfs are expected to be Hα emitters for at least a few hundred Myr and higher-mass stars will be Hα emitters for a smaller amount of time as they lose angular momentum faster upon approaching the main sequence. In young open clusters there is a limiting mass (or colour) beyond which chromospheric activity causes the line to be observed in emission for some stars. Using empirical data from several clusters of different ages Hawley et al. (1999) provide a log-linear fit to the age (in Myr) of a cluster and the $V-I$ at which stars first display Hα emission given as:

$$(V-I)_{\rm emission} = -6.42 + 0.99(\log {\rm age/Myr}) \tag{1.8}$$

This relationship can be inverted to estimate the *maximum* age of a star displaying Hα emission. That is, objects with a given $V-I$ colour and with Hα emission are unlikely to be older than the age implied by equation 1.8, provided that they are not close binaries.

At redder colours there is a point where no stars have Hα in absorption. Compiling data in 7 open clusters aged between 30 and 625 Myr, Binks et al. 2015 (in prep.) used an empirical relationship between the cluster age and the reddest intrinsic $V-I$ at which Hα absorption is still seen in some stars. This relationship can be used to estimate the *minimum* age of a star with a Hα absorption line:

$$(V-I)_{\rm absorption} = -4.19 + 0.68(\log {\rm age/Myr}) \tag{1.9}$$

1.4.2.4 Using activity to identify MG members and estimate MG ages

In an attempt to strengthen the age-activity-rotation connection for M-dwarfs, Kidder, Shkolnik & Skiff (2014) use the rotation periods of 59 stars of spectral-class M within 25 pc which are kinematically linked to at least one nearby MG. The scatter in rotation periods is large, ranging from 0.2 to 15 days, making Gyrochronology unfeasible for individual MG members. However, this is consistent with the expectation of angular momentum loss in young stars. This suggests that the technique may be useful for evaluating ages of groups of coeval stars.

Kastner et al. (2003) found that X-ray spectra for MG members soften with age, and combined with column densities, they can discriminate between T-Tauri, PMS and young main sequence sources. In a 25 pc volume-limited survey of nearby young M-dwarfs, Shkolnik et al. (2012) were able to tie the X-ray activity with kinematics and other empirical age indicators to identify 24 new members in 8 MGs.

Using coronal activity as partial criteria to identify MG members has yielded hit-rates $>$ 50 per cent (Schlieder, Lépine & Simon 2012). Large levels of chromospheric activity in MGs have been utilised to identify MG members and are capable of discerning between ages younger or older than the Hyades (625 Myr, Montes et al. 2001; López-Santiago, Micela & Montes 2009; Murgas et al. 2013). The mean and dispersion of $R'_{\rm HK}$ values in MGs appear consistent with their expected age and rotation rates (Gálvez-Ortiz et al. 2014). The use of activity in searching for MG members is discussed further in §2.3.

1.4.3 Lithium as a stellar clock

1.4.3.1 The astrophysics of Li depletion

Li is readily burned and practically never created in stars, a measurement of Li surface abundance can potentially serve as an excellent age indicator. Rapid convective mixing means the surface Li abundance reflects the abundance of the whole convection zone. The details of the p, α reaction responsible for Li burning are in §1.2.1.

Lithium depletion in PMS stars with spectral-types F, G and K has been studied extensively for several decades (Bodenheimer 1965; Pinsonneault, Kawaler & Demarque 1990; Bildsten et al. 1997; Somers & Pinsonneault 2014). In fully-convective, low-mass stars ($M < 0.35 M_{\odot}$), Li measurements can provide precise (or even accurate) age estimates that are relatively model-independent (see the LDB technique in §1.2.1, Burke, Pinsonneault & Sills 2004 and Jeffries 2006). The formation of a radiative core in FGK stars causes complications. If stars are still depleting Li at this stage, then models are often inconsistent and Li depletion becomes strongly dependent on convective efficiencies and opacities and cannot be used to estimate absolute ages.

During PMS contraction, the core temperature rises, causing a reduction in opacity and lowering the radiative temperature gradient. This creates a radiative core which expands to include an increasing fraction of the star. Low-mass stars ($0.4 < M/M_{\odot} < 1.1$) will have a short amount of time where the temperature at the base of the convective zone ($T_{\rm BCZ}$) is hot enough to deplete Li by convectively mixing Li-depleted material to the surface before the radiative zone expands and $T_{\rm BCZ}$ moves to temperatures below T_c. Objects with masses $> 1.1\,M_{\odot}$ have already developed a radiative core before the onset of Li-burning and will have a very short time in which they can deplete Li. If $M > 1.3\,M_{\odot}$, $T_{\rm BCZ}$ never becomes hot enough to ignite Li. Solar-type stars will commence Li depletion after a few Myr and would be expected to stop burning after $\sim 15\,$Myr. This leaves a fraction of the initial Li supply remaining in the convective envelope before emerging on the ZAMS. For stars in the range $0.4 < M/M_{\odot} < 0.6$, the radiative core does not push outwards quickly enough

to prevent total depletion within 30 Myr (Baraffe et al. 1998; Siess, Dufour & Forestini 2000), which is sooner than the time taken to reach the ZAMS. Table 1.3 shows the time taken for the initiation of a radiative core and to deplete 50, 95 and 99 per cent according to the models of Siess, Dufour & Forestini (2000).

If Li abundance was solely age dependent, then this would provide an excellent 'semi-fundamental' stellar clock. However, Li depletion is very sensitive to the conditions at the base of the shrinking SCZ, the physics of which are not yet fully known. Li depletion is also dependent on the treatment of assumed interior and surface opacities, metallicity and He abundance, but the dominant effect is convective efficiency (Pinsonneault 1997; Piau & Turck-Chièze 2002). Take the Baraffe et al. (2002) models as an example – at $T_{\rm eff} = 5000\,{\rm K}$, using mixing length parameters of 1.0 or 1.9 (scaled to match Solar luminosity at Solar age) results in Li depletion by a factor of 0.6 or 0.06 respectively at 125 Myr. It is clear that 'standard' convective mixing during the PMS is not the sole process responsible for Li depletion. The Sun is generally over-depleted compared to other Solar analogs, retaining only $1/140^{\rm th}$ of its proto-Solar amount (Richard et al. 1996), Israelian et al. (2009) suggest Li is more depleted in planet-hosting stars. In the Pleiades, Solar-type stars have depleted less than half their initial Li whilst on the PMS. Additional mechanisms to attempt to account for the extra loss in Li include rotationally induced mixing and meridonal circulation (Pinsonneault, Kawaler & Demarque 1990) and/or gravity waves (Chaboyer, Demarque & Pinsonneault 1995; Charbonnel & Talon 2005).

In order to measure the relative amount of Li present in a star compared to its initial value, a value for the initial abundance at a given mass is required. Measurements of meteoritic Li abundances provide useful estimates for the protostellar abundance of Li in population I stars. Asplund et al. (2009) measure a Solar meteoritic abundance of $\mathrm{A(Li)} = 3.26 \pm 0.05$. There is also evidence from very young (presumably undepleted) T-Tauri stars that the initial Li abundances are between 3.1 and 3.4 (e.g., Martin et al. 1994; Soderblom et al. 1999).

Lithium is mixed primarily via convection, but also meridional circulation and rotational mixing play a role in dredging up Li-poor material to the photosphere (Pin-

sonneault, Kawaler & Demarque 1990). At lower masses, metallicity should significantly affect Li depletion (Jeffries, Totten & James 2000; Mishenina & Soubiran 2005; Sestito & Randich 2005). An increase in metallicity increases the opacity, and the radiative gradient rises. As a result of the Schwarzchild criterion, this increases convective instability and the SCZ extends deeper, depleting more Li. Presently there are not enough young open clusters with differing metallicity to confirm or empirically quantify this dependency. Somers & Pinsonneault (2014) argue that metallicity impacts on the ZAMS Li pattern and there is observational evidence to suggest that the initial Li content may be positively correlated with metallicity (Ryan et al. 2001; Cummings et al. 2012). Prior to that there were actually contra-indicators to suggest metallicity was not important. Metallicity values of MG members are not expected to vary from the Solar value (Spina et al. 2014).

Observations of stars just reaching the ZAMS reveal the expected dependence of Li depletion on mass, but in the Pleiades, there is a clear, order of magnitude dispersion of Li abundance at a given $T_{\rm eff}$. A radius dispersion in stars of fixed mass

Mass ($M_\odot$)	Onset of radiative core (Myr)	Age/EW (50%) (Myr/mÅ)	Age/EW (90%) (Myr/mÅ)	Age/EW (99%) (Myr/mÅ)
0.3	remains fully convective	14.2/487	17.7/410	18.9/260
0.5	25	7.5/648	9.4/340	9.9/183
0.7	11	5.3/510	7.5/298	8.8/131
1.0	5	7.9/407	$> 10^4$/254	$> 10^4$/71

Table 1.3: Age at which a radiative zone begins to form and ages and corresponding equivalent widths for Li depletion by a factor of 50, 90 and 99 per cent, respectively. Ages for the radiative core onset correspond to the age at which the moment of inertia of the central radiative zone becomes greater than 0.01. When the core become radiative, the k_2 value drops as the core contracts faster than the surrounding envelope. The age at which this occurs (and 50, 90 and 99 percent Li depletion) is interpolated from the Siess, Dufour & Forestini (2000) models and corresponding equivalent widths were found using the curve of growth in Soderblom et al. (1993b) and the NLTE corrections provided by Carlsson et al. (1994) for masses $\geq 0.5\,M_\odot$ and the models of Palla et al. (2007) for $M = 0.3\,M_\odot$. The initial abundance, A(Li), is assumed to be 3.0.

and age as Li is being burned on the PMS may be responsible for the spread in Li abundances and the correlation between rotation and Li in young cool stars and there is supporting evidence that Li abundance and $v \sin i$ are strongly positively correlated (Do Nascimento, da Costa & de Medeiros 2010; Takeda et al. 2010). Somers & Pinsonneault (2014) attempt to reconcile the abundance spread by considering the various errors in the input physics and provide an updated model which lies within the dispersion for Solar-type stars. Standard models predict that cooler (K and M type) stars with the same metallicity and mass should destroy the same amount of Li on the PMS. In the situation of the Pleiades, it is apparent that the fast low-mass rotators can suppress Li depletion more effectively than the slower rotators (Soderblom et al. 1993a; King et al. 2003). If (as demonstrated by López-Morales 2007) rapid-rotators have inflated radii, this lowers $T_{\rm BCZ}$ and slows the Li-depletion. Somers & Pinsonneault (2014) demonstrate that inflated radii models can account for the large dispersions observed in 6 PMS clusters, ranging from $\sim 5 - 130\,$Myr.

1.4.3.2 Lithium as an empirical age indicator

The lack of an accurate stellar interior model does not preclude using Li depletion as an empirical age indicator. Lithium is measured by calculating the equivalent width (EW) of the Li I resonance doublet at 6708Å. More details about how this EW is measured in practice are provided in §4.2.2. To calculate the abundance, A(Li), curves of growth are used (e.g., Soderblom et al. 1993b; Palla et al. 2007). Even in cool stars, Li is almost completely ionised, and because the line strengths are temperature dependent they are subject to non-Local Thermodynamic Equilibrium (NLTE) effects, particularly in warmer stars (Carlsson et al. 1994). Depending on the photospheric Li abundance, temperature and metallicity, NLTE abundances can differ by as much as 0.3 dex compared with LTE curves of growth. Another problem in measuring accurate Li abundances lies in obtaining $T_{\rm eff}$, especially as young, active stars with starspots and chromospheric plages (and possibly discs) may cause photospheric variability.

It is possible to use Li-depletion in young open clusters as a means to rank groups

of stars in order of age. By measuring a star's colour and Li EW, one can obtain a mass-dependent age range. Sestito & Randich (2005) compiled Li data for a number of open clusters at different ages and displayed a clear progression of Li depletion from young clusters such as IC 2391/2602, α-Per and the Pleiades (30, 50 and 125 Myr, respectively) to older clusters including the Hyades and Praesepe (625 and 700 Myr, respectively). Figure 1.12 shows how PMS clusters vary in their Li EW as a function of $V - K$ colour and age.

If Li is undepleted then only an upper limit to an age is possible, whilst if all the Li has gone then only an age lower limit can be inferred. Figure 1.12 demonstrates the most effective mass ranges for which Li can be used as an empirical age.

F-stars – F-stars are observed to retain their Li in clusters as old as the Hyades with little separation in EW between ages of 30 to 625 Myr (EWs vary between $\sim$ 50 and 150 mÅ). Early F-stars are observed to have EWs < 100 mÅ in all clusters aged between 30 and 625 Myr. Scatter amongst each cluster between F0 and F4 is ≤ 50 mÅ for all clusters therefore precise EWs are needed to distinguish between clusters. The EWs of spectral-types between F5 and F9 in the Hyades are significantly smaller than younger clusters (generally < 100 mÅ compared to $100 - 150$ mÅ in the Pleiades and IC 2602 stars) and EWs in IC 2602 are marginally larger than Pleiades objects.

G-stars – In G0-G4 spectral-types, the pattern of EW versus $V - K$ is easily distinguishable between γ Vel (EW $\sim 300 - 400$ mÅ) and the older IC 2602 and the Pleiades (EW $\sim 150 - 250$ mÅ), however differences between IC 2602 and Pleiades objects are small and the scatter in each cluster overlaps. Li has largely depleted by a Hyades-like age, where EWs drop from ~ 100 mÅ at G0 to < 50 mÅ at G4. Between G5 and G9 spectral-types a clear separation in EW is still present between γ Vel (~ 400 mÅ) and IC 2602/Pleiades (EW $\sim 100 - 250$ mÅ). Whilst the EWs are on the whole increasing from G5 to G9 in γ Vel, IC 2602 and the Pleiades, a scatter as large as 200 mÅ is observed in IC 2602 and the Pleiades at later G-types and some Pleiades objects have significantly larger EWs than IC 2602. The EWs of late G-types in the Hyades is < 20 mÅ and practically unobservable.

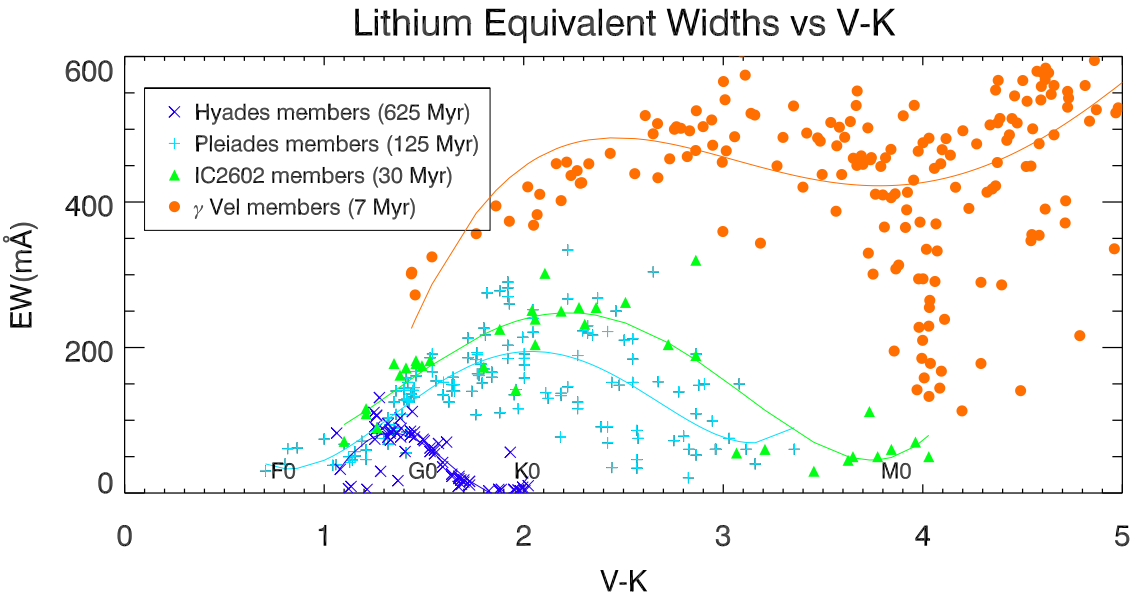

Figure 1.12: Lithium equivalent widths for age-calibrated open clusters as a function of their intrinsic $V-K$. To demonstrate the age evolution of Li depletion at a given colour, data from γ Vel ($5-10$ Myr, Jeffries et al. 2009), IC 2602 (30 Myr, Randich et al. 2001), Pleiades (125 Myr) and Hyades (625 Myr) are plotted. Lines indicate fourth-order polynomial fits to each cluster.

K-stars – K0 to K4 spectral-types in γ Vel increase in EW from 400 to 500 mÅ and the Li pattern plateaus at 500 mÅ from K5 to K9, although the scatter amongst γ Vel members is as large as 200 mÅ for mid-K types. These EWs are ≥ 200 mÅ larger than the EWs of IC 2602 members from K0 to K4, therefore an EW > 300 mÅ between K0 and K4 is likely younger than 30 Myr. Whilst the EWs in IC 2602 are slightly higher than the Pleiades (~ 250 mÅ compared to ~ 150 mÅ), the scatter in EW amongst early K-dwarfs in the Pleiades may be as much as 200 mÅ ($100 - 300$ mÅ). EWs peak at early K-types in both IC 2602 and the Pleiades (at ~ 250 mÅ), and fall to < 50 mÅ towards K9. Therefore whilst EWs in γ Vel remain fairly constant, the difference in EW between γ Vel and IC 2602 increases from ~ 250 mÅ at K5 to ~ 400 mÅ at K9. This means an EW measurement > 200 mÅ at K5 or > 100 mÅ at K9 is likely to be younger than 30 Myr. The scatter in the Pleiades objects towards late K-types has decreased (between $50 - 125$ mÅ) and a separation between IC 2602 and Pleiades is more distinguishable. For example, a K5-K9 star with an EW between $100 - 200$ mÅ is likely to be younger than the Pleiades. Hyades K-dwarfs have hardly any visible Li.
M-stars – M0-dwarfs in γ Vel have EWs as large as 600 mÅ, however, between M0 and M2 there is an extremely large scatter of EWs between 100 mÅ and 600 mÅ, possibly representative of the LDB in γ Vel. Table 1.3 shows that for early M-dwarfs, Li is expected to go from 50 to 99 per cent depletion in ~ 6 Myr which may explain the large observed scatter. Towards even later spectral-types (not accounting for several outliers), the scatter in EW amongst γ Vel members reduces to ~ 100 mÅ and EWs on average increase from 500 mÅ at M2 to 600 mÅ at M4. Observing an EW > 100 mÅ in early M-dwarfs generally indicates a star is not older than 20 Myr. In clusters older than (or equal to) IC 2602 almost no Li is detected in early to mid M-dwarfs.

Throughout this thesis, Li assumes an important role in assessing ages for stars < 200 Myr. Lithium has always been of high importance for identifying MG members and also for estimating the ages of young MGs. Previous studies using Li to identify MG members and assess their ages have used both models of Li depletion (e.g., Mentuch et al. 2008; Yee & Jensen 2010) and empirical data (e.g., Barrado y Navascues et al. 2004, 2006; Torres et al. 2006; da Silva et al. 2009).

1.4.4 Disc evolution on the pre-main sequence

The initial stages of star formation are discussed in §1.1. During the earliest visible stages of star formation, material accreting onto the stellar surface is transported to a surrounding disc. The prescence of near- to mid- IR excesses in young stars are signatures of warm dust at 0.1 to 10 AU in primordial circumstellar discs.

There are many factors that might cause disc dissipation and accretion to cease, but it appears to be an inevitable process. The strength of accretion/disc signatures and the frequency with which they are seen decay with time. Observations for primordial discs in $1 - 10$ Myr clusters have shown that the fraction of objects with excesses at near-IR decreases by a factor of 2 in $\sim$ 3 Myr, becoming asymptotic to zero after 10 Myr (Haisch, Lada & Lada 2001; Hillenbrand 2006; Dahm & Hillenbrand 2007; Hernández et al. 2008; Mamajek 2009). To quantify the decline in disc fractions with age, Mamajek (2009) use an exponential decay relation of the form $f = \exp(-\tau/\tau_{\rm disc})$, where f $(= n/N)$ is the fraction of stars in a cluster that have accreting discs. The time-constant, $\tau_{\rm disc}$ was estimated to be $\sim$ 2.5 Myr, using the available data. The decay of primordial discs as a function of time is displayed in Figure 1.13. More recent measurements of disc fractions and reevaluation of ages in young clusters suggest that $\tau_{\rm disc}$ could be twice as large (Pecaut, Mamajek & Bubar 2012; Bell et al. 2013). Absolute ages from this method are uncertain by factors of two, because of the age scale uncertainty.

Perhaps with the exception of η Cha, ϵ Cha and TWA ($\leq$ 10 Myr), the ages of MGs are older than the usual lifetimes for primordial discs, making these kinds of discs less effective as a probe for MG ages. On timescales of less than 1 Myr, km-sized planetesimals are expected to aggregate from the particles within the disc (Weidenschilling & Cuzzi 1993). Runaway accretion then occurs by oligarchic growth, which results in planetesimal objects that are tens to hundreds of km in size forming in their own 'feeding zones' (Klahr & Johansen 2008). The oligarchic growth phase may take as long as several Myr. At this stage accreting material falls either onto the star or onto the large protoplanetary cores, resulting in the formation of gas giant planets

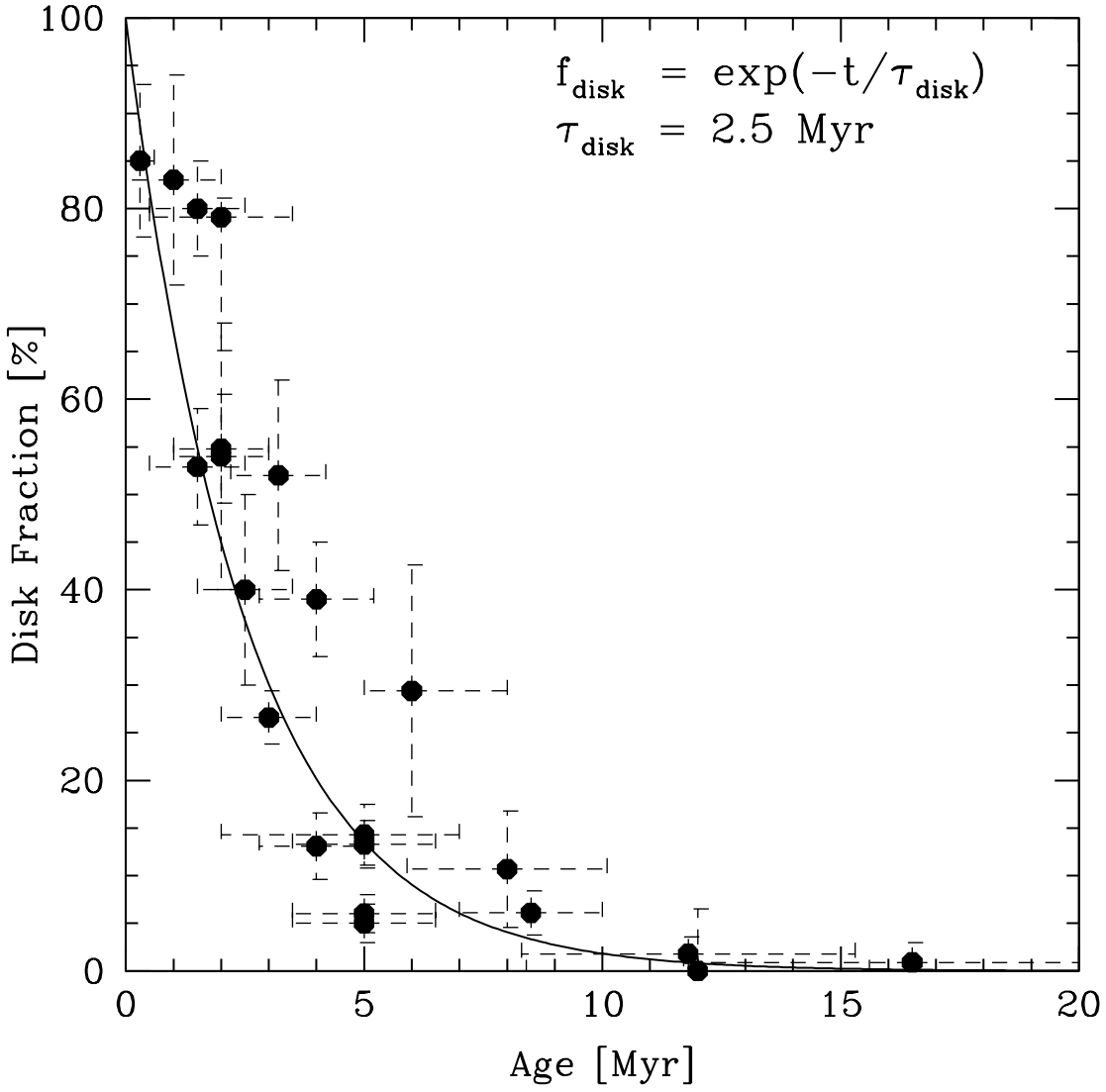

Figure 1.13: Figure from Mamajek (2009). Cluster ages versus the fraction of stars with primordial discs, based on either Hα or infrared diagnostics. The data is fitted with an exponential decay curve, with a timescale $\tau_{\rm disc} = 2.5\,$Myr. References for each cluster are available in figure 1 of Mamajek (2009).

(Hartmann et al. 1998). Collisions between these embryos can merge to form a few stable terrestrial planets in $10 - 100$ Myr (Weidenschilling 1997). Processes such as these are able to remove the primordial discs on timescales of $3 - 7$ Myr (Hernández et al. 2007; Hillenbrand, Bauermeister & White 2008; Currie & Kenyon 2009; Mamajek 2009).

By 10 Myr almost all the remaining discs around stars are optically-thin and comprised of dust and debris (see Wyatt 2008). Emission from these debris discs are from the second-generation dust formed in the collisions between planetesimals. These dust grains are heated by the parent star and reradiate at wavelengths $> 10\,\mu$m. On timescales of $10 - 100$ Myr debris discs will dissipate via loss mechanisms such as Poynting-Robertson drag and/or radiation pressure 'blow-out'. The timescales to remove debris discs are much shorter than this, which implies they are being replenished. Debris discs will persist until collisions between planetesimals cease. The presence of dust therefore implies the existence of higher mass planetesimals that can collide to produce the dusty debris which could signpost catastrophic collisions as well on top of a general age dependence (Backman & Paresce 1993; Lagrange, Backman & Artymowicz 2000; Zuckerman et al. 2001). Therefore any system with excess IR emission implies planet formation, or at least planetesimal formation.

Famous examples of debris discs in MGs (or in nearby associations) include: the directly imaged β Pic and AU Mic (BPMG, Smith & Terrile 1984; Kalas 2004), TW Hya (TWA, Weinberger et al. 1999), HR 8799 (Columba, Marois et al. 2008) and Formalhaut (Piscis Austrinus, Stern, Weintraub & Festou 1993). Surveys to characterise the mid-IR excess have benefitted from satellite based missions – primarily the InfraRed Astronomical Satellite (IRAS), the Mid-Infrared Photometric Survey (MIPS) on the Spitzer space telescope and more recently the Wide Infrared Survey Explorer (WISE). Zuckerman et al. (2011) used data from MIPS to characterise flux excesses at 24 and 70 μm for members of BPMG, TWA, ABDMG and the Tuc-Hor MG. SED fits to the photometry results in a diminishing fraction of stars with excess 24 μm flux with age. Table 11 in Zuckerman et al. (2011) summarises the fraction of debris disc objects. Using the WISE database, Schneider, Melis & Song (2012) identify excess emission at

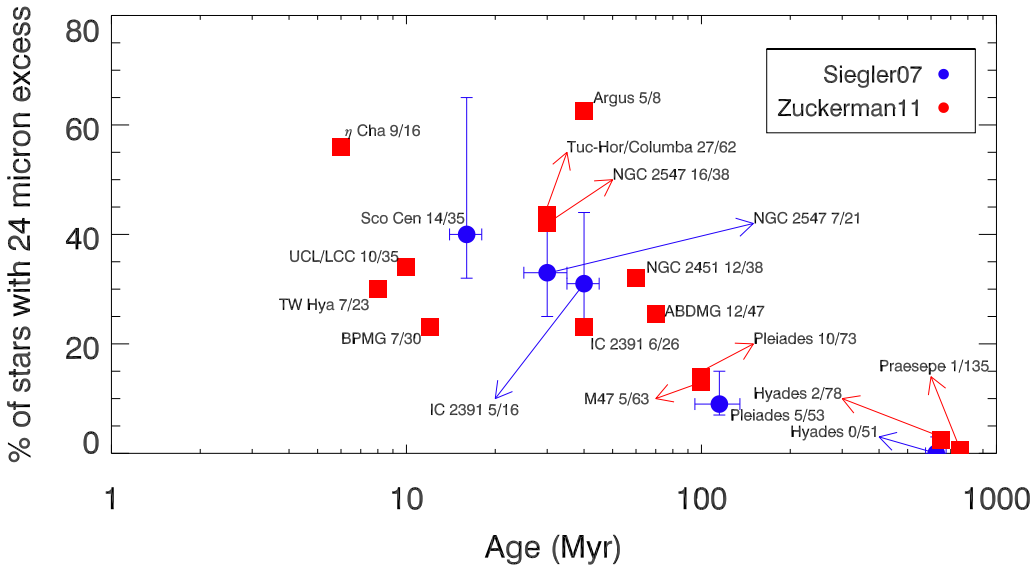

Figure 1.14: The fraction of Solar-type stars with 24 μm excess for several young open clusters and MGs. There is an overall declining trend in the fraction with age. Data are from the FGK stellar sample in Siegler et al. (2007) (blue circles) and Zuckerman et al. (2011) (red squares). Ages are extracted directly from the source publication. The numbers next to the labelled data correspond to the fraction of stars with an IR excess in each cluster. Error bars on the Siegler et al. (2007) sample are from table 4 in their paper.

12 and 22 μm for 4 members in TWA. The SEEDS MG survey (Brandt et al. 2014) is currently attempting to identify debris discs in MGs. In chapter 6, SED fits are made to seventeen M-dwarf MG members which exhibit IR excesses in the WISE database. As a means of estimating the ages of MGs, debris discs cannot provide absolute ages, and the time-dependence of disc dispersal is not fully known (Siegler et al. 2007; Currie & Kenyon 2009; Smith & Jeffries 2012). Figure 1.14 shows the fraction of Solar-type stars with debris discs for a range of young open clusters and MGs. This seems to show debris disc presence is a good youth indicator, however, the x-axis is logarithmic and even though discs are present 10 times less in older stars, there are ten times more of them.

1.5 Overview of all age techniques

The level to which an age indicator is effective usually depends on the mass and also the evolutionary stage of a star. For example, the LDB method is applicable only to M-dwarfs in stellar aggregates between 20 and 200 Myr, whereas MSTO ages can only be applied to stars of spectral-type A or earlier. For each technique discussed in this chapter, Table 1.4 provides a summary of the relative strengths and weaknesses/limitations for each method and the applicable mass and age ranges.

Method	Age range (Myr)	Mass range ($M/M_{\odot}$)	Strengths	Weaknesses/Limitations
Semi-Fundamental				
LDB	$20-200$	$0.1-0.4$	Involves few assumptions.	Requires moderate to high resolution spectra for very faint objects ($R > 3000$).
			Insensitive to observational uncertainties.	Does not extend to ages far past the ZAMS and does not cover star forming regions.
			Requires minimal analysis or interpretation: the Li feature is either clearly present or it is not.	Provides only age limits on single M-dwarfs.
			Age errors are usually $10-20$ per cent, but could be lowered to ~ 5 per cent with high quality observations.	
Traceback	< 20	All masses	Method is free from any interior stellar modelling, only kinematics are required.	Accurate radial velocities and parallaxes are required.
			Gaia should provide precise astrometry for many faint members of young groups.	The inclusion or exclusion of individual objects can significantly alter the determined age.
			Applicable for all spectral-types.	It is unclear whether any reliable (or repeatable) age for a group has ever been determined.
Model-Dependent				
HRD	All ages	All masses	Stellar luminosity changes rapidly and systematically during PMS contraction.	Many factors influence the apparent luminosity of a PMS star, with not all of them known to us. The resulting change in luminosity with time may not be monotonic.

Method	Age range (Myr)	Mass range ($M/M_\odot$)	Strengths	Weaknesses/Limitations
			When the above effects are small, CMDs may provide more precise ages if $T_{\rm eff}$ is well measured.	Ages can be very model-dependent.
			When applied to clusters, the technique may be more effective.	Reddening, variability and unresolved binaries add uncertainty to luminosities.
MSTO	5 − 1000 (providing there are stars near the turn-off)	> 1.0	Post-ZAMS models are in better agreement compared to PMS models.	Main sequence evolution is slow and higher mass stars are rare, leading to errors in inferred age that are driven mostly by the observational uncertainties and small number statistics.
			Easier to model higher-mass stars.	
Surface gravity	$1 - 100$	All masses	Potentially useful to measure ages for very low-mass stars	No absolute accuracy.
			Distance independent and relatively straightforward technique required.	May be difficult to separate genuine spectral features from noise artefacts.
Projected radii	$5 - 70$	All masses	Distance independent method.	Only provides an upper age-limit because of the $\sin i$ ambiguity.
			Precise rotation periods and high-resolution spectra can give precise measurements of $R \sin i$.	Method relies on correct modelling. Observations show that M-dwarfs are larger than their model predictions.
Empirical				
Rotation	> 100	> 0.5	Rotation periods can be measured precisely.	Large scatter in rotation periods in young clusters, particularly in low-mass stars.
			Once on the ZAMS, the rotation periods of solar-type stars scale with $t^{1/2}$. Calibratable with the Sun.	Lower-mass stars spin down on much longer timescales.
Activity	$50 - 5000$	> 0.5	Previous X-ray surveys have examined vast numbers of nearby, young stars. A measurement of $\log R^{'}_{\rm HK}$ or Hα is relatively uncomplicated.	Scatter in X-ray luminosity is present at all ages and is saturated for large X-ray emitters. Large levels of chromospheric variability in field stars (e.g. the Sun).
Li abundances	$1 - 1000$	< 1.2	Li abundances observed to decline on a mass and age dependent timescale.	Scatter at a given age and spectral-type may be as much as a factor of 10 (e.g. K-dwarfs in the Pleiades).
			Observing the Li 6708Å line is relatively uncomplicated.	Metallicity, rotation, binarity and surface inhomogeneities can alter Li abundances.

Method	Age range (Myr)	Mass range ($M/M_{\odot}$)	Strengths	Weaknesses/Limitations
			Large number of calibration clusters – Li abundances for FGKM stars available in the literature for > 20 open clusters younger than 625 Myr.	Models of Li depletion are not in agreement.
Discs	$< 10 - 15$	All masses	Presence of primordial discs easily evidenced by an IR excess.	Disc fractions are wavelength and mass dependent.
			A clear trend of exponential decay in primordial disc fractions is present for the first 10 Myr.	Primordial discs cannot be utilised as an age indicator beyond 10 Myr. Absolute ages are uncertain.
			Detection of a debris disc may be used as a secondary age indicator as supporting evidence for ages $>$ 10 Myr.	Disc fractions are calibrated data in clusters where ages must be accurately constrained. Recent work has suggested that in some cases, clusters ages may be older by of a factor of 2. Mechanism for disc dispersal is not fully known.

Table 1.4: Applicable age and mass ranges for the methods discussed in this chapter and a summary of the relative strengths and weaknesses/limitations for each technique.

2 Introduction: Moving Groups

2.1 A short history of identifying nearby, young stars

Young stars in star forming regions (SFRs) are hard to observe. These very young stars are relatively distant examples of PMS objects and obscuration by local, natal gas and dust clouds and interstellar reddening make their detailed study difficult. The closest SFRs all lie beyond 100 pc. To observe the products of recent star formation one must turn to the molecular clouds of ρ Ophiuchi ($120 - 160$ pc, Torres-Lopez et al. 2007; $0.3 - 3$ Myr, Parks et al. 2014) and Taurus-Auriga (140 pc, Kenyon, Dobrzycka & Hartmann 1994; $1 - 3$ Myr, Küçük & Akkaya 2010) and the SFRs of the Orion Nebular Cluster (389^{+24}_{-21} pc, Sandstrom et al. 2007; < 5 Myr, Jeffries et al. 2011), Lupus Complex (155 ± 8 pc, ≤ 3 Myr, Lombardi, Lada & Alves 2008), Chamaeleon (150 pc, Knude & Hog 1998; 2.6 Myr, Covey et al. 2010) and IC 348 (315 pc, Luhman et al. 2003; $4 - 5$ Myr, Mayne et al. 2007). Naturally, the question one asks at this stage is this: 'can examples of PMS stars be found more locally?'

The venerable history of detecting nearby young stars can arguably be traced back as early as 1869, when according to Eggen (1965), Proctor (1869) reported a number of comoving stars in the Hyades cluster and also five 'dipper' stars comoving in Ursa Major. In a review paper shortly following Eggen's, Sharpless (1965) notes that Proctor, in the same year, devised a model of 'stream' stars in the Galaxy, suggesting the existence of comoving stellar groups near to the Sun (Proctor 1869a).

In a series of publications titled *Stars and Stellar Systems*, Eggen (1961; 1965; 1965a) used the kinematics available at the time and identified a moving cluster of typically young (< 100 Myr) stellar objects sharing similar space motions, which he named the 'Local Association'. Also referred to as the Pleiades moving group, this association includes a number of bright B-type stars, stars in the Pleiades, α-Perseus and IC 2602 clusters, and objects in the Scorpio-Centaurus association. Although

the purported members of the Local Association share common kinematics, they span a large range of ages and are widely distributed in the Solar neighbourhood (within $\approx 300\,\mathrm{pc}$). This range in age and distance casts uncertainty as to whether the Local Association originated from one single molecular cloud, or if it is the remnant of several SFRs.

Following Eggen's hypothesis, detailed observations of several young, chromospherically active, fast-rotating, late-type stars led to the suggestion that they too were part of the Local Association (e.g., AB Dor and PZ Tel, Innis, Coates & Thompson 1988; BO Mic, Anders et al. 1993; LO Peg, Jeffries et al. 1994). Follow-up spectroscopy of optical counterparts to coronally active late-type stars found in EUV and X-ray surveys revealed a large fraction of these that were comoving with the Local Association (Jeffries & Jewell 1993); many were as young or younger than the Pleiades ($\sim 125\,\mathrm{Myr}$, Stauffer, Schultz & Kirkpatrick 1998) as evidenced by the presence of lithium in their photospheres (Jeffries 1995, see §1.4.3).

With the exception of the Local Association members, the only known groups of comoving, coeval PMS stars within 50 pc were the sparse Ursa Major group ($d \sim 25\,\mathrm{pc}$, Ammler-von Eiff & Guenther 2009; ages range from 300 Myr, Soderblom & Mayor 1993 to $500 \pm 100\,\mathrm{Myr}$, King et al. 2003) and the richly populated Hyades cluster ($d = 46.45 \pm 0.50\,\mathrm{pc}$, van Leeuwen 2009; age $= 625 \pm 50\,\mathrm{Myr}$, Perryman et al. 1998). Although these groups are nearby, their constituents are not as young as those in SFRs and are not useful for studying early PMS evolution.

Perhaps the first evidence that young stars could be identified far from SFRs and molecular clouds was provided by Rucinski & Krautter (1983), who carried out a spectroscopic investigation into the isolated variable star TW Hya. Their results supported the suggestion in Herbig (1978) that TW Hya is a T-Tauri star, based on the large photometric IR-excess and strong lithium absorption. The authors comment that 'TW Hya is outstanding in the sense that it has all the properties of a classical T-Tauri star but is located very far from any dark cloud'. This isolated case of a nearby T-Tauri star was to be the precursor to the identification of a large number of nearby post T-Tauri stars. Several years later, de la Reza et al. (1989) and Gregorio-Hetem

et al. (1992) carried out spectroscopic surveys of field stars with excess IR signatures from IRAS. As a result of these surveys, four additional T-Tauri stars within 10 degrees of TW Hya were identified, and found to be kinematically related. This small group of 5 T-Tauri stars in the vicinity of TW Hya was to be the first identification of a group of young, comoving stars within the Solar neighbourhood.

Throughout this thesis, MGs will be characterised as 'a comoving, coeval group of young stars that have similar chemical abundances'. These 'streams' of stars, typically containing some few dozen stellar systems have common Galactic motions which are defined in terms of their Galactic velocities, as described in §2.2.1. There are several reasons why astronomers are interested in finding MGs and their members:

•To study planets and debris discs around MG members. The typical age of a star in an MG is coincident with the epoch of giant and terrestrial planet formation ($\leq$ 10 and $20 - 50$ Myr, respectively), rendering such objects amenable to exoplanet and debris disc surveys (e.g., the SEEDS survey: Yamamoto et al. 2009; Janson et al. 2013; Brandt et al. 2014, the GEMINI/NICI campaign: Biller et al. 2008; 2013; Liu et al. 2010; Wahhaj et al. 2013, the PALMS survey: Bowler et al. 2012; 2015). Giant, young planets, which can form on timescales shorter than 10 Myr (Kataria & Simon 2010) are expected to be self-luminous and giant planets around low-mass (low-luminosity) nearby stars are ideal imaging candidates because they provide good brightness contrasts compared to higher-mass stars (Schlieder, Lépine & Simon 2012). The relative proximity of MG stars provide good spatial resolution for a given angular resolution, suitable for adaptive optics. There are two competing theories on how planets are formed in circumstellar discs; one is by core-accretion (Perri & Cameron 1974; Harris 1978; Mizuno 1980; Laughlin, Bodenheimer & Adams 2004; Mordasini et al. 2008; Nelson & Ruffert 2013) and the other is by disc instability (Cameron 1978; Boss 1998; Boss 2003; Durisen et al. 2007). Exoplanets around nearby PMS stars serve as excellent test beds to study unknown aspects of planet formation. Similarly, discs around low-mass stars evolve from their gas-rich protoplanetary phase to become debris discs at ages $\sim$ 10 Myr and their subsequent debris disc phase lasts for several 10s of Myr (see §1.4.4 and chapter 6 for an overview of PMS disc evolution).

•To provide observational tests for early stellar evolution. Isochronal models are most uncertain at low masses, therefore examples of low-mass MG members provide observational constraints on PMS evolution. Hillenbrand, Bauermeister & White (2008) find that models under-predict stellar masses by as much as 50 per cent. A sample of MG members with precise measurements of mass and age would serve as a benchmark for evolutionary models. Observing low-mass binaries in MGs would provide an age test to the group, as two coeval objects must be mapped on the same isochrone. MG binaries are close enough that they have both measurable orbital periods on timescales of decades or less, whilst still being resolvable (Fischer & Marcy 1992).

•To study how MGs form and by what processes clusters dissolve to populate the field. Lada & Lada (2003) observe that whilst > 90 per cent of stars that form in embedded clusters form in rich clusters with ≥ 100 members, less than 10 per cent remain gravitationally bound after $\sim 100\,\mathrm{Myr}$. If no nearby molecular clouds are present in the Solar neighbourhood, how did the young stars get there? Sterzik & Durisen (1995) postulate that nearby, young stars are high-velocity escapees in the decay of young multiple star systems. Alternatively, Feigelson (1996) suggested that they originate from smaller molecular clouds (cloudlets) that dispersed amongst the interstellar medium, such that their birthsites can no longer be detected. Mamajek & Feigelson (2001) suggest that kinematic data for several MGs point to a formation region near to the Scorpius-Centaurus (Sco-Cen) complex. This SFR is divided into 3 separate entities, the Upper Centaurus Lupus, the Upper Scorpius and the Lower Centaurus Crux. The orbits of MG members in TWA, BPMG, η Cha and ϵ Cha all have birthsites close to Sco-Cen (Mamajek, Lawson & Feigelson 2000; Ortega 2002, 2004; Jilinski, Ortega & de la Reza 2005; Fernández, Figueras & Torra 2008). Mamajek & Feigelson (2001) suggest that turbulence within a giant molecular cloud caused velocity dispersions of $\sim 5 - 10\,\mathrm{km\,s^{-1}}$, similar to the dispersion of space velocities observed in MGs comoving with the Local Association. Fernández, Figueras & Torra (2008) suggest that MGs originated from the impact of a Galactic spiral arm shock wave against a giant molecular cloud, triggering star formation in cloudlets slightly outside of the Sco-Cen complex.

2.2 Measuring kinematics and assessing MG membership

Given a set of young stars, how is it ascertained that they form a MG? There does not exist a single, solid definition for a MG that everybody agrees on. Whilst all MG searches have minimum requirements of common Galactic space velocities and coevality (e.g., Zuckerman & Song 2004; Zuckerman et al. 2011), some investigators also necessitate common XYZ positions (e.g., Torres et al. 2008; da Silva et al. 2009), arguing that the members of a MG have had little time to disperse through the Galaxy. In this thesis no spatial criteria are used to define MG membership. MGs should be chemically homogeneous but investigations have shown that sometimes they are not and one therefore presumes that the MG sample is contaminated, or concedes that MGs are not all born in the same natal cloud or cannot all have been dispersed from chemically homogeneous open clusters (e.g., Torres et al. 2008; Viana Almeida et al. 2009; Barenfeld et al. 2013; De Silva et al. 2013).

Another technique, known as the convergent point method (Eggen 1958; 1995), makes use of the positional coordinates, proper-motions and either a) the radial velocity (RV) of a star (the parallax is not needed, see §2.2.2) and/or b) a trigonometric parallax (the RV is not required, see §2.2.3) to test whether it is kinematically associated with a MG. Eggen developed several criteria for group membership in MGs, which he named the 'convergent point' test. The main assumption is that the total velocities of stars in MGs have negligible dispersion and apparent motion is directed towards a single convergent point. Given the total velocity and the convergent point of a MG, two quantities can be measured: the kinematic difference in RV between the star and the MG and the kinematic difference in tangential velocity between the star and the MG.

2.2.1 UVW velocities

Galactic space velocities are given in terms of UVW coordinates, centered on a heliocentric reference frame, which throughout this thesis will be measured in the following

way: U in the direction of the Galactic centre, V in the same direction as Galactic rotation and W directed towards the Galactic North pole. These velocities are calculated (and their uncertainties) using the prescription of Johnson & Soderblom (1987). The XYZ components of position are centered on the Sun and are have the same direction vectors as UVW, respectively. Principally, one must have sufficiently precise measurements of right ascension (α), declination (δ), proper-motion (μ_α, μ_δ), RV and parallax (π), along with their uncertainties (σ_{μ_α}, σ_{μ_δ}, σ_{RV}, σ_π, positional uncertainty can usually be ignored). The dispersion of UVW velocities amongst members of a MG is $\sim 2-3\,\mathrm{km\,s^{-1}}$ (Zuckerman & Song 2004; Torres et al. 2008; Zuckerman et al. 2011), therefore a candidate star within this dispersion would definitely be considered as a potential MG member. Figure 2.1 displays the spatial and velocity distribution for 10 MGs, these are summarised in §2.4.

The major challenges in measuring a sufficiently precise UVW lie in measuring precise RVs and proper-motions. For PMS stars it is hard to judge distances without a trigonometric parallax. Parallax measurements are not always available (or precise enough). If this is the case, one must turn to a photometric parallax. This method requires knowledge of the star's age and the correct use of model isochrones on a CMD. From the absolute magnitude, a distance (or parallax) can be estimated. However, because PMS stars are evolving along evolutionary tracks, the method relies on the assumptions that the age has been correctly estimated and the PMS evolutionary model used is reliable (model-to-model variations can be significant, see §1.3.1). The colour must also be measured to an appropriate accuracy. Reddening effects should not be an issue because MG members are within 100 pc, free from dust obscuration. In §5.7.1 spectroscopic/photometric parallaxes are measured, using the Siess, Dufour & Forestini (2000) evolutionary models and an M_K vs $V-K$ CMD.

Figure 2.1 shows that the range in U, V and W for MG members is generally no more than $\sim 3\,\mathrm{km\,s^{-1}}$. Zuckerman & Song (2004) identify a region in velocity space bounded by $-15 < U < 0, -34 < V < -10$ and $-20 < W < +3\,\mathrm{km\,s^{-1}}$ containing the majority of the currently known MGs, defined as the 'good box' (see Figure 2.1). Given that many of the MGs in the good box have similar UVW, in some cases the

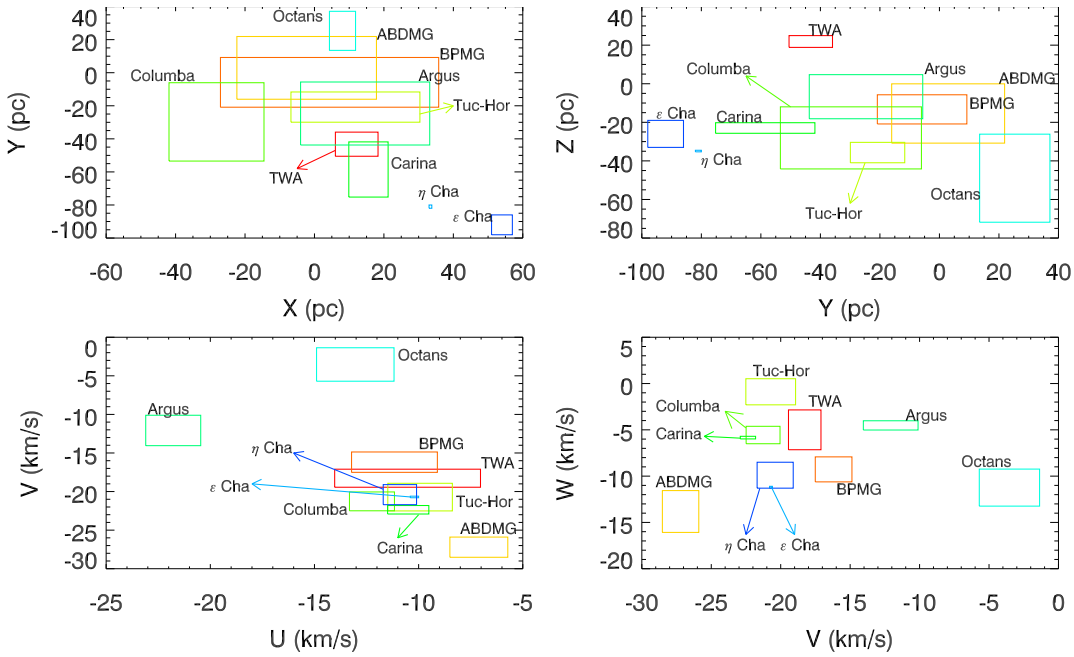

Figure 2.1: UVW space velocities and positions for the 10 MGs considered in this thesis, based on the Galactic space velocities, positions and associated 1σ uncertainties provided in Table 2.1.

UVW of a candidate may match with 2 or more MGs. In this circumstance, one must identify additional MG criteria to distinguish between groups.

2.2.2 Kinematic radial velocities

Given the position, proper-motion and RV of a star, one can compare the RV difference, ΔRV, between a star (RV_*) and the expected RV were it a member of a MG, using the following equation:

$$|\mathrm{RV}_* - V_T \cos\lambda| = \Delta\mathrm{RV}, \tag{2.1}$$

where V_T is the magnitude of the total velocity of the group ($\sqrt{U^2+V^2+W^2}$) and λ is the angular distance between the star and the convergent point of the proposed MG.

As a selection cut for potential MG candidates, Schlieder et al. (2010; 2012) set a value of $\Delta\mathrm{RV} < 5\,\mathrm{km\,s^{-1}}$. In chapters 4, 5 and 6 this criterion will be used to determine membership for MG candidates. The kinematic RV test is distance independent, however, a consistent RV cannot guarantee MG membership as the object may be a large distance away from the centroid of the MG. If ΔRV is too large, then an MG candidate can be rejected with certainty.

2.2.3 Kinematic tangential velocities

The difference in tangential velocity, ΔV_{TAN}, between a star and the expected tangential velocity were it part of a MG is given by :

$$|V_{\mathrm{TAN}} - V_T \sin\lambda| = \Delta V_{\mathrm{TAN}}. \tag{2.2}$$

The tangential velocity for the star is given by:

$$V_{\mathrm{TAN}} = \kappa\mu d, \tag{2.3}$$

where $\kappa = 4.74$ (no units), μ is the magnitude of the proper-motion vectors (in $\mathrm{mas\,yr^{-1}}$) and d is the distance (in pc). Ducourant et al. (2014) use a rejection threshold of $\Delta V_{\mathrm{TAN}}/V_{\mathrm{TAN}} < 0.05$ to qualify members of TWA (see §2.4.1). In §5.7.5 a criterion is used that MG candidates must have $\Delta V_{\mathrm{TAN}} < 5\,\mathrm{km\,s^{-1}}$.

2.2.4 Additional requirements for MG membership

Many interlopers risk inclusion in surveys searching for new MG members simply because they have similar kinematics. Additional criteria using ages and abundances are therefore essential. For example, Maldonado et al. (2010) found ~ 100 FGK stars within 25 pc that have UVW similar to at least one known MG, but only a quarter of these remained as potential MG candidates, as most of the sample had ages (based on Li, Hα and X-ray, see §1.4) that were incompatible with their kinematically associated MG. If stars in a MG are to have shared a common origin, they should also have similar chemical compositions. Viana Almeida et al. (2009) detect abundance dispersions of less than 0.1 dex in [Fe/H], [Ni/H] and [Si/H] amongst MG members. A study of ten objects comoving and coeval with ABDMG (see §2.4.3) by Barenfeld et al. (2013) found that half of the sample could not constitute a chemically homogeneous group, questioning whether one can confidently report these objects as genuine MG members.

2.3 Previous surveys to identify members of MGs

Surveys to identify new members of MGs can be broadly categorised into two philosophies. One is to initially identify targets with similar kinematics to a MG (using similar methodologies to those outlined in §2.2) and then carry out spectroscopy to identify objects with similar ages and chemical abundances. An example of this approach is given in Lépine & Simon (2009) who outline a procedure to identify objects with proper-motion vectors which point in a similar direction to the convergent point

of a MG and identify stars from that subsample for which photometric data shows a match between the hypothetical kinematic distance (using their equation 6) and the photometric distance (using their equation 9). Objects that satisfy these criteria are then assessed for youth indicators (e.g., X-ray, Hα, Li indicators; see §1.4), and an RV measurement determines if a candidate is a likely kinematic member (see, Equations 2.1 and 2.2). Based on these steps, Lépine & Simon (2009) uncovered four new members of BPMG, and further work by Schlieder (2010; 2012; 2012a) using a similar approach uncovered $\sim$ a dozen more likely members in BPMG and seven in ABDMG with spectral-types later than K3. A follow-up of 27 likely-new members in Schlieder, Lépine & Simon (2012a) revealed $\sim$ 50 per cent to be within $3\,\mathrm{km\,s^{-1}}$ in UVW of their corresponding MG. Similar approaches have been adopted by Kiss et al. (2011) and Moór et al. (2013) with similar detection rates for new MG members.

It is clear that kinematic surveys have been successful in unveiling a significant number of new low-mass MG members. Hundreds of highly probable new MG members have been reported with spectral-types K or later. Despite this, however, kinematic surveys inherently preclude the discovery of new MGs themselves. They may also be prone to contamination from field stars that happen to have similar space velocities as MGs. The number of returned candidates is sensitive to the restrictiveness of the initial kinematic criteria – a looser threshold may observe more MG members, however could return a significant number of interlopers, whereas a tighter threshold results in fewer interlopers but also risks overlooking a significant sample of genuine MG members.

Alternatively, one can approach the challenge of identifying new MGs by first selecting potentially young objects from wide-field surveys and then assessing their kinematics to group together objects in UVW space that share similar space velocities and use additional age-related proxies to further constrain their ages. This approach is exemplified in the Search for Associations Containing Young stars program (SACY, Torres et al. 2006; da Silva et al. 2009; Viana Almeida et al. 2009; De Silva et al. 2013; Elliott et al. 2014), initiated in 2000. SACY used X-ray bright sources in the ROSAT All-Sky Bright Source Catalogue with spectral-types later than G0 to identify $\sim$ 2000 potentially young, nearby stars. Spectroscopy of these objects provided radial

and rotational velocities and Li/Hα EWs. Ages and UVW velocities were calculated (see §1.4 and §2.2) and a metric based on distance and UVW used to qualify objects for group membership. Using this procedure, Torres et al. (2006) identified 13 potential new members of BPMG. Similar approaches were carried out by Maldonado et al. (2010) and Rodriguez et al. (2011) with broadly similar outcomes. An exception might be Shkolnik et al. (2012) who conducted a kinematic study of young M-dwarfs within 25 pc with ages ≤ 300 Myr, measuring their radial velocities and trigonometric parallaxes. They found a dozen objects with similar kinematics and age to a specific MG, 14 objects with similar kinematics but an ambiguous age and 27 objects with ages ≤ 150 Myr, but not matched in UVW to any of the MGs considered. This method demonstrates how a confluence of kinematics and age are fundamental requirements for MG membership.

The 'youth-targeted' approach usually produces a lower yield, but has the potential to reveal not only new members of known MGs, but also to discover entirely new groups themselves. An alternative approach based on a Bayesian inference model was presented in Malo et al. (2013). By taking into account (minimally) the position, proper-motion, magnitude and colour of 758 (spectral-type K5V-M5V) stars that initially displayed signposts of youth by virtue of either Hα emission or X-ray brightness (or both), membership probabilities were derived to identify new members in 7 MGs. The analysis calculates the probability of a candidate being a kinematic member of an MG at a given distance by comparing a set of observables to a set of $m \times n$ hypotheses, where m represents the number of groups and n represents the number of distances. Equally weighted prior probabilities are assigned to each hypothesis and a Gaussian distribution is used to model each observable (equation 6 in Malo et al. 2013) based on the mean and distribution in UVW and XYZ for the seven MGs. Where possible, additional observables (e.g., radial velocity, distance) were included in the Bayesian analysis to strengthen membership probabilities. The analysis uses XYZ as a criteria as well as UVW. From this strategy, 214 likely-new members of 7 different MGs were reported. The technique, whilst potentially useful at identifying kinematic matches to MGs still requires membership confirmation through a precise age and chemical abundance analy-

sis and not all MGs are taken into consideration (e.g., ϵ Cha, η-Cha and Octans-Near). A webtool to calculate kinematic membership probabilities, named 'BANYAN', has been made available at `http://www.astro.umontreal.ca/~malo/banyan.php` and is utilised in §5.7.5.

Young and old objects follow distinct sequences in the 2MASS-WISE CMDs. Gagné et al. (2014) modified the original BANYAN code to detect MG members with spectral-types later than M5 by using 2MASS and WISE photometry to produce an initial sample of 158 likely-young objects. The updated algorithm returns 25 likely-new members. Using the original BANYAN code, Malo et al. (2014) include radial and rotational velocities to confirm membership for 57 highly probable members suggested in Malo et al. (2013), whilst reporting a new sample of 130 likely-new members in 6 MGs. More recently, Gagné et al. (2015) have constructed a sample of $\sim$ 100 brown dwarf and planetary-mass MG candidates and find tentative evidence for mass segregation in ABDMG, Tuc-Hor and Columba (the BANYAN All-Sky Survey, BASS). To date, BANYAN has potentially more than tripled the number of MG members with spectral-types later than K5. For the remainder of this chapter, BANYAN will refer to the combined work of Malo et al. 2013 (M13); Malo et al. 2014 (M14a); Malo et al. 2014a (M14b); Gagné et al. 2014a (G14a); Gagné et al. 2014 (G14b) and Gagné et al. 2015 (G15).

2.4 Young moving groups within 100 pc

2.4.1 TW Hya (TWA)

Discovery - Subsequent to the identification of the five T-Tauri stars around TW Hya (see §2.1), Kastner et al. (1997) used data from ROSAT and noted that all five were very strong X-ray emitters (see §1.4.2.1). With follow up optical spectroscopy, he also identified strong lithium absorption (§1.4) in every object, deducing that the five stars formed a physical T-Tauri association with an age of 20 ± 10 Myr which was named the

TW Hya association (TWA). Using isochronal tracks (see §1.3.1), a distance of ~ 50 pc was calculated. In a similar spirit, Webb et al. (1999) surveyed X-ray bright sources in the ROSAT All-Sky Survey (RASS, Voges et al. 1999) near to TW Hya, and combined with strong chromospheric activity and lithium absorption (§1.4.2 and §1.4.3), they identified 6 additional stellar systems (7 stars and a brown dwarf). Both the Kastner and Webb work concluded that TW Hya was not a high-velocity escapee from a distant SFR, rather TW Hya and its companions were created in a nearby region now devoid of interstellar material.

Membership status - Additional searches in the vicinity of TW Hya revealed more members (Sterzik et al. 1999; Makarov & Fabricius 2001; Zuckerman et al. 2001; Gizis, Reid & Hawley 2002; Reid 2003; Song, Zuckerman & Bessell 2003). A list of the nearby MGs provided by Torres et al. (2008) qualified 22 star systems as members of TWA. Seven additional candidates were proposed by Nakajima & Morino (2012) within 30 pc. Based on the above surveys, the list stands at > 30. Ducourant et al. (2014) use a convergent point test to identify 31 stars in TWA. The BANYAN analysis has identified 36 possible new members of TWA with spectral-types later than K5 (1 in M13, 1 in G14a, 2 in G14b and 32 in G15), including an L4 brown-dwarf candidate reported in G15; which would so far be the lowest mass member of the group.

Age and origin - Using PMS evolutionary models, Webb et al. (1999) provided an age of 8 Myr, however the isochrones mapped objects from as young as 1 Myr to as old as 100 Myr. Barrado y Navascués (2006) used Hα emission and lithium, re-evaluating the age to 10^{+10}_{-7} Myr. Mamajek (2005) attempted to trace-back the kinematics of TWA members to find an age in the past at which the members occupied a spatial minimum, providing weak evidence that the group is expanding. Based on the U velocity and X position of the members, this gives an expansion age of 20^{+25}_{-7} Myr. de la Reza, Jilinski & Ortega (2006) trace-back the orbits of a sample of TWA members to measure a kinematic age of 8.3 ± 0.8 Myr, however this analysis is based on only five proposed members, one of which is not confined to a group at this age. A revised age of 7.5 ± 0.7 Myr is provided by Ducourant et al. (2014), obtained from kinematic trace-backs of 16 stars with revised astrometry. Both Mamajek, Lawson & Feigelson

(2000) and Song, Zuckerman & Bessell (2012) suggested that TWA is near to the edge of a larger stellar population, possibly from subgroups of the Sco-Cen association. Soderblom et al. (2014) conclude that no reliable kinematic age for TWA has been established.

Notable objects - Gizis, Reid & Hawley (2002) identified two free-floating brown dwarfs members of TWA. One of these members, 2M 1207, was revealed to be the first imaged planetary-mass secondary (2M 1207b) outside of the Solar system (Chauvin et al. 2004). The measured mass of 2M 1207b ($5 \pm 2\,M_{\rm Jup}$) is based on an age of 8 Myr for TWA. Signatures of dust discs are prominent in several TWA members (e.g., Matthews, Kalas & Wyatt 2007; Riaz & Gizis 2008; 2012; Looper et al. 2010; Schneider et al. 2012; 2013) and the primary member of the group itself, TW Hya, is surrounding by a richly-studied protoplanetary disc. Over 75 publications have focused on the characteristics of the disc in TW Hya.

2.4.2 Beta Pictoris (BPMG)

Discovery - Utilising results in the Hipparcos catalog, with the PPM proper-motion catalog and newly measured RVs, Barrado y Navascués et al. (1999) assessed the kinematics of a large sample of stars suggested to be linked with β Pic. They found that from an extensive catalogue, only 2 stellar systems had Galactic space velocities similar to β Pic and were plausibly young based their large X-ray activity (see §1.4.2.1). These were GJ 799 AB (a resolved binary) and GJ 803, both spectral-type M. Placing these newly identified low-mass objects onto PMS evolutionary tracks, an age of 20 ± 10 Myr was reported for β Pic, consistent with some previous work in the literature (e.g., Jura et al. 1993; Lanz, Heap & Hubeny 1995).

Taking a cue from Barrado y Navascués et al. (1999), Zuckerman et al. (2001) identified more than 20 thousand stars whose UVW velocities could be calculated from data in the literature. Allowing only stars within a few km s^{-1} in U, V and W of β Pic that also displayed at least one strong indicator of youth (e.g., lithium, Hα, rotation), they reduced the sample to 18 comoving, coeval stellar systems linked to β Pic, which

they termed the β Pictoris moving group (BPMG). These objects were concentrated mainly in the Southern hemisphere but spread widely across the sky (see Figure 2.1).

Membership status - Zuckerman & Song (2004) extended the number of BPMG stars (including binaries) to 33 in their '*Young Stars near the Sun*' review. A considerable number of lower-mass counterparts to BPMG have been revealed, primarily through proper-motion selected and kinematically biased surveys (see §2.3 for a description). Additional searches significantly increased the number of BPMG members (carried out by Zuckerman & Song 2004; Teixeira et al. 2009; Rice, Faherty & Cruz 2010; Schlieder, Lépine & Simon 2010; Kiss et al. 2011; Faherty et al. 2012 and Schlieder, Lépine & Simon 2012). These range in distance from 10 to 70 pc. The BANYAN analysis has identified 81 possible new BPMG members with spectral-types later than K5 (37 in M13, 27 in M14a, 5 in G14a and 12 in G15). The top-left and top-right panel in Figure 2.1 display the positional data for all the reported BPMG stars with measured parallaxes. BPMG is one of the closest known MGs and encompasses a volume of $60 \times 30 \times 10$ pc in XYZ, respectively.

Age and origin - Since Barrado y Navascues' age of ~ 20 Myr, investigators have reported ages between 10 and 30 Myr based on various techniques. Zuckerman et al. (2001) placed their newly-identified BPMG objects on a HRD, and using isochronal fits deduced an age of 12^{+8}_{-4} Myr, consistent with Barrado y Navascués et al. (1999) and to date the most often cited in the literature. Ortega et al. (2002) measured an age of 11.5 Myr for the group based on a kinematic trace-back of BPMG members, however no formal errors are reported (see §1.2.2). They further speculate a dynamical link with the Lower Centaurus Crux and Upper Centaurus Lupus groups in the OB Sco-Cen complex. Other kinematic ages (12 Myr, Song, Zuckerman & Bessell 2003; 22 ± 12 Myr, Makarov 2007; 18 Myr, Torres et al. 2008, see also §1.2.2) are consistent, however are prone to methodology issues described in §1.2.2. Mamajek & Bell (2014) used revised astrometry from the BPMG sample in Zuckerman & Song (2004) to trace-back their orbits and failed to identify any evidence of a spatial minimum 12 Myr ago. They also use the sample to plot the AFG type members on a CMD and using four separate evolutionary models they identify an age of 22 ± 3 Myr (with an additional

± 1 Myr based on the choice of model). Ages obtained from the LDB method (Song, Bessell & Zuckerman 2002; Binks & Jeffries 2014; M14b) and a further analysis of the age of BPMG is provided in chapter 4.

Notable objects - Using the IR data from IRAS, launched in the previous year, Smith & Terrile (1984) combined mid- and far-IR excess with data from an optical coronagraph to directly image, for the first time, disc material surrounding a young star. The reported discovery of PSO J318.5-22 – a planet detached from the orbit of its parent star (Liu et al. 2013), may improve knowledge of planet-formation processes and how young planets can be dislocated from their host star and surrounding material. In §4.3.3 the potential mass range for this object is discussed in light of a revised older age for BPMG. Other notable objects in the BPMG include: the direct imaging of β Pic b (Lagrange et al. 2010; 2011; Bonnefoy et al. 2014, see also chapter 4.) and its disc, the sub-stellar mass object surrounding PZ Tel (Biller et al. 2010; Jenkins et al. 2012; Mugrauer et al. 2012) and the imaged disc around the M-dwarf AU Mic (Kalas 2004; Augereau & Beust 2006; MacGregor 2014).

2.4.3 AB Doradus (ABDMG)

Discovery - Whilst carrying out a kinematic analysis of the Hipparcos catalog, Zuckerman, Song & Bessell (2004) noted an ensemble of ~ 30 nearby star systems stars linked both in age and UVW to the well-studied young, rapid rotator AB Dor, hypothesising the existence of the AB Doradus moving group (ABDMG). At a distance of ~ 20 pc, the 'nucleus' of ABDMG, a couple of dozen stellar systems, was reported as the nearest known comoving young group. The top left and top right plots in Figure 2.1 show that the distance of ABDMG objects with measured parallaxes is ≤ 30 pc. Whilst many MGs occupy a similar location in UVW coordinates, the Boettlinger diagrams in the bottom left and bottom right panels of Figure 2.1 show that ABDMG occupies a unique location in UVW space - its V velocity is $\sim 10\,\mathrm{km\,s^{-1}}$ less than MGs in the 'good box'.

Membership status - Subsequent searches for low-mass counterparts of the ABDMG

have uncovered several tens of 'likely new members', largely via proper-motion based surveys with follow-up spectroscopy (see §2.3). Additional candidate members proposed by Torres et al. (2008), Schlieder (2010; 2012), Bowler et al. (2012), Nakajima & Morino (2012) and by Shkolnik et al. (2012) have extended the number of likely candidates to ~ 100, making ABDMG currently the most populated MG. BANYAN has revealed 78 candidates with spectral-types later than K5 (33 in M13, 18 in M14a, 6 in G14a and 21 in G15) and in the G14a analysis, 2 ultra-red L-dwarfs are classified as ABDMG members.

Age and origin - Since 2004, ages for ABDMG have been reported between 50 and 150 Myr. Zuckerman, Song & Bessell (2004) compared the relative strengths of Hα emission and location of objects on an M_K vs $V-K$ CMD with the Tucanae-Horologium MG (which they assumed to be ~ 30 Myr, see §2.4.4) to arrive at an age of ~ 50 Myr. However, Luhman, Stauffer & Mamajek (2005) note that the M-dwarfs in ABDMG are too under-luminous to be ~ 50 Myr and report an age of 100 to 125 Myr.

Luhman, Stauffer & Mamajek (2005), suggest that ABDMG is coeval with the Pleiades and Ortega et al. (2007) trace-back the orbits of the centres of the Pleiades and ABDMG, observing a minimum separation 119 ± 20 Myr ago, although the distance between their centres is ~ 75 pc. Whilst their analysis is unable to account for dispersion in individual group members, Luhman, Stauffer & Mamajek (2005) note that an older Pleiades-like age for the ABDMG would explain the discrepancy between the measured mass of the brown-dwarf AB Dor C and the over-estimates from model predictions. In the Barenfeld et al. (2013) analysis, a lower age limit of 110 Myr is found based on the PMS contraction times for the K-dwarf members. A revised isochronal age of 100 Myr for 10 F/G members is provided in McCarthy & Wilhelm (2014) who also observe a trace-back age of 125 Myr, coincident with the Pleiades, although 3 of these objects are outliers at 125 Myr and typical errors per star are ~ 75 pc.

Notable objects - The group is host to the $4-7\,M_{\rm Jup}$ free-floating planet CFBDSIR 2149-0403 (Delorme et al. 2012). The eponymous member of the group, AB Dor, is a quadruple system including the $0.090 \pm 0.005\,M_\odot$ AB Dor C (Close et al. 2005). Very low-mass objects such as AB Dor C serve as an excellent low-mass calibration

point for evolutionary models.

2.4.4 The Great Austral Young Association

The Great Austral Young Association (GAYA), an amalgamation of Tucana, Horologium, Columba and Carina was proposed by Torres (2003; 2006) as a result of the extensive SACY program. The combined association was proposed following the discovery of a large number of young Southern hemisphere stars with similar kinematic and photometric properties.

2.4.4.1 Tucana-Horologium, GAYA1 (Tuc-Hor)

Discovery - The Tucanae association (Zuckerman & Webb 2000) and Horologium (Torres et al. 2000) association were identified within a very short time of each other. They were combined into one association based on their age, position and Galactic space motion (Tuc-Hor, de la Reza et al. 2001). To identify the Tucanae portion, Zuckerman & Webb (2000) found 10 objects with similar space motions which also exhibited excess IR flux in the IRAS catalogue. Using the ROSAT catalogues, Torres et al. (2000) unveiled the Horologium component by identifying strong X-ray emitters nearby the active star EP Eri.

Membership status - The number of bona-fide Tuc-Hor members with measured a parallax in M13 stands at 42, following the surveys in Zuckerman & Song (2004), Torres et al. (2008), Kiss et al. (2011), Zuckerman et al. (2011) and Nakajima & Morino (2012). Kraus et al. (2014) used RV, Hα emission and Li absorption to identify 129 new members with spectral-types K3−M6, increasing the total number of Tuc-Hor members three-fold and the number of members with spectral-type $\geq$ K3 by a factor of $\sim$ 8. The BANYAN analysis identified 174 objects with spectral-types later than K5 (17 in M13, 22 in M14a, 13 in G14a and 122 in G15); 13 of these are reported as L-dwarfs in G15.

Age and origin - Measurements of the age of Tuc-Hor have varied from $>$ 10 to

40 Myr. Based on a variety of age proxies; lithium absorption, gyrochronology and Hα strengths, Zuckerman & Webb (2000) estimated an age of ~ 40 Myr. Using the members identified in Stelzer & Neuhäuser (2001) and Zuckerman, Song & Webb (2001), Torres et al. (2001) measured the spatial extent of Tuc-Hor to be ~ 70 pc, and suggest that if the initial velocity dispersion of members is similar to the modulus of the current velocity dispersion ($1.5\,\mathrm{km\,s^{-1}}$), the group would have an evolutionary age of at least 10 Myr. Kraus et al. (2014) provided an isochronal age of $20-30$ Myr and an LDB age of 41 ± 2 Myr (see §1.2.1). If all of these newly confirmed members are indeed part of the group, then the LDB age is the most statistically significant age for an MG based on the LDB technique.

Notable objects - Several L-dwarfs are assigned with high probability memberships (> 90 per cent) in G14a and G15. Given the deluge of new members presented in Kraus et al. (2014), Tuc-Hor is an excellent nearby association to calibrate PMS evolution.

2.4.4.2 Columba and Carina, GAYA2

Torres (2003; 2006) identify Columba and Carina as two similar, but distinct MGs as part of the wider GAYA complex. Whilst Tuc-Hor is compact and densely populated, both Columba and Carina are larger entities with fewer members (see, for example, the top left and top right panels of Figure 2.1. Torres et al. (2008) recounts how both Columba and Carina were discovered in the same manner as Tuc-Hor.

Torres et al. (2008) and Zuckerman et al. (2011) discovered a total of 53 star systems in Columba ranging in spectral-type from B to M, of which only a dozen are confirmed as members through a measured parallax. The BANYAN analysis revealed 67 new candidates later than K5 (20 in M13, 25 in M14a, 3 in G14a and 19 in G15). Its age is estimated to be close to that of Tuc-Hor. Torres et al. (2008) report an age of 30 Myr, however, this may be older given the more recent LDB age of 41 ± 2 Myr for Tuc-Hor).

Columba is host to the directly imaged multiple exoplanet system HR 8799bcde (Marois et al. 2008). HR 8799, an A5V star at 39.9 pc, is known to have at least four

orbiting planets, at orbital separations of 15, 24, 38 and 68 AU (Marois et al. 2010). There have been over 70 publications investigating HR 8799 since the initial direct imaging discovery in Marois et al. (2008). Based on several age indicators, Marois et al. gave an age for HR 8799 of $30 - 165$ Myr. However, a later analysis using astroseismology Moya et al. (2010) provided a much older ~ 1 Gyr, which, using luminosity cooling tracks, would increase the masses of the HR 8799 planetary companions to brown-dwarfs. Doyon et al. (2010) applied a maximum-likelihood analysis based on the kinematics and position in a CMD and calculated that it is > 98 per cent likely a member of the ~ 30 Myr Columba association, which would secure the planetary-mass nature of the four orbiting bodies.

Given the small number of confirmed members in Carina (only 4 confirmed with parallaxes) the association is less well defined compared to other more densely populated MGs, however, the BANYAN code has identified 27 possible new members later than K5 (6 in M13, 7 in M14a and 14 in G15). A more recent analysis to identify new members in five MGs by Moór et al. (2013) claim to have identified 11 and 16 new members of Columba and Carina, respectively. Their Li EW/colour measurements are consistent with the Tuc-Hor Association and four newly proposed Columba objects have parallaxes consistent with group membership.

2.4.5 Argus

Discovery - Makarov & Urban (2000) used proper-motion to detect several comoving stars in the proximity of Carina-Vela. Using the convergent point method, Torres et al. (2003) found that the kinematics of this group were similar to the UVW velocities of the IC 2391 cluster and proposed that the two populations were connected. Because of the distinct U velocity compared to other MGs they named the group the Argus association (see Figure 2.1).

Membership status - Zuckerman et al. (2011) and Desidera et al. (2011) increased the number of members by six and one, respectively, with spectral-types A0−G8. The BANYAN code has identified 73 possible new Argus members with spectral-types later

than K5 (50 in M13, 18 in M14a, 3 in G14a and 2 in G15). Malo et al. (2013) counted 11 Argus members with trigonometric parallax measurements.

Age and origin - Ages inferred from Li EWs and position in the HRD suggest coevality with IC 2391 (40 Myr; Torres et al. 2008). Barrado y Navascués, Stauffer & Jayawardhana (2004) used Li depletion and Hα emission to measure an age of 50 ± 5 Myr. De Silva et al. (2013), found that stars in both the Argus MG and IC 2391 have similar chemical abundances ([Fe/H]$= -0.06 \pm 0.04, -0.04 \pm 0.03$, respectively) and kinematics, which are used as strong evidence to support a common origin for for both groups of stars.

Notable objects - AP Col, the nearest known PMS object is a member of Argus, at a distance of 8.4 pc (Riedel et al. 2011). A directly imaged debris disc surrounding HD 61005 has been observed by Desidera et al. (2011) and is reported to be a highly probable member of Argus based on its kinematics and Li EW. An L4β brown-dwarf is identified as ~ 80 per cent likely to be a member of Argus in G14b.

2.4.6 Octans-Near

The Octans association is characterised by Torres et al. (2006) as a group of 15 stellar systems, ~ 20 Myr, and at a distance of ~ 140 pc. Searching the Hipparcos catalog for objects kinematically similar to the Octans association Zuckerman et al. (2013) noted 14 star systems with UVW velocities close to Octans, but with Hipparcos parallaxes within 100 pc; much closer than Octans. These 14 objects have ages $30 - 100$ Myr based on their Li content, X-ray flux and presence of IR-excess (in 5 sources) and are collectively termed the 'Octans-Near' association. The authors comment that the group is similar in UVW to the Castor moving group, although the two are considerably different in age, with Castor's members being ~ 200 Myr.

An investigation by K. McCarthy et al. (2014, priv. comm.) assessed the chemical abundances of 5 F/G members (SNR $\sim 200 - 300$, all with $v \sin i < 20\,\mathrm{km\,s^{-1}}$) in the Zuckerman et al. sample. The chemical abundances for all 5 stars were within 0.1 dex for 10 separate chemical elements. McCarthy et al. also trace-back these mem-

bers, observing a minimum separation of 50 pc between all 5 members ~ 40 Myr ago, however no errors are reported on these. A census of the original 14 Octans-Near members (Murphy & Lawson 2015) indicated that their Li abundances map onto empirical isochrones similar to Tuc-Hor and Argus, at an age of ~ 40 Myr.

A kinematically unbiased survey of rapidly rotating Li-rich members in the Northern hemisphere (Binks et al. 2015, in prep., see chapter 5) has revealed several objects with similar ages and kinematics to Octans-Near which were not identified in the Zuckerman et al. (2013) sample. This could provide a lower mass counterpart to the group.

2.4.7 η and ϵ Cha

Shortly after the identification of TWA, Mamajek, Lawson & Feigelson (1999) identified 12 young, highly active X-ray sources in the vicinity of η Chamaeleontis. These were composed of two early-type stars (η Cha and RS Cha) and 10 Li-rich, Hα emitting, late-type stars (K3-M5). An assessment of their Li content, Hα and X-ray emission, and their $1-2$ mag overluminosity compared to the main sequence led the authors to report an age of ≤ 10 Myr. Astrometric measurements from Hipparcos revealed that η Cha, RS Cha and HD 75505 were comoving at a distance of ~ 97 pc, making the group currently the second closest association of T-Tauri stars, after TWA and according to Lawson & Feigelson (2001), the fourth nearest compact open cluster after Ursa Major, the Hyades and Coma Ber. The angular extent of η Cha ($\sim 0.5°$, or 0.8 pc) was measured to be roughly one order of magnitude smaller than TWA ($\sim 20°$, or 18 pc). The compactness of η Cha is shown by the $X-Y$ and $Y-Z$ distributions in Figure 2.1.

Subsequent to the work of Mamajek, Lawson & Feigelson (1999), a compact group of PMS stars associated with HD 104237 was identified to be codistant and comoving with the B9 stars ϵ Chamaeleontis AB (~ 114 pc, Feigelson, Lawson & Garmire 2003) and the group was named the ϵ Cha association. Luhman (2004) found three new M-dwarf members of ϵ Cha from a survey covering a region with a radius of 0.5 degrees around ϵ Cha AB. Using Li absorption and gravity-sensitive absorption lines, ages of

$\leq 5\,\mathrm{Myr}$ were reported, making the ϵ Cha association younger than the η Cha group (η Cha $= 5 - 10\,\mathrm{Myr}$, Mamajek, Lawson & Feigelson 1999; Luhman & Steeghs 2004).

Jilinski, Ortega & de la Reza (2005) retrace the orbits of η and ϵ Cha, identifying a common spatial origin about 7 million years ago (see §1.2.2 for a description of the trace-back technique). The birthplace appears to be located close to the Sco-Cen OB region, initially suggested by Mamajek, Lawson & Feigelson (1999). Fang et al. (2013) observe disc-like IR excesses in 6 out of 11 ϵ Cha members, providing an age of $\sim 5\,\mathrm{Myr}$ based on the protoplanetary disc fraction (see Figure 1.13 for reference). Using kinematics, CMD placement and lithium abundances, Murphy, Lawson & Bessell (2013) re-examine the membership and origin of ϵ Cha, reporting 35 members from B9 to mid-M spectral-type. Murphy et al. calculate disc and accretion fractions (both ~ 30 per cent) that are both consistent with a typical $3 - 5$ Myr-old population. They find, contrary to the work of Jilinski, Ortega & de la Reza (2005), that the η and ϵ Cha groups were separated by $\sim 30\,\mathrm{pc}$ at the time η Cha was formed $\leq 3\,\mathrm{Myr}$ later.

Name	N	Age (Myr)	Distance (pc)	UVW ($\mathrm{km\,s^{-1}}$)	σ_{UVW} ($\mathrm{km\,s^{-1}}$)	XYZ (pc)	σ_{XYZ} (pc)	α_{CP} (°)	δ_{CP} (°)
TWA	12	8−12	42−92	−10.53, −18.27, −5.00	3.50, 1.17, 2.15	12.17, −43.23, 21.90	6.14, 7.30, 3.06	180.8692	−79.9330
BPMG	44	21−26*	9−73	−11.16, −16.19, −9.27	2.06, 1.32, 1.35	4.35, −5.82, −13.29	31.43, 15.04, 7.56	87.9999	−30.1565
ABDMG	48	70−120	11−64	−7.11, −27.21, −13.82	1.39, 1.31, 2.26	−2.25, 2.93, −15.42	20.10, 18.97, 15.37	92.8918	−47.7275
Tuc-Hor	42	39−43*	36−71	−9.93, −20.72, −0.89	1.55, 1.79, 1.41	11.80, −20.79, −35.68	18.57, 9.14, 5.29	116.2796	−28.8042
Columba	20	20−40	35−81	−12.24, −21.27, −5.56	1.08, 1.22, 0.94	−28.22, −29.74, −28.07	13.68, 23.70, 16.09	103.2744	−29.7906
Carina	5	20−40	46−88	−10.50, −22.36, −5.84	0.99, 0.55, 0.14	15.55, −58.53, −22.95	5.66, 16.69, 2.74	104.9270	−34.2478
Argus	11	30−50	8−68	−21.78, −12.08, −4.52	1.32, 1.97, 0.50	14.60, −24.67, −6.72	18.60, 19.06, 11.43	91.9289	−1.2375
Octans	14	30−100	24−98	−13.04, −3.53, −11.24	1.86, 2.17, 2.00	8.07, 25.32, −48.97	3.76, 11.81, 22.83	60.1242	−4.7423
η Cha	4	5−10	~ 97	−10.20, −20.70, −11.20	0.20, 0.10, 0.10	33.40, −81.00, −34.90	0.40, 1.00, 0.40	89.8605	−37.5539
ϵ Cha	35	3−5	100−120	−10.90, −20.40, −9.90	0.80, 1.30, 1.40	54.00, −92.00, −26.00	3.00, 6.00, 7.00	92.4842	−35.1341

Table 2.1: Properties of the nearest known MGs within 100 pc. Column 2 is the number of MG objects with a measured parallax, from Gagné et al. (2014a). The age ranges provided are the range of previously derived ages from different techniques except those labelled with '*' which are solely from the LDB technique. $UVWXYZ$ are from Gagné et al. (2014a), except for Octans (calculated from the available data in Zuckerman et al. 2013) and η and ϵ Cha (Murphy, Lawson & Bessell 2013). Columns 9 and 10 correspond to the convergent points in right ascension and declination, respectively.

2.5 Outline of work

The work undertaken in this thesis is split into three separate chapters. Firstly, the details of the instrumentation and spectroscopy obtained at both the Nordic Optical Telescope and the Isaac Newton Telescope are explained in chapter 3, along with the essential post-data reduction steps.

In chapter 4 optical spectra acquired of 48 M-dwarf candidates of either the BPMG or the ABDMG are used to assess their membership status. Confirmed M-dwarf members of the BPMG are combined with previously identified M-dwarf members in the literature to provide an LDB age which is almost double that of previously reported isochronal and kinematic ages. The implications of these revised ages are placed into a more general context for planetary-mass objects in BPMG. Confirmed members of the ABDMG are utilised to identify a potential LDB location for the first time. The ABDMG members confirmed in chapter 4 increase the number of M-dwarfs in the group with a lithium measurement by ~ 50 per cent.

Chapter 5 presents work carried out to search for new, nearby, young low-mass stars, by identifying objects present in the kinematically unbiased catalogues of ROSAT (for X-ray data) and the SuperWASP All-Sky Survey (for short rotation periods). The method is capable of identifying both new members of existing MGs and entirely new MGs themselves. Optical spectroscopy was acquired for 146 potentially-young FGK stars. The ages (based on their Li EWs) and kinematics of a subset of 26 likely-young FGK stars are presented and are compared with the ten MGs discussed in §2.4. The majority of the young subsample do not share kinematics with any MG, however, several objects have similar kinematics to the Octans-Near association.

In chapter 6, IR data are collated for M-dwarf members of MGs to identify IR excesses typical of debris discs. SED models were fitted to seventeen objects that were likely to have discs based their IR colour to derive disc temperatures and determine the nature of the IR excess. Only 9 of the 151 objects observed were found to evidence debris discs, all of which were < 40 Myr. The M-dwarf debris disc fractions in this work are compared with higher-mass stars to investigate their mass and age dependency.

3 Data reduction, analysis and technical information

Subsequent chapters in this thesis deal with optical spectroscopic data collected from two sources. This chapter describes the instruments and the data analysis techniques common to both.

3.1 Telescopes used to collate data

3.1.1 Nordic Optical Telescope – multi-echelle spectroscopy

Several objects in chapter 4 and the majority of the data in chapter 5 were obtained on two separate observing runs (consecutively $21-24$ June, 2010 and $27-29$ December, 2012) at the Ritchey-Chrétien 2.56 m Nordic Optical Telescope (NOT) in La Palma, combined with the Fibre-fed Echelle Spectrograph (FIES). Echelle spectrographs have the capability of measuring high-resolution spectra over a large wavelength range by cross-dispersing the incoming collimated light through a prism, which separates out the orders horizontally. Light is directed towards the fibres, $100\,\mu$m in size, providing an angular resolution of 1.3", which is then focused onto the charge-couple device (CCD). The CCD (name: CCD 42-40, Telting et al. 2014) has an array of 2k $\times$ 2k pixels, each of size $13.5\,\mu$m and samples a wavelength region of $370-730$ nm, whereas the spectrograph optics are designed for a wider wavelength range ($300-800$ nm). Towards the red-end of the CCD the dispersion is typically 0.045Å/pixel. The diffraction grating has 36.1 grooves/mm. In mid-resolution mode, this set-up provides a resolving power of $R \sim 46000$. FIES is protected and mounted in a heavily insulated building adjacent to the NOT and provides a high degree of mechanical and thermal stability (temperature variations are typically 0.02 K). This is particularly beneficial for precise RV measurements (see §3.3.1). The echelle grating utilises high orders to provide a high spectral dispersion for each order. These high-resolution data come

at the expense of potentially more complicated data reduction processes than those in conventional long-slit spectrographs as there is overlap between the edges of each order. Large losses of light in the fibres result in a low system efficiency, and once seeing effects and photon losses due to instrumentation are accounted for, the efficiency is ~ 9 per cent in the V-band in mid-resolution mode. Figure 3.1 is a diagram describing the basic operation of a multi-echelle spectrograph and its light path.

Data were reduced using FIESTOOL[1], a Python-based automated routine designed to extract spectra with FIES. The program automatically generates and utilises flats, biases and calibration lamp exposures (see §3.2 for an explanation of why these frames are required) using the following steps: firstly, a master bias frame was generated by averaging over 7 frames and any pixels that deviated by $> 5\sigma$ from the mean bias value were replaced by the mean. A master flat frame was created by averaging over a large number of flat frames ($\sim$ 25 for each night). FIESTOOL then allows the user to interactively define the location of the spectral orders using 'ECHELLE.APFIND' and 'ECHELLE.APEDIT' in IRAF.[2] The normalised flat is used to subtract the scattered light from the combined flat frame, which determines the 2 dimensional shape of each spectral order in the combined flat. Dividing the object frame by the normalised flat is a useful way to reduce fringing in the CCD and reduces the effect of the blaze shape present in each order, which is wavelength dependent. Each observing block consisted of a target exposure bracketed between 2 Th-Ar exposures either side to calibrate a wavelength scale. FIESTOOL invokes IRAF to map on a wavelength solution using the 'blue-atlas' available at `http://www.not.iac.es/instruments/fies/atlas/atlas_2.pdf`. Typical wavelength solutions are correct to easily within 0.05Å. The final reduced spectra spanned 78 orders, ranging from $\sim 3000 - 8000$Å, each with a wavelength range of $\sim$ 80Å. Figure 3.2 shows the separate echelle orders in the final reduced image of the RV standard star HD 190007. Sky subtraction was not used in the reduction

[1]software created and developed by E. Stempels (2005), details on data reduction are available at `http://www.not.iac.es/instruments/fies/fiestool/fiestool-manual-1.0.pdf`

[2]IRAF is distributed by the National Optical Astronomy Observatory, which is operated by the Association of Universities for Research in Astronomy (AURA) under cooperative agreement with the National Science Foundation.

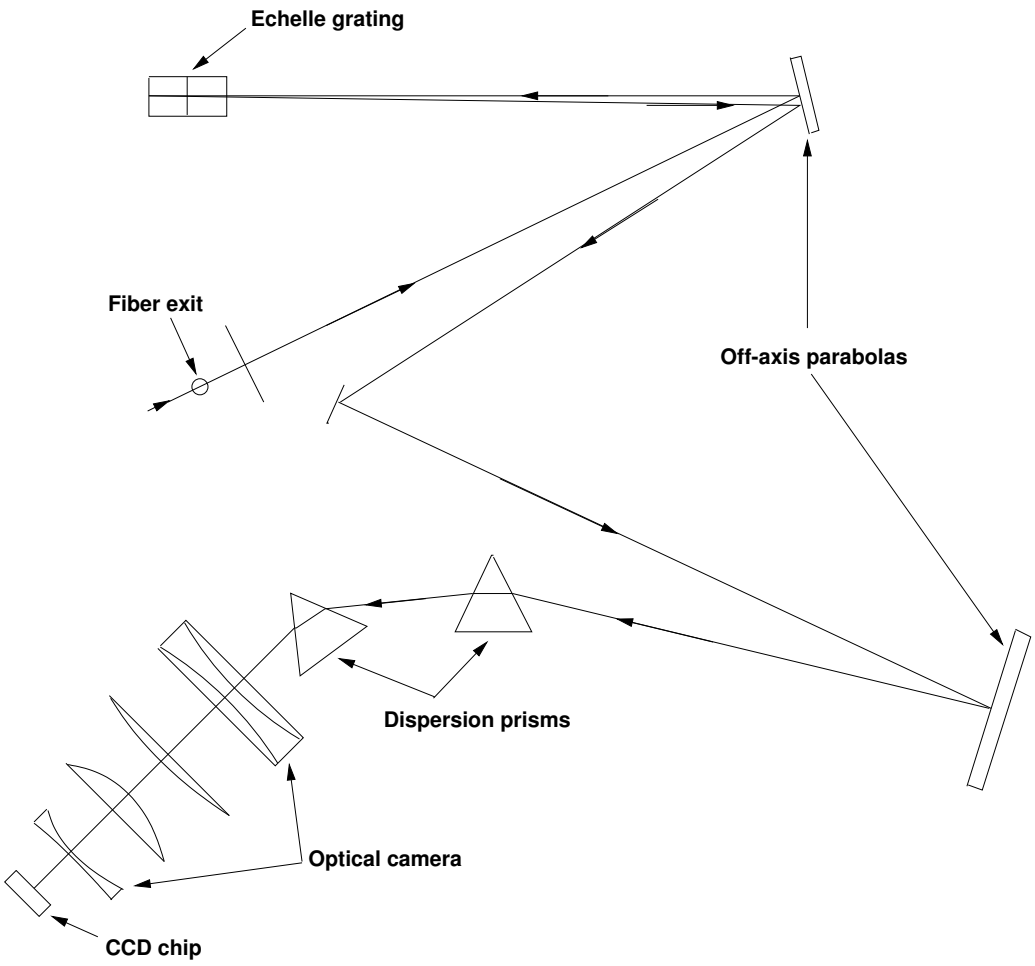

Figure 3.1:
A schematic showing the basic operation of a multi-echelle spectrograph. Light incident on the primary and secondary mirrors is focused towards an echelle grating, splitting the light into constituent wavelengths in a number of orders. This light travels through a set of dispersion prisms and lenses and is refocused using an optical camera. Finally, light from separate orders is detected by the CCD chip and is converted into photon counts per pixel.

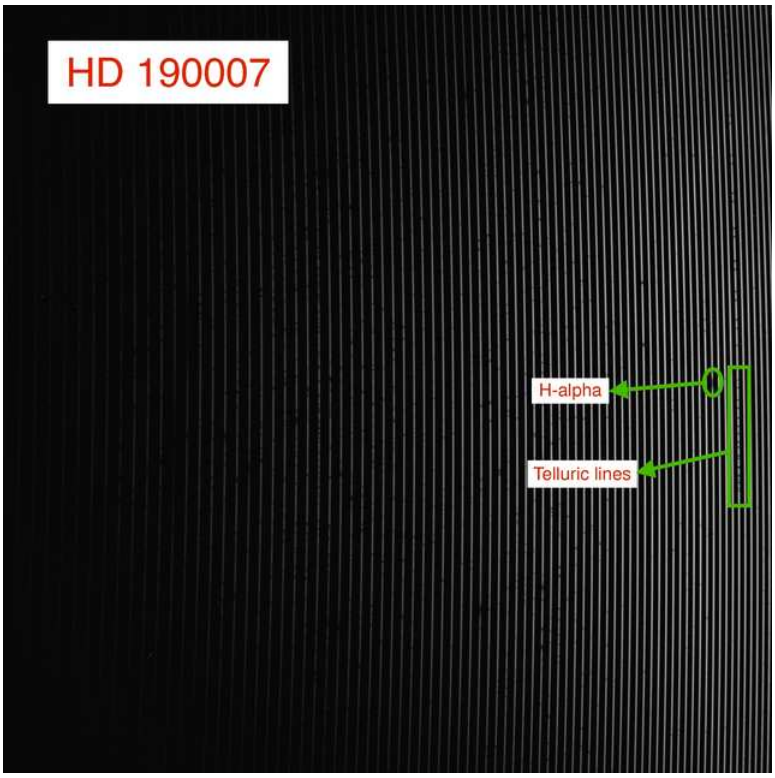

Figure 3.2:
The bias subtracted and flat-fielded echelle spectrum for one of the RV standard stars, HD 190007. The Hα feature is circled in order 70 and several features indicative of telluric absorption are located in orders 74 and 75.

process as flux calibration was unneccesary for the targets. The pixel size is 0.113Å. Signal-to-noise ratios (SNRs) improved greatly towards the red-end of the spectrum.

3.1.2 Isaac Newton Telescope – long-slit spectroscopy

Figure 3.3 demonstrates the layout of the long-slit Cassegrain spectrograph. Light incident on the telescope is focused through a slit of width 1.4 arcsec, which is then collimated and directed towards a diffraction grating, dispersing the light into con-

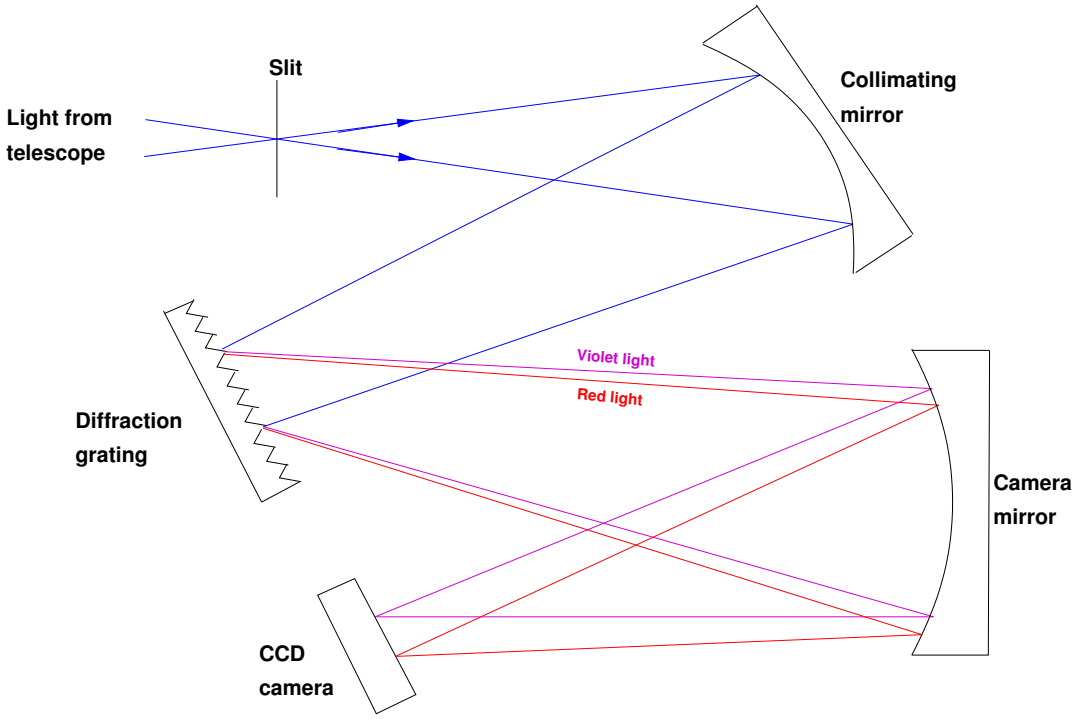

Figure 3.3:
A schematic to demonstrate the layout of a long-slit spectrograph. Light incident on the telescope is passed through the slit and directed towards a collimating mirror followed by a diffraction grating. The dispersed light is then focused towards the CCD camera where the image is recorded.

stituent wavelengths. The majority of targets observed in chapter 4 and follow up spectroscopy of a sub-sample of likely-young stars in chapter 5 were taken at the 2.5 m Isaac Newton Telescope (INT) in La Palma during a 7 night observing run from 20th March, 2013. The H1800V diffraction grating (1800 lines per mm) and a 1.4 arcsec slit gave a 2-pixel resolution of 0.7Å in the range $\lambda\lambda 6540 - 7170$Å.[3]

Observations were made on the Intermediate Dispersion Spectrograph (IDS), using the 235 mm camera and the RED+02 CCD. RED+02 has a pixel array of $\sim$2k $\times$

[3] http://www.ing.iac.es/Astronomy/instruments/ids/idsgrat_tables.html

4k, with each pixel 15 μm in size. The CCD is kept cool by liquid N_2 at temperatures around 158 K. At 6500Å the H1800V grating has an efficiency of $\sim$ 50 per cent and the RED+02 CCD has a quantum effiency of 90 per cent; much higher than the efficiency provided by the NOT set-up. However, both the spectrograph and the camera are mounted onto the telescope and this can result in increased RV variations. INT spectra were bracketed with Cu-Ne lamp exposures and extracted and wavelength calibrated using standard tasks from IRAF. Flats and biases were recorded at the start of the night, along with a sky exposure at twilight on a even region of sky near the zenith. A master flat frame was recorded separately for each night and applied to each target. The telluric standard, HD 60107 was observed each night in order to minimise telluric absorption lines due to mainly water vapour and the spectro-photometric standard Hiltner 600 was observed to allow for relative flux calibrated spectra. The spectra of a telluric standard and a spectro-photometric standard are presented in Figure 3.4.

3.2 Extracting wavelength-calibrated spectra from raw CCD images

A CCD is essentially a light sensitive semiconductor chip (usually made from Silicon), sub-divided into rows and columns each of several thousand pixels. When mounted to a telescope, incoming light passes through a narrow slit towards a collimating mirror, which is then directed towards a diffraction grating, dispersing the light into its constituent wavelengths. The dispersed light is then focused through a camera towards a CCD where photons impacting on the CCD pixels generate a small electric charge as a result of the photoelectric effect, which is stored and then read out onto a capacitor at the end of an exposure. The voltage reading scales linearly with the number of photons incident on the pixel. This signal is converted to digital units through a voltage amplifier, changing the units from e^-/pixel to counts/pixel (also known as analogue-to-digital units, ADU). The relationship between the two is known as the 'gain'.

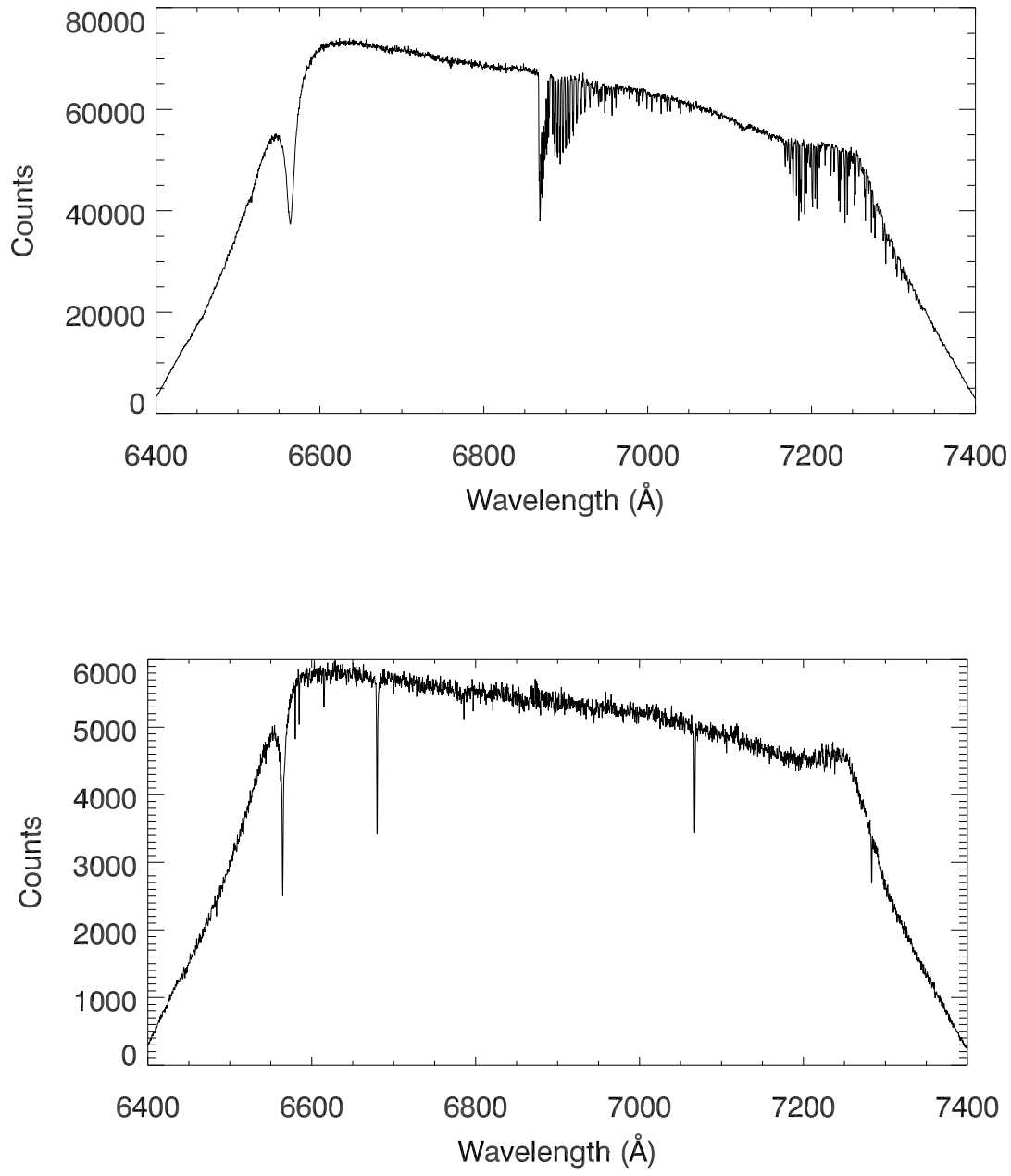

Figure 3.4:
Top: an example of a telluric standard, HD 60107, used to correct for water-vapour absorption lines in the INT spectra. Bottom: The spectro-photometric flux standard, Hiltner 600, used to provide relative flux calibrated spectra.

Before raw data files can be extracted from the CCD images, several correction frames are taken to remove effects specific to the detector:

Bias frames – A bias voltage is added as an offset to each image to ensure that all pixels contain a positive number of counts. This process is necessary for the correct conversion from e^-/pixel to counts/pixel. Bias frames are zero-second exposures taken with the camera shutter closed. Several exposures are median averaged, and the result is subsequently subtracted from the data to correct for the bias level.

Flat fields – Telescopes do not illuminate the CCD chip evenly. Surface inhomogeneities can cause shadowing effects, which are problematic for flux calibrations. To account for this, several exposures are made of a flat light source using a tungsten calibration lamp (used for data obtained at the NOT). Pixel-to-pixel sensitivity is improved by dividing the observations by a 'sensitivity map' created by stacking the flat fields. For INT observations a featureless region of sky at the zenith several minutes after sunset was recorded to account for dark sky emission lines.

The observed image on the CCD will only provide brightness as a function of pixel number. In order to accurately calibrate wavelengths of the observed spectra, short exposures of arc-lamps are taken before and after a science exposure. The arc lines are matched with an atlas of spectral lines, which are then mapped onto the data. Details of the arc-lamp exposures specific to the telescope observing run are provided in §3.1.1 and §3.1.2.

3.3 Determining parameters from spectroscopy

3.3.1 Radial velocities

Radial velocities (RVs) were measured by cross-correlating target spectra with standard stars similar in spectral-type that have precisely measured RVs (herein, RV standards). This is done by observing the relative shift in wavelength for a given number of spectral lines. In practice, one must characterise the peak of the cross-correlation function

(CCF) in terms of pixels between a target star and an RV standard to identify wavelength shift. A CCF uses all (unmasked) parts of the spectra to generate a lag that is given in pixels. To measure the lag at which the CCF reaches a peak, the FXCOR procedure was used in IRAF which bins spectra in equal velocity increments using the formulation in Tonry & Davis (1979). An example of the CCF measurement is provided in Figure 3.5.

RV standards were measured at the start of each night, and are listed in Tables 4.3 and 5.2 for INT and NOT observations, respectively. The RV standards were chosen to be within half a spectral class of the target being measured. For spectra obtained at the NOT the following strategy was employed to calculate an RV:

1) Measure the lag in RV between a target star and each RV standard ($\mathrm{RV_{lag}}$) for a given night of observing. This was done to ensure the observing conditions for each measurement were as similar as possible. SNR improves towards the red end of the spectrum, therefore measurements were made over 9 consecutive orders from 61 to 69 ($\lambda\lambda 5920 - 6520$Å), avoiding the saturated Na D lines at 5889.95Å and 5895.92Å(order 60), the broad Hα line at 6562.80Å (order 70) and contamination from telluric absorption in orders $74 - 78$. A weighted average relative RV for each target was then calculated over each order for each standard star correlation using the R quality factor in Tonry & Davis (1979). This is the ratio of the height of the true peak in the CCF compared to the average CCF value over the whole spectral order. Finally the RVs were transferred onto a heliocentric reference frame. Heliocentric RVs were obtained by calculating the heliocentric RV corrections for the positions of the target (C_{target}) and standard stars (C_{standard}) at the time of observation. The absolute heliocentric RV was calculated using $\mathrm{RV} = \mathrm{RV_{lag}} + \mathrm{RV_{standard}} + C_{\mathrm{standard}} - C_{\mathrm{target}}$.

2) Some orders match better than others. Poor CCF matches could be due to a spectral-type mismatch between an RV standard and a target, too much noise in the data, or, if the target is a spectroscopic binary, double line profiles may skew the CCF peak. The spectrum of a binary companion could be blended and more apparent in some orders than others. In some cases, no CCF peak was observed at all. In order to provide a more robust RV measurement (and also assess the precision) the clipped mean

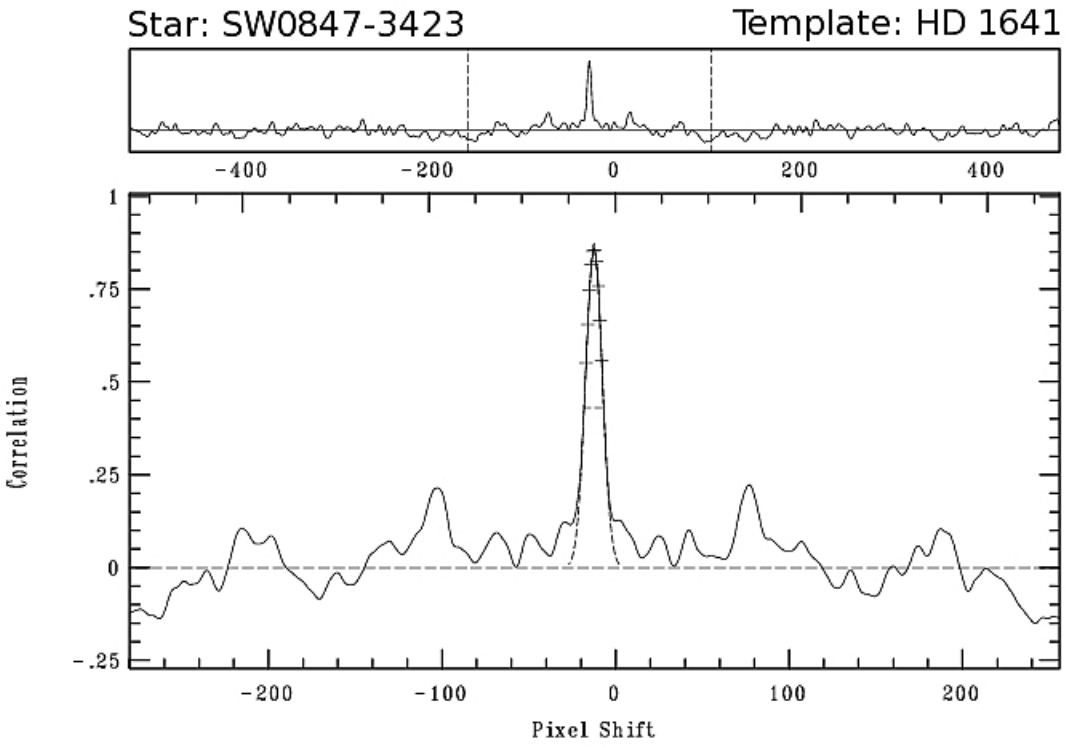

Figure 3.5:
An example of a CCF between a target star and an RV standard. The pixel shift required to produce the peak in the CCF corresponds to a shift in RV.

RV from 9 orders is taken. To account for the poor matches, the 'meanclip' routine in IDL was used. For each target the calculated RV between each RV standard was obtained for each spectral order. The combined mean velocity (over all 9 orders) was calculated and any measurements that were $> 2\sigma$ from the mean were clipped out, and the process was reiterated a maximum of 10 times.

3) Uncertainties were estimated from three independent sources. There were uncertainties in the RV standard, the standard deviation in RV measurement and a systematic error which was calculated after cross-correlation by measuring the average error between all RV standards (see §4.2.1 and 5.5.2). Each error source was added in quadrature.

A similar procedure was employed for RVs measured at the INT, although instead of using the whole 670Å spectral range as one block, the data were separated into 10 consecutive bins of 50Å from 6600Å to 7100Å (avoiding Hα at 6563Å), and the final RV was calculated by averaging the RV in each bin weighted by the R quality factor. To compensate for some telluric effects in the INT spectra, the A1V telluric standard HD 60107 was used to correct for spectral lines present due to atmospheric lines. The spectrum for the telluric standard is presented in Figure 3.4.

3.3.2 Rotational velocities

The line profile for a star rotating at a sufficiently large equatorial velocity will surpass the amount of broadening that can be attributable to solely thermal, collisional or turbulent effects. Spectral lines are broadened in rotating stars because there is a red-shift/blue-shift in RV between its two opposite limbs. As one cannot resolve the stellar surface, it is not observationally possible to detect the relative frequency shifts. Instead, the profile of the total emission across the surface is smeared out by an amount proportional to the rotation speed and thus the width of the broadened lines provides a measurement of rotation.

Projected rotational velocities ($v \sin i$) were estimated from the CCF full width half maxima (FWHM) using a set of simulations for objects observed on the NOT.

Broadened versions of a number of slowly rotating standard stars ($v \sin i$ standards, see Table 5.2) were produced by convolving high SNR spectra ($\simeq 100$) with a rotational broadening convolution kernel, using a limb-darkening parameter $\epsilon = 0.6$ (At 6000Å the solar value is $\epsilon = 0.56$). Because the $v \sin i$ standards all had a small finite rotational speed ($< 5\,\mathrm{km\,s^{-1}}$) a correction was made for the small $v \sin i$ values of the standards to set their non-rotating profiles at zero and artificial Gaussian noise was injected into the spun-up spectra. The high-frequency components in the spectra (wavenumber $k > 400$ was chosen after experimenting with several different values for k) were filtered out to minimise the effects of Gaussian noise (and also applied to the target spectra). Each standard was broadened in $1\,\mathrm{km\,s^{-1}}$ steps between 5 and $70\,\mathrm{km\,s^{-1}}$ and the FWHM of each broadened standard cross-correlation was recorded using FXCOR and repeated over the same echellogram orders as used in the RV analysis for NOT targets. Relationships between FWHM of the CCF and $v \sin i$ were derived using the means from the 9 orders weighted by the R quality factor (see Tonry & Davis 1979) for each standard. To ensure there were no spectral mismatches, only $v \sin i$ standard spectra within 5 spectral sub-classes of the target were used in each case. No $v \sin i$ values were measured from INT spectra because the SNR and resolution was not large enough.

4 Identifying low-mass members of the Beta Pictoris and AB Doradus Moving Groups

Significant parts of sections 4.1, 4.2 and 4.3 have appeared in Binks & Jeffries (2014).

Members of MGs like the BPMG and ABDMG represent some of the best observational targets for studying the early evolution of stars, their circumstellar environments and planetary systems. They are closer than equivalents in more spatially concentrated clusters and SFRs, offering better intrinsic sensitivity as well as angular and spatial resolution. Young gas giant planets around MG members are expected to be more luminous than in older systems, and young stars are frequently surrounded by debris discs that may evidence the formation of terrestrial planets or provide diagnostics of unseen planets. M-dwarfs are even better targets than G/K dwarfs for imaging planets because for planets of a given mass there will be a better contrast between planet and host star. Studies of BPMG members include: the identification and direct imaging of a planet (e.g., Lagrange et al. 2010; 2012; Bonnefoy et al. 2011; 2013) and debris disc (e.g., Smith & Terrile 1984; Holland et al. 1998; Golimowski et al. 2006) around its most luminous member, the A0 star β Pic; systematic surveys for planets, gas and debris discs using high angular resolution imaging or infrared diagnostics (e.g., Dent et al. 2013; Wahhaj et al. 2013; Brandt et al. 2014); and testing low-mass stellar and substellar evolutionary models using spatially resolved binary systems (e.g., Biller et al. 2010; Mugrauer et al. 2010). Objects in the ABDMG include CFBDSIR 2149-0403, a free-floating $4-7$ Jupiter-mass planet (Delorme et al. 2012); and the AB Doradus quadruple system, which includes the very-low mass AB Dor C ($0.090 \pm 0.005\,M_{\odot}$, Close et al. 2005). Details of both MGs are provided in §2.4.2 and §2.4.3.

Identifying low-mass candidates in MGs constrains the lithium depletion boundaries (LDBs, see §1.2.1) providing more precise and accurate ages, vital for interpreting the results from high spatial resolution imaging surveys or surveys for circumstellar material. This chapter describes new work to confirm the membership of published

candidates of the BPMG and the ABDMG using spectroscopy obtained at the INT and the NOT. ABDMG and BPMG candidates selected for observation are presented in §4.1 and the steps to calculate RVs, Hα and Li EWs and spectral-types are provided in §4.2 with the criteria required for MG membership. In §4.3.1 the method used to calculate the LDB age in BPMG is described and in §4.3.2 this is compared to the revised LDB age measured by Malo et al. (2014a) which incorporates surface magnetic fields. A comparison with previously measured ages for BPMG and implications for this updated age is presented in §4.3.3, focusing on the effect it has on the planetary-mass objects in BPMG. In §4.4 spectroscopic observations of a number of M-dwarf ABDMG candidates are assessed to ascertain membership. Candidates confirmed as ABDMG members from both these observations and previously reported members in the literature are presented and the LDB in ABDMG is located for the first time.

4.1 Observations

4.1.1 Target selection

In the last few years several dozen new M-dwarf candidates of BPMG and ABDMG have been identified through proper-motion based surveys (Lépine & Simon 2009; Schlieder et al. 2010; 2012a; Shkolnik et al. 2012; Malo et al. 2013; 2014a; 2014b; Gagné et al. 2014a; 2015). All targets chosen for observation were classed as likely new members in their respective surveys and had $V - K > 3.8$, corresponding to spectral-types later than M0 (Pecaut & Mamajek 2013). The initial candidate list consisted of 48 BPMG and 51 ABDMG candidates: 3 BPMG and 2 ABDMG targets from Shkolnik et al. (2012), 21 BPMG and 29 ABDMG from Schlieder, Lépine & Simon (2012) and 24 BPMG and 20 ABDMG from Malo et al. (2013). Spectra for 24 BPMG and 24 ABDMG candidates were obtained over 2 separate observing runs. All observed objects are listed in Tables 4.1 (BPMG) and 4.2 (ABDMG). Spectra for the confirmed BPMG and ABDMG members are presented in Figures 4.1 and 4.8, respectively.

Name	Ref	HJD	ET	M_K	V	J	K	RV	ΔRV	Hα EW	Li EW	Distance	SpT
(1)	(2)	(3)	(4)	(5)	(5)	(5)	(5)	(6)	(6)	(7)	(8)	(9)	(10)
BPMG candidates with $\Delta RV \leq 5\,km\,s^{-1}$													
J01351393−0712517	Sh12	291.400	2700	5.19 ± 0.14	13.43	8.96	8.08	6.5 ± 1.8[a]	2.7	−9.7	< 12	37.9 ± 2.4[h]	4.0
J02175601+1225266	S12	291.428	1800	4.93 ± 0.20	14.09	9.96	9.08	7.0 ± 1.4	1.4	−5.3	10	67.9 ± 6.1	4.0
J05015665+0108429[a1]	S12	291.515	1800	4.39 ± 0.12	11.74	7.21	6.37	19.7 ± 1.6	1.9	2.5	9	26.4 ± 2.1	2.9
J10141918+2104297[a2]	S12	291.714	1500	3.08 ± 0.09	10.08	7.07	6.26	3.1 ± 0.3	0.3	−0.9	< 9	43.3 ± 1.8[i]	−1.1
J05335981−0221323	M13	372.434	1500	4.60 ± 0.18	12.42	8.56	7.70	22.0 ± 1.3[b]	3.2	−3.3	< 31	41.8 ± 3.3	0.9
J16430128−1754272	M13	375.727	1200	4.69 ± 0.11	12.57	9.44	8.55	-10.0 ± 1.5[c]	3.5	−1.9	364	59.2 ± 2.8	0.6
J05015881+0958587**	M13	376.356	1800	4.39 ± 0.12	11.51	7.21	6.37	18.8 ± 1.5[d]	2.9	−5.2	15	24.9 ± 1.3[j]	4.1
J05241914−1601153**	M13	376.386	2100	5.34 ± 0.35	13.57	8.67	7.81	20.6 ± 4.1[e]	0.0	−6.7	217	31.7 ± 4.9	4.9
J05082729−2101444	M13	377.368	1800	6.42 ± 0.36	14.41	9.72	8.83	22.8 ± 3.8[f]	2.0	−13.6	618	30.8 ± 4.9	5.6
J19102820−2319484	M13	377.772	1800	4.02 ± 0.11	13.22	9.10	8.22	-7.9 ± 1.7	3.9	−5.7	< 38	69.2 ± 3.4	4.0
BPMG candidates with $\Delta RV > 5\,km\,s^{-1}$													
J11515681+0731262	S12	290.745	1500	5.24 ± 0.12	12.42	8.81	7.89	-11.1 ± 2.3	9.8	−3.3	< 31	34.0 ± 1.8	2.2
J00323480+0729271	Sh12	291.335	1700	4.36 ± 0.13	12.82	8.40	7.51	56.3 ± 1.4	54.6	−5.4	17	42.7 ± 2.6	4.1
J23512227+2344207	Sh12	291.361	1800	7.79 ± 0.10	14.18	9.68	8.82	38.6 ± 1.6	43.1	−5.0	17	16.1 ± 0.7	4.0
PYCJ 10019+6651	S12	291.655	1800	5.21 ± 0.14	12.29	9.07	8.22	-22.1 ± 1.3	15.6	−2.2	< 41	40.1 ± 2.6	1.2
J08224748+0757171	S12	291.701	1800	5.24 ± 0.22	14.29	10.06	9.21	-3.1 ± 1.9	16.2	−5.4	< 38	62.5 ± 6.2	4.2
1RXS J121151.0+124914	S12	291.746	1800	5.29 ± 0.24	12.60	9.50	8.80	-2.4 ± 3.8	5.4	−0.6	< 23	50.4 ± 2.1	0.5
J05320450−0305293**	M13	372.421	1500	3.73 ± 0.22	11.12	7.88	7.01	26.2 ± 1.6	7.2	−3.1	60	45.5 ± 4.5	2.8
J07293108+3556003 N	S12	372.455	700	4.80 ± 0.09	11.88	8.64	7.80	13.1 ± 1.4	5.7	−2.2	< 42	42.6 ± 2.6	1.1
J18495543−0134087	M13	374.734	900	4.57 ± 0.20	13.38	9.78	8.84	0.9 ± 2.2	18.6	−4.0	59	71.5 ± 6.9	2.4
J07264154+1850346	S12	375.399	1200	4.21 ± 0.19	13.83	9.98	9.13	-22.2 ± 1.3	34.8	−3.3	< 53	57.6 ± 5.2	2.9
J07293108+3556003S	S12	375.449	900	3.69 ± 0.12	11.88	8.64	7.80	14.0 ± 1.4	6.6	−2.3	< 30	39.9 ± 3.1	1.1
J04373746−0229282	Sh12	376.337	900	3.96 ± 0.32	10.53	7.13	6.41	25.1 ± 1.1	7.1	−3.4	12	31.2 ± 2.0	1.3
J05064946−2135038 N	M13	376.375	1800	4.69 ± 0.06	11.67	7.01	6.11	36.4 ± 1.5[g]	15.6	−6.2	< 41	19.2 ± 0.5[j]	4.6
J05064946−2135038 S	M13	376.375	900	4.70 ± 0.06	10.44	7.05	6.12	34.0 ± 1.4[g]	13.2	−6.4	< 41	19.2 ± 0.5[j]	2.1

Table 4.1: Observed BPMG candidates. (1) Object name prefixed by '2MASS' unless otherwise stated. (2) Reference paper: S12 = Schlieder, Lépine & Simon (2012), M13 = Malo et al. (2013), Sh12 = Shkolnik et al. (2012). (3) HJD is measured from 2456000 days. Measured in units of: (4) s (exposure time), (5) mag, (6) $km\,s^{-1}$, (7) Å, (8) mÅ. Where no Li EW was detected the 2σ upper limits is given, (9) pc, (10) spectral-type M-. (**) Unresolved binary. Previous radial velocity measurements of (a) $11.7 \pm 5.3\,km\,s^{-1}$ (Shkolnik et al. 2012), (b) $21.00 \pm 0.20\,km\,s^{-1}$ (Malo et al. 2014a), (c) $-11.3 \pm 3.5\,km\,s^{-1}$ (Zwitter et al. 2008), (d) $14.9 \pm 3.5\,km\,s^{-1}$ (Kharchenko et al. 2007), (e) $17.20 \pm 0.50\,km\,s^{-1}$ (Malo et al. 2014), (f) $26.60 \pm 0.43\,km\,s^{-1}$ (Malo et al. 2014), (g) $31.2 \pm 0.9\,km\,s^{-1}$ (Gizis, Reid & Hawley 2002). Trigonometric parallax reported in: (h) Shkolnik et al. (2012), (i) van Leeuwen (2007), (j) Riedel et al. (2014). Notes: (a1) Candidate rejected from group membership due to Hα absorption, (a2) Object removed from sample as it has a spectral-type earlier than M0. Spectral-types are calculated from TiO5 molecular band indices (see §4.2.3).

Name	Ref	HJD	ET	M_K	V	J	K	RV	ΔRV	Hα EW	Li EW	Distance	SpT
(1)	(2)	(3)	(4)	(5)	(5)	(5)	(5)	(6)	(6)	(7)	(8)	(9)	(10)
ABDMG candidates with $\Delta RV \leq 5\,km\,s^{-1}$													
J12574030+3513306 N**	S12	372.602	1500	6.07 ± 0.10	10.54	7.40	6.55	-14.1 ± 1.6	2.8	−1.8	< 51	17.6 ± 0.9	4.1
J12574030+3513306 S**	S12	372.602	700	6.07 ± 0.10	13.16	8.87	8.02	-18.0 ± 1.4	1.1	−1.8	< 47	17.6 ± 0.9	0.6
J15594729+4403595	M13	372.671	800	5.41 ± 0.21	11.83	8.51	7.62	-29.5 ± 3.8	0.4	−2.2	15	35.0 ± 2.5	1.3
PYC J16458+0343 AB	S12	372.685	700	6.56 ± 0.18	12.48	9.27	8.44	-23.3 ± 1.3	1.5	−1.5	184	49.1 ± 2.9	0.4
J10121768−0344404[a1]	M13	375.467	1500	5.52 ± 0.03	9.59	5.89	5.01	7.7 ± 1.0[a]	4.2	0.2	10	7.9 ± 0.1[d]	1.9
J12383713−2703349	M13	376.599	1200	6.60 ± 0.10	12.44	8.73	7.84	7.8 ± 1.2[b]	0.0	−1.8	< 63	25.2 ± 0.8	2.5
J09321267+3358285	S12	377.499	1200	5.84 ± 0.13	14.66	9.90	9.02	3.5 ± 1.2	4.8	−2.9	< 40	64.1 ± 3.5	3.7
ABDMG candidates with $\Delta RV > 5\,km\,s^{-1}$													
J09211104+4801538	S12	290.779	1800	6.59 ± 0.11	14.15	10.01	9.17	10.5 ± 2.1	17.7	−5.7	178	47.0 ± 2.0	4.1
1RXS J074450.5+000733	S12	372.509	1200	7.50 ± 0.15	14.30	10.09	9.23	4.2 ± 1.5	15.6	−4.6	10	39.2 ± 2.1	4.1
J09245082+3041373	S12	372.542	1800	6.93 ± 0.10	13.52	9.49	8.67	13.7 ± 2.3	13.1	−4.8	−100	33.3 ± 1.2	3.5
PYC J10043+5023	S12	372.576	1500	4.10 ± 0.13	11.67	8.08	7.20	-1.7 ± 1.5	8.6	−3.5	20	58.4 ± 3.0	2.5
PYC J13344+6956	S12	372.625	1500	5.73 ± 0.17	13.60	9.59	8.73	-14.1 ± 1.4	9.9	−6.3	< 38	47.0 ± 3.1	2.7
PYC J13351+5039N	S12	372.653	1800	5.31 ± 0.35	13.34*	9.31	8.37	-14.1 ± 1.3	8.5	−3.4	< 35	53.3 ± 3.6	3.7
PYC J13351+5039S	S12	372.653	1500	5.31 ± 0.35	12.72	10.33	9.43	-16.3 ± 1.4	6.4	−3.3	20	53.4 ± 3.6	2.5
J17520294+5637278	M13	372.713	1500	6.24 ± 0.24	13.32	9.23	8.38	-20.7 ± 1.3	10.2	−5.1	< 52	16.7 ± 2.1	3.8
J16232165+6149149**	M13	372.730	1200	6.32 ± 0.19	13.88	10.06	9.21	-18.3 ± 3.8	10.9	−4.9	< 38	35.9 ± 2.5	3.1
J05595569+5834155	S12	374.380	900	6.20 ± 0.22	13.56	9.03	8.18	469.3 ± 9.3	477.3	1.4	< 41	24.9 ± 0.8	−2.3
J06073185+4712266	S12	374.422	1800	7.18 ± 0.10	14.35	9.72	8.89	27.1 ± 1.8	28.9	−6.2	40	33.1 ± 1.2	4.6
J09022792+5848142	S12	374.480	1200	5.42 ± 0.15	13.30	9.85	8.95	0.1 ± 1.1	11.3	−2.1	< 38	70.4 ± 4.4	2.3
J09065515+4532299	S12	374.514	700	6.02 ± 0.13	13.27	9.87	9.04	9.2 ± 3.5	14.5	−3.2	< 51	58.3 ± 2.9	1.7
J14190331+6451463	M13	374.596	1800	7.04 ± 0.14	14.15	10.40	9.56	-12.0 ± 2.4	13.6	−4.6	54	37.0 ± 1.6	3.5
J15471191+4148218	S12	374.651	2100	6.62 ± 0.29	14.77	10.51	9.65	-11.5 ± 4.1	16.9	−5.5	40	54.7 ± 6.3	3.9
J16074132−1103073	M13	374.694	2000	7.38 ± 0.11	14.19	9.82	8.99	-19.4 ± 1.9[c]	5.2	−5.8	40	36.8 ± 1.4	4.2
PYC J08306+0421	S12	375.366	1200	6.46 ± 0.14	14.13	9.82	9.01	23.4 ± 4.9	7.5	−5.2	116	52.9 ± 3.1	3.8

Table 4.2: Observed ABDMG candidates. (1) Object name prefixed by '2MASS' unless otherwise stated. (2) Reference paper: S12 Schlieder, Lépine & Simon (2012), M13 = Malo et al. (2013), Sh12 = Shkolnik et al. (2012). (3) HJD is measured from 2456000 days. Measured in units of: (4) s (exposure time), (5) mag, (6) $km\,s^{-1}$, (7) Å, (8) mÅ. Where no Li EW was detected the 2σ upper limits is given, (9) pc, (10) spectral-type M-. (**) Unresolved binary. Radial velocity measurements of (a) $9.0 \pm 1.4\,km\,s^{-1}$ (Kharchenko et al. 2007), (b) $9.60 \pm 0.20\,km\,s^{-1}$ (Malo et al. 2014), (c) $-8.5 \pm 1.2\,km\,s^{-1}$ (Malo et al. 2014). Trigonometric parallax reported in (d) van Leeuwen (2007). (a1) Candidate rejected from group membership due to Hα absorption. Spectral-types are calculated from TiO5 molecular band indices (see §4.2.3). (*) No V magnitude, $V - K$ interpolated from table 5 in Pecaut & Mamajek (2013).

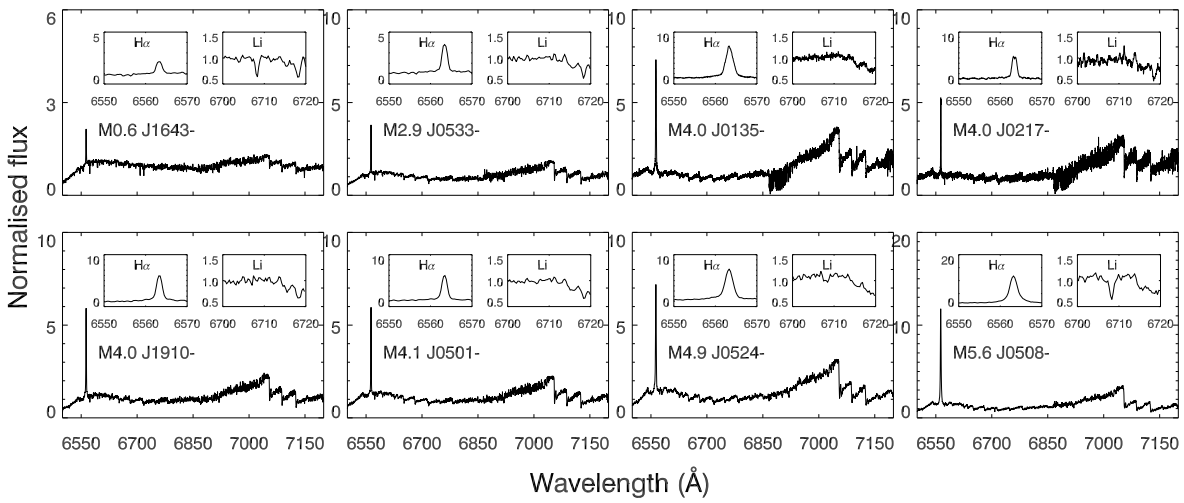

Figure 4.1: Spectra for the eight M-dwarf RV-confirmed BPMG members which also qualify from the requirements of Hα in emission and suitable placement on the CMD (see §4.2.4 for a description of the membership criteria). Full 2MASS names are given in Table 4.1. The inserts in each plot are normalised spectra in the regions of the Hα and Li I 6708Å line. All spectra (excluding objects 'J0135-' and 'J0217-', observed at the NOT, which have been blaze-corrected) have been subject to relative flux-calibration and telluric correction.

4.1.2 Spectroscopic data

Eleven BPMG candidates were observed on 28-29 December 2012 using the 2.56 m Nordic Optical Telescope (NOT) and Fibre-fed Echelle Spectrograph (FIES, $\lambda\lambda 3700 - 7400$Å, $R \sim 46000$, see §3.1.1 for the observational set-up). A second observing run on 20-26 March 2013 observed 24 ABDMG candidates and an additional 13 BPMG candidates, using the 2.5 m Isaac Newton Telescope (INT) and Intermediate Dispersion Spectrograph ($\lambda\lambda 6500 - 7200$Å. §3.1.2 provides details for the observational set-up). No objects were observed on both the NOT and the INT.

RV standards were measured at the beginning and end of each night. To avoid spectral-type mismatches, only M-dwarf RV standards were measured. These are all listed in Table 4.3. For the INT data, a telluric standard star, HD 60107 (spectral-type A1V, see Figure 3.4 and Table 4.3) was used to remove lines due to the Earth's atmosphere. In practice, this was achieved by normalising the spectra for both the telluric standard and target star. The spectrum of the inverted, normalised telluric standard was then multiplied by the normalised target spectrum. This has the effect of cancelling out the telluric lines such that they become level with the continuum. A spectro-photometric standard, Hiltner 600 (Figure 3.4), was observed to provide a relative flux-calibration of target spectra observed at the INT. Relative fluxes were measured using the IRAF routines STANDARD, SENSFUNC and CALIBRATE. Flux-calibration was necessary to measure spectral-types using the TiO5 feature around $\lambda\lambda 7100-7150$Å (see §4.2.3 and Figure 4.3). No flux-calibration was applied to objects observed at the NOT therefore the TiO5 band indices for these are likely to be less reliable because the normalised spectra may be less representative of the TiO5 band ratios (see §4.2.3).

4.2 Analysis

4.2.1 RVs

Heliocentric RVs were calculated by cross-correlating template stars with target stars using the FXCOR procedure in IRAF. The procedure to calculate RVs is outlined in §3.3.1. RVs from the NOT spectra were obtained by averaging over nine orders (orders $61-69$, consecutively between $\lambda\lambda 5880-6460$Å), using RV templates measured on the same night for which there was a spectral-type match within half a class. The RVs measured at the INT were carried out using the same cross-correlation technique using 10 successive wavelength bins of 50Å between 6600 and 7100Å. The final RVs were calculated using a weighting function for each wavelength bin based on the Tonry-Davis R factor (described in §3.3.1). RVs were averaged over all the template stars within half a spectral class of the target star. There were three major sources of error in the RV calculations: the uncertainty in RV of the template star (which at most

was $0.18\,\mathrm{km\,s^{-1}}$), the standard error in the relative RV based on several measurements of the same target star and an additional systematic error in the velocities of the RV standards, which was calculated by cross-correlating all of the RV standards with one another and producing a matrix of RV errors for each standard. These were measured to be 0.27 and $0.49\,\mathrm{km\,s^{-1}}$ for the NOT and INT, respectively. Each source of error was treated independently and added in quadrature.

4.2.2 Li and Hα EW measurement

The Li line observed in this thesis is the $1s^2 2s$ to $1s^2 2p$ transition, which emits photons with a wavelength of 6707.8Å (herein referred to as the 6708Å line). As a result of Russell-Saunders coupling, this line manifests as a doublet. The spin-up and spin-down

Name	Run	Spectral-type	RV ($\mathrm{km\,s^{-1}}$)	$v \sin i$ ($\mathrm{km\,s^{-1}}$)
HD 190007	NOT	M0.0V	18.275 ± 0.120	2.8 ± 1.0
GJ 686	INT	M1.0V	-9.499 ± 0.032	6.2 ± 3.7
HD 119850	INT	M1.5V	15.778 ± 0.061	1.8 ± 0.7
GJ 411	NOT	M2.0V	-84.683 ± 0.030	1.6 ± 1.0
HD 265866	INT	M3.0V	22.942 ± 0.055	2.4 (no error provided)
GJ 273	INT	M3.5V	18.210 ± 0.030	3.4 ± 2.1
GJ 526	NOT	M4.0V	15.778 ± 0.061	1.8 ± 0.7
GJ 699	INT	M4.0V	-110.416 ± 0.180	3.3 ± 1.5

Name	V (mag)	Spectral-type	Standard type
Hiltner 600	10.42	B1V	Spectro-photometric
HD 60107	5.27	A1V	Telluric

Table 4.3: Top: RV standards observed at the INT and NOT. All RVs are from (Chubak et al. 2012) and $v \sin i$ values are from (Glebocki & Gnacinski 2005). Bottom: The spectro-photometric and telluric standard observed at the INT.

states result in a fine splitting of the line, causing two lines at 6707.76Å and 6707.91Å. There is also an adjacent ^{6}Li doublet at 6707.92 and 6708.07Å, however, because ^{6}Li is destroyed very early in PMS evolution the abundance of ^{6}Li is very low (assumed to be absent) compared to ^{7}Li. In practice, none of the doublets surrounding the 6708Å line are resolved.

There is a weak Fe I contaminating line at 6707.45Å which often contributes to the 6708Å absorption line. Soderblom et al. (1993b) suggest a correction of $20(B-V)-3$mÅ to represent the EW of the Fe I line. It is also possible to account for the line using synthetic spectra. Although the work in this chapter does not account for Fe contamination (as it is only necessary to observe a strong Li absorption feature $>$ 200 mÅ when locating the LDB), in chapter 5 the Soderblom et al. (1993b) relationship is used to deblend the Fe line from the Li EWs at 6708 Å.

The Hα line, observed at 6562.8Å, is a direct result of photon emission in the $n_{3\rightarrow2}$ energy transition. Hα emission is a prominent feature in the atmospheres of young M-dwarfs (see Gizis 1997; Hawley et al. 2002). The use of Hα as an empirical youth indicator is reviewed in §1.4.2.3.

Other competing effects in stellar atmospheres give finite width to the absorption/emission profile. Usually rotation plays the dominant role in broadening the spectral lines, particularly in young M-dwarfs. Combined effects due to damping, micro- and macro-turbulence, pressure- and thermal-broadening are also present. Natural broadening is prevalent in all spectral lines but is relatively weak.

Although it is possible to measure abundances using synthetic spectral line fitting, in this thesis the relative abundance of an element from a spectral line is obtained by measuring the EW. This is done in practice by defining a rectangular area in an absorption profile and a continuum level across the spectral feature so that the rectangular area is equal to the area of the absorption profile. Formally this is given as:

$$\mathrm{EW}_\lambda = \int_{\lambda_1}^{\lambda_2} (1 - F_\lambda/F_c)\,\mathrm{d}\lambda, \tag{4.1}$$

where F_λ is the amount of flux at a given wavelength, F_C is the expected flux

from the continuum and λ_1 and λ_2 are wavelengths either side of the feature where the line profile becomes level with the continuum. Formally these wings should be infinitely large, however in practice lines are only measured until the wings become indistinguishable from the noise in the continuum level. For a large Li EW line ($\sim$ 250mÅ), this may lead to EW underestimates of up to 10 mÅ. Li and Hα EWs were measured relative to a pseudo-continuum using the SPLOT procedure in IRAF. EW uncertainties were approximated as $1.6\times\sqrt{\mathrm{FWHM}\times p}/\mathrm{SNR}$ (Cayrel de Strobel & Spite 1988), where FWHM, p and SNR are the full-width half maximum of the measured line, pixel size (in Å) and the signal-to-noise ratio, respectively. If no Li feature was seen, an upper limit was estimated as twice this uncertainty assuming a FWHM of 0.7Å. In this chapter no attempt is made to calculate Li abundance. Instead, the curve of growth table in Palla et al. (2007) is used to categorise objects as Li-rich/Li-poor. The criteria for an Li-rich object is described in §4.3.1 when attempting to locate the LDB in BPMG. The exposure times for observed candidates are listed in Tables 4.1 and 4.2. SNRs were typically $\sim$ 50 for spectra taken at the NOT and $\sim$ 30 for objects on the INT. Figure 4.1 displays the normalised spectra for the eight confirmed BPMG M-dwarf members observed either at the NOT or the INT that were used to define the LDB in §4.3.1. The top-left insert in each panel indicates the strength of the Hα emission, and the top-right insert displays a 20Å range close to the Li 6708Å feature. Spectra for two other objects that satisfied RV criteria but failed on other grounds (see §4.2.4) are presented in Figure 4.2. The spectra for confirmed ABDMG members are presented in the same format in Figure 4.8 and spectra for all other objects that failed to qualify as members of either BPMG or ABDMG are provided in Figures A.1 and A.2, respectively.

4.2.3 Spectral-types

Spectral-types were determined from the TiO5 molecular band flux ratio $f(\lambda\lambda7125-7136\text{Å})\,/\,f(\lambda\lambda7042-7046\text{Å})$ after spectra had been heliocentrically corrected. In early- to mid- M-dwarfs the depth of this feature becomes more pronounced for cooler stars

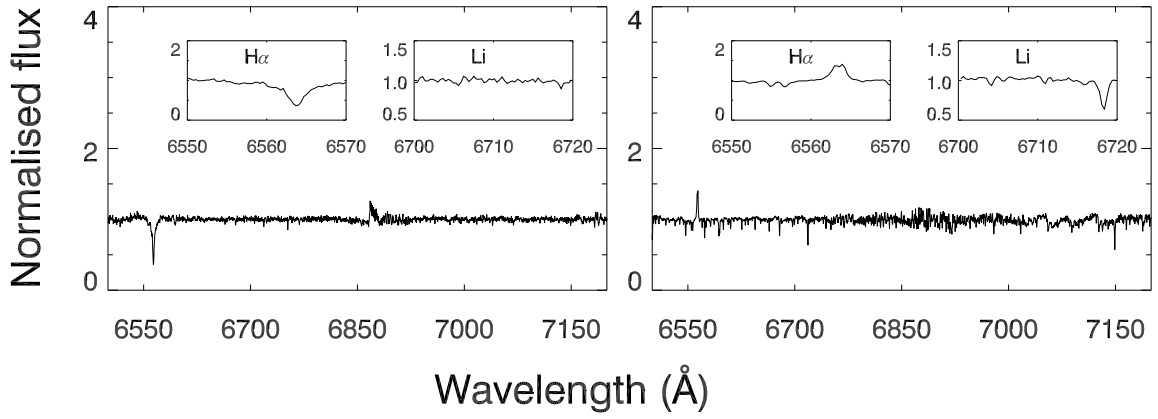

Figure 4.2: Spectra for the two BPMG candidates which satisfied the RV criterion, however failed on other grounds. The left panel, J05015665+0108429, has Hα in absorption rather than emission. The right panel, J10141918+2104297, was found to have a spectral-type earlier than M.

(see the sequence of M-dwarf spectra in Figure 4.1) and TiO5 ratios are calibrated for spectral-types K5-M7 (Gizis 1997). The TiO5-calibrated spectral-types for the newly observed targets were compared with published spectral-types for previously confirmed members from Zuckerman & Song (2004) and Malo et al. (2013). Plotted as a function of $V - K$ colour, Figure 4.3 suggests the calibration is consistent with literature values and that the precision is about half of a subclass.

4.2.4 Testing membership criteria

Measurements of RV, spectral-type, Hα EW and Li EW for all observed candidates are provided in Tables 4.1 (BPMG) and 4.2 (ABDMG). The mean Galactic space motion and convergent point of the BPMG and ABDMG (provided in Table 2.1) leads to a predicted RV for group members as a function of their sky position (see §2.2.2 for details). For 10 observed candidates in the BPMG and 7 in the ABDMG, the difference between this predicted RV and the measured RV (ΔRV in Tables 4.1 and 4.2) was found

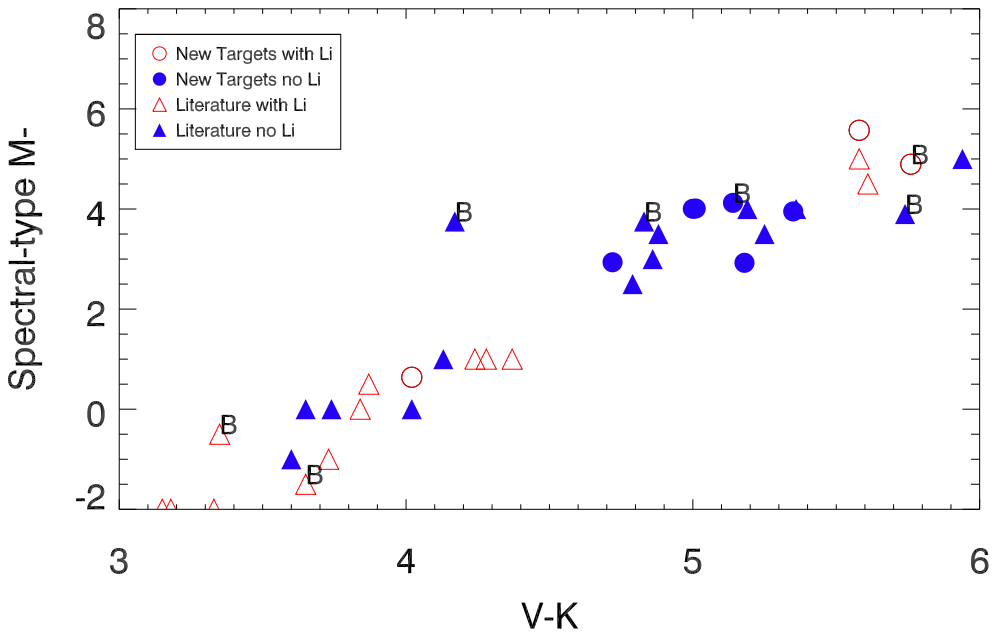

Figure 4.3: Comparison of $V - K$ with estimated spectral-types. Spectral-types for the observed candidates were calculated from the relative TiO5 band fluxes, using the prescription in Gizis (1997). Any objects known to be unresolved binaries are marked with a 'B'. Note that values of -2 and -1 correspond to spectral-types K5 and K7, respectively.

to be $< 5\,\mathrm{km\,s^{-1}}$ which, in common with previous work (e.g., Schlieder, Lépine & Simon 2012), is used as a required membership criterion. An extra requirement is that an M-dwarf member has Hα in emission, due to the strong chromospheric activity of young stars (Gizis, Reid & Hawley 2002; Kiraga & Stepien 2007). One object in BPMG (J0501-) and one in ABDMG (J1012-) satisfy RV criteria but fail membership because they have Hα in absorption. Finally, the predicted tangential velocity of a candidate combined with its proper-motion, taken from the source paper listed in Table 4.1, leads to a 'kinematic distance' (see §2.2.3). For 2 of the BPMG candidates that pass the RV and Hα tests, there is a trigonometric parallax that agrees reasonably well with this kinematic distance, both of which define the LDB in BPMG. For the rest, an assessment is made of an object's location on an absolute magnitude versus colour diagram using the kinematic distance. A true member must lie on or above the sequence defined by previously known members. Some latitude is allowed above the sequence, because targets may be unresolved binaries (two are known to be in BPMG and ABDMG – see Tables 4.1 and 4.2) up to 0.75 mag brighter than single stars of similar colour.

The colour-absolute-magnitude and spectral-type-magnitude diagrams for confirmed BPMG members are shown in Figures 4.4 and 4.5 and the M_K versus $V - K$ CMD for confirmed ABDMG members is provided in Figure 4.9. One object in BPMG (J1014-) was found to have a spectral-type earlier than M0 upon assessment of its TiO5 ratio. The remaining 8 objects in were consistent with all 3 group membership criteria, had spectral-types later than M0 and are all assumed to be BPMG members. These are listed in Table 4.1 and their spectra presented in Figure 4.1. Six objects were confirmed as ABDMG members. Observed BPMG and ABDMG members are supplemented with previously reported members from Zuckerman & Song (2004), Mentuch et al. (2008), Torres et al. (2008), Lépine & Simon (2009), Schlieder, Lépine & Simon (2010), Yee & Jensen (2010), Kiss et al. (2011) and Malo et al. (2013; 2014a). These were subjected to the same RV criteria to test for membership (no Hα measurements were available). All supplementary BPMG and ABDMG candidates from literature sources are provided in Tables 4.4 and 4.5 and are separated into two sub-tables of 'confirmed' and 'rejected' candidates.

Name (2MASS-)	Ref	RV ($\mathrm{km\,s^{-1}}$)	$\mathrm{RV_{pred}}$ ($\mathrm{km\,s^{-1}}$)	M_K (mag)	$V-K$ (mag)	Li EW (mÅ)	SpT
Literature candidates with $\Delta\mathrm{RV} \leq 5\,\mathrm{km\,s^{-1}}$							
HIP 21547	Z04	21.0 ± 4.5	18.0	2.20 ± 0.03	0.67 ± 0.02		F0V
HIP 560	Z04	6.5 ± 3.5	5.2	2.26 ± 0.04	0.94 ± 0.02	87	F2IV
HIP 10680	Z04	4.9 ± 1.4	4.4	3.11 ± 0.22	1.21 ± 0.03	138	F5V
HIP 99273	Z04	−5.8 ± 2.2	−9.1	2.48 ± 0.11	1.11 ± 0.03	58	F5V
HIP 95270	Z04	0.2 ± 0.4	−1.2	2.34 ± 0.08	1.12 ± 0.03	120	F5.5
HIP 25486	Z04	21.1 ± 1.6	20.2	2.77 ± 0.03	1.37 ± 0.02	135	F7
HIP 103311	Z04	−9.0 ± 3.0	−9.2	2.51 ± 0.08	1.49 ± 0.02	150	F8V
HIP 10679	Z04	5.0 ± 1.3	4.4	4.11 ± 0.36	1.48 ± 0.02	162	G2V
HD 161460	K11	1.4 ± 4.0	−2.5	2.32 ± 0.10	2.20 ± 0.03	320	K0IV
HIP 76629 A	Z04	3.6 ± 1.0	0.8	2.92 ± 0.10	2.29 ± 0.03	292	K0V
HIP 92680	L09	−4.2 ± 0.2	−3.2	2.81 ± 0.11	2.04 ± 0.03	287	K0Vp
CD−547336	K11	1.6 ± 1.4	−2.1	3.09 ± 0.10	2.14 ± 0.04	360	K1V
CD−2613904	T08	−8.1 ± 0.3	−11.0	2.85 ± 0.12	2.73 ± 0.04	320	K4Ve
J14142141−1521215	M13	−4.1 ± 0.0	−7.4	4.22 ± 0.33	3.63 ± 0.05		K5V
J22424896−7142211	M13	8.6 ± 0.5	8.4	3.98 ± 0.10	3.65 ± 0.04	440	K5V+K7Ve
BD +05 378	Z04	10.0 ± 4.0	11.2	3.96 ± 0.14	3.15 ± 0.04	450	K6Ve(sb1)
AO Men	Z04	16.2 ± 1.0	15.9	3.88 ± 0.08	3.20 ± 0.05	420	K6/7
CD−641208	Z04	2.0 ± 4.2	2.1	3.82 ± 0.03	3.33 ± 0.06	490	K7
J21212873−6655063	M13	3.3 ± 0.0	5.4	4.61 ± 0.10	3.60 ± 0.03		K7V
J18504448−3147472	M13	−6.0 ± 1.0	−9.6	3.85 ± 0.09	3.73 ± 0.03	492	K7Ve
J20560274−1710538	M13	−6.9 ± 0.0	−9.2	3.67 ± 0.12	3.35 ± 0.08	420	K7V+M0V
HIP 11437 A	Z04	6.7 ± 0.0	4.5	4.08 ± 0.20	3.22 ± 0.10		K8
HIP 11437 B	Z04	6.0 ± 0.0	4.5	4.92 ± 0.20	4.54 ± 0.30	270	M0
J19560438−3207376	M13	−7.2 ± 0.4	−7.8	4.05 ± 0.09	3.74 ± 0.03	110	M0V
HIP 23200	T08	19.8 ± 0.0	17.7	4.20 ± 0.15	3.84 ± 0.04	360	M0Ve
J23323085−1215513	M13	1.8 ± 0.7	0.6	4.32 ± 0.08	4.02 ± 0.10	185	M0Ve
J22004158+2715135	M13	−13.3 ± 2.4	−12.7	4.35 ± 0.11	3.65 ± 0.04		M0.0Ve
HIP 23309	Z04	19.4 ± 0.3	18.8	4.10 ± 0.07	3.87 ± 0.04	360	M0.5 kee
J11493184−7851011	M13	13.4 ± 1.3	10.6	3.74 ± 0.18	4.28 ± 0.09	560	M1V
J20013718−3313139	M13	−5.6 ± 1.8	−7.3	4.22 ± 0.10	4.13 ± 0.04	−100	M1V
HIP 102409	Z04	−4.1 ± 0.0	−6.0	4.55 ± 0.30	4.36 ± 0.04	80	M1Ve
GSC 07396−00759	T08	−5.7 ± 4.0	−9.7	3.57 ± 0.28	4.24 ± 0.30	200	M1Ve
J18465255−6210366	M13	2.4 ± 0.1	1.1	4.16 ± 0.09	4.37 ± 0.18	332	M1Ve
J21100535−1919573	M13	−5.1 ± 1.0	−7.9	4.62 ± 0.09	5.94 ± 0.04		M2V
BD−21 1074 A	T08	21.2 ± 0.9	20.8	4.62 ± 0.36	4.32 ± 0.04	20	M2V
HD 164249 B	Z04	−0.4 ± 0.5	−3.1	2.50 ± 0.06	4.10 ± 0.30	70	M2Ve
J00172353−6645124	M13	11.4 ± 0.8	10.6	4.84 ± 0.11	4.79 ± 0.04		M2.5V
HIP 11152	S10	10.4 ± 2.0	6.2	5.07 ± 0.18	3.97 ± 0.13		M3Ve
J17292067−5014529	M13	−0.4 ± 0.0	−3.5	3.77 ± 0.16	4.86 ± 0.06	50	M3Ve
HIP 84586 C	Z04	2.7 ± 1.8	2.7	5.14 ± 0.04	5.19 ± 0.30	20	M3Ve
J18420694−5554254	M13	1.0 ± 0.7	−1.3	4.89 ± 0.11	4.88 ± 0.30		M3.5V
J23500639+2659519	M13	−0.7 ± 2.8	−5.1	7.45 ± 0.09	5.25 ± 0.02		M3.5V
J05064946−2135038	M13	21.2 ± 0.9	20.8	4.69 ± 0.06	4.17 ± 0.30	20	M3.5Ve+M4V
J23172807+1936469	M13	−3.7 ± 0.0	−6.4	6.79 ± 0.09	4.83 ± 0.09		M3.5+M4.5
J20434114−2433534	M13	−6.0 ± 0.9	−8.0	5.54 ± 0.31	5.74 ± 0.30		M3.7+M4.1
HIP 112312 A	Z04	2.5 ± 0.6	1.3	5.10 ± 0.19	5.17 ± 0.03	0	M4IVe
J01365516−0647379	M13	12.2 ± 0.4	9.3	6.96 ± 0.04	5.19 ± 0.04		M4V
J23512227+2344207	M13	−2.1 ± 0.5	−4.5	7.84 ± 0.09	5.36 ± 0.05		M4V
HIP 102141 A	Z04	−3.7 ± 0.0	−5.9	4.79 ± 0.09	5.40 ± 0.30	0	M4Ve
HIP 102141 B	Z04	−5.1 ± 0.1	−5.9	4.79 ± 0.09	5.40 ± 0.30	0	M4Ve
HIP 76629 BC	Z04	0.1 ± 2.0	0.8	6.26 ± 0.10	5.61 ± 0.30	460	M4.5
HIP 112312 B	Z04	−1.7 ± 2.4	1.3	5.96 ± 0.19	5.58 ± 0.04	450	M5IVe
J01112542+1526214	M13	4.0 ± 0.1	3.1	6.52 ± 0.09	6.22 ± 0.04	629	M5V+M6V
TWA 22 AB	T08	13.6 ± 0.3	13.1	6.47 ± 0.03	6.27 ± 0.02	510	M6Ve+M6Ve
Literature candidates with $\Delta\mathrm{RV} > 5\,\mathrm{km\,s^{-1}}$ or lacking an RV measurement							
HIP 86598	K11	2.4 ± 1.1	−3.4	2.69 ± 0.14	1.36 ± 0.03		F9V
J06135773−2723550	M13	−6.8 ± 0.0	21.3	5.36 ± 0.11	2.96 ± 0.13	170	K5V
V* V4046 Sgr	T08		−9.7	2.98 ± 0.14	3.43 ± 0.08	440	K5V
J05224571−3917062	M13	36.4 ± 0.0	21.0	4.82 ± 0.12	3.39 ± 0.06	85	K7V
J18580415−2953045	M13	−4.9 ± 1.0	−10.1	3.55 ± 0.10	3.78 ± 0.03	483	M0Ve
V* V1311 Ori	T08		19.0	3.95 ± 0.20	4.11 ± 0.11	100	M2V
J19312434−2134226	M13	−26.0 ± 1.8	−11.7	5.46 ± 0.10	4.72 ± 0.04		M2.5V
J23301341−2023271	M13	−5.7 ± 0.0	2.0	5.29 ± 0.12	4.78 ± 0.04	0	M3V

Table 4.4: Supplementary BPMG objects from the literature. Ref column: Z04 = Zuckerman & Song (2004), T08 = Torres et al. (2008), L09 = Lépine & Simon (2009), S10 = Schlieder, Lépine & Simon (2010), K11 = Kiss et al. (2011), M13 = Malo et al. (2013). Spectral-types are from the source paper. Objects with Li EW = 0 do not have the data with which to estimate upper limits.

Name (2MASS-)	Ref	RV ($\mathrm{km\,s^{-1}}$)	$\mathrm{RV_{pred}}$ ($\mathrm{km\,s^{-1}}$)	M_K (mag)	$V-K$ (mag)	Li EW (mÅ)	SpT
Literature candidates with $\Delta\mathrm{RV} \leq 5\,\mathrm{km\,s^{-1}}$							
HIP 18859	Z04	17.6 ± 0.2	18.7	2.81 ± 0.04	1.21 ± 0.04	97	F5V
HIP 19183	Z04	15.9 ± 1.3	18.1	2.87 ± 0.11	1.21 ± 0.04		F5V
HIP 6276	Z04	8.3 ± 0.4	11.2	3.87 ± 0.08	1.85 ± 0.02	153	G0V
HIP 14684	T08	14.6 ± 0.7	19.1	3.84 ± 0.10	1.80 ± 0.04		G0V
HIP 82688	Z04	−16.5 ± 0.4	−18.9	3.01 ± 0.10	1.47 ± 0.02	133	G0V
HIP 113579	Z04	6.1 ± 0.2	4.3	3.50 ± 0.06	1.55 ± 0.04		G3V
HIP 115162	Z04	−19.7 ± 0.2	−18.6	3.72 ± 0.13	1.72 ± 0.03	160	G4V
HIP 12638	Z04	−4.2 ± 0.2	−3.5	3.76 ± 0.24	1.74 ± 0.02	158	G5V
HIP 14809	Z04	5.2 ± 0.2	5.8	3.32 ± 0.14	1.55 ± 0.04	150	G5V
HIP 116910	T08	11.1 ± 1.7	11.3	3.61 ± 0.16	1.77 ± 0.04		G8V
HIP 26373	Z04	32.2 ± 0.2	31.3	3.81 ± 0.08	2.11 ± 0.10		K0V
HIP 118008	Z04	12.1 ± 0.5	13.4	4.20 ± 0.05	2.34 ± 0.04		K3V
HIP 12635	Z04	−4.1 ± 0.3	−3.5	4.27 ± 0.29	2.52 ± 0.04	146	K3.5V
J01372322+2657119	M13	−5.9 ± 3.0	−2.9	4.74 ± 0.06	3.21 ± 0.07		K5Ve
HIP 26369	Z04	31.1 ± 1.1	31.3	4.61 ± 0.43	2.97 ± 0.04	44	K7V
HIP 31878	Z04	30.5 ± 0.7	31.3	4.75 ± 0.05	3.19 ± 0.02	50	K7V
J00340843+2523498	M14	−8.9 ± 1.3	−8.1	4.16 ± 0.07	3.44 ± 0.05		K7Ve
HIP 106231	Z04	−17.4 ± 1.0	−21.6	4.41 ± 0.06	2.87 ± 0.03	233	K8V
J20465795−0259320	M13	−13.8 ± 0.9	−15.5	4.93 ± 0.09	3.79 ± 0.05		M0V
HIP 86346	Z04	−26.7 ± 0.1	−30.3	4.21 ± 0.15	3.35 ± 0.07	28	M0V
J04554034−1917553	M14	22.2 ± 3.7	26.5	4.22 ± 0.29	4.17 ± 0.04		M0.5V
J04571728−0621564	M14	23.2 ± 0.6	23.1	5.32 ± 0.16	3.82 ± 0.04		M0.5V
J05240991−4223054	M14	33.4 ± 0.6	30.9	6.14 ± 0.22	4.00 ± 0.30		M0.5V
J05531299−4505119	M13	31.7 ± 0.0	31.4	5.07 ± 0.11	3.64 ± 0.30	140	M0.5V
HIP 81084	Z04	−15.0 ± 0.4	−15.9	5.12 ± 0.17	3.66 ± 0.04	0	M0.5V
J06091922−3549311	M13	31.4 ± 0.4	30.9	5.41 ± 0.15	3.99 ± 0.02	10	M0.5V+L4
HIP 114066	Z04	−23.7 ± 0.8	−22.9	5.04 ± 0.09	3.95 ± 0.02	30	M1V
J01484087−4830519	M14	21.5 ± 0.2	23.1	5.62 ± 0.24	4.21 ± 0.04		M1.5V
HIP 51317	T08	8.3 ± 0.5	8.8	6.06 ± 0.02	4.29 ± 0.04	0	M2V
J15244849−4929473	M14	6.7 ± 0.9	6.5	5.38 ± 0.07	4.34 ± 0.03		M2V
J21521039+0537356	M13	−15.1 ± 1.3	1.5	5.00 ± 0.39	4.74 ± 0.09	10	M2Ve
J23513366+3127229	M13	−13.5 ± 1.2	0.6	5.75 ± 0.07	4.63 ± 0.06	78	M2V+L0
HIP 17695	Z04	16.0 ± 1.7	18.6	5.89 ± 0.10	5.71 ± 0.02	74	M2.5V kee
J01034210+4051158	M14	−10.9 ± 0.4	−10.9	6.14 ± 0.15	4.60*		M2.6+M3.8
J01123504+1703557	M13	−1.5 ± 0.5	−0.9	5.88 ± 0.06	4.80 ± 0.10		M3V
J23320018−3917368	M13	11.6 ± 0.7	11.7	6.19 ± 0.16	4.90 ± 0.05		M3V
J04522441−1649219	M13	26.7 ± 1.5	26.3	5.83 ± 0.06	4.75 ± 0.06	20	M3Ve
J05301858−5358483	M14	31.3 ± 0.2	31.0		5.38 ± 0.02		M3+M6+M4
J01225093−2439505	M14	11.2 ± 0.3	15.8	6.57 ± 0.07	5.04 ± 0.08		M3.5V
J04141730−0906544	M13	23.4 ± 0.3	22.5	6.88 ± 0.13	5.12 ± 0.07	78	M3.5V
J21464282−8543046	M14	23.5 ± 0.7	22.2	7.13 ± 0.09	5.42 ± 0.04		M3.5V
J05254166−0909123	M14	28.4 ± 0.5	24.8	4.21 ± 0.24	4.95 ± 0.04		M3.5+M4
J02070786−1810077	M14	19.1 ± 3.7	17.0	6.90 ± 0.09	5.27 ± 0.02		M4V
J04363294−7851021	M14	26.5 ± 0.3	26.5	5.74 ± 0.53	5.38 ± 0.02		M4V
J08471906−5717547	M14	30.2 ± 0.2	28.4	7.01 ± 0.28	5.15 ± 0.03		M4V
J21471964−4803166	M14	10.4 ± 2.9	8.9	5.79 ± 0.11	5.15 ± 0.04		M4V
J11254754−4410267	M13	19.5 ± 2.0	18.7	5.89 ± 0.13	5.15 ± 0.03	0	M4+M4.5
Literature candidates with $\Delta\mathrm{RV} > 5\,\mathrm{km\,s^{-1}}$ or lacking an RV measurement							
J12194808+5246450	M13	−4.9 ± 1.2	−18.8	5.23 ± 0.13	3.66 ± 0.03		K7V
J01132958−0738088	M13		9.1	4.44 ± 0.06	3.54 ± 0.08		K7V+M5.5
J06022455−1634494	M13		27.4	4.65 ± 0.11	3.93 ± 0.05		M0.0V
J04554034−1917553	M13		27.0	5.48 ± 0.11	4.17 ± 0.04		M0.5V
J18553176−1622495	M13		−14.1	5.66 ± 0.09	3.95*		M0.5V
J04093930−2648489	M13		27.2	5.77 ± 0.10	4.36 ± 0.02		M1.5V
J02523096−1548357	M13		20.0	6.52 ± 0.08	4.65 ± 0.04		M2.5V
J06373215−2823125	M13		29.8	5.69 ± 0.20	4.51 ± 0.04		M2.5V
J02545247−0709255	M13		17.2	4.85 ± 0.12	4.63 ± 0.05		M3.0V
J04514615−2400087	M13		28.0	6.56 ± 0.12	4.78 ± 0.05		M3.0V
J07115917−3510157	M13		30.2	6.50 ± 0.26	4.86 ± 0.06		M3V+M3V
J04353618−2527347	M13		27.8	6.45 ± 0.15	5.00 ± 0.02		M3.5V
J19420065−2104051	M13		−10.5	6.08 ± 0.07	5.45 ± 0.05		M3.5V
J20223306−2927499	M13		−4.6	5.67 ± 0.06	6.12 ± 0.08		M3.5V
J05130132−7027418	M13		28.5	8.24 ± 0.15	5.10 ± 0.04		M3.5+M5.5
J04084031−2705473	M13		27.2	7.55 ± 0.11	5.48 ± 0.04		M4.0V
J04424932−1452268	M13		25.4	7.13 ± 0.10	5.14 ± 0.09		M4.0V
J20220177−3653014	M13		−0.9	7.26 ± 0.32	5.59*		M4.5V
J00354313+0233137	G14		1.3	7.39	8.35*		M4.8V
J22583200+1014589	G14		−11.2	7.68	7.06*		M4.9V
J23233072−2807141	G14		7.2	7.49	7.38*		M4.9V
J01243060−3355014	G14		18.3	7.66	3.87*		M5.2V
J22060961−0723353	G14		−7.8	7.92	7.50*		M5.3V
J22283837−3648372	G14		6.5	7.81	3.77*		M5.3V
J23523223−3413068	G14		11.7	7.94	7.06*		M5.3V
J23520507−1100435	G14		2.9	8.76	9.28*		M7.0V

Table 4.5: Supplementary ABDMG objects from the literature. M13, M14 and G14 refer to objects selected from the Malo et al. (2013; 2014b) and Gagné et al. (2015) sample, respectively. (*) No V magnitude, $V-K$ interpolated from table 5 in Pecaut & Mamajek (2013). Spectral-types are from the source paper. Objects with Li EW = 0 do not have the data with which to estimate upper limits.

4.3 Measuring an LDB age for BPMG

The procedures to obtain LDB ages for groups of young, coeval stars are described in §1.2.1. The LDB technique is most effective between 20 and 200 Myr, coincident with the ages of most MGs. Given the recent unveiling of a swathe of M-dwarf members in MGs (e.g., Shkolnik et al. 2012; Schlieder, Lépine & Simon 2012; Malo et al. 2013; Gagné et al. 2014a), objects observed at the NOT and INT and previous members in the literature were examined for (a) RV measurements (to ascertain kinematic membership to the group, see §2.2) and (b) Li EWs (either measured in this work or previously published, to determine the location of the LDB). The same criteria for group membership are used for the supplementary literature targets. The basic *modus operandi* was to confirm group membership based on the tests described in §4.2.4 and then identify the luminosity boundary between Li-rich and Li-poor stars. In this section, the literature data are from all sources prior to, and including Binks & Jeffries (2014). In the next section, this work is updated in the light of even more recent publications that add more objects to the mix.

Even if a boundary between Li-rich and Li-poor members cannot be identified, a detection (or lack) of Li in a star provides an upper (or lower) age limit to the group. For example, an Li-poor star at a given colour would set a lower age limit to the group (as there should be no Li-rich stars warmer than the coolest Li-poor star), and vice-versa for Li-rich objects. Using table 5 in Pecaut & Mamajek (2013), the LDB should be located at spectral-type ∼M4 ($M = 0.25\,M_{\odot}$) for objects at 20 Myr (e.g., NGC 1960, Jeffries et al. 2013) and for objects at 125 Myr (e.g., Pleiades, Stauffer, Schultz & Kirkpatrick 1998) the LDB should lie around M6.5/7 ($M \sim 0.1\,M_{\odot}$). Objects with masses less than $0.065\,M_{\odot}$ retain their initial Li content because the star is unable to reach the core temperatures for Li burning. Objects less massive than $0.075\,M_{\odot}$ are classed as brown dwarfs (Rebolo, Martin & Garcia Lopez 1994). For these reasons the search criteria for MG members was restricted to M0−M9 spectral-types only.

4.3.1 Locating the LDB in BPMG

In M-dwarfs, the Li 6708Å feature is expected to be strong where no depletion has occurred (EW $\simeq$ 0.6Å, Palla et al. 2007) and is observed to have this strength in very young T-Tauri stars (e.g., Sergison et al. 2013). Li-burning should begin at spectral-types M2–M3 after $\sim$ 10 Myr. Within a few Myr these stars should deplete Li by factors $>$ 100, resulting in an EW $<$ 0.2 Å, and Li burning progresses towards cooler, less luminous stars. The most model-independent way to define the LDB age (see §1.2.1 and Jeffries 2006), is to find the *luminosity* at which M-dwarf BPMG members make the transition from having depleted their Li by factors $>$ 100, to having undepleted Li at only slightly lower luminosities.

This is illustrated in Figures 4.4 and 4.5, where the absolute K magnitudes of Li-rich and Li-poor (EW $<$ 0.2 Å) members are plotted as a function of colour or spectral-type. Overplotted are curves of constant luminosity corresponding to the LDB (99 per cent Li depletion) at several ages. These are obtained from the theoretical models of Chabrier & Baraffe (1997) and transformed to absolute K magnitudes using quartic relationships fitted to tables of bolometric corrections for PMS stars as a function of colour or spectral-type (Pecaut & Mamajek 2013). In each diagram there is a reasonably clear boundary between Li-rich and Li-poor BPMG members. The LDB is identified as a rectangular region separating Li-poor from Li-rich stars. The upper bound is defined by the faintest Li-depleted star, the lower bound is defined by the brightest Li-rich star (excluding J05241914−1601153, which is known to be an unresolved binary and will be brighter than a single star at the same abcissa value – see Table 4.1). The width of the box is defined by the separation of these two stars, or twice their average uncertainty, whichever is larger. The Li-poor edge of the LDB is defined by the object J01351393−0712517 ($M_K = 5.19 \pm 0.14, V-K = 5.35 \pm 0.05, K = 8.08 \pm 0.03, d = 37.9 \pm 2.4$ pc) and the Li-rich edge is HIP 112312 B ($M_K = 5.96 \pm 0.19, V-K = 5.58 \pm 0.14, K = 7.80 \pm 0.03, d = 23.4 \pm 2.0$ pc).

The LDB age is calculated from the position of the central points of the boxes in Figures 4.4 and 4.5 by interpolating the LDB curves. Age uncertainties are estimated

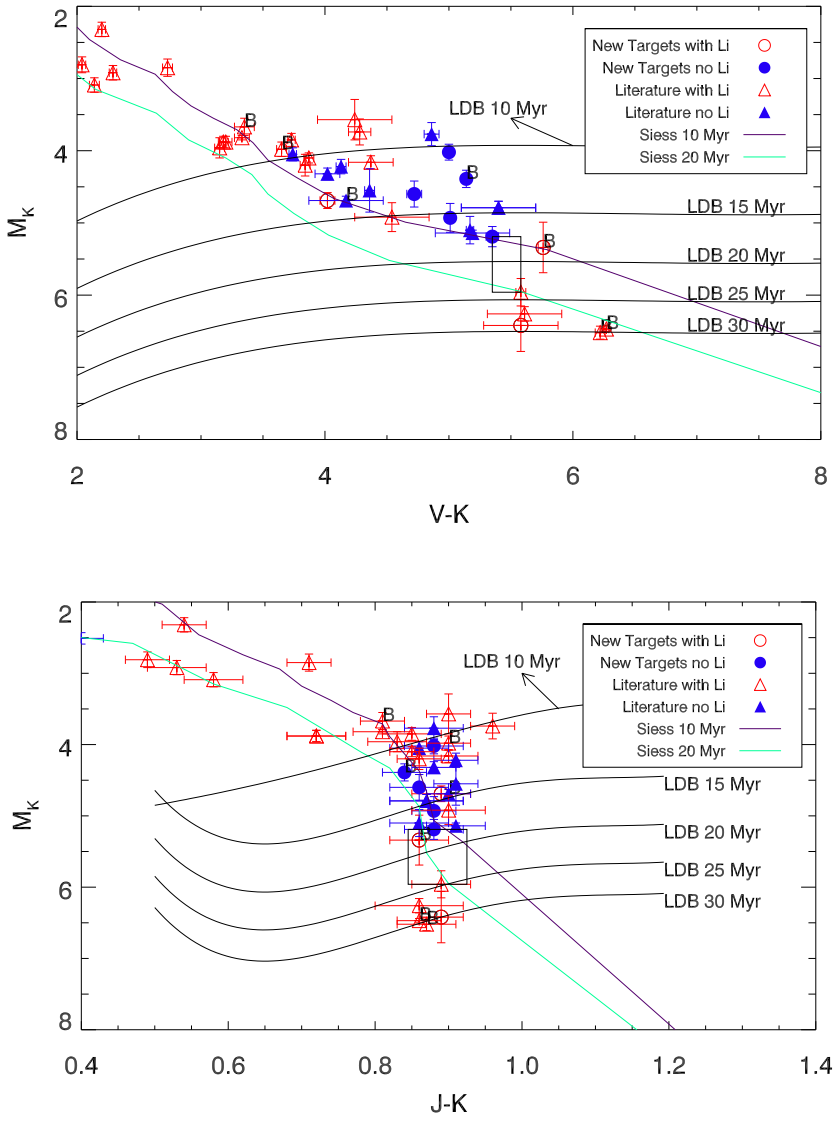

Figure 4.4: Locating the LDB for BPMG in 2 separate absolute K magnitude versus colour diagrams. New members from Table 4.1 and objects from the literature are indicated. Absolute magnitudes are calculated from 2MASS K and a trigonometric parallax where available or a kinematic distance otherwise. Known, unresolved binaries are marked with 'B'. Black lines represent constant luminosity loci from Chabrier et al. (1997), where Li is predicted to be 99 per cent depleted at the ages indicated. The green and maroon lines are 10 and 20 Myr isochrones from Siess et al. (2000). The rectangle in each diagram represents the estimated LDB location and its uncertainty, based on the faintest Li-depleted member and the brightest Li-rich member, but excluding the unresolved binary at $M_K = 5.3$, see §4.3.1.

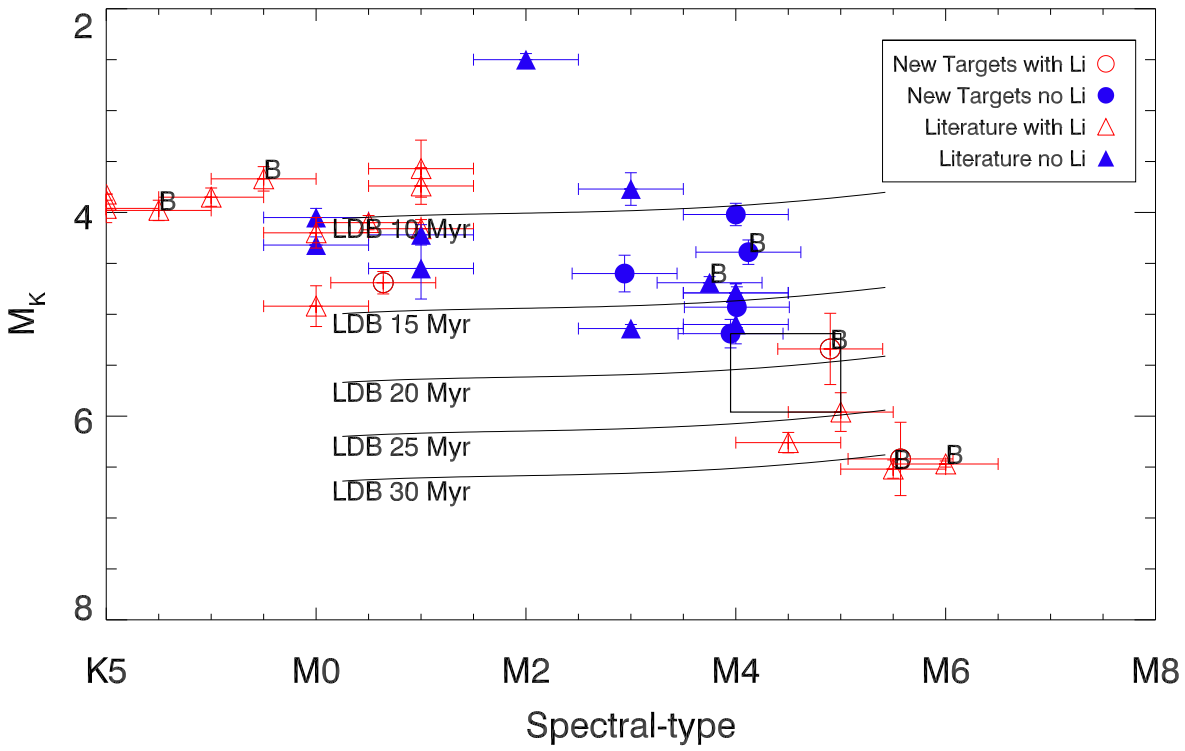

Figure 4.5: Locating the LDB for BPMG in an absolute K magnitude versus spectral-type diagram. Labels are the same as in Figure 4.4.

by perturbing the abcissae and ordinates according to the height and width of the LDB boxes and adding the resultant age perturbations in quadrature. A ± 0.1 mag of uncertainty in colour (or ± 0.5 subclasses in spectral-type) and magnitude is included to reflect errors in the calibration of these quantitities.

The results are given in the first row of Table 4.6 for the models of Chabrier & Baraffe (1997). To gain insight into any model dependency the process was repeated using the models of Siess et al. (2000, models with metallicity $Z = 0.02$) and Burke, Pinsonneault & Sills (2004). Table 4.6 shows that there is only ~ 2 Myr between the youngest and oldest age estimates from these models (compare the ages in a column). A comparison of the ages in each row shows differences of ≤ 0.6 Myr, attributable to small (0.1 mag) differences in the LDB location in each diagram; the applied bolometric corrections are similar to ≤ 0.04 mag. Finally, defining the LDB as the luminosity at which Li is depleted by 99.9 or 90 per cent would only change the age estimates by ± 1 Myr. All these uncertainties are small compared with the $3 - 4$ Myr observational error due to the size of the estimated LDB boxes. Adopting the Chabrier & Baraffe models, the final LDB age estimate is 21 ± 4 Myr, with an additional model dependent uncertainty of only ± 1 Myr.

	M_K vs $V-K$	M_K vs $J-K$	M_K vs SpT
LDB location	$M_K = 5.575 \pm 0.385$	$M_K = 5.575 \pm 0.385$	$M_K = 5.575 \pm 0.385$
	$V-K = 5.465 \pm 0.115$	$J-K = 0.885 \pm 0.040$	SpT$= 4.475 \pm 0.525$
$M_{\rm bol}$	8.280 ± 0.544	8.321 ± 0.556	8.307 ± 0.546
Ages (Myr)			
Chabrier & Baraffe 1997	$20.3^{+3.7}_{-3.2}$	$20.7^{+4.6}_{-4.1}$	$20.6^{+3.8}_{-3.2}$
Siess, Dufour & Forestini 2000	$19.9^{+4.1}_{-3.7}$	$20.5^{+5.0}_{-4.9}$	$20.2^{+4.1}_{-3.8}$
Burke, Pinsonneault & Sills 2004	$18.5^{+3.8}_{-3.0}$	$18.9^{+4.6}_{-3.8}$	$18.8^{+3.8}_{-3.0}$

Table 4.6: LDB ages for the BPMG. Each column corresponds to a diagram in Figure 4.4; each row gives ages based on a different evolutionary model.

4.3.2 BPMG revisited

Since the preparation and publication of Binks & Jeffries (2014) the sample of M-dwarf BPMG members has increased and a new generation of evolutionary models incorporating magnetic fields has been published. In this subsection the Binks & Jeffries (2014) analysis is revisited in the light of these developments. Malo et al. (2014a) calculate an LDB age of 26 ± 3 Myr based on newly identified members and incorporating the magnetic field models of Feiden & Chaboyer (2013). Magnetic fields act to inflate the radii of M-dwarfs, which, for a given luminosity drives the LDB to older ages. Malo et al. (2014a) estimate an average surface magnetic field in BPMG members of $< B >= 2.5$ kG (based on two BPMG members: AU Mic, $< B >= 2.3$ kG, Saar 1994 and HIP 23200, $< B >= 2.5$ kG, Reiners & Basri 2009).

The location of the LDB in Binks & Jeffries (2014) is reassessed using all newly identified objects in Malo et al. (2014a). In Table 4.7 the supplementary Malo et al. (2014a) objects are listed. To place the new objects onto the same M_K versus $V - K$ CMD, apparent V magnitudes were extracted from UCAC4 (Zacharias et al. 2012), except for 2MASS J20333759−2556521, which is from the SPM4 catalog (Girard et al. 2011) and K magnitudes from 2MASS (Cutri et al. 2003). Where possible, absolute K magnitudes were calculated from trigonometric parallaxes. If no parallax was available, the kinematic distance reported in Malo et al. (2014) was used. Objects classed as 'bonafide members' from the Malo et al. (2014a) have a parallax, RV and proper-motion measurement consistent with BPMG membership along with at least one strong empirical age indicator, whereas objects classed as 'candidates' either lack a parallax measurement or have ambiguous membership from at least one age indicator. All additional objects are displayed in Figure 4.6. Whilst there appear to be at least four objects in the vicinity of the original LDB box in Binks & Jeffries (2014), none of them constrain the LDB box further, and the original age of 21 ± 4 Myr would remain unaffected by LDB location. Additional members close to the LDB are useful to bolster the LDB location and provide a more statistically significant age.

Name (2MASS-)	RV ($\mathrm{km\,s^{-1}}$)	$\mathrm{RV_{pred}}$ ($\mathrm{km\,s^{-1}}$)	M_K (mag)	$V-K$ (mag)	Li EW (mÅ)	SpT
Bonafide members in Malo et al. (2014)						
J06182824−7202416	16.2 ± 1.0		4.21	3.38	420.00	K4Ve
J02412589+0559181	10.0		3.95	3.20	445.73 ± 3.67	K6Ve(sb1)
J20100002−2801410	−5.9 ± 0.4	−8.5	4.33	5.26	< 45.70	M2.5+M3.5
J06131330−2742054	22.8 ± 0.2	21.6	4.81	5.11	< 28.30	M3.5V*
J00275035−3233238	8.8 ± 0.2	8.3	5.57	5.04	< 28.70	M3.5Ve
J00275035−3233060	8.5 ± 0.2	8.3	5.46	4.86	< 25.55	M3.5Ve
J20333759−2556521	−8.8 ± 0.3	−8.1	5.46	5.91	504.21 ± 4.70	M4.5V
J10172689−5354265	13.6 ± 0.2		6.47	6.27	510.00	M6Ve+M6Ve
Candidate members in Malo et al. (2014)						
J00233468+2014282	−1.6 ± 0.2		3.72	3.66	338.65 ± 1.89	K7.5(sb2)
J18580415−2953045	−4.9	−10.1	3.61	3.78	466.26 ± 5.23	M0Ve
J19233820−4606316	−7.2 ± 0.2	−4.1	4.05	3.61	425.92 ± 3.02	M0V
J21100535−1919573	−5.6 ± 0.2	−7.9	4.67	4.55	< 21.20	M2V
J14252913−4113323	−1.2 ± 1.3		3.49	5.01	684.64 ± 15.15	M2.5Ve*
J04435686+3723033	6.4 ± 0.2	7.6	4.95	4.52	194.12 ± 4.04	M3Ve
J03323578+2843554	9.2 ± 0.3	8.2	4.77	5.30	< 31.35	M4+M4.5
J01365516−0647379	12.2 ± 0.4	9.5	6.96	5.14	< 22.85	M4+>L0
J21103147−2710578	−5.6 ± 0.2	−5.8	6.35	5.74	501.48 ± 9.30	M4.5V

Table 4.7: BPMG objects included in the Malo et al. (2014) sample. Li EWs prefixed with a '<' symbol are 2σ upper limits.

To investigate the 5 Myr discrepancy between the LDB ages reported in Binks & Jeffries (2014) versus Malo et al. (2014a), constant luminosity tracks at 99 per cent depletion were calculated using the Dartmouth stellar evolution models, using both the non-magnetic (Dotter et al. 2008) and $< B >= 2.5\,\mathrm{kG}$ (Feiden & Chaboyer 2013) flavours. The relationship between $\log L$ versus log age is almost linear, as observed in Figure 4.7. Adopting the value of $\log L_{\mathrm{LDB}} = -1.49$ from Malo et al. (2014a), a linear interpolation of the magnetic mass-tracks results in an age of exactly 25 Myr. The same analysis for the non-magnetic tracks gives an LDB age of 22 Myr. Therefore there is a difference of 3 Myr ($\sim$ 15 per cent) due to the magnetic nature of the model. To demonstrate model-consistency between non-magnetic models the Chabrier & Baraffe (1997) isochrones are overplotted in Figure 4.7. Interestingly, Jackson & Jeffries (2014) calculate a 15 per cent increase in age for any magnetic effect that inflates the radii of a PMS star by $\sim$ 15 per cent at a given luminosity and age. If the inflation were due to starspots, it would require 24 per cent coverage by dark spots to obtain the same change in LDB age induced by the magnetic models.

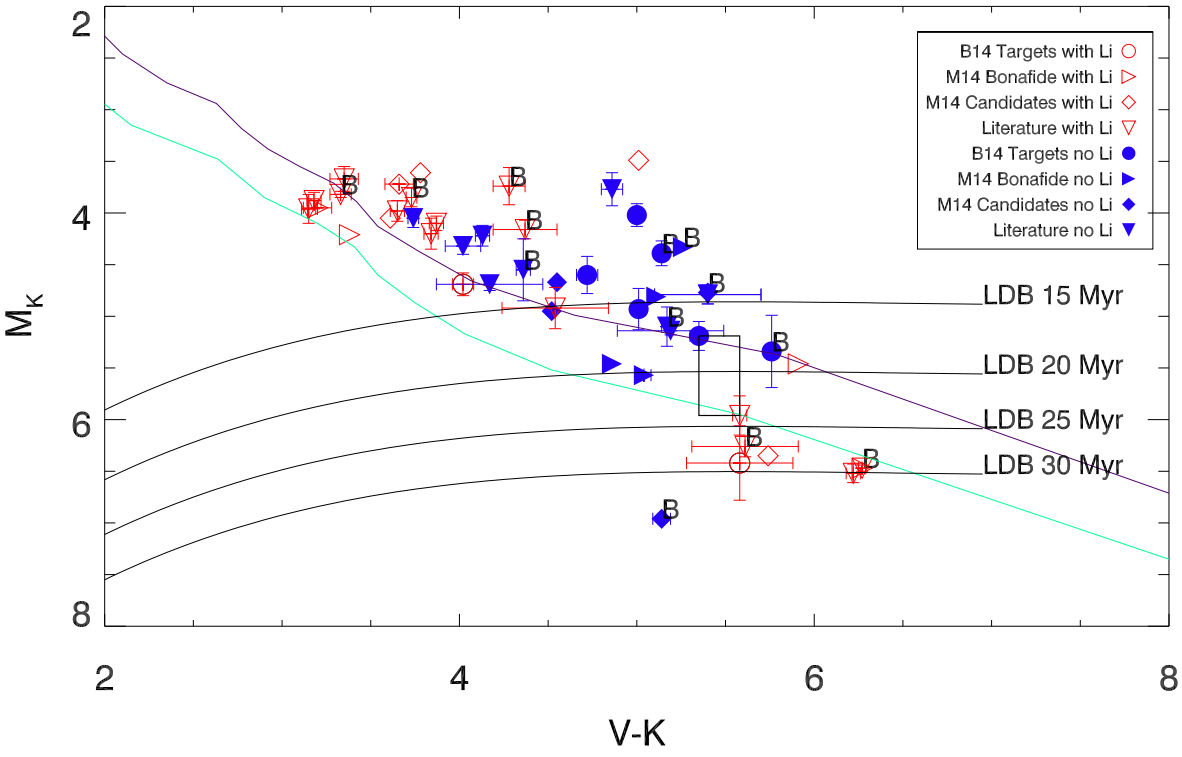

Figure 4.6: The revised CMD for BPMG using the newly identified members in Malo et al. (2014a). There is no alteration in the location and size of the LDB, however, at least four new objects are observed close to the box encompassing the LDB. This acts to secure the location of the LDB in BPMG, because any objects near to the LDB that are found to be non-members would be supported by a number of objects that are genuine BPMG objects. The green and maroon lines correspond to the 10 and 20 Myr isochrones from the Siess, Dufour & Forestini (2000) models. B14 = objects in Binks & Jeffries (2014), M14 Bonafide = objects referred to as bonafide BPMG members in Malo et al. (2014a), M14 Candidates = objects referred to as candidate BPMG members in Malo et al. (2014a).

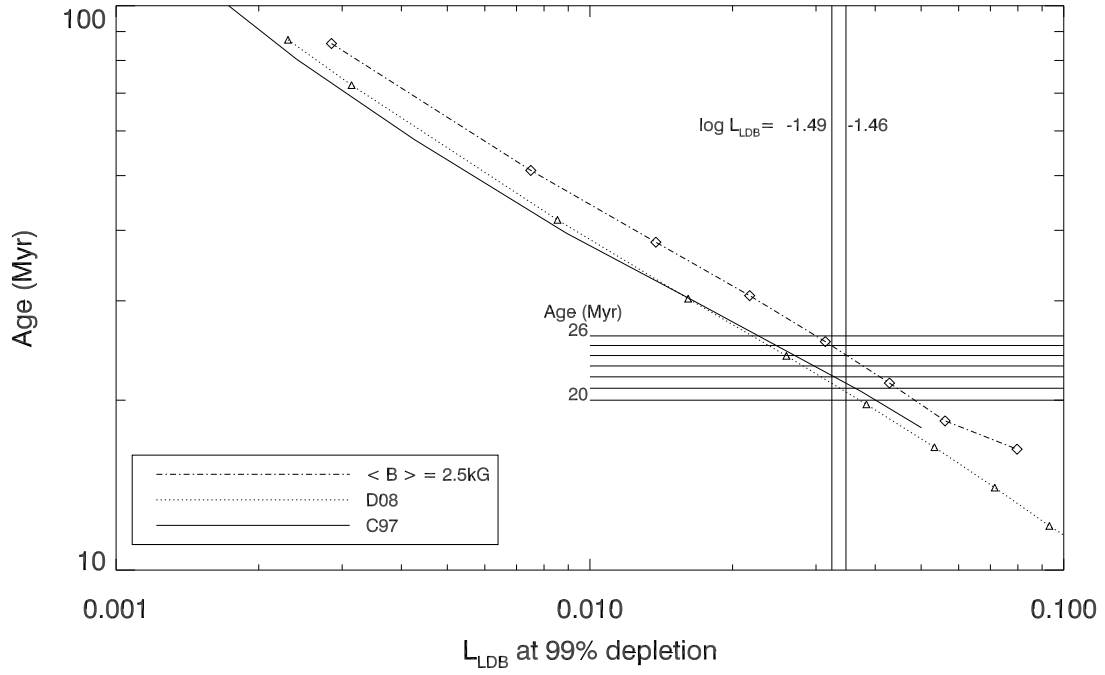

Figure 4.7: Comparison of the LDB location using the Dartmouth stellar evolutionary models. The dot-dash line represents a surface magnetic field of 2.5 kG and the dotted line (D08) is the non-magnetic Dartmouth evolutionary model (Dotter et al. 2008). The Chabrier & Baraffe (1997) models (solid line, C97) demonstrate the model consistency amongst non-magnetic models. Both the diamond and triangle symbols indicate the interpolated points (at 99 per cent Li depletion) in age and luminosity for each mass track. The difference between the magnetic models and the non-magnetic models is ~ 3 Myr and ~ 0.5 Myr between the non-magnetic models.

Malo et al. (2014a) calculate their luminosities for newly identified BPMG members by identifying a best-fit to synthetic spectra generated by BT-Settl models (Allard, Homeier & Freytag 2012). As a final check, bolometric luminosities for a sample of the newly observed targets were calculated using 2MASS K magnitudes and bolometric correction calibrations from Pecaut & Mamajek (2013). No overall systematic differences are found between the calculated luminosities and the LDB position remains unaffected.

The value for the LDB luminosity measured by Binks & Jeffries (2014) is $\log L = -1.46$. Using the same models for comparison results in a non-magnetic LDB age of 21 Myr and a magnetic LDB age of 24 Myr.

To summarise, the 5 Myr difference is likely to be due to:

a) The magnetic nature of the models (3 Myr).

b) An interpolation error (1 Myr).

c) A difference in LDB location (1 Myr).

4.3.3 Discussion and implications

The LDB age derived for the BPMG is reasonably precise, but could be improved by the addition of data for more members close to the LDB and an accurate assessment of their binary nature. More importantly, the LDB method yields an age likely to have a high degree of absolute accuracy. The physics involved in calculating the luminosity at the LDB versus age is well understood. Numerical experiments adjusting the physical inputs of models (convection efficiency, opacities, equation of state, etc.) within plausible bounds yield age uncertainties of only 8 per cent at ~ 20 Myr (Burke, Pinsonneault & Sills 2004), comparable with the model dependence identified in this work. The Burke et al. analysis did not account for magnetic activity, however, and the LDB age of BPMG in Malo et al. (2014a) suggests that magnetic models could increase LDB ages by ~ 20 per cent and starspot models (Jackson & Jeffries 2014) suggest that LDB ages are increased by $(1-\beta)^{0.5}$, where β is the fraction of flux blocked by starspots. Starspots definitely exist on stars (Messina et al. 2010), but the appropriate value of

β is uncertain.

Previous work to locate the LDB concluded that the age was > 30 Myr, incompatible with ages derived from fitting isochrones in the HRD or from kinematic trace-back, suggesting there could be gaps in our understanding of the physics of Li depletion (Song, Bessell & Zuckerman 2002; Yee & Jensen 2010). However, both of these works suffered from a sparse sample (only the binary pair HIP 112312 AB was considered by Song, Bessell & Zuckerman 2002); the new BPMG members confirmed here locate the LDB with more precision, particularly in defining the lowest luminosity objects that have lost their Li. However, all the objects considered in previous work are present in Table 4.1 and are entirely consistent with the 21 Myr LDB age. Even if the new members claimed in Binks & Jeffries (2014) are ignored, the presence of previously known Li-depleted objects at $M_K > 5.0$ constrains the LDB age to be > 15 Myr. The main reason that previous work found an older age was probably because comparison was made with Li depletion models as a function of $T_{\rm eff}$. This is a far more uncertain enterprise than comparing the *luminosity* of the LDB with models. Measuring $T_{\rm eff}$ in low-mass stars has systematic uncertainties of $100-200$ K at best, leading to large LDB age errors because the Hayashi tracks of stars with different mass are close together in $T_{\rm eff}$. Furthermore, theoretical $T_{\rm eff}$ predictions are extremely sensitive to adopted convection efficiencies and atmospheres, making any age estimate highly model-dependent (see §1.2.1 and §1.3.1).

The LDB age of 21 Myr is at the upper end of age estimates from some isochronal fits to low mass BPMG members in the HRD: 12^{+8}_{-4} Myr (Zuckerman et al. 2001). Isochronal ages are also model dependent, are very sensitive to adopted convective efficiencies, can vary depending on which mass range is considered, may be biased downwards by the neglect of unresolved binarity and also depend on how colours and spectral-types are translated into $T_{\rm eff}$ for comparison with models (or vice versa). The situation is well illustrated in Figure 4.4, where a single isochrone is incapable of fitting all the low-mass members. Nevertheless, Jeffries et al. (2013) and Bell et al. (2013) have recently shown that for NGC 1960, a rich open cluster with a similar LDB age to the BPMG, that isochronal fits to both low- and high-mass stars do agree with the LDB age

when these problems are carefully considered; the same may yet be true for the BPMG. Mamajek & Bell (2014) used revised parallaxes (van Leeuwen 2007) for the sample of BPMG members reported in Zuckerman & Song (2004) to relocate the A, F and G stars onto an M_V versus $B-V$ CMD. They combine 4 separate evolutionary models (Yonsei-Yale, Demarque et al. 2004; Dartmouth, Dotter et al. 2008; Pisa, Tognelli, Prada Moroni & Degl'Innocenti 2011; PARSEC, Bressan et al. 2012) and measure an age of 22 ± 3 Myr, with a 1 Myr additional systematic model uncertainty.

In principle, kinematic trace-back ages provide a model-independent age, or at least the time since the MG occupied a minimum spatial extent. The LDB age is older than trace-back ages of $10-12$ Myr reported by Ortega et al. (2012; 2014) and Song, Zuckerman & Bessell (2003), which have formal uncertainties as small as 0.3 Myr. However, other kinematic analyses do not concur with this age or this precision. Torres et al. (2006) find a group expansion consistent with an age of ~ 20 Myr; Makarov (2007) give a time of closest approach for pairs of BPMG members as 22 ± 12 Myr ago; and Mamajek & Bell (2014) found no significant evidence that BPMG was smaller in the past (see §1.2.2). The differing conclusions appear to arise from uncertain space motions combined with some subjectivity in which group members are included in the analyses. The forthcoming Gaia astrometry mission may reveal a precise kinematic age for the BPMG, but for now it appears an unreliable technique.

A key role for BPMG members is in testing evolutionary models for low-mass objects and circumstellar material at young ages. Adopting an older age of 21 Myr for the BPMG changes the inferred masses of substellar and planetary companions. Biller et al. (2010) find a faint companion to the BPMG member PZ Tel, estimating a mass for PZ Tel b of $36\,M_{\rm Jup}$ at an assumed age of 12 Myr. An age of 21 Myr would increase the inferred mass by ~ 30 per cent. Similarly, based on an age of 12^{+8}_{-4} Myr, Bonnefoy et al. (2013) estimate a mass of $10^{+3}_{-2}\,M_{\rm Jup}$ for β Pic b, the uncertainties largely arising from the assumed age. Again, an increase in age to 21 Myr results in a ~ 30 per cent increase in inferred mass, which is still below the upper limit of $15.5\,M_{\rm Jup}$ currently imposed by dynamical constraints (Lagrange et al. 2012).

4.4 ABDMG

Details of ABDMG are summarised in §2.4.3. In an attempt to identify new M-dwarf members in ABDMG and locate the LDB, spectra for 24 ABDMG candidates were obtained at the INT. Seventeen were from Schlieder, Lépine & Simon (2012a) and 7 from Malo et al. (2013). All candidates were analysed according the protocols set out in §4.2 and the RVs, predicted RVs, $V - K$ colour, Li EWs and spectral-types for objects observed on the INT are listed in Table 4.2. Only 6 of these objects satisfied the relevant group membership criteria for ABDMG, 2 of which were members of the Malo et al. sample and 4 from Schlieder et al. In Figure 4.8 the spectra for the 7 objects that satisfy RV criteria are presented. One of these objects, J10121768−0344404 has Hα in absorption. It also has a kinematic distance of 19 pc compared to the 7.9 ± 0.1 pc trigonometric distance (see Table 4.2), therefore the ABDMG membership status is unlikely and it is discarded from the analysis.

Supplementary candidates from literature sources were assessed in the same way. 44 objects from the literature were found with a spectral-type later than M0 (Malo et al. 2013; 2014a). Of these, 28 were found to satisfy the RV and Hα crtieria, but only 12 had an Li measurement. These were included with the 6 objects observed at the INT. The addition of the 6 confirmed objects observed at the INT represent a 50 per cent increase in the number of M-dwarf members with an Li EW measurment. The RVs, predicted RVs, $V - K$ colour, Li EWs and spectral-types for supplementary objects selected from literature sources are listed in Table 4.5.

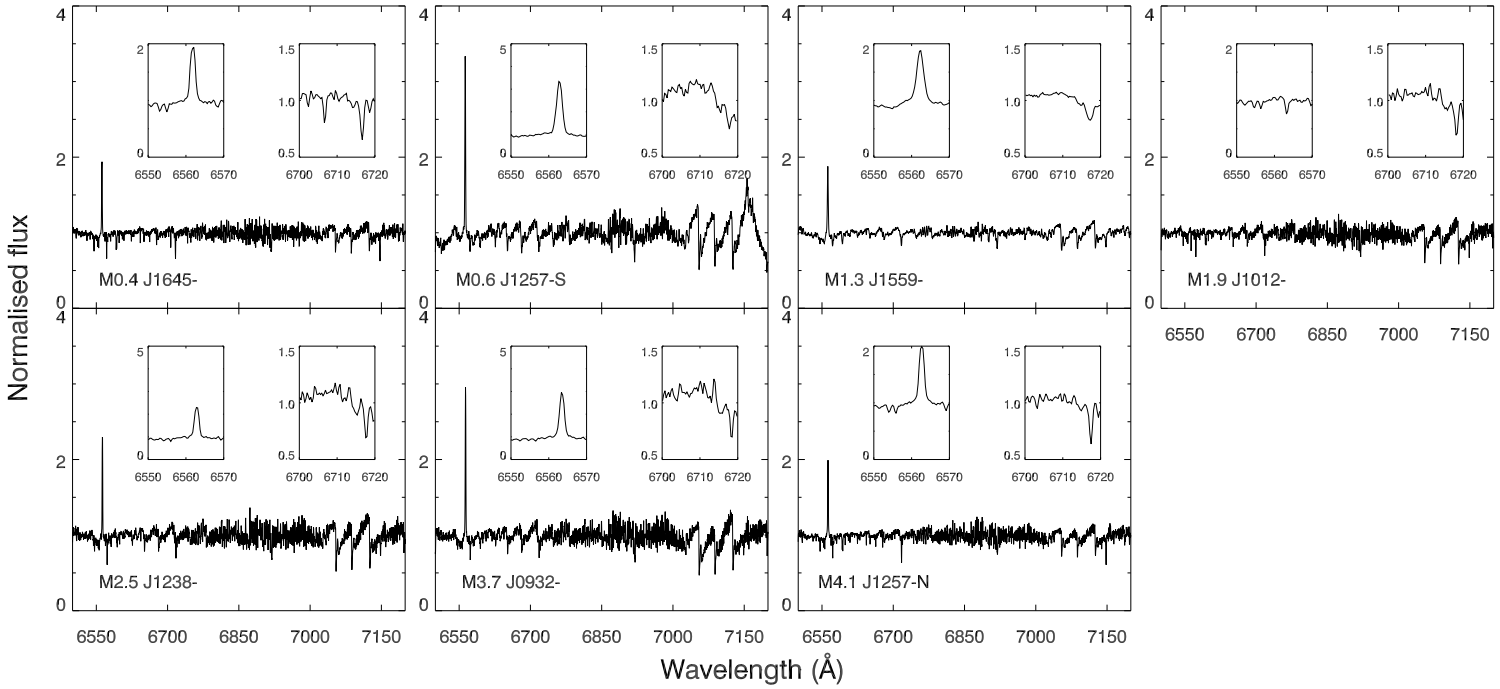

Figure 4.8: Spectra for the 7 RV-confirmed ABDMG members, all of which are spectral-type M. All objects display Hα in emission except J10121768−0344404.

Gagné et al. (2014) report an M8 ABDMG candidate (2MASS J0019262+4614078, herein J0019+4614) with an RV of $-19.5 \pm 2.0\,\mathrm{km\,s^{-1}}$, which gives a value of $\Delta RV = 3.2\,\mathrm{km\,s^{-1}}$. Reiners & Basri (2009) detect a strong Li feature around the 6708Å line in J0019+4614. An Li EW value is not reported, however an estimation of the EW by eye from the top-left panel in their figure 3 suggests it is $\gtrsim 625\,\mathrm{mÅ}$. This is comfortably large enough to report a non-depleted value, or at least less than 99 per cent depletion. Table 4.8 displays the 2MASS JHK photometry, RV and predicted RV (were it a member of ABDMG), spectral-type and Li EW. Gagné et al. (2015) reported 8 new likely-new members of ABDMG with spectral-types between M4.9 and M7.0. If these objects are indeed ABDMG members, an Li measurement would immediately provide a more precise age. The $V-K$ colours are interpolated from the provided $J-K$ colours in table 5 in Gagné et al. (2015) and are provided in Table 4.5 with the published spectral-types and M_K values. These are plotted as green squares in Figure 4.9.

Both the confirmed objects observed at the INT and confirmed members in the literature are placed onto a M_K versus $V-K$ CMD. There is a gap of several magnitudes in both colour and magnitude between an Li-poor object (2MASS J04141730−0906544, $M_K = 6.88, V-K = 5.12, K = 8.76 \pm 0.02$ and $d = 23.8 \pm 1.4\,\mathrm{pc}$) and an Li-rich object (J0019+4614, $M_K = 10.05, V-K = 8.71$ and $K = 11.50 \pm 0.01$). Treating the LDB as the centroid of this box results in an LDB age of $74^{+122}_{-39}\,\mathrm{Myr}$. Whilst this value is far from precise, it does provide at least some indication of a lower limit to the age. Taking into account only the Li-poor object, the lower LDB age would be 35 Myr (ignoring any errors). If only the Li-rich member is considered, the upper limit for ABDMG would be 196 Myr.

Name (2MASS-)	RV ($\mathrm{km\,s^{-1}}$)	$\mathrm{RV_{pred}}$ ($\mathrm{km\,s^{-1}}$)	J (mag)	H (mag)	K (mag)	Li EW (mÅ)	SpT
J00192626+4614078	−19.5 ± 2.0	−16.3	12.60 ± 0.02	11.94 ± 0.02	11.50 ± 0.01	> 625	M8

Table 4.8: The proposed M8 member of ABDMG reported in Gagné et al. (2014a).

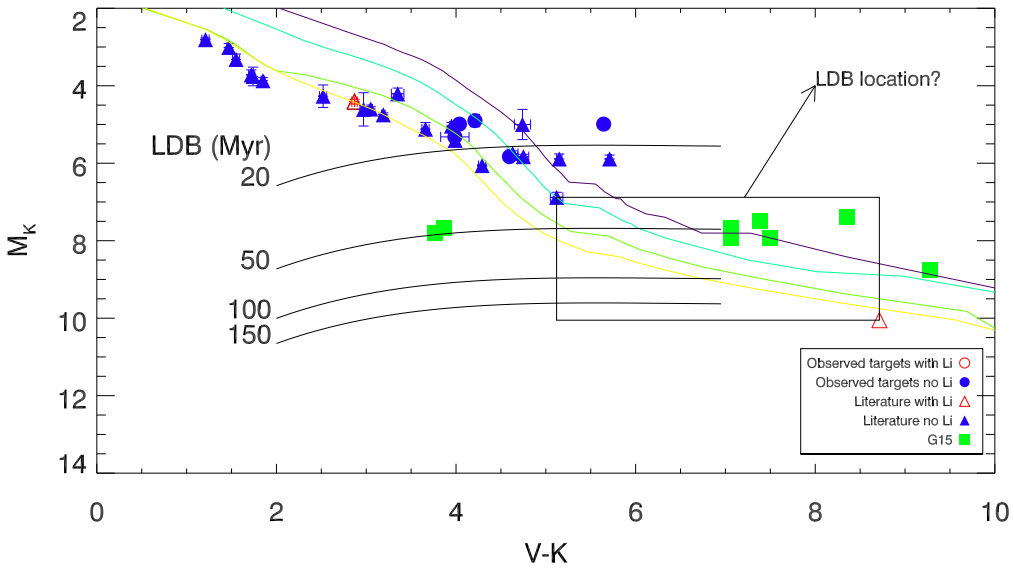

Figure 4.9: Current constraints on the location of the LDB in ABDMG. Green squares are the proposed candidates of ABDMG in Gagné et al. (2015, G15). Presently there are no Li data available in the critical M4−M8 region where the LDB is expected to be located. The LDB luminosity tracks are for 99 per cent depletion and the coloured lines represent isochrones from the Siess, Dufour & Forestini (2000) models, corresponding to the same ages as the LDB isochrones. The luminosity curves in the Chabrier & Baraffe (1997) models do not extend beyond $V - K \approx 7$, however this should have little effect on the overall LDB ages given that the boundary is so large.

Clearly the present situation for an LDB age for ABDMG is far from satisfactory. There is a striking void of RV-confirmed ABDMG objects between M4 and M8. Should such stars exist in ABDMG (current searches are ongoing – Gagné et al. 2014; 2015; Schlieder 2014, priv. comm.) an assessment of their Li content would almost certainly improve the location of the LDB and hence a more precise age.

5 A kinematically unbiased search for nearby young stars in the Northern hemisphere based on SuperWASP rotation periods

Accepted for publication in MNRAS (A. S. Binks, R. D. Jeffries & P. F. L. Maxted).

This chapter focuses on efforts to characterise the ages and kinematics of a sample of rapidly-rotating, X-ray active, nearby, low-mass stars using a kinematically-unbiased approach in the initial target selection. Based on optical spectroscopy of a sample of 146 nearby, potentially young stars, 26 are found that have lithium abundances consistent with an age of 200 Myr or younger, and ages are strengthened by estimates using Gyrochronology, Hα-emission and $R \sin i$/colour relationships (see §1.4.1, §1.4.2.3 and §1.3.4, respectively). Duplicate RV measurements for the vast majority of these objects indicate that they are unlikely to be members of tidally-locked spectroscopic binary systems. Fifteen likely-young objects are not linked with any MG considered in this analysis, which is tested by comparison of Galactic space velocity coordinates, their projected radial velocities and their ages (see §2.2). A grouping of seven targets appear to be comoving with space velocities similar to the Octans-Near MG. The initial search mechanism was $\sim$ 18 per cent efficient at identifying likely-single stars younger than 200 Myr. It is suggested that a more complete survey may result in the detection of new nearby MGs, particularly in the relatively undersampled Northern hemisphere.

5.1 Introduction

Finding young stars in the solar neighbourhood is important because they represent some of the best observational targets for advancing our understanding of the early evolution of stars and their surrounding circumstellar environments and planetary systems (e.g., Dent et al. 2013; Brandt et al. 2014; Bowler et al. 2015). They are much closer

than their equivalents in young clusters and star forming regions, offering advantages both in terms of sensitivity and angular resolution. If stars can be linked to particular coeval MGs, then their ages can reasonably be assumed similar to the MG as a whole, and these ages can then be estimated using the same battery of techniques available for young star clusters (see chapters 1 and 2 for an overview of age-dating techniques and MGs). At ages of $10 - 100$ Myr gas giant planets around MG members are expected to be much more luminous than in older systems, and young stars are frequently surrounded by debris discs that may evidence the formation of terrestrial planets or provide diagnostic indicators of unseen planets. Examples of work that utilise the youth and proximity of MG members include the high contrast infrared imaging detection of multiple planets surrounding the 30 Myr old A-type dwarf, HR 8799, a member of the Columba MG (Marois et al. 2008; 2010), and the identification of a planet around the A0 star β Pic; the eponymous member of the BPMG (Lagrange et al. 2010).

Much work has focused on finding new low-mass MG members by either targeting kinematically selected candidates comoving with MGs or searching for objects in kinematically unbiased surveys where each target has at least one signpost that it may be young (see §2.3 for details of several previous searches). Kinematically biased searches may be more efficient at discovering new members of known MGs, but they preclude the discovery of nearby, young objects that are not members of these groups. Kinematically (and spatially) unbiased searches are possible but less efficient (see §2.3). A more focused approach is to follow the early work that led to the discovery of low-mass stars in the Local Association, and pre-select stars which are likely to be young based on their magnetic activity. Young stars are magnetically active as a result of their fast rotation, convective zones and consequent dynamo-generated magnetic fields. This activity is manifested as chromospheric and coronal emission that can be detected via optical emission lines or UV and X-ray flux. Examples of this approach can be found in the earlier works of Jeffries (1995) and Montes et al. (2001), but more recently Torres et al. (2006), Lépine & Simon (2009), da Silva et al. (2009) and Shkolnik et al. (2011). Shkolnik et al. (2012) pre-selected a sample of nearby, X-ray active M-dwarfs, finding many new MG members but also finding that about 50 per cent of the young M-dwarfs

could not be assigned membership to any of the currently known MGs.

In this chapter a new, kinematically unbiased method is described which selects young stars in order to find new members of existing MGs, but also as a means to identify new MGs in the relatively unstudied Northern hemisphere. This technique relies on the fact that stellar rotation is strongly age dependent. At young ages, a large fraction of low-mass stars have very high rotation rates (rotation periods less than a few days – e.g., Patten & Simon 1996; Krishnamurthi et al. 1998). Angular momentum loss due to the interaction of their winds and strong magnetic fields leads to spin down of these fast rotators on a mass-dependent timescale, ranging from $\simeq 50$ Myr for G-stars to hundreds of Myr for M-dwarfs (see for example Barnes 2003 and §1.4.1). Messina et al. (2010) report rotation periods of several days or less for many known members of MGs, confirming that a selection based on a short rotation period is likely to contain a high fraction of young stars, although may be contaminated by members of short period, tidally-locked, binary systems. Candidates younger than 200 Myr can be confirmed by the presence of chromospheric/coronal activity and a high lithium abundance in the photosphere. Multiple spectra can rule out a tidally-locked, close binary nature if no RV variations are observed.

A description of the initial efforts to find young, nearby stars using this technique are presented, based on short rotation periods found as a by-product of objects with entries in both the ROSAT All-Sky Survey and SuperWASP transiting planet survey (Pollacco et al. 2006). These candidates were followed up with high resolution spectroscopy at the Nordic Optical Telescope and Isaac Newton Telescope in order to confirm their youth or uncover their close binary nature. §5.2 describes how periods were calculated from data in the SuperWASP photometry database and in §5.3 data from the ROSAT 1RXS and 2RXP catalogs are provided and the X-ray activity for all observed targets are assessed. The initial target selection is outlined in §5.4 along with details of the spectroscopic observations. §5.5 describes the techniques used to measure EWs, radial and rotational velocities, abundances and temperatures. The multiple methods that were used to constrain the ages of the observed targets are discussed in §5.6 and in §5.7 the space motions of the Li-rich (and hence potentially

young, see §1.4.3) targets are calculated and compared to known MGs. A discussion of individual objects is provided in §5.8. Finally, §5.9 discusses the potential of a repeat survey, focusing on the efficiency and relative success of this work at identifying kinematic sub-structure in the young sample. light-curves for the entire observed sample are presented in appendices A.3 (Li-rich) and A.4 (all other targets).

5.2 Period determination

The SuperWASP project (Pollacco et al. 2006) is a wide-field photometric survey for transiting exoplanets that has been operating since 2004. The wide field of view of its two cameras ($7.8^\circ \times 7.8^\circ$, one in each hemisphere) and typical observing cadence of ~ 10 minutes also make it proficient at identifying many types of stellar variability with timescales from one hour to several weeks (e.g., Norton et al. 2007; 2012). Data are available for tens of millions of objects with brightness in the approximate range $8 < V < 15$ covering most of the sky (avoiding the Galactic plane). An initial catalog of objects was generated by cross-correlating the ROSAT sky-survey (1RXS) and pointed phase (2RXP) catalogues (Voges et al. 1999; Rosat 2000) with objects in the SuperWASP archive (Butters et al. 2010). A sample of 5477 stars was created using the criteria that SuperWASP targets must be within either the 3σ position uncertainty or 10" of the X-ray source (whichever was larger), have declinations $> -20^\circ$ and contain more than 1000 photometric data points in the archive up to the 20^{th} July 2010 when the database query was performed.

Objects in the SuperWASP catalog may have correlated with ROSAT sources by random chance. To test this, the original positions of all objects observed in the SuperWASP catalog were offset by 1' and checked again for neighbouring ROSAT sources. The ROSAT error circles are about $10 - 20$", therefore a search radius of 15" was used to identify any neighbouring objects in the ROSAT catalog. Only one object (SW1000−0854) out of 146 had a neighbouring ROSAT source subsequent to being shifted by 1'. The chance of random correlation is 0.68 per cent.

Periodic variable stars were identified using the Lomb-Scargle periodogram technique described in Maxted et al. (2011). The Lomb-Scargle technique (Lomb 1976; Scargle 1982; Horne & Baliunas 1986; Zechmeister & Kürster 2009) searches for significant periodicities in unevenly sampled data. The SuperWASP light-curves are measured over several seasons of observation, each of which typically have $\sim$ 8000 unevenly sampled data points. To measure the period, the normalised power, $P_n(\omega)$ at a given angular frequency ($\omega = 2\pi\nu$) was calculated. The highest peaks in the calculated power spectrum correspond to candidate periodicities in the time series data. To obtain a solution for the light-curve, a least-squares fit of the sinusoidal function $y_i = a\sin(\omega t_i) + b\cos(\omega t_i)$ to magnitudes $m_i = 1, 2, ..., N$ was found. A power spectrum was obtained based on a χ^2 fit of the light-curve:

$$P_n(\omega) = \frac{\chi_0^2 - \chi^2(\omega)}{\chi_0^2}, \tag{5.1}$$

where

$$\chi_0^2 = \sum \frac{m_i^2}{\sigma_i^2},$$

and

$$\chi^2(\omega) = \sum \frac{(m_i - y_i)^2}{\sigma_i^2}$$

To ensure the signal is not a noise artefact, false alarm probabilities (FAPs) were calculated based on a bootstrap Monte Carlo technique developed by Collier Cameron et al. (2009). The FAP related to a given power P_n is taken as the fraction of randomised light-curves that have a highest power peak that exceeds P_n, which is the probability that a peak of a given height is merely caused by statistical variations (i.e., white noise). The spectrum of FAPs was used to estimate the power value in the periodogram for which this probability is 0.1, 1 and 10 per cent, all of which are labelled in the right panel of each light-curve presented in appendices A.3 and A.4.

Based on all the available periodograms, the periods were given a quality classification. If 3 or more seasons of data for an object resulted in an average period with a

standard error smaller than 5 per cent they were graded as 'A'. To assess the reliability of the period determination, the difference in χ^2 ($\Delta\chi^2$) between the second highest peak in each periodogram to the highest peak was calculated. If $\Delta\chi^2$, averaged over all observing seasons, was large enough (each light-curve contains ~ 8000 datapoints, so an average $\Delta\chi^2 > 1000$ was chosen as the minimum cut-off) and the value of the highest peak was larger than the FAP value at 0.1 per cent, this was considered a reliable period measurement. Objects with 1 or 2 seasons of data and satisfying the average $\Delta\chi^2$ criteria, and having a standard error smaller than 5 per cent were graded as 'B', whereas objects failing either the $\Delta\chi^2$ condition or resulting in large standard errors for their periods were graded 'C'.

For stars that were subsequently assessed as having ages less than 200 Myr (and unlikely to be spectroscopic binaries, see §5.6), the raw light-curves, periodograms and corresponding phase-folded light-curves are provided in §A.2. For the rest of the targets, the equivalent data are provided in §A.3. A summary of the period data, light-curve quality and binarity status (see §5.4.3) is provided in Table 5.1. The initial analysis of rotation periods that were used for target selection (see §5.4.1) were based on SWASP data up to 20$^{\text{th}}$ July 2010. The final results reported in this thesis are based on a reanalysis of the spectroscopically observed targets, based on all the data available up until December 2012. In most cases these agree with the original periods, however there are a handful of significant discrepancies.

The main source of B and V magnitudes are from the AAVSO All-Sky Photometric Survey (APASS, Henden et al. 2012), which covers the magnitude range $10 < V < 17$. All objects with V magnitudes < 10 that were unavailable in the APASS catalog were instead sourced from the NOMAD catalog (Zacharias et al. 2005). All K magnitudes are from 2MASS (Cutri et al. 2003). Proper-motions are extracted from the PPMXL catalog of positions and proper motions (Roeser, Demleitner & Schilbach 2010). BVK photometry and proper motions for the entire observed sample are presented in Tables 5.5 and 5.7, respectively. Figure 5.5 displays the entire observed sample plotted in terms of their rotation periods and $V - K$.

Table 5.1: Measured rotation periods for the final target sample. Periods are the reanalysed values (and standard errors) using the analysis in §5.2. Error bars on the periods are indicate the standard deviation of 2 or more light-curves. $\Delta\chi^2$ values are described in §5.2 and 'N' refers to the number of seasonal light-curves analysed for each target star. The column labelled 'Q' refers to the quality of the period determination and 'B' is a measure of the likelihood of the target being part of a spectroscopic binary system and is described in §5.4.3. $P_{\rm bin}$ is the probability that the star is a SB with an RV difference less than $5\,{\rm km\,s^{-1}}$ over the timescale between two observations. This is described in more detail in §5.4.4. The columns labelled 'CR', 'ET' and 'HR1' correspond to the X-ray count rate, exposure time and hardness ratios from the ROSAT database and $L_X/L_{\rm bol}$ is the fractional X-ray luminosity. The 'Date' column refers to the month and year when the first observation of the target in this work took place, J11 = June 2011, and D12 = December 2012.

ROSAT (1RXS-)	V (mag)	$V-K$ (mag)	Period (days)	$\Delta\chi^2$	N	Q	B	$P_{\rm bin}$	CR (s^{-1})	ET (min)	HR1	$L_X/L_{\rm bol}$ ($\times10^{-4}$)	Date
J001630.7+054626	11.678	2.175	0.765 ± 0.269	246	4	C	3		6.8	7	−0.29	6.56	D12
J001745.3−010255	9.820	1.560	1.358 ± 0.012	7725	3	A	1	0.12	9.7	6	−0.05	2.40	D12
J001825.5+232432	10.031	1.861	1.538	8302	2	C	2		23.9	4	0.44	8.77	D12
J003130.0+312352	10.044	1.530	0.843 ± 0.235	447	4	C	4		6.0	6	0.60	2.62	D12
J004713.7+381211	10.960	3.142	5.753	2771	2	B	2		10.0	8	−0.09	3.58	D12
J010823.3+313752	11.675	1.924	0.730 ± 0.040	1307	4	A	5	0.10	3.9	7	0.63	6.97	D12
J012458.8+255703	10.718	1.811	3.048 ± 0.026	1711	2	B	1	0.11	6.4	6	0.42	4.45	D12
J012757.8+185928	9.477	1.622	0.776 ± 0.012	1392	2	B	3		36.3	6	0.23	7.62	D12
J013324.9+493711	9.815	1.778	2.681	1833	4	C	4		26.4	4	0.30	7.56	D12
J013514.5+211611	10.788	1.490	1.871 ± 0.004	1994	3	A	1	0.09	1.4	7	1.00	1.43	D12
J014028.6+421159	10.390	2.412	1.061 ± 0.002	5979	3	A	2		30.8	6	−0.05	9.79	D12
J014454.5+282440	11.150	2.621	1.213	1007	4	A	4		6.3	6	0.31	4.52	D12
J015609.0−050044	9.837	2.547	1.922 ± 0.004	17554	3	A	4		11.2	6	0.34	2.53	D12
J022132.9+340449	9.781	1.975	3.618 ± 0.018	9682	3	A	2		11.4	6	0.57	3.42	D12
J022733.2+285834	9.808	1.801	4.312 ± 0.055	20549	4	A	2		7.4	5	0.48	2.29	D12
J023504.2+313927	10.337	1.743	1.274 ± 0.002	2038	4	A	1	0.10	15.2	6	0.17	6.59	D12
J025740.5+235755	9.834	2.280	3.357 ± 0.016	13011	2	B	2		39.6	2	−0.06	7.90	D12
J030405.0+300312	10.875	1.807	1.806 ± 0.005	1518	2	B	1	0.09	6.5	8	0.66	5.84	D12
J031627.0+563901	10.667	2.103	3.850	584	2	C	1	0.15	8.4	9	0.34	4.86	D12
J032231.4+285330	10.672	2.013	1.654 ± 0.011	281	2	C	1	0.12	5.9	7	0.86	4.54	D12
J033027.3+541741	9.190	1.910	0.790	137	2	C	5		9.4	9	0.10	1.30	D12
J033154.4+483135	10.245	1.227	0.332	159	1	C	1	0.10	4.3	8	1.00	2.78	D12
J033442.2+475319	10.669	1.463	0.701	746	1	C	1	0.11	5.5	8	1.00	5.14	D12
J033850.3+463627	10.069	1.312	0.711	460	1	C	5	0.13	5.9	8	0.76	2.92	D12
J034057.7+311756	11.146	2.420	4.267	148	2	C	4		3.8	7	0.78	3.72	D12
J034145.2+271855	11.622	2.769	2.639	5610	2	B	4		10.1	7	−0.15	7.92	D12
J034318.7+222704	11.571	2.545	2.893	1075	1	B	1	0.10	5.6	6	1.00	8.43	D12
J034433.9+504343	10.769	2.294	0.897	2001	2	B	3		7.6	9	0.88	5.80	D12
J034514.5+561535	11.444	2.678	0.752 ± 0.336	334	2	C	3		11.1	11	0.00	8.54	D12
J034630.6+330238	10.634	3.023	1.120	95	1	C	3		7.2	86	1.00	3.55	D12
J040105.2+343906	10.602	3.165	0.922 ± 0.023	2417	4	A	2		0.5	357	1.00	0.24	D12
J041702.1+353116	10.677	2.606	1.742	5288	1	B	2		21.4	9	−0.25	7.04	D12
J041946.0+231750	10.712	2.346	2.197	323	1	C	2		15.8	9	0.02	7.27	D12
J042315.8+555652	9.775	1.602	1.351	524	1	C	1	0.09	11.4	9	0.29	3.27	D12
J043119.5+375143	11.219	1.945	2.397 ± 2.692	702	3	C	3		5.7	8	0.69	6.80	D12
J050205.8+311111	10.792	2.218	4.531	4169	1	B	1	0.10	6.7	7	−0.07	3.31	D12
J052036.6+244731	11.515	2.443	0.694	2489	1	B	3		5.3	7	1.00	7.87	D12
J052146.7+240036	10.393	2.323	3.436	9955	1	C	1	0.11	29.8	7	−0.08	9.65	D12
J052405.8+540403	10.212	2.698	3.066	332	1	C	3		5.1	7	1.00	2.02	D12
J052638.7+223151	11.760	2.420	4.655	701	1	C	1	0.12	9.8	7	0.08	11.90	D12
J053103.9+231232	9.374	1.971	0.950	654	1	C	4		54.2	7	0.17	9.12	D12
J053506.4+394644	10.442	2.345	4.452	7473	2	B	3		6.8	7	0.87	3.74	D12
J054629.4+504005	10.502	1.458	4.096	904	1	C	1	0.12	1.2	135	0.38	0.72	D12
J055632.8+230554	11.817	2.533	0.754	614	1	C	2		10.7	7	0.37	15.25	D12
J064039.3+251851	10.740	2.617	5.505	1966	1	B	4		5.2	7	1.00	3.52	D12
J074610.3+285826	10.109	2.608	2.259 ± 0.020	2898	3	A	2		42.6	7	−0.21	8.56	D12
J080657.4+253204	9.909	2.699	1.185	22902	1	B	2		11.5	7	−0.12	1.96	D12
J081539.3+294641	10.782	2.415	1.071 ± 0.003	563	2	C	2		9.9	3	0.08	4.89	D12
J081714.0+324152	12.546	2.440	0.555	579	4	C	2		6.0	7	0.03	14.37	D12
J082814.5−084343	9.165	3.119	3.404 ± 3.605	14166	2	B	2		5.6	5	0.73	0.61	D12
J082808.7+422247	10.094	2.736	3.324	1673	3	A	4		5.8	8	0.62	1.74	D12
J083336.3+322450	11.648	2.444	2.505 ± 0.877	303	3	C	5	0.10	9.5	4	0.41	12.38	D12
J083336.1+335029	9.987	2.281	2.381	11166	1	B	4		33.6	5	0.09	8.50	D12
J083843.1−074110	10.741	1.678	1.947 ± 0.026	1827	4	A	4		6.1	5	0.57	4.83	D12
J084748.1+342357	10.304	1.686	4.231	996	2	C	1	0.12	3.4	48.	−0.08	1.26	D12
J085231.1+390718	11.170	1.838	1.478 ± 0.713	45296	2	C	2		8.6	7	0.35	8.69	D12
J085922.5−091632	10.251	2.525	4.971	216	1	C	1	0.15	6.0	6	0.21	1.86	D12
J090610.7+333748	9.791	1.304	3.969 ± 0.044	216	2	C	1	0.09	1.3	365	−0.02	0.33	D12
J095945.7+384910	10.002	2.467	0.759	1126	2	B	2		30.7	8	0.00	6.88	D12
J100035.3−085442	11.502	2.428	4.218 ± 0.020	4477	5	A	5	0.15	8.3	7	0.63	10.51	D12
J105541.8+424603	10.805	2.536	0.979	160	1	C	3		17.7	7	−0.23	6.87	D12
J105933.7+231548	11.078	2.545	0.638	956	1	C	3		47.2	4	0.03	28.03	D12
J113033.9−022656	10.946	2.622	0.884 ± 0.002	1601	5	A	4		18.2	7	−0.09	8.53	D12
J113352.8+361331	11.706	3.001	1.447	592	2	C	4		11.0	5	0.17	10.00	J11
J114608.2+400156	12.680	4.563	1.369	1001	1	B	2		15.3	5	0.15	10.96	J11
J114804.0−081850	10.404	1.803	2.036 ± 0.006	552	2	C	2		7.4	6	0.49	3.98	D12
J120803.6+311055	11.799	2.744	0.232	1791	1	B	3		6.8	8	−0.24	5.95	J11
J122105.7+200541	10.662	2.361	5.753	7436	2	B	2		5.8	8	0.13	2.70	D12
J123740.0+345055	12.017	3.510	3.985 ± 0.022	871	2	C	1	0.15	5.0	9	−0.12	3.71	D12
J125146.8+223240	10.534	3.282	3.434 ± 0.011	1141	2	B	2		42.0	8	−0.20	8.66	J11
J125128.7+250532	11.335	2.550	0.966	766	1	C	2		1.7	135	−0.37	0.96	D12
J132117.1+210116	11.745	2.485	1.346 ± 0.001	611	3	C	4		5.6	5	−0.15	5.62	J11

Table 5.1: *continued.*

ROSAT (1RXS-)	V (mag)	$V-K$ (mag)	Period (days)	$\Delta\chi^2$	N	Q	B	$P_{\rm bin}$	CR (s^{-1})	ET (min)	HR1	$L_X/L_{\rm bol}$	Date
J132713.0+455826	11.174	3.136	2.159	639	1	C	1	0.15	16.0	10	−0.11	6.80	J11
J132838.0+353303	11.902	2.064	0.200 ± 0.001	1892	4	A	2		3.5	27	−0.05	5.14	J11
J132943.2−045418	9.783	2.132	3.025 ± 0.007	29256	3	A	5	0.14	28.8	4	0.59	8.28	J11
J133241.6+223007	9.655	2.808	1.040	186	1	C	1	0.12	84.4	6	−0.13	10.70	J11
J133318.7+230110	9.800	1.783	0.214 ± 0.001	5513	1	B	3		9.5	6	0.25	2.61	J11
J133707.9+444449	11.050	1.954	4.376	301	1	C	1	0.17	7.2	11	−0.11	4.75	D12
J134327.7+391131	11.456	2.157	3.052 ± 0.001	4181	2	B	2		7.5	10	0.00	7.30	J11
J135458.3−054348	9.231	2.091	5.361 ± 0.040	319	2	C	1	0.18	8.8	4	−0.60	0.69	D12
J141913.3−163420	9.489	2.292	0.673 ± 0.001	8636	3	A	3		34.1	5	0.24	5.91	J11
J142057.2+345958	9.233	2.619	2.032 ± 0.001	2922	3	A	2		27.0	9	0.00	2.78	J11
J142903.2+335033	9.233	1.869	3.808 ± 0.074	3710	4	A	4		17.7	10	0.16	2.67	J11
J143711.9−033121	10.944	2.726	1.109 ± 0.001	2729	2	B	1	0.13	11.0	5	0.94	8.31	J11
J143854.8+330022	11.036	2.219	5.095 ± 0.036	3576	2	B	1	0.13	5.5	7	0.40	4.41	D12
J144522.9−085425	10.613	2.648	5.261 ± 0.082	10865	3	A	1	0.13	16.9	3	0.31	7.31	D12
J150206.0−120206	11.200	3.247	2.686 ± 0.003	24962	2	B	1	0.19	11.2	4	0.64	7.01	J11
J152807.3−101035	11.460	2.747	1.430 ± 0.009	6005	4	A	5		7.6	6	0.85	8.80	J11
J153144.1−073451	10.774	1.883	1.377	920	1	C	5		7.0	6	0.94	6.30	J11
J154841.1−031040	10.859	2.615	1.906 ± 0.002	1292	2	B	3		3.6	164	0.94	2.65	J11
J155007.4−022229	10.050	2.538	2.241 ± 0.007	37160	3	A	1	0.13	48.3	7	−0.09	10.33	J11
J160714.4+340123	10.895	3.159	0.742 ± 0.007	19661	3	A	2		26.8	10	−0.28	7.84	J11
J162255.0+224559	10.646	2.052	1.740	439	1	C	4		10.8	10	0.61	7.15	J11
J162506.5+300218	10.205	3.022	1.002 ± 0.098	51786	2	B	1	0.52	22.0	10	0.29	5.31	D12
J162640.6+335033	9.622	2.492	19.88 ± 3.443	2987	6	C	5	0.45	77.7	12	0.13	1.32	J11
J162946.1+281034	10.654	1.925	1.426 ± 0.003	5023	4	A	1	0.12	9.2	9	0.87	7.17	J11
J163739.5+221104	10.761	2.468	2.089	18635	1	B	2		14.8	7	0.35	8.18	J11
J163741.2+291946	11.440	2.862	0.825	7687	1	B	3		7.9	8	0.29	6.53	J11
J165000.2+412217	10.928	2.141	1.828 ± 0.014	5582	5	A	2		11.3	11	−0.09	6.38	J11
J165921.7+342822	10.580	1.240	1.569 ± 0.008	184	5	C	2		1.7	97	0.01	0.92	J11
J170303.1+320320	11.362	1.824	2.513 ± 0.745	1542	6	C	4		5.9	13	0.44	7.49	J11
J170420.7+392909	11.362	2.453	0.753 ± 0.077	4046	3	A	3		6.2	15	0.21	5.56	J11
J171331.0+232021	11.373	2.865	2.789	2278	1	B	2	0.14	10.2	11	0.46	8.62	J11
J171807.5+250610	10.614	3.027	2.420 ± 0.008	5432	2	B	1	0.09	27.2	11	0.04	8.27	J11
J172228.5+365843	10.504	2.800	1.229 ± 0.001	10864	9	A	1	0.12	24.8	14	−0.06	7.24	J11
J172413.5+402616	11.253	2.574	0.289 ± 0.010	6715	10	A	3	0.10	5.5	16	0.44	4.79	J11
J173103.4+281510	10.213	2.402	1.263 ± 0.002	13828	3	A	2	0.12	28.7	12	−0.05	7.78	J11
J174432.1+131259	11.335	2.652	2.698	1152	1	B	2		5.8	8	0.33	4.91	J11
J174704.1+332126	11.456	2.495	3.169 ± 0.036	6283	3	A	5	0.27	5.4	14	−0.32	3.64	J11
J174947.6+335056	10.528	1.874	1.355 ± 0.008	10284	3	A	4		6.5	14	0.06	3.03	J11
J175133.3+414121	9.836	2.645	4.666 ± 0.018	6775	4	A	3		6.7	18	0.26	1.38	J11
J175242.3+232724	10.245	2.446	1.549 ± 0.005	873	3	C	3		12.4	11	0.78	5.26	J11
J175718.5+313314	10.545	1.791	0.698 ± 0.002	31927	5	A	3	0.08	14.4	13	0.25	7.84	J11
J175758.9+550608	11.216	2.885	0.637 ± 0.001	4426	5	A	3		11.8	37	0.10	7.04	J11
J175809.3+092241	10.750	2.277	0.728 ± 0.339	90	2	C	1	0.10	10.2	5	0.85	7.61	J11
J180028.5+510002	9.742	1.224	1.194 ± 0.004	1307	5	A	3		2.2	171	0.16	0.61	J11
J180426.3+393044	11.532	2.365	1.547 ± 0.004	3260	5	A	1	0.12	7.3	16	0.01	7.07	J11
J181258.6+410604	11.840	2.691	0.655 ± 0.005	680	3	C	4	0.09	6.4	17	0.00	7.08	J11
J181511.0+294827	9.187	1.387	2.663 ± 0.006	3829	3	A	2		6.0	10	0.07	0.92	J11
J181537.9+381927	9.885	1.597	3.161 ± 0.024	945	4	C	4		7.1	15	0.05	1.97	J11
J183018.1+344633	10.530	1.724	3.099 ± 0.082	5139	7	A	2		7.2	13	0.48	4.41	J11
J183139.0+541843	9.929	1.810	0.636 ± 0.001	1313	4	A	3		14.6	29	0.25	4.49	J11
J191302.4+443629	10.283	2.117	3.520 ± 0.058	12092	4	A	3		8.0	10	0.73	3.91	J11
J192502.2+442948	9.939	2.398	1.205 ± 0.001	11141	2	B	1	0.11	24.2	10	0.18	5.89	J11
J202823.9+113115	9.681	1.645	2.390	5957	2	B	3		10.2	7	0.39	1.83	J11
J202843.1−094317	9.317	2.186	0.510 ± 1.086	23965	3	C	3		5.1	5	1.00	1.71	J11
J204404.5+131413	10.538	1.911	2.156 ± 0.005	4208	4	A	4		8.4	8	0.02	3.85	J11
J204859.5−064453	9.588	2.318	2.049 ± 0.008	22539	2	B	5	0.12	36.4	6	0.24	6.84	J11
J205831.1−090233	11.180	2.071	2.251 ± 0.012	5173	6	A	1	0.13	11.2	6	0.28	10.25	J11
J210707.1+063247	9.869	2.000	6.331 ± 2.413	3677	7	C	5	0.19	5.5	8	0.93	2.08	J11
J210747.5+135735	10.613	1.892	14.10 ± 1.254	518	3	C	3		5.4	7	0.89	4.08	J11
J212136.2+094834	10.333	1.904	3.564 ± 0.056	11894	3	A	5	0.15	5.8	8	0.77	3.25	J11
J214539.0+271124	11.425	2.305	1.267 ± 0.225	1152	3	B	1	0.12	5.6	6	0.29	5.94	D12
J214810.6+191013	10.734	2.967	1.165 ± 0.002	7003	2	B	5	0.14	23.9	5	−0.21	7.11	J11
J220459.1+074940	11.810	3.083	2.707 ± 0.005	26239	5	A	4		8.2	4	0.77	10.51	J11
J222229.1+281432	9.926	1.537	2.287 ± 0.011	5425	5	A	4		29.1	9	0.22	9.36	J11
J224446.2+302927	10.241	2.000	3.556	269	1	C	4		8.8	9	0.42	3.71	D12
J225617.9+205257	11.410	2.731	1.100 ± 0.003	1164	4	A	2		8.2	4	0.06	6.20	J11
J230752.8+171033	10.780	2.881	1.073 ± 0.002	980	3	C	2		30.9	7	−0.25	9.72	J11
J231037.8+205531	10.033	2.252	0.923 ± 0.002	13079	3	A	3		41.4	8	0.01	10.49	J11
J231229.1+170935	11.057	3.325	3.094 ± 0.015	49598	3	A	2		31.6	6	−0.32	9.36	J11
J231713.2+055107	10.305	2.928	2.226	4426	2	B	4		7.3	7	0.97	2.77	D12
J232048.8+292151	11.400	1.581	1.098 ± 0.451	1420	3	C	1	0.15	5.3	8	0.41	7.30	D12
J233907.3+220355	10.382	2.454	4.107 ± 0.051	1301	3	A	4		17.7	7	0.24	6.51	D12
J234008.0−022906	9.893	1.490	2.893	5762	2	B	1	0.14	8.8	6	0.68	3.48	D12
J235750.3+334401	11.271	2.625	1.420	15441	1	B	2		8.6	5	0.06	5.97	J11

5.3 X-ray activity in the ROSAT catalog

The initial target selection described in §5.4 were selected based on having short rotation periods and displaying rotational modulation in light-curves. All objects have entries in both ROSAT and SuperWASP. Throughout the selection process no criteria were used based on any specific X-ray property – a database entry in either the 1RXS or 2RXP catalog was deemed sufficient. Data were available for all the selected targets and were analysed subsequent to the telescope observations. §1.4.2.1 describes how X-ray data can be utilised as an age proxy and its effectiveness/limitations at ages $< 1\,\mathrm{Gyr}$. $L_\mathrm{X}/L_\mathrm{bol}$ was calculated for each object using:

$$\frac{L_\mathrm{X}}{L_\mathrm{bol}} = \frac{f_\mathrm{X}}{2.48 \times 10^{-5} \times 10^{-0.4 m_\mathrm{bol}}} \tag{5.2}$$

To obtain values of $L_\mathrm{X}/L_\mathrm{bol}$ for each target star the ROSAT catalogs were revisited to obtain count rates, exposure times and hardness ratios (all provided in Table 5.1). X-ray fluxes (f_X) were calculated by multiplying the count rate by the energy conversion factor (ECF) provided in Stelzer & Neuhäuser (2001):

$$\mathrm{ECF} = (8.31 + 5.30\,\mathrm{HR1}) \times 10^{-12} \mathrm{erg\,cm^{-2}\,cr^{-1}} \tag{5.3}$$

Bolometric magnitudes were found using V magnitudes and a main-sequence bolometric correction interpolated from $V - K$ using table 5 in Pecaut & Mamajek (2013). Main-sequence conversions should be appropriate for the F, G and K stars in this sample, however, objects younger than 30 Myr may result in a small calibration error on the order of ~ 0.1 dex.

Figure 5.1 shows $L_\mathrm{X}/L_\mathrm{bol}$ as a function of $V-K$ and Rossby number. Convective turnover times were calculated using the τ_C versus $B-V$ empirical relation (equation 4) in Noyes et al. (1984). For reference, the 10^th and 90^th percentile $L_\mathrm{X}/L_\mathrm{bol}$ range for F, G and K stars in NGC 2547, the Pleiades and the Hyades (based on figure 12 in Jeffries et al. 2006) are represented by light blue/blue/dark blue lines (respectively). $L_\mathrm{X}/L_\mathrm{bol}$ is a relatively crude age indicator and largely rotation-dependent in any case. Almost

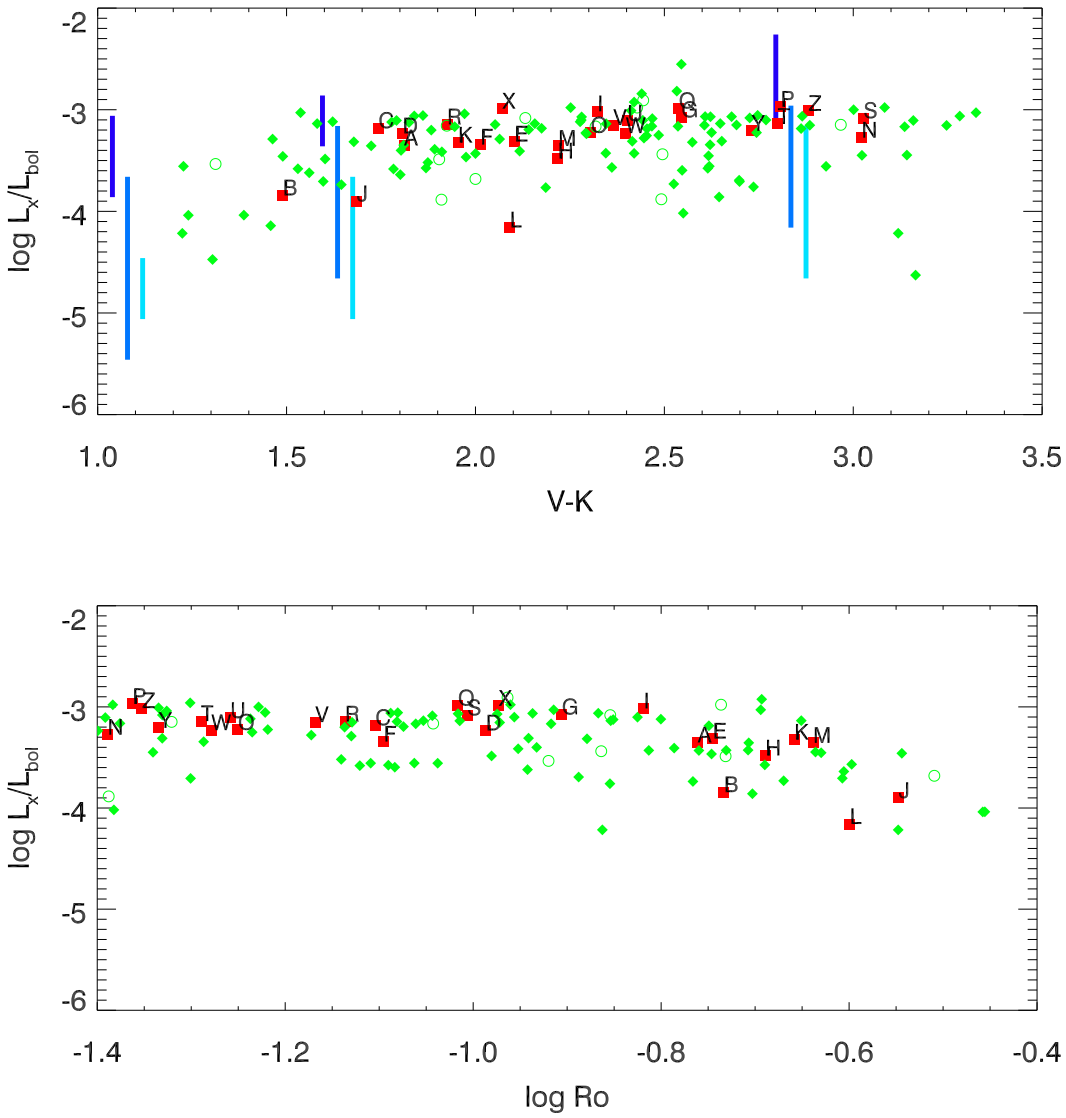

Figure 5.1: Top: $\log L_{\rm X}/L_{\rm bol}$ as a function of $V-K$. The $10^{\rm th}$ to $90^{\rm th}$ percentile range of $L_{\rm X}/L_{\rm bol}$ values in NGC 2547, the Pleiades and the Hyades are represented by the dark blue/blue/light blue lines, respectively. Bottom: $\log L_{\rm X}/L_{\rm bol}$ as a function of Rossby number. Rossby numbers are calculated from the relationship in Noyes et al. (1984). Red squares represent 26 objects that were later identified to be likely-young and were considered likely-single stars (referred to as the 'likely-young sample' in §5.6). All these objects are labelled from A to Z and their names correspond to those in Table 5.8. Any objects that had two or more separate RV measurements that varied by more than $5\,{\rm km\,s^{-1}}$ were assumed to be close-in spectroscopic binaries and are denoted here by open green circles. All other objects are designated by filled green diamonds. This symbol scheme for all other plots will remain the same throughout this chapter.

all of the candidates could be consistent with a Pleiades age (as expected for their rotation rates). Figure 5.1 shows that the genuinely young objects (red squares) have values of $\log L_{\rm X}/L_{\rm bol} \sim 0.5\,$dex greater than the average object in the entire sample.

5.4 Spectroscopic observations and sample selection

5.4.1 Sample selection

Prior to selecting targets for spectroscopy, the light-curves for the sample available in the SuperWASP catalog were checked to identify objects most likely to be showing variability in their light-curves as a result of starspot modulation. These were more likely to be objects with several seasonal light-curves. Whilst some objects had consistent periods measured from many seasons of data, with clear sinusoidal behaviour, some of the sample had sparse, poor quality data and sometimes inconsistent period determinations. Because of the range of quality in data the selection process was entirely subjective. Any objects indicating a sharp dip in their light-curve over any part of their phase were flagged as eclipsing binaries and discarded.

From the initial catalog of 5477 targets, 146 were chosen for spectroscopic investigation based on inspection of their light-curves, period analysis, and their visibility at the time of observation[1]. Rapidly-rotating, late-type stars with periods less than 5 days were considered for target selection. The observed targets are listed in Table 5.1. Note that for the purposes of this chapter, the light-curves were reanalysed after the observing run using a larger dataset (see §5.2) and nine of the redetermined periods were subsequently found to have periods > 5 days (see Table 5.1).

The range of target spectral-types is restricted to the range mid-F to late-K (approximately $1.0 < V - K < 3.5$) for two reasons. First, because Li was to be

[1]for the rest of this chapter the nomenclature for the targets are 'SW' followed by the hours and minutes in right ascension and the degrees and minutes in declination given in the ROSAT catalog, e.g., 1RXS J001630.7+054626 = SW0016+0546.

used as a primary youth indicator, this range contains stars where significant and measurable Li depletion is expected on timescales of $10-100$ Myr (see Soderblom 2010 and §1.4.3.1). The hot boundary is where Li-depletion timescales become very long and poorly understood diffusive or other non-standard mixing processes may become dominant (Boesgaard & Tripicco 1986), whilst the cool boundary marks the point where Li depletion occurs extremely rapidly and even very young stars may have depleted their Li (e.g., Jeffries 2006). Secondly, low-mass MG stars will usually rotate very rapidly; FGK stars typically have spin-down timescales of $\sim 50-100$ Myr, and M-dwarfs ~ 300 Myr or longer (this is illustrated by the gyrochrones in Figure 5.5, see also §1.4.1). Thus fast rotation in M-dwarfs is not necessarily a sign of youth and the targetting of such objects could lead to high contamination with older stars. The basis for choosing the objects in terms of colour and rotation period is discussed in more detail in §5.6.1 where 'gyrochronology' is used to provide age estimates.

An important point is that the nature of the target selection, from an all-sky survey, allows for a *kinematically unbiased* sample, independent of proper-motion or RV criteria. This provides an opportunity to identify young stars that do not share the Galactic space motions of previously identified MGs. The sample is not spatially unbiased, however, because the SuperWASP survey avoids Galactic latitudes between $\pm 20°$.

5.4.2 Observation strategy

High-resolution echelle spectroscopy of 146 objects was obtained over 2 telescope runs using the Fibre-fed Echelle Spectrograph (FIES) on the 2.56 m Nordic Optical Telescope (NOT). The first observing run of 68 targets lasted 4 consecutive nights from the 21$^{\rm st}$ June 2011, and a further 78 targets were observed on the 27$^{\rm th}$, 28$^{\rm th}$ and 29$^{\rm th}$ December 2012 (these are listed in the 'Date' column in Table 5.1). Details of the observational set-up and the telescope/instrument capabilities are discussed in §3.1.1.

The observing strategy was to obtain a single observation of a target, reduce the data in real time at the telescope and inspect the spectrum for the presence of the

Li I 6708Å doublet. If Li was clearly present then, if necessary, a further exposure was performed to obtain a signal-to-noise ratio (SNR) per pixel of ≥ 50 around the Li line. Objects where Li was detected were observed again on a subsequent night in order to check for short-term RV changes that might betray their close binary nature (see §5.4.3 for further details on spectroscopic binaries).

To further identify whether or not objects were spectroscopic binaries (SBs, see §5.3.3), several of the most probable young objects were later re-examined using long-slit spectroscopy on the Isaac Newton Telescope (INT) on the 23$^{\rm rd}$ and 24$^{\rm th}$ March 2013 (these observations are labelled 'M13' and the observational set-up is described in §3.1.2), in combination with the H1800V grating and IDS-235 wide-field camera. This allowed for a RV precision of $\sim 1-2\,{\rm km\,s^{-1}}$ and these measurements were compared to the RVs measured at the NOT. In this chapter, the RV measurements on the INT are not incorporated into the averaged final RV, rather they are used to check for RV consistency and Li content. All individually measured RVs are presented in column 4 of Table 5.7 and INT observations are subscripted with an 'i'.

Observations were also made of several RV and low-activity standard stars (selected for their low levels of chromospheric Ca II H and K emission) over a similar spectral-type range as the targets. Standards chosen for low-activity exhibited $\log R'_{\rm HK}$ values that were generally less active than solar-types in the Hyades (see table 3 in Mamajek & Hillenbrand 2008) and were largely consistent with old inactive field stars. These were subsequently used to calibrate RVs and projected rotational velocities ($v \sin i$). Spectral-type, RV, $v \sin i$ and $\log R'_{\rm HK}$ values for all the standards used are listed Table 5.2.

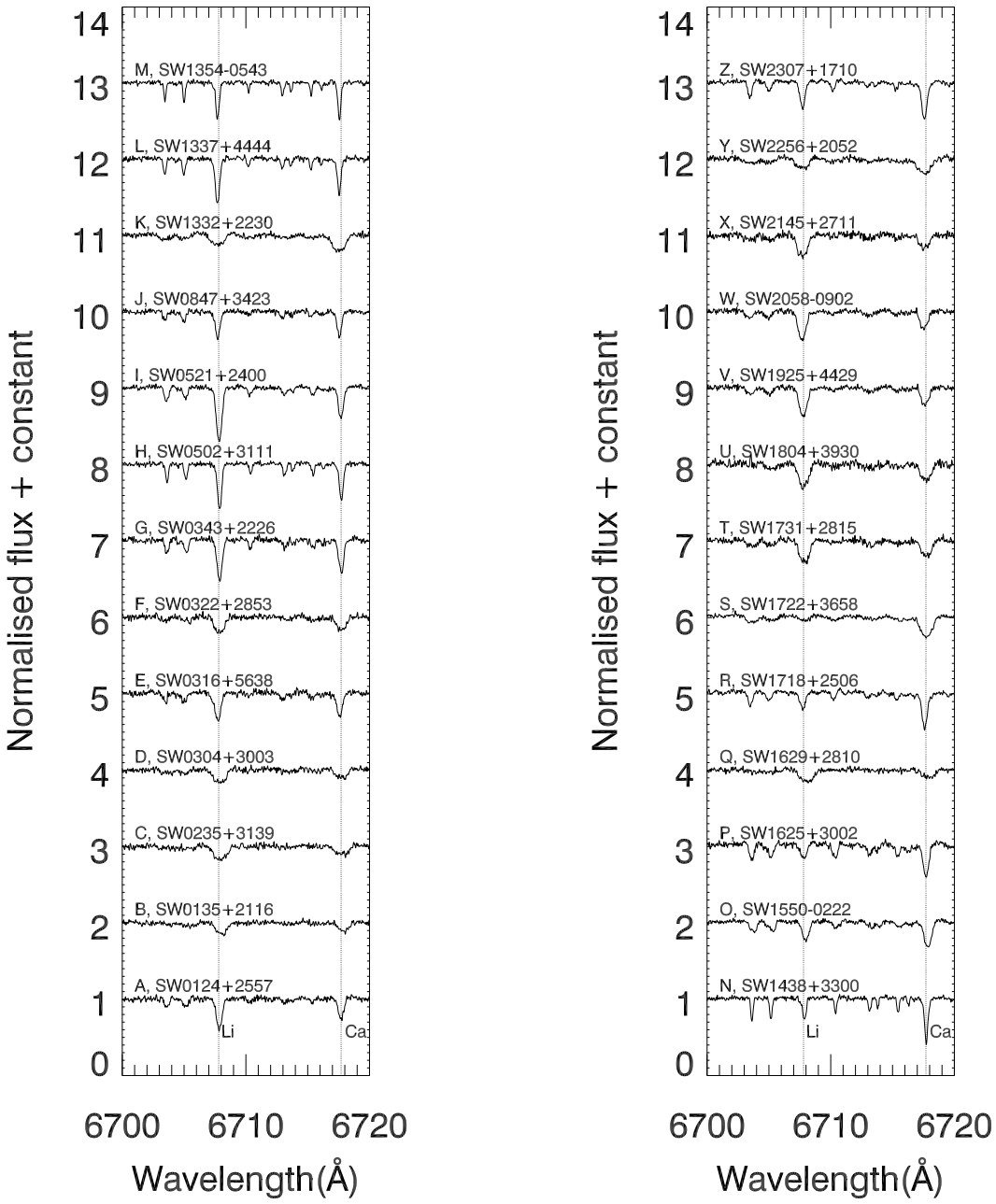

Figure 5.2: Heliocentrically-corrected and normalised spectra for the likely-young sample near the Li I 6708Å line.

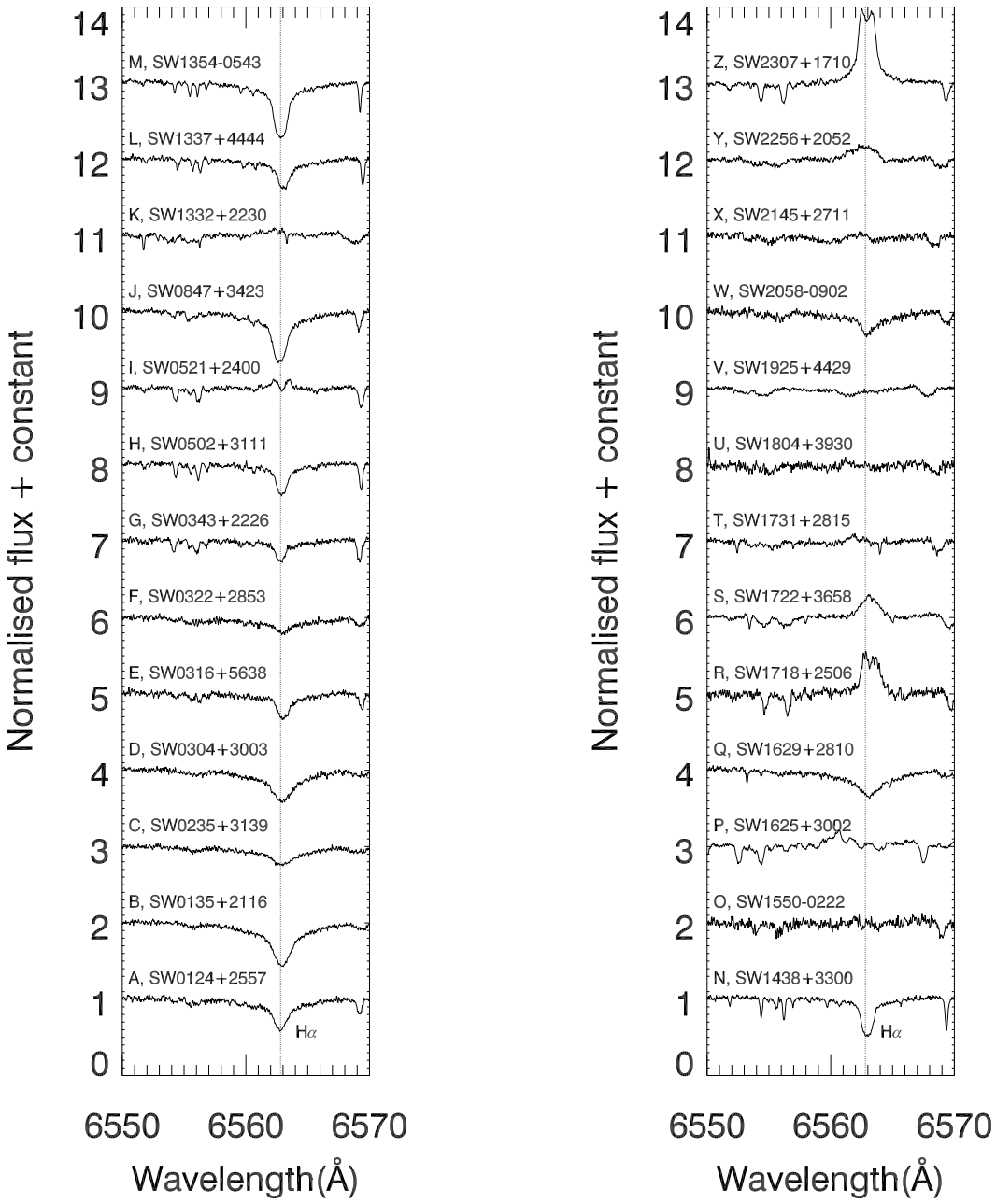

Figure 5.3: Heliocentrically-corrected and normalised spectra for the likely-young sample near the Hα 6563Å line.

Standard	Spectral-type	RV $\mathrm{km\,s^{-1}}$	σ_{RV} $\mathrm{km\,s^{-1}}$	$v \sin i$ $\mathrm{km\,s^{-1}}$	$\log R'_{\mathrm{HK}}$
HD 114762	F8V	49.4	0.5	1.7	−4.902
HD 1461	G0V	−10.158	0.116	5.0	−5.008
HD 95128	G1V	11.293	0.108	3.1	−4.973
HD 217014	G2.5IVa	−33.118	0.128	2.8	−5.054
HD 197076	G5V	−35.402	0.030	2.9	−4.872
HD 9407	G6V	−33.313	0.124	0.0	−4.986
HD 115617	G7V	−7.844	0.128	0.5	−4.962
HD 101501	G8V	−5.464	0.105	2.3	−4.483
HD 3651	K0V	−32.940	0.042	0.6	−4.849
HD 10780	K0V	2.814	0.086	0.9	−4.700
HD 131509	K0V	−44.749	0.167	6.4	−5.142
HD 4628	K2.5V	−10.229	0.030	1.6	−4.979
HD 190007	K4Vk	−30.270	0.105	2.8	−4.592
HD 209290	M0V	18.275	0.120	3.8	
HD 119850	M1.5V	15.778	0.061	1.8	
GJ 411	M2.0V	−84.683	0.030	1.6	
GJ 526	M4.0V	15.778	0.061	1.8	

Table 5.2: RV and minimum activity standards. All RVs are from Chubak et al. (2012), except for HD 114762 (Udry, Mayor & Queloz 1999). All $v \sin i$ values are from Glebocki & Gnacinski (2005). All $\log R'_{\mathrm{HK}}$ are from Isaacson & Fischer (2010), except for HD 3651 (Pace 2013) and HD 190007 (Mittag et al. 2011).

5.4.3 Binary contaminants

Tidally-locked SBs maintain large amounts of angular momentum well into their main sequence lifetimes and therefore retain short rotation periods. Solar-mass binaries starting from the birthline that have periods ≤ 8 days will have circular orbits and synchronous rotation upon reaching the main sequence (Stahler & Palla 2005). Short period SBs are expected to be the main contaminants in the survey, but should have large RV variations detectable by two observations separated by ~ 24 hours.

It is generally acknowledged that higher than normal Li abundance is common among magnetically active stars, and in this work high levels of rotationally-induced activity could be from either young, single rapid rotators, or tidally-locked SBs. Strass-

meier et al. (2012) find that Li abundances in cool binary stars generally increase with effective temperatures and follow a different overall trend compared to single stars, however they find that binaries exhibit 0.25 dex less Li abundance on average than single stars for a given $T_{\rm eff}$. Comparing Li abundances with rotational periods they observe a trend of $\log N({\rm Li}) = -0.6 \log P_{\rm rot}$ for binaries, but with dispersions as large as $3-4$ dex for periods less than 5 days. There is some observational evidence that tidally-locked SBs in the Hyades (0.6 Myr) and M67 (3.7 Gyr) have larger Li abundances than their single counterparts (Barrado y Navascués, Deliyannis & Stauffer 2001, Canto Martins et al. 2011), however this has yet to be empirically quantified. In this work, the EWs, colours and periods of Li-rich objects likely to be SBs are provided but their ages are not assessed and they are not used in further kinematic analyses.

The process of measuring RVs is described in §5.5.2. In general, the RVs of likely-single, slow rotators with a reasonable SNR could be measured to precisions $\leq 1\,{\rm km\,s^{-1}}$. An RV difference $> 5\,{\rm km\,s^{-1}}$ between 2 measurements of the same object on separate nights is treated as sufficient to flag these objects as SB systems. A numerical grading system is used to distinguish likely single stars (allocated a grade of 1) from those very likely to be binaries (allocated a grade of 5). A score of 5 was given if RV differences of $> 5\,{\rm km\,s^{-1}}$ are detected for a target on separate nights or if there were literature sources indicating that either the object is an SB or has a published RV measurement $> 5\,{\rm km\,s^{-1}}$ discrepant with the RV measurements from this work. In addition, to score 5, the average error in RV measurement must be less than $5\,{\rm km\,s^{-1}}$. Objects graded 4 result from obtaining only one spectrum which results in a) a cross-correlation function (CCF) with a template that appeared multiple-peaked and b) an RV error $< 5\,{\rm km\,s^{-1}}$. A grade of 3 was given if the status of the star from the CCF was unclear (presumably as a result of poor SNR and/or large $v \sin i$), resulting in either an indeterminate RV or an average RV error $> 5\,{\rm km\,s^{-1}}$. A grade of 2 was used for objects which had a single spectrum, an RV error less than $5\,{\rm km\,s^{-1}}$ and a distinct single-lined peak in the CCF. Finally, objects scoring 1 had consistent RV measurements for 2 or more spectra. Binary scores for each object are presented in column 8 of Table 5.1 and the individual RV measurements are provided in column 4 of Table 5.7.

From the entire observed sample of 146 objects, 14 scored 5, 26 of them scored either 4, 29 scored 3, 38 scored 2 and 39 objects scored 1. Any objects that scored 5 were automatically assumed to be SBs, and are listed in Table 5.7 with their individual RV measurements for comparison. All targets selected for further analyses in §5.7 have binary scores of either 1 or 2. However, 2 or more consistent RV values for an object is not a guarantee that the object is single. Given that some of the objects in this sample have orbital periods of the order of $\sim$ 24 hours, consistent RV measurements could be a result of measuring two points at the same phase on an RV curve. To fully determine the binary nature of the targets one must obtain long-term observations to fully detect RV variations (should they exist).

5.4.4 Binary simulation

Although the criterion that two separate observations resulting in RV differences $> 5\,\mathrm{km\,s^{-1}}$ is sufficient to flag these objects as SBs, a fraction of SBs with RV differences $< 5\,\mathrm{km\,s^{-1}}$ may remain undetected. Given that these observations are incapable of distinguishing between tidally-locked, short-period SBs and single stars, a simulation was carried out to calculate the probability that an object is an SB with an RV variation $< 5\,\mathrm{km\,s^{-1}}$ over the time between observations.

The RV equation was used to identify the difference in RV at two points on the RV curve separated by a phase equal to the cadence (cad) between observations:

$$\mathrm{RV} = \frac{2\pi a \sin i}{P\sqrt{1-e^2}}[\cos(\theta+\omega) + e\cos\omega], \tag{5.4}$$

where a is the semi-major axis of the elliptic orbit, i is the angle of inclination of the binary system (randomly chosen between 0 and 90°), P is the orbital period (in days, equal to the rotation period for tidally-locked, circular orbits), e is the eccentricity of the ellipse (set at zero for circular orbits), θ is the time-dependent true anomaly and ω is the time-independent argument of periastron. The simulation used 10^6 iterations

using a flat mass-ratio between 0.20 and 0.95 (Hogeveen 1990) and the primary mass was estimated from its spectral-type. Tidally-locked binaries will be circular, therefore $e = 0$ in all calculations. A value between 0 and 2π was randomly assigned for θ. A second RV measurement was calculated by shifting θ by $2\pi/\mathrm{cad}$.

The simulation was carried out for all objects that had 2 separate RV measurements at the NOT. For some targets a poor choice was made for the cadence between observations because they were similar to the rotation period and perhaps a third observation is needed to rule out most of these as being binary. There is a ~ 10 per cent chance that a tidally-locked binary with an orbital period equal to the rotation period may not have have yielded an RV difference of $> 5\,\mathrm{km\,s^{-1}}$. Column 9 in Table 5.1 lists the binary probabilities (P_{bin}) for each object with 2 observations. Simulationss for two objects, SW1332+2230 ($P = 1.04\,\mathrm{days}$, $\mathrm{cad} = 2.00\,\mathrm{days}$, $P_{\mathrm{bin}} = 0.12$) and SW0316+5638 ($P = 3.85\,\mathrm{days}$, $\mathrm{cad} = 0.97\,\mathrm{days}$, $P_{\mathrm{bin}} = 0.15$) are presented in Figure 5.4. In the initial target selection, light-curves indicative of eclipsing binaries were filtered out, therefore simulations with high inclination angles can probably be ruled out. For example, a $0.7M_{\odot}/0.5M_{\odot}$ binary system with an orbital period of 3 days would be at least partially eclipsing if $i > 60°$. The probability of observing an object with $i > 60°$ is $\cos 60° = 0.5$, therefore P_{bin} could be over-estimated by a factor of 2.

An extra simulation was made to compare these results with a general field star population using a period distribution of $\log P(\mathrm{days}) = 5.03 \pm 2.28$ (Raghavan et al. 2010), e randomly ranging from 0 to 1, the same mass-ratio distribution and a 24 hour cadence. The true anomaly was solved iteratively using the Newton-Raphson method. Using a binary fraction of 0.46 (Raghavan et al. 2010), the fraction of 2 point trials that resulted in a velocity difference $> 5\,\mathrm{km\,s^{-1}}$ was 2.2 per cent for binary field stars. Of the 55 objects observed twice in this sample, 11 have RV differences $> 5\,\mathrm{km\,s^{-1}}$, a factor of 10 larger. The larger fraction of SBs observed in this sample is likely because objects were selected with short rotation periods. The sample is probably biased in the sense that objects suspected to be young are observed twice and objects with only one observation may be more likely to be binaries because they are generally as X-ray active as young stars (see Figure 5.1) but were not Li-rich. There is a 7.2 per cent

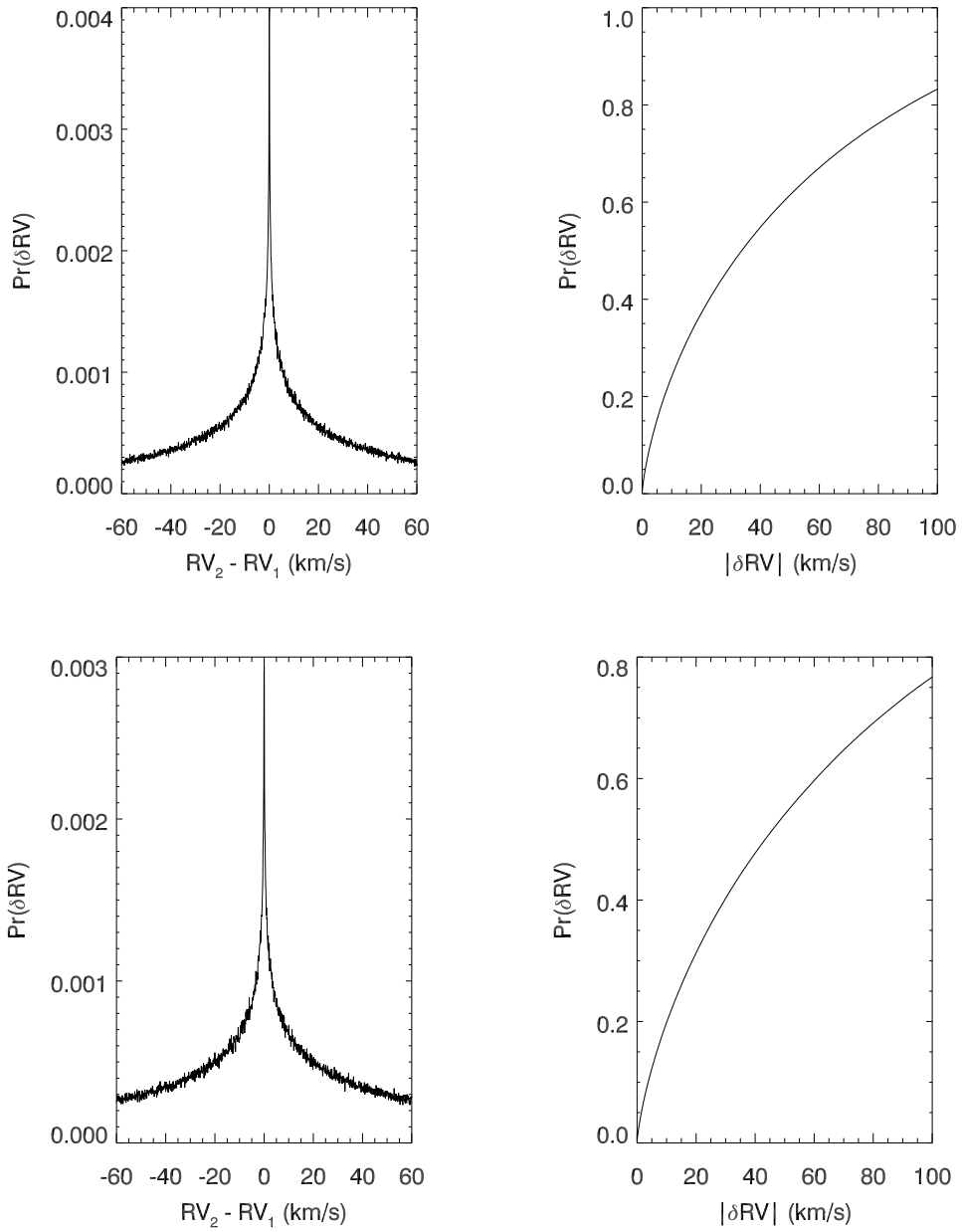

Figure 5.4: Simulations to calculate the fraction of binary objects that would result in an RV difference $< 5\,\mathrm{km\,s^{-1}}$ over the cadence of two observations for SW0316+5638 (top) and SW1332+2230 (bottom). The input parameters and a description of the simulation is provided in §5.4.4. The left panel demonstrates the probability that a binary star has an RV difference ($\mathrm{RV}_2 - \mathrm{RV}_1$) of a certain value. The right panel is the cumulative probability that an object has $|\mathrm{RV}_2 - \mathrm{RV}_1|$ less than a given value.

chance that a star has 2 RV measurements within $5\,\mathrm{km\,s^{-1}}$ but $> 5\,\mathrm{km\,s^{-1}}$ from the average centre-of-mass RV. All binary simulations assume the RV uncertainties are negligible.

5.5 Data analysis and results

5.5.1 Equivalent widths

Li EWs were obtained using the procedure outlined in §4.2.2. A correction for the contaminating Fe I line at 6707.4Å, EW(Fe) = $20(B-V)-3$ mÅ was applied (Soderblom et al. 1993a) and errors were estimated using the Cayrel de Strobel & Spite (1988) formula (provided in §4.2.2). The pixel size for the CCD used in the NOT observations is 0.113Å and 0.35Å for INT observations. The SNR was calculated empirically from the RMS of fits to continuum regions and had an average value of 50 around the Li I 6708Å line. For objects with Li EW $<$ 20mÅ, 2σ upper limits are provided. Measurements of the 6563Å Hα line EW were made by direct integration above a surrounding pseudo-continuum. Both the Li and Hα EW measurements are listed in Table 5.5.

5.5.2 Radial and rotational velocities

To measure RVs and $v \sin i$ the FXCOR procedure in IRAF was used, which is described in §3.3.1 and §3.3.2, respectively. RVs were heliocentrically corrected and uncertainties were a function of SNR, spectral-type and rotational broadening. There were three sources of error: the standard error measured over the 9 echellogram orders (weighted by the 'R' factor described in §3.3.1), the published RV uncertainty of the RV standard used in the calibration and a systematic uncertainty measured by cross-correlating all the RV standards with one another. These errors were treated as independent and were added in quadrature. RV measurements and errors for all targets are provided in Table 5.7, along with any previous literature values. The RV measurements for

each RV standard relative to one another formed a matrix of cross-correlation values. These matrices from the J11 and D12 runs are given in Tables 5.3 and 5.4, respectively. The systematic uncertainty was calculated as $0.36\,\mathrm{km\,s^{-1}}$ for the standards used in the June 2011 run and $0.27\,\mathrm{km\,s^{-1}}$ for the standards used in the December 2012 run. To avoid any spectral mismatch between target and template calibrations, standards are restricted to within 0.5 spectral classes of the target star in each case. RVs from the INT were measured following the procedure in §4.2.1, however, because the resolving power is much less than the NOT, the INT RVs were used only to support data obtained at the NOT and were not included in the final averaged RV.

From the initial sample of 146 targets, 30 were found to have indeterminate RVs (as a result of poorly constrained cross-correlation peaks) and 12 objects were observed to have RVs that varied by more than $5\,\mathrm{km\,s^{-1}}$ on the timescale of the observing run, presumably as a result of binarity (see §5.4.3). The indeterminate RVs were a result of either noisy data, binarity or large $v \sin i$.

Projected rotational velocities ($v \sin i$) were estimated from the CCF widths using a set of simulations. Broadened versions of a number of slowly rotating standard stars (see Table 5.2) were produced by convolving high SNR spectra with a rotational broadening convolution kernel. The details of the technique used to measure $v \sin i$ are provided in §3.3.2. Relationships were derived between FWHM of the CCF and $v \sin i$ using the means from the 9 orders weighted by the R quality factor (see Tonry & Davis 1979 and §3.3.1) for each standard. To ensure there were no spectral mismatches that would lead to badly calibrated CCFs only the spectra for standards within 0.5 of a spectral class of the target in each case were used. The resolving power and SNR for spectra on the INT were insufficient to obtain $v \sin i$ measurements. The measured $v \sin i$ values are presented in Table 5.7.

		Target star							
		GJ 526	HD 114762	GJ 411	HD 95128	HD 190007	HD 217014	HD 9407	HD 114762
Standard star	GJ 526	0.00	0.39	1.67	0.75	0.30	0.07	0.34	0.75
	HD 114762	0.38	0.00	1.60	0.27	0.15	0.02	0.27	0.30
	GJ 411	1.64	1.53	0.00	1.20	1.42	1.67	1.32	1.17
	HD 95128	0.75	0.27	0.07	0.00	0.24	0.34	0.03	0.07
	HD 190007	0.27	0.10	1.42	0.03	0.00	0.10	0.20	0.24
	HD 217014	0.03	0.09	1.67	0.38	0.14	0.00	0.34	0.40
	HD 9407	0.32	0.23	1.32	0.05	0.20	0.33	0.00	0.14
	HD 114762	0.73	0.30	1.23	0.04	0.19	0.34	0.09	0.00
	HD 119850	0.42	0.70	2.05	0.95	0.61	0.47	0.78	1.18
	HD 131509	0.14	0.21	1.74	0.45	0.27	0.10	0.44	0.56
	HD 3651	0.75	0.03	1.57	0.28	0.12	0.09	0.23	0.38
	HD 101501	0.47	0.34	1.23	0.05	0.30	0.47	0.17	0.80
	HD 114762	0.34	0.02	1.64	0.36	0.12	0.08	0.26	0.29
	HD 131509	0.07	0.18	1.72	0.43	0.19	0.03	0.37	0.49
	HD 190007	0.16	0.10	1.33	0.25	0.00	0.20	0.17	0.29

		HD 119850	HD 131509	HD 3651	HD 101501	HD 114762	HD 131509	HD 190007	Average
Standard star	GJ 526	0.39	0.13	0.11	0.48	0.34	0.07	0.19	0.40
	HD 114762	0.67	0.18	0.04	0.40	0.02	0.15	0.15	0.31
	GJ 411	2.02	1.73	1.57	1.21	1.58	1.72	1.33	1.41
	HD 95128	0.95	0.44	0.25	0.06	0.35	0.42	0.23	0.30
	HD 190007	0.59	0.27	0.12	0.31	0.07	0.19	0.00	0.26
	HD 217014	0.45	0.10	0.09	0.49	0.14	0.03	0.20	0.30
	HD 9407	0.76	0.43	0.23	0.18	0.21	0.37	0.16	0.33
	HD 114762	1.17	0.53	0.32	0.09	0.28	0.46	0.24	0.40
	HD 119850	0.00	0.30	0.53	0.91	0.76	0.37	0.71	0.72
	HD 131509	0.28	0.00	0.20	0.57	0.24	0.07	0.33	0.37
	HD 3651	0.50	0.20	0.00	0.38	0.04	0.13	0.07	0.35
	HD 101501	0.91	0.57	0.36	0.00	0.35	0.50	0.25	0.45
	HD 114762	0.76	0.21	0.02	0.36	0.00	0.13	0.16	0.32
	HD 131509	0.35	0.07	0.13	0.50	0.17	0.00	0.27	0.33
	HD 190007	0.68	0.32	0.07	0.26	0.11	0.27	0.00	0.28

Table 5.3: RV cross-correlation table for the June 2011 NOT observing run. All values are in $\mathrm{km\,s^{-1}}$ and are residuals after subtraction of the previously catalogued RVs of the target-template correlation. The final averaged cross-correlation error is $0.36\mathrm{km\,s^{-1}}$. NB: Spectral-types later than M0 were not used as RV standards in any RV measurement.

		Target star							
		HD 1461	HD 3651	HD 4628	HD 114762	HD 197076	HD 190007	HD 209290	HD 114762
Standard star	HD 1461	0.00	0.07	0.07	0.25	0.08	0.15	0.44	0.23
	HD 3651	0.07	0.00	0.08	0.36	0.06	0.11	0.32	0.33
	HD 4628	0.07	0.08	0.00	0.24	0.08	0.14	0.38	0.22
	HD 114762	0.25	0.37	0.24	0.00	0.30	0.33	0.60	0.04
	HD 197076	0.07	0.07	0.08	0.30	0.00	0.16	0.45	0.27
	HD 190007	0.13	0.10	0.12	0.33	0.17	0.00	0.27	0.32
	HD 209290	0.45	0.33	0.38	0.59	0.44	0.26	0.00	0.60
	HD 114762	0.20	0.30	0.21	0.03	0.28	0.31	0.60	0.00
	HD 115617	0.21	0.19	0.21	0.50	0.11	0.11	0.28	0.47
	HD 9407	0.07	0.04	0.05	0.26	0.13	0.21	0.45	0.22
	HD 10780	0.11	0.05	0.09	0.34	0.05	0.12	0.33	0.31
	HD 1461	0.02	0.08	0.06	0.22	0.11	0.17	0.46	0.22
	GJ 411	0.73	0.46	0.45	0.86	0.77	0.38	0.13	0.88
	GJ 526	0.75	0.74	0.70	1.00	0.86	0.62	0.22	1.02
	HD 114762	0.24	0.33	0.22	0.09	0.30	0.35	0.62	0.02

		HD 115617	HD 9407	HD 10780	HD 1461	GJ 411	GJ 526	HD 114762	Average
Standard star	HD 1461	0.20	0.06	0.09	0.04	0.74	0.76	0.27	0.23
	HD 3651	0.17	0.03	0.04	0.09	0.46	0.68	0.38	0.21
	HD 4628	0.22	0.05	0.09	0.07	0.47	0.68	0.25	0.20
	HD 114762	0.52	0.27	0.34	0.23	0.90	0.99	0.02	0.36
	HD 197076	0.12	0.13	0.04	0.08	0.78	0.87	0.29	0.25
	HD 190007	0.12	0.24	0.14	0.18	0.36	0.62	0.35	0.23
	HD 209290	0.27	0.45	0.34	0.45	0.09	0.22	0.62	0.37
	HD 114762	0.48	0.22	0.31	0.20	0.87	1.01	0.03	0.34
	HD 115617	0.00	0.15	0.11	0.21	0.55	0.66	0.50	0.28
	HD 9407	0.16	0.00	0.05	0.07	0.69	0.76	0.25	0.23
	HD 10780	0.13	0.04	0.00	0.11	0.56	0.65	0.34	0.22
	HD 1461	0.23	0.06	0.12	0.00	0.77	0.80	0.23	0.24
	GJ 411	0.55	0.71	0.56	0.75	0.00	0.33	0.88	0.56
	GJ 526	0.65	0.75	0.64	0.79	0.26	0.00	1.02	0.67
	HD 114762	0.48	0.24	0.33	0.23	0.90	1.03	0.00	0.36

Table 5.4: RV cross-correlation table for the December 2012 NOT observing run, generated in the same manner as described in Table 5.3. The final averaged cross-correlation error is $0.27\mathrm{km\,s^{-1}}$.

5.5.3 Effective temperatures and Li abundance calculations

Temperatures were estimated based on $V - K$ (using the empirical calibrations in Alonso, Arribas & Martinez-Roger 1996), assuming no reddening. There is evidence to suggest that the metallicities of young, nearby stars do not vary much from the solar value (Spina et al. 2014) and FGK stars should be very close to the ZAMS by 20 Myr. Therefore temperatures are calibrated using solar metallicity and $\log g = 4.5$. The EW of the Li I 6708Å line is transformed into logarithmic Li abundances (on the usual scale where $\log N(\mathrm{H}) = 12$) using the curves of growth from Soderblom et al. (1993a) and correcting for non-local thermodynamic equilibrium effects using the code provided in Carlsson et al. (1994). Table 5.5 displays the temperatures, abundances and their associated uncertainties. Any previous Li EW or Hα EW measurements found in the literature are listed in the footnotes of Table 5.5.

Table 5.5: EWs, BVK photometry, temperatures, spectral-types (SpT) and Li abundances. Hα EWs have typical error of ~ 10 mÅ. Objects with no observed Li line (Li EW < 20 mÅ) are prefixed with a '<' to represent 2σ upper limits. Li $\mathrm{EW_{corr}}$ is the final EW after correcting for the blended Fe I line.

Name	Li EW (mÅ)	Li $\mathrm{EW_{corr}}$ (mÅ)	Hα EW (Å)	B (mag)	V (mag)	K (mag)	$T_{\rm eff}$ (K)	SpT	A(Li)
SW0016+0546	< 14		−0.94	12.471 ± 0.052	11.678 ± 0.063	9.503 ± 0.021	4920	K2	
SW0017−0102	< 13		2.07	10.451 ± 0.085	9.820 ± 0.007	8.260 ± 0.023	5660	G5	
SW0018+2324	< 10		0.85	10.696 ± 0.055	10.031 ± 0.045	8.170 ± 0.033	5250	K0	
SW0031+3123	< 12		2.21	10.671 ± 0.034	10.044 ± 0.057	8.514 ± 0.019	5700	G3	
SW0047+3812	< 9		0.06	12.274 ± 0.045	10.960 ± 0.058	7.818 ± 0.029	4140	K6	
SW0108+3138	216	213 ± 27	0.47	12.434 ± 0.042	11.675 ± 0.070	9.751 ± 0.015	5180	K1	$2.66^{+0.15}_{-0.20}$
SW0124+2557	223	213 ± 13	1.28	11.470 ± 0.045	10.718 ± 0.042	8.907 ± 0.019	5310	G9	$2.78^{+0.10}_{-0.13}$
SW0127+1859	165	157 ± 43	2.06	10.030 ± 0.098	9.477 ± 0.119	7.855 ± 0.024	5540	G7	$2.73^{+0.28}_{-0.28}$
SW0133+4937	< 12		1.27	10.500 ± 0.018	9.815 ± 0.019	8.037 ± 0.018	5350	G9	
SW0135+2116	154	144 ± 21	2.22	11.387 ± 0.008	10.788 ± 0.020	9.298 ± 0.016	5760	G2	$2.85^{+0.10}_{-0.14}$
SW0140+4212	< 8		−0.25	11.316 ± 0.028	10.390 ± 0.054	7.978 ± 0.027	4700	K4	
SW0144+2824	< 26		−0.29	12.128 ± 0.006	11.150 ± 0.026	8.529 ± 0.017	4530	K5	
SW0156−0500	< 12		0.57	10.774 ± 0.051	9.837 ± 0.033	7.290 ± 0.020	4590	K4	
SW0221+3404	< 6		1.30	10.601 ± 0.032	9.781 ± 0.063	7.806 ± 0.023	5130	K1	
SW0227+2858	< 13		1.79	10.524 ± 0.012	9.808 ± 0.047	8.007 ± 0.023	5320	G9	
SW0235+3139	209	197 ± 20	0.99	10.980 ± 0.061	10.337 ± 0.049	8.594 ± 0.017	5390	G9	$2.78^{+0.11}_{-0.16}$
SW0257+2357	< 15		−0.03	10.671 ± 0.044	9.834 ± 0.055	7.554 ± 0.021	4820	K3	
SW0304+3003	193	186 ± 21	1.77	11.579 ± 0.087	10.875 ± 0.076	9.068 ± 0.018	5320	G9	$2.66^{+0.14}_{-0.18}$
SW0316+5638	222	211 ± 13	0.82	11.482 ± 0.049	10.667 ± 0.023	8.564 ± 0.020	5000	K2	$2.49^{+0.08}_{-0.12}$
SW0322+2853	184	174 ± 25	0.71	11.356 ± 0.050	10.672 ± 0.059	8.659 ± 0.019	5090	K2	$2.41^{+0.13}_{-0.17}$
SW0330+5417$_{\rm a}$	48	38 ± 18	2.09	9.512 ± 0.056	9.190 ± 0.007	7.280 ± 0.020	5200	K0	$1.66^{+0.26}_{-0.23}$
SW0331+4831	121	113 ± 24	2.60	10.910 ± 0.039	10.245 ± 0.073	9.018 ± 0.021	6190	F8	$3.02^{+0.18}_{-0.20}$
SW0334+4753	142	128 ± 29	1.16	11.530 ± 0.031	10.669 ± 0.082	9.206 ± 0.022	5810	G2	$2.81^{+0.20}_{-0.22}$
SW0338+4636	< 27		2.58	10.888 ± 0.052	10.069 ± 0.093	8.757 ± 0.018	6050	F9	
SW0340+3118	137	129 ± 12	2.02	12.044 ± 0.031	11.146 ± 0.026	8.726 ± 0.019	4700	K4	$1.80^{+0.08}_{-0.12}$
SW0341+2718$_{\rm b}$	36	15 ± 17	−0.58	12.641 ± 0.058	11.622 ± 0.084	8.853 ± 0.020	4410	K5	
SW0343+2226	267	246 ± 25	0.49	12.537 ± 0.056	11.571	9.026 ± 0.020	4590	K4	$2.22^{+0.09}_{-0.17}$
SW0344+5043	136	118 ± 26	1.11	11.556 ± 0.020	10.769 ± 0.021	8.475 ± 0.021	4810	K3	$1.87^{+0.13}_{-0.18}$
SW0345+5615	239	226 ± 28	−0.38	12.250 ± 0.209	11.444 ± 0.117	8.766 ± 0.019	4480	K5	$2.02^{+0.17}_{-0.22}$
SW0346+3302	< 25		1.14	11.806 ± 0.050	10.634 ± 0.057	7.611 ± 0.027	4220	K6	
SW0401+3439	26	11 ± 26	1.28	11.836 ± 0.047	10.602 ± 0.038	7.437 ± 0.024	4120	K7	
SW0417+3531	< 6		−0.06	11.793 ± 0.156	10.677 ± 0.072	8.071 ± 0.020	4540	K5	
SW0419+2317	22	8 ± 7	0.21	11.494 ± 0.056	10.712 ± 0.084	8.366 ± 0.018	4760	K3	$0.51^{+0.73}_{-0.34}$

Table 5.5: *continued.*

Name	Li EW (mÅ)	Li EW_{corr} (mÅ)	Hα EW (Å)	B (mag)	V (mag)	K (mag)	T_{eff} (K)	SpT	A(Li)
SW0423+5556	137	140 ± 28	2.18	10.343 ± 0.192	9.775 ± 0.102	8.173 ± 0.031	5560	G6	$2.67^{+0.24}_{-0.23}$
SW0431+3751	210	207 ± 25	0.80	12.059 ± 0.006	11.219	9.274 ± 0.020	5160	K1	$2.62^{+0.09}_{-0.15}$
SW0502+3111	249	238 ± 16	0.80	11.671 ± 0.078	10.792 ± 0.017	8.574 ± 0.021	4880	K3	$2.50^{+0.08}_{-0.13}$
SW0520+2447	21	5 ± 5	0.78	12.531 ± 0.044	11.515 ± 0.038	9.072 ± 0.017	4680	K4	
SW0521+2400$_c$	386	366 ± 14	−0.05	11.367 ± 0.045	10.393 ± 0.043	8.070 ± 0.021	4780	K3	$3.09^{+0.09}_{-0.14}$
SW0524+5404	< 9		−2.04	11.245 ± 0.032	10.212 ± 0.056	7.514 ± 0.018	4460	K5	
SW0526+2231$_d$	285	265 ± 11	−0.20		11.760 ± 0.300	9.340 ± 0.017	4700	K4	$2.44^{+0.32}_{-0.33}$
SW0531+2312$_e$	215	207 ± 32	0.78	9.930 ± 0.079	9.374 ± 0.129	7.403 ± 0.024	5130	K1	$2.59^{+0.21}_{-0.25}$
SW0535+3946	< 18		1.06	11.392 ± 0.036	10.442 ± 0.035	8.097 ± 0.023	4760	K3	
SW0546+5040	116	107 ± 13	2.20	11.131 ± 0.017	10.502 ± 0.013	9.044 ± 0.019	5810	G2	$2.70^{+0.08}_{-0.12}$
SW0556+2305	< 5		−0.42	12.793 ± 0.084	11.817 ± 0.065	9.284 ± 0.020	4600	K4	
SW0640+2518	< 16		0.43	11.784 ± 0.060	10.740 ± 0.055	8.123 ± 0.021	4530	K5	
SW0746+2858	< 54		−0.07	11.048 ± 0.040	10.109 ± 0.033	7.501 ± 0.018	4540	K5	
SW0806+2532	< 10		0.14	10.933 ± 0.036	9.909 ± 0.061	7.210 ± 0.017	4460	K5	
SW0815+2946	34	20 ± 15	−0.16	11.647 ± 0.050	10.782 ± 0.044	8.367 ± 0.018	4700	K4	$0.87^{+0.61}_{-0.32}$
SW0817+3241	< 6		−0.07	13.406 ± 0.090	12.546 ± 0.058	10.100 ± 0.018	4680	K4	
SW0828−0843	< 24		1.22	9.899 ± 0.156	9.165 ± 0.242	6.046 ± 0.020	4160	K6	
SW0828+4222	< 6		0.39	11.135 ± 0.092	10.094 ± 0.034	7.358 ± 0.018	4430	K5	
SW0833+3224	128	104 ± 18	0.43	12.602 ± 0.057	11.648 ± 0.060	9.204 ± 0.016	4680	K4	$1.65^{+0.13}_{-0.18}$
SW0833+3350	51	33 ± 18	0.39	10.872 ± 0.039	9.987 ± 0.021	7.706 ± 0.021	4820	K3	$1.22^{+0.34}_{-0.25}$
SW0838−0741	< 9		1.50	11.389 ± 0.023	10.741 ± 0.033	9.063 ± 0.019	5470	G8	
SW0847+3423	165	155 ± 15	1.83	10.958 ± 0.023	10.304 ± 0.038	8.618 ± 0.022	5460	G8	$2.66^{+0.10}_{-0.14}$
SW0852+3907	< 7		0.96	11.962 ± 0.016	11.170 ± 0.046	9.332 ± 0.020	5280	K0	
SW0859−0916	20	1 ± 14	0.46	11.250 ± 0.044	10.251 ± 0.034	7.726 ± 0.023	4610	K4	
SW0906+3337	102	93 ± 23	3.02	10.271 ± 0.049	9.791 ± 0.026	8.487 ± 0.022	6060	F9	$2.81^{+0.15}_{-0.18}$
SW0959+3849	< 17		−0.69	11.026 ± 0.060	10.002 ± 0.032	7.535 ± 0.029	4660	K4	
SW1000−0854	< 5		−0.15	12.199 ± 0.043	11.502 ± 0.043	9.074 ± 0.021	4690	K4	
SW1055+4246	< 7		−0.16	11.721 ± 0.029	10.805 ± 0.037	8.269 ± 0.013	4600	K4	
SW1059+2315	< 9		−0.30	11.967 ± 0.086	11.078 ± 0.061	8.533 ± 0.018	4590	K4	
SW1130−0227	< 6		−0.26	11.868 ± 0.058	10.946 ± 0.046	8.324 ± 0.021	4520	K5	
SW1133+3613	26	10 ± 3	−0.67	12.836 ± 0.044	11.706 ± 0.068	8.705 ± 0.020	4240	K6	$-0.05^{+0.20}_{-0.21}$
SW1146+4001	38	6 ± 3	−2.30		12.680 ± 0.092	10.368 ± 0.018	4790	K3	$0.44^{+0.43}_{-0.41}$
SW1148−0818	< 4		1.45	11.084 ± 0.037	10.404 ± 0.024	8.601 ± 0.021	5320	G9	
SW1208+3111	20	6 ± 2	0.03	12.803 ± 0.043	11.799 ± 0.018	9.055 ± 0.019	4430	K5	$-0.06^{+0.16}_{-0.21}$
SW1221+2005	23	8 ± 19	0.48	11.543 ± 0.076	10.662 ± 0.056	8.301 ± 0.017	4750	K3	
SW1237+3450	< 2		−0.74	13.021 ± 0.318	12.017 ± 0.178	8.507 ± 0.013	3910	K9	
SW1251+2232	28	4 ± 2	−0.57	11.760 ± 0.053	10.534 ± 0.048	7.252 ± 0.016	4050	K7	$-0.62^{+0.35}_{-0.24}$
SW1251+2505	< 9		1.12	12.403 ± 0.036	11.335 ± 0.042	8.785 ± 0.019	4580	K4	
SW1321+2101	21	7 ± 7	−0.04	12.592 ± 0.220	11.745 ± 0.148	9.260 ± 0.020	4640	K4	$0.30^{+0.82}_{-0.40}$
SW1327+4558	25	4 ± 2	−1.17	12.354 ± 0.053	11.174 ± 0.041	8.038 ± 0.026	4140	K6	$-0.58^{+0.40}_{-0.27}$
SW1328+3533	< 3		0.75	12.711 ± 0.175	11.902 ± 0.124	9.838 ± 0.020	5040	K2	
SW1329−0454	< 10		0.69	10.301 ± 0.044	9.783 ± 0.003	7.651 ± 0.024	4970	K2	
SW1332+2230$_f$	159	142 ± 14	−0.62	10.669 ± 0.043	9.655 ± 0.024	6.847 ± 0.023	4380	K5	$1.50^{+0.10}_{-0.15}$
SW1333+2300	< 3		−0.28	10.527 ± 0.042	9.800 ± 0.031	8.017 ± 0.033	5340	G9	
SW1337+4444	260	245 ± 10	1.07	11.852 ± 0.027	11.050 ± 0.022	9.096 ± 0.018	5150	K1	$2.78^{+0.07}_{-0.11}$
SW1343+3911	< 6		0.51	12.021 ± 0.102	11.456 ± 0.076	9.299 ± 0.017	4940	K2	
SW1354−0543	169	159 ± 12	1.98	10.089 ± 0.144	9.231 ± 0.104	7.140 ± 0.020	5010	K2	$2.27^{+0.15}_{-0.19}$
SW1419−1634	< 9		−0.22	10.373 ± 0.028	9.474 ± 0.022	7.197 ± 0.020	4830	K3	
SW1420+3459	< 16		0.13	11.212 ± 0.045	10.333 ± 0.029	7.714 ± 0.033	4530	K5	
SW1429+3350	< 4		1.25	9.951 ± 0.022	9.233 ± 0.016	7.364 ± 0.021	5240	K0	
SW1437−0331	< 7		−0.08	11.718	10.790 ± 0.007	8.218 ± 0.027	4570	K4	
SW1438+3300	106	93 ± 8	0.96	11.934 ± 0.055	11.036 ± 0.048	8.817 ± 0.020	4880	K3	$1.80^{+0.11}_{-0.14}$
SW1445−0854	< 5		0.25	11.531 ± 0.124	10.613 ± 0.113	7.965 ± 0.021	4500	K5	
SW1502−1201	< 5		−4.87	12.334 ± 0.203	11.200 ± 0.212	7.953 ± 0.027	4070	K7	
SW1528−1010	20	7 ± 1	0.21	12.120 ± 0.200	11.460 ± 0.200	8.713 ± 0.021	4430	K5	$0.03^{+0.29}_{-0.32}$
SW1531−0734	< 8		0.87	11.454 ± 0.066	10.774 ± 0.070	8.891 ± 0.021	5230	K0	
SW1548−0310	< 5		0.60	11.865 ± 0.056	10.859 ± 0.027	8.244 ± 0.031	4530	K5	
SW1550−0222	174	155 ± 23	−0.01	10.939 ± 0.041	10.050 ± 0.058	7.512 ± 0.023	4590	K4	$1.82^{+0.13}_{-0.18}$
SW1607+3401	20	3 ± 2	−0.89	12.065 ± 0.055	10.895 ± 0.042	7.736 ± 0.020	4130	K6	$-0.66^{+0.28}_{-0.23}$
SW1622+2246	< 5		0.87	11.440 ± 0.026	10.646 ± 0.011	8.594 ± 0.021	5050	K2	
SW1625+3002	86	69 ± 15	−0.40	11.311 ± 0.032	10.132 ± 0.037	7.183 ± 0.027	4270	K6	$0.92^{+0.14}_{-0.19}$
SW1626+3350	42	31 ± 3	0.55	10.365 ± 0.029	9.622 ± 0.020	7.130 ± 0.024	4630	K4	$0.99^{+0.08}_{-0.12}$
SW1629+2810	208	196 ± 18	1.14	11.394 ± 0.062	10.654 ± 0.041	8.729 ± 0.020	5180	K1	$2.59^{+0.11}_{-0.15}$
SW1637+2211	20	6 ± 2	0.30	11.659	10.761	8.293 ± 0.018	4650	K4	$0.29^{+0.15}_{-0.18}$
SW1637+2919	25	6 ± 2	−0.25	12.557 ± 0.034	11.440 ± 0.058	8.578 ± 0.021	4340	K5	$-0.14^{+0.18}_{-0.22}$
SW1649+4122	25	6 ± 3	−0.12	11.912 ± 0.043	10.928 ± 0.050	8.787 ± 0.017	4960	K2	$0.55^{+0.29}_{-0.24}$
SW1659+3428	< 5		2.08	11.053 ± 0.083	10.580 ± 0.025	9.340 ± 0.015	6170	F8	
SW1703+3203	< 9		0.74	12.052 ± 0.186	11.362 ± 0.107	9.538 ± 0.021	5300	K0	
SW1704+3928	< 3		−0.15	12.052 ± 0.186	11.362 ± 0.107	8.909 ± 0.023	4670	K4	

Table 5.5: *continued.*

Name	Li EW (mÅ)	Li EW_{corr} (mÅ)	Hα EW (Å)	B (mag)	V (mag)	K (mag)	T_{eff} (K)	SpT	A(Li)
SW1713+2320	< 5		0.45	10.647 ± 0.049	11.373 ± 0.062	8.508 ± 0.021	4340	K5	
SW1718+2506	135	117 ± 4	−1.22	11.533 ± 0.184	10.614 ± 0.069	7.587 ± 0.020	4210	K6	$1.18^{+0.12}_{-0.12}$
SW1722+3658	62	44 ± 7	−0.34	11.601 ± 0.046	10.504 ± 0.039	7.704 ± 0.017	4380	K5	$0.84^{+0.12}_{-0.16}$
SW1724+4026	21	4 ± 2	0.10	12.142 ± 0.074	11.253 ± 0.057	8.679 ± 0.017	4560	K4	$0.00^{+0.31}_{-0.27}$
SW1731+2815	278	265 ± 36	0.19	11.069 ± 0.026	10.213 ± 0.011	7.811 ± 0.016	4710	K4	$2.46^{+0.15}_{-0.25}$
SW1744+1312	27	4 ± 2	0.04	12.357 ± 0.038	11.335 ± 0.075	8.683 ± 0.019	4500	K5	$-0.14^{+0.27}_{-0.28}$
SW1747+3321	224	208 ± 36	0.05	12.380 ± 0.102	11.456 ± 0.098	8.961 ± 0.020	4630	K4	$2.10^{+0.19}_{-0.25}$
SW1749+3350	22	9 ± 3	0.07	11.366 ± 0.060	10.528 ± 0.042	8.654 ± 0.018	5240	K0	$1.03^{+0.16}_{-0.19}$
SW1751+4141	86	67 ± 8	0.16	10.999 ± 0.025	9.836 ± 0.051	7.191 ± 0.021	4510	K5	$1.22^{+0.11}_{-0.17}$
SW1752+2327	< 6		0.08	11.141 ± 0.042	10.245 ± 0.026	7.799 ± 0.026	4670	K4	
SW1757+3133	60	49 ± 7	0.62	11.247 ± 0.051	10.545 ± 0.039	8.754 ± 0.017	5330	G9	$1.89^{+0.10}_{-0.13}$
SW1757+5506	< 20		−0.41	12.355 ± 0.084	11.216 ± 0.083	8.331 ± 0.016	4320	K6	
SW1758+0922	21	8 ± 2	0.26	11.655 ± 0.035	10.750 ± 0.029	8.473 ± 0.039	4830	K3	$0.56^{+0.15}_{-0.18}$
SW1800+5100	< 7		0.04	10.231 ± 0.004	9.742 ± 0.033	8.518 ± 0.025	6200	F8	
SW1804+3930	269	252 ± 36	−0.18	12.603 ± 0.066	11.532 ± 0.046	9.167 ± 0.017	4750	K3	$2.51^{+0.17}_{-0.26}$
SW1812+4105	< 4		−0.51	12.948 ± 0.069	11.840 ± 0.062	9.149 ± 0.017	4470	K5	
SW1815+2948	57	49 ± 6	1.82	9.744 ± 0.022	9.187 ± 0.016	7.800 ± 0.024	5930	G0	$2.38^{+0.09}_{-0.12}$
SW1815+3819$_g$	25	14 ± 3	0.80	10.599 ± 0.036	9.885 ± 0.027	8.288 ± 0.017	5600	G6	$1.55^{+0.12}_{-0.16}$
SW1830+3446	20	9 ± 3	0.88	11.208 ± 0.053	10.530 ± 0.041	8.806 ± 0.018	5410	G9	
SW1831+5418	< 6		0.01	10.748 ± 0.013	9.929 ± 0.031	8.119 ± 0.024	5310	G9	
SW1913+4436	< 6		1.41	11.189 ± 0.047	10.283 ± 0.042	8.166 ± 0.020	4980	K2	
SW1925+4429$_h$	222	208 ± 20	0.01	11.011 ± 0.047	9.939 ± 0.061	7.541 ± 0.018	4720	K4	$2.19^{+0.12}_{-0.17}$
SW2028−0943	< 6		1.72	10.278 ± 0.103	9.681 ± 0.115	8.036 ± 0.017	5510	G7	
SW2028+1131	< 10		−0.36	10.140 ± 0.031	9.317 ± 0.021	7.131 ± 0.024	4910	K3	
SW2044+1314	65	53 ± 4	0.70	11.231 ± 0.018	10.538 ± 0.030	8.627 ± 0.017	5200	K1	$1.81^{+0.08}_{-0.11}$
SW2048−0644	63	50 ± 1	0.09	10.427 ± 0.08	9.588 ± 0.074	7.270 ± 0.023	4790	K3	$1.38^{+0.13}_{-0.14}$
SW2058−0902	337	279 ± 42	0.76	12.208 ± 0.252	11.180 ± 0.112	9.109 ± 0.021	5030	K2	$2.82^{+0.23}_{-0.29}$
SW2107+0632	68	57 ± 8	1.15	10.556	9.869	7.869 ± 0.027	5100	K2	$1.76^{+0.08}_{-0.12}$
SW2107+1357	115	102 ± 6	0.66	11.346 ± 0.064	10.613 ± 0.093	8.721 ± 0.016	5220	K1	$2.18^{+0.14}_{-0.16}$
SW2121+0948	46	32 ± 4	0.73	11.143 ± 0.029	10.333 ± 0.053	8.429 ± 0.049	5210	K1	$1.58^{+0.14}_{-0.16}$
SW2145+2711	254	242 ± 24	−0.08	12.014 ± 0.032	11.279 ± 0.037	9.120 ± 0.018	4940	K3	$2.58^{+0.11}_{-0.17}$
SW2148+1910	38	21 ± 2	−0.20	11.750 ± 0.027	10.734 ± 0.059	7.767 ± 0.017	4260	K6	$0.33^{+0.12}_{-0.13}$
SW2205+0749	25	4 ± 1	−0.22	12.945 ± 0.101	11.810 ± 0.069	8.727 ± 0.020	4180	K6	$-0.56^{+0.16}_{-0.17}$
SW2222+2814	21	3 ± 1	1.86	10.466 ± 0.033	9.926 ± 0.027	8.389 ± 0.019	5690	G4	
SW2244+3029	< 4		0.80	10.984 ± 0.049	10.225 ± 0.060	8.241 ± 0.027	5120	K1	
SW2256+2052	141	122 ± 8	−0.36	12.390 ± 0.071	11.410 ± 0.072	8.679 ± 0.016	4440	K5	$1.48^{+0.13}_{-0.17}$
SW2307+1710	163	146 ± 30	−1.50	11.867 ± 0.054	10.780 ± 0.024	7.899 ± 0.027	4320	K6	$1.45^{+0.14}_{-0.21}$
SW2310+2055	< 3		−0.01	10.833 ± 0.077	10.033 ± 0.054	7.781 ± 0.016	4850	K3	
SW2312+1709	29	2 ± 2	−0.49	12.254 ± 0.025	11.057 ± 0.019	7.732 ± 0.027	4020	K7	$-1.09^{+0.22}_{-0.35}$
SW2317+0551$_i$	< 4		0.15	11.207 ± 0.041	10.175 ± 0.043	7.377 ± 0.029	4390	K5	
SW2320+2921	145	135 ± 32	1.41	12.006 ± 0.066	11.400 ± 0.053	9.819 ± 0.020	5630	G5	$2.70^{+0.18}_{-0.22}$
SW2339+2204	< 4		0.29	11.310 ± 0.047	10.382 ± 0.070	7.928 ± 0.019	4670	K4	
SW2340−0228$_j$	131	121 ± 27	2.24	10.447 ± 0.056	9.893 ± 0.046	8.403 ± 0.021	5760	G2	$2.74^{+0.16}_{-0.19}$
SW2357+3343	28	11 ± 2	−0.21	12.165 ± 0.064	11.271 ± 0.052	8.646 ± 0.016	4520	K5	$0.39^{+0.12}_{-0.18}$

a: Hα EW = −0.146 Å, Li EW = 70 mÅ (Guillout et al. 2009), b: Hα EW = −2.11 Å, Li EW = 80 mÅ(Li & Hu 1998), c: Hα EW = −2.14 Å, Li EW = 390 mÅ(Li & Hu 1998), d: Hα EW = −2.14 Å, Li EW = 290 mÅ (Li & Hu 1998), e: Hα EW = −1.78 Å, Li EW = 350 mÅ(Li & Hu 1998), f: Hα EW = 0.6 Å (Mason et al. 1995), g: Hα EW = −0.10 Å, Li EW = 15 mÅ (Guillout et al. 2009), h: Li EW = 270 ± 20 mÅ, Hα EW = 1.0Å (Frasca et al. 2011), i: Li EW = 0 mÅ (Torres et al. 2006), j: Li EW = 150 mÅ (Torres et al. 2006.

5.6 Age indicators

In the initial target selection a subset of objects were chosen which were rapidly rotating (periods shorter than 5 days) and had corresponding entries in the ROSAT 1RXS or 2RXP catalogs (see §5.4 for details on the X-ray activity of the sample). Gyrochronol-

ogy (see §1.4.1) is used in order to quantify a maximum age based on rotation periods, as outlined in Barnes (2003). From this initial upper age limit Li EW/abundances are used as the primary age diagnostic and are checked for age consistency using two other techniques based on the Hα EWs (see §1.4.2.3) and projected stellar radii ($R \sin i$, see §1.3.4). From the sample of 146 objects a subset of 26 are defined that have Li ages < 200 Myr and are unlikely to be members of SB systems (binary scores of 1 or 2) which are herein referred to as 'the likely-young sample'. These are listed in Table 5.6. Six targets were assessed as having Li ages ≤ 200 Myr but were assigned binary scores of 3 or 4.

5.6.1 Gyrochronology

Gyrochronology provides a rotation- and colour-dependent method to obtain an age estimate for single, late-type stars by using empirical fits to data in open clusters of known age (as described in §1.4.1). Figure 5.5 displays the rotation periods against $V - K$ for the entire observed sample, overplotted with curves for the interface (I) and convective (C) sequences discussed in Barnes (2003; 2007). The calibrations in Barnes (2003; 2007) were done in terms of $B - V$, therefore these were altered to $V - K$ by interpolating the tables in Kenyon & Hartmann (1995). Objects with scores of 5 in the binarity tests were likely SBs and ages based on gyrochronology are ineffective for these, because their rotational history is unlikely to track those that describe the evolution of single stars. The Gyrochronology ages for objects with binary scores of 4 or 5 are flagged in the Gyrochronology column in Table 5.6 and are not treated as reliable ages.

The bifurcation point is the point at which the C sequence meets the I sequence and the isochrones become bimodal redward of this point. To estimate an age using gyrochronology the following analysis is carried out (see Figure 5.5):

•If the object lies above the I sequence, it is definitely older than this gyrochrone.

•If the object lie below the I sequence and blueward of the the corresponding C sequence, then this target is younger than that gyrochrone.

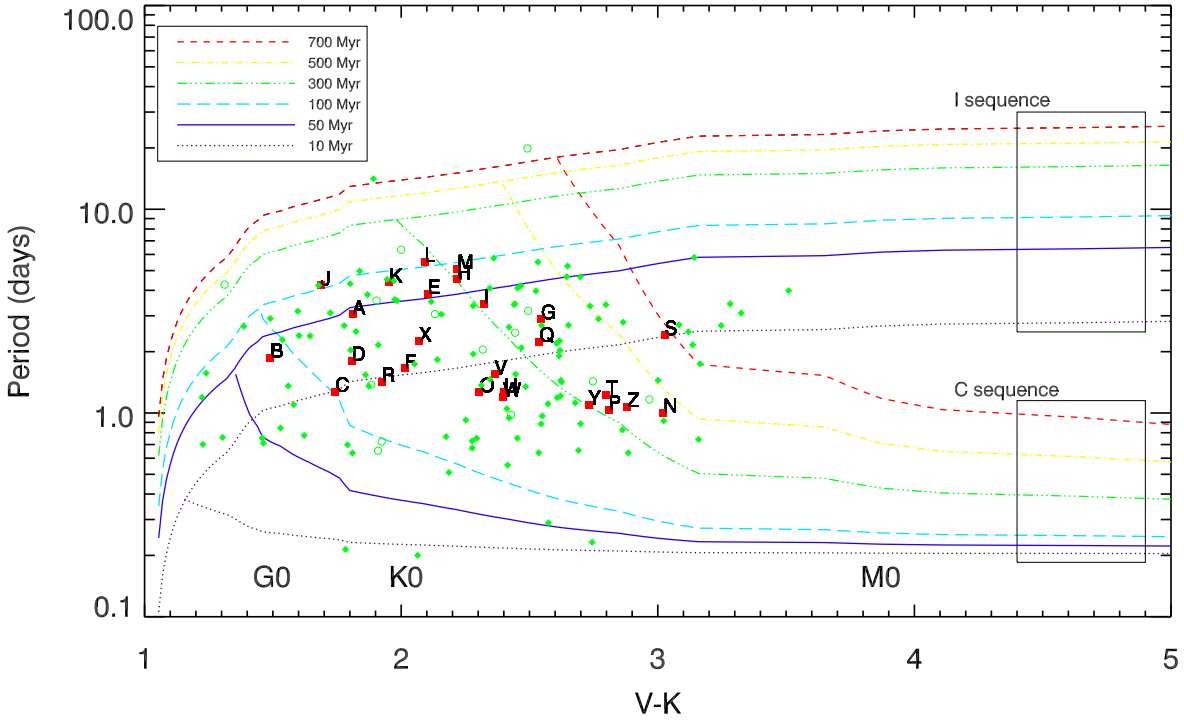

Figure 5.5: Rotation periods versus $V-K$ for the entire observed sample. The various lines represent the I- and C-sequence gyrochrones in Barnes (2003; 2007). The method of inferring an age range from the gyrochrones is described in §5.6.1 – note the three objects A, B and L which are used as examples to describe how to fit the age ranges.

•If the object lies below the I sequence and redward of the corresponding C sequence, there is an ambiguity and one must look for an older gyrochrone which satisfies the previous condition.

Three stars from the likely-young sample (targets A, B and L) are used to clarify how gyrochronology works in practice and are labelled in Figure 5.5 – these labels correspond to the designation of the likely-young sample in Table 5.8:

Target A - Target A lies below the 50 Myr I sequence, but above the 10 Myr I sequence. It is redward of the 10, 50 and 100 Myr C gyrochrones, but lies blueward of the 300 Myr C gyrochrone and the 300 Myr bifurcation point. Hence the age of target A is estimated to be < 300 Myr, with a lower limit of 10 Myr.

Target B - Target B has a minimum age of 10 Myr, as it lies above the I sequence of this isochrone. It is below the I sequence of all gyrochrones with ages ≥ 50 Myr but is only blueward of the C sequence for those with ages ≥ 300 Myr. Hence the age of B is estimated to be between 10 and 300 Myr.

Target L - Target L is at least older than 100 Myr, because it is above the I sequence at this age. Although it lies below all the I sequences ≥ 100 Myr it is only blueward of the C sequence at an age of 500 Myr. Hence L has a gyrochronology age between 100 and 500 Myr.

The limitations of the initial target selection in terms of colour and period now become clearer when examining Figure 5.5. A period < 5 days implies an age < 700 Myr for late F-stars with $1.0 < V-K < 1.5$; < 300 Myr for G-stars with $1.5 < V-K < 2.0$, but then increases again to < 700 Myr for K-stars with $2.0 < V-K < 3.5$ and even older for cooler M-dwarfs with $V-K > 3.5$. Reversing this argument, to be sure an object has an age ≤ 100 Myr would require it to have a period of < 1 day if it were a late F-star, < 2 days for a G-star and then less than 0.7 of a day for K-stars and less than 0.3 of a day for M-stars. The age limits from gyrochronology for the likely-young sample are provided in Table 5.6 on page 160.

5.6.2 Li EW measurements compared to known clusters

Whilst theoretical models partially capture the behaviour of PMS Li depletion in FGK types, they are strongly sensitive to the assumed opacities in the atmospheres and interiors of these stars and do not presently explain the spread in Li abundance that is seen at a given effective temperature in presumably coeval clusters of stars. For example, the spread in Li abundance amongst K-stars in the Pleiades is $1-2$ dex (see §1.4.3.2 for a discussion). For these reasons Li is only used as an empirical age estimator by comparing the Li EWs of the targets as a function of $B-V$ and $V-K$ and the Li abundances as a function of $T_{\rm eff}$ with stars observed in the well-studied Hyades (age $\sim$ 650 Myr) and Pleiades (age $\sim$ 125 Myr) clusters, using Li EW data obtained from Soderblom et al. (1990; 1993; 1993a; 1993b; 1995; 1995a; 1999), Jones et al. (1996; 1997; 1999) and Wilden et al. (2002). In addition to these two clusters, comparisons were made with three younger clusters; NGC 2264 ($\sim$ 5 Myr, King 1998; Soderblom et al. 1999; Dahm & Simon 2005), γ Vel ($\sim$ 10 Myr, Jeffries et al. 2014) and IC 2602 ($\sim$ 30 Myr, Meola et al. 2000; Randich et al. 2001a; 2001b). A large sample of objects in this work are of spectral-type G and K. This makes it particularly difficult to distinguish between Pleiades-like stars and those in younger clusters because of the relatively large scatter in Li EW amongst these spectral-types (see the scatter in Figure 5.6 and 5.7 for Li-rich K stars). Therefore most of the Li-rich objects at these spectral-types are cautiously assigned ages between 30 and 200 Myr.

In Figure 5.6 the Li EWs and colours are presented for the entire sample of observed stars, and ages are estimated using comparisons to the Li patterns in the aforementioned open clusters. One object with duplicate, consistent RV measurements has a Li EW/$B-V$ (and also Li EW/$V-K$) indicative of stars younger than the Pleiades (more similar to the pattern observed in IC 2602 at $\sim$ 30 Myr). Twenty-five targets with binary scores of 1 or 2 have Li EWs/colours (or Li abundances/temperatures) consistent with a Pleiades age. A plot of A(Li) versus $T_{\rm eff}$ is shown in Figure 5.7. As this is essentially the data from Figure 5.6 folded through a simple transformation, it contains no new information on the ages, but does illustrate that the most Li-rich stars

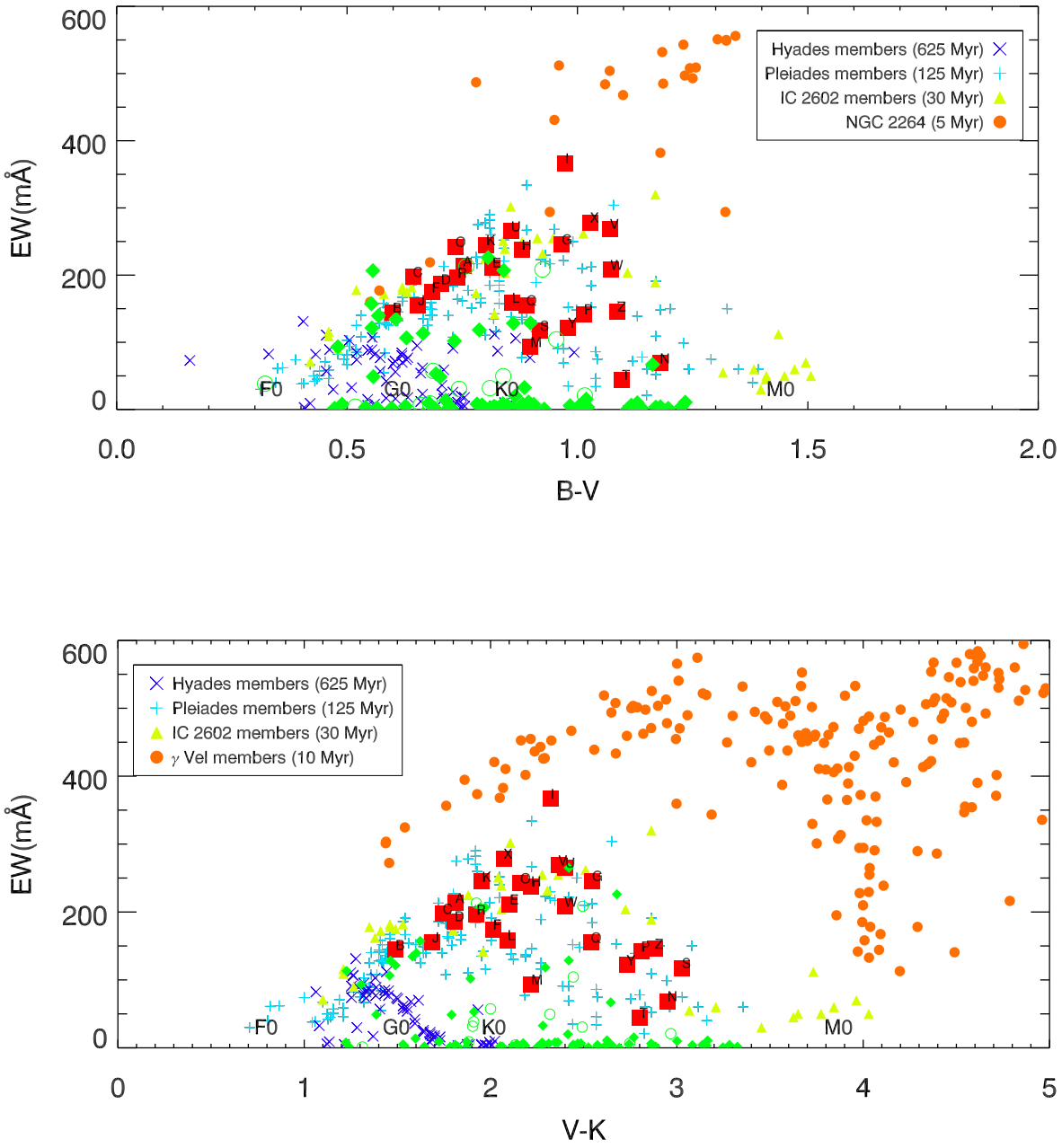

Figure 5.6: Li EWs as a function of $B-V$ and $V-K$. Objects are compared to members in the Hyades (625 Myr), the Pleiades (125 Myr), IC 2602 (30 Myr) and either NGC 2264 for $B-V$ (5 Myr) or γ Vel for $V-K$ (10 Myr, see text for references) to estimate an Li-based age range. Error bars are not included, but are provided in Table 5.5. Red squares, green closed diamonds and green open circles have the same designation as described in the caption of Figure 5.1.

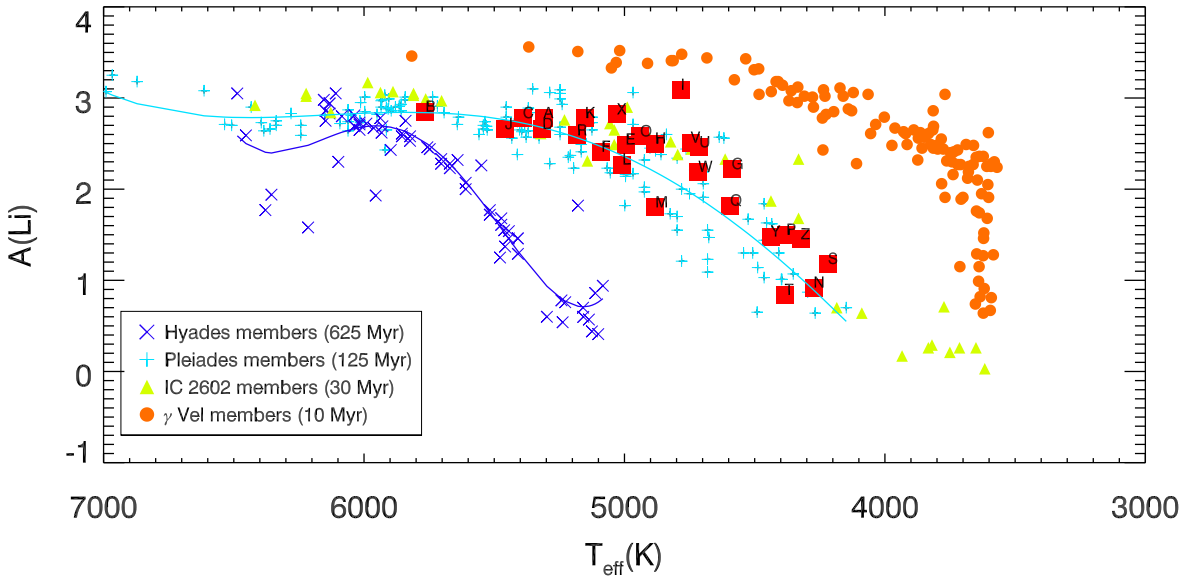

Figure 5.7: Li abundances as a function of surface temperature. Both the target sample and all ancillary data from the open clusters are folded through the same curve of growth (described in §5.5.3). Fourth-order polynomial fits are overplotted for the Hyades and Pleiades, however these are only intended as visual aids and are not implied to represent the trend of Li abundances in these clusters. Only red squares (corresponding to the 'likely-young sample') are overplotted. Li abundances and temperatures for all other objects are listed in Table 5.5.

found are still depleted from an assumed initial level of about A(Li)=3.3, so are probably not very young PMS stars. The estimated Li age ranges for the entire observed sample are presented in Table 5.6 on page 160.

5.6.3 Hα emission

In §5.3, $L_{\rm X}/L_{\rm bol}$ relationships are found to be relatively crude age estimators and are largely rotation-dependent. Figure 5.1 shows a large scatter and considerable overlap in $L_{\rm X}/L_{\rm bol}$ for all FGK stars in NGC 2547, the Pleiades and the Hyades, and also many objects in the sample have values of $\log(L_{\rm X}/L_{\rm bol}) > -3$, which is in the saturated X-ray regime. A potentially more direct activity-age dependent probe is to observe the strength of the Hα line at 6563 Å. Hα emission lines are diagnostic of strong magnetic activity in the photospheres of stars, which are linked to rotation and young ages. In §1.4.2.3 the usefulness and limitations of Hα as an empirical age indicator are discussed.

Using data from several open clusters ranging from 30 to 625 Myr, a log-linear relationship for both Hα emission (upper age limit) and absorption (lower age limit) as a function of $V-K$ and age are provided in §1.4.2.3. This relationship can be used to estimate the minimum/maximum age of a star with an Hα absorption/emission line. Hα EW > 200 mÅ are treated as absorption (providing a minimum age) and Hα EW < -200 mÅ as emission (a maximum age). Targets with Hα EWs in the range $\pm$ 200 mÅ were considered as 'filled-in' lines and Equations 1.8 and 1.9 were used to provide an age *range*. In Table 5.5 the Hα EWs for all 146 targets in the initial sample are presented, and the ages based on Hα for the entire sample are provided in Table 5.6. The Hα EWs of the entire observed sample are plotted as a function of $V-K$ in Figure 5.8.

There are quite a few examples of cool, K-type objects with Hα in emission, but weak Li. The implication is that these are 'young' according to Hα, yet not young according to Li. Because magnetic activity really tracks rotation and not age, the implication is that that these are probably tidelly-locked binary systems. Indeed, several such objects are identified as class 4/5. Conversely, the identification of K-type

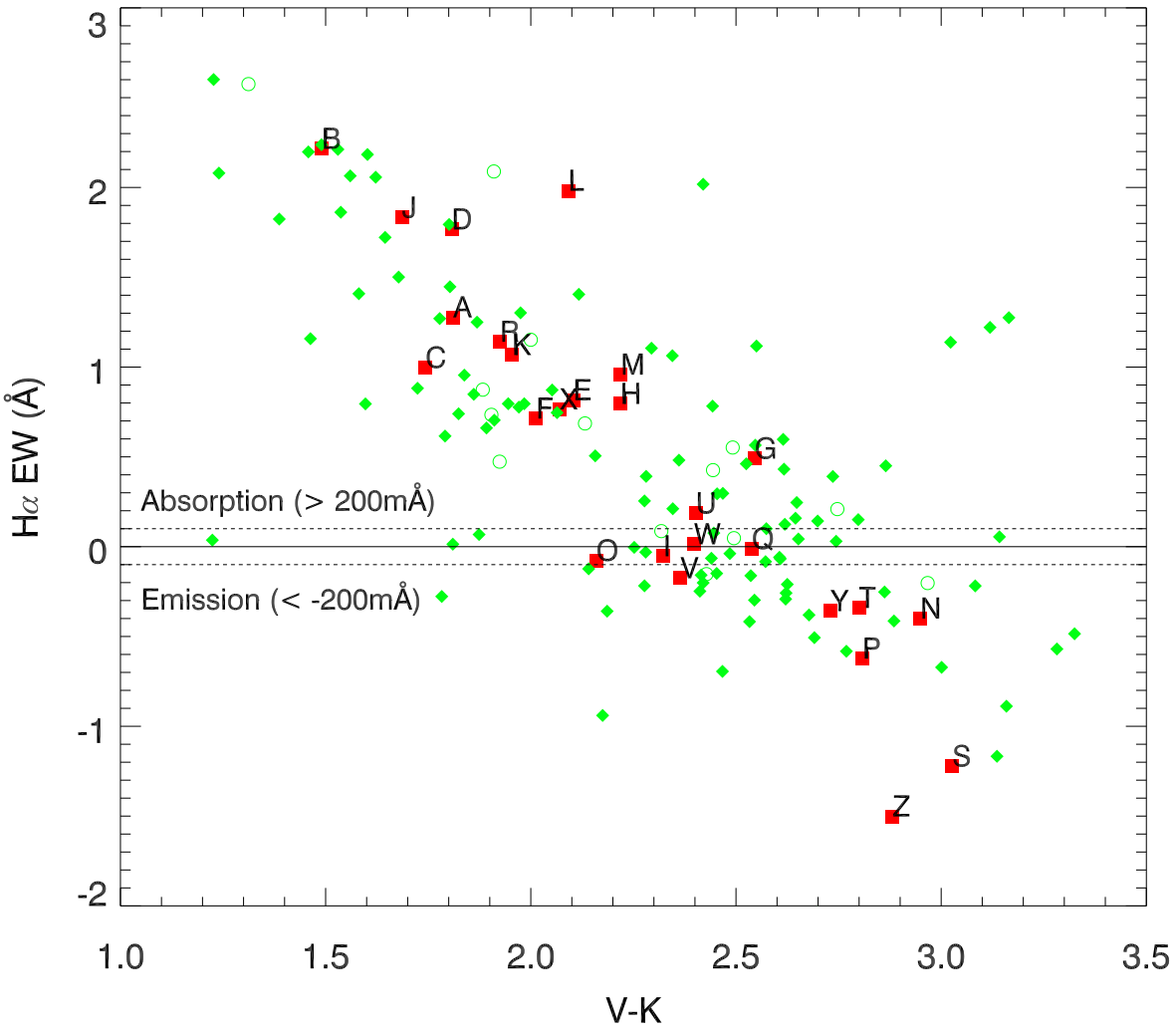

Figure 5.8: Hα EW as a function of $V - K$. Objects displaying emission may be compared to an upper age limit based on chromospheric activity and a lower age limit for Hα absorption. Only objects with EWs $> 200\,$mÅ ($< -200\,$mÅ) were identified as true absorption (or emission) lines.

objects with Hα in emission and strong Li absorption is an extremely strong indication of the stellar youth.

5.6.4 Radii-colour isochrones

Projected rotational velocities ($v \sin i$) were calculated following the procedures in §3.3.2 and multiplied by the rotational period to obtain measurements of the projected stellar radius $R \sin i = Pv \sin i$. Because of the $\sin i$ ambiguity, this technique is only capable of providing lower limits to the radius. Values of $R \sin i$ are compared to radii/$V - K$ isochrones from the models of Siess, Dufour & Forestini (2000). Between ages of $10 - 100$ Myr a star is contracting on the PMS, and because the radii calculated from $R \sin i$ is a lower limit, this method can only provide an upper age limit (details of which are described in §1.3.4). The $R \sin i$ value used corresponds to the 1σ lower limit based on both the period and $v \sin i$ measurement. The $v \sin i$ values for six objects were indeterminate, presumably as a result of either poor SNR or extremely rapid rotation (which would affect the shape of the CCF). The remainder of the entire sample (140 objects) are presented in Figure 5.9. The targets that displayed no Li yet appear to have large values of $R \sin i$ are more likely to be SBs as opposed to being genuinely young. Depending on the difference it could be that binary components are inflated with respect to ZAMS predictions by magnetic effects (but this might only be $10 - 20$ per cent). It could be that there is some problem with the period (although it is difficult to see why it should be too large) or maybe a single $v \sin i$ measurement has been made when the components of a binary were almost, but not quite coincident in RV space, thus leading to a mistakenly broad line estimate. One object in Figure 5.9, SW1438+3300, has an Li age < 200 Myr and an apparent $R \sin i$ age between $5 - 10$ Myr. This object does show evidence for some Li depletion, so it is highly unlikely at this spectral-type that it could be as young as 5 Myr.

5.6.5 Combined age estimation

In terms of an overall age indicator for low-mass stars between $10 - 200$ Myr (coincident with MG ages) only Li can provide an effective age *range* consistently for the entire observed sample, regardless of the object's binarity status. Whilst effects due to rota-

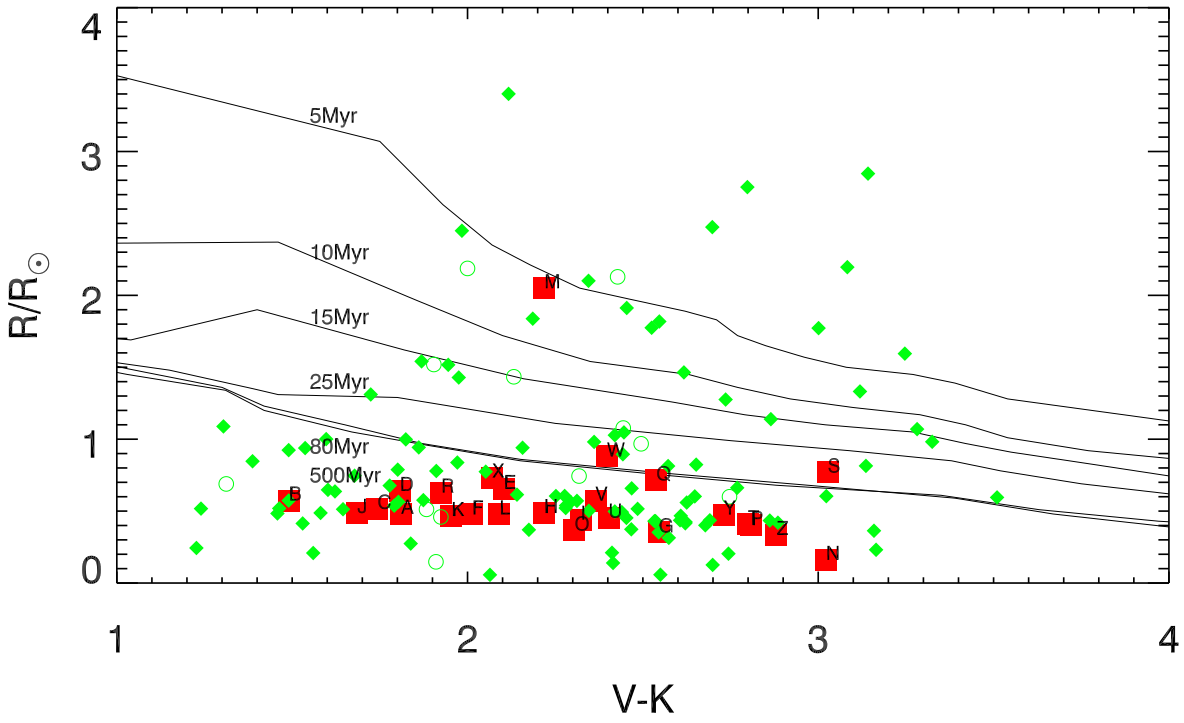

Figure 5.9: Radii versus $V - K$ for the entire observed sample (minus the six objects with an indeterminate $v \sin i$ measurement). Continuous lines represent isochrones generated from the models in Siess, Dufour & Forestini (2000). The plotted points are $R \sin i$ and therefore lower limits to the true radius.

tion cause scatter in Li EW (particularly for K stars), the scatter in the age-dependent variable is less pronounced compared to Hα- and $R \sin i$-based ages. *Therefore the procedure was to use Li to provide the age for the entire sample and utilise the alternative methods in this section to support (or contradict) the Li age.* If no Li is present in the spectra, then the object is automatically assumed to be older than the Hyades and is assigned an age of 1 Gyr (for the purpose of a parallax estimation, see §5.7.1).

Each age estimate is provided in Table 5.6. From herein within this chapter, subsequent analysis is restricted to the likely-young sample described at the beginning of this section (objects with an age estimated from Li as < 200 Myr and binary scores of 1 or 2). Table 5.6 shows that, with the exception of SW0521+2400, all of the likely-young sample have Li-based ages consistent with the ages measured from Hα. $R \sin i$ values are only identified as younger than main-sequence for 3 objects, two of which (SW1718+2506 and SW1925+4429) are consistent with Li and Hα and the other, SW1438+3300, is discussed in §5.6.4. SW0521+2400 has an age range of $5 - 30$ Myr, significantly younger than the rest of the sample.

Table 5.6: Age estimates in Myr for the entire observed sample, based on Gyrochronology, Hα, Li EW and $R \sin i$/colour. The final age estimate is solely from the Li EW age, other age indicators are used only as supporting evidence for the Li age. Gyrochronology and $R \sin i$ ages are upper limits. SBs, (with binary scores of 5) are not expected to have reliable ages. Target names with a '4' subscript have binary scores of 4, making their ages less reliable than likely-single stars.

Name	Gyrochronology (Myr)	Li EW (Myr)	Hα (Myr)	$R \sin i$ (Myr)
Likely-young sample				
A, SW0124+2557	< 300	30–150	>21	
B, SW0135+2116	< 100	30–200	>17	
C, SW0235+3139	< 100	30–200	>20	
D, SW0304+3003	< 300	30–200	>21	
E, SW0316+5638	< 300	30–200	>27	
F, SW0322+2853	< 300	30–200	>24	
G, SW0343+2226	< 500	30–150	>41	
H, SW0502+3111	< 500	30–150	>32	
I, SW0521+2400	< 300	5–30	35–50	
J, SW0847+3423	< 300	30–150	>19	
K, SW1337+4444	< 300	30–150	>22	
L, SW1354−0543	< 300	30–150	>27	
M, SW1438+3300	< 500	100–200	>32	< 5
N, SW1625+3002	< 500	30–150	<189	

Table 5.6: *continued.*

Name	Gyrochronology (Myr)	Li EW (Myr)	Hα (Myr)	$R \sin i$ (Myr)
O, SW2145+2711	< 300	30–150	29–39	
P, SW1332+2230		30–150	66–127	
Q, SW1550−0222	< 700	30–150	41–64	
R, SW1629+2810	< 300	30–150	>22	
S, SW1718+2506		30–150	<233	< 80
T, SW1722+3658		100–200	<123	
U, SW1731+2815	< 300	30–150	>37	
V, SW1804+3930	< 500	30–150	<53	
W, SW1925+4429	< 500	30–150	37–55	< 80
X, SW2058−0902	< 500	30–150	>26	
Y, SW2256+2307	< 700	30–150	<99	
Z, SW2307+1710		30–150	<158	
All other objects				
SW0016+0546	< 300		<40	
SW0017−0102	< 100		>18	
SW0018+2324	< 300		>21	
SW0031+3123$_4$	< 100		>17	
SW0047+3812			>122	5
SW0127+1859	< 100	30–200	>18	
SW0133+4937$_4$	< 300		>21	
SW0140+4212	< 300		<56	
SW0144+2824$_4$	< 300		<71	
SW0156−0500$_4$	< 500		>42	< 10
SW0221+3404	< 300		>23	25
SW0227+2858	< 300		>21	
SW0257+2357	< 300		>34	
SW0331+4831	< 100	100–700	>12	
SW0334+4753	< 100	30–500	>17	
SW0340+3118$_4$	< 700	30–200	>37	< 25
SW0341+2718$_4$	< 500		<111	
SW0344+5043	< 300	100–300	>34	
SW0345+5615	< 300	30–150	<83	
SW0346+3302	< 500		>99	
SW0401+3439	< 700		>127	
SW0417+3531	< 500		43–69	
SW0419+2317	< 300		>35	
SW0423+5556	< 100		>18	
SW0431+3751	< 500	30–150	>22	
SW0520+2447	< 100		>38	80
SW0524+5404	< 500		<89	5
SW0526+2231	< 500		<56	
SW0531+2312$_4$	< 300	30–150	>22	
SW0535+3946	< 300		>35	
SW0546+5040	< 300	100–700	>17	
SW0556+2305	< 300		<64	
SW0640+2518$_4$	< 500		>44	< 15

Table 5.6: *continued.*

Name	Gyrochronology (Myr)	Li EW (Myr)	Hα (Myr)	$R \sin i$ (Myr)
SW0746+2858	<500		44–70	
SW0806+2532	<300		>52	
SW0815+2946	<300		>37	
SW0817+3241	<300		38–58	
SW0828+4222$_4$	<500		>56	<15
SW0828−0843	<500		>117	15
SW0833+3350$_4$	<300		>34	
SW0838−0741$_4$	<300		>19	
SW0852+3907	<300		>21	
SW0859−0916	<500		>41	
SW0906+3337	<700	30–700	>13	
SW0959+3849	<300		<59	
SW1055+4246	<300		<64	
SW1059+2315	<300		<65	
SW1130−0227$_4$	<300		<71	
SW1148−0818	<300		>21	
SW1221+2005	<500		>36	80
SW1237+3450			<531	80
SW1251+2505	<300		>41	
SW1445−0854	<500		>46	
SW2244+3029$_4$	<300		>23	<10
SW2317+0551$_4$	<700		>64	<5
SW2320+2921	<100	30–700	>18	
SW2339+2204$_4$	<500		>39	<10
SW2340−0228	<300	100–300	>17	
SW1133+3613$_4$			<218	<5
SW1146+4001	<500		<49	
SW1208+3111			57–103	
SW1251+2232			<387	15
SW1321+2101$_4$	<700		40–61	
SW1327+4558			<308	<80
SW1328+3533	<700		>26	
SW1333+2300	<300		<23	
SW1343+3911	<500		>29	<80
SW1419−1634	<500		<47	
SW1420+3459	<700		>44	
SW1429+3350$_4$	<300		>21	<25
SW1437−0331	<700		42–67	<80
SW1502−1201			<369	<5
SW1548−0310	<700		>44	
SW1607+3401			<326	
SW1622+2246$_4$	<300		>25	
SW1637+2211	<700		>39	
SW1637+2919			<150	
SW1649+4122	<500		<38	
SW1659+3428	<100		>12	

Table 5.6: *continued.*

Name	Gyrochronology (Myr)	Li EW (Myr)	Hα (Myr)	$R \sin i$ (Myr)
SW1703+3203$_4$	<300		>21	
SW1704+3928	<500		<58	
SW1713+2320			>74	80
SW1724+4026	<700		>42	
SW1744+1312			47–77	50
SW1749+3350$_4$	<300	500–700	22–25	
SW1751+4141	<700	100–200	>46	
SW1752+2327	<500		38–58	<80
SW1757+3133	<300	300–700	>21	
SW1757+5506			<160	
SW1758+0922	<500		>34	
SW1800+5100	<100		11–12	
SW1812+4105$_4$	<700		<87	
SW1815+2948	<100		>15	
SW1815+3819$_4$	<300		>18	
SW1830+3446	<300		>19	25
SW1831+5418	<300		21–24	
SW1913+4436	<500		>28	<5
SW2028+1131	<500		>18	<15
SW2028−0943	<300		<41	
SW2044+1314$_4$	<300	200–700	>22	
SW2107+1357		100–300	>22	<10
SW2204+0749$_4$			<269	<5
SW2222+2814$_4$	<300		>18	
SW2310+2055	<500		33–46	
SW2312+1709			<411	<25
SW2357+3343		200–700	<71	
Spectroscopic binaries				
SW0108+3138	<300	30–150	>22	
SW0330+5417	<100	500–700	>22	
SW0338+4636	<100		>13	
SW0833+3224	<300	100–200	>38	
SW1000−0854	<500		<57	<5
SW1329−0454	<500		>28	
SW1528−1010			>57	
SW1531−0734	<300		>22	
SW1626+3350		100–300	>40	
SW1747+3321		30–150	40–61	<80
SW2048−0644	<500	100–300	35–50	
SW2107+0632	<300		>23	
SW2121+0948	<300	200–700	>22	<25
SW2148+1910		100–300	<199	

5.7 Kinematic analysis

5.7.1 Parallax estimation

Only four objects from the entire observed sample were found to have a previously measured trigonometric parallax. These are listed in column 6 of Table 5.7 with a subscript 't'. For the rest of the objects parallaxes were determined using $V - K$ (assuming no reddening) and a maximum and minimum age (see Table 5.6). Using the Siess, Dufour & Forestini (2000) evolutionary models (with solar metallicity and no convective overshoot) a maximum and minimum absolute K magnitude was calculated by interpolating M_K for the youngest and oldest isochrone corresponding to the estimated age range, and a 'photometric' parallax was calculated.

In Figure 5.10 the M_K range is plotted for the likely-young sample, along with all other objects and SBs. The plot shows that the younger objects span a larger range in M_K due to PMS contraction. For example, target I, with an age range from 5 to 30 Myr increases in M_K by ~ 1.5 mag, whereas target V, with an age ranging between 30 and 70 Myr results in a difference in M_K of ~ 0.5 mag. Redward of $V - K = 3.0$ isochrones are separated by no more than 0.7 mag between 30 Myr and the ZAMS and no more than 0.3 mag between 50 Myr and the ZAMS.

To test the precision of the photometric parallaxes, absolute K magnitudes were calculated for the 4 objects with trigonometric parallaxes and are plotted as purple downwards-pointing triangles. For each measurement the absolute K magnitude from the photometric parallax appears to under-predict the absolute K magnitude based on trigonometric parallaxes but to within 0.5 mag. Given the model dependency of the photometric parallaxes and that different evolutionary models can have log-age variances of as much as 0.6 dex at the ZAMS (see Hillenbrand, Bauermeister & White 2008 and §1.3.1.2), the differences in M_K here are within model uncertainties. Another issue could be binarity. If the 4 objects with trigonometric parallaxes are binaries, they would be estimated to be closer than for single stars. If the 4 objects with trigonometric parallaxes are not young then they could be older than 1 Gyr and the isochrones may

have moved back upwards above the ZAMS, such that the isochrone could be consistent with their position in the absolute CMD. The parallax range for all objects are provided in column 6 of Table 5.7.

5.7.2 Calculating Galactic space velocities

The inputs required to measure Galactic space velocities are the right ascension and declination (α, δ, in decimal format), their corresponding proper motions (μ_α, μ_δ in units of $\mathrm{mas\,yr^{-1}}$), an RV measurement (in $\mathrm{km\,s^{-1}}$), a parallax (π, measured in mas) and their associated errors (σ_{μ_α}, σ_{μ_δ}, σ_{RV} and σ_π; positional errors are considered negligible). All but four objects lack a measured trigonometric parallax, therefore the photometric parallax range (described in §5.7.1) is used if no trigonometric parallax is available.

Using the prescription in Johnson & Soderblom (1987) Galactic space velocities (and their errors) were computed (where UVW has the same convention as described in §2.2.1). Table 5.7 lists all input parameters and resulting UVW. Columns 7, 8 and 9 are the calculated UVW values and have two separate error bars, the first incorporates the σ_{μ_α}, σ_{μ_δ} and σ_{RV} uncertainties and the second corresponds to half of the range in each velocity coordinate resulting from the extrema of the maximum and minimum photometric parallaxes (provided in column 6). Should a trigonometric parallax exist, or if an object is assigned a single-valued main-sequence age (1 Gyr) then all errors are incorporated into one single error bar.

Figures 5.11 and 5.12 are the $U-V$ and $V-W$ Boettlinger diagrams for the likely-young sample. To compare their space motions with nearby MGs, the UVW ranges for the 10 MGs in Table 2.1 are overplotted. With the exception of SW1332+2230 (target P, which has a measured parallax), velocity error bars on this plot do not include an error due to the parallax uncertainty. Instead, a line connects UVW points calculated at the extrema of the distances inferred from the photometric parallaxes. The object plotted in blue is SW0521+2400 (target I) which had an age range significantly younger than the rest of the sample (see Table 5.6).

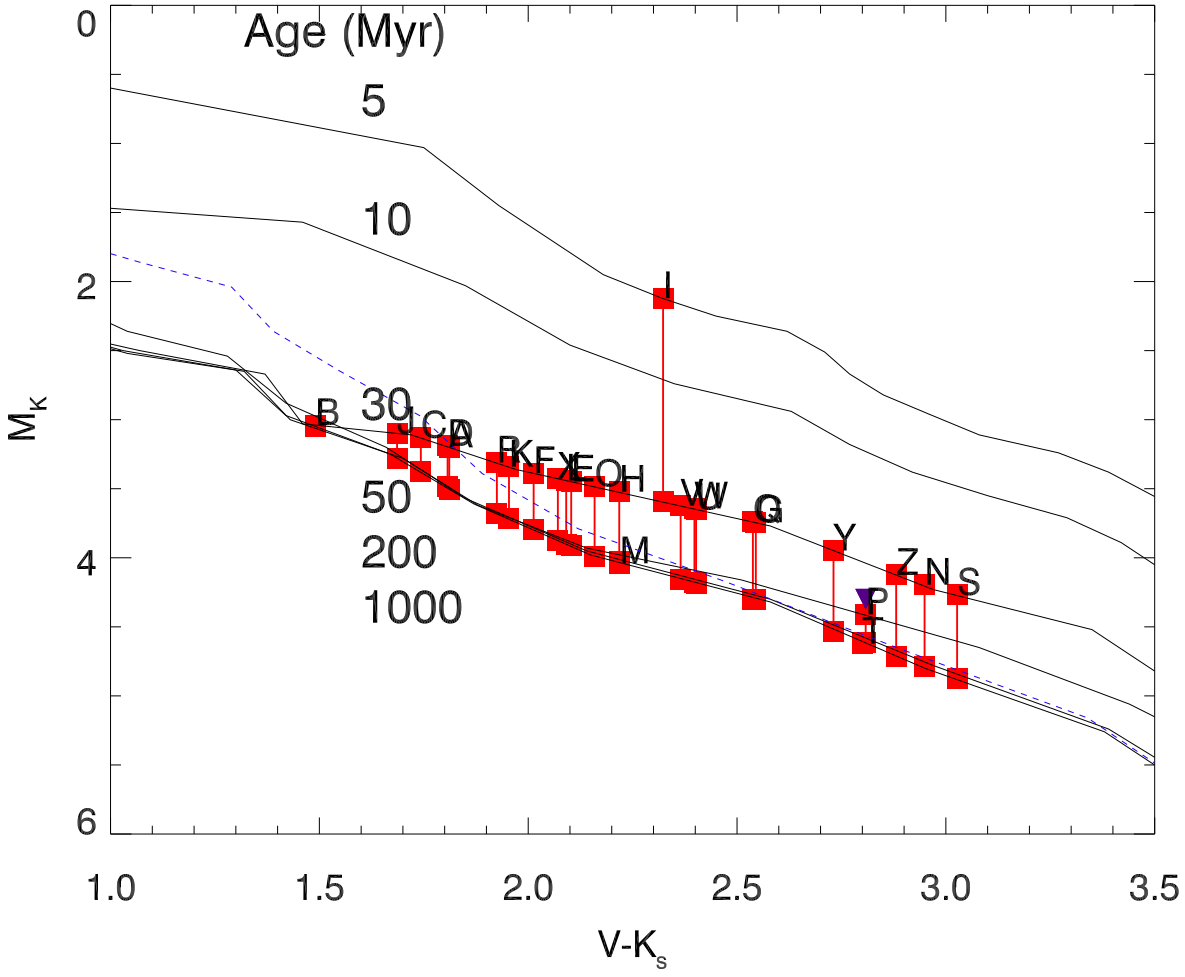

Figure 5.10: M_K versus $V-K$ CMD for the entire observed sample. With the exception of four stars with a parallax, the absolute K magnitude has not been measured for any of these stars. Rather, they are placed on isochrones appropriate to the ages inferred from their Li abundance. Red lines indicate the range in M_K for the likely-young sample based on the age range for each object. The model isochrones of Siess, Dufour & Forestini (2000) are overplotted at 5, 10, 30, 200 and 1000 Myr and the dotted blue line is the ZAMS. Purple downwards-facing triangles represent objects which were found to have a previously measured trigonometric parallax.

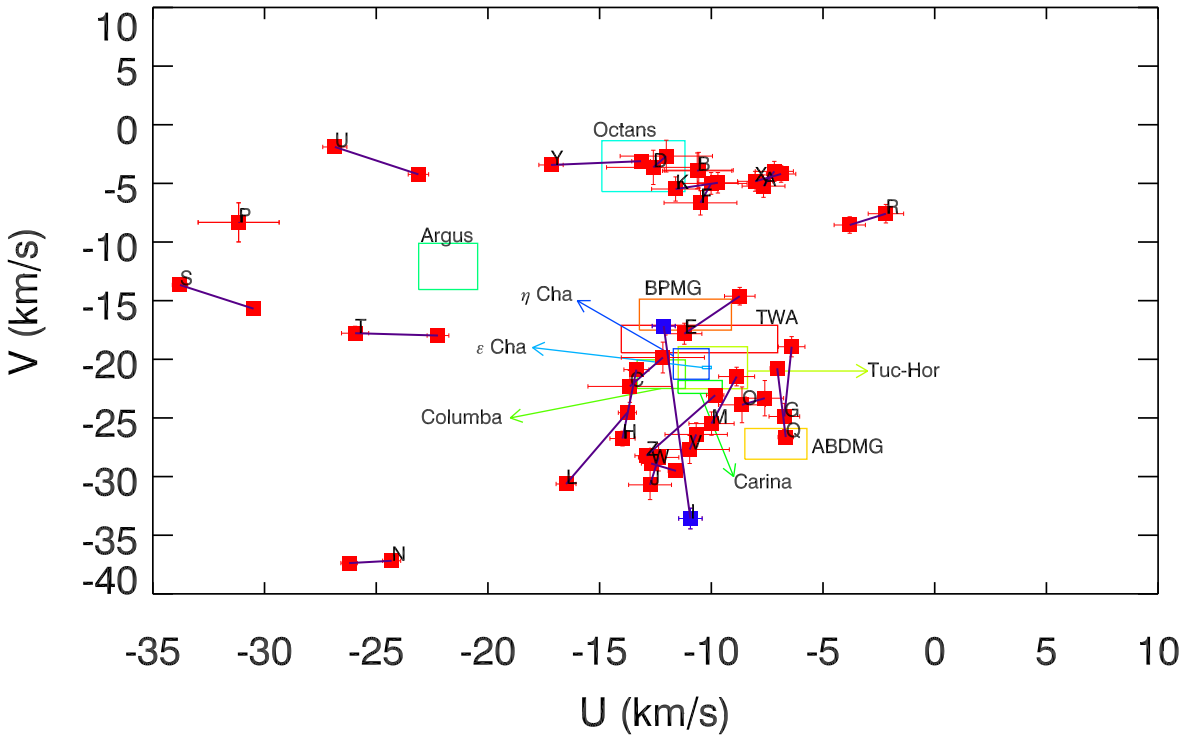

Figure 5.11: $U-V$ Boettlinger diagram for the likely-young sample in this work. Each object is connected by a solid purple line which indicates distance uncertainties due to the photometric parallax method described in §5.7.1. Labels are the same as in Table 5.8.

The dispersion in U, V and W is within $\sim 3\,\mathrm{km\,s^{-1}}$ for the known MGs (see Table 2.1). On initial inspection of Figures 5.11 and 5.12, only 10 objects overlap with a MG in $U-V$ and 12 objects in $V-W$. Eleven do not appear kinematically linked to any of the MGs considered in the analysis and seven objects appear to have similar space velocities to Octans-Near association identified by Zuckerman et al. (2013). Figure 5.13 shows the objects that were measured to be younger than 200 Myr but were assigned binary scores of 3 or 4.

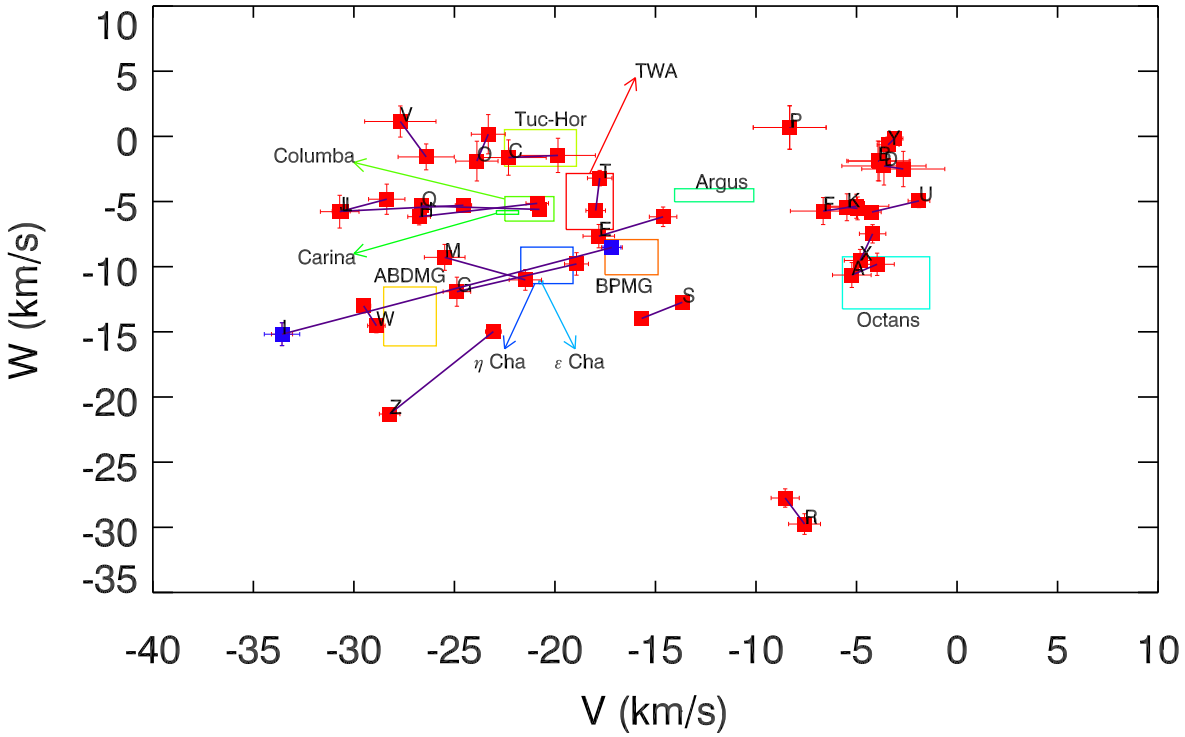

Figure 5.12: $V-W$ Boettlinger diagram for the likely-young sample in this work. Each object is connected by a solid purple line which indicates distance uncertainties due to the photometric parallax method described in §5.7.1. Labels are the same as in Table 5.8.

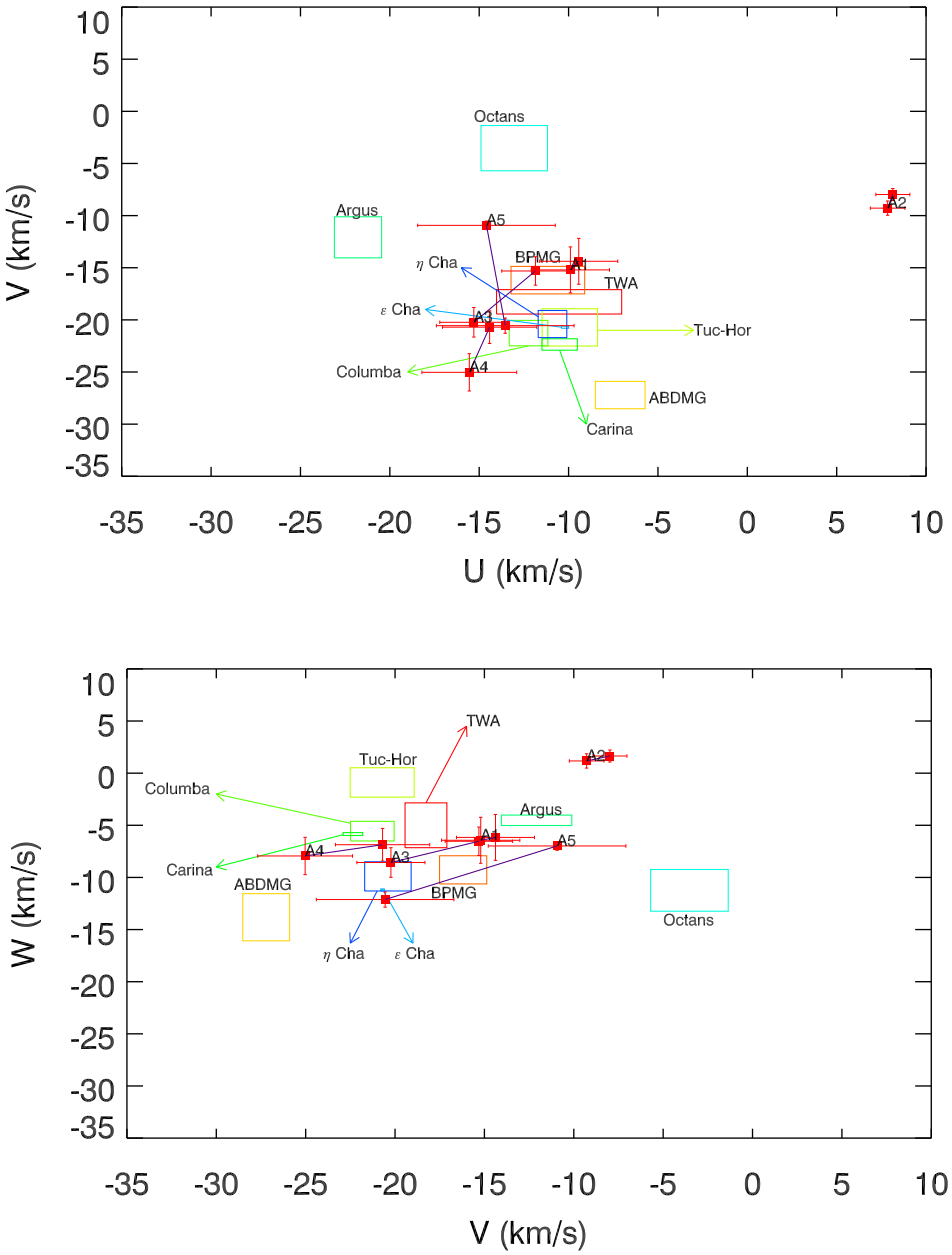

Figure 5.13: $U-V$ and $V-W$ Boettlinger diagrams for objects younger than 200 Myr which had ambiguous CCFs, with binary scores of 3 or 4. Each object is connected by a solid purple line which indicates distance uncertainties due to the photometric parallax method described in §5.7.1. The labels correspond to the following targets: A1 = SW0127+1859; A2 = SW0340+3118; A3 = SW0345+5615; A4 = SW0431+3751; A5 = SW0531+2312. One object, SW1751+4141 was measured to have an age younger than 200 Myr, however a calculation of UVW was not possible because it has an indeterminate RV.

Table 5.7: Proper-motions, RVs, UVW and $v \sin i$ measurements for the entire observed sample. RV values with an 'i' subscript are INT measurements. Parallaxes with a 't' subscript are trigonometric parallaxes.

Name	μ_α (mas yr^{-1})	μ_δ (mas yr^{-1})	RV (individual) (km s^{-1})	RV (final) (km s^{-1})	π (mas)	U (km s^{-1})	V (km s^{-1})	W (km s^{-1})	$v \sin i$ (km s^{-1})
Likely-young sample									
SW0124+2557	11.9 ± 1.6	−14.0 ± 1.7	7.2 ± 0.7, 7.4 ± 0.7	7.3 ± 0.7	7.22−8.31	−7.4 ± 0.9 ± 0.2	−4.6 ± 0.9 ± 0.6	−10.2 ± 0.9 ± 0.4	8.0 ± 1.1
SW0135+2116$_a$	12.2 ± 1.5	−0.6 ± 1.5	5.0 ± 1.9, 5.0 ± 2.2	5.0 ± 2.0	5.60−5.62	−10.6 ± 1.5	−3.9 ± 1.5	−1.9 ± 1.6	35.5 ± 0.5
SW0235+3139	38.9 ± 1.4	−21.9 ± 1.4	0.3 ± 2.5, 0.2 ± 2.3	0.3 ± 2.4	8.08−9.04	−12.9 ± 1.9 ± 0.7	−21.1 ± 1.3 ± 1.2	−1.5 ± 1.3 ± 0.1	20.5 ± 1.1
SW0304+3003	11.9 ± 1.7	−4.2 ± 1.7	9.8 ± 2.4, 9.8 ± 2.4	9.8 ± 2.4	6.67−7.64	−12.3 ± 2.1 ± 0.3	−3.2 ± 1.4 ± 0.5	−2.4 ± 1.4 ± 0.1	18.0 ± 0.5
SW0316+5638$_b$	27.5 ± 2.1	−35.1 ± 2.1	−2.0 ± 0.6, −2.1 ± 0.6	−2.1 ± 0.6	9.48−11.75	−10.0 ± 0.7 ± 1.2	−16.2 ± 0.8 ± 1.6	−6.9 ± 1.0 ± 0.7	8.6 ± 0.5
SW0322+2853	12.4 ± 1.6	−14.6 ± 1.7	8.2 ± 1.8, 9.9 ± 1.9	9.0 ± 1.8	8.82−10.65	−10.2 ± 1.6 ± 0.2	−5.8 ± 1.0 ± 0.8	−5.5 ± 1.0 ± 0.2	14.6 ± 0.6
SW0343+2226$_c$	22.5 ± 2.1	−46.2 ± 2.1	6.0 ± 0.5	6.0 ± 0.5	8.78−11.37	−6.6 ± 0.6 ± 0.2	−21.9 ± 1.0 ± 3.0	−10.9 ± 0.9 ± 1.1	6.2 ± 0.5
SW0502+3111	27.2 ± 1.3	−52.5 ± 1.3	11.2 ± 0.6, 14.2 ± 2.2$_i$	11.2 ± 0.6	9.76−12.34	−13.7 ± 0.6 ± 0.3	−23.8 ± 0.6 ± 2.9	−5.6 ± 0.6 ± 0.5	5.4 ± 0.2
SW0521+2400$_d$	10.0 ± 1.2	−48.0 ± 1.2	13.5 ± 0.5, 17.1 ± 2.2$_i$	13.5 ± 0.5	6.46−12.74	−11.5 ± 0.5 ± 0.6	−25.4 ± 0.7 ± 8.2	−11.9 ± 0.7 ± 3.3	6.5 ± 0.4
SW0847+3423	−17.1 ± 2.2	−50.6 ± 2.1	10.1 ± 0.6, 10.2 ± 0.6, 11.6 ± 1.5$_i$	10.2 ± 0.6	7.87−8.55	−12.5 ± 0.9 ± 0.2	−29.5 ± 1.2 ± 1.2	−5.3 ± 1.1 ± 0.5	5.8 ± 1.2
SW1337+4444	−16.9 ± 1.6	7.4 ± 1.6	−6.4 ± 0.6, −6.4 ± 0.6, −1.2 ± 3.5$_i$	−6.4 ± 0.6	7.06−8.39	−10.7 ± 1.0 ± 0.9	−5.2 ± 1.0 ± 0.3	−5.5 ± 0.7	5.4 ± 0.5
SW1354−0543	−115.3 ± 1.4	−69.2 ± 1.5	−4.1 ± 0.6, −4.2 ± 0.6, −2.3 ± 1.6$_i$	−4.2 ± 0.6	18.20−22.50	−15.1 ± 0.4 ± 1.4	−27.6 ± 0.4 ± 3.0	−5.5 ±0.5 ± 0.2	4.3 ± 1.2
SW1438+3300	−35.7 ± 1.9	−17.5 ± 1.9	−19.2 ± 0.6, −19.3 ± 0.6	−19.2 ± 0.6	11.02−11.08	−8.9 ± 0.8	−21.4 ± 0.8	−11.0 ± 0.6	20.4 ± 1.3
SW1625+3002	39.4 ± 1.6	−37.7 ± 1.6	−68.0 ± 0.7, −69.1 ± 0.7	−68.5 ± 0.7	25.25−33.18	−25.0 ± 0.4 ± 1.0	−37.2 ±0.4 ± 0.1	−52.6 ±0.5 ± 0.7	8.1 ± 0.9
SW2145+2711	16.6 ± 1.7	−7.5 ± 1.7	−22.5 ± 1.8, −23.4 ± 1.4	−22.9 ± 1.6	7.45−9.42	−8.3 ± 1.0 ± 0.5	−23.7 ±1.5 ± 0.3	−1.3 ± 1.1 ± 1.0	14.6 ± 0.5
SW1332+2230$_e$	−135.0 ± 1.1	55.2 ± 1.1	−5.1 ± 0.7, −5.0 ± 2.2$_i$	−5.1 ± 0.7	21.71 ± 1.64$_t$	−20.2 ± 0.2 ± 0.9	−5.4 ± 0.2 ± 0.2	−1.4 ± 0.7 ± 0.2	19.6 ± 0.4
SW1550−0222$_f$	−62.8 ± 1.2	−72.5 ± 1.2	−10.3 ± 0.3, −10.9 ± 0.4, −10.4 ± 2.3$_i$	−10.6 ± 0.4	17.57−22.84	−6.9 ± 0.3 ± 0.2	−23.7 ± 0.3 ± 3.0	−5.5 ±0.3 ± 0.1	16.2 ± 0.5
SW1629+2810	28.2 ± 1.4	−12.4 ± 1.4	−25.3 ± 0.8, −25.1 ± 0.7, −20.3 ± 2.2$_i$	−25.2 ± 0.8	8.25−9.76	−3.0 ± 0.7 ± 0.8	−8.1 ± 0.7 ± 0.5	−28.8 ±0.8 ± 1.0	22.3 ± 0.4
SW1718+2506	−4.0 ± 1.7	76.3 ± 1.6	−34.7 ± 0.3, −34.9 ± 0.3	−34.8 ± 0.3	21.69−28.66	−32.1 ± 0.3 ± 1.7	−14.7 ± 0.3 ± 1.0	−13.4 ± 0.3 ± 0.6	16.1 ± 0.5
SW1722+3658	−37.3 ± 2.5	63.4 ± 2.4	−24.6 ± 0.6, −26.0 ± 0.6	−25.3 ± 0.6	24.10−24.19	−22.2 ± 0.5	−18.0 ± 0.5	−5.7 ± 0.5	16.8 ± 0.5
SW1731+2815	5.0 ± 1.5	63.2 ± 1.7	−18.2 ± 0.5	−18.2 ± 0.5	14.71−18.86	−25.0 ± 0.5 ± 1.9	−3.1 ± 0.5 ± 1.2	−5.4 ±0.5 ± 0.4	18.3 ± 0.5
SW1804+3930	−22.4 ± 3.1	4.1 ± 3.1	−25.5 ± 0.6, −27.3 ± 0.7	−26.4 ± 0.6	7.78−9.95	−10.8 ± 1.6 ± 0.1	−0.6 ± 1.1 ± 27.0	−0.2 ±1.6 ± 1.4	18.8 ± 0.5
SW1925+4429$_g$	30.9 ± 1.5	7.1 ± 1.5	−33.5 ± 0.6	−33.5 ± 0.6	16.61−21.26	−12.1 ± 0.4 ± 0.6	−29.2 ± 0.5 ± 0.3	−13.8 ± 0.4 ± 0.8	37.0 ± 0.4
SW2058−0902	18.9 ± 1.5	−7.0 ± 1.5	−3.0 ± 0.4, −2.4 ± 0.4	−2.7 ± 0.4	7.31−8.98	−7.5 ± 0.7 ± 0.6	−4.5 ±0.8 ± 0.3	−8.5 ±0.8 ± 1.0	16.5 ± 0.5
SW2256+2052	38.1 ± 1.3	16.2 ± 1.3	−2.5 ± 0.6	−2.5 ± 0.6	11.31−14.84	−15.1 ± 0.5 ± 2.0	−3.3 ± 0.5 ± 0.2	−0.4 ± 0.5 ± 0.2	21.9 ± 0.4
SW2307+1710	105.7 ± 2.0	−85.7 ± 1.4	−8.4 ± 0.3	−8.4 ± 0.3	17.58−23.06	−11.4 ± 0.5 ± 1.5	−25.6 ±0.3 ± 2.6	−18.1 ± 0.4 ± 3.2	15.8 ± 0.5
All other targets									
SW0016+0546	10.7 ± 1.9	−28.4 ± 1.9	−4.1 ± 7.7	−4.1 ± 7.7	7.96	3.1 ± 1.7	−17.0 ± 4.2	−6.7 ± 6.4	24.5 ± 0.9
SW0017−0102	−23.1 ± 1.2	−20.2 ± 1.2	8.7 ± 0.7, 8.8 ± 0.7	8.7 ± 0.7	9.15	14.5 ± 0.6	1.7 ± 0.6	−10.8 ± 0.7	7.8 ± 3.9
SW0018+2324	35.5 ± 1.2	−13.2 ± 1.2	10.7 ± 3.6	10.7 ± 3.6	12.10	−13.3 ± 1.2	−1.6 ± 2.6	−12.5 ± 2.3	31.1 ± 0.5
SW0031+3123	10.5 ± 1.4	−15.6 ± 1.4	33.5 ± 1.4	33.5 ± 1.4	7.99−8.14	−15.8 ± 0.9	18.3 ± 1.2 ± 0.1	−25.7 ± 1.0 ± 0.1	24.9 ± 4.4
SW0047+3812	117.7 ± 2.2	−56.6 ± 2.2	−11.7 ± 0.7	−11.7 ± 0.7	26.89	−9.5 ± 0.5	−23.5 ± 0.6	−4.5 ± 0.5	24.3 ± 3.4
SW0127+1859	37.4 ± 1.3	−24.8 ± 1.3	−1.4 ± 15.2, −7.7 ± 17.2		11.09−11.69				41.6 ± 1.1
SW0133+4937	−25.8 ± 1.5	−22.9 ± 1.5	11.8 ± 1.5	11.8 ± 1.5	11.90	0.8 ± 1.0	12.5 ± 1.2	−13.0 ± 0.7	12.8 ± 1.0
SW0140+4212	−1.7 ± 1.3	−76.9 ± 1.3	−14.3 ± 0.9	−14.3 ± 0.9	17.27	11.0 ± 0.6	−17.6 ± 0.7	−14.7 ± 0.4	10.2 ± 0.4
SW0144+2824	6.5 ± 1.6	−35.9 ± 1.6	−80.2 ± 1.3	−80.2 ± 1.3	14.59	50.1 ± 0.9	−53.5 ± 0.9	34.6 ± 0.9	17.3 ± 0.5
SW0156−0500	40.7 ± 1.4	−17.9 ± 1.4	21.4 ± 2.8	21.4 ± 2.8	24.87	−13.1 ± 1.2	−4.3 ± 0.5	−18.5 ± 2.5	34.2 ± 0.3
SW0221+3404	9.0 ± 1.2	−29.3 ± 1.3	−7.1 ± 2.5	−7.1 ± 2.5	15.28	4.1 ± 1.9	−10.5 ± 1.4	−3.7 ± 1.1	20.1 ± 0.9
SW0227+2858	−1.4 ± 1.5	−39.1 ± 1.5	−36.1 ± 0.7	−36.1 ± 0.7	12.39	29.0 ± 0.7	−25.6 ± 0.6	5.7 ± 0.6	9.3 ± 1.1
SW0257+2357$_h$	−24.9 ± 0.9	−91.7 ± 0.8	−83.1 ± 0.5	−83.1 ± 0.5	15.07 ± 1.39$_t$	73.0 ± 0.4	−38.9 ± 0.3	23.7 ± 0.3	7.9 ± 0.8
SW0331+4831$_i$	28.5 ± 1.2	−25.9 ± 1.2	0.1 ± 3.0	0.1 ± 3.0	5.06−5.22	−18.2 ± 2.6 ± 0.3	−30.2 ± 1.8 ± 0.5	−4.3 ± 1.2 ± 0.1	18.9 ±0.9
SW0334+4753$_j$	21.0 ± 2.2	−25.2 ± 2.3	1.1 ± 2.2	1.1 ± 2.2	5.72−5.82	−13.7 ± 2.1 ± 0.1	−22.2 ± 2.0 ± 0.2	−6.8 ± 1.9 ± 0.1	37.5 ± 1.4
SW0340+3118	6.7 ± 1.3	−11.6 ± 1.3	−10.3 ± 1.0	−10.3 ± 1.0	9.71−12.40	8.0 ± 1.0 ± 0.1	−8.6 ± 0.6 ± 0.6	1.4 ±0.6 ± 0.2	12.2 ± 0.2
SW0341+2718$_k$	73.3 ± 1.2	−113.1 ± 1.2	89.8 ± 0.9	89.8 ± 0.9	13.61	−87.9 ± 0.8	−20.6 ± 0.5	−45.9 ± 0.5	12.7
SW0344+5043	25.4 ± 1.7	−30.4 ± 1.7	−1.1 ± 5.2	−1.1 ± 5.2	13.20−13.37	−6.1 ± 4.4	−12.4 ± 2.7 ± 0.1	−3.0 ± 0.7	31.8 ± 0.9
SW0345+5615	32.8 ± 1.6	−49.5 ± 1.7	2.9 ± 10.0		10.52−13.79				27.0 ± 0.7
SW0346+3302	15.2 ± 1.1	−9.8 ± 1.2	−114.0 ± 92.5		27.85				27.3 ± 0.5
SW0401+3439	4.1 ± 1.7	−10.3 ± 1.8	−43.6 ± 1.0	−43.6 ± 1.0	32.38	39.9 ± 0.9	−14.9 ± 0.4	9.6 ± 0.4	12.8
SW0417+3531	−81.5 ± 2.4	−127.3 ± 2.5	−12.4 ± 0.8	−12.4 ± 0.8	17.81	16.2 ± 0.8	−13.9 ± 0.7	−36.3 ± 0.7	12.7 ± 0.4
SW0419+2317	3.4 ± 1.3	−74.7 ± 1.3	−7.9 ± 0.9	−7.9 ± 0.9	14.08	10.1 ± 0.8	−20.8 ± 0.4	−12.6 ± 0.5	11.6 ± 0.5
SW0423+5556	26.4 ± 7.5	−13.0 ± 7.5	−2.0 ± 3.4, −2.3 ± 3.4	−2.2 ± 3.4	9.76	−4.7 ± 3.5	−12.9 ± 3.6	4.5 ± 3.6	22.4 ± 0.7

Table 5.7: *continued.*

Name	μ_α (mas yr^{-1})	μ_δ (mas yr^{-1})	RV (individual) (km s^{-1})	RV (final) (km s^{-1})	π (mas)	U (km s^{-1})	V (km s^{-1})	W (km s^{-1})	$v \sin i$ (km s^{-1})
SW0431+3751$_{\rm l}$	19.4 ± 2.3	−34.9 ± 2.3	8.8 ± 5.7, 8.3 ± 4.2, 8.8 ± 5.8	8.8 ± 2.7	6.47−7.69	−15.0 ± 2.6 ± 0.6	−22.9 ± 1.7 ± 2.2	−7.4 ± 1.6 ± 0.5	32.1 ± 1.3
SW0520+2447	−0.3 ± 1.6	−18.0 ± 1.6	24.3 ± 6.8, 7.0 ± 7.1		10.55				65.4 ± 1.1
SW0524+5404	1.6 ± 1.3	−13.4 ± 1.5	23.3 ± 18.7, 29.8 ± 22.4		24.23				40.8 ± 4.6
SW0526+2231	8.3 ± 1.5	−18.5 ± 1.5	28.7 ± 0.6, 29.9 ± 3.2$_{\rm i}$	28.7 ± 0.6	9.26	−27.7 ± 0.6	−11.8 ± 0.8	−5.2 ± 0.8	5.4 ± 0.3
SW0531+2312$_{\rm m}$	3.1 ± 1.1	−37.5 ± 1.2	70.1 ± 2.9	15.8 ± 3.9	7.95 ± 1.29$_{\rm t}$	−14.1 ± 3.8 ± 0.5	−15.7 ± 0.6 ± 4.8	−9.6 ± 0.7 ± 2.6	44.9 ± 4.0
SW0535+3946	14.3 ± 1.6	−16.4 ± 1.6	57.0 ± 4.0, 78.0 ± 6.6	70.1 ± 2.9	15.94	−69.9 ± 2.9	6.3 ± 0.7	5.7 ± 0.5	23.9 ± 0.4
SW0546+5040	10.0 ± 1.9	−40.7 ± 1.9	−1.4 ± 0.6, −1.9 ± 0.6	−1.7 ± 0.6	6.06−6.19	−10.1 ± 0.8 ± 0.1	−29.5 ± 1.4 ± 0.3	−8.9 ± 1.4 ± 0.1	6.0 ± 1.2
SW0556+2305	−6.1 ± 1.3	−31.0 ± 1.3	57.9 ± 2.4	57.9 ± 2.4	9.89	−56.1 ± 2.4	−17.6 ± 0.7	−10.9 ± 0.6	28.9 ± 0.3
SW0640+2518	−0.7 ± 1.7	−8.3 ± 1.7	18.8 ± 1.4	18.8 ± 1.4	17.49	−18.2 ± 1.4	−4.9 ± 0.5	1.8 ± 0.5	13.5 ± 0.6
SW0746+2858	−72.7 ± 1.6	−67.2 ± 1.6	57.6 ± 0.6	57.6 ± 0.6	23.16	−57.4 ± 0.6	−19.8 ± 0.3	6.4 ± 0.4	10.5 ± 0.4
SW0806+2532	−82.5 ± 1.6	−120.2 ± 1.7	−2.4 ± 0.6	−2.4 ± 0.6	27.87	−2.4 ± 0.5	−16.2 ± 0.3	−18.8 ± 0.3	5.4 ± 0.3
SW0815+2946	−15.1 ± 1.6	−54.0 ± 1.7	5.5 ± 0.7	5.5 ± 0.7	14.44	−6.0 ± 0.6	−17.4 ± 0.6	−5.5 ± 0.6	8.0 ± 0.6
SW0817+3241	−16.0 ± 3.4	9.0 ± 3.3	−33.7 ± 4.4	−33.7 ± 4.4	6.55	21.9 ± 4.0	12.9 ± 2.4	−25.7 ± 3.1	45.0
SW0828−0843	−6.0 ± 1.4	−29.0 ± 1.4	26.2 ± 1.8	26.2 ± 1.8	59.91	−15.6 ± 1.1	−21.6 ± 1.4	2.7 ± 0.5	19.3 ± 0.8
SW0828+4222	−51.1 ± 1.4	−42.7 ± 1.4	−55.1 ± 2.1	−55.1 ± 2.1	26.63	43.9 ± 1.7	−6.2 ± 0.2	−33.1 ± 1.2	19.8 ± 0.4
SW0833+3350	−104.8 ± 2.0	−56.5 ± 2.2	90.4 ± 0.9	90.4 ± 0.9	18.67	−88.2 ± 0.8	−22.8 ± 0.6	28.0 ± 0.7	11.0 ± 0.4
SW0838−0741	−7.6 ± 1.8	12.6 ± 1.7	88.6 ± 3.0	88.6 ± 3.0	6.78	−58.4 ± 2.0	−60.4 ± 2.4	30.1 ± 1.5	19.4 ± 1.0
SW0852+3907	32.0 ± 1.7	−105.7 ± 1.8	−25.5 ± 0.7	−25.5 ± 0.7	6.92	33.4 ± 0.9	−72.4 ± 1.2	−4.5 ± 1.0	9.4 ± 0.8
SW0859−0916$_{\rm n}$	−0.1 ± 1.6	−9.3 ± 1.7	−22.1 ± 2.2		20.20	−9.7 ±1.1	−18.5 ± 1.7	7.5 ± 0.9	18.1 ± 0.5
SW0906+3337	−28.0 ± 1.2	−32.1 ± 1.2	18.4 ± 1.3, 17.4 ± 1.2	17.9 ± 1.3	6.67−6.74	−24.3 ± 1.1 ± 0.1	−24.6 ± 0.9 ± 0.1	−5.2 ± 1.1 ± 0.1	13.9 ± 1.0
SW0959+3849	−29.3 ± 1.5	−6.1 ± 1.5	−3.3 ± 1.1	−3.3 ± 1.1	21.57	−2.9 ± 0.8	−2.1 ± 0.3	−6.4 ± 0.9	24.9 ± 0.4
SW1055+4246	−57.1 ± 1.3	−32.8 ± 1.3	58.7 ± 72.7		15.79				22.3 ± 0.3
SW1059+2315	47.8 ± 2.0	−28.2 ± 2.0	60.9 ± 14.5		14.03				28.0 ± 0.1
SW1130−0227	−39.7 ± 1.9	−91.1 ± 2.0	5.4 ± 2.6	5.4 ± 2.6	16.03	2.6 ± 0.6	−27.0 ± 1.6	−12.4 ± 2.2	24.3 ± 0.4
SW1133+3613	−142.5 ± 1.7	−55.0 ± 1.7	30.8 ± 0.6	30.8 ± 0.6	14.45	−51.0 ± 0.6	−16.5 ± 0.6	24.2 ± 0.6	62.1 ± 10.1
SW1146+4001	46.6 ± 4.0	−127.8 ± 4.0	−31.9 ± 0.4	−31.9 ± 0.4	5.54	85.4 ± 3.3	−85.2 ± 3.4	1.6 ± 1.2	21.1 ± 1.9
SW1148−0818	−61.4 ± 1.6	−4.1 ± 1.7	−64.3 ± 1.2	−64.3 ± 1.2	9.43	−31.1 ± 0.8	25.5 ± 1.0	−59.0 ± 1.1	14.0 ± 1.0
SW1208+3111	79.4 ± 1.5	−24.0 ± 1.6			12.26				44.6 ± 2.9
SW1221+2005	26.6 ± 1.1	−1.2 ± 1.1	−5.4 ± 0.6	−5.4 ± 0.6	14.61	7.9 ± 0.4	4.8 ± 0.4	−4.4 ± 0.6	8.6 ± 0.3
SW1237+3450$_{\rm o}$	−67.8 ± 2.7	−43.8 ± 2.7	7.9 ± 0.6	7.9 ± 0.6	24.61	−5.9 ± 0.5	−14.6 ± 0.5	−7.4 ± 0.6	7.6
SW1251+2232	35.7 ± 1.0	1.4 ± 0.9	−6.6 ± 0.3	−6.6 ± 0.3	25.39	3.4 ± 0.1	3.0 ± 0.1	−6.6 ± 0.3	15.8 ± 0.5
SW1251+2505	−8.3 ± 1.7	0.8 ± 1.7	−35.8 ± 0.6	−35.8 ± 0.6	12.54	−3.5 ± 0.6	−0.4 ± 0.6	−35.8 ± 0.6	3.0 ± 0.4
SW1321+2101	52.0 ± 1.2	4.9 ± 1.2	−13.9 ± 0.5	−13.9 ± 0.5	8.35	19.8 ± 0.7	19.9 ± 0.7	−16.8 ± 0.5	19.4 ± 0.6
SW1327+4558$_{\rm p}$	−88.4 ± 1.7	−52.6 ± 1.7	14.7 ± 0.4	14.7 ± 0.4	19.80	−11.3 ± 0.4	−13.6 ± 0.4	30.1 ± 0.4	19.1 ± 0.4
SW1328+3533	51.2 ± 2.4	−29.0 ± 2.4	−7.6 ± 0.3	−7.6 ± 0.3	6.33	43.4 ± 1.8	4.6 ± 1.8	−9.9 ± 0.5	14.4 ± 0.6
SW1333+2300	−109.6 ± 1.2	−7.1 ± 1.2			12.12				
SW1343+3911	−117.8 ± 1.8	−13.9 ± 1.8	−74.8 ± 0.3	−74.8 ± 0.3	8.55	−46.9 ± 1.0	−66.7 ± 1.0	−57.3 ± 0.4	15.6 ± 0.7
SW1419−1634	−14.0 ± 2.0	−18.6 ± 1.9			23.51				45.6 ± 5.0
SW1420+3459	−49.0 ± 2.0	−77.2 ± 1.9	−43.3 ± 0.5	−43.3 ± 0.5	21.11	−2.6 ± 0.4	−32.5 ± 0.4	−35.1 ± 0.5	
SW1429+3350	−74.6 ± 1.7	4.4 ± 1.7	33.1 ± 0.4	33.1 ± 0.4	17.53	−7.9 ± 0.8	−2.8 ± 1.0	35.7 ± 2.8	20.5 ± 0.6
SW1437−0331$_{\rm q}$	−57.9 ± 1.6	−6.1 ± 1.7	−60.9 ± 1.2	−60.9 ± 1.2	14.27	−49.5 ± 0.9	−5.1 ± 0.6	−40.1 ± 1.0	37.2 ± 1.9
SW1445−0854$_{\rm r}$	−79.8 ± 1.7	−50.6 ± 1.7	−36.0 ± 0.6	−36.0 ± 0.6	19.13	−32.1 ±0.5	−15.3 ± 0.4	−24.0 ± 0.5	5.8 ± 0.4
SW1502−1201$_{\rm s}$	−77.3 ± 2.0	−52.2 ± 2.0	60.9 ± 0.7	60.9 ± 0.7	26.58	4.8 ±0.4	58.9 ± 0.7	−22.1 ± 0.4	30.1 ± 1.0
SW1548−0310	−7.2 ± 2.7	−26.0 ± 2.8			16.54				
SW1607+3401	98.3 ± 2.7	1.5 ± 2.4	−85.3 ± 0.8	−85.3 ± 0.8	28.07	−27.3 ± 0.5	−36.0 ±0.6	−74.2 ± 0.6	24.8 ± 0.4
SW1622+2246	−37.0 ± 1.3	9.0 ± 1.3	−84.0 ± 1.1	−84.0 ± 1.1	11.16	−55.5 ± 0.8	−47.6 ±0.7	−44.5 ± 0.8	22.6 ± 0.6
SW1637+2211	−18.6 ± 1.5	−48.6 ± 1.5	56.4 ± 0.4	56.4 ± 0.4	16.34	42.8 ± 0.4	16.8 ± 0.4	36.0 ± 0.4	16.0 ± 0.5
SW1637+2919	42.2 ± 1.7	10.9 ± 1.7			16.34				26.7 ± 0.6
SW1649+4122	−8.6 ± 1.5	95.8 ± 1.6	−95.3 ± 0.6	−95.3 ± 0.6	10.78	−70.0 ± 0.7	−53.1 ± 0.6	−56.1 ± 0.6	17.0 ± 0.6
SW1659+3428	12.9 ± 2.5	−14.5 ± 2.4	1.9 ± 0.4	1.9 ± 0.4	4.31	17.4 ± 2.4	2.6 ± 2.0	−12.2 ± 2.2	16.7 ± 0.7
SW1703+3203	−8.8 ± 1.7	4.7 ± 1.5	−128.1 ± 0.9	−128.1 ± 0.9	6.23	−64.6 ± 1.1	−86.6 ± 1.1	−69.1 ± 1.2	20.1 ± 0.5
SW1704+3928	−44.4 ± 1.7	5.5 ± 1.7			11.41				30.5 ± 0.7
SW1713+2320	−1.8 ± 1.5	−31.9 ± 1.5	38.3 ± 0.9	38.3 ± 0.9	16.88	−30.2 ± 0.8	10.8 ± 0.5	−22.8 ± 0.5	20.7 ± 0.6
SW1724+4026	−7.5 ± 1.5	−4.2 ± 1.5			13.26				55.1 ± 9.8
SW1744+1312	−47.5 ± 1.1	−7.1 ± 1.1	−15.6 ± 0.4	−15.6 ± 0.4	13.82	−10.0 ± 0.4	−18.9 ± 0.4	7.4 ± 0.4	15.5 ± 0.5
SW1749+3350	−13.8 ± 1.6	−31.5 ± 1.7	10.2 ± 0.6	10.2 ± 0.6	9.71−9.72	18.4 ± 0.8	−1.6 ± 0.7	6.6 ± 0.8	21.5 ± 0.7
SW1751+4141	−5.0 ± 1.6	−17.4 ± 1.6			27.63−28.00				
SW1752+2327	−29.0 ± 1.3	−0.9 ± 1.2			18.96				34.3 ± 1.3

Table 5.7: *continued.*

Name	μ_α (mas yr^{-1})	μ_δ (mas yr^{-1})	RV (individual) (km s^{-1})	RV (final) (km s^{-1})	π (mas)	U (km s^{-1})	V (km s^{-1})	W (km s^{-1})	$v \sin i$ (km s^{-1})
SW1757+3133	-11.2 ± 1.5	-11.7 ± 1.4	-19.1 ± 8.0	-19.1 ± 8.0	8.71−8.76	-3.6 ± 4.0	-20.3 ± 6.1	-4.5 ± 3.4	39.0 ± 1.7
SW1757+5506	-11.2 ± 1.5	-11.7 ± 1.4	19.1 ± 8.8	19.1 ± 8.8	18.52	12.1 ± 4.3	12.0 ± 6.7	9.6 ± 3.7	33.4 ± 1.2
SW1758+0922	-28.1 ± 2.0	-2.9 ± 2.0	-18.9 ± 0.6, -20.3 ± 0.6	19.6 ± 0.6	12.59	-14.1 ± 0.7	-17.0 ± 0.7	3.3 ± 0.7	32.0 ± 1.4
SW1800+5100	-8.2 ± 1.2	10.7 ± 1.2			6.24−6.37				
SW1812+4105	12.2 ± 15.0	-11.0 ± 15.0	-83.9 ± 2.0	-83.9 ± 2.0	11.48	-24.5 ± 5.9	-69.8 ± 3.7	-40.1 ± 5.7	33.7 ± 1.4
SW1815+2948	12.8 ± 1.5	6.0 ± 1.5	-22.1 ± 0.4	-22.1 ± 0.4	9.92	-14.5 ± 0.6	-13.3 ± 0.5	-12.1 ± 0.7	16.1 ± 0.7
SW1815+3819$_{\rm t}$	20.9 ± 1.9	100.7 ± 2.2	-35.6 ± 0.3	-35.6 ± 0.3	9.91	-58.9 ± 1.0	-11.2 ± 0.6	-9.6 ± 0.9	16.0 ± 0.6
SW1830+3446	-1.1 ± 2.1	6.1 ± 2.1	-69.3 ± 0.6	-69.3 ± 0.6	7.98	-32.8 ± 1.2	-57.4 ± 0.9	-20.9 ± 1.2	21.4 ± 0.4
SW1831+5418	-5.4 ± 1.6	7.8 ± 1.6			11.87				
SW1913+4436	-6.9 ± 1.4	4.4 ± 1.3			14.09				49.0 ± 3.6
SW2028−0943	7.4 ± 1.4	-7.4 ± 1.4			10.65				50.9 ± 7.7
SW2028+1131	5.8 ± 1.3	-32.7 ± 1.3			23.45				52.8 ± 7.9
SW2044+1314	34.6 ± 0.8	12.5 ± 0.8	80.6 ± 0.7	80.6 ± 0.7	7.55−7.87	$22.2 \pm 0.6 \pm 0.4$	$71.7 \pm 0.6 \pm 0.1$	$-37.1 \pm 0.5 \pm 0.3$	18.3 ± 1.0
SW2107+1357	-2.1 ± 0.8	-20.3 ± 0.8			9.54−9.62				24.7 ± 1.7
SW2205+0749$_{\rm u}$	-15.5 ± 11.9	-8.9 ± 11.9	-87.6 ± 2.5	-87.6 ± 2.5	17.17	-21.8 ± 3.2	-66.1 ± 2.9	53.5 ± 3.0	41.1 ± 4.1
SW2222+2814	48.6 ± 1.6	59.9 ± 1.5	-21.0 ± 0.9	-21.0 ± 0.9	8.46	-42.4 ± 0.9	-12.6 ± 0.9	18.7 ± 0.9	20.8 ± 0.4
SW2244+3029	18.2 ± 1.3	-0.7 ± 1.3	-70.4 ± 1.2	-70.4 ± 1.2	12.59	-2.3 ± 0.5	-65.7 ± 1.1	26.3 ± 0.7	34.9 ± 1.0
SW2310+2055	72.2 ± 1.5	-15.2 ± 1.5			17.84				33.2 ± 1.0
SW2312+1709	12.8 ± 1.6	-9.2 ± 1.7	64.2 ± 0.4	64.2 ± 0.4	30.64	-2.4 ± 0.2	48.0 ± 0.3	42.7 ± 0.3	16.1 ± 0.4
SW2317+0551$_{\rm v}$	8.2 ± 1.3	-5.4 ± 1.3	-21.2 ± 3.6	-21.2 ± 3.6	27.31	-2.0 ± 0.3	-14.8 ± 2.3	15.2 ± 2.8	41.0
SW2320+2921	8.0 ± 1.7	-14.0 ± 1.7	3.0 ± 1.1, 1.7 ± 2.2	2.3 ± 1.7	4.46−4.57	-0.8 ± 1.8	$-6.5 \pm 1.7 \pm 0.1$	$-15.8 \pm 1.8 \pm 0.2$	22.5 ± 0.4
SW2339+2204	-86.8 ± 1.6	-63.3 ± 1.6	19.6 ± 2.0	19.6 ± 2.0	17.94	24.6 ± 0.5	16.1 ± 1.5	-18.1 ± 1.2	23.6 ± 0.7
SW2340−0228$_{\rm w}$	27.7 ± 1.7	-11.1 ± 1.8	18.2 ± 2.5, 18.5 ± 2.5	18.4 ± 2.5	8.48−8.51	-9.5 ± 1.0	-2.3 ± 1.5	-22.8 ± 2.3	16.1 ± 0.8
SW2357+3343	104.3 ± 3.7	9.8 ± 3.6	-28.8 ± 1.3	-28.8 ± 1.3	13.97	$-23.6 \pm 1.3 \pm 0.2$	$-38.5 \pm 1.3 \pm 0.1$	9.0 ± 1.2	20.0 ± 0.4
Spectroscopic binaries									
SW0108+3138	5.6 ± 1.3	-13.9 ± 1.3	-10.2 ± 3.1, 9.1 ± 3.3		5.15−6.10				32.2 ± 1.9
SW0330+5417$_{\rm x}$	148.0 ± 0.8	-121.7 ± 0.9	66.4 ± 0.6		$12.68 \pm 1.11_{\rm t}$				9.5 ± 0.6
SW0338+4636$_{\rm y}$	20.0 ± 1.5	-26.4 ± 1.5	2.5 ± 3.6, -7.5 ± 3.9		5.90				49.1 ± 9.3
SW0833+3224	-31.4 ± 1.7	-30.9 ± 1.7	39.1 ± 6.4, 77.1 ± 2.5, $45.3 \pm 2.9_{\rm i}$		10.02−10.12				21.8 ± 0.9
SW1000−0854$_{\rm z}$	-13.3 ± 1.6	1.4 ± 1.6	57.2 ± 2.7, 75.6 ± 3.5		10.47				25.6 ± 8.5
SW1329−0454	-29.2 ± 1.4	2.4 ± 1.5	31.8 ± 1.8, -75.2 ± 0.3		18.08				24.0 ± 0.7
SW1528−1010$_{\rm aa}$	22.0 ± 2.4	-82.5 ± 2.4	-40.2 ± 11.2		14.35				21.3 ± 0.5
SW1531−0734$_{\rm ab}$	-38.1 ± 1.7	-7.8 ± 2.0	-58.0 ± 0.9	-58.0 ± 0.9	8.78	-54.0 ± 0.9	-14.3 ± 1.0	-26.2 ± 1.0	18.9 ± 0.6
SW1626+3350	-21.8 ± 1.6	-37.4 ± 1.6	-119.5 ± 0.4, -125.3 ± 0.3		26.34−26.82				14.1 ± 0.6
SW1747+3321	-8.7 ± 2.5	-1.8 ± 2.5	10.6 ± 0.4, -14.4 ± 0.3		8.91−11.54				15.5 ± 0.5
SW2048+1910	18.2 ± 1.4	-149.0 ± 1.4	-27.9 ± 2.1, -50.6 ± 0.9		23.16−23.47				
SW2107+0632	-24.1 ± 1.9	-9.8 ± 1.9	4.6 ± 0.4, -0.9 ± 0.4		15.12				17.5 ± 0.7
SW2121+0948	-23.6 ± 1.8	-28.1 ± 1.9	12.0 ± 0.6, -54.0 ± 0.7		10.98−11.07				21.6 ± 0.7
SW2148+1910	72.2 ± 1.5	-15.2 ± 1.5	-86.0 ± 0.5, -71.8 ± 0.7		25.62				

a: $v \sin i = 34.0\,\mathrm{km\,s^{-1}}$ (Glebocki & Gnacinski 2005), b: Likely α Persei member (Hoogerwerf & Blaauw 2000), c: Possible Pleiades member (Sarro et al. 2014), $v \sin i = 11.0 \pm 3.00\,\mathrm{km\,s^{-1}}$ (Glebocki & Gnacinski 2005), $RV = 6.06 \pm 0.29\,\mathrm{km\,s^{-1}}$; $v \sin i = 12.2 \pm 1.0\,\mathrm{km\,s^{-1}}$ (Mermilliod, Mayor & Udry 2009), d: $RV = 14.2 \pm 1.4\,\mathrm{km\,s^{-1}}$, $v \sin i = 15.6 \pm 1.0\,\mathrm{km\,s^{-1}}$ (Biazzo et al. 2012), e: Parallax from de Bruijne & Eilers (2012), f: $RV = -13.6 \pm 1.8\,\mathrm{km\,s^{-1}}$ (Kordopatis et al. 2013), g: $\log g = 4.39$; [Fe/H] $= -1.35$ (Pinsonneault et al. 2012); $RV = -33.1, -33.1, -32.2\,\mathrm{km\,s^{-1}}$, $v \sin i = 39.3 \pm 2.4\,\mathrm{km\,s^{-1}}$ (Frasca et al. 2011), h: Parallax from Anderson & Francis (2012), i: $v \sin i = 38.0 \pm 3.0\,\mathrm{km\,s^{-1}}$ (Glebocki & Gnacinski 2005), likely α Persei member (Zuckerman et al. 2012), $RV = 3.67\,\mathrm{km\,s^{-1}}$ (Makarov 2006), j: $v \sin i = 65.0 \pm 3.0\,\mathrm{km\,s^{-1}}$ (Glebocki & Gnacinski 2005), likely α Persei member (Zuckerman et al. 2012), $RV = 4.06\,\mathrm{km\,s^{-1}}$ (Makarov 2006), k: Possible Pleiades member (Hartman et al. 2010), l: Member of the Per OB2 SFR (Belikov et al. 2002), m: Parallax from de Bruijne & Eilers (2012), n: $RV = -26.0 \pm 2.6\,\mathrm{km\,s^{-1}}$, o: Reported as a likely-new-member of ABDMG; $RV = 9.7 \pm 0.6\,\mathrm{km\,s^{-1}}$; $v \sin i = 8\,\mathrm{km\,s^{-1}}$ (Schlieder, Lépine & Simon 2012), p: Reported as a likely-new-member of ABDMG; $RV = 17.6 \pm 2.0\,\mathrm{km\,s^{-1}}$; $v \sin i = 10 \pm 2\,\mathrm{km\,s^{-1}}$ (Schlieder, Lépine & Simon 2012), q: $RV = -26.6 \pm 3.4\,\mathrm{km\,s^{-1}}$ (Kordopatis et al. 2013), r: $RV = 13.3 \pm 2.0\,\mathrm{km\,s^{-1}}$ (Kordopatis et al. 2013), s: $RV = -30.3 \pm 4.3\,\mathrm{km\,s^{-1}}$ (Kordopatis et al. 2013), t: $v \sin i = 16.7 \pm 0.5\,\mathrm{km\,s^{-1}}$; $\log g = 4.27\,\mathrm{cm\,s^{-2}}$; [Fe/H] $= -0.13$ (Guillout et al. 2009), u: SB2? (Zickgraf et al. 2005), v: SB2?; $v \sin i = 40.0 \pm 5.0\,\mathrm{km\,s^{-1}}$ (Torres et al. 2006), w: $RV = 17.7\,\mathrm{km\,s^{-1}}$; $v \sin i = 33.6 \pm 3.4\,\mathrm{km\,s^{-1}}$ (Torres et al. 2006), x: Parallax from Kharchenko & Roeser (2009), SB1?; $v \sin i = 18.2\,\mathrm{km\,s^{-1}}$; $\log g = 4.25\,\mathrm{cm\,s^{-2}}$; [Fe/H] $= -0.05$; $RV = 33.93\,\mathrm{km\,s^{-1}}$ (de Bruijne & Eilers 2012), y: Likely α Persei member (Zuckerman et al. 2012), $RV = 4.78\,\mathrm{km\,s^{-1}}$ (Makarov 2006), z: $RV = -7.2 \pm 5.8\,\mathrm{km\,s^{-1}}$ (Kordopatis et al. 2013), aa: $RV = 18.8, -27.8, 35.6, 23.2\,\mathrm{km\,s^{-1}}$ (Kordopatis et al. 2013), ab: $RV = -24.5, -5.9\,\mathrm{km\,s^{-1}}$ (Kordopatis et al. 2013).

5.7.3 Comparison with MG space velocities

To test if a star is kinematically matched in UVW to a known MG, a reduced χ^2 fitting statistic is used, as described in Shkolnik et al. (2012):

$$\bar{\chi}^2_{\rm T} = \frac{1}{3}\left(\frac{(U_* - U_{\rm MG})^2}{\sigma^2_{U_*} + \sigma^2_{U_{\rm MG}}} + \frac{(V_* - V_{\rm MG})^2}{\sigma^2_{V_*} + \sigma^2_{V_{\rm MG}}} + \frac{(W_* - W_{\rm MG})^2}{\sigma^2_{W_*} + \sigma^2_{W_{\rm MG}}}\right) \tag{5.5}$$

$UVW_{\rm MG}$ and errors are provided in Table 2.1. With the exception of SW1332+2230, the UVW midpoint values are used as inputs for UVW and σ_{UVW}. Table 5.8 provides the reduced $\bar{\chi}^2_{\rm T}$ values for all of the likely-young sample. To interpret these results, given there are 3 degrees of freedom, a $\bar{\chi}^2_{\rm T}$ value larger than 3.78 rejects the null hypothesis at 99 per cent confidence. Any candidate/MG test where $\bar{\chi}^2_{\rm T} > 3.78$ results in rejection for MG membership.

5.7.4 Predicted radial velocity comparisons with known MGs

The Boettlinger diagrams require distances, which, with one exception for the likely-young sample, could only be inferred using photometric parallaxes. Therefore a *distance independent* criterion was used to strengthen the case for MG membership. Given the UVW and convergent point of an MG and the position of a candidate member, the predicted RV for a group member is then $V_T \cos\lambda$, where V_T is the total velocity of the group ($\sqrt{U^2+V^2+W^2}$) and λ is the angle between the convergent point and the target position (see §2.2.1).

The average RV error for the likely-young sample is $\sim 1\,{\rm km\,s^{-1}}$ and the dispersion amongst MG members in UVW is $\lesssim 3\,{\rm km\,s^{-1}}$. Therefore true MG members are required to have RVs that are within $5\,{\rm km\,s^{-1}}$ of the predicted RV ($\Delta{\rm RV} = |{\rm RV} - V_T\cos\lambda| < 5\,{\rm km\,s^{-1}}$). Any candidates with $\Delta{\rm RV} > 5\,{\rm km\,s^{-1}}$ are rejected as MG members. Objects that have RVs within this threshold are flagged as possible members, although even if they satisfy this criterion, a discrepancy in distance, age or chemical abundances may result in a rejection. For this reason the technique can be used to

eliminate membership. The UVW and convergent point of each MG is provided in Table 2.1 and values of ΔRV for each candidate/MG are given in Table 5.9.

In §5.4.4, it was calculated that there is a 7.2 per cent chance that a star has 2 RV measurements within $5\,\mathrm{km\,s^{-1}}$ but $> 5\,\mathrm{km\,s^{-1}}$ from the average centre-of-mass RV. This implies that out of a sample of 26 Li-rich stars likely to be single based on repeat RV measurements, ~ 2 may be shifted in UVW by $\sim 5\,\mathrm{km\,s^{-1}}$ which would affect their membership status to MGs.

5.7.5 Combined MG membership criteria

If a candidate is a true member of an MG then it must satisfy the conditions set in §2.1. In this work a candidate only remains as a possible member of a MG if it satisfies all of the following criteria:

1. The $\bar{\chi}^2_T$ value in Table 5.8 is no more than 3.78.
2. ΔRV values in Table 5.9 are no more no than $5\,\mathrm{km\,s^{-1}}$.
3. The estimated age range for the candidates (provided in Table 5.6) must overlap with the age range of the MG (see Table 2.1).

In Table 5.10 the outcome for each criteria is given. A ✔ indicates a successful criterion match and an ✘ represents a failure.

Target	Label	TWA	BPMG	ABDMG	Tuc-Hor	Columba	Carina	Argus	Octans-Near	η Cha	ϵ Cha
SW0124+2557	A	45.9	22.2	81.5	38.3	62.3	186.8	68.2	3.2	240.5	45.7
SW0135+2116	B	63.1	38.8	116.9	29.6	73.4	638.7	38.8	7.9	11511.3	64.6
SW0235+3139	C	16.1	13.5	18.2	1.1	6.1	230.8	27.9	24.3	1808.2	13.0
SW0304+3003	D	62.1	37.3	111.8	31.0	67.2	346.4	28.5	6.6	1490.7	61.9
SW0316+5638	E	10.8	0.9	13.0	5.9	3.2	5.1	17.4	9.4	13.4	2.7
SW0322+2853	F	36.8	17.3	69.4	22.6	37.6	92.4	28.7	3.7	346.5	33.1
SW0343+2226	G	10.4	3.0	1.4	12.2	13.6	12.4	55.8	12.3	65.6	9.6
SW0502+3111	H	16.9	4.4	11.6	5.5	0.8	3.2	16.5	12.8	67.7	6.5
SW0521+2400	I	14.1	0.6	3.0	3.5	1.3	1.4	19.1	2.4	1.6	0.3
SW0847+3423	J	29.9	21.8	10.1	9.5	8.0	12.1	35.8	39.9	91.3	13.7
SW1337+4444	K	50.9	24.8	96.3	28.1	55.5	264.8	20.9	3.4	1901.8	47.0
SW1354−0543	L	18.3	7.3	10.1	6.9	2.2	3.9	11.3	16.8	176.9	7.1
SW1438+3300	M	13.9	3.4	2.4	10.8	6.4	8.4	40.8	16.4	1.7	1.3
SW1625+3002	N	265.1	361.1	146.2	403.5	602.5	1599.4	1039.7	216.4	5716.4	342.3
SW2145+2711	O	16.8	18.9	11.6	1.2	8.9	10.5	45.6	37.3	69.7	13.8
SW1332+2230	P	44.8	29.2	83.5	24.1	47.5	132.2	10.4	10.8	245.2	47.4
SW1550−0222	Q	9.2	5.9	4.9	5.0	8.2	5.6	46.5	16.6	436.3	11.7
SW1629+2810	R	59.8	60.5	77.1	107.4	144.6	310.8	206.9	30.0	347.7	82.5
SW1718+2506	S	47.0	23.9	64.0	56.8	55.7	103.5	49.4	27.2	73.6	50.4
SW1722+3658	T	25.5	10.1	39.1	13.5	12.9	35.8	3.2	23.2	161.6	18.3
SW1731+2815	U	54.9	29.2	87.1	38.6	50.3	90.2	6.4	9.6	153.7	51.9
SW1804+3930	V	28.0	25.7	11.2	3.8	9.9	16.0	43.0	43.4	55.8	15.2
SW1925+4429	W	45.7	33.5	4.5	29.4	28.6	74.6	74.1	46.2	227.6	16.9
SW2058−0902	X	52.4	25.8	96.3	33.7	65.7	271.0	41.8	3.3	832.5	51.4
SW2256+2052	Y	68.8	46.0	124.9	32.9	81.3	495.3	27.3	9.8	3401.3	73.2
SW2307+1710	Z	17.1	5.8	1.9	9.2	5.7	5.6	20.6	15.6	3.0	3.0

Table 5.8: $\bar{\chi}^2_{\rm T}$ values for each candidate/MG match in the likely-young sample.

Target	Label	TWA	BPMG	ABDMG	Tuc-Hor	Columba	Carina	Argus	Octans-Near	η Cha	ϵ Cha
SW0124+2557	A	21.0	5.5	11.5	13.8	10.1	11.5	0.1	4.3	7.5	7.7
SW0135+2116	B	17.2	1.4	6.4	9.8	5.8	7.2	3.6	7.6	3.0	3.3
SW0235+3139	C	14.8	4.5	1.9	2.4	1.2	0.5	12.4	12.8	2.4	2.5
SW0304+3003	D	23.6	3.2	9.0	9.5	5.9	7.6	5.1	4.1	5.0	4.8
SW0316+5638	E	17.4	1.0	8.9	2.9	1.3	3.4	11.8	10.3	2.5	1.8
SW0322+2853	F	22.1	1.2	6.6	7.1	3.5	5.2	7.4	5.4	2.8	2.6
SW0343+2226	G	16.8	4.5	0.7	1.1	2.9	1.2	12.7	9.6	3.6	3.7
SW0502+3111	H	23.2	1.1	6.0	3.8	1.1	2.9	9.3	2.5	2.4	1.8
SW0521+2400	I	22.9	0.9	4.1	3.1	0.2	1.8	9.0	0.9	1.5	1.0
SW0847+3423	J	19.2	5.2	9.8	0.4	1.4	2.8	5.5	6.5	6.6	5.2
SW1337+4444	K	5.0	7.2	15.4	0.9	5.4	6.1	0.8	4.7	10.6	9.2
SW1354−0543	L	10.9	4.3	2.7	4.4	0.4	0.6	7.2	10.6	4.1	3.4
SW1438+3300	M	11.2	2.8	4.0	9.2	4.2	4.1	5.9	4.7	0.2	0.9
SW1625+3002	N	59.9	47.9	40.6	51.8	47.2	47.2	48.5	52.7	44.6	45.3
SW2145+2711	O	9.5	9.1	1.2	2.4	3.1	2.4	9.6	21.3	5.8	5.5
SW1332+2230	P	1.6	6.4	10.5	1.9	3.1	3.1	3.5	8.4	8.3	7.1
SW1550−0222	Q	14.4	5.1	5.6	0.6	4.1	3.0	10.2	6.8	5.9	5.6
SW1629+2810	R	17.1	4.5	2.6	8.3	3.7	3.8	4.6	9.2	1.2	1.9
SW1718+2506	S	26.8	13.3	6.4	15.5	11.4	11.6	12.2	19.2	10.1	10.5
SW1722+3658	T	13.4	3.9	5.1	5.6	1.7	1.4	5.2	11.3	0.1	0.5
SW1731+2815	U	8.9	3.4	11.0	1.8	5.7	5.7	4.1	3.3	7.0	6.5
SW1804+3930	V	13.0	5.0	4.6	5.3	1.9	1.6	6.5	13.9	0.8	1.3
SW1925+4429	W	17.5	13.6	3.0	11.5	9.4	8.7	16.1	24.7	9.1	9.5
SW2058−0902	X	2.5	8.3	9.1	14.4	13.7	13.0	15.5	1.7	9.1	10.1
SW2256+2052	Y	9.7	5.6	12.1	14.1	11.9	12.7	5.0	5.9	8.2	8.7
SW2307+1710	Z	2.7	1.7	4.0	7.1	4.5	5.2	2.0	12.8	0.6	1.1

Table 5.9: ΔRV values for all MG/candidate comparisons. UVW and convergent points ($\alpha_{\rm CP}$ and $\delta_{\rm CP}$) for each MG are provided in Table 2.1.

		TWA			BPMG			ABDMG			Tuc-Hor			Columba			Carina			Argus			Octans-Near			η Cha			ϵ Cha		
Target	Label	1	2	3	1	2	3	1	2	3	1	2	3	1	2	3	1	2	3	1	2	3	1	2	3	1	2	3	1	2	3
SW0124+2557	A	✘	✘	✘	✘	✘	✘	✘	✘	✔	✘	✘	✔	✘	✘	✔	✘	✘	✔	✘	✔	✔	✔	✔	✔	✘	✘	✘	✘	✘	✘
SW0135+2116	B	✘	✘	✘	✘	✔	✘	✘	✘	✔	✘	✘	✔	✘	✘	✔	✘	✘	✔	✘	✔	✔	✘	✘	✔	✘	✔	✘	✘	✔	✘
SW0235+3139	C	✘	✘	✘	✘	✔	✘	✘	✔	✔	✔	✔	✔	✘	✔	✔	✘	✔	✔	✘	✘	✔	✘	✘	✔	✘	✔	✘	✘	✔	✘
SW0304+3003	D	✘	✘	✘	✘	✔	✘	✘	✘	✔	✘	✘	✔	✘	✘	✔	✘	✘	✔	✘	✘	✔	✘	✔	✔	✘	✔	✘	✘	✔	✘
SW0316+5638	E	✘	✘	✘	✔	✔	✘	✘	✘	✔	✘	✔	✔	✔	✔	✔	✘	✔	✔	✘	✘	✔	✘	✘	✔	✘	✔	✘	✔	✔	✘
SW0322+2853	F	✘	✘	✘	✘	✔	✘	✘	✘	✔	✘	✘	✔	✘	✔	✔	✘	✘	✔	✘	✘	✔	✔	✘	✔	✘	✔	✘	✘	✔	✘
SW0343+2226	G	✘	✘	✘	✔	✔	✘	✔	✔	✔	✘	✔	✔	✘	✔	✔	✘	✔	✔	✘	✘	✔	✘	✘	✔	✘	✔	✘	✘	✔	✘
SW0502+3111	H	✘	✘	✘	✘	✔	✘	✘	✘	✔	✘	✔	✔	✔	✔	✔	✔	✔	✔	✘	✘	✔	✘	✔	✔	✘	✔	✘	✘	✔	✘
SW0521+2400	I	✘	✘	✔	✔	✔	✔	✔	✔	✘	✔	✔	✔	✔	✔	✔	✔	✔	✔	✘	✘	✔	✔	✔	✔	✔	✔	✔	✔	✔	✔
SW0847+3423	J	✘	✘	✘	✘	✘	✘	✘	✘	✔	✘	✔	✔	✘	✔	✔	✘	✔	✔	✘	✘	✔	✘	✘	✔	✘	✘	✘	✘	✘	✘
SW1337+4444	K	✘	✔	✘	✘	✘	✘	✘	✘	✔	✘	✔	✔	✘	✘	✔	✘	✘	✔	✘	✔	✔	✔	✔	✔	✘	✘	✘	✘	✘	✘
SW1354−0543	L	✘	✘	✘	✘	✔	✘	✘	✔	✔	✘	✔	✔	✔	✔	✔	✘	✔	✔	✘	✘	✔	✘	✘	✔	✘	✔	✘	✘	✔	✘
SW1438+3300	M	✘	✘	✘	✔	✔	✘	✔	✔	✔	✘	✘	✔	✘	✔	✔	✘	✔	✔	✘	✘	✔	✘	✔	✔	✔	✔	✘	✔	✔	✘
SW1625+3002	N	✘	✘	✘	✘	✘	✘	✘	✘	✔	✘	✘	✔	✘	✘	✔	✘	✘	✔	✘	✘	✔	✘	✘	✔	✘	✘	✘	✘	✘	✘
SW2145+2711	O	✘	✘	✘	✘	✘	✘	✘	✔	✔	✔	✔	✔	✘	✔	✔	✘	✔	✔	✘	✘	✔	✘	✘	✔	✘	✘	✘	✘	✘	✘
SW1332+2230	P	✘	✔	✘	✘	✘	✘	✘	✘	✔	✘	✔	✔	✘	✔	✔	✘	✔	✔	✘	✔	✔	✘	✘	✔	✘	✘	✘	✘	✘	✘
SW1550−0222	Q	✘	✘	✘	✘	✘	✘	✘	✘	✔	✘	✔	✔	✘	✔	✔	✘	✔	✔	✘	✘	✔	✘	✘	✔	✘	✘	✘	✘	✘	✘
SW1629+2810	R	✘	✘	✘	✘	✔	✘	✘	✔	✔	✘	✘	✔	✘	✔	✔	✘	✔	✔	✘	✔	✔	✘	✘	✔	✘	✔	✘	✘	✔	✘
SW1718+2506	S	✘	✘	✘	✘	✘	✘	✘	✘	✔	✘	✘	✔	✘	✘	✔	✘	✘	✔	✘	✘	✔	✘	✘	✔	✘	✘	✘	✘	✘	✘
SW1722+3658	T	✘	✘	✘	✘	✔	✘	✘	✘	✔	✘	✘	✔	✘	✔	✔	✘	✔	✔	✔	✘	✔	✘	✘	✔	✘	✔	✘	✘	✔	✘
SW1731+2815	U	✘	✘	✘	✘	✔	✘	✘	✘	✔	✘	✔	✔	✘	✘	✔	✘	✘	✔	✘	✔	✔	✘	✔	✔	✘	✘	✘	✘	✘	✘
SW1804+3930	V	✘	✘	✘	✘	✔	✘	✘	✔	✔	✔	✘	✔	✘	✔	✔	✘	✔	✔	✘	✘	✔	✘	✘	✔	✘	✔	✘	✘	✔	✘
SW1925+4429	W	✘	✘	✘	✘	✘	✘	✘	✔	✔	✘	✘	✔	✘	✘	✔	✘	✘	✔	✘	✘	✔	✘	✘	✔	✘	✘	✘	✘	✘	✘
SW2058−0902	X	✘	✔	✘	✘	✘	✘	✘	✘	✔	✘	✘	✔	✘	✘	✔	✘	✘	✔	✘	✘	✔	✔	✔	✔	✘	✘	✘	✘	✘	✘
SW2256+2052	Y	✘	✘	✘	✘	✘	✘	✘	✘	✔	✘	✘	✔	✘	✘	✔	✘	✘	✔	✘	✔	✔	✘	✘	✔	✘	✘	✘	✘	✘	✘
SW2307+1710	Z	✘	✔	✘	✘	✔	✘	✔	✔	✔	✘	✘	✔	✘	✔	✔	✘	✘	✔	✘	✔	✔	✘	✘	✔	✔	✔	✘	✔	✔	✘

Table 5.10: The full list of candidate/MG criteria matches for the likely-young sample. A ✔ marks a successful match and a ✘ denotes a failed criteria. The columns labelled '1, 2 and 3' are the criteria listed in §5.7.5. An object was only considered a potential member of an MG if all three were satisfied.

Even if an object satisfies all three of these criteria, they may subsequently be ruled out if they are inconsistent in terms of position or abundance. The tangential velocity ($V_{\rm TAN}$) of the one target with a trigonometric parallax (SW1332+2230) was compared with the projected tangential velocities for each MG using Equation 2.2. The comparison reveals only one potential match with ABDMG ($\delta V_{\rm TAN} = 4.6\,{\rm km\,s^{-1}}$).

5.7.6 BANYAN

All members in the likely-young sample were subsequently analysed using the web-based tool 'BANYAN'[2]. BANYAN returns membership probabilities for 7 MGs (TWA, BPMG, Tuc-Hor, Columba, Carina, Argus and ABDMG) by taking into account (minimally) sky positions and proper motions. RVs and parallaxes are optional additional criteria which can be used to provide a more robust probability. Probabilities are calculated using the formulation described in Malo et al. (2013) and sum to 100 per cent across the field and the seven considered MGs. To attain membership probabilities for the likely-young sample, sky position, proper motion and RV are used as inputs. Parallaxes are not used as an input unless a trigonometric parallax is available. The results are listed in Table 5.11. The BANYAN tool uses only kinematic and positional criteria for group membership, therefore additional age and abundance criteria are required to fully assess membership status. According to the BANYAN analysis, 15 objects result in a zero per cent kinematic match for any MG. The BANYAN code takes into account the XYZ positions of candidates and compares them with the mean and dispersion of XYZ for MGs. Objects which have been identified in the Northern hemisphere may not be detected as MG members by BANYAN because they are too distant from the centroids of most MGs as most MG members are in the Southern hemisphere. A few candidates have no matches to a MG based on work in this chapter, but BANYAN detects a finite probability. This may be due to the strictness of the kinematic criteria applied in this chapter or because an object is located close to a MG in XYZ but not in

[2]see §2.3, available at `http://www.astro.umontreal.ca/~malo/banyan.php`

Target	Label	TWA	BPMG	TucHor	COL	CAR	Argus	ABDMG	Field star
SW0124+2557	A								100.00
SW0135+2116	B								100.00
SW0235+3139	C								100.00
SW0304+3003	D								100.00
SW0316+5638	E	1.05							98.95
SW0322+2853	F								100.00
SW0343+2226	G		59.66					0.11	40.23
SW0502+3111	H		23.42		30.85				45.72
SW0521+2400	I		99.56						0.44
SW0847+3423	J								100.00
SW1337+4444	K								100.00
SW1354−0543	L	24.31	0.11						74.81
SW1438+3300	M								100.00
SW1625+3002	N								100.00
SW2145+2711	O								100.00
SW1332+2230	P								100.00
SW1550−0222	Q		2.64						97.35
SW1629+2810	R								100.00
SW1718+2506	S								100.00
SW1722+3658	T		35.80				0.10		64.10
SW1731+2815	U		12.69				0.01		87.30
SW1804+3930	V		0.70		0.01			0.63	98.66
SW1925+4429	W							75.48	24.52
SW2058−0902	X								100.00
SW2256+2052	Y								100.00
SW2307+1710	Z	61.15						34.83	4.02

Table 5.11: Membership probabilities (in per cent) for the 7 MGs considered in the BANYAN code developed by Malo et al. (2013). This analysis takes into account right ascension, declination, proper motions and RVs but do not include the photometric parallaxes. Only kinematic data is used to calculate probabilities.

UVW. In §5.8 the results of the work in this chapter are compared to the probabilities in Table 5.11.

5.8 Individual objects

5.8.1 Individual objects linked to at least one MG

This section focuses on objects that satisfied all 3 criteria in §5.7.5 for at least one MG. For each candidate/MG match the membership feasibility is further examined and any additional data in the literature is used. From the likely-young sample of 26 objects

identified in this work, 12 were linked to at least one MG.

Target A, SW0124+2557 - All three criteria are matched for the Octans-Near association. The BANYAN code does not associate this object with any MG, although BANYAN not take Octans-Near into consideration. It has a spectral-type G9 and its Li age-range is estimated as $30 - 150$ Myr.

Target C, SW0235+3139 - All three criteria are matched for Tuc-Hor, however BANYAN assigns a zero probability (herein $P_{\rm BANYAN}$) of it being a Tuc-Hor member (or any other MG). It is possible that BANYAN does not predict Tuc-Hor membership because the XYZ is a long way from the members used for definition of the MG by Malo et al. (2013). Figures 5.11 and 5.12 show that this object is within the 1σ dispersion in V and W for Tuc-Hor but this is not the case for U velocity. Because of its G9 spectral-type, an age-range of 30 to 200 Myr is assigned and although this encompasses the age of Tuc-Hor ($\sim$ 40 Myr), a more precise age is necessary before membership can properly be assigned.

Target E, SW0316+5638 - This K2 object matches all three criteria for Columba. However, $P_{\rm BANYAN}$ is zero for Columba and only TWA returns a non-zero probability (1.05 per cent). The large difference in XYZ between target E and Columba may explain why BANYAN did not recover any membership probability for Columba. The age of Columba is $20 - 40$ Myr (see Table 2.1) and although this target has a large Li EW (222 mÅ) an age range of $30 - 200$ Myr is inferred because of the overlap in Li EWs amongst clusters between 30 and 125 Myr for K-dwarfs.

Target G, SW0343+2226 - All three criteria are successfully matched with ABDMG. $P_{\rm BANYAN} = 0.11$ per cent for ABDMG, however this much higher for BPMG (59.66 per cent). Its low $P_{\rm BANYAN}$ value for ABDMG is due to its large difference in XYZ. Although target G satisfies both the $\bar{\chi}^2_T$ and RV criteria, membership to BPMG is ruled out because its age is measured between 30 and 150 Myr (Figure 5.6 shows that its Li EW/colour is between the lower envelope of IC 2602 and the upper envelope of the Pleiades), not coeval with BPMG, whose age is < 30 Myr. The age of this object is more likely to be coeval with ABDMG (between 70 and 125 Myr). There is an uncertainty of $\sim 4\,{\rm km\,s^{-1}}$ in V velocity, which means the object could have kinematic

matches to Tuc-Hor or TWA (but not BPMG). A literature search for this object using the SIMBAD[3] database reveals that it was classified as a Pleiades member (Pels 22) by van Leeuwen, Alphenaar & Brand (1986) and has since been acknowledged as a member of the Pleiades cluster in at least 7 subsequent publications. Target G is very close to the centroid of the Pleiades cluster (α, δ = 03h 47m 00s, +24d 07m 00s), however the parallax range used in this chapter ($8.78 - 11.37$ mas) does not encompass the Pleiades ($6.66 - 8.33$ mas).

Target H, SW0502+2111 - The three criteria in §5.7.5 matched successfully for Columba and Carina. The BANYAN analysis returns $P_{\rm BANYAN} = 30.85$ per cent for Columba, $P_{\rm BANYAN} = 23.42$ per cent for BPMG, but zero probability for Carina. It is close to Columba in UVW, but not matched with BPMG. An upper age of 150 Myr is estimated and a lower bound of 30 Myr is estimated based on Li. This lower age limit is not coeval with BPMG, but could still be a Columba member. At a spectral-type of K3 it lies in a part of the diagram where a large scatter is present between Pleiades and IC 2602 members, however the object appears slightly closer to the IC 2602 pattern.

Target I, SW0521+2400 - Although this K3 spectral-type object matches all three criteria for seven MGs (BPMG, Tuc-Hor, Columba, Carina, Octans, η Cha and ϵ Cha), there is a large uncertainty in V velocity. BANYAN predicts it is a BPMG member with 99.56 per cent probability, the highest probability of any group membership for the likely-young sample. Figures 5.11 and 5.12 show that membership with Tuc-Hor, Carina, Columba and Octans-Near cannot be ruled out, however a more accurate parallax is required to identify which group it may belong to. The object has an Li EW (> 300 mÅ), large enough to set a cautious upper age of 30 Myr. Although a lower age of 5 Myr was assigned, this object may turn out to be younger than this. Li & Hu (1998) identify this object as a weak-lined T-Tauri star (WTTS) in the surrounding area of the Taurus-Auriga region. It is classified as a T-Tauri star in the pre-main sequence catalog developed by Ducourant et al. (2005).

Santos et al. (2008) located the object in the Taurus SFR and derive chemical

[3] `http://simbad.u-strasbg.fr/simbad/`

abundances. To test for abundance matches with MGs, the mean and standard deviations of [Fe/H], [Si/H] and [Ni/H] for members of the MGs in tables 2 and 3 in Viana Almeida et al. (2009) were compared to SW0521+2400. The abundances are consistent with any of the considered MGs. Biazzo et al. (2012) identify this target as part of a $2-10$ Myr stellar aggregrate within 15° of Taurus-Auriga, which they name 'X-Clump 0534+22'. Should the age turn out to be between $2-10$ Myr then only η Cha, ϵ Cha and TWA would satisfy the age criterion.

Target K, SW1337+4444 - This object successfully matches all three criteria for Octans-Near membership, however BANYAN does not provide a match to any MG (although Octans-Near is not part of the BANYAN analysis). It has a K1 spectral-type with a Li EW of 260 mÅ, therefore its age is estimated as $30-150$ Myr. Figures 5.11 and 5.12 show that it is within the 1σ range of Octans-Near in U and V, however it is $\sim 5\,\mathrm{km\,s^{-1}}$ larger in W velocity.

Target L, SW1354−0543 - All three criteria are matched with Columba, although BANYAN predicts $P_{\mathrm{BANYAN}} = 24.31$ per cent for TWA, $P_{\mathrm{BANYAN}} = 0.11$ for BPMG, and zero for all other MGs. It has a Li EW of 169 mÅ, which at spectral-type K2 can only provide an age-range of $30-200$ Myr, which is too old to be a TWA member. A more precise age is essential to further test membership status to Columba. Neither the U, V or W velocity are within the 1σ range of Columba (see Figures 5.11 and 5.12) and because there is a large error in V velocity, this prevents a conclusive membership status for any MG.

Target M, SW1438+3300 - Although this object satisfies all criteria for ABDMG, all MG probabilities are given as zero in BANYAN. This may be because target M is too far away in XYZ from ABDMG to be detected by BANYAN. The age range for the object is $30-200$ Myr (which encompasses the age of ABDMG), because at spectral-type K3 a Li EW of ~ 100 mÅ appears older than IC 2602 and much more consistent with a Pleiades-like age.

Target O, SW2145+2711 - This target satisfies all criteria for Tuc-Hor. However, BANYAN returns zero membership probabilities for any MG, probably because of the large difference in XYZ between target O and any MG. An age of $30-150$ Myr is

estimated based on the spectral-type (K3) and Li EW (254 mÅ) and the Hα age range is estimated as $29 - 39$ Myr. Figures 5.11 and 5.12 show that each UVW coordinate for this object is within $5\,\mathrm{km\,s^{-1}}$ of the Tuc-Hor range, within the 1σ dispersion in U and W and within 2σ in V.

Target X, SW2058−0902 - Whilst this target matches all criteria for the Octans-Near association, the BANYAN analysis returns zero probability for all MGs (although Octans-Near is not considered in BANYAN). It has an Li EW of 337 mÅ, which at a spectral-type of K3 sets an age range of $30 - 150$ Myr, however, the Li pattern observed in Figure 5.6 suggests the object is more consistent with IC 2602 (at ~ 30 Myr) rather than the Pleiades (~ 125 Myr). The U velocity is $\sim 5\,\mathrm{km\,s^{-1}}$ from Octans-Near, but V and W are within 1σ of Octans-Near (see Figure 5.12).

Target Z, SW2307+1710 - This target is matched with ABDMG, and BANYAN returns a 34.83 per cent chance of it being an ABDMG member, however a 61.15 per cent probability is calculated for TWA. Membership is rejected for TWA because target Z is too old to be coeval with TWA. The Li EW and $V - K$ of the target lies between the upper envelope of the Pleiades and the lower envelope of IC 2602, setting an age range of $30 - 150$ Myr (see Figure 5.6). Li, Hu & Chen (2000) identify the object as a possible WTTS and Ducourant et al. (2005) include it as a member in the PMS stars proper-motion catalog. The UVW values all lie outside the ABDMG box in Figures 5.11 and 5.12, however, the UVW uncertainties from parallax estimation are large. A more precise age and parallax are necessary to test if it is an ABDMG member.

5.8.2 Individual objects not linked to any MG

Target B, SW0135+2116 - BANYAN returned a zero probability for all of the seven MGs considered. At a spectral-type of G2 and Li EW of 154 mÅ this target is assigned an age range of $30 - 200$ Myr, supported by a Hα EW lower age limit of 20 Myr. In terms of UVW velocity, it appears consistent in $U - V$ with Octans-Near, however the W velocity of the target is $\sim 10\,\mathrm{km\,s^{-1}}$ larger than Octans-Near. Favata et al.

(1995) measure a $v \sin i$ value of $34\,\mathrm{km\,s^{-1}}$, which is $1.5\,\mathrm{km\,s^{-1}}(3\sigma)$ slower than the measurement in this work.

Target D, SW0304+3003 - All MG membership probabilities in BANYAN are zero. The age for the target is measured between $30 - 200\,\mathrm{Myr}$. It has a spectral-type G9 and a Li EW of $193\,\mathrm{m\AA}$, where there is large overlap between IC 2602 and Pleiades objects. This age is supported by a Hα lower age limit of 20 Myr. It is in the range of Octans-Near members in terms of U and V velocity, but is $\sim 10\,\mathrm{km\,s^{-1}}$ larger in W. It is flagged as a candidate WTTS in Taurus-Auriga region in Li & Hu (1998).

Target F, SW0322+2853 - BANYAN returned zero probability for membership with any MG. Because it has a spectral-type K2 and a Li EW of $184\,\mathrm{m\AA}$ its age is estimated between 30 and 200 Myr, and is supported by a lower Hα age limit of 25 Myr. In UVW space it appears consistent with the U and V velocities of Octans-Near, but is around $5\,\mathrm{km\,s^{-1}}$ larger in W than Octans-Near.

Target J, SW0847+3423 - All MG membership probabilities for this object were returned as zero using BANYAN. An age range of $30-150\,\mathrm{Myr}$ was estimated, however this object may be more consistent with an IC 2602 age given the G8 spectral-type and Li EW of $168\,\mathrm{m\AA}$. Its age is consistent a lower age limit of 20 Myr set by Hα. Its UVW velocity is $> 5\,\mathrm{km\,s^{-1}}$ from the centroid of any of the 10 MGs considered.

Target N, SW1625+3002 - BANYAN returns zero probability for all MGs considered in the analysis. Although it has an Li EW of $86\,\mathrm{m\AA}$, because it is a late-K dwarf it is estimated to have an age of $30 - 150\,\mathrm{Myr}$, with a Hα age younger than 189 Myr. The W velocity is matched to a few MGs, however, both the U and V are at least $\sim 15\,\mathrm{km\,s^{-1}}$ from any MG.

Target P, SW1332+2230 - Zero membership probabilities are returned for all MGs considered in the BANYAN analysis. At spectral-type K5 and a Li EW of $159\,\mathrm{m\AA}$ an age between 30 and 150 Myr was estimated and supported by a Hα age range of $65 - 125\,\mathrm{Myr}$. It has a U, V and W velocity at least $10\,\mathrm{km\,s^{-1}}$ from any MG. Xing & Xing (2012) include this target as a young K4V object with a Li EW of $17\,\mathrm{m\AA}$ which is almost $150\,\mathrm{m\AA}$ lower than the measurement in this work. It is listed as a possible visual binary in Makarov (2003), however, two consistent RV measurements in this

analysis suggest the object is not a SB.

Target Q, SW1550−0222 - BANYAN returns a $P_{\rm BANYAN}$ of 2.64 per cent for BPMG. The age range of $30 - 150$ Myr may be more consistent with the pattern observed in IC 2602 given the spectral-type K4 and Li EW of 174 mÅ. The Hα age is estimated between 40 and 65 Myr. The U and V velocities are consistent with ABDMG, however its W velocity is too large by $\sim 10\,{\rm km\,s^{-1}}$.

Target R, SW1629+2810 - BANYAN returns zero membership probabilities to any MG. Given the spectral-type (K1) and Li EW (208 mÅ), an age of $30 - 150$ Myr was estimated and supported by a lower age limit of 20 Myr from Hα. It is at least $10\,{\rm km\,s^{-1}}$ from any MG in either U, V or W.

Target S, SW1718+2506 - All membership probabilities using BANYAN are zero. Because the object has a late-K spectral-type, its Li EW (135 mÅ) leads to an age estimate between 30 and 150 Myr. Figure 5.6 shows that it may be more consistent with IC 2602. This age is supported by a Hα upper limit of 230 Myr and an $R \sin i$ upper limit of 80 Myr. It is $> 5\,{\rm km\,s^{-1}}$ from any MG in U, V or W.

Target T, SW1722+3658 - BANYAN returns membership probabilities of 35.80 per cent for BPMG and 0.10 per cent for Argus. Its Li EW is only 62 mÅ, however, as it is a late-K type, it was estimated to have an age of $100 - 200$ Myr. This is too old to be a BPMG member. An upper limit of 120 Myr is provided because Hα is in emission. There are no matches $< 5\,{\rm km\,s^{-1}}$ in all UVW velocities for any MG.

Target U, SW1731+2815 - A 12.69 per cent probability for BPMG and 0.01 per cent probability for Argus are calculated in the BANYAN analysis. It has an age range of $30-150$ Myr, however given the large Li EW (278 mÅ), this could be more associated with a 30 Myr cluster. It has a Hα age older than 35 Myr. There are no matches within $5\,{\rm km\,s^{-1}}$ for U, V or W for any MG and BPMG membership can be ruled out based on both the kinematics and age.

Target V, SW1804+3930 - BANYAN returns $P_{\rm BANYAN} = 0.70, 0.01$ and 0.63 per cent for BPMG, Col and ABDMG, respectively. Although its age range is given as $30 - 150$ Myr, the Li EW (269 mÅ) pattern at K3 suggests it may be more consistent with a 30 Myr cluster. The object has a Hα emission line which provides an upper

limit of 50 Myr. Target V is not within $5\,\mathrm{km\,s^{-1}}$ in U, V or W for any MG.

Target W, SW1925+4429 - BANYAN predicts $P_{\mathrm{BANYAN}} = 75.48$ per cent for ABDMG. This object satisfies the RV criteria in §5.7.4 for ABDMG (see Table 5.9) and its location in $U-V$ and $V-W$ velocity space suggests that it is similar to ABDMG in V and W but is more than $5\,\mathrm{km\,s^{-1}}$ from ABDMG in U velocity and therefore fails membership test 1, although only marginally ($\bar{\chi}^2_T = 4.5$, the membership criteria is 3.78). The U, V and W are precise to within $1\,\mathrm{km\,s^{-1}}$ in each velocity coordinate. The Li EW measurement of 222 mÅ at an early-K spectral-type results in an age range of 30 to 150 Myr and although there is significant scatter amongst IC 2602 and Pleiades objects at this spectral-type, this target is more consistent with the lower envelope of IC 2602. The Hα age range is $35-55$ Myr and an upper age limit of 80 Myr is calculated based on $R\sin i$.

Frasca et al. (2011) identify differential rotation in the star based on data from the *Kepler* mission. Their Li EW measurement is ~ 50 mÅ larger and their 1.0Å Hα EW is certainly not consistent with the 0.1Å absorption line measured in this work. The $v\sin i$ measurements match to 1σ and their calculated inclination angle, i, provides a stellar radius of $0.93R_{\odot}$. Figure 5.9 suggests an age between 25 and 80 Myr, where the $\sin i$ ambiguity has been resolved. This is at least 40 Myr younger than ABDMG (if indeed ABDMG is coeval with the Pleiades), making membership for ABDMG unlikely.

The object is flagged as an equal-magnitude visual binary system in the WDS Catalog (Worley & Douglass 1997) and the Tycho Double Star Catalog (Fabricius et al. 2002). Frasca et al. (2011) find a separation of 0.3", which corresponds to 25 AU and measure an inclination angle $i = 70°$. An equal mass binary would be expected to have RV variations $> 5\,\mathrm{km\,s^{-1}}$ over $3-4$ years. The RVs reported in Frasca et al. (2011) are from 3 separate observation between 2007 and 2009 and the measurement of $-33.5 \pm 0.6\,\mathrm{km\,s^{-1}}$ in this work carried out in June 2011 indicate that RVs are consistent to within 1σ over a four year period, suggesting that the object is not in a equal-mass visual binary system.

Target Y, SW2256+2052 - Zero membership probabilities were returned for all MGs using BANYAN. It has a spectral-type K5 and a Li EW of 141 mÅ from which an age

range of $30 - 150$ Myr was estimated, and a Hα emission line sets an upper limit of 100 Myr. It is within the range of Octans-Near in U and V velocity, however it has a W velocity $\sim 5\,\mathrm{km\,s^{-1}}$ larger than Octans-Near.

5.8.3 Connection with the Octans-Near association

In a Hipparcos-based survey, Zuckerman et al. (2013) report 14 star systems with spectral-types between G5 and A0 and distances ranging from 24 to 98 pc that have ages between $\sim 30 - 100$ Myr and have Galactic space velocities similar to the mean space motion of Octans ($UVW_{\mathrm{Octans}} = -14.5{\pm}0.9, -3.6{\pm}1.6, -11.2{\pm}1.4\,\mathrm{km\,s^{-1}}; UVW_{\mathrm{sample}} = -13.0 \pm 1.9, -3.5 \pm 2.2, -11.2 \pm 2.0\,\mathrm{km\,s^{-1}}$). Torres et al. (2008) measure the distance of Octans to be 141 ± 34 pc and given that the 14 star systems in Zuckerman et al. (2013) are closer than the Octans association (all within 100 pc), the authors describe this stellar aggregate as the 'Octans-Near' group.

In §5.7.5, four objects – A, I, K and X – pass tests for Octans-Near membership, however, target I is unlikely to be an Octans-Near member on account of its large UVW uncertainties (see §5.8.1). Whether these objects are connected to either the Octans, the Octans-Near or not, there nevertheless still exists a sub-grouping of 7 objects in the sample (A, B, D, F, K, X and Y) which are all younger than 200 Myr and have UVW values of $U = -10.5 \pm 2.7(\pm 1.8); V = -4.3 \pm 1.0(\pm 1.4); W = -4.9 \pm 3.6(\pm 1.3)\,\mathrm{km\,s^{-1}}$, relatively close to Octans/Octans-Near but not to any other known MG (error bars are the standard deviations and the values in parentheses are the average UVW uncertainties).

In principle, if the 7 kinematically consistent objects identified here were born from the same molecular cloud, then given their $UVWXYZ$ coordinates, it would be possible to trace-back their motions under a reasonable gravitational potential and identify a time at which all these objects occupied a spatial minimum. Adopting the epicyclic orbit equations in Fuchs et al. (2006) and a trace-back model provided by E. Mamajek an attempt is made to identify the time of minimum separation. Figure 5.14 shows no clear evidence of spatial convergence in the past 100 Myr. However, this

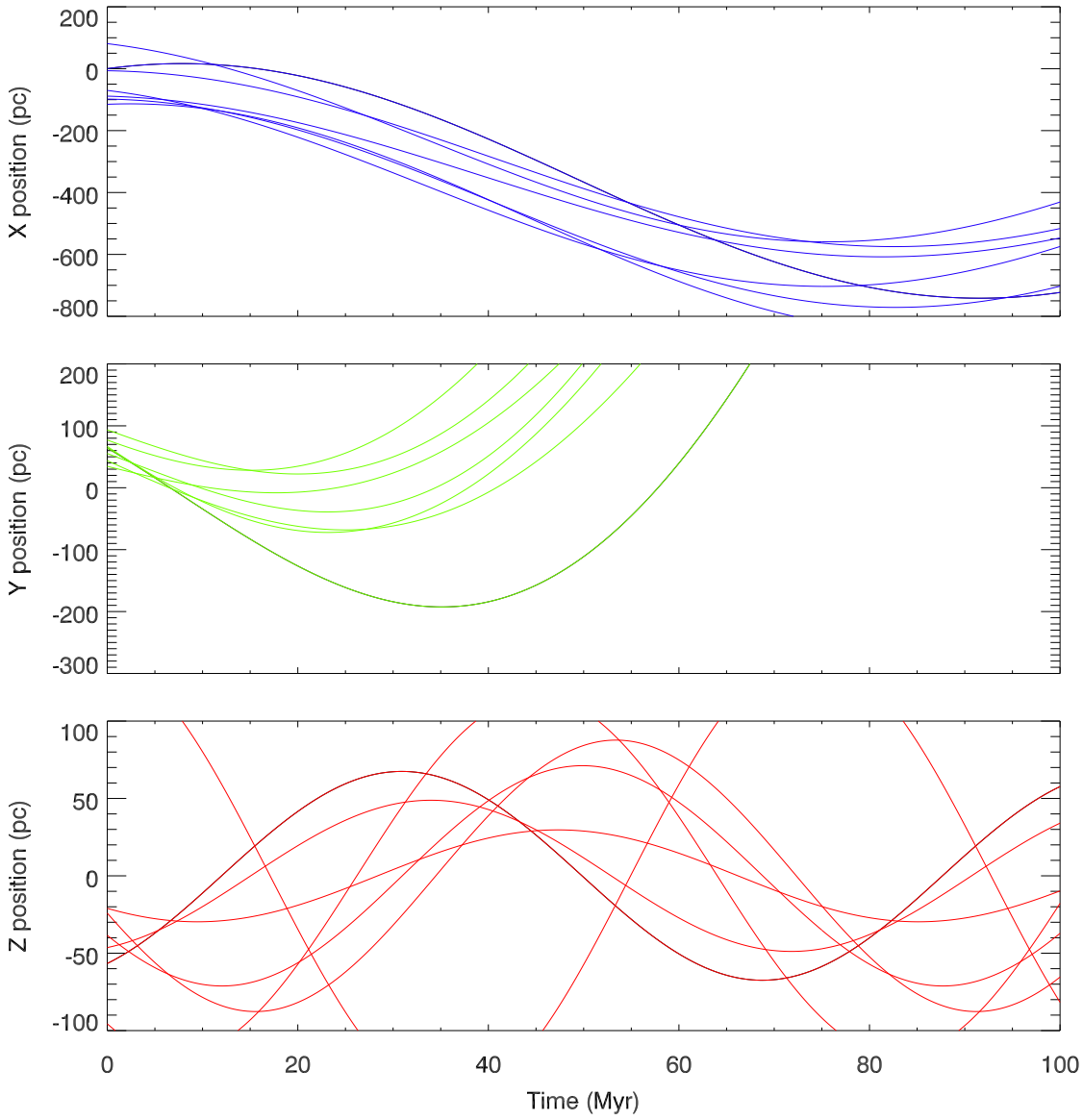

Figure 5.14: Kinematic trace-backs of the seven objects which appear to form a subgrouping close to Octans-Near in Boettlinger diagrams. Their initial $UVWXYZ$ coordinates are propagated backwards in time using the procedure outlined in Mamajek & Bell (2014). Here, no evidence is found for this group converging in the past, however, the errors in distance over time may rapidly overpower any genuine kinematic subgrouping. Precise astrometry is required to fully benefit from the trace-back method.

method is unlikely to be robust, and the initial UVW and parallaxes in Table 5.7 are not sufficiently precise (for a discussion of error analysis in the trace-back method, see §1.2.2). A $1\,\mathrm{km\,s^{-1}}$ error in velocity results in a 10 pc distance uncertainty in only 10 Myr of trace-back.

5.9 Conclusions

From an initial sample of 146 spectroscopically observed short-period FGK stars in the SuperWASP All Sky Survey, twenty-six were found to be younger than 200 Myr (by assessment of their relative Li EW compared with open clusters) and were unlikely to be SBs based on consistent RV measurements (for 24 objects) or were observed to have a clear, single peak in their CCF if only one measurement was available (this was the case for 2 objects). Five objects were G-stars and the remaining 21 ranged from K1 to K6.

Twelve objects from the initial observed sample had 2 or more RV measurements that varied by more than $5\,\mathrm{km\,s^{-1}}$ on the timescale of the observing run and were subsequently assumed to be SBs. If a significant Li line was not observed at the telescope, then usually a repeat measurement was not made. Only 41 targets had more than one RV measurement. Therefore the bulk of the sample (72 per cent) could be binaries that have yet to be detected.

The simulations show there is < 10 per cent (on average) chance of atidally locked binary going undetected. If that was the case, these objects could have very different systemic velocities to the RV that was measured. The Li-rich targets could also be in much wider binary systems and would also betray no RV variation. In this case there could still be considerable RV uncerainties because even objects with orbital periods of years could have an RV departing from the systemic RV by $\sim 10\,\mathrm{km\,s^{-1}}$. Only 2.2 per cent of random field stars have $|\mathrm{RV}| > 5\,\mathrm{km\,s^{-1}}$. This shows the objects selected for observation are not random, but have a very high proportion of close (probably tidally-locked) binaries. There is 7.2 per cent chance that despite finding two consistent RV

observations in a twice-measured star, the true RV is at least $5\,\mathrm{km\,s^{-1}}$ away from the measured average center-of-mass RV, thus possibly displacing ~ 2 of the Li-rich objects in Boettlinger diagrams by $\sim 5\,\mathrm{km\,s^{-1}}$. This cannot explain all the objects unassociated with known MGs.

With the exception of one target (SW1332+2230), distances were calculated using isochronal tracks on CMDs (see §5.7.1 and Figure 5.10). Distances of the likely-young sample members ranged from 30 to 180 pc and had a mean distance of 92 ± 38 pc. The majority of the likely-young sample were estimated to have ages between 30 and 200 Myr. There is a large scatter in Li EW measurements in G and K stars between 30 Myr clusters (e.g., IC 2602) and clusters at 125 Myr (e.g., Pleiades), and because most of the sample have G and K spectral-types, this prohibited a more precise age range. Age estimations from Gyrochronology, Hα and $R \sin i$ (§5.6.1, §5.6.3 and §5.6.4, respectively) were used to supplement the Li-derived age, however, binarity could be a major complicating issue for these age indicators. In most cases these rotation-based ages agreed, but there were several cases where $R \sin i$ ages were much lower than Li ages.

Lower-mass, nearby, young stars are favourable as targets to follow-up with high-resolution imaging to detect the presence of brown-dwarf binaries, or even exoplanets. There are 16 objects in the likely-young sample with ages < 200 Myr, later than K0 and within 100 pc that would be ideal candidates for imaging surveys.

Fifty-four per cent of the observed sample had rotation periods < 2 days (77 out of 146) and there were fourteen objects in the likely-young sample that had rotation periods less than 2 days. The fraction of young stars detected with periods shorter/longer than 2 days is similar, and one cannot infer whether a future search would be more efficient by restricting the catalog to stars with periods less than 2 days. Messina et al. (2010) measure the median rotation period of objects in BPMG and TWA as 4.83 days (≤ 30 Myr) and 2.29 days in the Pleiades. It is also possible that some young stars do not show rotational modulation for the light-curves assessed in this analysis but may reveal modulation over many epochs of WASP data. Jackson, Jeffries & Maxted (2009) find that in NGC 2516, single epoch light-curves only recovered ~ 50 per cent

of the young stars. The majority of the likely-young sample (58 per cent) were later than K0, and Li becomes a more useful empirical age indicator between $10 - 100$ Myr for late-K/early-M stars. A future search may therefore attempt to identify generally lower-mass stars than the targets observed in this sample.

Eleven targets are identified which satisfy kinematic and age criteria with at least one MG (see §5.7.5) and fifteen fail at least one criteria for membership to *any* MG considered in this analysis. There is tentative evidence for a sub-grouping of seven objects whose location in UVW space appears close to the 'Octans-Near' association (Zuckerman et al. 2013) in terms of U and V but larger on average in W by $\sim 5\,\mathrm{km\,s^{-1}}$. However, only four of these satisfy all criteria for Octans-Near membership. Regardless of whether some of these objects are connected to Octans-Near or not, a grouping of stars exist around $U = -10.5 \pm 2.7; V = -4.3 \pm 1.0; W = -4.9 \pm 3.6\,\mathrm{km\,s^{-1}}$.

In light of results from the analysis of these 146 objects, additional substantial surveys of MG candidates in the Northern hemisphere are necessary. The kinematically unbiased search mechanism was ~ 18 per cent efficient at detecting likely-single G and K-type stars younger than 200 Myr and can be used to identify stars that are not associated with previously studied MGs. More widespread searches for MG candidates in the Northern hemisphere may provide additional useful samples of young stars, and could unveil important kinematic substructure in the Solar neighbourhood. In §7.3 suggestions on improving the search mechanism for young nearby stars based on work in this chapter are discussed.

6 The debris disc fraction for M-dwarfs in nearby, young, Moving Groups

6.1 Introduction

Debris discs are circumstellar discs comprised of small dust particles that orbit a star. They are initially formed from primordial discs containing gas and small grains, which coalesce under gravity to form dust particles (see §1.4.4 for a review of debris discs as empirical age indicators). Primordial discs are the progenitors of debris discs and are expected to have dissipated by ages ≤ 10 Myr (Haisch, Lada & Lada 2001; Hillenbrand 2006; Dahm & Hillenbrand 2007; Hernández et al. 2008; Mamajek 2009). It is expected that the gas and small dust grains should have accreted to km-sized planetesimals in less than 1 Myr (Weidenschilling & Cuzzi 1993) and it takes up to a few Myr to form objects in the disc $10 - 100$ km in size via oligarchic growth (Klahr & Johansen 2008). Mechanisms such as Poynting-Robertson drag, radiation pressure 'blow-out' and photoevaporation are expected to remove debris on timescales of several tens of Myr, however, collisions between planetesimals and the incidence of falling evaporating bodies may act to replenish the debris and some debris discs can be observed well into a star's main sequence phase (Vega, for example, has a clearly resolved debris disc at an age of ~ 350 Myr and several old white dwarfs have been observed to have discs - e.g., Barber et al. 2013; Wang et al. 2014).

By the time a debris disc has formed the star is well into its class III phase and is undergoing contraction onto the main sequence. Light from the star is re-radiated by dust and debris in the disc predominantly at IR wavelengths. The amount of IR flux which emanates from the disc surface depends on both the size and temperature of the disc and most debris discs outshine their parent star at mid-IR wavelengths. Observations at a range of IR wavelengths are able to probe different regions of the disc and reveal the evolutionary sequence from primordial discs to debris discs. Near-IR observations probe hot accreting gas in protoplanetary discs (Wood et al. 2002; Vinković

et al. 2006; Carmona et al. 2008), mid-IR observations can identify transitional discs (Kim et al. 2009; Espaillat et al. 2011; Gräfe et al. 2011) and mid-/far-IR observations are capable of revealing dusty debris discs (Sitko et al. 2004; Currie et al. 2008). The dispersal of gas and dust surrounding optically-thick young T-Tauri objects eventually result in an optically-thin source, potentially resolvable with ground-based telescopes and optical coronographs.

Wide-field surveys to detect sources in the mid-IR have benefitted from satellite based missions – primarily the Infrared Astronomical Stellite (IRAS), the AKARI satellite and more recently the Wide Infrared Survey Explorer (WISE). Other mid-IR surveys such as the Infrared Array Camera (IRAC) and the Mid-Infrared Photometric Survey (MIPS) on the Spitzer space telescope have available photometric data, although these missions did not map the entire sky. Table 6.1 summarises the capabilities and resolution limits for each satellite.

The frequency of observed debris discs appears to be dependent on both age and spectral-type. Generally speaking, debris discs are more common around early-type stars and around young stars (Wyatt 2008). Figure 1.14 shows the fraction of FGK stars in nearby, young associations that have 24 μm fluxes in excess of the photospheric level. From 10 to 100 Myr there is an overall decline from $\sim$ 40 to 10 per cent, although a large scatter remains present throughout this age range. It takes from 10 Myr to 500 Myr for the same level of decline in A-stars (Siegler et al. 2007). Sierchio et al. (2014) find that in a sample of 255 Solar-type stars, none of the objects older than 5 Gyr had *any* 24 μm excess (significant at the 3σ level) and only 5 per cent had an excess at 70 μm.

Whilst much work has focused on the disc frequencies for Solar-type stars, little is known of M-dwarf debris disc fractions, because most are too faint to be studied in open clusters and until recently few were confirmed as members of MGs. Young field M-dwarfs are rare, however, WISE photometry has revealed IR excesses in some older M-dwarf field stars, albeit $<$ 1 per cent (Theissen & West 2014). WISE has been successful in uncovering hundreds of Solar-type objects with an IR excess in the Solar-neighbourhood (Patel, Metchev & Heinze 2014), however, very few young,

nearby M-dwarfs have been reported with IR excesses (Avenhaus, Schmid & Meyer 2012). Disc fractions for young M-dwarfs have been reported to be both smaller than FGK-types (Lestrade et al. 2009) and larger (Forbrich et al. 2008), however, both are limited by small number statistics. Although some work has investigated the disc fractions in MGs (Simon et al. 2012; Schneider, Melis & Song 2012), few have been able to provide large M-dwarf samples. Theoretical studies of the evolution of dust around M-dwarfs suggest the timescales of dust dissipation are more rapid than in earlier-types (Plavchan, Jura & Lipscy 2005; Trilling et al. 2008). Simulations to predict the occurence of planetesimals around M-dwarfs suggest that WISE should be capable of detecting debris discs around M stars with ages $\sim 10\,\mathrm{Myr}$ (Heng & Malik 2013).

Name	Launch year	$\lambda_{\mathrm{central}}$ (μm)	Sensitivity (mJy)	FOV (arcmin)	Bandwidth (μm)	Detector
IRAS	1983	12	700 (10σ)	0.75×4.5	$8.5 - 15$	Si:As
		25	650	0.75×4.6	$19 - 30$	Si:Sb
		60	850	1.5×4.7	$40 - 80$	Ge:Ga
		100	3000	3.0×5.0	$83 - 120$	Ge:Ga
IRAC	2003	3.6	0.032 (1σ)	5.2×5.2	$3.2 - 4.0$	In:Sb
		4.5	0.038	5.2×5.2	$4.0 - 5.0$	In:Sb
		5.8	0.15	5.2×5.2	$5.0 - 6.4$	Si:As
		8.0	0.092	5.2×5.2	$6.4 - 9.3$	Si:As
MIPS	2003	24	0.110 (5σ)	5.4×5.5	$22 - 27$	Si:As
		70	7.2	5.25×2.6	$60 - 80$	Ge:Ga
		160	29	0.53×5.33	$140 - 180$	Ge:Ga
AKARI	2006	9	0.076 (5σ)	10×10	$6.7 - 11.6$	Si:As
		18	0.273	10×10	$13.9 - 25.6$	Si:As
		90	550	44.2×44.2	$60 - 110$	Ge:Ga
WISE	2010	3.4	0.068 (5σ)	47×47	$2.8 - 4.0$	HgCdTe
		4.6	0.098	47×47	$4.0 - 5.6$	HgCdTe
		12	0.86	47×47	$7.2 - 18$	Si:As
		22	5.4	47×47	$19 - 28$	Si:As

Table 6.1: Properties of the IRAS, IRAC, MIPS, AKARI and WISE data from IR satellites. The sensitivity is the limit of the lowest flux that can be detected in a given photometric band. The IRAC sensitivities are for a 2 second exposure with low background count, whereas MIPS sensitivities are 500 second on-source exposures. IRAS, WISE and AKARI sensitivities are averages over the survey.

Motivated by the lack of a robust M-dwarf disc fraction and the recent swathe of new M-dwarfs discovered in MGs, the work in this chapter makes use of IR photometry from the WISE satellite to measure the occurence of discs in MGs. §6.2 describes how the initial target catalog of M-dwarfs is compiled. The WISE photometry collated for all targets is presented in §6.3 with a description of the photometric criteria required for the detection of an IR excess. In §6.4 SED models and single temperature black-body fits are made to stars qualifying from the photometric cut. A final assessment of the nature of the IR excess in each target is discussed in §6.5 and the observed debris disc fractions are calculated in §6.6. The M-dwarf fractions are placed into a more general context with Solar-type stars to investigate both the age and mass dependency of the presence of debris discs.

6.2 Target selection

Several recent kinematic surveys of MGs have revealed hundreds of new candidate M-dwarf members (see §2.3 for a description of these searches). The initial criteria for inclusion in *this analysis* was that an object has to be M-type, but also has to belong to a known MG, where that membership is tested using the RV criterion in Equation 2.1. Where possible, ages quoted for the MGs were based on the LDB technique, or from isochronal ages if an LDB age was not available. The following MGs were chosen for analysis (the source paper from which the targets were extracted are in parenthesis: ϵ Cha ($3-5$ Myr, Murphy, Lawson & Bessell 2013), η Cha ($5-10$ Myr, Luhman 2004), TWA ($8-12$ Myr, Nakajima & Morino 2012; Malo et al. 2013; Ducourant et al. 2014), BPMG ($21-26$ Myr, Barrado y Navascués et al. 1999; Zuckerman et al. 2001; Schlieder, Lépine & Simon 2010; Schlieder et al. 2012; Shkolnik et al. 2012; Malo et al. 2013; 2014b), Carina ($20-40$ Myr, Malo et al. 2013), Columba ($20-40$ Myr, Malo et al. 2013), Tuc-Hor ($39-43$ Myr, Malo et al. 2013; Kraus et al. 2014), Argus ($30-50$ Myr, De Silva et al. 2013; Malo et al. 2013) and ABDMG ($70-120$ Myr, Zuckerman, Song & Bessell 2004; Schlieder, Lépine & Simon 2012; Shkolnik et al. 2012; Malo et al. 2013).

These included newly identified members of BPMG and ABDMG established in chapter 4. JHK photometry is from the 2MASS catalog (Cutri et al. 2003). M-dwarfs in the Octans association were not detectable with WISE photometry.

WISE (Wright et al. 2010) is a NASA IR-wavelength telescope which mapped $>$ 99 per cent of the sky at 3.4, 4.6, 12 and 22 μm ($W1, W2, W3, W4$) in 2010 with angular resolutions of 6.1", 6.4", 6.5" and 12.0" in the four bands; respectively. It is capable of providing 5σ point-source sensitivities of 0.068, 0.098, 0.86 and 5.4 mJy, which, compared to previous satellite-based surveys such as IRAS and MIPS is $\sim$2 orders of magnitude deeper (see Table 6.1). Only objects with SNR values greater than 5.0 in the $W4$ band were considered for analysis. In Table 6.2 the 2MASS and WISE photometry are presented for all objects with SNR $>$ 5.0. This table also includes the measured and predicted RV and the spectral-type. Of the 292 RV-confirmed M-dwarfs in the nine MGs, 151 have SNR $>$ 5.0 in the $W4$ band (herein referred to simply as 'SNR'); 9 in ϵ Cha, 8 in η Cha, 30 in TWA, 35 in BPMG, 2 in Carina, 8 in Columba, 31 in Tuc-Hor, 10 in Argus and 18 in ABDMG (see Table 6.6 for reference). Any objects from the likely-young sample in §5 with SNR $>$ 5 were also examined for disc excess.

JHK magnitudes were converted to fluxes (all in units of erg/s/cm^2/Å) using the 2MASS isophotal bandpasses and zero-point magnitude fluxes from table 2 in Cohen, Wheaton & Megeath (2003). For the WISE data, zero-magnitude fluxes are taken from Jarrett et al. (2011) and colour corrections are available in Wright et al. (2010). Following the work in Theissen & West (2014) and the advisory notes in Wright et al. (2010), $W4$ fluxes are reduced by 10 per cent. For objects with $W1 - W4 > 1.0$, additional photometry/flux values were searched for in the IRAS, AKARI, Spitzer IRAC and Spitzer MIPS catalogs and any additional fluxes are listed in Table 6.3. The fluxes for IRAS sources were extracted directly from the IRAS point source catalog (Helou 1988). For the AKARI IRC bands (9 and 18 μm), zero magnitude fluxes are from table 8 in Tanabé et al. (2008) and the AKARI FIS (90 μm), IRAC and MIPS zero magnitude fluxes were extracted from the calibration tables available at `http://irsa.ipac.caltech.edu/`. All fluxes red-ward of the K band have a 10 per cent calibration error added in quadrature to the photometric uncertainties.

Table 6.2: 2MASS JHK and WISE photometry for the entire sample of disc candidates in MGs with SNR > 5.0. The SNR value in the $W4$ band is listed in the $W4$ column. The E_{W4} values in column 11 is the observed $W4$ flux subtracted by the expected $W4$ flux from a photosphere at a given spectral-type and divided this by the flux error (see §6.3). Objects with E_{W4} greater than 3.0 are discussed in §6.6.3. . All spectral-types listed are derived from the source publication.

Name (WISE-)	RV (km s^{-1})	$RV_{\rm p}$ (km s^{-1})	J (mag)	H (mag)	K (mag)	$W1$ (mag)	$W2$ (mag)	$W3$ (mag)	$W4$ (mag, SNR)	E_{W4}	SpT M-
ϵ Cha (3 − 5 Myr)											
J111835.64−793554.8	19.3 ± 1.6	15.1	10.50 ± 0.03	9.89 ± 0.02	9.62 ± 0.02	9.42 ± 0.02	9.14 ± 0.02	7.67 ± 0.02	4.47 ± 0.02, 46.9	46.5	4.5
J114326.57−780445.5	15.6 ± 1.0	14.7	11.62 ± 0.02	10.97 ± 0.02	10.60 ± 0.02	10.24 ± 0.02	9.84 ± 0.02	8.71 ± 0.02	7.12 ± 0.07, 15.7	14.4	4.7
J114931.74−785101.0	13.4 ± 1.3	14.6	9.45 ± 0.02	8.72 ± 0.05	8.49 ± 0.02	8.20 ± 0.02	7.67 ± 0.02	4.54 ± 0.01	1.82 ± 0.01, 99.2	98.3	0.0
J115504.71−791911.0	14.0 ± 1.3	14.5	11.22 ± 0.02	10.47 ± 0.03	10.08 ± 0.02	9.87 ± 0.02	9.65 ± 0.02	9.27 ± 0.03	6.84 ± 0.05, 19.9	18.1	3.0
J120055.08−782029.5	10.7 ± 1.3	14.3	11.96 ± 0.02	11.40 ± 0.03	11.01 ± 0.02	10.62 ± 0.02	10.16 ± 0.02	8.52 ± 0.02	6.61 ± 0.05, 23.0	22.2	5.8
J120144.32−781926.7	14.9 ± 1.1	14.3	11.68 ± 0.02	11.12 ± 0.03	10.78 ± 0.03	10.16 ± 0.02	9.74 ± 0.02	8.35 ± 0.02	6.70 ± 0.05, 21.4	20.0	5.0
J120203.59−785301.3	11.0 ± 6.0	14.3	9.22 ± 0.02	8.46 ± 0.04	8.31 ± 0.02	8.10 ± 0.02	8.04 ± 0.02	7.92 ± 0.02	8.13 ± 0.19, 5.8	0	0.0
J121943.62−740357.3		13.7	9.75 ± 0.03	9.05 ± 0.03	8.86 ± 0.02	8.75 ± 0.02	8.67 ± 0.02	8.55 ± 0.02	8.28 ± 0.21, 5.3	0.9	0.0
J122021.70−740739.5		13.7	9.26 ± 0.02	8.61 ± 0.03	8.37 ± 0.02	8.26 ± 0.02	8.15 ± 0.02	8.04 ± 0.02	8.11 ± 0.16, 6.6	0	0.0
η Cha (5 − 10 Myr)											
J084130.24−785306.3		17.3	11.81 ± 0.03	11.24 ± 0.03	10.98 ± 0.02	10.71 ± 0.02	10.35 ± 0.02	8.98 ± 0.02	7.34 ± 0.07, 15.8	14.7	4.8
J084223.67−790402.7		17.3	9.53 ± 0.02	8.78 ± 0.06	8.61 ± 0.02	8.51 ± 0.02	8.45 ± 0.02	8.31 ± 0.02	7.76 ± 0.10, 11.0	3.6	1.8
J084227.02−785747.7		17.3	10.78 ± 0.02	10.10 ± 0.02	9.85 ± 0.02	9.72 ± 0.02	9.48 ± 0.02	7.86 ± 0.02	5.19 ± 0.03, 40.3	39.3	4.0
J084318.52−790518.0		17.3	10.51 ± 0.03	9.83 ± 0.02	9.43 ± 0.02	8.55 ± 0.02	7.84 ± 0.02	5.51 ± 0.01	3.40 ± 0.02, 68.9	67.0	3.3
J084409.09−783345.6		17.4	12.51 ± 0.02	11.98 ± 0.02	11.62 ± 0.02	11.19 ± 0.02	10.68 ± 0.02	9.09 ± 0.03	7.25 ± 0.07, 15.6	15.1	5.8
J084416.33−785907.8		17.3	10.26 ± 0.03	9.67 ± 0.03	9.34 ± 0.02	9.10 ± 0.02	8.75 ± 0.02	7.24 ± 0.02	5.49 ± 0.03, 40.7	38.2	4.5
J084431.82−784630.9	15.0 ± 1.1	17.3	9.65 ± 0.02	8.92 ± 0.06	8.73 ± 0.02	8.60 ± 0.02	8.58 ± 0.02	8.46 ± 0.02	8.32 ± 0.17, 6.2	0	1.0
J084756.68−785452.9		17.3	9.32 ± 0.02	8.68 ± 0.08	8.41 ± 0.03	8.29 ± 0.02	8.15 ± 0.02	8.01 ± 0.02	7.94 ± 0.11, 10.1	0	3.3
TWA (8 − 12 Myr)											
J015218.43−595016.9	8.1 ± 1.8	9.9	8.94 ± 0.02	8.33 ± 0.04	8.14 ± 0.03	7.96 ± 0.02	7.87 ± 0.02	7.78 ± 0.02	7.67 ± 0.08, 13.0	0	2.0
J020012.84−084052.4	4.8 ± 0.2	3.0	8.77 ± 0.02	8.14 ± 0.04	7.87 ± 0.02	7.78 ± 0.02	7.68 ± 0.02	7.59 ± 0.02	7.54 ± 0.12, 9.5	0	2.5
J021558.99−092912.5	2.5 ± 0.3	4.5	8.43 ± 0.03	7.80 ± 0.03	7.55 ± 0.02	7.37 ± 0.03	7.26 ± 0.02	7.17 ± 0.02	7.03 ± 0.07, 15.1	0	2.5
J022244.32−602247.7	13.1 ± 0.9	11.8	8.99 ± 0.02	8.39 ± 0.04	8.10 ± 0.03	7.94 ± 0.02	7.79 ± 0.02	7.68 ± 0.02	7.55 ± 0.10, 11.0	0.2	4.0
J024147.39−525930.7	12.7 ± 1.2	11.8	8.48 ± 0.03	7.85 ± 0.03	7.64 ± 0.03	7.45 ± 0.03	7.35 ± 0.02	7.27 ± 0.02	7.09 ± 0.07, 16.0	0.3	2.5
J043657.44−161306.7	15.7 ± 0.5	16.3	9.12 ± 0.03	8.47 ± 0.05	8.26 ± 0.02	8.12 ± 0.02	7.97 ± 0.02	7.89 ± 0.02	7.71 ± 0.16, 6.7	0.3	3.5
J044401.08−662403.2	16.7 ± 0.4	15.8	9.47 ± 0.02	8.75 ± 0.03	8.58 ± 0.02	8.50 ± 0.02	8.47 ± 0.02	8.38 ± 0.02	8.25 ± 0.15, 7.2	0	0.5
J101209.04−312445.3	14.6 ± 0.6	15.9	8.85 ± 0.02	8.26 ± 0.05	7.99 ± 0.03	7.81 ± 0.02	7.54 ± 0.02	6.14 ± 0.01	4.80 ± 0.03, 39.2	35.3	4.0
J104230.01−334016.4	11.4 ± 0.0	14.3	7.79 ± 0.02	7.13 ± 0.03	6.90 ± 0.03	6.82 ± 0.03	6.71 ± 0.02	6.60 ± 0.02	6.01 ± 0.03, 27.7	16.1	2.0
J111027.80−373152.0	14.5 ± 0.2	12.9	7.65 ± 0.02	7.04 ± 0.03	6.77 ± 0.02	6.60 ± 0.04	6.34 ± 0.02	3.88 ± 0.02	1.73 ± 0.01, 77.5	76.3	4.0
J111326.18−452342.8	15.8 ± 2.0	13.1	9.41 ± 0.03	8.73 ± 0.04	8.49 ± 0.03	8.36 ± 0.02	8.26 ± 0.02	8.16 ± 0.02	8.05 ± 0.16, 7.0	0.3	0.0
J112117.15−344645.4	12.3 ± 1.2	11.3	8.43 ± 0.04	7.73 ± 0.07	7.49 ± 0.04	7.64 ± 0.05	7.55 ± 0.03	7.43 ± 0.03	7.00 ± 0.14, 7.7	2.0	1.0
J113155.20−343627.3	12.7 ± 3.8	11.4	7.67 ± 0.03	6.99 ± 0.03	6.74 ± 0.02	6.65 ± 0.04	6.51 ± 0.02	6.41 ± 0.02	6.32 ± 0.05, 21.9	0.2	2.0
J113218.24−301952.0	15.8 ± 2.0	13.1	9.64 ± 0.02	9.03 ± 0.02	8.77 ± 0.02	8.80 ± 0.02	8.44 ± 0.02	7.07 ± 0.02	5.16 ± 0.03, 38.1	36.8	5.0
J113241.20−265156.1	9.3 ± 1.0	10.5	8.34 ± 0.02	7.66 ± 0.04	7.43 ± 0.02	7.36 ± 0.03	7.22 ± 0.02	7.13 ± 0.01	7.04 ± 0.09, 11.8	0	3.0
J120727.32−324700.4	8.5 ± 1.2	8.8	8.62 ± 0.03	8.02 ± 0.04	7.75 ± 0.03	7.64 ± 0.03	7.51 ± 0.02	7.41 ± 0.02	7.23 ± 0.09, 12.8	0.7	3.0
J120733.42−393254.2	11.2 ± 2.0	9.6	12.99 ± 0.03	12.39 ± 0.03	11.94 ± 0.03	11.56 ± 0.02	11.01 ± 0.02	9.46 ± 0.03	8.03 ± 0.13, 8.2	7.6	8.0
J121530.66−394842.8	7.5 ± 0.1	9.1	8.17 ± 0.03	7.50 ± 0.04	7.31 ± 0.02	7.26 ± 0.03	7.21 ± 0.02	7.13 ± 0.02	7.08 ± 0.08, 14.4	0	1.0
J123138.03−455859.6	8.1 ± 4.0	8.6	9.33 ± 0.03	8.69 ± 0.06	8.41 ± 0.03	8.32 ± 0.02	8.20 ± 0.02	8.08 ± 0.02	7.76 ± 0.10, 10.8	1.9	3.0
J123456.26−453807.7	9.0 ± 0.4	8.6	8.99 ± 0.03	8.33 ± 0.04	8.09 ± 0.02	7.94 ± 0.02	7.86 ± 0.02	7.74 ± 0.02	7.54 ± 0.10, 10.5	0.8	1.5
J123504.19−413638.8	6.6 ± 0.8	8.1	9.12 ± 0.02	8.48 ± 0.04	8.19 ± 0.03	8.09 ± 0.02	7.96 ± 0.02	7.87 ± 0.02	7.75 ± 0.11, 10.2	0.1	2.0
J170808.73−693619.3	6.3 ± 3.3	4.9	9.06 ± 0.02	8.42 ± 0.03	8.20 ± 0.02	8.02 ± 0.02	7.89 ± 0.02	7.77 ± 0.02	7.64 ± 0.13, 8.1	0.1	3.5
J213708.89−603606.4	2.3 ± 0.2	0.9	9.64 ± 0.02	9.01 ± 0.05	8.76 ± 0.02	8.59 ± 0.02	8.45 ± 0.02	8.32 ± 0.02	8.15 ± 0.20, 5.5	0.4	3.0
J220216.29−421034.0	−2.6 ± 0.5	−4.9	8.93 ± 0.03	8.23 ± 0.04	7.99 ± 0.02	7.90 ± 0.02	7.86 ± 0.02	7.76 ± 0.02	7.66 ± 0.14, 7.5	0	1.0
J224408.79−541319.0	1.6 ± 1.6	0.6	9.36 ± 0.03	8.71 ± 0.04	8.47 ± 0.03	8.30 ± 0.02	8.13 ± 0.02	8.01 ± 0.02	7.97 ± 0.20, 5.5	0	4.0
J231316.77−493316.3	1.9 ± 0.3	0.4	9.76 ± 0.02	9.14 ± 0.02	8.92 ± 0.02	8.76 ± 0.02	8.58 ± 0.02	8.44 ± 0.02	8.07 ± 0.21, 5.2	1.3	4.0
J232047.18−672321.4	6.6 ± 0.3	5.7	9.99 ± 0.04	9.39 ± 0.05	8.96 ± 0.03	8.52 ± 0.02	8.33 ± 0.02	8.22 ± 0.02	7.99 ± 0.14, 7.9	0.9	5.0
J232610.84−732350.5	8.0 ± 1.9	7.3	8.84 ± 0.03	8.20 ± 0.05	7.94 ± 0.03	7.87 ± 0.02	7.81 ± 0.02	7.71 ± 0.02	7.64 ± 0.12, 9.4	0	0.0
J232857.75−680234.5	10.8 ± 3.4	7.3	9.26 ± 0.02	8.64 ± 0.04	8.38 ± 0.02	8.27 ± 0.02	8.15 ± 0.02	8.03 ± 0.02	8.05 ± 0.17, 6.3	0	2.5
J234747.06−651725.3	6.2 ± 0.5	5.9	9.10 ± 0.02	8.39 ± 0.03	8.17 ± 0.03	8.07 ± 0.02	8.02 ± 0.02	7.91 ± 0.02	8.04 ± 0.17, 6.4	0	1.5
BPMG (21 − 26 Myr)											
J001723.69−664512.4	10.7 ± 0.2	10.9	8.56 ± 0.02	7.93 ± 0.04	7.70 ± 0.02	7.60 ± 0.02	7.49 ± 0.02	7.41 ± 0.01	7.33 ± 0.10, 11.3	0	2.5
J002750.43−323324.4	8.5 ± 0.2	8.3	8.97 ± 0.03	8.39 ± 0.03	8.12 ± 0.03	7.95 ± 0.02	7.76 ± 0.02	7.66 ± 0.02	7.61 ± 0.13, 8.3	0.5	0.0
J011125.54+152620.7	3.1 ± 1.6	3.4	9.08 ± 0.03	8.51 ± 0.04	8.21 ± 0.03	8.00 ± 0.02	7.79 ± 0.02	7.64 ± 0.02	7.60 ± 0.13, 8.6	0	5.0
J011328.27−382102.9	14.3 ± 0.5	11.9	8.49 ± 0.02	7.84 ± 0.02	7.60 ± 0.02	7.50 ± 0.03	7.46 ± 0.02	7.37 ± 0.02	7.25 ± 0.08, 12.9	0	3.0
J013513.98−071251.9	6.5 ± 1.8	9.2	8.96 ± 0.02	8.39 ± 0.03	8.08 ± 0.03	7.97 ± 0.02	7.80 ± 0.02	7.69 ± 0.02	7.48 ± 0.11, 10.0	1.1	4.0

Table 6.2: *continued.*

Name (WISE-)	RV (km s^{-1})	$RV_{\rm p}$ (km s^{-1})	J (mag)	H (mag)	K (mag)	$W1$ (mag)	$W2$ (mag)	$W3$ (mag)	$W4$ (mag, SNR)	E_{W4}	SpT M-
J013655.28−064738.8	12.2 ± 0.4	9.5	9.71 ± 0.02	9.14 ± 0.03	8.86 ± 0.02	8.68 ± 0.02	8.52 ± 0.02	8.41 ± 0.02	8.21 ± 0.18, 6.0	0.6	4.0
J015350.81−145950.6	10.5 ± 0.4	12.0	7.94 ± 0.03	7.30 ± 0.03	7.07 ± 0.02	6.81 ± 0.03	6.73 ± 0.02	6.67 ± 0.01	6.60 ± 0.05, 22.5	0	4.0
J022326.71+224405.7	10.4 ± 2.0	6.8	8.18 ± 0.02	7.56 ± 0.02	7.35 ± 0.02	7.26 ± 0.03	7.24 ± 0.02	7.18 ± 0.02	7.27 ± 0.09, 11.5	0	3.0
J044356.87+372302.7	6.4 ± 0.3	7.6	9.71 ± 0.02	9.03 ± 0.02	8.80 ± 0.02	8.65 ± 0.02	8.56 ± 0.02	8.35 ± 0.02	7.55 ± 0.16, 6.9	3.4	3.5
J045934.85+014659.7	19.8 ± 0.0	18.3	7.12 ± 0.02	6.45 ± 0.03	6.26 ± 0.02	6.17 ± 0.05	6.08 ± 0.02	6.05 ± 0.02	6.00 ± 0.05, 23.0	0	0.0
J050047.16−571524.7	19.4 ± 0.3	19.0	7.09 ± 0.02	6.43 ± 0.03	6.24 ± 0.02	6.13 ± 0.05	6.09 ± 0.02	6.06 ± 0.01	5.93 ± 0.03, 34.7	0	0.5
J050649.50−213504.3	21.1 ± 1.7	21.2	7.00 ± 0.02	6.39 ± 0.02	6.11 ± 0.02	5.45 ± 0.05	4.78 ± 0.02	4.67 ± 0.01	5.11 ± 0.03, 38.1	0	3.5
J061313.30−274205.6	22.5 ± 0.2	21.6	8.00 ± 0.03	7.43 ± 0.07	7.14 ± 0.02	7.04 ± 0.04	6.85 ± 0.02	6.76 ± 0.02	6.67 ± 0.07, 16.3	0.1	4.0
J081738.97−824328.8	15.6 ± 1.5	12.8	7.47 ± 0.02	6.84 ± 0.04	6.59 ± 0.03	6.46 ± 0.04	6.29 ± 0.02	6.20 ± 0.01	5.98 ± 0.03, 37.7	3.3	4.5
J101726.70−535426.5	13.6 ± 0.3	13.3	8.55 ± 0.02	8.09 ± 0.05	7.69 ± 0.02	7.49 ± 0.02	7.27 ± 0.02	7.10 ± 0.01	6.81 ± 0.06, 19.4	4.1	6.0
J135453.61−712148.9	5.7 ± 0.2	7.3	8.55 ± 0.02	7.92 ± 0.03	7.67 ± 0.03	7.61 ± 0.02	7.49 ± 0.02	7.40 ± 0.02	7.47 ± 0.12, 9.2	0	2.5
J165720.25−534332.4	1.4 ± 0.2	−2.0	8.69 ± 0.02	8.07 ± 0.02	7.79 ± 0.02	7.68 ± 0.02	7.57 ± 0.02	7.47 ± 0.02	7.40 ± 0.11, 9.7	0	3.0
J171731.26−665706.8	2.7 ± 1.8	2.8	8.54 ± 0.03	7.92 ± 0.04	7.63 ± 0.02	7.53 ± 0.02	7.38 ± 0.02	7.22 ± 0.02	6.96 ± 0.07, 14.6	3.1	3.0
J172920.64−501453.4	−0.1 ± 0.9	−3.5	8.87 ± 0.03	8.19 ± 0.04	7.99 ± 0.03	7.84 ± 0.02	7.70 ± 0.02	7.47 ± 0.02	7.09 ± 0.08, 13.4	4.1	3.0
J181422.07−324610.6	−5.7 ± 0.8	−9.8	9.44 ± 0.02	8.77 ± 0.04	8.54 ± 0.02	8.46 ± 0.02	8.38 ± 0.02	8.32 ± 0.02	8.02 ± 0.19, 5.7	0.7	1.0
J181515.65−492747.9	0.3 ± 3.6	−3.8	8.92 ± 0.02	8.24 ± 0.03	8.04 ± 0.02	7.91 ± 0.02	7.78 ± 0.02	7.69 ± 0.02	7.74 ± 0.16, 6.7	0	3.0
J184652.56−621037.3	2.4 ± 0.1	1.2	8.75 ± 0.02	8.05 ± 0.04	7.85 ± 0.02	7.75 ± 0.02	7.70 ± 0.02	7.63 ± 0.02	7.66 ± 0.14, 8.0	0	1.0
J192338.22−460632.1	0.0 ± 0.4	−4.1	9.11 ± 0.03	8.44 ± 0.03	8.27 ± 0.03	8.15 ± 0.02	8.16 ± 0.02	8.06 ± 0.02	8.14 ± 0.17, 6.4	0	0.0
J195602.95−320719.3	−3.7 ± 2.2	−7.8	8.96 ± 0.03	8.34 ± 0.04	8.11 ± 0.03	7.91 ± 0.02	7.75 ± 0.02	7.66 ± 0.02	7.63 ± 0.15, 7.3	0	4.0
J195604.39−320738.3	−7.2 ± 0.5	−7.8	8.71 ± 0.03	8.03 ± 0.04	7.85 ± 0.02	7.72 ± 0.02	7.72 ± 0.02	7.63 ± 0.02	7.32 ± 0.11, 10.0	1.1	0.0
J200137.19−331314.5	−3.7 ± 0.2	−7.3	9.15 ± 0.02	8.46 ± 0.05	8.24 ± 0.02	8.14 ± 0.02	8.10 ± 0.02	8.03 ± 0.02	7.87 ± 0.19, 5.7	0	1.0
J201000.06−280141.6	−5.8 ± 0.6	−8.5	8.65 ± 0.02	8.01 ± 0.05	7.73 ± 0.03	7.61 ± 0.03	7.44 ± 0.02	7.37 ± 0.02	7.23 ± 0.12, 9.5	0.4	2.5
J204341.18−243353.8	−5.8 ± 0.6	−7.9	8.60 ± 0.02	8.00 ± 0.02	7.76 ± 0.02	7.60 ± 0.02	7.40 ± 0.02	7.39 ± 0.02	7.14 ± 0.11, 10.2	0.8	3.7
J204509.76−312030.9	−4.1 ± 0.0	−6.0	5.44 ± 0.02	4.83 ± 0.02	4.53 ± 0.02	4.50 ± 0.09	4.00 ± 0.05	4.31 ± 0.01	4.14 ± 0.03, 43.6	3.4	1.0
J211005.41−191958.4	−5.7 ± 0.4	−7.9	8.11 ± 0.03	7.45 ± 0.03	7.20 ± 0.02	7.05 ± 0.03	6.99 ± 0.02	6.94 ± 0.02	6.90 ± 0.11, 9.5	0	2.0
J220041.64+271513.4	−13.3 ± 2.4	−12.8	8.56 ± 0.03	7.95 ± 0.02	7.72 ± 0.02	7.60 ± 0.03	7.60 ± 0.02	7.54 ± 0.02	7.28 ± 0.11, 9.8	0.5	0.0
J224500.20−331527.2	2.0 ± 0.0	1.5	8.68 ± 0.02	8.06 ± 0.03	7.79 ± 0.03	7.65 ± 0.02	7.43 ± 0.02	7.31 ± 0.02	7.20 ± 0.10, 10.3	0.4	5.0
J231728.40+193645.7	−3.7 ± 0.0	−6.4	8.02 ± 0.02	7.41 ± 0.02	7.17 ± 0.02	7.00 ± 0.03	6.86 ± 0.02	6.78 ± 0.02	6.66 ± 0.06, 18.1	0	3.5
J233230.95−121552.0	1.2 ± 0.6	0.8	7.45 ± 0.02	6.77 ± 0.04	6.57 ± 0.02	6.49 ± 0.04	6.43 ± 0.02	6.39 ± 0.02	6.25 ± 0.05, 21.7	0	0.0
J235122.50+234419.9	−2.1 ± 0.5	−4.5	9.68 ± 0.02	9.08 ± 0.02	8.82 ± 0.02	8.66 ± 0.02	8.50 ± 0.02	8.37 ± 0.02	8.00 ± 0.17, 6.4	1.5	4.0
Carina (20 − 40 Myr)											
J061130.01−721338.2	6.0 ± 1.1	4.0	9.55 ± 0.02	8.96 ± 0.03	8.70 ± 0.03	8.54 ± 0.02	8.35 ± 0.02	8.23 ± 0.02	8.19 ± 0.09, 11.4	0	4.0
J090324.30−634832.9	20.7 ± 0.4	20.8	9.57 ± 0.03	8.86 ± 0.05	8.69 ± 0.02	8.57 ± 0.02	8.53 ± 0.02	8.44 ± 0.02	8.35 ± 0.15, 7.2	0	0.5
Columba (20 − 40 Myr)											
J030509.79−372505.8	14.3 ± 0.6	17.0	9.54 ± 0.02	8.88 ± 0.04	8.65 ± 0.02	8.55 ± 0.02	8.45 ± 0.02	8.33 ± 0.02	8.32 ± 0.16, 6.8	0	1.5
J034137.39+551305.7	−3.2 ± 0.6	−1.8	8.35 ± 0.03	7.65 ± 0.03	7.50 ± 0.02	7.44 ± 0.03	7.45 ± 0.02	7.37 ± 0.02	7.52 ± 0.16, 6.9	0	0.5
J042400.99−551222.2	20.1 ± 0.5	20.2	9.80 ± 0.02	9.16 ± 0.02	8.95 ± 0.02	8.79 ± 0.02	8.67 ± 0.02	8.52 ± 0.02	8.29 ± 0.12, 9.0	1.2	2.5
J045153.05−464730.8	24.0 ± 0.8	22.0	9.80 ± 0.02	9.14 ± 0.02	8.89 ± 0.02	8.79 ± 0.02	8.74 ± 0.02	8.63 ± 0.02	8.52 ± 0.20, 5.4	0	0.0
J051004.29−234040.9	24.3 ± 0.3	23.0	9.24 ± 0.03	8.58 ± 0.03	8.36 ± 0.02	8.19 ± 0.02	8.06 ± 0.02	7.95 ± 0.02	7.68 ± 0.12, 9.1	1.2	3.0
J051004.90−234015.1	24.4 ± 0.2	23.0	9.60 ± 0.04	8.93 ± 0.04	8.54 ± 0.02	8.36 ± 0.02	8.23 ± 0.02	8.15 ± 0.02	8.27 ± 0.20, 5.5	0	2.0
J060023.07−440121.7	22.3 ± 1.6	24.0	10.31 ± 0.04	9.58 ± 0.03	9.26 ± 0.03	9.06 ± 0.02	8.88 ± 0.02	8.74 ± 0.02	8.52 ± 0.20, 5.4	0.7	4.0
J070657.72−535345.9	22.4 ± 0.6	22.9	8.54 ± 0.03	7.90 ± 0.05	7.67 ± 0.03	7.59 ± 0.03	7.57 ± 0.02	7.48 ± 0.02	7.39 ± 0.08, 13.8	0	0.0
Tuc−Hor (39 − 43 Myr)											
J001527.62−641455.2	6.7 ± 0.3	6.2	9.32 ± 0.03	8.69 ± 0.02	8.44 ± 0.02	8.33 ± 0.02	8.24 ± 0.02	8.12 ± 0.02	8.13 ± 0.18, 5.9	0	1.8
J003025.74−623602.3	9.4 ± 0.7	11.5	8.44 ± 0.02	7.80 ± 0.03	7.55 ± 0.02	7.23 ± 0.03	7.17 ± 0.02	7.07 ± 0.01	6.90 ± 0.07, 15.3	0	2.2
J003935.87−381659.0	3.3 ± 0.4	3.6	8.78 ± 0.02	8.09 ± 0.03	7.86 ± 0.02	7.76 ± 0.02	7.67 ± 0.02	7.60 ± 0.02	7.48 ± 0.13, 8.4	0	1.4
J004935.79−634742.0	8.1 ± 0.3	7.9	9.28 ± 0.03	8.66 ± 0.04	8.43 ± 0.03	8.32 ± 0.02	8.23 ± 0.02	8.15 ± 0.02	8.01 ± 0.16, 6.7	0	1.7
J010243.86−623534.8	7.0 ± 2.0	5.4	9.64 ± 0.02	9.04 ± 0.02	8.80 ± 0.02	8.61 ± 0.02	8.43 ± 0.02	8.29 ± 0.02	8.19 ± 0.21, 5.1	0.3	2.9
J010335.75−551556.6	7.3 ± 2.6	7.0	10.16 ± 0.02	9.58 ± 0.03	9.24 ± 0.02	9.03 ± 0.02	8.79 ± 0.02	8.56 ± 0.02	7.86 ± 0.15, 7.4	3.9	5.0
J011340.44−593934.8	11.9 ± 6.7	14.1	9.95 ± 0.02	9.34 ± 0.03	9.06 ± 0.03	8.87 ± 0.02	8.69 ± 0.02	8.59 ± 0.02	8.40 ± 0.21, 5.1	0.5	3.7
J012245.24−631845.0	7.8 ± 1.4	6.0	9.83 ± 0.02	9.21 ± 0.03	8.98 ± 0.02	8.83 ± 0.03	8.67 ± 0.02	8.54 ± 0.02	8.31 ± 0.19, 5.7	0.8	3.5
J015057.01−584403.4	11.1 ± 0.5	12.0	9.54 ± 0.02	8.87 ± 0.05	8.64 ± 0.02	8.55 ± 0.02	8.42 ± 0.02	8.29 ± 0.02	8.39 ± 0.19, 5.6	0	3.0
J015218.43−595016.9	10.3 ± 0.3	10.2	8.94 ± 0.02	8.33 ± 0.04	8.14 ± 0.03	7.96 ± 0.02	7.87 ± 0.02	7.78 ± 0.02	7.67 ± 0.08, 13.0	0	1.6
J020012.84−084052.4	4.5 ± 0.4	5.5	8.77 ± 0.02	8.14 ± 0.04	7.87 ± 0.02	7.78 ± 0.02	7.68 ± 0.02	7.59 ± 0.02	7.54 ± 0.12, 9.5	0	2.1
J020701.85−440638.3	11.1 ± 2.0	11.6	9.27 ± 0.03	8.69 ± 0.04	8.40 ± 0.02	8.26 ± 0.02	8.11 ± 0.02	8.00 ± 0.02	8.10 ± 0.20, 5.3	0	1.9
J021258.28−585118.3	9.1 ± 0.8	7.0	9.32 ± 0.02	8.65 ± 0.05	8.44 ± 0.02	8.30 ± 0.02	8.20 ± 0.02	8.10 ± 0.02	7.98 ± 0.13, 8.1	0	1.9
J022051.50−582341.3	12.1 ± 0.6	11.6	9.67 ± 0.02	9.09 ± 0.02	8.83 ± 0.02	8.67 ± 0.02	8.51 ± 0.02	8.40 ± 0.02	8.06 ± 0.15, 7.2	1.5	3.2
J022424.69−703321.2	11.8 ± 0.3	11.5	10.37 ± 0.02	9.75 ± 0.02	9.49 ± 0.02	9.33 ± 0.02	9.13 ± 0.02	8.97 ± 0.02	8.71 ± 0.21, 5.2	1.1	3.3
J024147.39−525930.7	12.6 ± 0.7	12.9	8.48 ± 0.03	7.85 ± 0.03	7.64 ± 0.03	7.45 ± 0.03	7.35 ± 0.02	7.27 ± 0.02	7.09 ± 0.07, 16.0	0.4	2.1

Table 6.2: *continued.*

Name (WISE-)	RV ($\mathrm{km\,s^{-1}}$)	RV_p ($\mathrm{km\,s^{-1}}$)	J (mag)	H (mag)	K (mag)	$W1$ (mag)	$W2$ (mag)	$W3$ (mag)	$W4$ (mag, SNR)	E_{W4}	SpT M-
J024746.49−580427.4	13.1 ± 0.5	12.8	9.36 ± 0.02	8.67 ± 0.02	8.45 ± 0.02	8.34 ± 0.02	8.23 ± 0.02	8.13 ± 0.02	8.10 ± 0.14, 7.8	0	1.8
J025433.25−510831.4	13.8 ± 0.4	14.9	8.67 ± 0.03	8.07 ± 0.05	7.78 ± 0.03	7.61 ± 0.02	7.52 ± 0.02	7.43 ± 0.01	7.39 ± 0.08, 13.4	0	1.1
J025647.15−634302.5	16.7 ± 4.7	20.2	9.86 ± 0.03	9.22 ± 0.03	9.01 ± 0.03	8.80 ± 0.02	8.62 ± 0.02	8.50 ± 0.02	8.29 ± 0.15, 7.2	0.9	3.6
J030509.79−372505.8	14.2 ± 0.5	15.6	9.54 ± 0.02	8.88 ± 0.04	8.65 ± 0.02	8.55 ± 0.02	8.45 ± 0.02	8.33 ± 0.02	8.32 ± 0.16, 6.8	0	1.4
J041333.21−523158.5	18.4 ± 0.2	20.1	10.00 ± 0.03	9.35 ± 0.02	9.12 ± 0.02	9.00 ± 0.02	8.87 ± 0.02	8.75 ± 0.02	8.68 ± 0.16, 6.7	0	2.4
J042400.99−551222.2	19.0 ± 0.7	21.1	9.80 ± 0.02	9.16 ± 0.02	8.95 ± 0.02	8.79 ± 0.02	8.67 ± 0.02	8.52 ± 0.02	8.29 ± 0.12, 9.0	1.3	2.0
J043657.44−161306.7	16.6 ± 1.9	16.5	9.12 ± 0.03	8.47 ± 0.05	8.26 ± 0.02	8.12 ± 0.02	7.97 ± 0.02	7.89 ± 0.02	7.71 ± 0.16, 6.7	0.3	3.3
J044401.08−662403.2	16.0 ± 0.5	15.7	9.47 ± 0.02	8.75 ± 0.03	8.58 ± 0.02	8.50 ± 0.02	8.47 ± 0.02	8.38 ± 0.02	8.25 ± 0.15, 7.2	0	0.0
J053925.08−424521.0	21.7 ± 0.2	22.9	9.45 ± 0.02	8.80 ± 0.02	8.60 ± 0.02	8.45 ± 0.02	8.37 ± 0.02	8.27 ± 0.02	8.12 ± 0.14, 7.9	0.1	1.7
J213708.89−603606.4	0.2 ± 0.4	−0.9	9.64 ± 0.02	9.01 ± 0.05	8.76 ± 0.02	8.59 ± 0.02	8.45 ± 0.02	8.32 ± 0.02	8.15 ± 0.20, 5.5	0.4	3.0
J220216.29−421034.0	−2.8 ± 0.3	−1.1	8.93 ± 0.03	8.23 ± 0.04	7.99 ± 0.02	7.90 ± 0.02	7.86 ± 0.02	7.76 ± 0.02	7.66 ± 0.14, 7.5	0	0.7
J231246.53−504924.8	4.1 ± 11.9	6.0	9.12 ± 0.02	8.53 ± 0.05	8.30 ± 0.03	8.08 ± 0.02	7.90 ± 0.02	7.77 ± 0.02	7.87 ± 0.17, 6.4	0	3.9
J231316.77−493316.3	0.3 ± 0.7	−0.2	9.76 ± 0.02	9.14 ± 0.02	8.92 ± 0.02	8.76 ± 0.02	8.58 ± 0.02	8.44 ± 0.02	8.07 ± 0.21, 5.2	1.4	3.5
J232857.75−680234.5	8.0 ± 1.5	9.4	9.26 ± 0.02	8.64 ± 0.04	8.38 ± 0.02	8.27 ± 0.02	8.15 ± 0.02	8.03 ± 0.02	8.05 ± 0.17, 6.3	0	2.3
J234747.06−651725.3	6.1 ± 0.3	5.7	9.10 ± 0.02	8.39 ± 0.03	8.17 ± 0.03	8.07 ± 0.02	8.02 ± 0.02	7.91 ± 0.02	8.04 ± 0.17, 6.4	0	1.0
Argus (30 − 50 Myr)											
J005033.39+244900.3	6.0 ± 1.1	4.0	7.95 ± 0.02	7.35 ± 0.01	7.12 ± 0.02	6.88 ± 0.03	6.72 ± 0.02	6.64 ± 0.01	6.49 ± 0.05, 20.6	0.5	3.5
J030336.86−253531.6	20.1 ± 0.8	16.1	8.00 ± 0.02	7.34 ± 0.03	7.11 ± 0.03	7.01 ± 0.03	7.00 ± 0.02	6.93 ± 0.01	6.87 ± 0.06, 19.4	0	0.0
J044649.74−603409.7	15.5 ± 3.5	12.1	8.55 ± 0.02	7.95 ± 0.03	7.72 ± 0.02	7.59 ± 0.02	7.50 ± 0.02	7.41 ± 0.01	7.33 ± 0.06, 18.1	0	1.5
J050903.58−420919.2	16.8 ± 1.7	18.5	9.58 ± 0.02	8.98 ± 0.02	8.76 ± 0.02	8.58 ± 0.02	8.42 ± 0.02	8.33 ± 0.02	8.25 ± 0.13, 8.1	0	3.5
J061345.36−235206.3	22.9 ± 0.2	23.4	8.37 ± 0.03	7.79 ± 0.04	7.53 ± 0.02	7.36 ± 0.03	7.21 ± 0.02	7.08 ± 0.01	6.95 ± 0.07, 16.2	0.8	3.5
J120929.80−750540.2	1.9 ± 0.5	0.5	9.91 ± 0.02	9.24 ± 0.02	9.01 ± 0.02	8.86 ± 0.02	8.75 ± 0.02	8.61 ± 0.02	8.23 ± 0.16, 6.6	1.5	3.0
J155531.60+351204.3	−15.5 ± 0.7	−17.6	8.93 ± 0.02	8.26 ± 0.03	8.04 ± 0.03	7.82 ± 0.02	7.68 ± 0.02	7.54 ± 0.02	7.49 ± 0.09, 12.5	0	4.0
J184500.95−140905.9	−23.0 ± 0.3	−24.1	8.47 ± 0.04	7.94 ± 0.04	7.57 ± 0.03	7.30 ± 0.03	7.09 ± 0.02	7.05 ± 0.02	6.81 ± 0.14, 7.5	0.6	5.0
J193124.38−213423.8	−25.6 ± 1.5	−21.8	8.69 ± 0.02	8.09 ± 0.05	7.83 ± 0.03	7.70 ± 0.02	7.59 ± 0.02	7.52 ± 0.02	7.43 ± 0.14, 8.0	0	2.5
J201633.88−071145.5	−23.0 ± 0.2	−21.2	8.59 ± 0.03	7.96 ± 0.05	7.71 ± 0.02	7.61 ± 0.02	7.60 ± 0.02	7.54 ± 0.02	7.51 ± 0.13, 8.2	0	0.0
ABDMG (70 − 120 Myr)											
J010342.25+405114.2	−10.9 ± 0.4	−11.5	9.37 ± 0.04	8.84 ± 0.05	8.51 ± 0.03	8.09 ± 0.02	7.94 ± 0.02	7.88 ± 0.02	7.72 ± 0.10, 10.3	0.3	2.6
J012251.01−243951.8	11.2 ± 0.3	15.6	10.08 ± 0.03	9.47 ± 0.02	9.20 ± 0.03	9.01 ± 0.03	8.84 ± 0.02	8.75 ± 0.03	8.20 ± 0.21, 5.1	1.7	3.5
J034723.45−015822.7	16.0 ± 1.7	17.8	7.80 ± 0.03	7.17 ± 0.05	6.93 ± 0.02	6.81 ± 0.04	6.68 ± 0.02	6.63 ± 0.02	6.51 ± 0.07, 16.4	0	2.5
J045224.49−164924.0	26.7 ± 1.5	25.8	7.74 ± 0.02	7.15 ± 0.03	6.89 ± 0.03	6.76 ± 0.04	6.60 ± 0.02	6.53 ± 0.02	6.42 ± 0.05, 20.8	0	3.0
J045717.30−062157.5	23.4 ± 0.3	22.5	9.51 ± 0.02	8.83 ± 0.04	8.64 ± 0.02	8.52 ± 0.02	8.52 ± 0.02	8.36 ± 0.02	8.04 ± 0.18, 5.9	1.0	0.5
J052541.69−090914.4	26.3 ± 0.3	24.1	8.45 ± 0.03	7.88 ± 0.03	7.62 ± 0.03	7.48 ± 0.03	7.32 ± 0.02	7.22 ± 0.02	7.13 ± 0.09, 12.3	0	3.5
J055313.01−450512.1	31.7 ± 0.8	31.3	8.60 ± 0.03	7.94 ± 0.04	7.73 ± 0.02	7.62 ± 0.02	7.59 ± 0.02	7.50 ± 0.02	7.53 ± 0.09, 11.8	0	0.5
J084718.88−571754.5	30.2 ± 0.2	28.4	9.41 ± 0.02	8.81 ± 0.05	8.55 ± 0.02	8.36 ± 0.02	8.19 ± 0.02	8.05 ± 0.02	7.80 ± 0.11, 9.9	1.6	4.0
J123837.00−270336.9	7.8 ± 1.2	7.8	8.73 ± 0.04	8.08 ± 0.03	7.84 ± 0.03	7.68 ± 0.02	7.57 ± 0.02	7.47 ± 0.02	7.35 ± 0.10, 11.2	0.1	1.5
J125740.02+351328.7	−14.1 ± 1.6	−11.3	7.40 ± 0.02	6.73 ± 0.02	6.55 ± 0.02	6.37 ± 0.04	6.39 ± 0.02	6.30 ± 0.01	6.20 ± 0.05, 23.7	0	4.0
J152448.37−492949.9	10.3 ± 0.2	7.4	8.16 ± 0.03	7.53 ± 0.03	7.30 ± 0.02	7.11 ± 0.03	7.02 ± 0.02	6.97 ± 0.01	6.96 ± 0.08, 13.4	0	2.0
J155947.24+440359.6	−18.0 ± 1.4	−16.9	8.51 ± 0.02	7.84 ± 0.02	7.62 ± 0.02	7.50 ± 0.03	7.44 ± 0.02	7.35 ± 0.01	7.28 ± 0.06, 17.4	0	1.0
J163341.57−093313.6	−15.0 ± 0.4	−15.0	8.38 ± 0.02	7.78 ± 0.05	7.55 ± 0.03	7.45 ± 0.02	7.44 ± 0.02	7.40 ± 0.02	7.40 ± 0.14, 7.8	0	0.5
J173839.62+611416.5	−26.7 ± 0.1	−30.4	7.62 ± 0.02	7.00 ± 0.02	6.81 ± 0.02	6.73 ± 0.04	6.70 ± 0.02	6.64 ± 0.01	6.52 ± 0.04, 24.9	0	0.0
J214644.83−854306.3	23.5 ± 0.7	22.2	8.84 ± 0.02	8.28 ± 0.03	7.99 ± 0.02	7.82 ± 0.02	7.64 ± 0.02	7.52 ± 0.02	7.26 ± 0.08, 13.8	2.3	3.5
J215210.48+053734.4	−15.1 ± 0.2	−14.3	8.25 ± 0.03	7.65 ± 0.04	7.39 ± 0.03	7.21 ± 0.03	7.07 ± 0.02	7.01 ± 0.02	6.83 ± 0.07, 16.0	0.7	2.0
J230605.11+635533.7	−23.7 ± 0.8	−23.3	7.82 ± 0.02	7.17 ± 0.04	6.98 ± 0.02	6.93 ± 0.03	6.91 ± 0.02	6.85 ± 0.02	6.74 ± 0.05, 21.1	0	1.0
J233200.34−391738.9	11.1 ± 0.2	11.9	8.90 ± 0.03	8.26 ± 0.03	8.02 ± 0.02	7.88 ± 0.02	7.75 ± 0.02	7.62 ± 0.02	7.71 ± 0.15, 7.3	0	3.0

6.3 Identifying IR-excesses

Flux ratios in the $W4$ band (E_{W4}) were measured by subtracting the observed $W4$ flux by the expected $W4$ flux from a photosphere at a given spectral-type and dividing this by the flux error. The flux error is the quadrature sum of the $W4$ photometric uncertainty and the scatter in $W1 - W4$ for a disc-less star at a given spectral-type (see Figure 6.1). Objects with E_{W4} greater than 3.0 are discussed in §6.6.3.

Schneider, Melis & Song (2012) apply a criteria of $W1 - W4 > 1.0$ mag to identify circumstellar discs around M-dwarf TWA members. A typical $W1-W4$ colour for an M-dwarf field star without an excess is usually between 0 and 1. Figure 6.1 shows that $W1 - W4$ is likely to be the best colour indicator to pick out objects with discs. This work will utilise the same photometric cut, however, should an object with $W1 - W4 < 1.0$ have an E_{W4} value > 3.0, then they will be assumed to have debris discs. Seventeen objects survive the $W1 - W4 > 1.0$ cut: 6 in ϵ Cha, 5 in η Cha, 4 in TWA, 1 in BPMG and 1 in Tuc-Hor (see Table 6.5 on page 218). No objects from the likely-young sample in §5 were found to have any IR excess. To represent the general M-dwarf field star population a sample of M-dwarfs from the third catalogue of nearby stars (Gliese & Jahreiss 1991) is used (cross symbols). These are used to inform the error bar that is used to judge the significance of any excess. A sample of primordial and transitional discs in the Taurus SFR (Esplin, Luhman & Mamajek 2014) are used to try and distinguish the tranisitional disc sequence from primordial sources (filled left-facing and open right-facing triangles, respectively).

Figure 6.1 shows 4 separate colour-colour diagrams for the entire sample used in this analysis. Large $K - W1$ and $K - W2$ colours are indicative of large amounts of near-IR flux, synonymous with the general trend observed in primordial discs. The bottom-right panel in Figure 6.1 ($W1-W4$ versus $K-W1$) may be the most effective way of separating debris discs from primordial discs as it can potentially probe both hot discs ($K - W1$) and cooler discs ($W1 - W4$). These colour-colour diagrams as discussed in more detail in §6.6.1.

Discs contribute very little to the flux at optical wavelengths, therefore to identify

the amount of colour excess for each target, the tables in Pecaut & Mamajek (2013) were used to estimate the expected WISE colours for a given spectral-type if it had no disc. Spectral-types for the entire sample of MG members are from the literature source and are listed in the final column of Table 6.2. The colour excesses were calculated by subtracting the expected 'disc-less' colour from the observed colour and are presented in Figure 6.2. This criterion did not change the disc classification for any of the objects and was not subsequently used to identify the type of disc excess.

Because discs contribute large amounts of IR flux compared to the star, the flux gradient observed in spectral energy diagrams (SEDs) is shallower than for objects without discs. The slope of the SED at IR wavelengths is characterised by α, where $\alpha = \mathrm{d}\log\lambda F_\lambda / \mathrm{d}\log\lambda$. In identifying the disc frequencies amongst brown-dwarfs in the Upper Scorpius OB association Riaz et al. (2012) suggest that objects with $\alpha_{K-W3} \geq -0.2, -0.2 > \alpha_{K-W3} > -1.8$ and $\alpha_{K-W3} \leq -2.0$ correspond to class I/II/III sources, respectively. This method was calibrated for objects as early as M3.5 and should be applicable to most M-dwarfs in this work. There is an overlap of class II/III sources between $-2.0 < \alpha < -1.8$. Should an object have $-2.0 < \alpha_{K-W3} < -1.8$ it will be assumed to be class III.

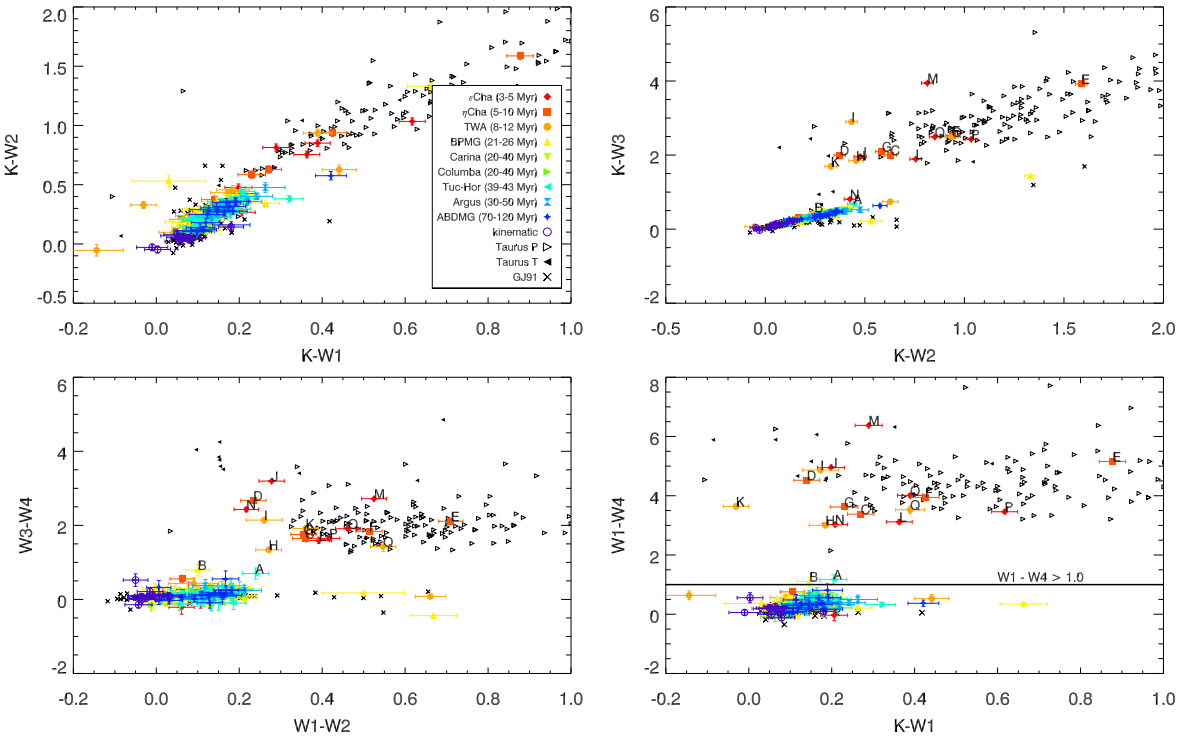

Figure 6.1:
Colour-colour diagrams for the entire sample of M-dwarfs in this analysis with SNR values > 5.0. Taurus P and Taurus T refer to the primordial and transitional disc sample in Esplin, Luhman & Mamajek (2014). Black crosses represent M-type field stars from the Gliese & Jahreiss (1991) catalog. Objects labelled 'kinematic' are from the likely-young sample of stars identified in §5. Objects labelled with initials in the $W1 - W4$ versus $K - W1$ plot correspond to the targets chosen for further analysis, listed in Table 6.4.

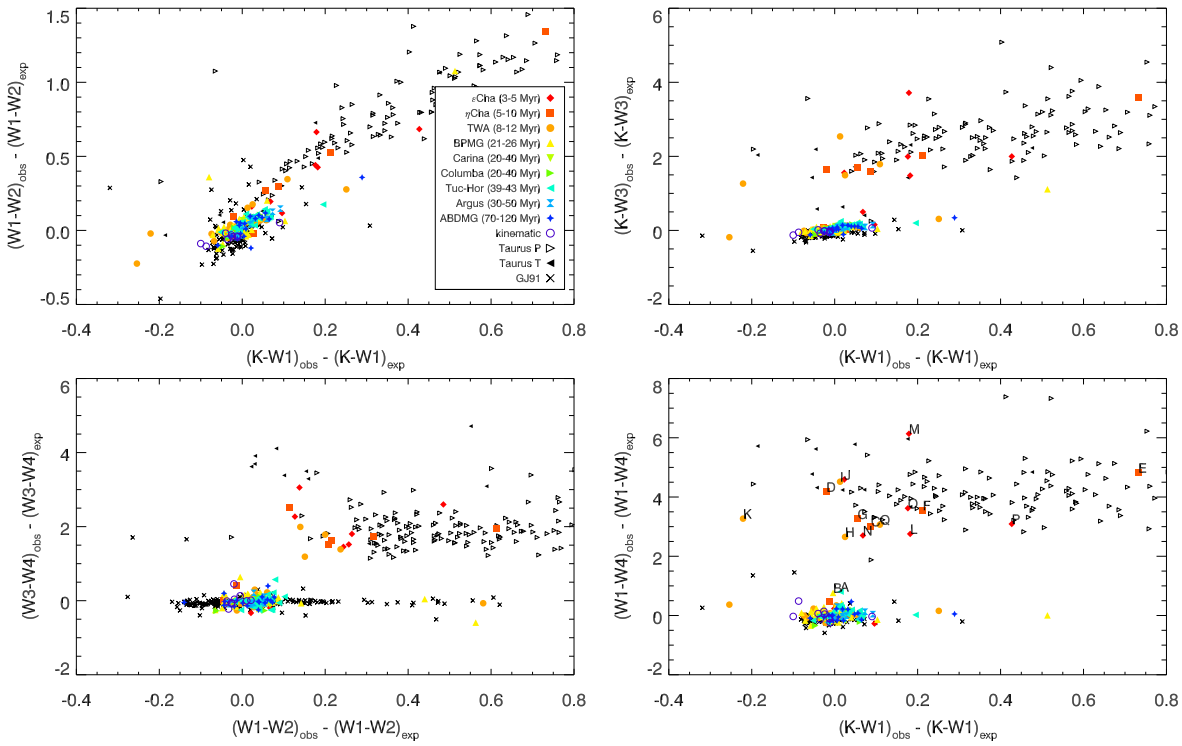

Figure 6.2:
Similar to Figure 6.1, but here the plotted values are the expected colour for an object at a given spectral-type (based on table 5 in Pecaut & Mamajek 2013) subtracted from the observed colour to provide a colour excess.

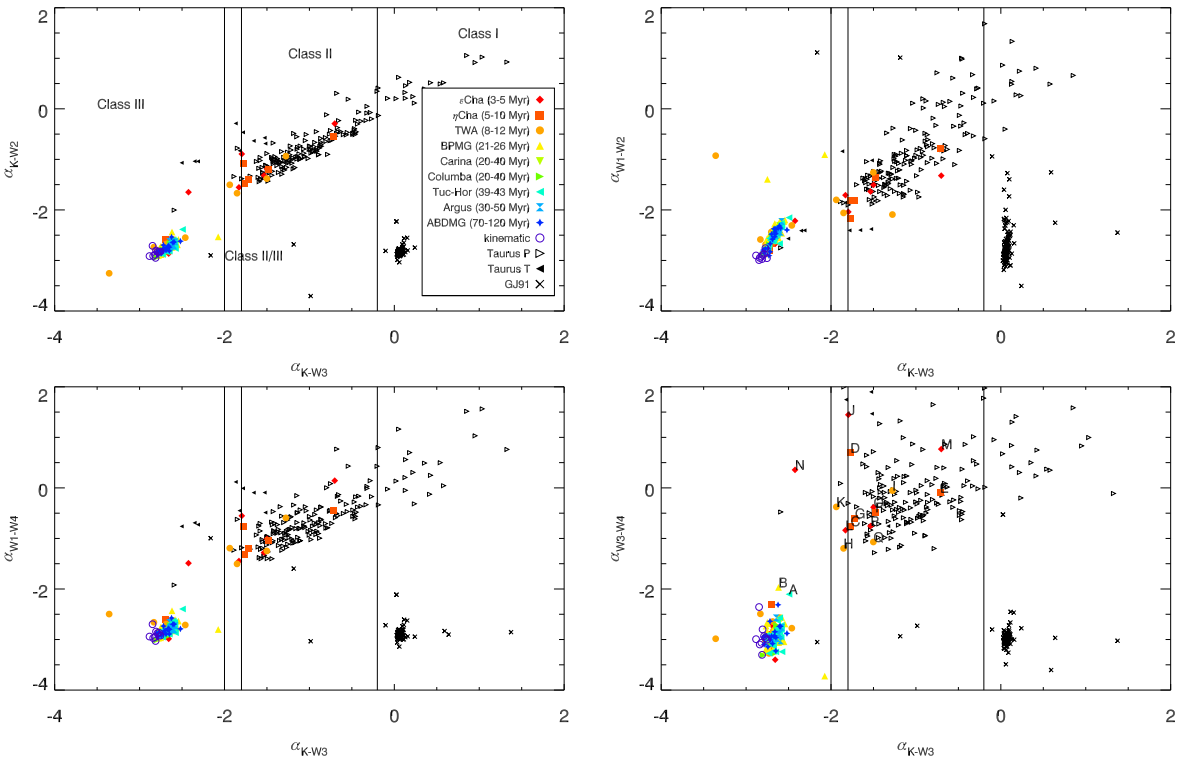

Figure 6.3:
Flux gradient (α) values for the entire sample using α_{K-W3} as the ordinate in each panel. The vertical lines at $\alpha_{K-W3} = -2.0, -1.8$ and -0.2 represent the boundaries for class I/II/III objects in Riaz et al. (2012).

6.4 SED models

SED models were generated to provide a best-fit star and single-temperature disc to the available photometry. To simulate the photosphere the BT-Settl model atmospheres were used for $T_{\rm eff} > 2700\,{\rm K}$ (Allard 2014) and the AMES-DUSTY models were used for $T_{\rm eff} \leq 2700\,{\rm K}$ (Chabrier & Baraffe 2000). All SEDs were fit using a metallicity of [M/H] = 0.0 and $\log g = 4.5$. The flux profiles of the single-temperature discs were generated from black-body Planck functions. Model fluxes for each photometry point were calculated by integrating the relative spectral response (RSR) curve with the combined stellar and disc flux over the photometric bandwidth and dividing this by the integral of the RSR curve, as below:

$$f_{\rm mod}(\lambda) = \frac{\int_{\lambda_1}^{\lambda_2} RSR(\lambda) f(\lambda)\, d\lambda}{\int_{\lambda_1}^{\lambda_2} RSR(\lambda)\, d\lambda}, \tag{6.1}$$

where $f(\lambda)$ is the sum of the model stellar and disc flux. $T_{\rm eff}$ was calculated by comparing spectral-types with the colour-$T_{\rm eff}$ tables in Pecaut & Mamajek (2013). There were three free parameters to constrain: the disc temperature ($T_{\rm d}$), the surface area of the star and the surface area of the disc. The stellar and disc components are treated separately. Because the fitted SEDs were calibrated for a source at 10 pc, the flux profiles were multiplied by a normalisation parameter of 10^{α} to characterise the stellar surface area. Using 2MASS JHK photometry to constrain the photosphere, a χ^2_* value was obtained for fits at each value of α, which was altered in steps of 0.0001. The code then used the α value which returned the lowest χ^2_* for the final fit. As $T_{\rm eff}$ is fixed throughout the final fitting process there are 2 degrees of freedom for the stellar fit (from fitting JHK photometry), so dividing by 2 provides the reduced χ^2_* ($\chi^2_{\rm r,*}$). Error bars for α were calculated using a parabolic interpolation of $\chi^2_{\rm r,*}$ and α. The α and $T_{\rm eff}$ values are listed in Table 6.4 and all α errors were ~ 0.01.

The final fitted disc contribution minimised $\chi^2_{\rm d}$, but this time using the WISE photometry and any supplementary IR data available (see Table 6.3). Once $T_{\rm eff}$ and α

had been minimised, a single-temperature Planck function was fit to model the disc. Because the Planck function is calculated as the spectral radiance emitted from the source, the disc fits required a correction to account for the disc surface area. This was done by multiplying the Planck function by a factor of 10^{β}, altering β in steps of 0.05 and $T_{\rm d}$ in steps of 10 K to provide the lowest $\chi^2_{\rm d}$. Error bars for β and $T_{\rm d}$ were calculated only for objects that had IR data either side of the peak of the disc fit (8 out of 17) because if no IR data were available red-ward of the peak flux, the disc fits could not be constrained and β and $T_{\rm d}$ were degenerate. In Figure 6.5 contour plots are provided for 1, 2 and 3σ errors for the simultaneous fits of β and $T_{\rm d}$ and the maximum/minimum values of β and $T_{\rm d}$ which provide 1σ errors in the fit are used as estimates of the error bar on both of these parameters. This method is likely to slightly over-predict 1σ errors.

Table 6.4 displays χ^2 values for the best stellar fit and the best disc fit, the corresponding α and β values, $T_{\rm eff}$ and $T_{\rm d}$. The amount flux radiating from the disc compared to the star ($f_{\rm d}/f_*$, herein 'flux fraction') is calculated by integrating the best-fit flux profiles for the disc and star between 0.1 and 200 μm. In Figure 6.4, the best-fit SED and disc models are displayed for all 17 objects that had a photometric IR excess that satisfied the criteria in §6.2. In the situation where only WISE data were available and the SED fit was not constrained by any wavelength points longer than the peak flux wavelength, the fit was much less constrained and the models more subject to degeneracies. These objects are flagged in Table 6.4.

Name WISE-	Fluxes ($\times 10^{-14}$ erg/s/cm^2/Å)
J114931.74−785101.0	1.50 (9) 1.03 (12) 1.09 (18) 0.84 (25) 0.12 (60) 0.04 (90)
J111835.64−793554.8	0.12 (18)
J084227.02−785747.7	0.96 (3.6) 0.43 (4.5) 0.19 (5.8) 0.08 (8) 0.03 (24) 0.006 (70) 0.002 (160)
J084416.33−785907.8	1.67 (3.6) 0.82 (4.5) 0.40 (5.8) 0.20 (8) 0.02 (24) 0.003 (70)
J084130.24−785306.3	0.41 (3.6) 0.21 (4.5) 0.10 (5.8) 0.05 (8)
J084318.52−790518.0	0.74 (9) 0.70 (18) 0.30 (90) 2.94 (3.6) 1.87 (4.5) 1.15 (5.8) 0.76 (8) 0.12 (24) 0.01 (70) 0.0008 (160) 0.16 (25)
J084409.09−783345.6	0.26 (3.6) 0.14 (4.5) 0.07 (5.8) 0.04 (8) 0.004 (24)
J101209.04−312445.3	0.46 (9)
J111027.80−373152.0	2.60 (9) 2.06 (12) 1.28 (18) 0.84 (25) 0.08 (60) 0.02 (90)

Table 6.3: Additional fluxes used for SED modelling. Values in parentheses are the wavelengths (in μm) for each data point: 3.6, 4.5, 5.8 and 8 are from IRAC: 12, 25, 60 and 100 are from IRAS, 24, 70 and 160 are from MIPS and 9, 18 and 90 are from AKARI.

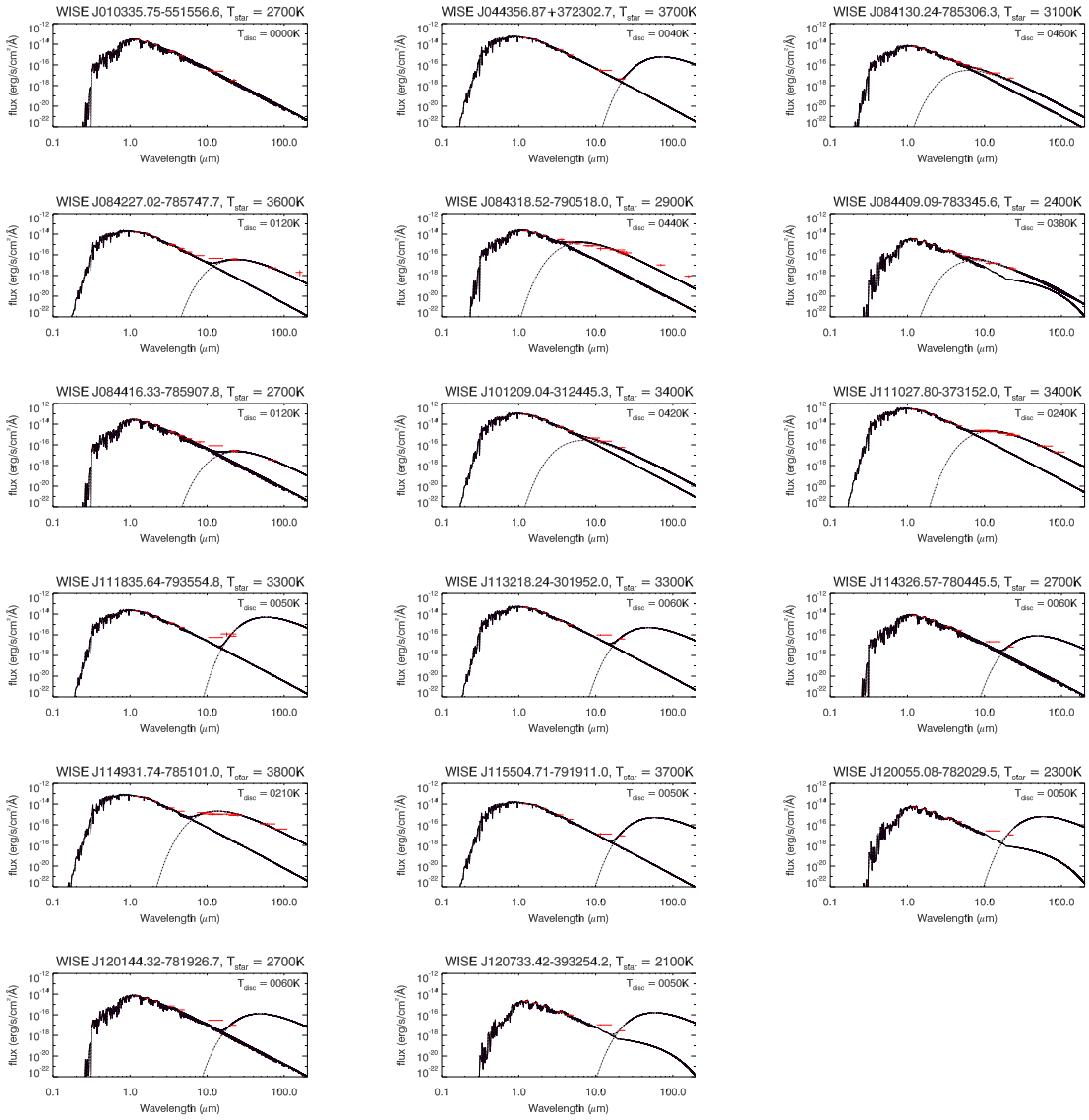

Figure 6.4: SED models for the 17 objects identified with $W1 - W4 > 1.0$. Red lines represent the flux data and the best-fit stellar SED, single-temperature black-body and their sum are overplotted as solid black lines. The fitting parameters for each SED are provided in Table 6.4.

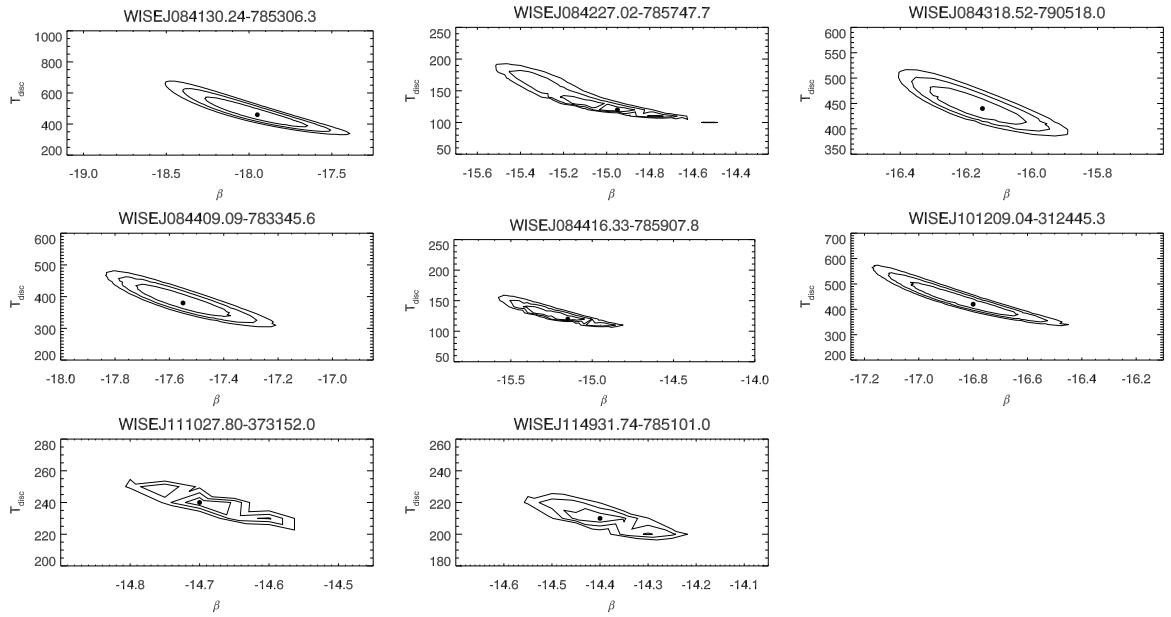

Figure 6.5: Contour plots indicating the 1, 2 and 3σ errors from simultaneously fitting β and $T_{\rm eff}$ in the SED models. These were only available for 8 objects because in all other cases there was not enough far-IR data to constrain the fits to the disc.

Name WISE-	MG	$N_{\rm IR}$	χ^2_*	$\chi^2_{\rm d}$	α	β	$T_{\rm eff}$ (K)	$T_{\rm d}$ (K)	$f_{\rm IR}/f_*$
J010335.75−551556.6	Tuc-Hor	4*	5.30	N/A	−18.94	N/A	2700	0	
J044356.87+372302.7	BPMG	4*	3.21	56.79	−19.19	−11.35	3700	40	
J084130.24−785306.3	η Cha	8	0.51	46.61	−19.80	$-17.95^{+0.30}_{-0.62}$	3100	460^{+110}_{-80}	$0.036^{+0.014}_{-0.009}$
J084227.02−785747.7	η Cha	11	4.28	95.04	−19.58	$-14.95^{+0.21}_{-0.27}$	3600	120^{+20}_{-10}	$0.053^{+0.010}_{-0.010}$
J084318.52−790518.0	η Cha	14	33.13	210.81	−19.14	$-16.15^{+0.13}_{-0.16}$	2900	440^{+40}_{-30}	$0.543^{+0.011}_{-0.096}$
J084409.09−783345.6	η Cha	9	0.74	64.60	−19.74	-17.55 ± 0.18	2400	380^{+60}_{-40}	$0.096^{+0.033}_{-0.018}$
J084416.33−785907.8	η Cha	9	5.21	26.63	−18.98	$-15.15^{+0.20}_{-0.28}$	2700	120^{+20}_{-10}	$0.028^{+0.007}_{-0.005}$
J101209.04−312445.3	TWA	5	1.41	38.61	−18.75	$-16.80^{+0.17}_{-0.23}$	3400	420^{+90}_{-50}	$0.021^{+0.007}_{-0.003}$
J111027.80−373152.0	TWA	10	3.30	24.08	−18.27	$-14.70^{+0.10}_{-0.02}$	3400	240 ± 10	$0.092^{+0.004}_{-0.010}$
J111835.64−793554.8	ϵ Cha	5*	2.98	6.84	−19.36	−10.90	3300	50	
J113218.24−301952.0	TWA	4*	3.20	14.79	−19.02	−12.30	3300	60	
J114326.57−780445.5	ϵ Cha	4*	22.04	24.83	−19.50	−13.10	2700	60	
J114931.74−785101.0	ϵ Cha	10	7.17	148.86	−19.11	$-14.40^{+0.11}_{-0.07}$	3800	210 ± 10	$0.475^{+0.062}_{-0.059}$
J115504.71−791911.0	ϵ Cha	4*	50.90	64.00	−19.75	−11.90	3700	50	
J120055.08−782029.5	ϵ Cha	4*	1.20	20.30	−19.44	−11.80	2300	50	
J120144.32−781926.7	ϵ Cha	4*	2.45	52.47	−19.56	−12.90	2700	60	
J120733.42−393254.2	TWA	4*	1.64	9.68	−19.69	−12.40	2100	50	

Table 6.4: Best-fit parameters to SED models for the sample of objects with $W1 - W4 > 1.0$. The number of flux points at wavelengths longer than K are provided in column 3. Error bars are ~ 0.01 for α and $\sim 200\,$K for $T_{\rm eff}$. *No data available to constrain the disc at wavelengths longer than the peak wavelength of the black-body fit.

6.5 Sensitivity limits for detecting debris discs

A working definition for debris discs is that they have $f_{\rm d}/f_*$ less than 0.01 (Lagrange, Backman & Artymowicz 2000). Optically thick primordial discs will generally have much higher values than this ratio. Given that the objects in this work are relatively faint M-dwarfs, there will be a limiting $W1-W4$ colour for which objects can be observed with $f_{\rm d}/f_* \leq 0.01$.

To explore the relationship between $f_{\rm d}/f_*$ and $W1-W4$, a simulation was made in which the emitting area of the disc was altered to give $f_{\rm d}/f_* = 0.01$, and this gave a corresponding $W1-W4$. To characterise the disc-less $W1-W4$ photometry for a given spectral-type the following objects were used: J055313.01−450512.1 (M0.5V, ABDMG), J125740.02+351328.7 (M4V, ABDMG) and DEN 1048-3956 (M8.5, field brown dwarf – see Avenhaus, Schmid & Meyer 2012). Photospheres were fit using the same procedure described in §6.4. The disc temperature was fixed at either 100 K or 300 K and the $W4$ magnitude and the disc area were outputs from the model. The disc normalisation was altered until $f_{\rm d}/f_*$ reached 0.01.

The results are presented in Figure 6.6. They indicate that a value of $W1-W4 = 1.0$ would correspond to $f_{\rm d}/f_* = 1\times10^{-3}$ for M-dwarfs and 5×10^{-4} for G and K stars. At some value of $W1-W4$, $f_{\rm d}/f_* = 0.01$. Debris discs generally have a smaller value of $W1-W4$ than this. However, if $W1-W4$ is too small it becomes indistinguishable from field stars (see Figure 6.1). The simulations provide a 'window' of $W1-W4$ that can indicate debris discs between the error threshold at the bottom, to where $f_{\rm d}/f_* = 0.01$ at the top.

The $W1-W4$ colour at which $f_{\rm d}/f_*$ reaches 0.01 is ≈ 2.5 for early to mid-M spectral-types and ≈ 2.2 for late M-dwarfs. Given that M8/9 represents the faintest object in the MG sample, $W1-W4 \approx 2.2$ suggest that debris discs will have $W1-W4$ values somewhere between these upper limits and the $W1-W4$ values of disc-less field stars. Primordial discs would likely have higher $W1-W4$ values. For comparison, the same simulation was carried out for an F5, a G3 and a K7 star (HIP 19183, HIP 113579 and HIP 31878, respectively, all members of ABDMG). For F and G stars the sensitivity

improves, and debris disc objects with $W1-W4<3.7$ are detectable. Observations of K stars are only slightly more sensitive than M-dwarfs and have a detection threshold of $W1-W4<2.8$. There were small differences of $W1-W4\sim0.1$ in the results between 100 K and 300 K discs. The models do not take into account disc gaps or disc orientation.

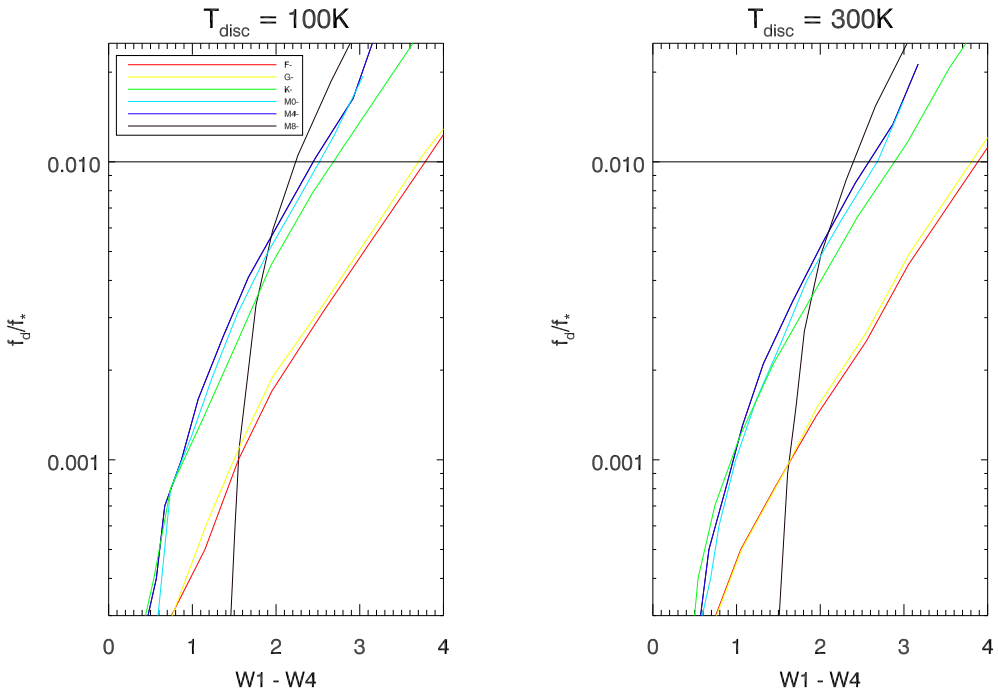

Figure 6.6:
Sensitivity limits for detecting debris discs in M-dwarfs with a disc temperature of 100 K (left) and 300 K (right). The $W1-W4$ for which $f_{\rm d}/f_*=0.01$ is ≈2.2 for M8 stars, ≈2.5 for M0/M4, ≈2.8 for K-stars and ≈3.7 for G and F-stars.

6.6 Nature of the IR excess

6.6.1 Disc criteria

This section and §6.6.2 focuses on objects that have $W1 - W4 > 1.0$. In §6.6.3 objects with $W1 - W4 < 1.0$ and a $E_{W4} > 3.0$ are discussed. To determine whether the IR excess is evidence of a debris disc, a primordial disc or some other artefact, an assessment for each object was made based on colour-colour diagrams (Figure 6.1), spectral energy slopes (α, Figure 6.3), flux fractions ($f_{\rm d}/f_*$, calculated from SED models) and data available in the literature. The final disc designation for each target is listed in Table 6.5 on page 218.

Debris discs generally have $f_{\rm d}/f_* < 10^{-2}$ (Lagrange, Backman & Artymowicz 2000), whereas Cieza et al. (2012) estimate primordial discs to have $f_{\rm d} \gtrsim 0.1$. In this work objects with $f_{\rm d}/f_* > 0.1$ are primordial, $0.01 < f_{\rm d}/f_* < 0.1$ are either primordial or transitional and $f_{\rm d}/f_* < 10^{-2}$ are debris discs. In §6.5 it was shown that M-dwarfs with $W1{-}W4 \gtrsim 2.5$ have $f_{\rm d}/f_* > 0.01$, *therefore only two objects in the* $W1{-}W4 > 1.0$ *sample could be debris discs.* The remaining 15 objects are therefore either primordial or transitional (unless there is strong evidence in the literature to suggest otherwise).

Figure 6.1 shows that both primordial and transitional discs in Taurus have colours of $3 < W1 - W4 < 6$, which is consistent with the simulations in §6.5. Overall it appears that transitional discs have slightly larger $W1 - W4$ values ($\sim$ 4.5 to 6.0) although not enough to strongly distinguish them from primordial discs. The $K - W1$ versus $K - W2$ plot (top-left plot) is ineffective at separating the sequences and is not used for analysis, however, the top-right plot shows that at $K - W2$ all but 2 primordial discs are blue-ward of $K - W2 \simeq 0.6$ and only one transitional disc is red-ward of this point. The majority of transitional discs in $W1 - W2$ (bottom-left plot) lie blue-ward of ~ 0.2 and all but one of the primordial discs are red-ward of ~ 0.3. In the bottom-right plot all but 2 primordial discs are blue-ward of $K - W1 \simeq 0.2$ and all but 2 transitional discs are red-ward of this point. This is no clear separation between primordial and transitional discs for *any* of the colour-colour diagrams and it is not

possible to characterise a debris disc in this way, however, based on the colour boundaries discussed here the following classification is set for all objects with $W1-W4 > 1.0$:

1) If $K - W2$ is greater than/less than 0.6 – transitional/primordial disc.
2) If $W1 - W2$ is greater than/less than 0.25 – transitional/primordial disc.
3) If $K - W1$ is greater than/less than 0.2 – transitional/primordial disc.

Table 6.5 lists whether an object is more likely to be primordial or transitional based on the top-right, bottom-left and bottom-right plots of Figure 6.1. No attempt was made to identify disc types based on Figure 6.2.

Figure 6.3 shows that eleven of the objects with $W1 - W4 > 1.0$ are class II and six are class III sources based on the α slopes described in §6.2. Whilst the majority of debris discs are class III, usually in systems older than 10 Myr, there are counter-examples of this; for example, Scicluna et al. (2014) observe some 30 Myr old class II protoplanetary discs, and there are examples of class III debris discs in young regions like Upper Sco ($5 - 10$ Myr, Carpenter et al. 2009; Luhman & Mamajek 2012). Therefore, this method is used only as secondary evidence and certainly does not assume primacy in classifying the disc type.

Each object was searched for any additional material in the literature that may point to the type of disc excess. Classification based on literary sources only assumes primacy if data has been used which wasn't available for this work. Any parameters derived in this work are compared to results in the literature if they are available. Ultimately, the final designation of a disc type will be subjective in some cases, particularly if there is a dearth of mid-/far-IR photometry to constrain SED fits, however, if a sufficient amount of IR data is available then $f_{\rm d}/f_*$ will be used as the primary indicator. Based on previous searches for debris discs around M-dwarfs (Lestrade et al. 2009; Avenhaus, Schmid & Meyer 2012) a low-fraction is to be expected, therefore if the disc type is uncertain but it *could* be a debris disc then this category is adopted.

6.6.2 Individual objects with $W1 - W4 > 1.0$

Target A: J010335.75−551556.6 - Tuc-Hor, M5.0 - Although this member qualified from the initial photometric cut, its $W1-W4$ value of 1.17 is ~ 2 magnitudes lower than the bulk of objects with similar spectral-types that qualified (see Figure 6.1). No IR photometry/flux data were found at wavelengths $> 25\,\mu$m and the shape of the SED displays shows little sign of a disc excess, however, it may be that a cold disc is present and the excess is stronger at longer wavelengths. Despite this, a value of $E_{W4} = 3.9$ is indicative of a significant excess at $22\,\mu$m. Riedel et al. (2014) have measured a trigonometric parallax of 21.18 ± 1.37 mas and identify the target as a member of a triple system comprised of two equal mass M-dwarfs and a $12 - 14\,M_{\rm Jup}$ tertiary brown dwarf, claiming that it may be a member of Carina, although they note that the object is overluminous compared to the BPMG sequence, implying an age < 20 Myr, incompatible with current estimates of Carina's age. Both the BANYAN analysis and Delorme et al. (2013) attribute its membership to Tuc-Hor and the latter work notes that this is the first object to be imaged around a binary system at a separation compatible with disc formation (< 100 AU, Pearce, Wyatt & Kennedy 2013). Despite this, no previous indications of a disc was found in the literature. Some of the excess emission may be from the brown dwarf companion, however, this would be much hotter than a debris and would contribute at shorter wavelengths. This work will assume it has a debris disc because it has a significant E_{W4} and is within the sensitivity limits for debris disc detection.

Target B: J044356.87+372302.7 - BPMG, M3.5 - This object has little evidence of disc excess in Figures 6.1, 6.2 and 6.3 and is most likely to be a BPMG member (96 per cent membership probability quoted in Malo et al. 2013). No evidence of a disc was identified in any previous work, however many of the stellar properties $(R, \log L, \log g, T_{\rm eff})$ have been calculated in Malo et al. (2014). The SED is poorly constrained as there are no data beyond $W4$. The $W1 - W4$ value of 1.10 is below the detection threshold for a debris disc and it has an $E_{W4} = 3.4$. Therefore this object is classed as a debris disc.

Target C: J084130.24−785306.3 - η Cha, M4.8 - In Figure 6.1 this object is amongst both primordial and transitional discs in Taurus, therefore it is not possible to distinguish what type of disc it has based on colour-colour diagrams. The α_{K-W3} value is consistent with a class II source. The $f_{\rm d}/f_*$ value of 0.036 is $\sim 3\sigma$ from the debris disc threshold of 0.01 and is consistent to within 1σ of the $f_{\rm d}/f_*$ value of 0.04 in Gautier et al. (2008). At least ten publications in the past 10 years have identified this object as an M-dwarf member of η Cha with a surrounding primordial disc. It has a $W1 - W4 = 3.39$ which would result in $f_{\rm d}/f_* < 0.01$. Given the large amount of previous work that has identified it as a primordial disc, this work will presume the same.

Target D: J084227.02−785747.7 - η Cha, M4.0 - The colour-colour diagrams in Figure 6.1 suggest this object has the same photometric properties as transitional discs, however, this target is reported as a primordial disc in η Cha in tens of publications. A calculated flux fraction of 0.053 is compatible with the work of Gautier et al. (2008), who calculate a value of 0.06. The object is classed as a primordial disc on the basis of both this work and much previous work in the literature.

Target E: J084318.52−790518.0 - η Cha, M3.3 - This target is easily the reddest object with a disc excess in this survey in terms of $K - W1$, $K - W2$ and $K - W3$ and has similar colours as the primordial discs in Taurus. Photometry/flux data are available up to 160 μm and the SED indicates a strong IR excess. The flux fraction calculated in this chapter is 0.543, $\sim$ triple the value calculated in Gautier et al. (2008). Lawson & Feigelson (2001) categorise this object as a CTTS in η Cha, and over 20 publications in the past five years indicate a primordial disc surrounding it; therefore this work will presume the same disc category.

Target F: J084409.09−783345.6 - η Cha, M5.8 - All 3 colour-colour diagrams suggest this target has similar colours as primordial discs in Taurus. The SED model calculates a flux fraction of ~ 0.096, which is $\sim 3\sigma$ from the value of 0.04 calculated in Gautier et al. (2008) and $\sim 5\sigma$ larger the debris disc threshold of 0.01. Some publications indicate primordial disc excess, however Rhee, Song & Zuckerman (2007) identify warm dusty material in the disc and suggest it could be either a debris or

primordial disc. Based on Spitzer IRS spectra, Currie & Sicilia-Aguilar (2011) classify the object as a primordial disc because 1) it lacks evidence for an inner hole/gap as inferred from SED modelling and 2) its mid-IR emission exceeds the optically thick, flat disc limit. This work presumes it is a primordial disc.

Target G: J084416.33−785907.8 - η Cha, M4.5 - The disc nature of this object cannot be determined from colour-colour diagrams because both it is close to primordial and transitional discs in all colour-colour diagrams, although two out of three plots suggests it is located more towards the primordial disc sequence. Data is available up to 70 μm and SED fits show a clear IR excess. The flux fraction of 0.028 calculated in this work is $\sim 2\sigma$ from the value of 0.04 calculated in Gautier et al. (2008) and suggests the disc type is either primordial or transitional. Sicilia-Aguilar et al. (2009) and Currie & Sicilia-Aguilar (2011) identify that the star is a CTTS with a homogeneously depleted transitional disc. In this work a transitional disc is assumed.

Target H: J101209.04−312445.3 - TWA, M4.0 - This object was confirmed as a new TWA member in Malo et al. (2014) based on consistent kinematic (RV and parallax match with their predicted values) and age indicators (Li, Hα). It has similar colours as the tranisitional discs in Taurus in all three colour-colour diagrams. There are no data beyond 25 μm, however the SED model is marginally constrained either side of the peak of the disc flux and a $f_{\rm d}/f_*$ value of 0.021 is $\sim 3\sigma$ from the threshold of 0.01. No evidence of disc presence has been recorded in the literature for this object, however, the $W1 - W4$ value of 3.01 is too large to detect $f_{\rm d}/f_* < 0.01$. Since the value of $f_{\rm d}/f_*$ is less than 0.1, the object is designated as a transitional disc, although it may turn out to be a primordial disc.

Target I: J111027.80−373152.0 - TWA, M4.0 - All three colour-colour diagrams place this object amongst Taurus transitional discs, and there is photometry available up to 90 μm. The SED fit calculates a disc temperature of 240 ± 10 K, compared with previous estimates of 301 $\pm$ 4 K, 229 K and 280 $\pm$ 5 K (Schegerer et al. 2006, Sargent et al. 2006 and Riviere-Marichalar et al. 2013, respectively). The $f_{\rm d}/f_*$ is calculated as 0.092, not indicative of a debris disc. This is within 1σ of the value calculated in Riviere-Marichalar et al. (2013) of 0.098. Schneider, Melis & Song (2012) and Dent

et al. (2013) report dusty circumstellar material, however, whether this is debris or primordial is not confirmed, although based on this analysis it is very unlikely to be a debris disc. Using Herschel PACS spectroscopy, Riviere-Marichalar et al. (2013) identify a disc 'gap' in this object, which resembles a transitional disc, and this work will presume the excess is from a transitional disc.

Target J: J111835.64−793554.8 - ϵ Cha, M4.5 - The colour-colour diagrams in Figure 6.1 all suggest this object has $K-W1$, $K-W2$ and $W1-W2$ colours typical of transitional discs in Taurus. Luhman (2007) identify this object as a WTTS, likely to be a member of ϵ Cha based on age and kinematic properties. No data are available beyond 22 μm and SED models are unable to determine the disc nature. Using IR photometry from DENIS, 2MASS, IRAC, and Spitzer MIPS and Spitzer IRS spectroscopy, Manoj et al. (2011) suggest the object has a transitional disc with a hole in the inner disc, and this work will presume the same.

Target K: J113218.24−301952.0 - TWA, M0.0 - This target is located close to Taurus transitional discs in two colour-colour diagrams ($K-W2$ and $K-W1$), but closer to the primordial sequence in $W1-W2$. The α_{K-W3} value is marginally larger than -2.0, suggesting the object is a class III source. The SED in Figure 6.4 does indicate small levels of IR excess for the WISE photometry, however there are no data for wavelengths beyond $W4$. Schneider, Melis & Song (2012) classify it as a debris disc in their TWA census, however, $W1-W4=3.64$; too large for $f_{\rm d}/f_{*}<0.01$. In this work the object is classed as a transitional disc.

Target L: J114326.57−780445.5 - ϵ Cha, M4.7 - Although all three colour-colour plots suggest this object may be a primordial disc, the SED models were not capable of identifying the disc nature due to the lack of IR data beyond 25 μm. Based on Spitzer IRS spectra and IR photometry the object is described as a class II source (consistent with the classification based on the α slopes in Figure 6.3) with a transitional disc in Manoj et al. (2011) and this designation will be used in this analysis. The $W1-W4=4.95$; too large for a debris disc.

Target M: J114931.74−785101.0 - ϵ Cha, M0.0 - All three colour-colour diagrams in Figures 6.1 show this target has colours similar to primordial discs in Taurus and

photometric/flux data are available at wavelengths up to 90 μm. The SED model is well constrained by mid-/far-IR data and a single black-body fit provides a disc temperature of 210 ± 10 K, with an $f_{\rm d}/f_*$ value of 0.475, indicative of a primordial disc. Wahhaj et al. (2010) calculate a value of 0.280 for $f_{\rm d}/f_*$. In total, 7 publications were found between 2000 and 2014 that identified a disc as part of the system. Both Brandner et al. (2000) and Luhman et al. (2008) identify it as a post-T Tauri M1 star located in the nearby Chamaeleon associtation and Murphy, Lawson & Bessell (2013) suggest that although Malo et al. (2013) characterise it as a BPMG member, its kinematics are better matched with ϵ Cha (ϵ Cha was not considered in the Malo et al. analysis). Figure 6 in Wahhaj et al. (2010) reveals distinct mid-/far-IR excess in their SED models. Simon et al. (2012) identify this target as a debris disc, however, given the large flux fraction calculated and that a $W1-W4$ colour of 6.38 would be incapable of detecting flux fractions < 0.01, this analysis predicts that the disc is primordial in nature.

Target N: J115504.71−791911.0 - ϵ Cha, M3.0 - Two colour-colour diagrams suggest that the colours of this object are similar to transitional discs in Taurus ($K-W2$ and $W1-W2$), however it appears to be more 'primordial' in the $K-W1$ diagram. The α_{K-W3} value suggests it is a class III object. No excess is identified in the SED models, and only WISE photometry is available for the source. Its $W1-W4$ value of 3.03 is too large for $f_{\rm d}/f_* < 0.01$. Both the works of Huélamo et al. (2011) and Kastner et al. (2012) identify a transitional disc around J115504.71−791911.0. This work will therefore assume that the object has a weak transitional disc.

Target O: J120055.08−782029.5 - ϵ Cha, M5.8 - In all three colour-colour diagrams (Figure 6.1) this object has colours similar to primordial discs in Taurus. Only WISE photometry was available for this target, and the SED models were incapable of distiguishing the type of excess. Fang et al. (2013) identify it as an ϵ Cha member and the globally depleted SED suggests dust settling and Spitzer IRS spectra show an optically thick primordial disc. It has a $W1-W4$ of 4.01; too large to detect $f_{\rm d}/f_* < 0.01$. A primordial disc is assumed in this analysis.

Target P: J120144.32−781926.7 - ϵ Cha, M5.0 - This object has $W1-W4 = 3.46$,

which is similar to those observed in Taurus primordial discs for all three colour-colour diagrams, and the SED shows large excess flux at both $W3$ and $W4$, although only WISE photometry is available for this source. The SED from Fang et al. (2013) looks similar to Target O and many of the disc characteristics are similar. Its $W1 - W4$ of 3.64 is too large for $f_{\rm d}/f_* < 0.01$ and this object is assumed to be an optically thick primordial disc.

Target Q: J120733.42−393254.2 - TWA, M8.0 - This target is the lowest-mass member in the sample with a $W1 - W4$ greater than 1.0 ($W1 - W4 = 3.53$) and the colour-colour diagrams in Figure 6.1 are all similar to the Taurus primordial disc sequence. Similar to target P, there is a clear excess of flux at $W3$ and $W4$, however only WISE photometry was available for it. Literature searches for any additional evidence for a disc revealed that this target was the brown dwarf 2M1207, which is host to the giant exoplanet candidate 2M1207b (Mamajek 2005; Barman et al. 2011, see §2.4.1). Riaz & Gizis (2012) suggest that 2M1207 has a transition disc with an inner disc evacuation due to grain growth/dust settling. Its $W1 - W4$ of 3.53 is too large for $f_{\rm d}/f_* < 0.01$. This work will assume it has a transitional disc.

Name WISE-	Initial	Group	$W1-W4$	Excess	α	$f_{\rm IR}/f_*$	Literature	Final
J010335.75−551556.6	A	Tuc-Hor	1.17	TTT	II	N	N/A	D
J044356.87+372302.7	B	BPMG	1.10	TTT	II	N/A	N/A	D
J084130.24−785306.3	C	η Cha	3.39	PPP	II	P/T	P	P
J084227.02−785747.7	D	η Cha	4.53	TTT	III	P/T	P	P
J084318.52−790518.0	E	η Cha	5.15	PPP	II	P	P	P
J084409.09−783345.6	F	η Cha	3.94	PPP	II	P/T	P	P
J084416.33−785907.8	G	η Cha	3.61	TPP	II	P/T	P	P
J101209.04−312445.3	H	TWA	3.01	TPP	III	P/T	N/A	T
J111027.80−373152.0	I	TWA	4.87	TTT	II	P/T	T	T
J111835.64−793554.8	J	ϵ Cha	4.95	TTT	III	N/A*	T	T
J113218.24−301952.0	K	TWA	3.64	TPT	III	N/A*	D	T
J114326.57−780445.5	L	ϵ Cha	3.12	PPP	III	N/A*	T	T
J114931.74−785101.0	M	ϵ Cha	6.38	PPP	II	P	P/D	P
J115504.71−791911.0	N	ϵ Cha	3.03	TTP	III	N/A*	T	T
J120055.08−782029.5	O	ϵ Cha	4.01	PPP	II	N/A*	P	P
J120144.32−781926.7	P	ϵ Cha	3.46	PPP	II	N/A*	P	P
J120733.42−393254.2	Q	TWA	3.53	PPP	II	N/A*	T	T

Table 6.5: Final designation for the nature of the disc excess. The excess column is based on the three criteria in the colour-colour diagrams of Figure 6.1. The entries in column 6 detect whether an object is a class II or class III source based on the α slopes calculated in §6.3. D = debris disc, P = primordial disc, T = transitional disc, N = no evidence for a disc, N/A = no information available. *Although there are no data available for SED fits beyond 25 μm the $W1 - W4$ colour is beyond the limit for a debris disc and can only be classed as either P or T.

6.6.3 Other disc candidates identified with W4 excess

A description of how flux excesses were calculated is described in §6.3. Objects with $E_{W4} > 3.0$ are considered as having disc excess. All objects with $W1 - W4 > 1.0$ had $E_{W4} > 3.0$. In addition there were 7 objects with $W1 - W4 < 1.0$ and $E_{W4} > 3.0$. In light of the sensitivity limits calculated for M-dwarfs in §6.5, these additional objects are likely to be debris discs. Of these seven objects, there is one member of η Cha, one TWA member and there are five BPMG members (one of which is AU Mic, host to a well-studied debris disc). The η Cha object is J084223.67−790402.7 (M1.8) and previous IR searches using Spitzer MIPS photometry (Gautier et al. 2008) and Herschel photometry up to 500 μm (Cieza et al. 2013) calculate $f_{\rm d}/f_* \sim 3 \times 10^{-5}$, typical of a debris disc. Based on MIPS photometry, Low et al. (2005) identify a small IR excess at 24 μm and $f_{\rm d}/f_* = 10^{-3}$ for the TWA member J104230.01−334016.4. The five BPMG members with $W1 - W4 < 1.0$ and $E_{W4} > 3.0$ are J081738.97−824328.8 (M4.5), J101726.70−535426.5 (M6.0), J171731.26−665706.8 (M3.0), J172920.64−501453.4 (M3.0) and J204509.76−312030.9 (M1.0, AU Mic). Of the BPMG objects, only AU Mic had any information in the literature pertaining to a debris disc.

SEDs were fit for the seven objects which had $W1 - W4 > 1.0$ and $E_{W4} > 3.0$ using the same procedure described in §6.4. These are all displayed in Figure 6.7. Where possible, additional data from IRAC, IRAS, MIPS and AKARI were used. As discussed in §6.4, flux fractions could only be calculated if IR data was available at longer wavelengths than the peak of the disc flux. Three out of the 7 objects had a measurable $f_{\rm d}/f_*$, all of which were less than 0.01 (J081738.97−824328.8, $f_{\rm d}/f_* = 0.003$; J171731.26−665706.8, $f_{\rm d}/f_* = 0.0004$; J204509.76−312030.9, $f_{\rm d}/f_* = 0.0003$). No flux fractions could be measured for J084223.67−790402.7 or J104230.01−334016.4, however, previous measurements are consistent with a debris disc. In all of the seven objects no evidence was found that was inconsistent with a debris disc, therefore all of these were assumed to have debris discs.

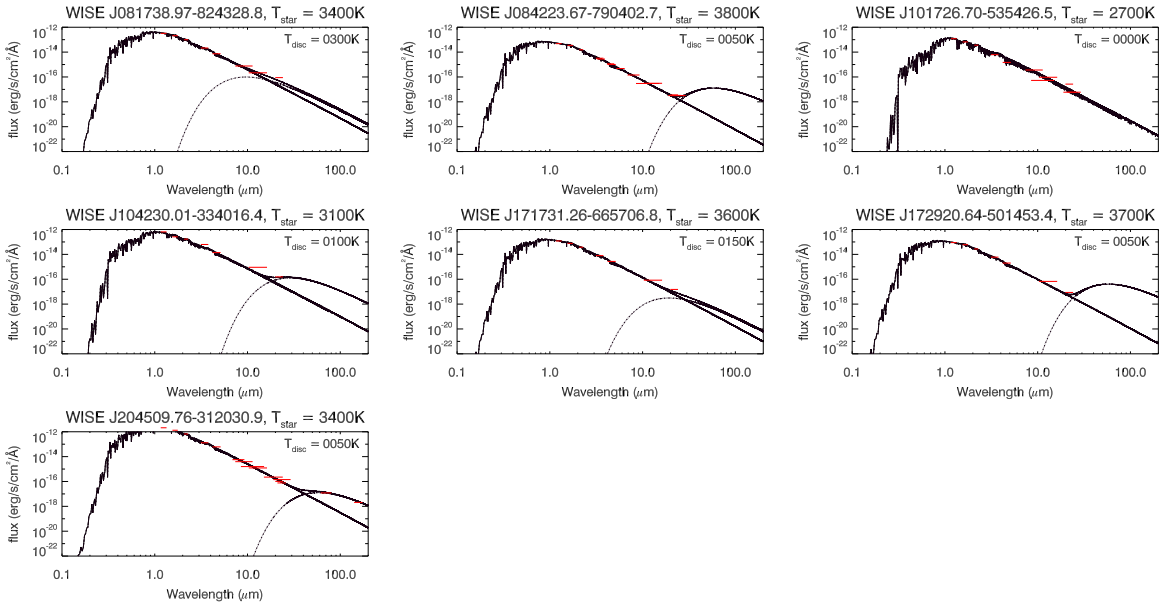

Figure 6.7: SEDs for objects with $W1 - W4 < 1.0$ and $E_{W4} > 3.0$. Only in the case of J204509.76−312030.9 was there data available beyond 25 μm. Three objects have data for wavelengths longer than the peak disc flux, therefore could have flux fractions calculated.

6.7 Discussion

Table 6.6 shows the statistics for all 292 objects analysed in this work. 151 (51 per cent) had SNR values > 5.0, of which 17 had $W1 - W4$ colours > 1.0. The colour-colour diagrams show that the majority of objects in Taurus with discs have $W1 - W4 \geq 3.0$ and, with the exception of one BPMG and one Tuc-Hor object, the $W1 - W4$ colours for all objects satisfying $W1 - W4 > 1.0$ were all larger than 3.0. A simulation revealed, however, that only objects with $W1 - W4 < 2.5$ would be expected to have $f_{\rm d}/f_* < 0.01$, typical of debris discs.

Of the 141 objects with SNR < 5.0, only one target in ϵ Cha had a $W1 - W4$ colour > 2.5 (J115054.81−741130.6), which suggests that all but one of the objects with a primoridal or transitional disc have been uncovered in this work. Only 8 objects out of the 17 investigated for disc excess had any mid-/far-IR data available at wavelengths beyond $W4$. This suggests that even for young, nearby M-dwarfs in MGs, most of them are too faint for mid-/far-IR observations beyond $25\,\mu$m.

Only 2 of the objects with $W1 - W4 > 1.0$ had $W1 - W4$ values small enough to have $f_{\rm d}/f_* < 0.01$, because the $W1 - W4$ for all other objects were too large to be debris discs. In addition, 7 objects with $W1 - W4 < 1.0$ were classed as debris discs

Name	SNR > 5			SNR < 5		
	$W1 - W4 > 1.0$	$W1 - W4 < 1.0$	Total	$W1 - W4 > 1.0$	$W1 - W4 < 1.0$	Total
ϵ Cha	6	3	9	3	5	8
η Cha	5	3	8	1	3	4
TWA	4	26	30	1	8	9
BPMG	1	34	35	0	8	8
Carina	0	8	8	1	10	11
Columba	0	2	2	0	2	2
Tuc-Hor	1	30	31	29	55	84
Argus	0	10	10	0	2	2
ABDMG	0	18	18	1	12	13
Total	17	134	151	36	105	141

Table 6.6: The statistics of objects with/without discs based on photometric and SNR criteria for the entire sample.

based on excess fluxes in $W4$ ($E_{W4} > 3.0$, see §6.6.1) and $f_{\rm d}/f_*$ (where possible). Only four MGs were found to have any debris discs; η Cha, TWA, BPMG and Tuc-Hor. In η Cha 6 out of 8 targets had discs, but only one was a debris disc, in TWA there was one debris disc and 4 transitional discs (out of 30), 6 (out of 35) BPMG objects had debris discs, and one debris disc was found in Tuc-Hor (out of 31). In ϵ Cha there were 3 transitional and 3 primordial discs found (out of 9), but no debris discs. The total fraction of MG members with debris discs identified in this chapter is 9/151 (5.96 per cent), however, it can only be used as a lower limit as it is quite possible for debris discs to avoid detection with a very small $W1 - W4$ excess. If the objects identified as transitional discs actually turned out to be debris discs, then these numbers change to 3 in ϵ Cha, 1 in η Cha, 5 in TWA, 6 in BPMG and 1 in Tuc-Hor. The total debris disc fraction would be increased to 16/151 (10.60 per cent). Only five objects have $f_{\rm d}/f_* < 0.01$, J104230.01−334016.4. If only these objects were used, then a lower limit of 5/151 (3.31 per cent) would be set.

Lestrade et al. (2009) found that out of a sample of 19 M-dwarfs younger than 200 Myr, $5.3^{+10.5}_{-5.0}$ per cent had cold debris discs, consistent with the findings in this work. Conversely, following a deep Spitzer MIPS survey of NGC 2547 (35 ± 3 Myr, Jeffries & Oliveira 2005) Forbrich et al. (2008) claim a larger debris disc fraction for M-dwarfs in NGC 2547, setting a lower limit of 4.3 per cent, although their work only uses 24 μm excesses to characterise debris discs by identifying $K - W4$ sources that are larger than the 3σ dispersion amongst Pleiades stars of similar spectral-type. This may suggest that the M-dwarf debris disc fractions are lower than FGK stars at a similar age because they are more difficult to detect. Meanwhile, in terms of MG members over spectral-types B to M, Simon et al. (2012) observe larger debris disc fractions in ϵ and η Cha (35 per cent), TWA (20 per cent) and BPMG (15 per cent), although their work only uses WISE colour excesses to define debris discs.

To test the significance of a null detection of debris discs in all MGs older than 40 Myr, one must show that enough M-dwarfs in MGs with ages > 40 Myr have been observed in order to be able to claim that there are fewer debris discs than in the younger MGs. Young and old samples were observed with similar sensitivity, so that

even if debris discs were missed at low values of $f_{\rm d}/f_*$, it is still possible to measure the fractional decline of debris discs with age amongst M-dwarfs and compare this with higher-mass stars. If there have been zero detections and the number of observations is n, then the probability of obtaining a frequency, f in n detections is $\exp(-fn)$. Taking this into account, no MGs older than 40 Myr were found to have any debris discs (see Table 6.6) in which there were 38 objects in total. The confidence to which one can claim $f < 6$ per cent is $1 - \exp(-38 \times 6/100) = 90$ per cent. In this chapter, one sample of 113 stars younger than 40 Myr were found to have 9 debris discs, whereas in the sample of stars older than 40 Myr there were zero debris disc detections in 38 objects. To test the statistical significance of this, a 2×2 chi-squared contingency test was performed on both samples. The chi-square statistic is 3.22 and the P-value is 0.07. This result rejects the null hypothesis with > 90 per cent confidence. A major finding of work in this chapter is that the time taken for disc fractions to fall from 40 to 10 per cent is 500 Myr for A-type stars, ~ 100 Myr for FGK stars, and based on this work, < 40 Myr for M-dwarfs.

Studies of the behaviour and evolution of dust around M-dwarfs suggest that the timescales for dust dissipation and the disc frequencies might be considerably different from what is observed in earlier type stars. The lack of excess around M-dwarfs has been suggested to originate from the enhanced stellar wind drag of late-type stars (Plavchan, Jura & Lipscy 2005). Stellar wind drag can dominate the Poynting-Robertson effect in removing small grains from discs around late-type stars and the remaining larger grains in the disc that the wind does not blow out would necessitate observations at longer wavelengths (Matthews et al. 2014). Stellar mass loss rates in young M-dwarfs are hard to determine but are expected to be up to 1000 times that of the current Solar wind (Wood et al. 2002) and are much larger than higher-mass stars of a similar age. Heng & Malik (2013) generate survival models to determine if a disc will survive a series of dynamical process up to a certain age and the IR excesses are computed. They attribute the lack of observed field M-dwarf debris discs identified by WISE to the sensitivity of the data to the ~ 1 AU region of the disc, where the planetesimals are not expected to persist for longer than 300 Myr. Despite this, a handful of debris discs have

been observed around old M-dwarfs (Lestrade et al. 2006; 2012).Using $f_{\rm d}/f_* < 0.01$ as the threshold for debris disc detection, Wyatt (2008) have shown that debris disc material around M0 stars are only detectable to $\sim 10\,$AU at $24\,\mu$m, whereas in A0 stars this material can be detected up to $\sim 500\,$AU. Material closer to the star will form planets or dissipate much faster (Kenyon & Bromley 2002); this could explain the lack of material detected when probing debris discs around M-dwarfs at $\sim 10\,$AU.

Recently, Gagné et al. (2015) have released a catalog of 228 candidate members of MGs with spectral-types between M4 and L6, of which there are 28 TWA, 8 BPMG and 112 Tuc-Hor candidates. Whilst these objects require membership confirmation through the means of an RV measurment, one could expect an extra ~ 1 object in TWA and ~ 4 objects in Tuc-Hor with a debris disc from this sample based on the debris disc fractions observed in in this work. M-dwarfs are ideal candidates for direct imaging surveys (see §2.2) and TWA objects have distances between ~ 40 and $90\,$pc. Observations on the 1.0" scale would be able to resolve material at $50\,$AU for a TWA object at $50\,$pc. For comparison, dusty material is observed in the β Pictoris disc out to $\sim 400\,$AU (Smith & Terrile 1984). Direct imaging surveys such as SEEDS, Gemini/NICI and PALMS (see §2.1) should be capable of resolving disc material around M-dwarfs in TWA.

6.8 Summary

In this chapter work has been carried out to identify debris discs amongst M-dwarfs in MGs. Debris discs are detected in the mid-IR where they usually outshine their parent star, therefore a photometric cut of $W1 - W4 > 1.0$ was used in the initial crtieria. However, it is difficult to identify debris discs because the size of a $W1 - W4$ excess from a debris disc around an M-dwarf is much smaller than that for a debris disc around a more massive star. There is a risk that a significant number of debris discs remain undetected because their $W1 - W4$ excess is indistinguishable from field stars.

Within these narrow detection limits several stars were identified with a modest excess; too small to be a primordial disc, and in some cases there is longer wavelength data that supports the classification as a debris disc. Without knowing how many undetected debris discs have been unaccounted for it is difficult to provide a robust M-dwarf debris disc fraction. The fraction of debris discs is small, smaller than claimed for A-K stars at similar ages, but it is hard to compare the two because of a lack of comparable sensistivity to $f_{\rm d}/f_*$ for stars for different masses. Higher-mass stars contribute less relative flux at IR wavelengths and are more easily detectable from a field star population of similar spectral-type.

For objects younger than 40 Myr, debris discs were detected in 9 out of 113 (8 per cent) and no debris discs were detected in the 38 objects older than 40 Myr. This is a significant difference and the confidence to which one can claim a detection rate of < 6 per cent in M-dwarfs older than 40 Myr is 90 per cent. Despite the sensitivity problems it is clear that the M-dwarf discs are evolving and that the evolutionary timescale for debris disc dissipation appears to be faster than for higher mass stars.

7 Conclusions and future work

"*When I heard the learn'd astronomer,*
When the proofs, the figures, were ranged in columns before me,
When I was shown the charts and diagrams, to add, divide, and
Measure them,
When I sitting heard the astronomer where he lectured with much
Applause in the lecture-room,
How soon unaccountable I became tired and sick,
Till rising and gliding out I wander'd off by myself,
In the mystical moist night-air, and from time to time,
Look'd up in perfect silence at the stars."
– Walt Whitman, Leaves of Grass

7.1 Conclusions

Optical spectroscopy has been used in this thesis to identify and characterise samples of young, nearby, low-mass stars; many of which are members of nearby MGs. Low-mass stars that belong to MGs are young and nearby, and are critically important as they offer optimal conditions to directly image sub-stellar objects (brown dwarfs, exoplanets, discs) and act as immediate empirical test studies for theoretical models of PMS evolution. Given a normal IMF and the fact that high-mass MG members have been found it was expected that there must be a low-mass accompanying population, and this work goes some way towards establishing it, though it is by no means complete.

Observations at the INT and the NOT were carried out to obtain spectroscopy of M-dwarfs that had been identified in previous surveys as candidates in either the BPMG and ABDMG (24 were taken in each). These were combined with previously confirmed candidate members in the literature and criteria based on RV and Hα (if available) confirmed 63 BPMG and 54 ABDMG members.

Objects confirmed as BPMG members with a measured Li EW were selected to locate the LDB. Absolute magnitudes were calculated using kinematic parallaxes (unless a trigonometric parallax was available) and two CMDs (M_K versus $V-K$ and M_K versus $J-K$, see §4.3.1) and an M_K versus spectral-type diagram were used to identify the LDB in BPMG. All three LDB locations provided an age of 21 ± 4 Myr, with an additional model-dependent uncertainty of only ± 1 Myr. This is older than previously thought and makes the inferred mass of very low-mass and planetary companions of BPMG members about 30 per cent larger.

Magnetic activity and star spots inflate the radii of M-dwarfs and models incorporating magnetic fields predict older LDB ages. Using the Dartmouth evolutionary models with an empirically-constrained surface magnetic field of 2.5 kG, Malo et al. (2014) report a revised LDB age of 26 ± 3 Myr at almost the same LDB luminosity as the one published in Binks & Jeffries (2014). An analysis of both works suggests that a difference of 3 Myr is due to the magnetic nature of the evolutionary model. The same procedure was used for confirmed members of ABDMG and an LDB between spectral-types M4 and M8 is identified. This results in a large LDB age range between 35 and 196 Myr which could be improved if Li measurements were made for objects in the critical mass range.

Kinematically unbiased searches for young, nearby stars provide an excellent opportunity to identify new members of existing MGs and also to discover entirely new MGs (see chapter 5). Low-mass MG members are X-ray active and have rotation periods of several days or less. An initial sample of 146 short-period FGK stars were selected for observation (§5.4). Optical spectroscopy was obtained on the NOT and the INT for the entire sample in order to assess their ages and kinematics. Twenty-six were found to be younger than 200 Myr (by assessment of their relative Li strengths compared with open clusters, see §5.6.2) and were unlikely to be spectroscopic binaries based on consistent duplicate RV measurements (named the 'likely-young sample').

The large Li EW scatter observed amongst early-K dwarfs for clusters younger than $\sim$ 200 Myr restricted the ages for the majority of the likely-young sample to between 30 and 200 Myr. Additional age estimations from Gyrochronology, Hα and

$R \sin i$ were less precise and only used to supplement the Li-derived age. The lack of a trigonometric parallax is a major limitation in measuring Galactic space velocities, and with the exception of one target, distances for objects in the likely-young sample were calculated by interpolating absolute magnitudes on isochronal tracks in an M_K versus $V - K$ CMD for an age range (see §5.7.1). The precision of photometric parallaxes depends on the reliability of the isochronal model and the precision of the age for an object, making the method less reliable than parallaxes obtained from astrometry. The majority of the likely-young sample (~ 60 per cent) had spectral-types later than K0, and Li-based age estimates become more effective between $10 - 100$ Myr for late-K/early-M stars. A future search may therefore attempt to identify generally lower-mass stars than the targets observed in this sample.

The search mechanism was 18 per cent efficient at detecting likely-single G and K-type stars younger than 200 Myr and within ~ 100 pc. The fraction of young stars that have rotation periods shorter/longer than two days are similar, suggesting that there may be no advantage to restricting the search to shorter rotation periods. The survey identified 11 stars that were similar in age and kinematics to least one MG and 15 that were not linked to any known MG. More widespread searches for MG candidates in the Northern hemisphere may provide additional useful samples of young stars, and could unveil important kinematic substructure in the solar neighbourhood. Sub-stellar objects around low-mass, nearby, young stars would provide angular and spatial resolutions and brightness contrasts capable of detection with high-resolution imaging. This work has revealed 16 objects younger than 200 Myr, within 100 pc and with spectral-types later than K0 which are ideal candidates for direct imaging surveys.

Seven objects are close in U and V velocity to the Octans-Near association (Zuckerman et al. 2013; Murphy & Lawson 2015, see §5.8.3), but are a few km s^{-1} faster on average in W velocity. Only four of these have RVs similar to their predicted RV were they part of Octans-Near. Whether or not they are connected to an MG, these seven objects occupy a kinematic sub-grouping with dispersions less than 5 km s^{-1} in all 3 velocity coordinates.

Mid- and near-IR photometry in the WISE catalog was obtained for RV-confirmed

M-dwarf members of MGs to identify IR excesses indicative of debris disc structure. To identify IR excess, a photometric cut of $W1 - W4 > 1.0$ in the WISE channels was applied and colour-colour diagrams, spectral indices and SED models with single temperature black-body fits were made to these objects to find whether the IR excess was due to a primordial, transition or a debris disc. The same criteria used in Lagrange, Backman & Artymowicz (2000) that debris discs must have $f_{\rm d}/f_* < 0.01$ was applied in this work and of the seventeen objects identified with IR excess, only 2 were found that could feasibly evidence a debris disc, both of which had $W1 - W4 \sim 1.0$; the remaining objects were found to be either transitional or primordial with $W1 - W4 > 3.0$. For the objects with $W1 - W4 < 1.0$, 7 of them had evidence of debris discs based on their $W4$ flux excess; this included the known debris disc around AU Mic. This work suggests a more restrictive cut of $W1 - W4 > 3.0$ would be more efficient at identifying primordial and transitional discs in M-dwarfs. A simulation to identify the maximum $W1 - W4$ that would result in $f_{\rm d}/f_* < 0.01$ revealed that no M-dwarfs with debris discs are expected to have $W1 - W4 \geq 2.5$.

The fraction of debris discs amongst M-dwarfs in MGs observed in this work is ~ 6 per cent, which is similar to some previous studies (Lestrade et al. 2009; Simon et al. 2012) but not as comparable with the fraction observed in a deep MIPS photometric survey of NGC 2547 members ($\sim$ 4.3 per cent based on 24 μm excesses, Forbrich et al. 2008). A number of objects may have escaped detection, however, because the $W1 - W4$ colour of debris discs around M-dwarfs may be indistinguishable from the field star sample. It is possible that a deeper photometric survey may unveil more debris discs amongst the MG members studied in this work, however they would still be limited to $W1 - W4 < 2.5$ based on the simulations in §6.5. No debris discs were observed in groups older than 40 Myr and a debris disc fraction of < 6 per cent can be stated with > 90 per cent confidence, suggesting that the dispersal timescales for debris discs in M-dwarfs is more rapid than in higher-mass stars.

The rest of this chapter focuses on the potential for future work in light of the results obtained in this thesis. §7.2 considers the opportunity to apply the LDB technique to other MGs, particularly in anticipation of spectroscopy from the Gaia ESO

Survey (GES). The potential to investigate the identity of the sample of stars possibly connected with Octans-Near is reviewed in §7.3, as well as a consideration to repeating the process in chapter 5 to identify additional nearby MGs. In §7.4 the proposal of a 'maximum-likelihood' technique to derive Li ages is presented. Astrometry from the Gaia mission and spectroscopy from the GES is anticipated for 2016 and their potential applications to improve work presented in this thesis is discussed in §7.5.

7.2 Measuring LDB ages for MGs

7.2.1 An improved LDB measurement for BPMG

In this subsection, the terms 'Li-rich' and 'Li-poor' refer to objects with Li EWs greater/less than 0.2Å (see §4.3.1). In chapter 4 an LDB age of 21 ± 4 Myr was calculated for BPMG based on optical spectroscopy of a sample of recently identified M-dwarf candidates. Whilst model-to-model variations and colour and magnitude uncertainties resulted in age errors of ~ 1 Myr, the age error bar is largely governed by the size of the gap in colour/magnitude between the lowest luminosity Li-poor ($M_K = 5.19, V-K = 5.35$) and the brightest Li-rich object ($M_K = 5.96, V-K = 5.58$) on either side of the LDB.

There are two ways to constrain the LDB age: a) identify new objects inside the LDB gap and/or b) provide improved parallaxes for objects critically near to the LDB. If additional objects are revealed to lie within this gap then any Li measurement would further constrain the LDB age (provided it is indeed a bonafide member), especially if these have parallax measurements. Gaia will provide parallaxes for all these stars, and their data release is anticipated in 2017 (see §7.5).

More recently, Malo et al. (2014) reevaluate the BPMG age to be 26 ± 3 Myr based on surface magnetic fields. Their sample of BPMG 'bonafide' objects (see their table 3) between spectral-types M4 and M5 include 2 Li-rich objects that were not present in the Binks & Jeffries (2014) analysis – one is at a spectral-type of M4.5 and

has a reported distance of 48.3 ± 3.3 pc in Riedel et al. (2014). Although neither of these targets tighten the LDB gap, they do act to *support* the LDB location and provide a more statistically significant age.

Table 4.2 shows that 2 of the 8 confirmed BPMG candidates observed in Binks & Jeffries (2014) had measured trigonometric parallaxes, both similar to their statistical parallaxes. One of these, J05015881−0958587, is the Li-poor member at M4.1 which defines the Li-poor edge of the the LDB. The Li-rich side of the LDB is defined by HIP 76629B at M4.5. This resolved binary has a parallax of 25.95 ± 1.14 mas (van Leeuwen 2007).

There are twelve RV-confirmed members in Malo et al. (2014a) with spectral-types between M1 and M5 that are yet to have any Li measurement. More recently, Gagné et al. (2015) presented 7 objects between M4.9 and M9.0 that were claimed to be likely-new members of BPMG. These are all listed in Table 7.1. Li measurements in any of these targets would be useful to identify the pattern of Li depletion amongst M-dwarf BPMG members. Figure 7.1 shows both the Malo et al. (2014a) and Gagné et al. (2015) objects on a M_K versus $V - K$ CMD with the location of the LDB in Binks & Jeffries (2014). No objects are inside the LDB box, however, Li measurements of several of the mid-M Malo et al. (2014a) objects would be useful to support the LDB location. Absolute K magnitudes have been calculated from the predicted distances in the source publication and $V - K$ magnitudes have been interpolated from $J - K$ colours if a V magnitude is not available.

Name (2MASS-)	Ref	RV ($\mathrm{km\,s^{-1}}$)	$\mathrm{RV_{pred}}$ ($\mathrm{km\,s^{-1}}$)	M_K (mag)	$V-K$ (mag)	SpT
J00172353−6645124	M14	10.7 ± 0.2	10.9	4.75	4.65	M2.5V
J01132817−3821024	M14	14.3 ± 0.5	11.9	5.28	4.17	M0.0+M1.0
J01535076−1459503	M14	10.5 ± 0.4	12.0	4.84	4.90	M3V+M3V
J08173943−8243298	M14	15.6 ± 1.5	12.8	4.43	5.03	M4*
J08224744−5726530	M14	14.7 ± 0.2	17.2	3.91	9.12	M4.5+>L0
J13545390−7121476	M14	5.7 ± 0.2	7.3	6.06	3.85	M2.5V
J16572029−5343316	M14	1.4 ± 0.2	−2.0	4.26	7.25	M3V
J18420694−5554254	M14	2.4 ± 0.5	1.2	4.92	4.95	M3.5V
J19243494−3442392	M14	−3.7 ± 0.2	−8.0	5.12	3.91	M4V
J19560294−3207186	M14	−3.7 ± 2.2	−7.8	4.41	5.19	M4V
J20013718−3313139	M14	−3.7 ± 0.2	−7.3	4.32	4.07	M1V
J23500639+2659519	M14	−0.7 ± 2.8	−5.1	7.40	3.46	M3.5V
J03445673−1145126	G15		16.9	8.63	7.38*	M6.0
J04433761+0002051	G15	17.1 ± 3.0	17.1	9.66	10.69*	M9
J08025781−8330076	G15		11.0	8.15	8.11*	M5.4
J19444417−4359015	G15		−2.9	7.47	7.99*	M4.9
J20004841−7523070	G15	11.8 ± 1.0	11.8	9.03	10.17*	M9
J20330186−4903105	G15		−0.5	8.13	7.62*	M5.6
J20334670−3733443	G15		−4.6	7.32	7.32*	M0

Table 7.1: M-dwarf BPMG candidates that lack Li measurements. M14 and G15 refer to objects selected from the Malo et al. (2014a) and Gagné et al. (2015) sample, respectively. RVs and spectral-types are from the source paper. (*) No V magnitude available - $V-K$ interpolated from $J-K$ colours using table 5 in Pecaut & Mamajek (2013).

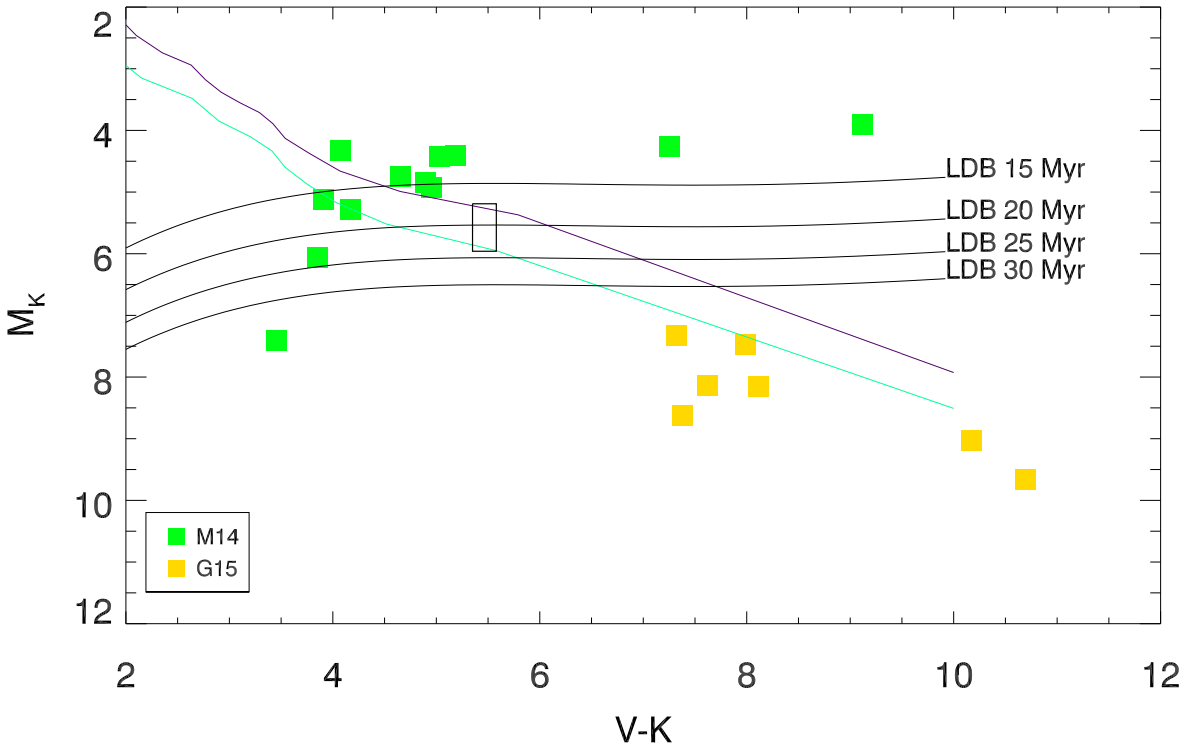

Figure 7.1: BPMG candidates in Malo et al. (2014a) and Gagné et al. (2015) which lack an Li measurement. Filled green squares represent objects from Malo et al. (2014a) and filled yellow squares are objects from Gagné et al. (2015). The LDB defined by Binks & Jeffries (2014) is given by the rectangular box. Purple and turquoise lines are the 10 and 20 Myr isochrones from Siess, Dufour & Forestini (2000), respectively.

7.2.2 An LDB age for Argus

The properties of the Argus MG are described in §2.4.5. Previous age estimates for Argus have ranged from 30 Myr (Torres et al. 2008) to 50 Myr (Barrado y Navascués, Stauffer & Jayawardhana 2004). Sixty-seven Argus candidates were intially chosen for analysis that had previously measured RVs and a spectral-type later than K0; 52 were chosen from Malo et al. (2013) and 15 from the De Silva et al. (2013) survey. Twenty-six qualified as members based on the RV criteria in §2.2.2; 13 from Malo et al. (2013) and 13 from De Silva et al. (2013). Sixteen of these also had published Li EWs in the literature – 3 from Malo et al. (2013) and all 13 from De Silva et al. (2013). Twelve new Argus candidates identified in Malo et al. (2014) satisfied the RV criteria and are overplotted as green squares in Figure 7.2. These do not have a Li EW, but would serve to constrain the LDB were a measurement to be made.

Figure 7.2 shows that the LDB in Argus is presently constrained by the Li-poor 2MASS J03033668−2535329 ($M_K = 5.05, V - K = 3.95$) and the Li-rich AP Col ($M_K = 7.25, V - K = 6.08$), which provides an LDB age of 26^{+15}_{-10} Myr using the Chabrier & Baraffe (1997) models. Presently, errors due to the size of the LDB gap are much larger than any uncertainties in magnitude/colour measurements. An Li measurement for any of the objects represented by the green squares would reduce the age uncertainty for Argus. All Argus candidates used in this analysis are listed in Table 7.2. In December 2014 and January 2015 spectroscopy has been acquired for 5 Argus candidate members using the South African Large Telescope, all of which are within the LDB gap in Figure 7.2.

Name (2MASS-)	Ref	RV ($km\,s^{-1}$)	RV_{pred} ($km\,s^{-1}$)	M_K (mag)	$V-K$ (mag)	Li EW (mÅ)	SpT
V* AP Col	M13	22.4 ± 0.3	21.2	7.25 ± 0.03	6.08 ± 0.04	280	M5V
J03033668−2535329	M14	20.1	16.1	5.05 ± 0.22	3.95 ± 0.04	0	M0.0+M6.0
J12170465−5743558	M14	−1.6 ± 0.8	−0.1	4.08 ± 0.09	3.22 ± 0.09	160	K7V
CD−29 2360	D13	26.0	22.0	3.84 ± 0.02	2.58 ± 0.04	180	K3.5V
CD−56 1438	D13	14.0	14.5	3.89 ± 0.02	2.07 ± 0.01	230	K3V
CD−43 3604	D13	21.4	17.0	3.62 ± 0.02	3.01 ± 0.05	320	K5.5V
CD−57 2315	D13	11.7	10.7	2.80 ± 0.02	2.60 ± 0.04	308	K3.5V
TYC 7695−335−1	D13	14.0	12.6	3.25 ± 0.02	2.45 ± 0.02	300	K3V
TYC 9217−641−1	D13	6.7	5.0	3.88 ± 0.02	2.52 ± 0.03	240	K3.5V
CD−39 5833	D13	15.0	11.5	3.65 ± 0.02	1.87 ± 0.01	260	G9V
CD−74 673	D13	2.0	0.2	5.02 ± 0.03	2.62 ± 0.04	230	K3.5V
CD−52 9381	D13	−13.3	−13.1	5.02 ± 0.03	3.18 ± 0.07	60	K6V
PMM 2456	D13	14.8	12.5	3.90 ± 0.02	2.59 ± 0.11	301	K3.5V
PMM 4467	D13	15.2	12.4	3.72 ± 0.02	2.10 ± 0.02	190	K2V
PMM 4636	D13	13.6	12.4	4.56 ± 0.02	3.07 ± 0.03	100	K6V
PMM 4902	D13	14.7	12.2	4.35 ± 0.02	2.70 ± 0.04	204	K4V
J05090356−4209199	M14	16.8 ± 1.7	18.5	5.03 ± 0.39	4.97 ± 0.06		M3.5V
J00503319+2449009	M14	6.0 ± 1.1	4.0	5.04 ± 0.02	5.04 ± 0.01		M3.5+M4.5
J04464970−6034109	M14	15.5 ± 3.5	12.2	4.93 ± 0.11	4.26 ± 0.05		M1.5V
J06134539−2352077	M14	22.9 ± 0.2	23.4	6.06 ± 0.26	4.93 ± 0.16		M3.5+M5
J09423823−6229028	M14	11.7 ± 0.2	7.4	6.95 ± 0.18	5.05 ± 0.01		M3.5+M3.5
J09445422−1220544	M14	13.5 ± 0.4	14.5	7.11 ± 0.12	6.15 ± 0.06		M5V
J12092998−7505400	M14	1.9 ± 0.5	0.5	4.69 ± 0.28	5.59 ± 0.16		M3V
J13591045−1950034	M13	−15.8	−10.9	5.49 ± 0.06	5.49 ± 0.04		M4.5V
J15553178+3512028	M14	−15.5 ± 0.7	−17.7	5.04 ± 0.15	5.62 ± 0.03		M4+M7
J19224278−0515536	M14	−26.3 ± 0.2	−28.3	5.48 ± 0.39	4.98 ± 0.06		K5V
J19312434−2134226	M14	−25.6 ± 1.5	−21.8	4.91 ± 0.17	4.71 ± 0.07		M2.5V
J20163382−0711456	M14	−23.0 ± 0.2	−21.2	3.81 ± 0.03	3.82 ± 0.06		M0V+M2V
J22332264−0936537	M14	−4.4 ± 1.4	−9.4	4.70 ± 0.30	4.70 ± 0.08		M3+M3
J23205766−0147373	M14	−7.2 ± 0.4	−5.1	5.20 ± 0.02	5.20 ± 0.01		M4+M4
J23532520−7056410	M14	0.6 ± 2.4	−0.0	6.60 ± 0.09	5.22 ± 0.02		M3.5V

Table 7.2: M-dwarf Argus candidates chosen for analysis. D13, M13 and M14 refer to objects selected from the De Silva et al. (2013), Malo et al. (2013) and Malo et al. (2014a) sample, respectively. RVs and spectral-types are from the source paper.

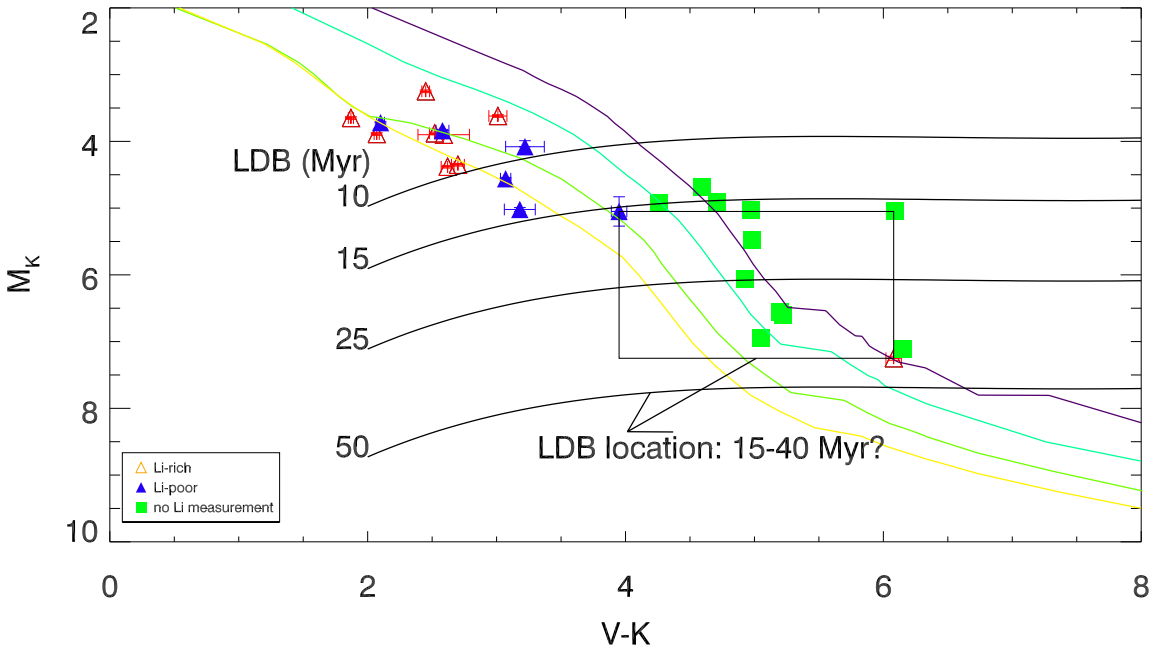

Figure 7.2: Locating the LDB in the Argus MG. Currently available RV, colour and Li measurements provide an LDB age between 15 and 40 Myr. The filled green squares represent objects from the Malo et al. (2014) sample that have been confirmed based on their RVs but do not have any Li data. Purple, turquoise, green and yellow lines are the 10, 20, 50 and 100 Myr isochrones from Siess, Dufour & Forestini (2000), respectively.

7.2.3 An LDB age for Columba

In §2.4.4.2 the properties of the Columba MG are discussed. Columba's age has been previously estimated between 20 and 40 Myr (Torres et al. 2008; Doyon et al. 2010). In an attempt to identify the LDB in Columba, candidate members cooler than K0, with a measured RV in Torres et al. (2008), Malo et al. (2013) and Malo et al. (2014a) are assessed for RV-based membership criteria and Li measurements. Only 7 RV-qualified objects have Li EW measurements, one from Torres et al. (2008), four from Malo et al. (2013) and two from Malo et al. (2014a). The lowest mass object in this sample, 2MASS J04515303−4647309 has a spectral-type M0 and is Li-poor.

All Columba candidates are listed in Table 7.3. In Figure 7.3 the Li-rich (Li-poor) objects are designated by red (or blue) triangles. Filled green squares denote the 18 M-dwarf members that satisfied RV-criteria but lack an Li measurement (1 from Malo et al. 2013 and 17 from Malo et al. 2014a). There are 15 objects with spectral-types between M3.9 and M8.0 in Gagné et al. (2015) that are claimed as likely new members but lack an RV. An Li measurement in any of these will help identify the LDB. If the age of Columba is 20 Myr, as claimed in Torres et al. (2008), then the LDB is expected to be observed at spectral-types between M4 and M5.

Name (2MASS-)	Ref	RV ($\mathrm{km\,s^{-1}}$)	$\mathrm{RV_{pred}}$ ($\mathrm{km\,s^{-1}}$)	M_K (mag)	$V-K$ (mag)	Li EW (mÅ)	SpT
BD-16 351	T08	13.4 ± 1.9	9.5	3.65 ± 0.09	2.28 ± 0.06	190	K1V
J02303239−4342232	M13	16.3 ± 1.1	15.0	3.66 ± 0.07	3.08 ± 0.05	50	K5Ve
J03241504−5901125	M13	17.5 ± 1.3	17.6	3.79 ± 0.10	3.39 ± 0.05	235	K7V
J09331427−4848331	M13	22.0 ± 0.0	20.5	4.25 ± 0.11	3.39 ± 0.06	0	K7V
J04515303−4647309	M14	24.0 ± 0.8	22.0	4.37 ± 0.22	3.41 ± 0.30	80	M0V
CD−44 753	T08	14.5 ± 2.4	15.0	3.59 ± 0.09	3.08 ± 0.05		K5V
CD−52 381	T08	14.4 ± 3.4	13.3	3.56 ± 0.12	2.55 ± 0.09		K2V
J05064991−2135091	M13	23.7 ± 1.7	22.6	2.57 ± 0.06	3.97 ± 0.04		M1Ve
J02335984−1811525	M14	12.4 ± 0.3	12.6	4.65 ± 0.12	4.76 ± 0.04		M3.0+M3.5
J03050976−3725058	M14	14.3 ± 0.6	17.0	4.30 ± 0.09	4.43 ± 0.02		M1.5+M3.0
J04091413−4008019	M14	21.3 ± 0.5	20.6	5.72 ± 0.12	5.01 ± 0.03		M3.5V
J04240094−5512223	M14	20.1 ± 0.5	20.2	4.72 ± 0.13	4.62 ± 0.03		M2.5V
J05100427−2340407	M14	24.3 ± 0.3	22.9	4.93 ± 0.24	4.67 ± 0.04		M3.0+M3.5
J05100488−2340148	M14	24.4 ± 0.2	22.9	4.73 ± 0.15	4.78 ± 0.04		M2.0+M2.5
J05111098−4903597	M14	21.2 ± 0.2	22.3	5.75 ± 0.17	4.99 ± 0.03		M3.5V
J05142736−1514514	M14	21.2 ± 0.4	22.3	5.80 ± 0.35	4.94 ± 0.04		M3.5V
J05142878−1514546	M14	21.4 ± 0.3	22.3		5.16 ± 0.03		M3.5V
J05164586−5410168	M14	21.9 ± 0.4	21.8	5.30 ± 0.16	4.63 ± 0.06		M3V
J05195695−1124440	M14	23.4 ± 0.5	21.9	4.83 ± 0.21	4.73 ± 0.04		M3.5V
J05241317−2104427	M14	24.5 ± 0.3	23.4	5.67 ± 0.28	5.06 ± 0.04		M4V
J05331130−2914199	M14	25.4 ± 0.4	24.0	5.53 ± 0.22	5.24 ± 0.02		M4V
J05395494−1307598	M14	24.9 ± 0.4	22.9		4.74 ± 0.04		M3V
J05470650−3210413	M14	21.9 ± 0.6	24.3	5.32 ± 0.19	4.75 ± 0.06		M2.5V
J06002304−4401217	M14	22.3 ± 1.6	24.9	5.52 ± 0.37	5.14 ± 0.05		M4V+M4V
J07065772−5353463	M14	22.4 ± 0.6	23.1	4.13 ± 0.14	3.75 ± 0.04		M0V

Table 7.3: M-dwarf Columba candidates satisfying RV criteria and chosen for analysis. T08, M13, M14 and G15 refer to objects selected from the Torres et al. (2008), Malo et al. (2013), Malo et al. (2014a) and Gagné et al. (2015) sample, respectively. RVs and spectral-types are from the source paper.

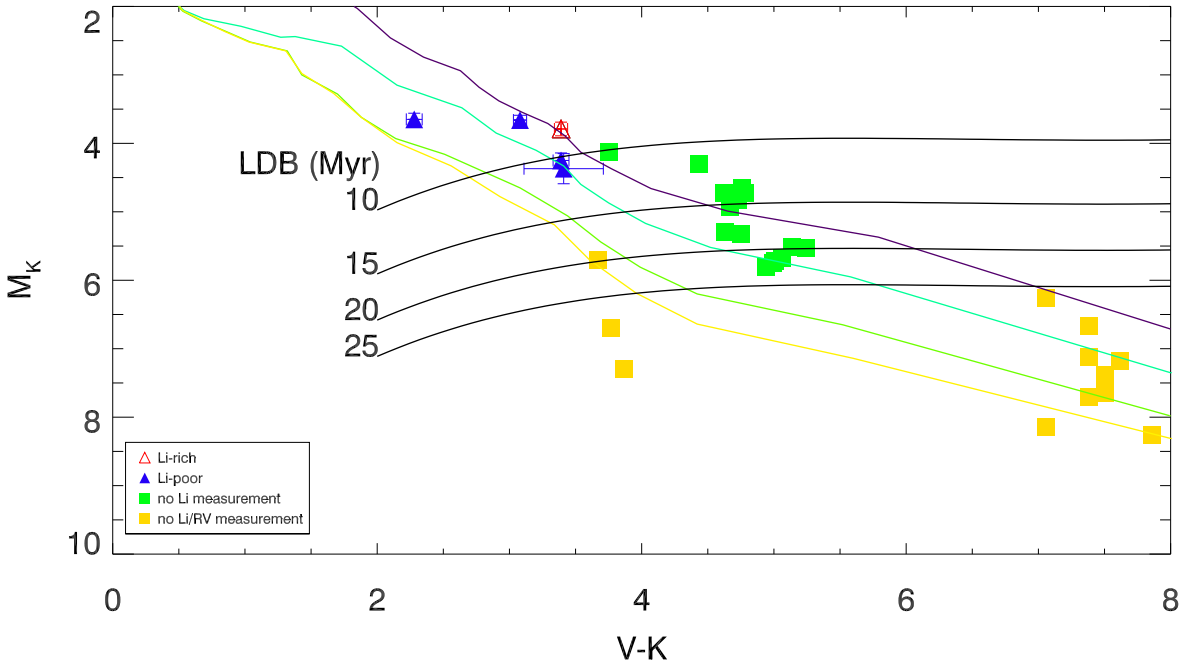

Figure 7.3: Locating the LDB in the Columba MG. Red (blue) triangles represent Li-rich (poor) objects that qualify as Columba members based on their RVs. The only M-dwarf with an Li measurement is an Li-poor object at M0. Filled green squares represent objects that have been confirmed based on their RVs but do not have any Li data. Yellow squares are from Gagné et al. (2015) and do not have an Li or an RV measurement. Purple, turquoise, green and yellow lines are the 10, 20, 50 and 100 Myr isochrones from Siess, Dufour & Forestini (2000), respectively.

7.3 Identifying the kinematics of young, nearby stars

Tentative evidence was found in §5 for a kinematic subgroup of 7 objects younger than 200 Myr with a mean UVW of $-11, -4, -5\,\mathrm{km\,s^{-1}}$; close to the Octans-Near MG, but not to any other known MGs. The Boettlinger diagrams in Figure 5.1 also indicate several objects that have do not have Galactic space velocities similar to *any* previously identified MG. X-ray active stars with periods less than 5 days were chosen from an initial catalog containing period data for 5477 objects. From this initial sample there remain 777 objects that have yet to be assessed for spectroscopic follow up that have rotation periods < 5 days and errors < 20 per cent.

Given that ~ 15 per cent of the objects in chapter 5 were later found to be younger than 200 Myr (and unlikely to be SBs) then one could expect ~ 100 similar objects from the remaining catalog entries yet to be observed. Applying the same procedure as chapter 5 for new targets will help identify the kinematic structure of nearby, young stars, particularly in the Northern hemisphere. Some searches for nearby, young stars include XYZ as a MG membership criterion (e.g., BANYAN, see §5.7.6). By defining a group besed on XYZ it often misses out on adding Northern hemisphere objects to the mix, as the majority on MG members are in the Southern hemisphere.

Although short rotation periods were chosen as an initial proxy to identify young stars, 12 objects had 2 or more RV measurements that varied by more than $5\,\mathrm{km\,s^{-1}}$, presumably as a result of binarity. It is not possible to completely rule out binarity for stars that were measured to have consistent RVs because the cadence of the observations may be on the same timescale as an orbital period for a tidally-locked binary system. A simulation showed that the probability that an object with two consistent RV measurements is actually a spectroscopic binaries with RV variations $> 5\,\mathrm{km\,s^{-1}}$ is ~ 10 per cent, although this value varies from star-to-star. The only truly robust way to rule out (or confirm) binarity is to perform multiple RV measurements over several nights to identify RV variability (if present).

Constituents of MGs must share similar chemical abundances if they are to have come from the same star-birth event. Viana Almeida et al. (2009) measure overall dispersions of < 0.1 dex for [Fe/H], [Si/H] and [Ni/H] for Solar-type stars in 6 MGs. One could therefore reason that chemical abundances for MG candidates should be no more than 0.1 dex from the mean. The Gaia ESO Survey (GES) is building up a catalogue of 100,000 abundances for field stars with magnitudes $V < 19$, and $\sim 10,000$ of these will have high-resolution spectra (Gilmore et al. 2012). The available data provides an opportunity to identify chemical sub-structure in the catalog which could form the basis of a kinematically-unbiased initial target search for MGs. Samples of chemically homogeneous stars in the catalog could be identified using a minimum spanning tree algorithm. To provide a more efficient search mechanism one could demand that objects in chemical homogeneous samples exhibited at least one property indicative of youth (e.g., short rotation period, high chromospheric and/or coronal activity). This procedure would be capable of detecting new MG members and would not preclude the discovery of new MGs.

7.4 Improved Li-based age estimates

Throughout this thesis Li has assumed a central role in estimating the ages of young, low-mass stars. Whilst the LDB method is capable of providing precise and potentially accurate ages, the use of Li at higher masses is more problematic because the development of a radiative core during the PMS phase complicates the physics of Li depletion. Model dependency is a critical issue for FGK stars and currently no evolutionary model can claim to provide accurate ages (see §1.4.3).

In spite of this, it is still possible to use Li as an *empirical* age indicator by observing the pattern of Li EW as a function of colour for young clusters of previously derived ages. Generally, one identifies an Li EW and colour for a star (or group of coeval stars) and then makes a visual comparison with the Li patterns observed in a number of clusters to estimate an age. This technique leads to objectivity issues

because ultimately the user must identify an age by eye and no statistically meaningful uncertainties for parameter estimates can be derived.

With the exception of the work by Sestito & Randich (2005), little (or perhaps no) effort has been made to place Li EWs on a more quantitative footing. By placing stars in open clusters (between ages of 5 Myr to 8 Gyr) into 3 separate temperature bins between 5500 K and 6350 K, Sestito & Randich (2005) measure the average Li abundance in each open cluster for each temperature bin. The results are provided in their table 3. This work is resticted to a narrow temperature range and a sparse number of open clusters younger than 200 Myr. A more focused, quantitative approach may provide more statistically meaningful ages and will demonstrate the relative effectiveness of Li as an age measurement at different masses and Li EWs.

The technique of fitting two dimensional model distributions has already been used for CMDs. Naylor & Jeffries (2006) present a maximum-likelihood method for fitting two dimensional models to stellar data in colour-magnitude space. Their techniques may be generalised to any two-dimensional data set, and would be applicable to the problem of fitting Li EW and $V-K$ data.

Given a set of clusters with ages known apriori, one could use the Li EW and $V-K$ (referred to as 'W' and 'C') data in each cluster to simulate empirical isochrones with a large number of data points using the mean and standard deviation value of W at a given C. One could then grid the data into bins of size ΔW and ΔC and normalise the data to produce a probability density function $\rho(\mathrm{W}, \mathrm{C})$ for each bin in a given cluster. The formal definition for the likelihood that an object with an observed W ($W_m \pm \sigma_{W_m}$) and C ($C_m \pm \sigma_{C_m}$) follows the same W and C trend as a cluster (and hence has the same age) is:

$$P = \int_{W_0}^{W_1} \int_{C_0}^{C_1} U(W - W_m, C - C_m)\rho(W, C)\, dW\, dC, \tag{7.1}$$

where U could be assumed to take the form of a 2D Gaussian probability function given by:

$$U = \exp\left\{-[(W - W_m)^2/2\sigma^2_{W_m}] - [(C - C_m)^2/2\sigma^2_{C_m}]\right\}. \quad (7.2)$$

Values for P would then be measured for clusters at different ages and a maximum-likelihood age could be derived along with appropriate confidence intervals. It is anticipated that a swathe of new homogeneously measured Li data from the GES will help provide more statistically meaningful Li-derived ages.

7.5 The potential of Gaia

The Gaia satellite, successfully launched in December 2013, is now obtaining astrometric data for ~ 1 billion stars in the Milky Way and beyond. For stars with spectral-type G0V and V magnitudes < 13, positions are expected to be measured down to precisions of $6\,\mu$as (a factor of several hundred times better than Hipparcos), proper-motions to within $5\,\mu\mathrm{as\,yr}^{-1}$ and parallaxes to within $8\,\mu$as (Lindegren et al. 2008). RV measurements will be made for ~ 150 million stars with $V < 16.5$ using the slitless radial-velocity spectrometer. The spectrometer has a resolution of $R \simeq 11,500$) and a wavelength range of $847 - 874\,$nm, which provides RV precisions of $1 - 15\,\mathrm{km\,s}^{-1}$ for a range of spectral-types. An object of spectral-type M6 at $V = 15$ is expected to provide a parallax precision of $9.6\,\mu$as and a K1 star at $V = 13.5$ is expected to have an RV precision of $0.6\,\mathrm{km\,s}^{-1}$.

The completeness of Gaia down to $V \sim 20$ is expected to provide parallaxes for *all* of the objects considered in this thesis. Significantly improved parallaxes and proper motion will improve on work in this thesis in the following respects:

•Many objects that qualified as BPMG or ABDMG members in chapter 4 did not have a parallax measurement. Gaia is expected to provide parallaxes to precisions of less than $10\,\mu$as and these could be utilised to provide kinematic membership tests

based on Equation 2.3. A CMD for BPMG and ABDMG objects with precise parallaxes can serve as an empirical isochrone at their respective ages and can provide a test for PMS evolutionary models. The location of the LDB in BPMG in chapter 4 is defined between two objects which both have previously measured parallaxes precise to several mas. A more precise parallax could lead to a slightly improved LDB age, however, the LDB uncertainty would remain dominated by the size of the gap between the dimmest Li-poor objects and the brightest Li-rich object. Recent surveys to identify low-mass stars in MGs have revealed hundreds of 10^{th} to 15^{th} magnitude M-dwarf candidates that require parallaxes to confirm their membership. These could be followed up spectroscopically to measure their RV and Li content.

•The main uncertainty in calculating UVW is usually due to the lack of a parallax measurement. Only 2 objects in the young sample in §5 had a trigonometric parallax, the rest were based on their estimated age range (see §5.7.1). Results from Gaia are expected to include precise parallaxes for all of the young stars included in the sample in chapter 5 and would significantly improve the Boettlinger diagrams in Figure 5.1, particularly for the youngest stars because the errors would only be from the projected components of the RV error. High-precision parallax data from Gaia would also provide improved XYZ positional data with which kinematic trace-back ages could be established. The membership criteria for MGs in chapter 5 does not take into account tangential velocities or XYZ positions, which rely on accurate parallaxes (see §2.2). A thorough examination of MG membership status should account for some minimum spatial volume occupied by the MG. Gaia astrometry would be able to test these extra criteria and examine the hypothesis that the MGs are not single entities, as hinted at by the lack of chemical coherence in the ABDMG.

Bibliography

Allard F., Homeier D., Freytag B., 2012, Royal Society of London Philosophical Transactions Series A, 370, 2765

Allard F., 2014, in Booth, M., Matthews, B. C., and Graham, J. R., eds., IAU Symp. 299, Exploring the formation and evolution of planetary systems, 271

Allers K. N., Jaffe D. T., Luhman K. L., Liu M. C., Wilson J. C., Skrutskie M. F., Nelson M., Peterson D. E., Smith J. D., Cushing M. C., 2007, Astrophysical Journal, 657, 511

Alonso A., Arribas S., Martinez-Roger C., 1996, Astronomy and Astrophysics, 313, 873

Ammler-von Eiff M., Guenther E. W., 2009, Astronomy and Astrophysics, 508, 677

Anders G. J., Coates D. W., Jeffries R. D., Kellett B. J., 1993, Monthly Notices of the RAS, 265, 941

Anderson E., Francis C., 2012, Astronomy Letters, 38, 331

André P., Ward-Thompson D., Barsony M., 1993, Astrophysical Journal, 406, 122

André P., Ward-Thompson D., Barsony M., 2000, in Mannings, V., Boss, A. P., Russell, S. S., eds., Protostars and Planets IV, 59

Asplund M., Grevesse N., Sauval A. J., Scott P., 2009, Annual Review of Astron and Astrophys, 47, 481

Augereau J.-C., Beust H., 2006, Astronomy and Astrophysics, 455, 987

Avenhaus H., Schmid H. M., Meyer M. R., 2012, Astronomy and Astrophysics, 548, A105

Backman D. E., Paresce F., 1993, in Levy E. H., Lunine J. I., eds., Protostars and Planets III, 1253

Baker J., Bizzarro M., Wittig N., Connelly J., Haack H., 2005, Nature, 436, 1127

Bally J., Reipurth B., 2006, The Birth of Stars and Planets, Cambridge University Press

Baraffe I., Chabrier G., Allard F., Hauschildt P. H., 1998, Astronomy and Astrophysics, 337, 403

Baraffe I., Chabrier G., Allard F., Hauschildt P. H., 2002, Astronomy and Astrophysics, 382, 563

Baraffe I., Chabrier G., Barman T. S., Allard F., Hauschildt P. H., 2003, Astronomy and Astrophysics, 402, 701

Baraffe I., Chabrier G., Gallardo J., 2009, Astrophysical Journal, Letters, 702, L27

Baraffe I., Chabrier G., 2010, Astronomy and Astrophysics, 521, A44

Baraffe I., Vorobyov E., Chabrier G., 2012, Astrophysical Journal, 756, 118

Barber S. D., Patterson A. J., Kilic M., Leggett S. K., Dufour P., Bloom J. S., Starr D. L., 2013, in Krzesiń, ski J., Stachowski G., Moskalik P., Bajan K., eds., 18th European White Dwarf Workshop. 457

Barenfeld S. A., Bubar E. J., Mamajek E. E., Young P. A., 2013, Astrophysical Journal, 766, 6

Barman T. S., Macintosh B., Konopacky Q. M., Marois C., 2011, Astrophysical Journal, Letters, 735, L39

Barnes S. A., 2003, Astrophysical Journal, 586, 464

Barnes S. A., 2007, Astrophysical Journal, 669, 1167

Barnes S. A., 2009, in Mamajek E. E., Soderblom D. R., Wyse R. F. G., eds., IAU Symp. 258, The Ages of Stars, 345

Barnes S. A., Kim Y.-C., 2010, Astrophysical Journal, 721, 675

Barrado y Navascués D., Stauffer J. R., Song I., Caillault J.-P., 1999, Astrophysical Journal, Letters, 520, L123

Barrado y Navascués D., Deliyannis C. P., Stauffer J. R., 2001, Astrophysical Journal, 549, 452

Barrado y Navascués D., Stauffer J. R., Jayawardhana R., 2004, Astrophysical Journal, 614, 386

Barrado y Navascués D., 2006, Astronomy and Astrophysics, 459, 511

Barry D. C., Cromwell R. H., Hege E. K., 1987, Astrophysical Journal, 315, 264

Barsony M., Kenyon S. J., 1992, Astrophysical Journal, Letters, 384, L53

Basri G., Marcy G. W., Graham J. R., 1996, Astrophysical Journal, 458, 600

Basri G., 1997, Mem. Societa Astronomica Italiana, 68, 917

Belikov A. N., Kharchenko N. V., Piskunov A. E., Schilbach E., Scholz R.-D., Yatsenko A. I., 2002, Astronomy and Astrophysics, 384, 145

Bell C. P. M., Naylor T., Mayne N. J., Jeffries R. D., Littlefair S. P., 2013, Monthly Notices of the RAS, 434, 806

Bertelli G., Nasi E., Girardi L., Marigo P., 2009, Astronomy and Astrophysics, 508, 355

Biazzo K., Alcalá J. M., Covino E., Sterzik M. F., Guillout P., Chavarría-K. C., Frasca A., Raddi R., 2012, Astronomy and Astrophysics, 542, A115

Bildsten L., Brown E. F., Matzner C. D., Ushomirsky G., 1997, Astrophysical Journal, 482, 442

Biller B., Artigau É., Wahhaj Z., Hartung M., Liu M. C., Close L. M., Chun M. R., Ftaclas C., Toomey D. W., Hayward T., 2008, in Hubin N., Max C. E., Wizinowich, P. L., eds., Society of Photo-Optical Instrumentation Engineers (SPIE) Conf. 7015., 70156Q

Biller B. A., Liu M. C., Wahhaj Z., Nielsen E. L., Close L. M., Dupuy T. J., Hayward T. L., Burrows A., Chun M., Ftaclas C., Clarke F., Hartung M., Males J., Reid I. N., Shkolnik E. L., Skemer A., Tecza M., Thatte N., Alencar S. H. P., Artymowicz P., Boss A., de Gouveia Dal Pino E., Gregorio-Hetem J., Ida S., Kuchner M. J., Lin D., Toomey D., 2010, Astrophysical Journal, Letters, 720, L82

Biller B. A., Liu M. C., Wahhaj Z., Nielsen E. L., Hayward T. L., Males J. R., Skemer A., Close L. M., Chun M., Ftaclas C., Clarke F., Thatte N., Shkolnik E. L., Reid I. N., Hartung M., Boss A., Lin D., Alencar S. H. P., de Gouveia Dal Pino E., Gregorio-Hetem J., Toomey D., 2013, Astrophysical Journal, 777, 160

Binks A. S., Jeffries R. D., 2014, Monthly Notices of the RAS, 438, L11

Blaauw A., 1952, Bulletin Astronomical Institute of the Netherlands, 11, 414

Blaauw A., 1978, in L. V. Mizoyan, ed, (Yeravan: Armenian Academy of Sciences), 101

Bodenheimer P., 1965, Publications of the ASP, 77, 124

Boesgaard A. M., Tripicco M. J., 1986, Astrophysical Journal, 303, 724

Böhm-Vitense E., 1958, Zeitschrift fuer Astrophysik, 46, 108

Böhm-Vitense E., 1992, Journal of the British Astronomical Association, 102, 109

Bonnefoy M., Lagrange A.-M., Boccaletti A., Chauvin G., Apai D., Allard F., Ehrenreich D., Girard J. H. V., Mouillet D., Rouan D., Gratadour D., Kasper M., 2011, Astronomy and Astrophysics, 528, L15

Bonnefoy M., Boccaletti A., Lagrange A.-M., Allard F., Mordasini C., Beust H., Chauvin G., Girard J. H. V., Homeier D., Apai D., Lacour S., Rouan D., 2013, Astronomy and Astrophysics, 555, A107

Bonnefoy M., Boccaletti A., Lagrange A.-M., Allard F., Mordasini C., Beust H., Chauvin G., Girard J. H. V., Homeier D., Apai D., Lacour S., Rouan D., Rameau J., Klahr H., 2014, in Booth M., Matthews B. C., Graham J. R., eds., IAU Symp. 299, Exploring the formation and evolution of planetary systems, 241

Boss A. P., 1998, Earth Moon and Planets, 81, 19

Boss A. P., 2003, Astrophysical Journal, 599, 577

Bouvier J., 2007, in Bouvier J., Appenzeller I., eds., IAU Symp. 243, Star-Disk Interaction in Young Stars, 231

Bouvier J., 2013, in Hennebelle P., Charbonnel C., eds.,.EAS Publications Series Vol. 62, Role and Mechanisms of Angular Momentum Transport During the Formation and Early Evolution of Stars, 143

Bouvier J., Matt S. P., Mohanty S., Scholz A., Stassun K. G., Zanni C., 2014, in Mannings, V., Boss, A. P., Russell, S. S., eds., Protostars and Planets IV, 433

Bowler B. P., Liu M. C., Shkolnik E. L., Dupuy T. J., Cieza L. A., Kraus A. L., Tamura M., 2012, Astrophysical Journal, 753, 142

Bowler B. P., Liu M. C., Shkolnik E. L., Tamura M., 2015, Astrophysical Journal, Supplement, 216, 7

Bozhinova I., Helling C., Stark C., 2013, Mem. Societa Astronomica Italiana, 84, 1094

Brandner W., Zinnecker H., Alcalá J. M., Allard F., Covino E., Frink S., Köhler R., Kunkel M., Moneti A., Schweitzer A., 2000, Astronomical Journal, 120, 950

Brandt T. D., Kuzuhara M., McElwain M. W., Schlieder J. E., Wisniewski J. P., Turner E. L., Carson J., Matsuo T., Biller B., Bonnefoy M., Dressing C., Janson M., Knapp G. R., Moro-Martín A., Thalmann C., Kudo T., Kusakabe N., Hashimoto J., Abe L., Brandner W., Currie T., Egner S., Feldt M., Golota T., Goto M., Grady C. A., Guyon O., Hayano Y., Hayashi M., Hayashi S., Henning T., Hodapp K. W., Ishii M., Iye M., Kandori R., Kwon J., Mede K., Miyama S., Morino J.-I., Nishimura T., Pyo T.-S., Serabyn E., Suenaga T., Suto H., Suzuki R., Takami M., Takahashi Y., Takato N., Terada H., Tomono D., Watanabe M., Yamada T., Takami H., Usuda T., Tamura M., 2014, Astrophysical Journal, 786, 1

Bressan A., Marigo P., Girardi L., Salasnich B., Dal Cero C., Rubele S., Nanni A., 2012, Monthly Notices of the RAS, 427, 127

Brown T. M., 2014, Astrophysical Journal, 789, 101

Brown A. G. A., Dekker G., de Zeeuw P. T., 1997, Monthly Notices of the RAS, 285, 479

Burke C. J., Pinsonneault M. H., Sills A., 2004, Astrophysical Journal, 604, 272

Burrows A., Marley M., Hubbard W. B., Lunine J. I., Guillot T., Saumon D., Freedman R., Sudarsky D., Sharp C., 1997, Astrophysical Journal, 491, 856

Burrows A., Hubbard W. B., Lunine J. I., Liebert J., 2001, Reviews of Modern Physics, 73, 719

Butters O. W., West R. G., Anderson D. R., Collier Cameron A., Clarkson W. I., Enoch B., Haswell C. A., Hellier C., Horne K., Joshi Y., Kane S. R., Lister T. A., Maxted P. F. L., Parley N., Pollacco D., Smalley B., Street R. A., Todd I., Wheatley P. J., Wilson D. M., 2010, Astronomy and Astrophysics, 520, L10

Cameron A. G. W., 1978, Moon and Planets, 18, 5

Canto Martins B. L., Lèbre A., Palacios A., de Laverny P., Richard O., Melo C. H. F., Do Nascimento, Jr. J. D., de Medeiros J. R., 2011, Astronomy and Astrophysics, 527, A94

Cargile P. A., James D. J., 2010, Astronomical Journal, 140, 677

Cargile P. A., James D. J., Jeffries R. D., 2010, Astrophysical Journal, Letters, 725, L111

Carlsson M., Rutten R. J., Bruls J. H. M. J., Shchukina N. G., 1994, Astronomy and Astrophysics, 288, 860

Carmona A., van den Ancker M. E., Henning T., Pavlyuchenkov Y., Dullemond C. P., Goto M., Fedele D., Stecklum B., Thi W.-F., Bouwman J., Waters L. B. F. M., 2008, in Sun Y.-S., Ferraz-Mello S., Zhou J.-L., eds, IAU Symp. 249, Exoplanets: Detection, Formation and Dynamics, 359

Carpenter J. M., Mamajek E. E., Hillenbrand L. A., Meyer M. R., 2009, Astrophysical Journal, 705, 1646

Casagrande L., Ramírez I., Meléndez J., Bessell M., Asplund M., 2010, Astronomy and Astrophysics, 512, A54

Casagrande L., Portinari L., Glass I. S., Laney D., Silva Aguirre V., Datson J., Andersen J., Nordström B., Holmberg J., Flynn C., Asplund M., 2014, Monthly Notices of the RAS, 439, 2060

Cayrel de Strobel G., Spite M., 1988, in Cayrel de Strobel G., Spite M., eds., IAU Symp. 132, The Impact of Very High S/N Spectroscopy on Stellar Physics, 345

Chaboyer B., Demarque P., Pinsonneault M. H., 1995, Astrophysical Journal, 441, 876

Chabrier G., Baraffe I., 1997, Astronomy and Astrophysics, 327, 1039

Chabrier G., Baraffe I., 2000, Annual Review of Astron and Astrophys, 38, 337

Chabrier G., Gallardo J., Baraffe I., 2007, Astronomy and Astrophysics, 472, L17

Chambers J. E., 2001, Icarus, 152, 205

Charbonnel C., Talon S., 2005, Science, 309, 2189

Chauvin G., Lagrange A.-M., Dumas C., Zuckerman B., Mouillet D., Song I., Beuzit J.-L., Lowrance P., 2004, Astronomy and Astrophysics, 425, L29

Chubak C., Marcy G., Fischer D. A., Howard A. W., Isaacson H., Johnson J. A., Wright J. T., 2012, ArXiv e-prints (arXiv:1207.6212)

Cieza L. A., Schreiber M. R., Romero G. A., Williams J. P., Rebassa-Mansergas A., Merín B., 2012, Astrophysical Journal, 750, 157

Cieza L. A., Olofsson J., Harvey P. M., Evans, II N. J., Najita J., Henning T., Merín B., Liebhart A., Güdel M., Augereau J.-C., Pinte C., 2013, Astrophysical Journal, 762, 100

Clem J. L., VandenBerg D. A., Grundahl F., Bell R. A., 2004, Astronomical Journal, 127, 1227

Close L. M., Lenzen R., Guirado J. C., Nielsen E. L., Mamajek E. E., Brandner W., Hartung M., Lidman C., Biller B., 2005, Nature, 433, 286

Cohen M., Wheaton W. A., Megeath S. T., 2003, Astronomical Journal, 126, 1090

Collier Cameron A., Davidson V. A., Hebb L., Skinner G., Anderson D. R., Christian D. J., Clarkson W. I., Enoch B., Irwin J., Joshi Y., Haswell C. A., Hellier C., Horne K. D., Kane S. R., Lister T. A., Maxted P. F. L., Norton A. J., Parley N., Pollacco D., Ryans R., Scholz A., Skillen I., Smalley B., Street R. A., West R. G., Wilson D. M., Wheatley P. J., 2009, Monthly Notices of the RAS, 400, 451

Covey K. R., Lada C. J., Román-Zúñiga C., Muench A. A., Forbrich J., Ascenso J., 2010, Astrophysical Journal, 722, 971

Cummings J. D., Deliyannis C. P., Anthony-Twarog B., Twarog B., Maderak R. M., 2012, Astronomical Journal, 144, 137

Currie T., Kenyon S. J., Balog Z., Rieke G., Bragg A., Bromley B., 2008, Astrophysical Journal, 672, 558

Currie T., Kenyon S. J., 2009, Astronomical Journal, 138, 703

Currie T., Sicilia-Aguilar A., 2011, Astrophysical Journal, 732, 24

Cutri R. M., Skrutskie M. F., van Dyk S., Beichman C. A., Carpenter J. M., Chester T., Cambresy L., Evans T., Fowler J., Gizis J., Howard E., Huchra J., Jarrett T., Kopan E. L., Kirkpatrick J. D., Light R. M., Marsh K. A., McCallon H., Schneider S., Stiening R., Sykes M., Weinberg M., Wheaton W. A., Wheelock S., Zacarias N., 2003, 2MASS All Sky Catalog of point sources.. Available at `http://www.ipac.caltech.edu/2MASS/`, ed. Cutri R. M., et al.

Da Rio N., Gouliermis D. A., Gennaro M., 2010, Astrophysical Journal, 723, 166

da Silva L., Torres C. A. O., de La Reza R., Quast G. R., Melo C. H. F., Sterzik M. F., 2009, Astronomy and Astrophysics, 508, 833

Dahm S. E., Hillenbrand L. A., 2007, Astronomical Journal, 133, 2072

Dahm S. E., Simon T., 2005, Astronomical Journal, 129, 829

D'Antona F., Mazzitelli I., 1997, Mem. Societa Astronomica Italiana, 68, 807

de Bruijne J. H. J., Eilers A.-C., 2012, Astronomy and Astrophysics, 546, A61

de la Reza R., Torres C. A. O., Quast G., Castilho B. V., Vieira G. L., 1989, Astrophysical Journal, Letters, 343, L61

de la Reza R., da Silva L., Jilinski E., Torres C. A. O., Quast G., 2001, in Jayawardhana R., Greene T., eds., ASP Conf. 244., Young Stars Near Earth: Progress and Prospects, 37

de la Reza R., Jilinski E., Ortega V. G., 2006, Astronomical Journal, 131, 2609

De Silva G. M., D'Orazi V., Melo C., Torres C. A. O., Gieles M., Quast G. R., Sterzik M., 2013, Monthly Notices of the RAS, 431, 1005

Delorme P., Gagné J., Malo L., Reylé C., Artigau E., Albert L., Forveille T., Delfosse X., Allard F., Homeier D., 2012, Astronomy and Astrophysics, 548, A26

Delorme P., Gagné J., Girard J. H., Lagrange A. M., Chauvin G., Naud M.-E., Lafrenière D., Doyon R., Riedel A., Bonnefoy M., Malo L., 2013, Astronomy and Astrophysics, 553, L5

Demarque P. R., Larson R. B., 1964, Astronomical Journal, 69, 136

Demarque P., Woo J.-H., Kim Y.-C., Yi S. K., 2004, Astrophysical Journal, Supplement, 155, 667

Denissenkov P. A., Pinsonneault M., Terndrup D. M., Newsham G., 2010, Astrophysical Journal, 716, 1269

Dent W. R. F., Thi W. F., Kamp I., Williams J. P., Menard F., Andrews S., Ardila D., Aresu G., Augereau J.-C., Barrado y Navascues D., Brittain S., Carmona A., Ciardi D., Danchi W., Donaldson J., Duchene G., Eiroa C., Fedele D., Grady C., de Gregorio-Molsalvo I., Howard C., Huélamo N., Krivov A., Lebreton J., Liseau R., Martin-Zaidi C., Mathews G., Meeus G., Mendigutía I., Montesinos B., Morales-Calderon M., Mora A., Nomura H., Pantin E., Pascucci I., Phillips N., Pinte C., Podio L., Ramsay S. K., Riaz B., Riviere-Marichalar P., Roberge A., Sandell G., Solano E., Tilling I., Torrelles J. M., Vandenbusche B., Vicente S., White G. J., Woitke P., 2013, Publications of the ASP, 125, 477

Desidera S., Covino E., Messina S., D'Orazi D'Orazi V., Alcalá J. M., Brugaletta E., Carson J., Lanzafame A. C., Launhardt R., 2011, Astronomy and Astrophysics, 529, A54

Do Nascimento J. D., da Costa J. S., de Medeiros J. R., 2010, Astronomy and Astrophysics, 519, A101

Dobbie P. D., Lodieu N., Sharp R. G., 2010, Monthly Notices of the RAS, 409, 1002

Dotter A., Chaboyer B., Jevremović D., Kostov V., Baron E., Ferguson J. W., 2008, Astrophysical Journal, Supplement, 178, 89

Doyon R., Lafrenière D., Artigau E., Malo L., Marois C., 2010, p. In the Spirit of Lyot 2010, Direct Detection of Exoplanets and Circumstellar Disks, 42

Ducourant C., Teixeira R., Périé J. P., Lecampion J. F., Guibert J., Sartori M. J., 2005, Astronomy and Astrophysics, 438, 769

Ducourant C., Teixeira R., Galli P. A. B., Le Campion J. F., Krone-Martins A., Zuckerman B., Chauvin G., Song I., 2014, Astronomy and Astrophysics, 563, A121

Durisen R. H., Boss A. P., Mayer L., Nelson A. F., Quinn T., Rice W. K. M., 2007, in Reipurth B., Jewitt D., Keil K., eds., Protostars and Planets V, 607

Durney B. R., Latour J., 1977, Geophysical and Astrophysical Fluid Dynamics, 9, 241

Eggen O. J., 1958, Monthly Notices of the RAS, 118, 65

Eggen O. J., 1961, Royal Greenwich Observatory Bulletins, 41, 245

Eggen O. J., 1965, in Blaauw A., Schmidt M., eds, Galactic Structure, 111

Eggen O. J., 1965a, Annual Review of Astron and Astrophys, 3, 235

Eggen O. J., 1995, Astronomical Journal, 110, 1749

Ekström S., Georgy C., Eggenberger P., Meynet G., Mowlavi N., Wyttenbach A., Granada A., Decressin T., Hirschi R., Frischknecht U., Charbonnel C., Maeder A., 2012, Astronomy and Astrophysics, 537, A146

Elliott P., Bayo A., Melo C. H. F., Torres C. A. O., Sterzik M., Quast G. R., 2014, Astronomy and Astrophysics, 568, A26

Elmegreen B. G., Efremov Y. N., 1996, Astrophysical Journal, 466, 802

Epstein C. R., Pinsonneault M. H., 2014, Astrophysical Journal, 780, 159

Espaillat C., Furlan E., D'Alessio P., Sargent B., Nagel E., Calvet N., Watson D. M., Muzerolle J., 2011, Astrophysical Journal, 728, 49

Esplin T. L., Luhman K. L., Mamajek E. E., 2014, Astrophysical Journal, 784, 126

Evans, II N. J., Dunham M. M., Jørgensen J. K., Enoch M. L., Merín B., van Dishoeck E. F., Alcalá J. M., Myers P. C., Stapelfeldt K. R., Huard T. L., Allen L. E., Harvey P. M., van Kempen T., Blake G. A., Koerner D. W., Mundy L. G., Padgett D. L., Sargent A. I., 2009, Astrophysical Journal, Supplement, 181, 321

Fabricius C., Høg E., Makarov V. V., Mason B. D., Wycoff G. L., Urban S. E., 2002, Astronomy and Astrophysics, 384, 180

Faherty J. K., Burgasser A. J., Walter F. M., Van der Bliek N., Shara M. M., Cruz K. L., West A. A., Vrba F. J., Anglada-Escudé G., 2012, Astrophysical Journal, 752, 56

Fang M., van Boekel R., Bouwman J., Henning T., Lawson W. A., Sicilia-Aguilar A., 2013, Astronomy and Astrophysics, 549, A15

Favata F., Barbera M., Micela G., Sciortino S., 1995, Astronomy and Astrophysics, 295, 147

Favata F., Micela G., Baliunas S. L., Schmitt J. H. M. M., Güdel M., Harnden, Jr. F. R., Sciortino S., Stern R. A., 2004, Astronomy and Astrophysics, 418, L13

Feiden G. A., Chaboyer B., 2012, Astrophysical Journal, 757, 42

Feiden G. A., Chaboyer B., 2013, Astrophysical Journal, 779, 183

Feiden G. A., Chaboyer B., 2014, Astrophysical Journal, 789, 53

Feigelson E. D., 1996, Astrophysical Journal, 468, 306

Feigelson E. D., Montmerle T., 1999, Annual Review of Astron and Astrophys, 37, 363

Feigelson E. D., Lawson W. A., Garmire G. P., 2003, Astrophysical Journal, 599, 1207

Fernández D., Figueras F., Torra J., 2008, Astronomy and Astrophysics, 480, 735

Fischer D. A., Marcy G. W., 1992, Astrophysical Journal, 396, 178

Flaccomio E., Micela G., Sciortino S., 2003, Astronomy and Astrophysics, 402, 277

Flaccomio E., Micela G., Sciortino S., 2012, Astronomy and Astrophysics, 548, A85

Forbrich J., Lada C. J., Muench A. A., Teixeira P. S., 2008, Astrophysical Journal, 687, 1107

Frasca A., Fröhlich H.-E., Bonanno A., Catanzaro G., Biazzo K., Molenda-Żakowicz J., 2011, Astronomy and Astrophysics, 532, A81

Fuchs B., Breitschwerdt D., de Avillez M. A., Dettbarn C., Flynn C., 2006, Monthly Notices of the RAS, 373, 993

Gagné J., Lafrenière D., Doyon R., Malo L., Artigau É., 2014, Astrophysical Journal, 783, 121

Gagné J., Faherty J. K., Cruz K., Lafrenière D., Doyon R., Malo L., Artigau É., 2014, Astrophysical Journal, Letters, 785, L14

Gagné J., Lafrenière D., Doyon R., Malo L., Artigau É., 2015, Astrophysical Journal, 798, 73

Gallet F., Bouvier J., 2013, Astronomy and Astrophysics, 556, A36

Gálvez-Ortiz M. C., Kuznetsov M., Clarke J. R. A., Pavlenko Y. V., Folkes S. L., Pinfield D. J., Jones H. R. A., Jenkins J. S., Barnes J. R., Burningham B., Day-Jones A. C., Martín E. L., García Pérez A. E., del Burgo C., Pokorny R. S., 2014, Monthly Notices of the RAS, 439, 3890

Gautier, III T. N., Rebull L. M., Stapelfeldt K. R., Mainzer A., 2008, Astrophysical Journal, 683, 813

Georgy C., Granada A., Ekström S., Meynet G., Anderson R. I., Wyttenbach A., Eggenberger P., Maeder A., 2014, Astronomy and Astrophysics, 566, A21

Gilmore G., Randich S., Asplund M., Binney J., Bonifacio P., Drew J., Feltzing S., Ferguson A., Jeffries R., Micela G., Negueruela I., Prusti T., Rix H.-W., Vallenari A., Alfaro E., Allende-Prieto C., Babusiaux C., Bensby T., Blomme R., Bragaglia A., Flaccomio E., François P., Irwin M., Koposov S., Korn A., Lanzafame A., Pancino E., Paunzen E., Recio-Blanco A., Sacco G., Smiljanic R., Van Eck S., Walton N., 2012, The Messenger, 147, 25

Girard T. M., van Altena W. F., Zacharias N., Vieira K., Casetti-Dinescu D. I., Castillo D., Herrera D., Lee Y. S., Beers T. C., Monet D. G., López C. E., 2011, Astronomical Journal, 142, 15

Girardi L., Eggenberger P., Miglio A., 2011, Monthly Notices of the RAS, 412, L103

Gizis J. E., 1997, Astronomical Journal, 113, 806

Gizis J. E., Reid I. N., Hawley S. L., 2002, Astronomical Journal, 123, 3356

Glebocki R., Gnacinski P., 2005, VizieR Online Data Catalog, 3244

Gliese W., Jahreiss H., 1991, NASA STI/Recon Technical Report A, 92, 33932

Golimowski D. A., Ardila D. R., Krist J. E., Clampin M., Ford H. C., Illingworth G. D., Bartko F., Benítez N., Blakeslee J. P., Bouwens R. J., Bradley L. D., Broadhurst T. J., Brown R. A., Burrows C. J., Cheng E. S., Cross N. J. G., Demarco R.,

Feldman P. D., Franx M., Goto T., Gronwall C., Hartig G. F., Holden B. P., Homeier N. L., Infante L., Jee M. J., Kimble R. A., Lesser M. P., Martel A. R., Mei S., Menanteau F., Meurer G. R., Miley G. K., Motta V., Postman M., Rosati P., Sirianni M., Sparks W. B., Tran H. D., Tsvetanov Z. I., White R. L., Zheng W., Zirm A. W., 2006, Astronomical Journal, 131, 3109

Gräfe C., Wolf S., Roccatagliata V., Sauter J., Ertel S., 2011, Astronomy and Astrophysics, 533, A89

Gray D. F., 1992, The observation and analysis of stellar photospheres (Second Edition), Cambridge University Press

Greene T. P., Wilking B. A., Andre P., Young E. T., Lada C. J., 1994, Astrophysical Journal, 434, 614

Gregorio-Hetem J., Lepine J. R. D., Quast G. R., Torres C. A. O., de La Reza R., 1992, Astronomical Journal, 103, 549

Güdel M., 2007, Living Reviews in Solar Physics, 4, 3

Guillout P., Klutsch A., Frasca A., Freire Ferrero R., Marilli E., Mignemi G., Biazzo K., Bouvier J., Monier R., Motch C., Sterzik M., 2009, Astronomy and Astrophysics, 504, 829

Haisch, Jr. K. E., Lada E. A., Lada C. J., 2001, Astrophysical Journal, Letters, 553, L153

Harris A. W., 1978, Lunar and Planetary Science Conference IX, 459

Hartman J. D., Bakos G. Á., Kovács G., Noyes R. W., 2010, Monthly Notices of the RAS, 408, 475

Hartmann L., Calvet N., Gullbring E., D'Alessio P., 1998, Astrophysical Journal, 495, 385

Hauck B., Mermilliod M., 1998, Astronomy and Astrophysics, Supplement, 129, 431

Hauschildt P. H., Allard F., Baron E., 1999, Astrophysical Journal, 512, 377

Hawley S. L., Reid I. N., Gizis J. E., Byrne P. B., 1999, in Butler C. J., Doyle J. G., eds., Solar and Stellar Activity: Similarities and Differences, 63

Hawley S. L., Covey K. R., Knapp G. R., Golimowski D. A., Fan X., Anderson S. F., Gunn J. E., Harris H. C., Ivezić Ž., Long G. M., Lupton R. H., McGehee P. M., Narayanan V., Peng E., Schlegel D., Schneider D. P., Spahn E. Y., Strauss M. A., Szkody P., Tsvetanov Z., Walkowicz L. M., Brinkmann J., Harvanek M., Hennessy G. S., Kleinman S. J., Krzesinski J., Long D., Neilsen E. H., Newman P. R., Nitta A., Snedden S. A., York D. G., 2002, Astronomical Journal, 123, 3409

in Helou G., Walker D. W., eds, Infrared astronomical satellite (IRAS) catalogs and atlases. Volume 7: The small scale structure catalog, 1988

Henden A. A., Levine S. E., Terrell D., Smith T. C., Welch D., 2012, Journal of the American Association of Variable Star Observers (JAAVSO), 40, 430

Heng K., Malik M., 2013, Monthly Notices of the RAS, 432, 2562

Herbig G. H., 1978, Can Post-T Tauri Stars Be Found?, in Mirzoyan L. V., ed., Problems of Physics and Evolution of the Universe, Yerevan, Publishing House of the Armenian Academy of Sciences, 171

Hernández J., Calvet N., Briceño C., Hartmann L., Vivas A. K., Muzerolle J., Downes J., Allen L., Gutermuth R., 2007, Astrophysical Journal, 671, 1784

Hernández J., Hartmann L., Calvet N., Jeffries R. D., Gutermuth R., Muzerolle J., Stauffer J., 2008, Astrophysical Journal, 686, 1195

Hillenbrand L. A., 2006, in Livio M., ed., STScI Symposium Series #19, A Decade of Discovery: Planets Around Other Stars,

Hillenbrand L. A., Bauermeister A., White R. J., 2008, in van Belle G., ed., 14th Cambridge Workshop on Cool Stars, Stellar Systems, and the Sun, 200

Hogeveen S. J., 1990, Astrophysics and Space Science, 173, 315

Holland W. S., Greaves J. S., Zuckerman B., Webb R. A., McCarthy C., Coulson I. M., Walther D. M., Dent W. R. F., Gear W. K., Robson I., 1998, Nature, 392, 788

Holloway L. E., Prato L., Song I., Walter F. M., 2005, American Astronomical Society Meeting 207, 74.27; Bulletin of the American Astronomical Society, Vol. 37, 1288

Hoogerwerf R., Blaauw A., 2000, Astronomy and Astrophysics, 360, 391

Horne J. H., Baliunas S. L., 1986, Astrophysical Journal, 302, 757

Huélamo N., Lacour S., Tuthill P., Ireland M., Kraus A., Chauvin G., 2011, Astronomy and Astrophysics, 528, L7

Iben, Jr. I., 1967, Annual Review of Astron and Astrophys, 5, 571

Innis J. L., Coates D. W., Thompson K., 1988, Monthly Notices of the RAS, 233, 887

Isaacson H., Fischer D., 2010, Astrophysical Journal, 725, 875

Israelian G., Delgado Mena E., Santos N. C., Sousa S. G., Mayor M., Udry S., Domínguez Cerdeña C., Rebolo R., Randich S., 2009, Nature, 462, 189

Jackson R. J., Jeffries R. D., Maxted P. F. L., 2009, Monthly Notices of the RAS, 399, L89

Jackson R. J., Jeffries R. D., 2013, Monthly Notices of the RAS, 431, 1883

Jackson R. J., Jeffries R. D., 2014, Monthly Notices of the RAS, 445, 4306

Janson M., Brandt T. D., Moro-Martín A., Usuda T., Thalmann C., Carson J. C., Goto M., Currie T., McElwain M. W., Itoh Y., Fukagawa M., Crepp J., Kuzuhara M., Hashimoto J., Kudo T., Kusakabe N., Abe L., Brandner W., Egner S., Feldt

M., Grady C. A., Guyon O., Hayano Y., Hayashi M., Hayashi S., Henning T., Hodapp K. W., Ishii M., Iye M., Kandori R., Knapp G. R., Kwon J., Matsuo T., Miyama S., Morino J.-I., Nishimura T., Pyo T.-S., Serabyn E., Suenaga T., Suto H., Suzuki R., Takahashi Y., Takami M., Takato N., Terada H., Tomono D., Turner E. L., Watanabe M., Wisniewski J., Yamada T., Takami H., Tamura M., 2013, Astrophysical Journal, 773, 73

Jarrett T. H., Cohen M., Masci F., Wright E., Stern D., Benford D., Blain A., Carey S., Cutri R. M., Eisenhardt P., Lonsdale C., Mainzer A., Marsh K., Padgett D., Petty S., Ressler M., Skrutskie M., Stanford S., Surace J., Tsai C. W., Wheelock S., Yan D. L., 2011, Astrophysical Journal, 735, 112

Jeffries R. D., Jewell S. J., 1993, Monthly Notices of the RAS, 264, 106

Jeffries R. D., Byrne P. B., Doyle J. G., Anders G. J., James D. J., Lanzafame A. C., 1994, Monthly Notices of the RAS, 270, 153

Jeffries R. D., 1995, Monthly Notices of the RAS, 273, 559

Jeffries R. D., Totten E. J., James D. J., 2000, Monthly Notices of the RAS, 316, 950

Jeffries R. D., Naylor T., 2001, in Montmerle T., André P., eds., ASP Conf. 243., From Darkness to Light: Origin and Evolution of Young Stellar Clusters, 633

Jeffries R. D., Oliveira J. M., 2005, Monthly Notices of the RAS, 358, 13

Jeffries, R. D. 2006, Pre-Main-Sequence Lithium Depletion (Chemical Abundances and Mixing in Stars in the Milky Way and its Satellites, ESO ASTROPHYSICS SYMPOSIA. ISBN 978-3-540-34135-2. Springer-Verlag, 2006, p. 163), 163

Jeffries R. D., Evans P. A., Pye J. P., Briggs K. R., 2006, Monthly Notices of the RAS, 367, 781

Jeffries R. D., Naylor T., Walter F. M., Pozzo M. P., Devey C. R., 2009, Monthly Notices of the RAS, 393, 538

Jeffries R. D., Littlefair S. P., Naylor T., Mayne N. J., 2011, Monthly Notices of the RAS, 418, 1948

Jeffries R. D., Naylor T., Mayne N. J., Bell C. P. M., Littlefair S. P., 2013, Monthly Notices of the RAS, 434, 2438

Jeffries R. D., 2014, in Lebreton Y., Valls-Gabaud D., Charbonnel C., eds., EAS Publications Series Vol. 65, The Ages of Stars, 289

Jeffries R. D., Jackson R. J., Cottaar M., Koposov S. E., Lanzafame A. C., Meyer M. R., Prisinzano L., Randich S., Sacco G. G., Brugaletta E., Caramazza M., Damiani F., Franciosini E., Frasca A., Gilmore G., Feltzing S., Micela G., Alfaro E., Bensby T., Pancino E., Recio-Blanco A., de Laverny P., Lewis J., Magrini L., Morbidelli L., Costado M. T., Jofré P., Klutsch A., Lind K., Maiorca E., 2014, Astronomy and Astrophysics, 563, A94

Jenkins J. S., Pavlenko Y. V., Ivanyuk O., Gallardo J., Jones M. I., Day-Jones A. C., Jones H. R. A., Ruiz M. T., Pinfield D. J., Yakovina L., 2012, Monthly Notices of the RAS, 420, 3587

Jilinski E., Ortega V. G., de la Reza R., 2005, Astrophysical Journal, 619, 945

Johnson D. R. H., Soderblom D. R., 1987, Astronomical Journal, 93, 864

Jones B. F., Shetrone M., Fischer D., Soderblom D. R., 1996, Astronomical Journal, 112, 186

Jones B. F., Fischer D., Shetrone M., Soderblom D. R., 1997, Astronomical Journal, 114, 352

Jones B. F., Fischer D., Soderblom D. R., 1999, Astronomical Journal, 117, 330

Juarez A. J., Cargile P. A., James D. J., Stassun K. G., 2014, Astrophysical Journal, 795, 143

Jura M., Zuckerman B., Becklin E. E., Smith R. C., 1993, Astrophysical Journal, Letters, 418, L37

Kalas P., Liu M. C., Matthews, B. C., 2004, Science, 303, 1990

Kastner J. H., Zuckerman B., Weintraub D. A., Forveille T., 1997, Science, 277, 67

Kastner J. H., Crigger L., Rich M., Weintraub D. A., 2003, Astrophysical Journal, 585, 878

Kastner J. H., Thompson E. A., Montez R., Murphy S. J., Bessell M. S., Sacco G. G., 2012, Astrophysical Journal, Letters, 747, L23

Kataria T., Simon M., 2010, Astronomical Journal, 140, 206

Kawaler S. D., 1988, Astrophysical Journal, 333, 236

Kenyon S. J., Dobrzycka D., Hartmann L., 1994, Astronomical Journal, 108, 1872

Kenyon S. J., Hartmann L., 1995, Astrophysical Journal, Supplement, 101, 117

Kenyon S. J., Bromley B. C., 2002, Astronomical Journal, 123, 1757

Kharchenko N. V., Scholz R.-D., Piskunov A. E., Roeser S., Schilbach E., 2007, VizieR Online Data Catalog, 3254

Kharchenko N. V., Roeser S., 2009, VizieR Online Data Catalog, 1280

Kidder B., Shkolnik E., Skiff B., 2014, American Astronomical Society Meeting Abstracts 223, 215.04

Kim K. H., Watson D. M., Manoj P., Furlan E., Najita J., Forrest W. J., Sargent B., Espaillat C., Calvet N., Luhman K. L., McClure M. K., Green J. D., Harrold S. T., 2009, Astrophysical Journal, 700, 1017

King J. R., 1998, Astronomical Journal, 116, 254

King J. R., Villarreal A. R., Soderblom D. R., Gulliver A. F., Adelman S. J., 2003, Astronomical Journal, 125, 1980

Kippenhahn R., 1967, in Hack M., ed., Late-Type Stars, 319

Kiraga M., Stepien K., 2007, Acta Astronomica, 57, 149

Kiss L. L., Moór A., Szalai T., Kovács J., Bayliss D., Gilmore G. F., Bienaymé O., Binney J., Bland-Hawthorn J., Campbell R., Freeman K. C., Fulbright J. P., Gibson B. K., Grebel E. K., Helmi A., Munari U., Navarro J. F., Parker Q. A., Reid W., Seabroke G. M., Siebert A., Siviero A., Steinmetz M., Watson F. G., Williams M., Wyse R. F. G., Zwitter T., 2011, Monthly Notices of the RAS, 411, 117

Klahr H., Johansen A., 2008, Physica Scripta Volume T, 130(1), 014018

Knude J., Hog E., 1998, Astronomy and Astrophysics, 338, 897

Kordopatis G., Gilmore G., Steinmetz M., Boeche C., Seabroke G. M., Siebert A., Zwitter T., Binney J., de Laverny P., Recio-Blanco A., Williams M. E. K., Piffl T., Enke H., Roeser S., Bijaoui A., Wyse R. F. G., Freeman K., Munari U., Carrillo I., Anguiano B., Burton D., Campbell R., Cass C. J. P., Fiegert K., Hartley M., Parker Q. A., Reid W., Ritter A., Russell K. S., Stupar M., Watson F. G., Bienaymé O., Bland-Hawthorn J., Gerhard O., Gibson B. K., Grebel E. K., Helmi A., Navarro J. F., Conrad C., Famaey B., Faure C., Just A., Kos J., Matijevič G., McMillan P. J., Minchev I., Scholz R., Sharma S., Siviero A., de Boer E. W., Žerjal M., 2013, Astronomical Journal, 146, 134

Kraft R. P., 1967, Astrophysical Journal, 150, 551

Kraus A. L., Shkolnik E. L., Allers K. N., Liu M. C., 2014, Astronomical Journal, 147, 146

Krishnamurthi A., Terndrup D. M., Pinsonneault M. H., Sellgren K., Stauffer J. R., Schild R., Backman D. E., Beisser K. B., Dahari D. B., Dasgupta A., Hagelgans

J. T., Seeds M. A., Anand R., Laaksonen B. D., Marschall L. A., Ramseyer T., 1998, Astrophysical Journal, 493, 914

Kroupa P., 2002, Science, 295, 82

Kubát J., Korcáková D., 2004, in Zverko J., Ziznovsky J., Adelman S. J., Weiss W. W., eds., IAU Symp. 224, The A-Star Puzzle, Cambridge Univ. Press, 13

Küçük I., Akkaya I., 2010, Revista Mexicana de Astronomia y Astrofisica, 46, 109

Lachaume R., Dominik C., Lanz T., Habing H. J., 1999, Astronomy and Astrophysics, 348, 897

Lada C. J., 1987, in Peimbert M., Jugaku J., eds, Star Forming Regions, 1

Lada C., 2000, in Murdin P., ed., Young Stellar Objects, Bristol: Institute of Physics Publishing

Lada C. J., Lada E. A., 2003, Annual Review of Astron and Astrophys, 41, 57

Lagrange A.-M., Backman D. E., Artymowicz P., 2000, in Mannings, V., Boss, A. P., Russell, S. S., eds., Protostars and Planets IV, 639

Lagrange A.-M., Bonnefoy M., Chauvin G., Apai D., Ehrenreich D., Boccaletti A., Gratadour D., Rouan D., Mouillet D., Lacour S., Kasper M., 2010, Science, 329, 57

Lagrange A.-M., Bonnefoy M., Chauvin G., Apai D., Ehrenreich D., Boccaletti A., Gratadour D., Rouan D., Mouillet D., Lacour S., Kasper M., 2011, in Sozzetti A., Lattanzi M. G., Boss A. P., eds, IAU Symp. 276, The Astrophysics of Planetary Systems: Formation, Structure, and Dynamical Evolution, 60

Lagrange A.-M., De Bondt K., Meunier N., Sterzik M., Beust H., Galland F., 2012, Astronomy and Astrophysics, 542, A18

Lanz T., Heap S. R., Hubeny I., 1995, Astrophysical Journal, Letters, 447, L41

Laughlin G., Bodenheimer P., Adams F. C., 2004, Astrophysical Journal, Letters, 612, L73

Lawson W., Feigelson E. D., 2001, in Montmerle T., André P., eds., ASP Conf. 243., From Darkness to Light: Origin and Evolution of Young Stellar Clusters, 591

Lawson W. A., Crause L. A., 2005, Monthly Notices of the RAS, 357, 1399

Lawson W. A., Lyo A.-R., Bessell M. S., 2009, Monthly Notices of the RAS, 400, L29

Lépine S., Simon M., 2009, Astronomical Journal, 137, 3632

Lestrade J.-F., Wyatt M. C., Bertoldi F., Dent W. R. F., Menten K. M., 2006, Astronomy and Astrophysics, 460, 733

Lestrade J.-F., Wyatt M. C., Bertoldi F., Menten K. M., Labaigt G., 2009, Astronomy and Astrophysics, 506, 1455

Lestrade J.-F., Matthews B. C., Sibthorpe B., Kennedy G. M., Wyatt M. C., Bryden G., Greaves J. S., Thilliez E., Moro-Martín A., Booth M., Dent W. R. F., Duchêne G., Harvey P. M., Horner J., Kalas P., Kavelaars J. J., Phillips N. M., Rodriguez D. R., Su K. Y. L., Wilner D. J., 2012, Astronomy and Astrophysics, 548, A86

Li J. Z., Hu J. Y., 1998, Astronomy and Astrophysics, Supplement, 132, 173

Li J. Z., Hu J. Y., Chen W. P., 2000, Astronomy and Astrophysics, 356, 157

Lindegren L., Babusiaux C., Bailer-Jones C., Bastian U., Brown A. G. A., Cropper M., Høg E., Jordi C., Katz D., van Leeuwen F., Luri X., Mignard F., de Bruijne J. H. J., Prusti T., 2008, in Jin W. J., Platais I., Perryman M. A. C., eds, IAU Symp. 248, A Giant Step: from Milli- to Micro-arcsecond Astrometry, 217

Liu M. C., 2004, Science, 305, 1442

Liu M. C., Wahhaj Z., Biller B., Chun M., Close L., Ftaclas C., Hartung M., Hayward T., Nielsen E., Toomey D., Shkolnik E., Reid I., NICI Planet-Finding Campaign Team, 2010, American Astronomical Society Meeting Abstracts, 215, 449.01

Liu M. C., Magnier E. A., Deacon N. R., Allers K. N., Dupuy T. J., Kotson M. C., Aller K. M., Burgett W. S., Chambers K. C., Draper P. W., Hodapp K. W., Jedicke R., Kaiser N., Kudritzki R.-P., Metcalfe N., Morgan J. S., Price P. A., Tonry J. L., Wainscoat R. J., 2013, Astrophysical Journal, Letters, 777, L20

Lomb N. R., 1976, Astrophysics and Space Science, 39, 447

Lombardi M., Lada C. J., Alves J., 2008, Astronomy and Astrophysics, 480, 785

Looper D. L., Mohanty S., Bochanski J. J., Burgasser A. J., Mamajek E. E., Herczeg G. J., West A. A., Faherty J. K., Rayner J., Pitts M. A., Kirkpatrick J. D., 2010,Astrophysical Journal, 714, 45

López-Morales M., 2007, Astrophysical Journal, 660, 732

López-Santiago J., Micela G., Montes D., 2009, Astronomy and Astrophysics, 499, 129

Low F. J., Smith P. S., Werner M., Chen C., Krause V., Jura M., Hines D. C., 2005, Astrophysical Journal, 631, 1170

Lucas P. W., Roche P. F., Allard F., Hauschildt P. H., 2001, Monthly Notices of the RAS, 326, 695

Luhman K. L., 1999, Astrophysical Journal, 525, 466

Luhman K. L., Stauffer J. R., Muench A. A., Rieke G. H., Lada E. A., Bouvier J., Lada C. J., 2003, Astrophysical Journal, 593, 1093

Luhman K. L., 2004, Astrophysical Journal, 616, 1033

Luhman K. L., Steeghs D., 2004, Astrophysical Journal, 609, 917

Luhman K. L., Stauffer J. R., Mamajek E. E., 2005, Astrophysical Journal, Letters, 628, L69

Luhman K. L., 2007, Astrophysical Journal, Supplement, 173, 104

Luhman K. L., Allen L. E., Allen P. R., Gutermuth R. A., Hartmann L., Mamajek E. E., Megeath S. T., Myers P. C., Fazio G. G., 2008, Astrophysical Journal, 675, 1375

Luhman K. L., Mamajek E. E., 2012, Astrophysical Journal, 758, 31

Lyra W., Moitinho A., van der Bliek N. S., Alves J., 2006, Astronomy and Astrophysics, 453, 101

MacDonald J., Mullan D., 2013, ArXiv e-prints (arXiv:1311.3246)

MacGregor M., 2014, in Booth M., Matthews B. C., Graham J. R., eds., IAU Symp. 299, Exploring the Formation and Evolution of Planetary Systems, 313

Maeder A., 1976, Astronomy and Astrophysics, 47, 389

Makarov V. V., Urban S., 2000, Monthly Notices of the RAS, 317, 289

Makarov V. V., Fabricius C., 2001, Astronomy and Astrophysics, 368, 866

Makarov V. V., 2003, Astronomical Journal, 126, 1996

Makarov V. V., 2006, Astronomical Journal, 131, 2967

Makarov V. V., 2007, Astrophysical Journal, Supplement, 169, 105

Maldonado J., Martínez-Arnáiz R. M., Eiroa C., Montes D., Montesinos B., 2010, Astronomy and Astrophysics, 521, A12

Malo L., Doyon R., Lafrenière D., Artigau É., Gagné J., Baron F., Riedel A., 2013, Astrophysical Journal, 762, 88

Malo L., Artigau É., Doyon R., Lafrenière D., Albert L., Gagné J., 2014a, Astrophysical Journal, 788, 81

Malo L., Doyon R., Feiden G. A., Albert L., Lafrenière D., Artigau É., Gagné J., Riedel A., 2014b, Astrophysical Journal, 792, 37

Mamajek E. E., Lawson W. A., Feigelson E. D., 1999, Astrophysical Journal, Letters, 516, L77

Mamajek E. E., Lawson W. A., Feigelson E. D., 2000, Astrophysical Journal, 544, 356

Mamajek E. E., Feigelson E. D., 2001, in Jayawardhana R., Greene T., eds., ASP Conf. 244., Young Stars Near Earth: Progress and Prospects, 104

Mamajek E. E., 2005, Astrophysical Journal, 634, 1385

Mamajek E. E., Hillenbrand L. A., 2008, Astrophysical Journal, 687, 1264

Mamajek E. E., 2009, in Usuda T., Tamura M., Ishii M., eds., American Institute of Physics Conference Series Vol. 1158, 3

Mamajek E. E., 2012, Astrophysical Journal, Letters, 754, L20

Mamajek E. E., Bell C. P. M., 2014, Monthly Notices of the RAS, 445, 2169

Manoj P., Kim K. H., Furlan E., McClure M. K., Luhman K. L., Watson D. M., Espaillat C., Calvet N., Najita J. R., D'Alessio P., Adame L., Sargent B. A., Forrest W. J., Bohac C., Green J. D., Arnold L. A., 2011, Astrophysical Journal, Supplement, 193, 11

Manzi S., Randich S., de Wit W. J., Palla F., 2008, Astronomy and Astrophysics, 479, 141

Marois C., Macintosh B., Barman T., Zuckerman B., Song I., Patience J., Lafrenière D., Doyon R., 2008, Science, 322, 1348

Marois C., Zuckerman B., Konopacky Q. M., Macintosh B., Barman T., 2010, Nature, 468, 1080

Martin E. L., Rebolo R., Magazzu A., Pavlenko Y. V., 1994, Astronomy and Astrophysics, 282, 503

Mason K. O., Hassall B. J. M., Bromage G. E., Buckley D. A. H., Naylor T., O'Donoghue D., Watson M. G., Bertram D., Branduardi-Raymont G., Charles P. A., Cooke B., Elliott K. H., Hawkins M. R. S., Hodgkin S. T., Jewell S. J., Jomaron C. M., Sekiguchi K., Kellett B. J., Lawrence A., McHardy I., Mittaz J. P. D., Pike C. D., Ponman T. J., Schmitt J., Voges W., Wargau W., Wonnacott D., 1995, Monthly Notices of the RAS, 274, 1194

Matthews B. C., Kalas P. G., Wyatt M. C., 2007, Astrophysical Journal, 663, 1103

Matthews B. C., Krivov A. V., Wyatt M. C., Bryden G., Eiroa C., 2014, Protostars and Planets VI, 521

Maxted P. F. L., Anderson D. R., Collier Cameron A., Hellier C., Queloz D., Smalley B., Street R. A., Triaud A. H. M. J., West R. G., Gillon M., Lister T. A., Pepe F., Pollacco D., Ségransan D., Smith A. M. S., Udry S., 2011, Publications of the ASP, 123, 547

Mayne N. J., Naylor T., Littlefair S. P., Saunders E. S., Jeffries R. D., 2007, Monthly Notices of the RAS, 375, 1220

McCarthy K., Wilhelm R. J., 2014, Astronomical Journal, 148, 70

Meibom S., Mathieu R. D., Stassun K. G., 2009, Astrophysical Journal, 695, 679

Melis C., Zuckerman B., Rhee J. H., Song I., 2010, Astrophysical Journal, Letters, 717, L57

Mentuch E., Brandeker A., van Kerkwijk M. H., Jayawardhana R., Hauschildt P. H., 2008, Astrophysical Journal, 689, 1127

Meola G., Randich S., Pallavicini R., Stauffer J. R., Balachandran S., 2000, in Pallavicini R., Micela G., Sciortino S., eds., ASP Conf. 198., Stellar Clusters and Associations: Convection, Rotation, and Dynamos, 285

Mermilliod J. C., 1981, Astronomy and Astrophysics, 97, 235

Mermilliod J.-C., Mayor M., Udry S., 2009, Astronomy and Astrophysics, 498, 949

Messina S., Desidera S., Turatto M., Lanzafame A. C., Guinan E. F., 2010, Astronomy and Astrophysics, 520, A15

Messina S., Desidera S., Lanzafame A. C., Turatto M., Guinan E. F., 2011, Astronomy and Astrophysics, 532, A10

Mishenina T. V., Soubiran C., 2005, in Hill V., Francois P., Primas F., eds., IAU Symp. 228, From Lithium to Uranium: Elemental Tracers of Early Cosmic Evolution, 97

Mittag M., Hempelmann A., González-Pérez J. N., Schmitt J. H. M. M., Hall J. C., 2011, in Johns-Krull C., Browning M. K., West A. A., eds, 16th Cambridge Workshop on Cool Stars, Stellar Systems, and the Sun, 1187

Mizuno H., 1980, Progress of Theoretical Physics, 64, 544

Montes D., López-Santiago J., Fernández-Figueroa M. J., Gálvez M. C., 2001, Astronomy and Astrophysics, 379, 976

Montesinos B., Thomas J. H., Ventura P., Mazzitelli I., 2001, Monthly Notices of the RAS, 326, 877

Moór A., Szabó G. M., Kiss L. L., Kiss C., Ábrahám P., Szulágyi J., Kóspál Á., Szalai T., 2013, Monthly Notices of the RAS, 435, 1376

Mordasini C., Alibert Y., Benz W., Naef D., 2008, in Fischer D., Rasio F. A., Thorsett S. E., Wolszczan A., eds., ASP Conf. 398., Extreme Solar Systems, 235

Moya A., Amado P. J., Barrado D., García Hernández A., Aberasturi M., Montesinos B., Aceituno F., 2010, Monthly Notices of the RAS, 405, L81

Mugrauer M., Vogt N., Neuhäuser R., Schmidt T. O. B., 2010, Astronomy and Astrophysics, 523, L1

Mugrauer M., Röll T., Ginski C., Vogt N., Neuhäuser R., Schmidt T. O. B., 2012, Monthly Notices of the RAS, 424, 1714

Murgas F., Jenkins J. S., Rojo P., Jones H. R. A., Pinfield D. J., 2013, Astronomy and Astrophysics, 552, A27

Murphy S. J., Lawson W. A., Bessell M. S., 2013, Monthly Notices of the RAS, 435, 1325

Murphy S. J., Lawson W. A., 2015, Monthly Notices of the RAS, 447, 1267

Nakajima T., Morino J.-I., 2012, Astronomical Journal, 143, 2

Naylor T., Jeffries R. D., 2006, Monthly Notices of the RAS, 373, 1251

Naylor T., Mayne N. J., Jeffries R. D., Littlefair S. P., Saunders E. S., 2009, in Mamajek E. E., Soderblom D. R., Wyse R. F. G., eds, IAU Symp. 258, The Ages of Stars, 103

Nelson A. F., Ruffert M., 2013, Monthly Notices of the RAS, 429, 1791

Norton A. J., Wheatley P. J., West R. G., Haswell C. A., Street R. A., Collier Cameron A., Christian D. J., Clarkson W. I., Enoch B., Gallaway M., Hellier C., Horne K., Irwin J., Kane S. R., Lister T. A., Nicholas J. P., Parley N., Pollacco D., Ryans R., Skillen I., Wilson D. M., 2007, Astronomy and Astrophysics, 467, 785

Norton A. J., 2012, in Griffin, E., Hanisch, R., Seaman, R., eds, IAU Symp. 285, New Horizons in Time Domain Astronomy, 382

Noyes R. W., Hartmann L. W., Baliunas S. L., Duncan D. K., Vaughan A. H., 1984, Astrophysical Journal, 279, 763

Opitz D., Gallardo J., 2011, Boletin de la Asociacion Argentina de Astronomia La Plata Argentina, 54, 93

Ortega V. G., de la Reza R., Jilinski E., Bazzanella B., 2002, Astrophysical Journal, Letters, 575, L75

Ortega V. G., de la Reza R., Jilinski E., Bazzanella B., 2004, Astrophysical Journal, 609, 243

Ortega V. G., Jilinski E., de La Reza R., Bazzanella B., 2007, Monthly Notices of the RAS, 377, 441

Pace G., 2013, Astronomy and Astrophysics, 551, L8

Palla F., Stahler S. W., 1999, Astrophysical Journal, 525, 772

Palla F., Randich S., Pavlenko Y. V., Flaccomio E., Pallavicini R., 2007, Astrophysical Journal, Letters, 659, L41

Pallavicini R., Golub L., Rosner R., Vaiana G. S., Ayres T., Linsky J. L., 1981, Astrophysical Journal, 248, 279

Parks J. R., Plavchan P., White R. J., Gee A. H., 2014, Astrophysical Journal, Supplement, 211, 3

Patel R. I., Metchev S. A., Heinze A., 2014, Astrophysical Journal, Supplement, 212, 10

Patten B. M., Simon T., 1996, Astrophysical Journal, Supplement, 106, 489

Pearce T., Wyatt M., Kennedy G., 2013, Protostars and Planets VI Posters, Poster #2K015

Pecaut M. J., Mamajek E. E., Bubar E. J., 2012, Astrophysical Journal, 746, 154

Pecaut M. J., Mamajek E. E., 2013, Astrophysical Journal, Supplement, 208, 9

Peres G., Orlando S., Reale F., Rosner R., Hudson H., 2000, Astrophysical Journal, 528, 537

Perri F., Cameron A. G. W., 1974, Icarus, 22, 416

Perryman M. A. C., Lindegren L., Kovalevsky J., Hoeg E., Bastian U., Bernacca P. L., Crézé M., Donati F., Grenon M., Grewing M., van Leeuwen F., van der Marel H., Mignard F., Murray C. A., Le Poole R. S., Schrijver H., Turon C., Arenou F., Froeschlé M., Petersen C. S., 1997, Astronomy and Astrophysics, 323, L49

Perryman M. A. C., Brown A. G. A., Lebreton Y., Gomez A., Turon C., Cayrel de Strobel G., Mermilliod J. C., Robichon N., Kovalevsky J., Crifo F., 1998, Astronomy and Astrophysics, 331, 81

Piau L., Turck-Chièze S., 2002, Astrophysical Journal, 566, 419

Pinsonneault M. H., Kawaler S. D., Demarque P., 1990, Astrophysical Journal, Supplement, 74, 501

Pinsonneault M., 1997, Annual Review of Astron and Astrophys, 35, 557

Pinsonneault M. H., An D., Molenda-Żakowicz J., Chaplin W. J., Metcalfe T. S., Bruntt H., 2012, Astrophysical Journal, Supplement, 199, 30

Pizzolato N., Maggio A., Micela G., Sciortino S., Ventura P., 2003, Astronomy and Astrophysics, 397, 147

Plavchan P., Jura M., Lipscy S. J., 2005, Astrophysical Journal, 631, 1161

Pollacco D. L., Skillen I., Collier Cameron A., Christian D. J., Hellier C., Irwin J., Lister T. A., Street R. A., West R. G., Anderson D. R., Clarkson W. I., Deeg H., Enoch B., Evans A., Fitzsimmons A., Haswell C. A., Hodgkin S., Horne K., Kane S. R., Keenan F. P., Maxted P. F. L., Norton A. J., Osborne J., Parley N. R., Ryans R. S. I., Smalley B., Wheatley P. J., Wilson D. M., 2006, Publications of the ASP, 118, 1407

Preibisch T., Feigelson E. D., 2005, Astrophysical Journal, Supplement, 160, 390

Prisinzano L., Micela G., Sciortino S., Affer L., Damiani F., 2012, Astronomy and Astrophysics, 546, A9

Proctor R. A., 1869, Royal Society of London Proceedings Series I, 18, 169

Proctor R. A., 1869a, Monthly Notices of the RAS, 30, 50

Raghavan D., McAlister H. A., Henry T. J., Latham D. W., Marcy G. W., Mason B. D., Gies D. R., White R. J., ten Brummelaar T. A., 2010, Astrophysical Journal, Supplement, 190, 1

Rajpurohit A. S., Reylé C., Allard F., Scholz R.-D., Homeier D., Schultheis M., Bayo A., 2014, Astronomy and Astrophysics, 564, A90

Ramírez I., Meléndez J., 2005, Astrophysical Journal, 626, 465

Randich S., 2000, in Pallavicini R., Micela G., Sciortino S., eds, Stellar Clusters and Associations: Convection, Rotation, and Dynamos, 401

Randich S., 2001, Astronomy and Astrophysics, 377, 512

Randich S., Pallavicini R., Meola G., Stauffer J. R., Balachandran S. C., 2001, Astronomy and Astrophysics, 372, 862

Raymond S. N., Quinn T., Lunine J. I., 2004, Icarus, 168, 1

Rebolo R., Martin E. L., Magazzu A., 1993, in Weiss W. W., Baglin A., eds., IAU Colloq. 137: Inside the Stars, 171

Rebolo R., Martin E. L., Garcia Lopez R. J., 1994, in Caillault J.-P., ed., Cool Stars, Stellar Systems, and the Sun, 297

Reid N., 2003, Monthly Notices of the RAS, 342, 837

Reiners A., Basri G., 2009, Astrophysical Journal, 705, 1416

Rhee J. H., Song I., Zuckerman B., 2007, Astrophysical Journal, 671, 616

Riaz B., Gizis J. E., 2008, Astrophysical Journal, 681, 1584

Riaz B., Gizis J. E., 2012, Astronomy and Astrophysics, 548, A54

Riaz B., Lodieu N., Goodwin S., Stamatellos D., Thompson M., 2012, Monthly Notices of the RAS, 420, 2497

Ribas I., Guinan E. F., Güdel M., Audard M., 2005, Astrophysical Journal, 622, 680

Rice E. L., Faherty J. K., Cruz K. L., 2010, Astrophysical Journal, Letters, 715, L165

Richard O., Vauclair S., Charbonnel C., Dziembowski W. A., 1996, Astronomy and Astrophysics, 312, 1000

Riedel A. R., Murphy S. J., Henry T. J., Melis C., Jao W.-C., Subasavage J. P., 2011, Astronomical Journal, 142, 104

Riedel A. R., 2012, PhD thesis, Georgia State University

Riedel A. R., Finch C. T., Henry T. J., Subasavage J. P., Jao W.-C., Malo L., Rodriguez D. R., White R. J., Gies D. R., Dieterich S. B., Winters J. G., Davison C. L., Nelan E. P., Blunt S. C., Cruz K. L., Rice E. L., Ianna P. A., 2014, Astronomical Journal, 147, 85

Riviere-Marichalar P., Pinte C., Barrado D., Thi W. F., Eiroa C., Kamp I., Montesinos B., Donaldson J., Augereau J. C., Huélamo N., Roberge A., Ardila D., Sandell G., Williams J. P., Dent W. R. F., Menard F., Lillo-Box J., Duchêne G., 2013, Astronomy and Astrophysics, 555, A67

Rodriguez D. R., Bessell M. S., Zuckerman B., Kastner J. H., 2011, Astrophysical Journal, 727, 62

Roeser S., Demleitner M., Schilbach E., 2010, Astronomical Journal, 139, 2440

Rosat C., 2000, VizieR Online Data Catalog, 9030

Rucinski S. M., Krautter J., 1983, Astronomy and Astrophysics, 121, 217

Ryan S. G., Kajino T., Beers T. C., Suzuki T. K., Romano D., Matteucci F., Rosolankova K., 2001, Astrophysical Journal, 549, 55

Saar S. H., 1994, in Rabin D. M., Jefferies J. T., Lindsey C., eds., IAU Symp. 154, Infrared Solar Physics, 493

Salpeter E. E., 1955, Astrophysical Journal, 121, 161

Sandage A., 1962, Astrophysical Journal, 136, 319

Sandstrom K. M., Peek J. E. G., Bower G. C., Bolatto A. D., Plambeck R. L., 2007, Astrophysical Journal, 667, 1161

Santos N. C., Melo C., James D. J., Gameiro J. F., Bouvier J., Gomes J. I., 2008, Astronomy and Astrophysics, 480, 889

Sargent B., Forrest W. J., D'Alessio P., Li A., Najita J., Watson D. M., Calvet N., Furlan E., Green J. D., Kim K. H., Sloan G. C., Chen C. H., Hartmann L., Houck J. R., 2006, Astrophysical Journal, 645, 395

Sarro L. M., Bouy H., Berihuete A., Bertin E., Moraux E., Bouvier J., Cuillandre J.-C., Barrado D., Solano E., 2014, Astronomy and Astrophysics, 563, A45

Scandariato G., Da Rio N., Robberto M., Pagano I., Stassun K., 2012, Astronomy and Astrophysics, 545, A19

Scargle J. D., 1982, Astrophysical Journal, 263, 835

Schaller G., Schaerer D., Meynet G., Maeder A., 1992, Astronomy and Astrophysics, Supplement, 96, 269

Schatzman E., 1962, Annales d'Astrophysique, 25, 18

Schegerer A., Wolf S., Voshchinnikov N. V., Przygodda F., Kessler-Silacci J. E., 2006, Astronomy and Astrophysics, 456, 535

Schlieder J. E., Lépine S., Simon M., 2010, Astronomical Journal, 140, 119

Schlieder J. E., Lépine S., Simon M., 2012, Astronomical Journal, 144, 109

Schlieder J. E., Lépine S., Simon M., 2012a, Astronomical Journal, 143, 80

Schlieder J. E., Lépine S., Rice E., Simon M., Fielding D., Tomasino R., 2012, Astronomical Journal, 143, 114

Schmidt E. G., Langan S., Rogalla D., Thacker-Lynn L., 2007, Astronomical Journal, 133, 665

Schneider A., Song I., Melis C., Hufford T., Zuckerman B. M., Bessell M. S., 2013, American Astronomical Society Meeting Abstracts, 325.06

Schneider A., Melis C., Song I., 2012, Astrophysical Journal, 754, 39

Schwarzschild K., 1906, Nachrichten von der Königlichen Gesellschaft der Wissenschaften zu Göttingen. Math.-phys. Klasse, 195, p. 41-53, 195, 41

Scicluna P., Rosotti G., Dale J. E., Testi L., 2014, Astronomy and Astrophysics, 566, L3

Semkov E. H., 2011, Bulgarian Astronomical Journal, 15, 65

Sergison D. J., Mayne N. J., Naylor T., Jeffries R. D., Bell C. P. M., 2013, Monthly Notices of the RAS, 434, 966

Sestito P., Randich S., 2005, Astronomy and Astrophysics, 442, 615

Sharpless S., 1965, in Blaauw A., Schmidt M., eds., Galactic Structure, University of Chicago Press, Chicago, 131

Shkolnik E. L., Liu M. C., Reid I. N., Dupuy T., Weinberger A. J., 2011, Astrophysical Journal, 727, 6

Shkolnik E. L., Anglada-Escudé G., Liu M. C., Bowler B. P., Weinberger A. J., Boss A. P., Reid I. N., Tamura M., 2012, Astrophysical Journal, 758, 56

Sicilia-Aguilar A., Bouwman J., Juhász A., Henning T., Roccatagliata V., Lawson W. A., Acke B., Feigelson E. D., Tielens A. G. G. M., Decin L., Meeus G., 2009, Astrophysical Journal, 701, 1188

Siegler N., Muzerolle J., Young E. T., Rieke G. H., Mamajek E. E., Trilling D. E., Gorlova N., Su K. Y. L., 2007, Astrophysical Journal, 654, 580

Sierchio J. M., Rieke G. H., Su K. Y. L., Gáspár A., 2014, Astrophysical Journal, 785, 33

Siess L., 2001, in Montmerle T., André P., eds., ASP Conf. 243., From Darkness to Light: Origin and Evolution of Young Stellar Clusters, 581

Siess L., Dufour E., Forestini M., 2000, Astronomy and Astrophysics, 358, 593

Simon T., Patten B. M., 1998, Publications of the ASP, 110, 283

Simon M., Schlieder J. E., Constantin A.-M., Silverstein M., 2012, Astrophysical Journal, 751, 114

Sitko M. L., Lynch D. K., Russell R. W., Grady C. A., 2004, in Penny A., ed., Planetary Systems in the Universe, 368

Skumanich A., 1972, Astrophysical Journal, 171, 565

Slesnick C. L., Hillenbrand L. A., Carpenter J. M., 2004, Astrophysical Journal, 610, 1045

Smith B. A., Terrile R. J., 1984, Science, 226, 1421

Smith R., Jeffries R. D., 2012, Monthly Notices of the RAS, 420, 2884

Soderblom D. R., Oey M. S., Johnson D. R. H., Stone R. P. S., 1990, Astronomical Journal, 99, 595

Soderblom D. R., Duncan D. K., Johnson D. R. H., 1991, Astrophysical Journal, 375, 722

Soderblom D. R., Mayor M., 1993, Astronomical Journal, 105, 226

Soderblom D. R., Pilachowski C. A., Fedele S. B., Jones B. F., 1993, Astronomical Journal, 105, 2299

Soderblom D. R., Jones B. F., Balachandran S., Stauffer J. R., Duncan D. K., Fedele S. B., Hudon J. D., 1993a, Astronomical Journal, 106, 1059

Soderblom D. R., Fedele S. B., Jones B. F., Stauffer J. R., Prosser C. F., 1993b, Astronomical Journal, 106, 1080

Soderblom D. R., Fedele S. B., Jones B. F., Stauffer J. R., Prosser C. F., 1995, Astronomical Journal, 109, 1402

Soderblom D. R., Jones B. F., Stauffer J. R., Chaboyer B., 1995a, Astronomical Journal, 110, 729

Soderblom D. R., King J. R., Siess L., Jones B. F., Fischer D., 1999, Astronomical Journal, 118, 1301

Soderblom D. R., 2010, Annual Review of Astron and Astrophys, 48, 581

Soderblom D. R., Hillenbrand L. A., Jeffries R. D., Mamajek E. E., Naylor T., 2014, Protostars and Planets VI, 219

Somers G., Pinsonneault M. H., 2014, Astrophysical Journal, 790, 72

Song I., Bessell M. S., Zuckerman B., 2002, Astrophysical Journal, Letters, 581, L43

Song I., Zuckerman B., Bessell M. S., 2003, Astrophysical Journal, 599, 342

Song I., Zuckerman B., Bessell M. S., 2012, Astronomical Journal, 144, 8

Spina L., Randich S., Palla F., Sacco G. G., Magrini L., Franciosini E., Morbidelli L., Prisinzano L., Alfaro E. J., Biazzo K., Frasca A., González Hernández J. I., Sousa S. G., Adibekyan V., Delgado-Mena E., Montes D., Tabernero H., Klutsch A., Gilmore G., Feltzing S., Jeffries R. D., Micela G., Vallenari A., Bensby T., Bragaglia A., Flaccomio E., Koposov S., Lanzafame A. C., Pancino E., Recio-Blanco A., Smiljanic R., Costado M. T., Damiani F., Hill V., Hourihane A., Jofré P., de Laverny P., Masseron T., Worley C., 2014, Astronomy and Astrophysics, 567, A55

Spruit H. C., Weiss A., 1986, Astronomy and Astrophysics, 166, 167

Stahler S. W., Palla F., 2005, The Formation of Stars, Wiley-VCH

Stauffer J. R., Schild R. A., Baliunas S. L., Africano J. L., 1987, Publications of the ASP, 99, 471

Stauffer J. R., Schultz G., Kirkpatrick J. D., 1998, Astrophysical Journal, Letters, 499, L199

Stauffer J. R., Barrado y Navascués D., Bouvier J., Morrison H. L., Harding P., Luhman K. L., Stanke T., McCaughrean M., Terndrup D. M., Allen L., Assouad P., 1999, Astrophysical Journal, 527, 219

Stelzer B., Neuhäuser R., 2001, Astronomy and Astrophysics, 372, 117

Stern S. A., Weintraub D. A., Festou M. C., 1993, AAS/Division for Planetary Sciences Meeting Abstracts 25, 1124

Sterzik M. F., Durisen R. H., 1995, Astronomy and Astrophysics, 304, L9

Sterzik M. F., Alcalá J. M., Covino E., Petr M. G., 1999, Astronomy and Astrophysics, 346, L41

Strassmeier K. G., Weber M., Granzer T., Järvinen S., 2012, Astronomische Nachrichten, 333, 663

Su K. Y. L., Rieke G. H., Stansberry J. A., Bryden G., Stapelfeldt K. R., Trilling D. E., Muzerolle J., Beichman C. A., Moro-Martin A., Hines D. C., Werner M. W., 2006, Astrophysical Journal, 653, 675

Takagi Y., Itoh Y., Oasa Y., Sugitani K., 2011, Publications of the ASJ, 63, 677

Takeda Y., Honda S., Kawanomoto S., Ando H., Sakurai T., 2010, Astronomy and Astrophysics, 515, A93

Tanabé T., Sakon I., Cohen M., Wada T., Ita Y., Ohyama Y., Oyabu S., Uemizu K., Takagi T., Ishihara D., Kim W., Ueno M., Matsuhara H., Onaka T., 2008, Publications of the ASJ, 60, 375

Teixeira R., Ducourant C., Chauvin G., Krone-Martins A., Bonnefoy M., Song I., 2009, Astronomy and Astrophysics, 503, 281

Telting J. H., Avila G., Buchhave L., Frandsen S., Gandolfi D., Lindberg B., Stempels H. C., Prins S., NOT staff, 2014, Astronomische Nachrichten, 335, 41

Theissen C. A., West A. A., 2014, Astrophysical Journal, 794, 146

Tognelli E., Prada Moroni P. G., Degl'Innocenti S., 2011, Astronomy and Astrophysics, 533, A109

Tonry J., Davis M., 1979, Astronomical Journal, 84, 1511

Torres C. A. O., da Silva L., Quast G. R., de la Reza R., Jilinski E., 2000, Astronomical Journal, 120, 1410

Torres C. A. O., Quast G. R., de La Reza R., da Silva L., Melo C. H. F., 2001, in Jayawardhana R., Greene T., eds., ASP Conf. 244., Young Stars Near Earth: Progress and Prospects, 43

Torres C. A. O., Quast G. R., de La Reza R., da Silva L., Melo C. H. F., Sterzik M., 2003, in Lépine J., Gregorio-Hetem J., eds., Astrophysics and Space Science Library, 83

Torres C. A. O., Quast G. R., da Silva L., de La Reza R., Melo C. H. F., Sterzik M., 2006, Astronomy and Astrophysics, 460, 695

Torres C. A. O., Quast G. R., Melo C. H. F., Sterzik M. F., Young Nearby Loose Associations, 757, 2008

Torres-Lopez R. M., Mioduszewki A. J., Loinard L. R., Rodriguez L. F., 2007, American Astronomical Society Meeting Abstracts, 147.01

Tout C. A., Livio M., Bonnell I. A., 1999, Monthly Notices of the RAS, 310, 360

Trilling D. E., Bryden G., Beichman C. A., Rieke G. H., Su K. Y. L., Stansberry J. A., Blaylock M., Stapelfeldt K. R., Beeman J. W., Haller E. E., 2008, Astrophysical Journal, 674, 1086

Udry S., Mayor M., Queloz D., 1999, in Hearnshaw J. B., Scarfe C. D., eds., IAU Colloq. 170: Precise Stellar Radial Velocities, 367

Ushomirsky G., Matzner C. D., Brown E. F., Bildsten L., Hilliard V. G., Schroeder P. C., 1998, Astrophysical Journal, 497, 253

van Leeuwen F., Alphenaar P., Brand J., 1986, Astronomy and Astrophysics, Supplement, 65, 309

van Leeuwen F., 2007, Astronomy and Astrophysics, 474, 653

van Leeuwen F., 2009, Astronomy and Astrophysics, 497, 209

Ventura P., Zeppieri A., Mazzitelli I., D'Antona F., 1998, Astronomy and Astrophysics, 331, 1011

Viana Almeida P., Santos N. C., Melo C., Ammler-von Eiff M., Torres C. A. O., Quast G. R., Gameiro J. F., Sterzik M., 2009, Astronomy and Astrophysics, 501, 965

Vinković D., Ivezić Ž., Jurkić T., Elitzur M., 2006, Astrophysical Journal, 636, 348

Voges W., Aschenbach B., Boller T., Bräuninger H., Briel U., Burkert W., Dennerl K., Englhauser J., Gruber R., Haberl F., Hartner G., Hasinger G., Kürster M., Pfeffermann E., Pietsch W., Predehl P., Rosso C., Schmitt J. H. M. M., Trümper J., Zimmermann H. U., 1999, Astronomy and Astrophysics, 349, 389

Wahhaj Z., Cieza L., Koerner D. W., Stapelfeldt K. R., Padgett D. L., Case A., Keller J. R., Merín B., Evans, II N. J., Harvey P., Sargent A., van Dishoeck E. F., Allen L., Blake G., Brooke T., Chapman N., Mundy L., Myers P. C., 2010, Astrophysical Journal, 724, 835

Wahhaj Z., Liu M. C., Nielsen E. L., Biller B. A., Hayward T. L., Close L. M., Males J. R., Skemer A., Ftaclas C., Chun M., Thatte N., Tecza M., Shkolnik E. L., Kuchner M., Reid I. N., de Gouveia Dal Pino E. M., Alencar S. H. P., Gregorio-Hetem J., Boss A., Lin D. N. C., Toomey D. W., 2013, Astrophysical Journal, 773, 179

Wang B., Justham S., Liu Z.-W., Zhang J.-J., Liu D.-D., Han Z., 2014, Monthly Notices of the RAS, 445, 2340

Webb R. A., Zuckerman B., Platais I., Patience J., White R. J., Schwartz M. J., McCarthy C., 1999, Astrophysical Journal, Letters, 512, L63

Weidenschilling S. J., Cuzzi J. N., 1993, in Levy E. H., Lunine J. I., eds., Protostars and Planets III, 1031

Weidenschilling S. J., 1997, Lunar and Planetary Science Conference, 1517

Weinberger A. J., Schneider G., Becklin E. E., Smith B. A., Hines D. C., 1999, American Astronomical Society Meeting Abstracts 194, 934

Weise P., Launhardt R., Setiawan J., Henning T., 2010, Astronomy and Astrophysics, 517, A88

Wilden B. S., Jones B. F., Lin D. N. C., Soderblom D. R., 2002, Astronomical Journal, 124, 2799

Wilking B. A., Lada C. J., Young E. T., 1989, Astrophysical Journal, 340, 823

Wolk S. J., Harnden, Jr. F. R., Flaccomio E., Micela G., Favata F., Shang H., Feigelson E. D., 2005, Astrophysical Journal, Supplement, 160, 423

Wood K., Lada C. J., Bjorkman J. E., Kenyon S. J., Whitney B., Wolff M. J., 2002, Astrophysical Journal, 567, 1183

Worley C. E., Douglass G. G., 1997, Astronomy and Astrophysics, Supplement, 125, 523

Wright E. L., Eisenhardt P. R. M., Mainzer A. K., Ressler M. E., Cutri R. M., Jarrett T., Kirkpatrick J. D., Padgett D., McMillan R. S., Skrutskie M., Stanford S. A., Cohen M., Walker R. G., Mather J. C., Leisawitz D., Gautier, III T. N., McLean I., Benford D., Lonsdale C. J., Blain A., Mendez B., Irace W. R., Duval V., Liu F., Royer D., Heinrichsen I., Howard J., Shannon M., Kendall M., Walsh A. L., Larsen M., Cardon J. G., Schick S., Schwalm M., Abid M., Fabinsky B., Naes L., Tsai C.-W., 2010, Astronomical Journal, 140, 1868

Wright N. J., Drake J. J., Mamajek E. E., Henry G. W., 2011, Astrophysical Journal, 743, 48

Wyatt M. C., 2008, Annual Review of Astron and Astrophys, 46, 339

Xing L.-F., Xing Q.-F., 2012, Astronomy and Astrophysics, 537, A91

Yamamoto K., Matsuo T., McElwain M., Tamura M., Morishita H., Nakashima A., Shibai H., Fukagawa M., Kato E., Kanoh T., Itoh Y., Kaneko Y., Shimoura M., Itoh Y., Funayama H., Hashiguchi T., 2009, in Usuda T., Tamura M., Ishii M., eds, American Institute of Physics Conference Series, 273

Yang W., Bi S., Meng X., Liu Z., 2013, Astrophysical Journal, 776, 112

Yee J. C., Jensen E. L. N., 2010, Astrophysical Journal, 711, 303

Yi S. K., Kim Y.-C., Demarque P., 2003, Astrophysical Journal, Supplement, 144, 259

Yorke H. W., Bodenheimer P., Laughlin G., 1993, Astrophysical Journal, 411, 274

Zacharias N., Monet D. G., Levine S. E., Urban S. E., Gaume R., Wycoff G. L., 2005, VizieR Online Data Catalog, 1297, 0

Zacharias N., Finch C. T., Girard T. M., Henden A., Bartlett J. L., Monet D. G., Zacharias M. I., 2012, VizieR Online Data Catalog, 1322, 0

Zechmeister M., Kürster M., 2009, Astronomy and Astrophysics, 496, 577

Zickgraf F.-J., Krautter J., Reffert S., Alcalá J. M., Mujica R., Covino E., Sterzik M. F., 2005, Astronomy and Astrophysics, 433, 151

Zuckerman B., Webb R. A., 2000, Astrophysical Journal, 535, 959

Zuckerman B., Song I., Webb R. A., 2001, Astrophysical Journal, 559, 388

Zuckerman B., Song I., Bessell M. S., Webb R. A., 2001, Astrophysical Journal, Letters, 562, L87

Zuckerman B., Song I., 2004, Annual Review of Astron and Astrophys, 42, 685

Zuckerman B., Song I., Bessell M. S., 2004, Astrophysical Journal, Letters, 613, L65

Zuckerman B., Rhee J. H., Song I., Bessell M. S., 2011, Astrophysical Journal, 732, 61

Zuckerman B., Melis C., Rhee J. H., Schneider A., Song I., 2012, Astrophysical Journal, 752, 58

Zuckerman B., Vican L., Song I., Schneider A., 2013, Astrophysical Journal, 778, 5

Zwitter T., Siebert A., Munari U., Freeman K. C., Siviero A., Watson F. G., Fulbright J. P., Wyse R. F. G., Campbell R., Seabroke G. M., Williams M., Steinmetz M., Bienaymé O., Gilmore G., Grebel E. K., Helmi A., Navarro J. F., Anguiano B., Boeche C., Burton D., Cass P., Dawe J., Fiegert K., Hartley M., Russell K.,

Veltz L., Bailin J., Binney J., Bland-Hawthorn J., Brown A., Dehnen W., Evans N. W., Re Fiorentin P., Fiorucci M., Gerhard O., Gibson B., Kelz A., Kujken K., Matijevič G., Minchev I., Parker Q. A., Peñarrubia J., Quillen A., Read M. A., Reid W., Roeser S., Ruchti G., Scholz R.-D., Smith M. C., Sordo R., Tolstoi E., Tomasella L., Vidrih S., Wylie-de Boer E., 2008, Astronomical Journal, 136, 421

A Appendices

A.1 RV-failed BPMG and ABDMG candidates

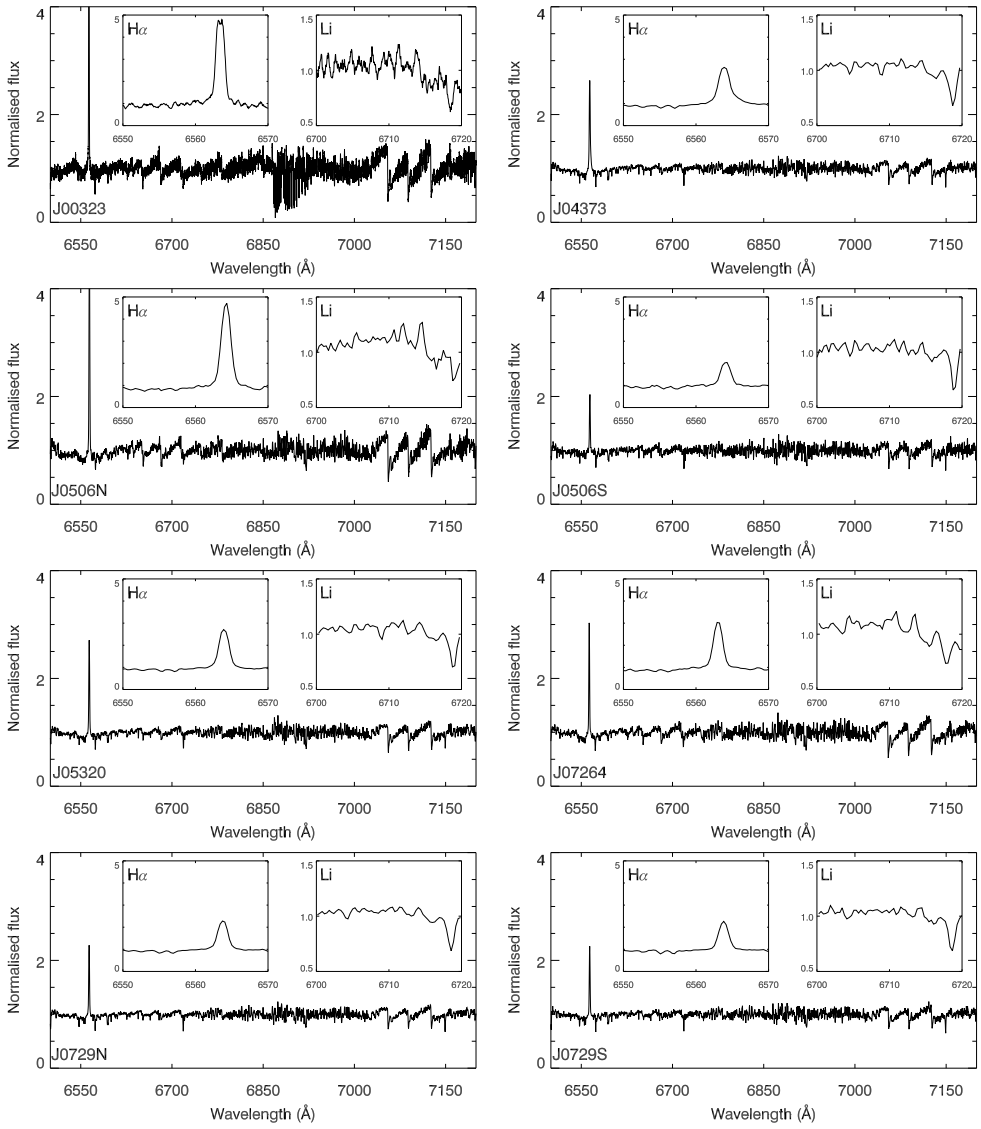

Figure A.1: Spectra for BPMG candidates failing the RV criterion.

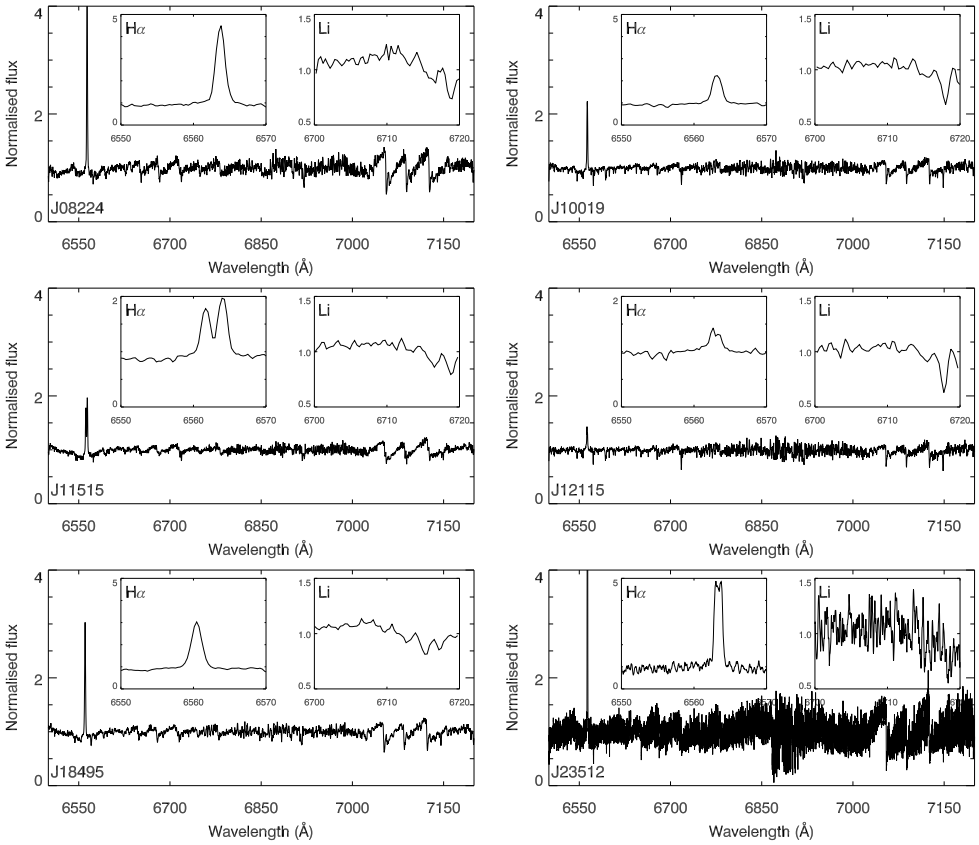

Figure A.1 *continued.*

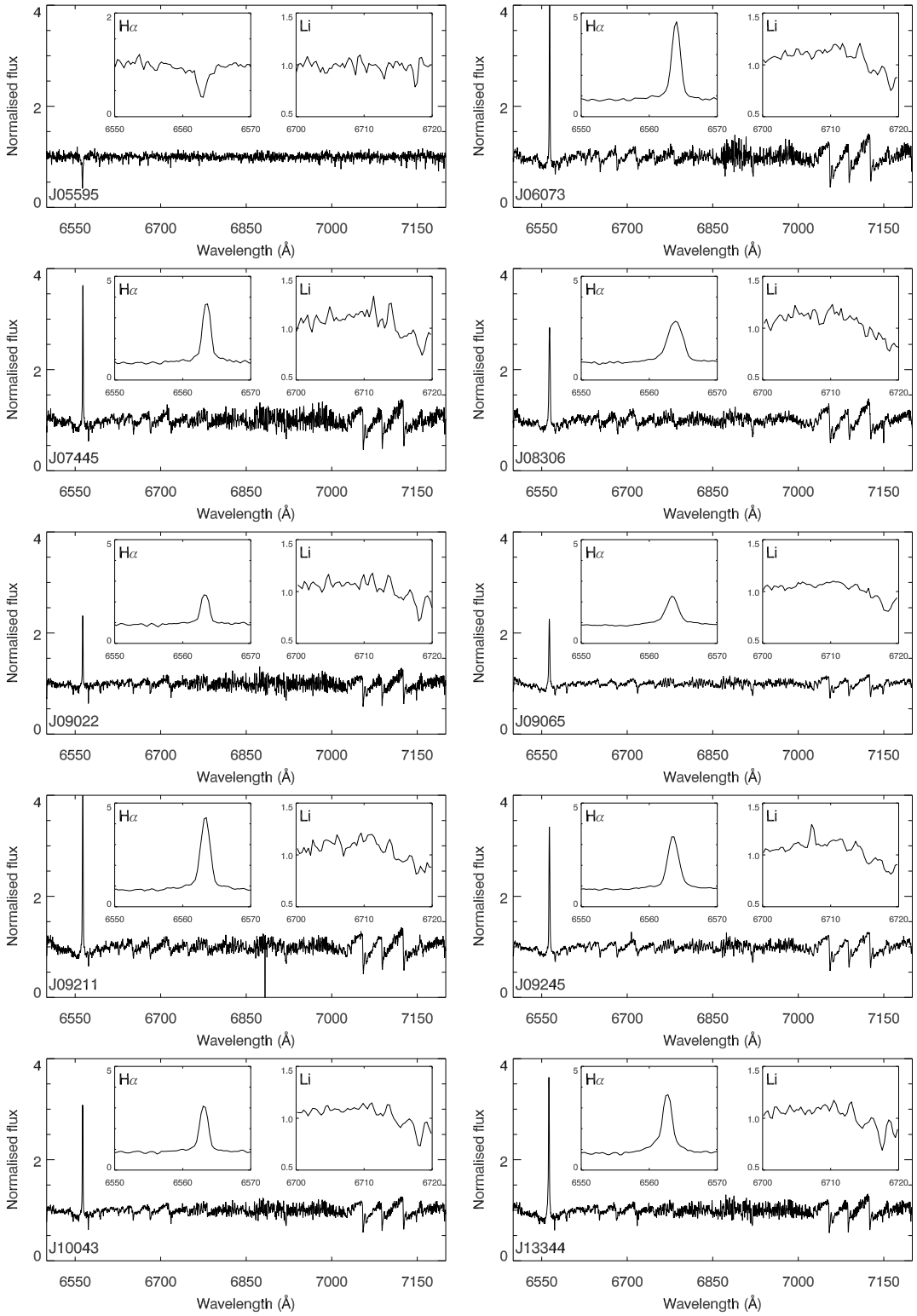

Figure A.2: Spectra for ABDMG candidates failing the RV criterion.

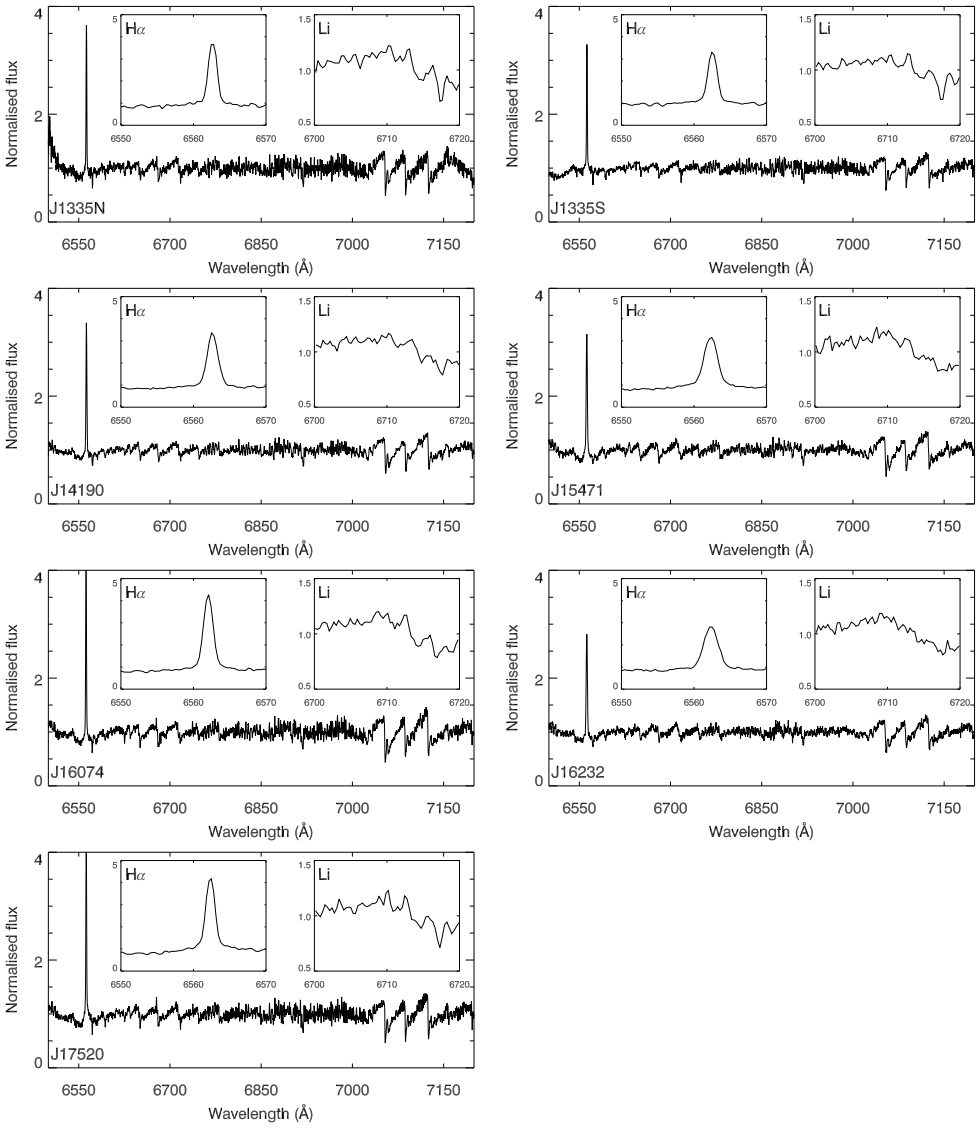

Figure A.2 *continued.*

A.2 Light-curves for the likely-young sample

The data output contains three panels: firstly the raw photometric data measured over each season is displayed in the left window. Each of these time series photometry plots are titled under the naming convention of the target name, followed by the SuperWASP camera number and then by the start and final date over which the measurement took place (given in terms of heliocentric julian date (HJD) - 2450000). The middle plot represents the variation in magnitude over one phase, with a $y_i = a\sin(\omega t_i) + b\cos(\omega t_i)$ fit to calculate the period. The corresponding power spectrum is displayed on the right panel with the highest power value labelled in the title. Also superimposed on these plots are the FAP values at 0.1, 1 and 10 per cent. Note that the periods reported here are the original measured periods before the reanalysis in §5.2.

A, SW0124+2557

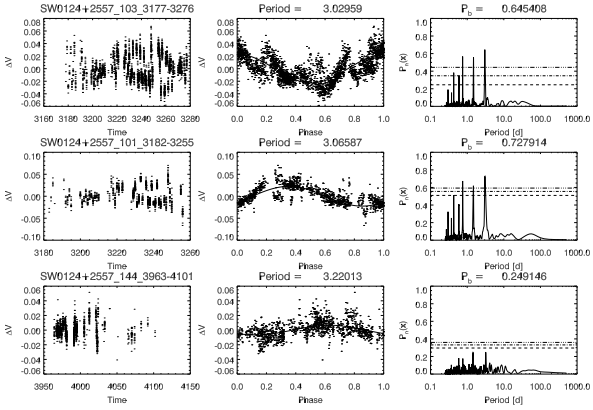

B, SW0135+2116

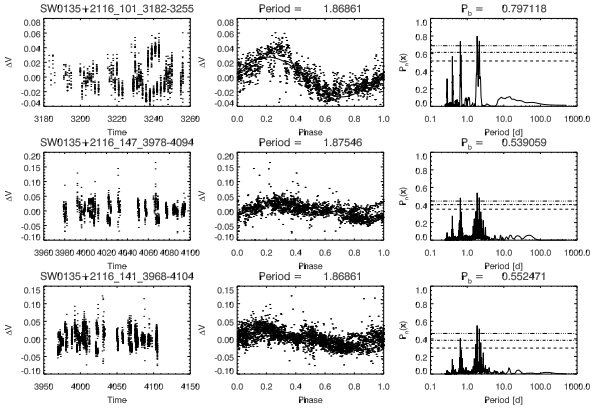

C, SW0235+3139

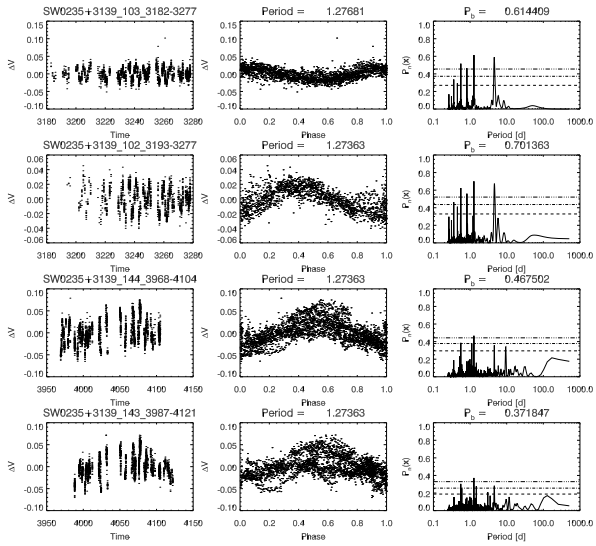

E, SW0316+5638

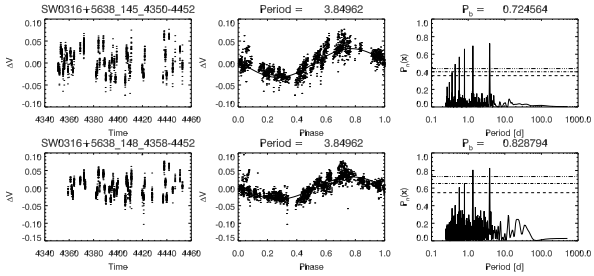

F, SW0322+2853

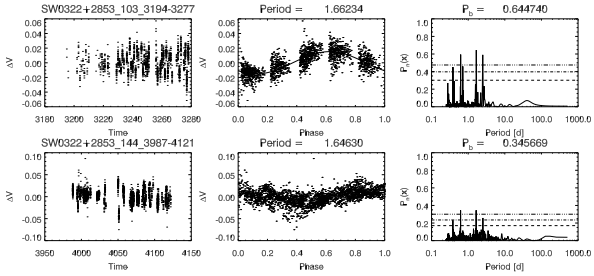

D, SW0304+3003

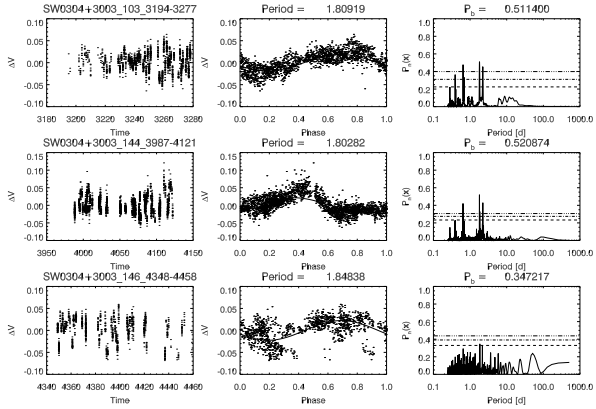

G, SW0343+2226

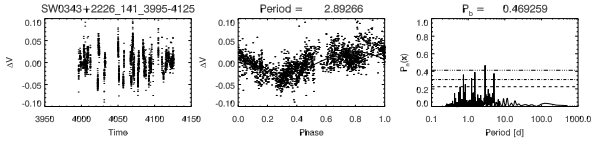

H, SW0502+3111

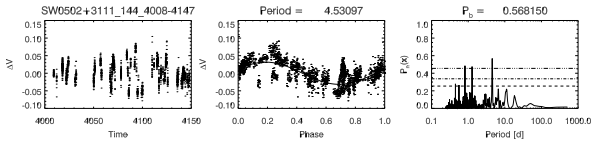

I, SW0521+2400

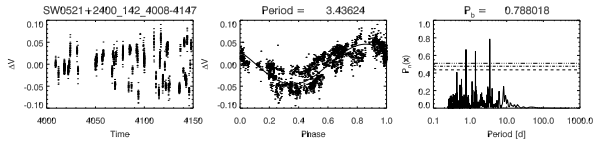

J, SW0847+3423

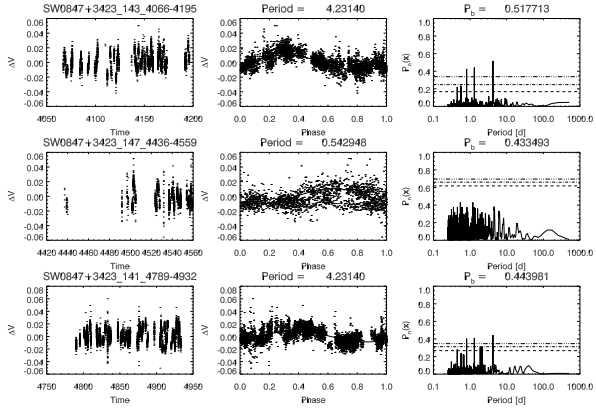

K, SW1337+4444

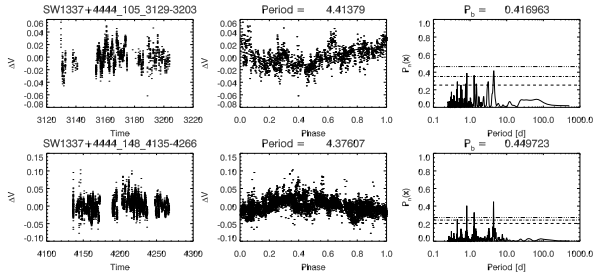

L, SW1354−0543

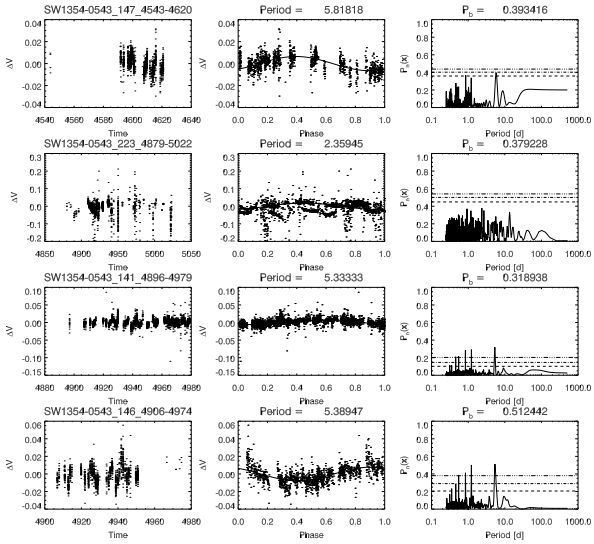

M, SW1438+3300

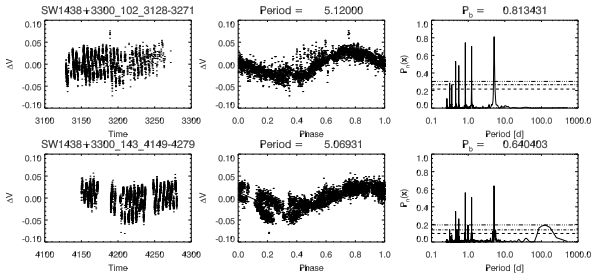

N, SW1625+3002

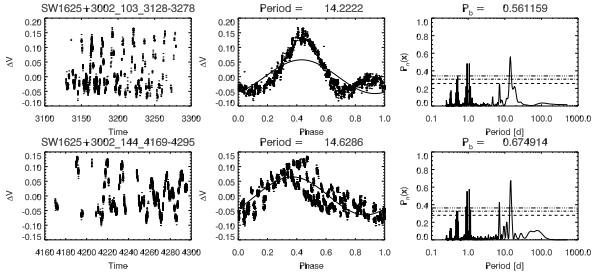

O, SW2145+2711

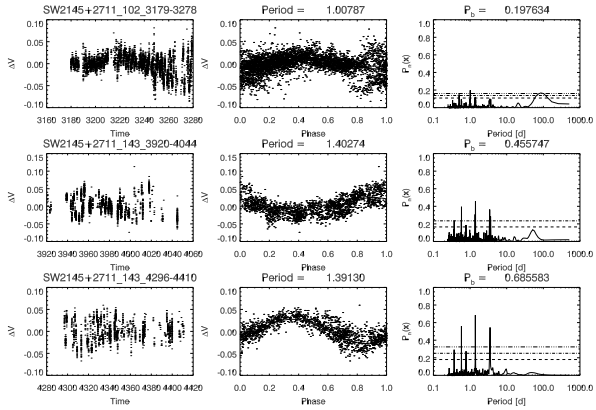

P, SW1332+2230

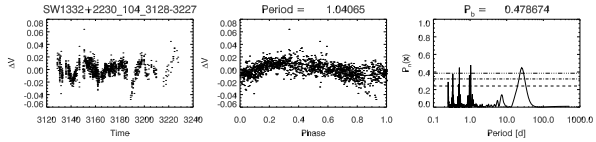

Q, SW1550−0222

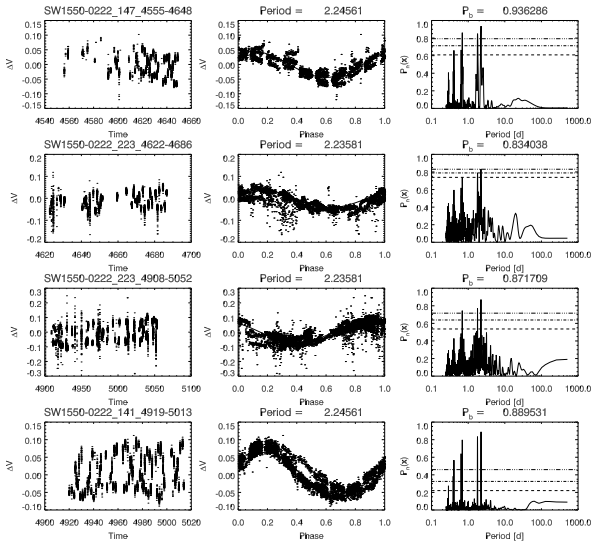

R, SW1629+2810

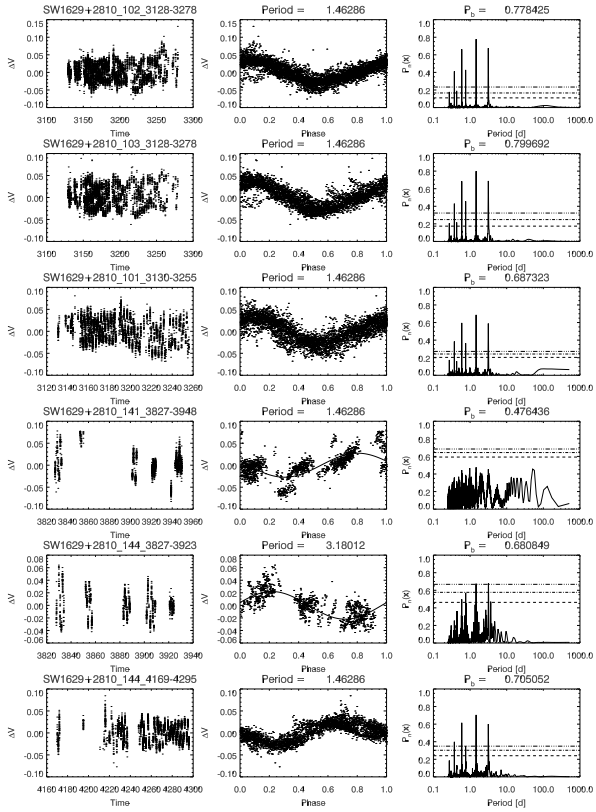

T, SW1722+3658

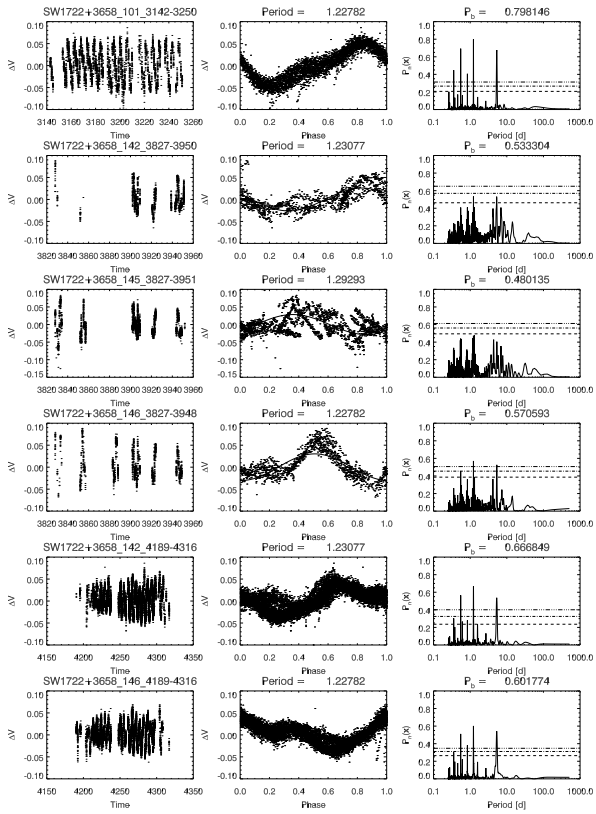

S, SW1718+2506

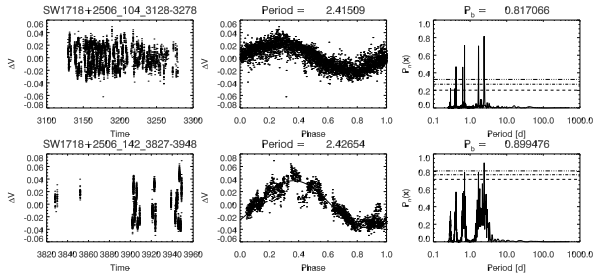

T, SW1722+3658 (cont.)

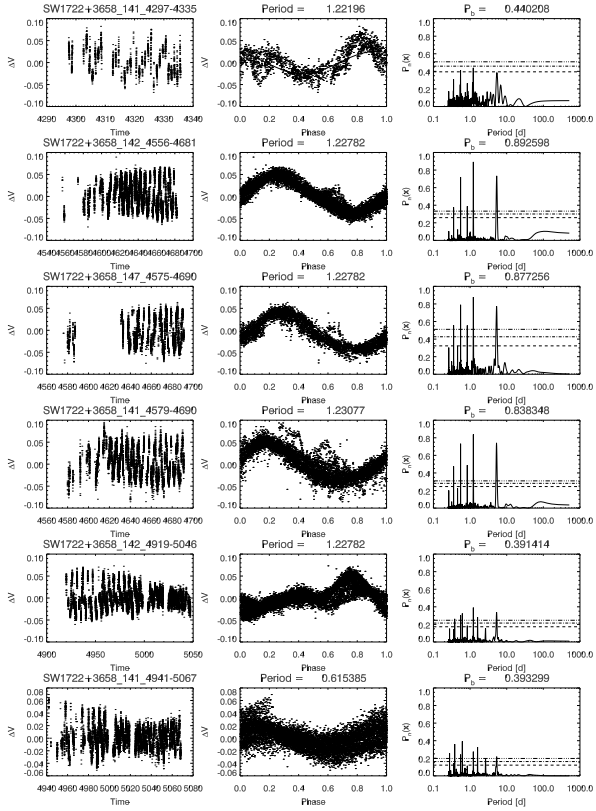

V, SW1804+3930

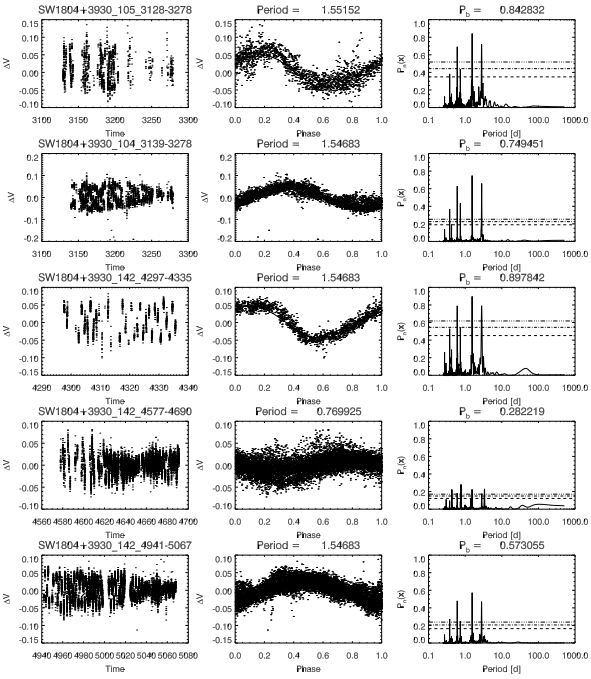

U, SW1731+2815

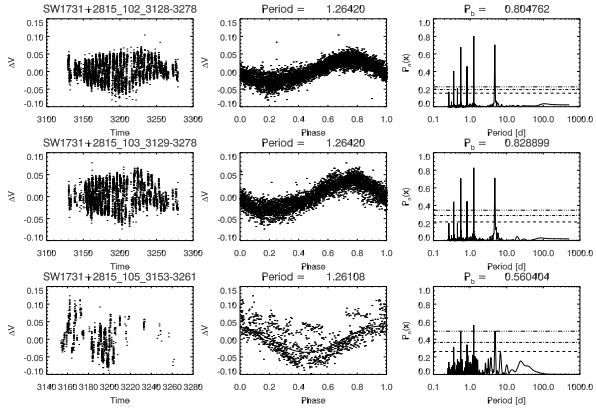

W, SW1925+4429

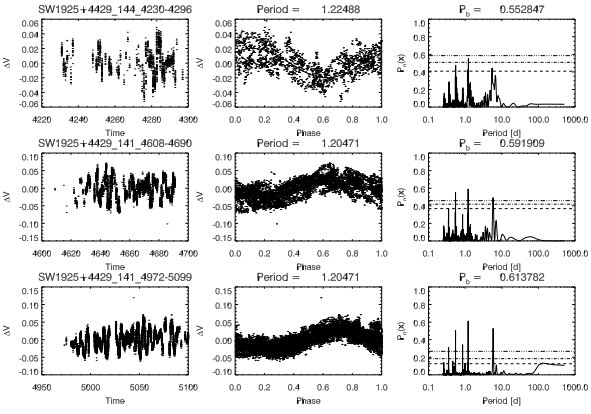

X, SW2058−0902

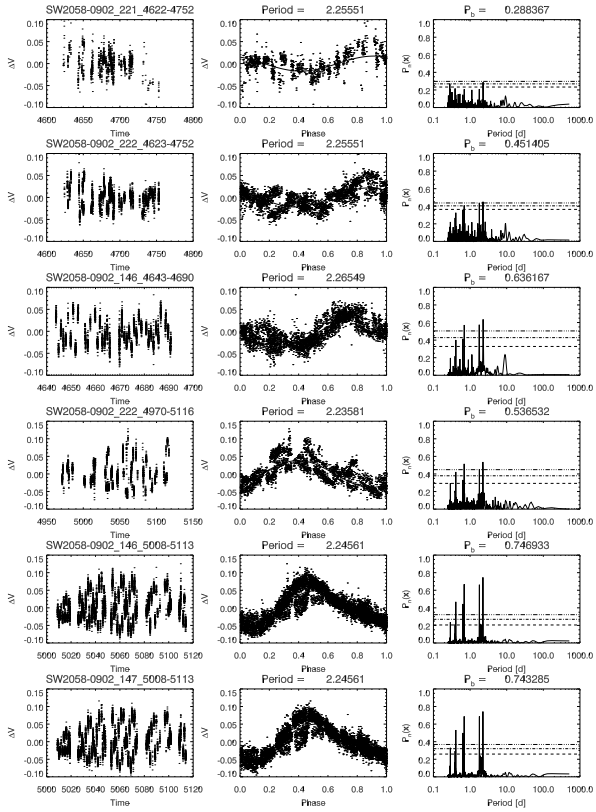

Y, SW2256+2052

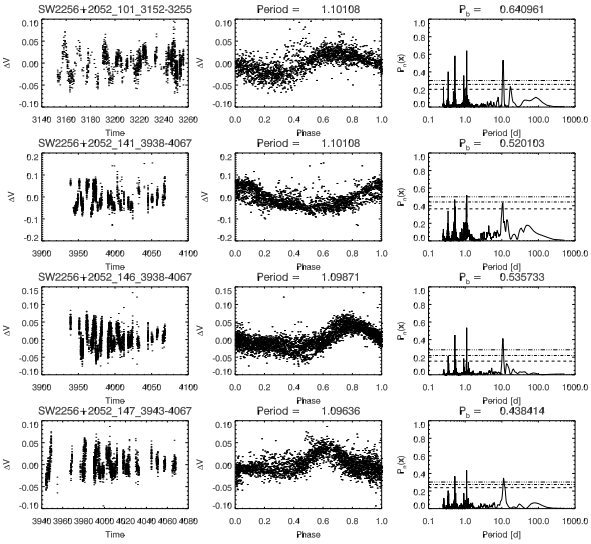

Z, SW2307+1710

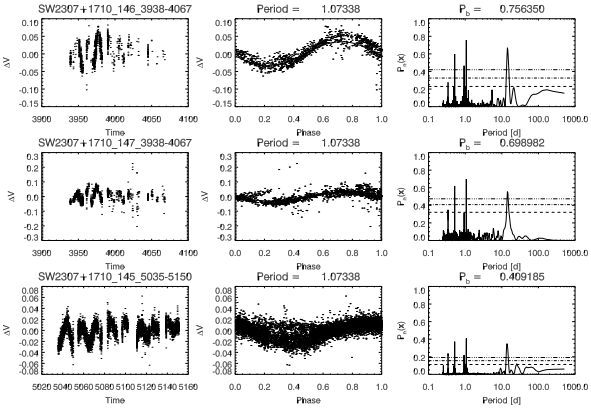

A.3 Supplementary light-curves for the remaining objects

The data output are in the same format as described in Appendix A.3.

SW0016+0546

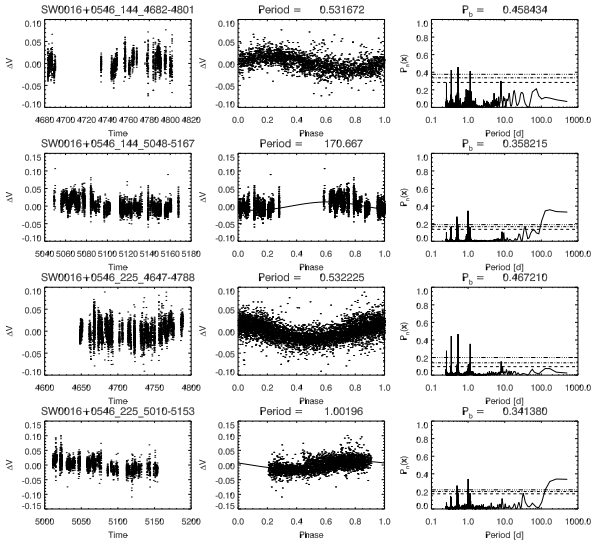

SW0017−0102

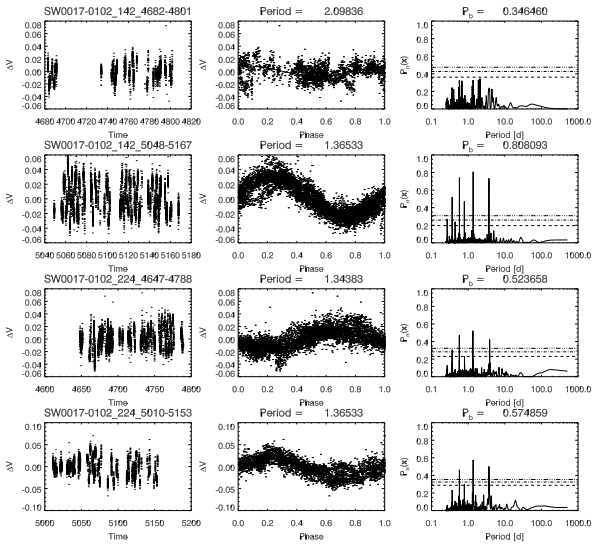

SW0018+2324

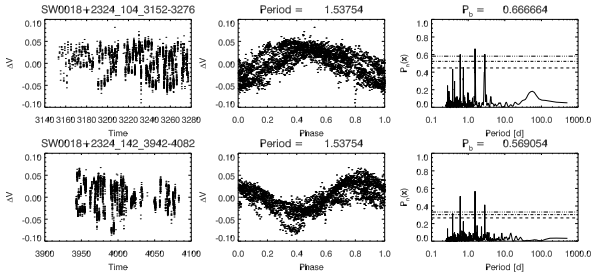

SW0031+3123

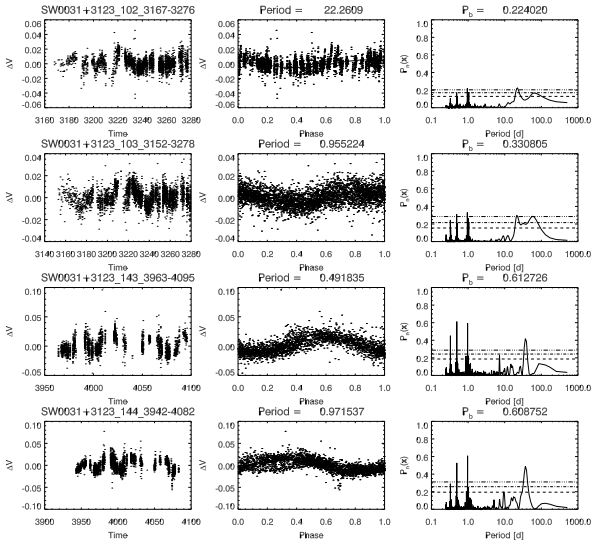

SW0108+3138

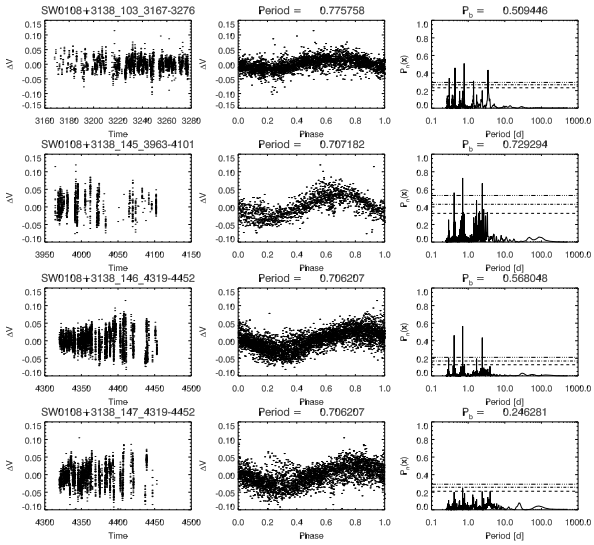

SW0127+1859

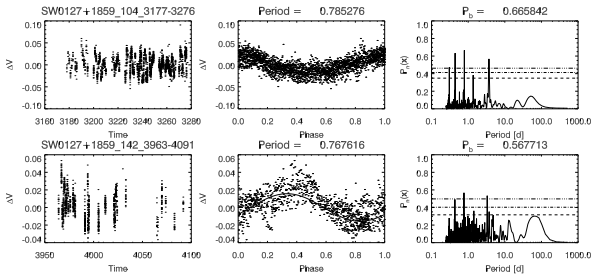

SW0047+3812

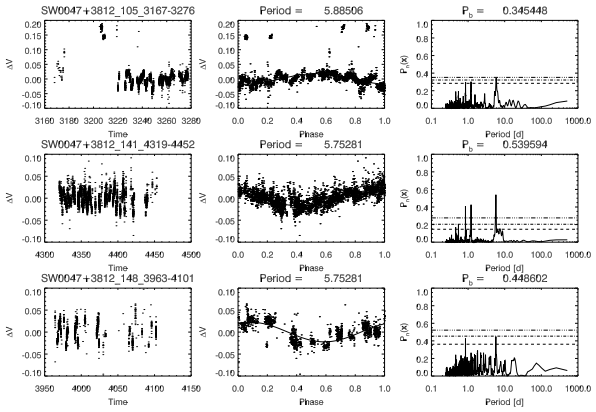

SW0133+4937

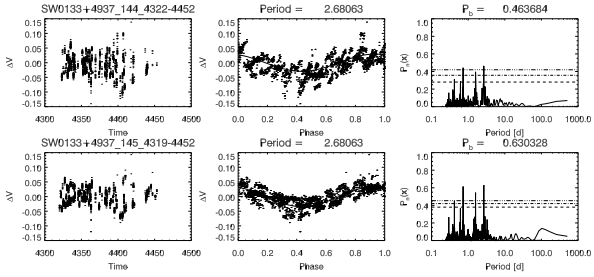

SW0140+4212

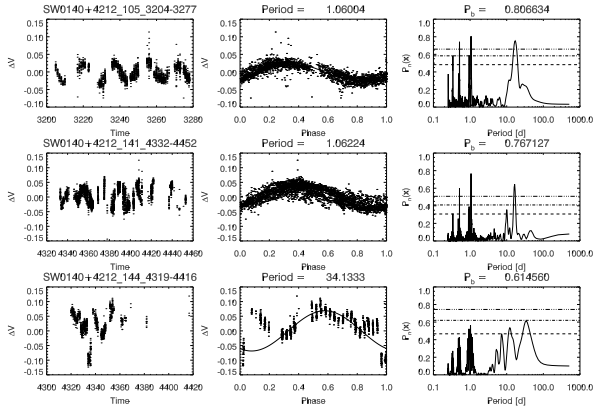

SW0144+2824

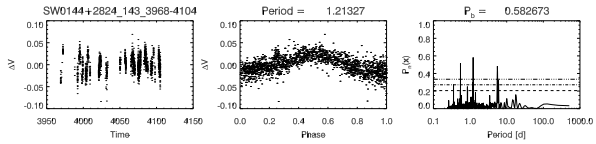

SW0156−0500

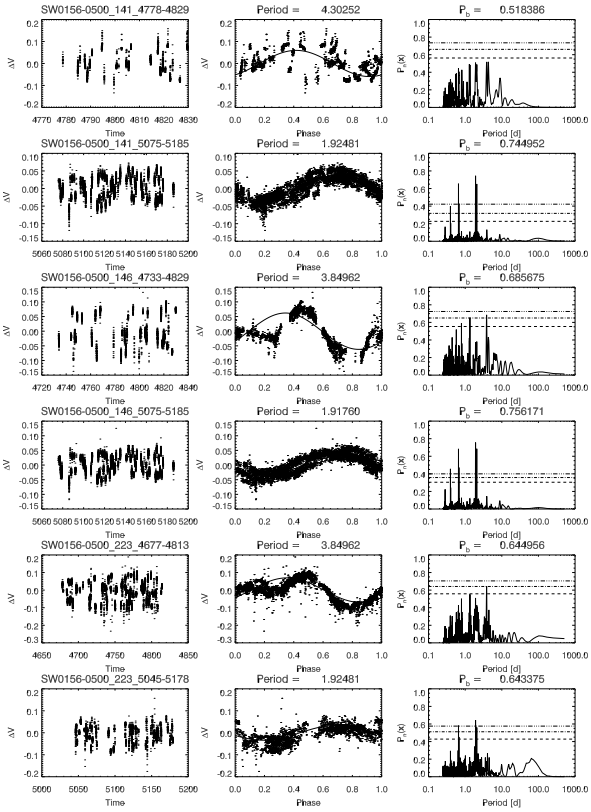

SW0221+3404

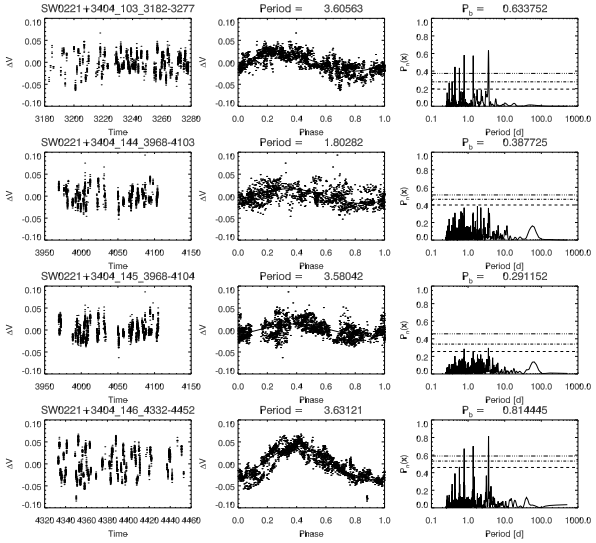

SW0257+2357

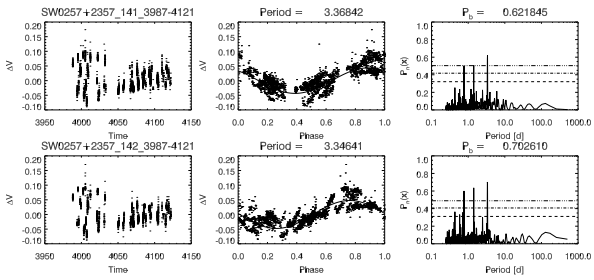

SW0330+5417

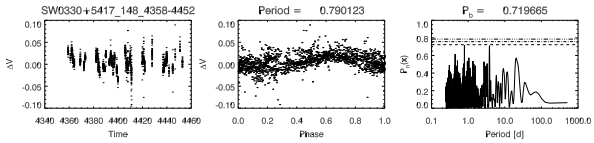

SW0227+2858

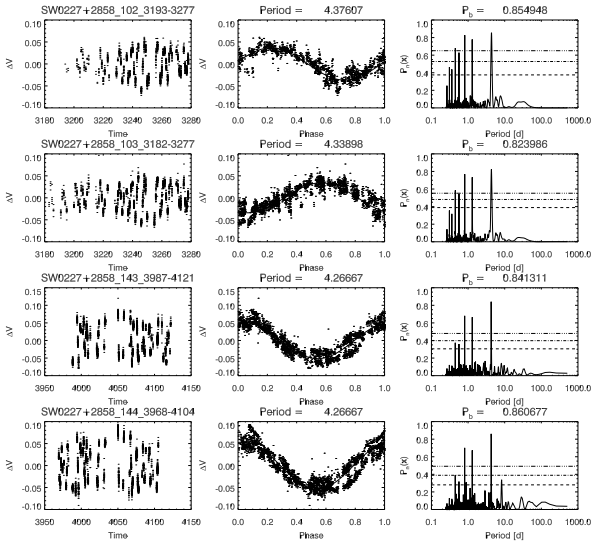

SW0331+4831

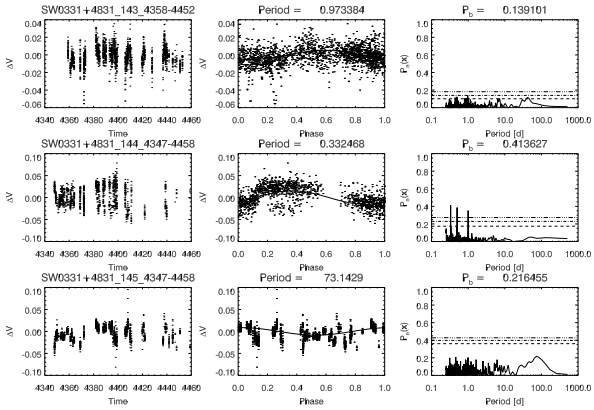

SW0334+4753

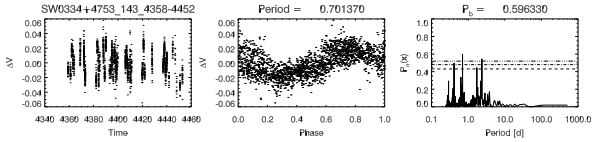

SW0338+4636

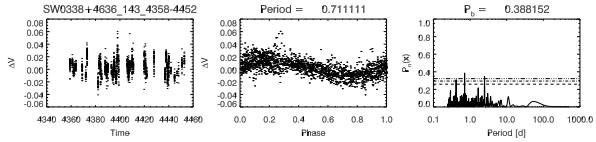

SW0344+5043

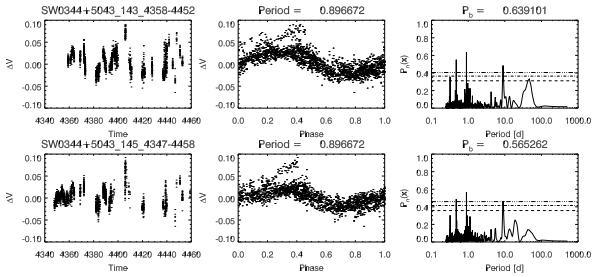

SW0340+3118

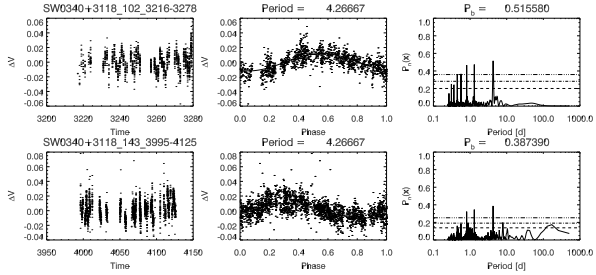

SW0345+5615

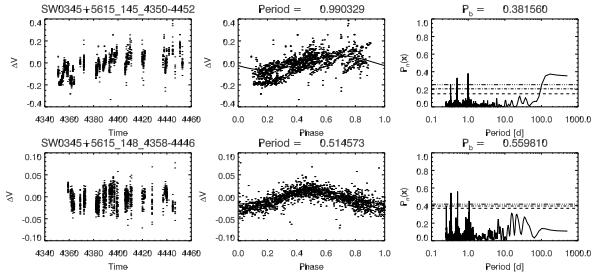

SW0340+2718

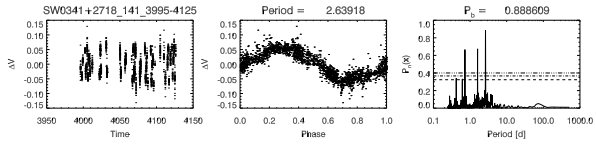

SW0346+3302

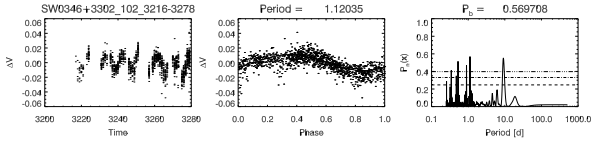

SW0401+3439

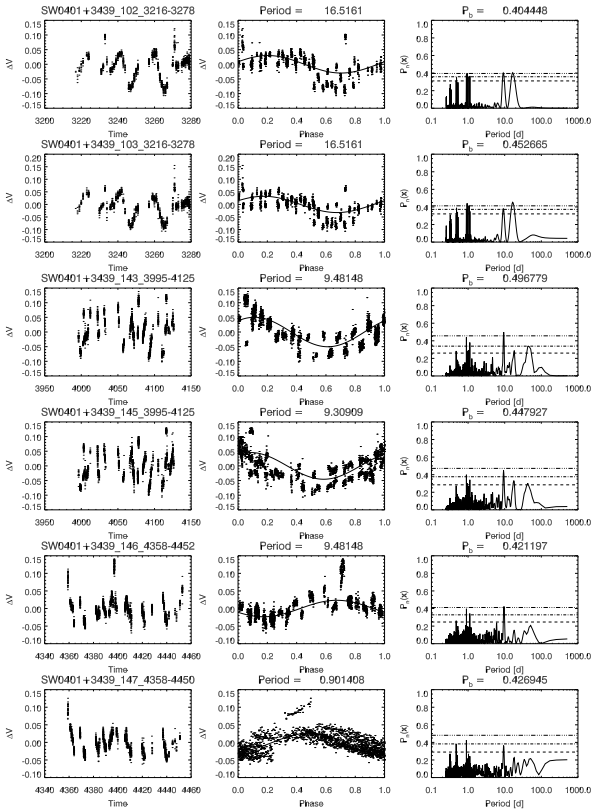

SW0417+3531

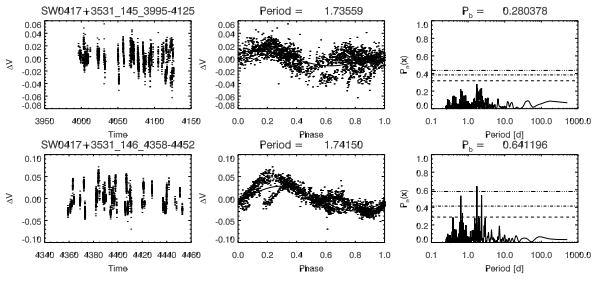

SW0419+2317

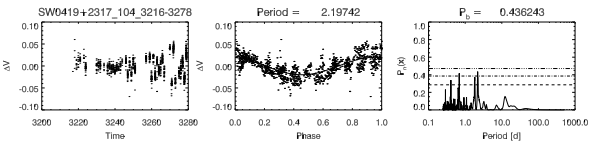

SW0423+5556

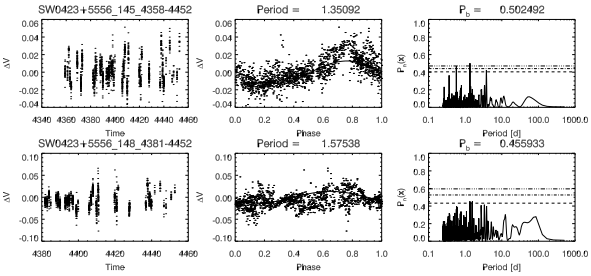

SW0431+3751

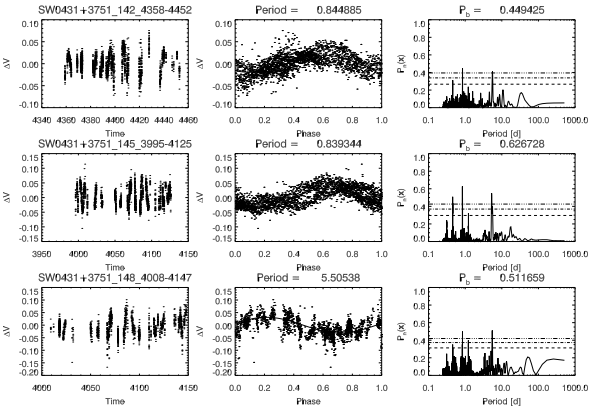

SW0520+2447

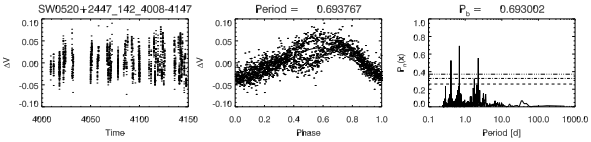

SW0524+5404

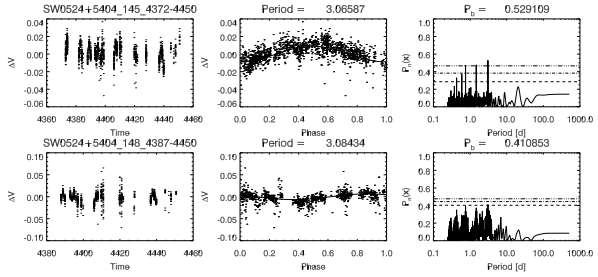

SW0535+3946

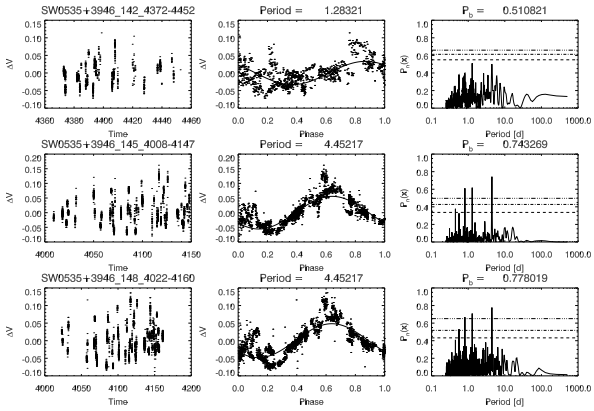

SW0526+2231

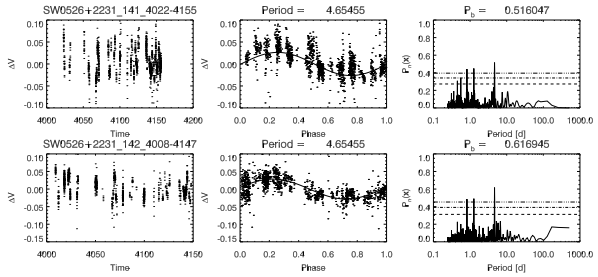

SW0546+5040

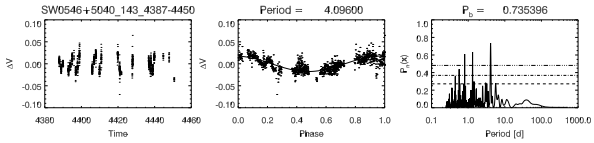

SW0531+2312

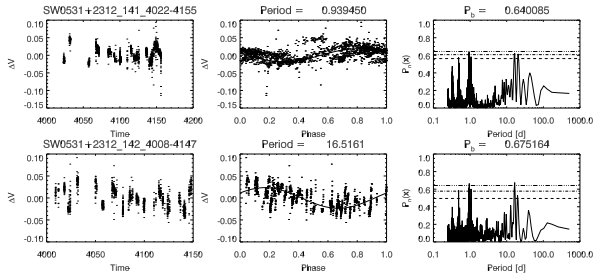

SW0556+2305

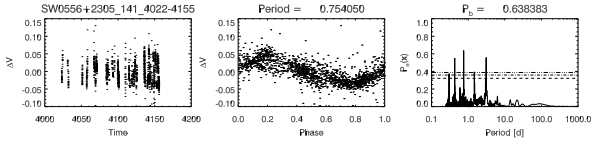

SW0640+2518

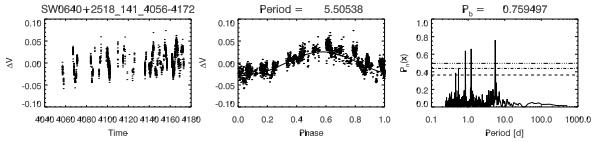

SW0746+2858

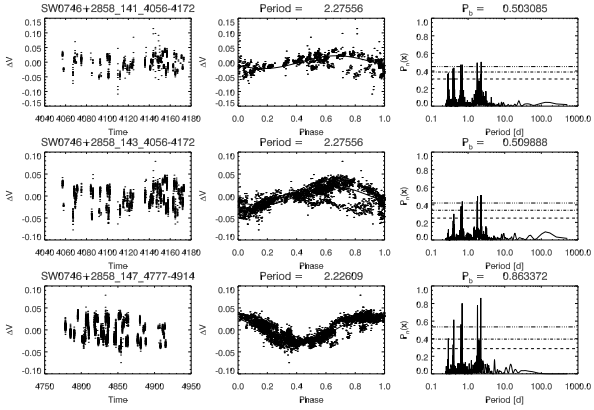

SW0806+2532

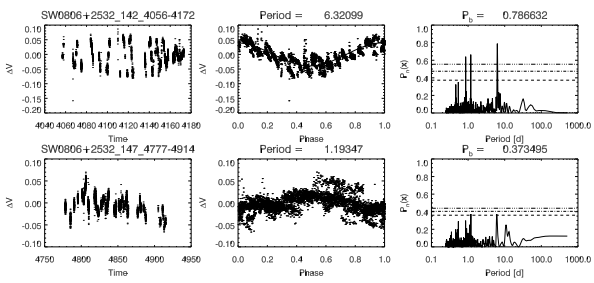

SW0815+2946

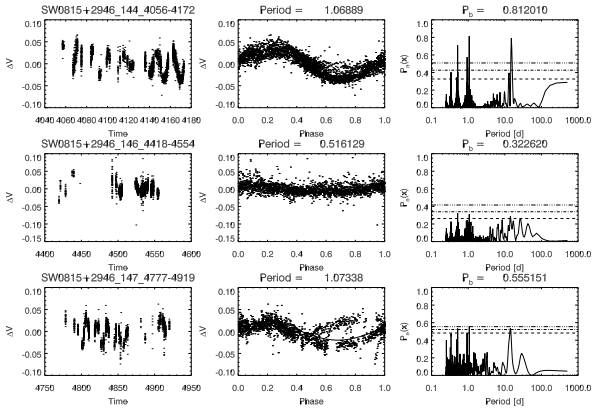

SW0817+3241

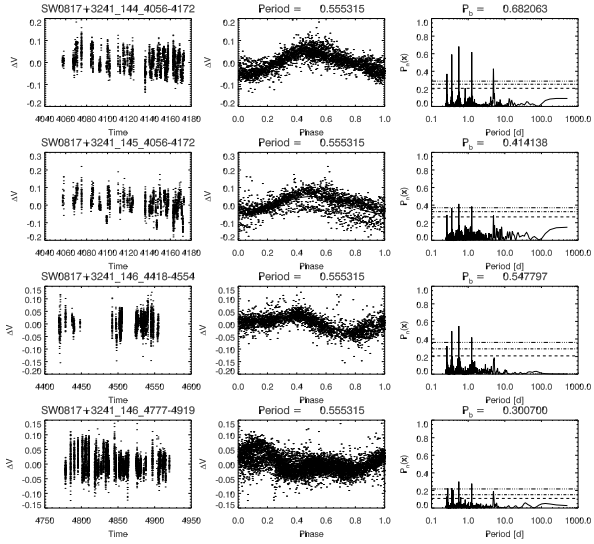

SW0828−0843

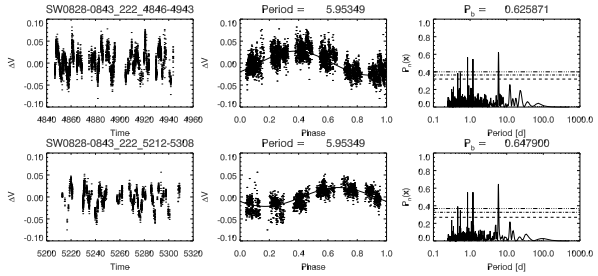

SW0833+3224

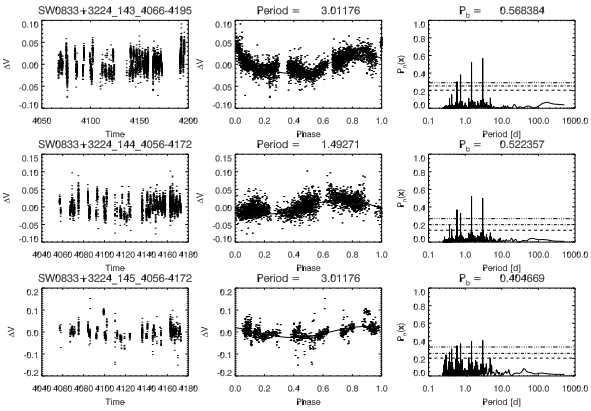

SW0828+4222

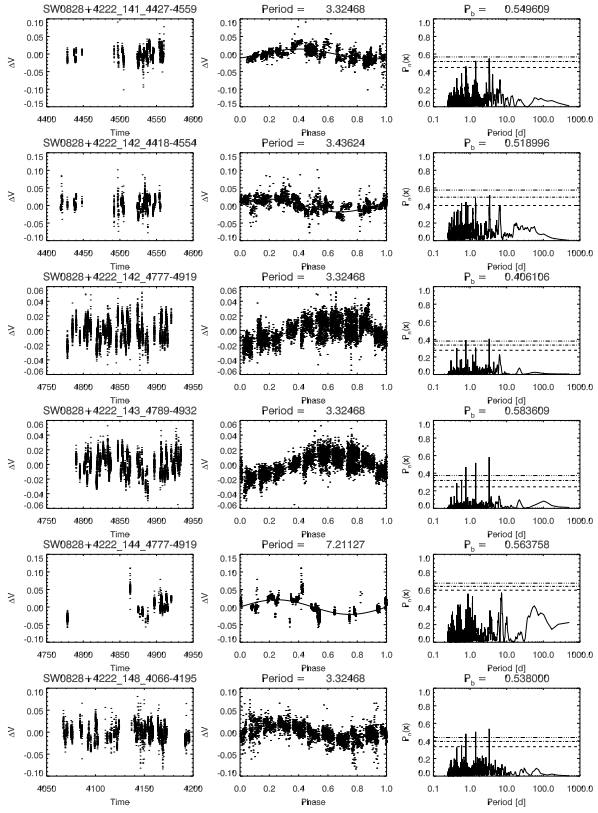

SW0833+3350

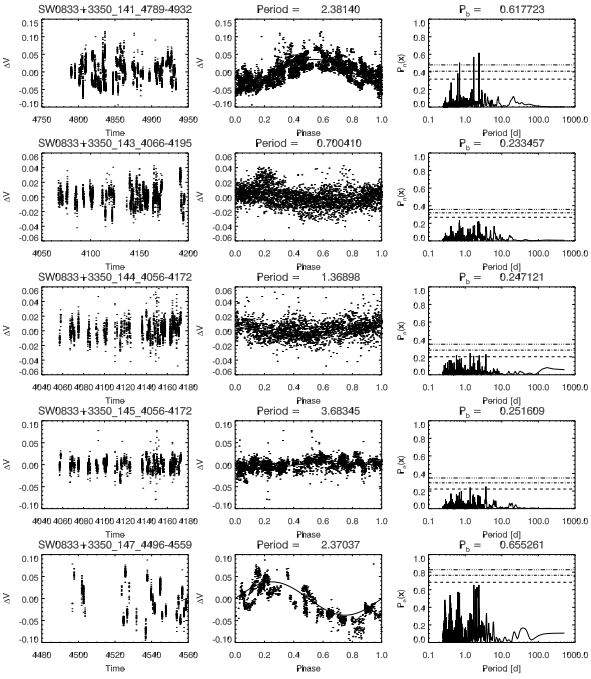

SW0838−0741

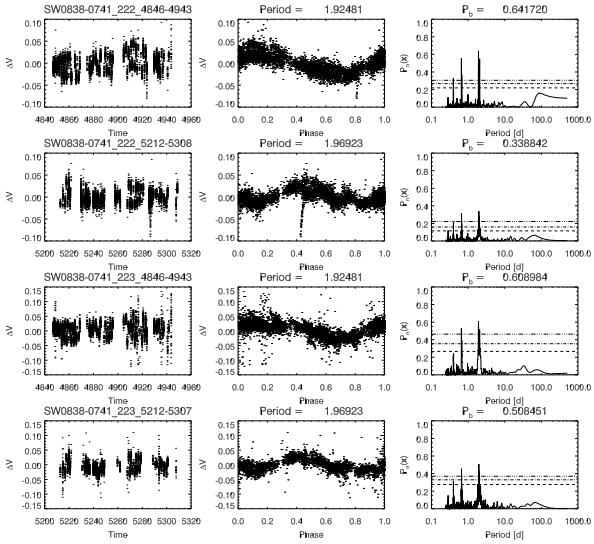

SW0906+3337

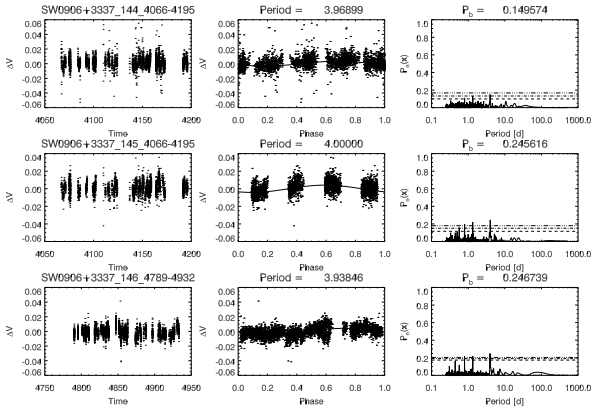

SW0852+3907

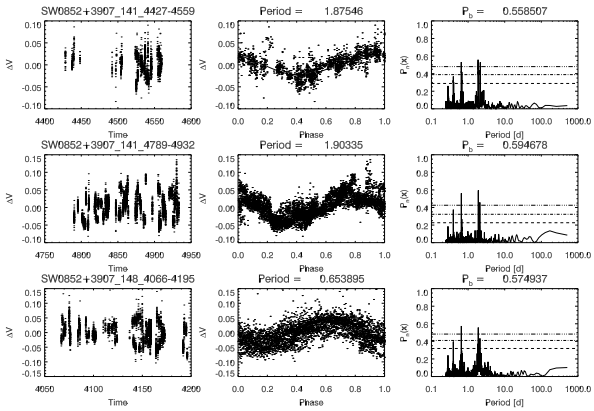

SW0959+3849

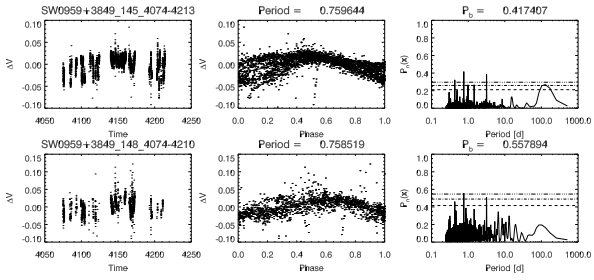

SW0859−0916

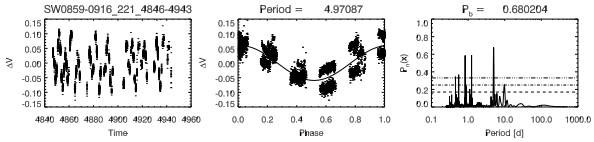

SW1000−0854

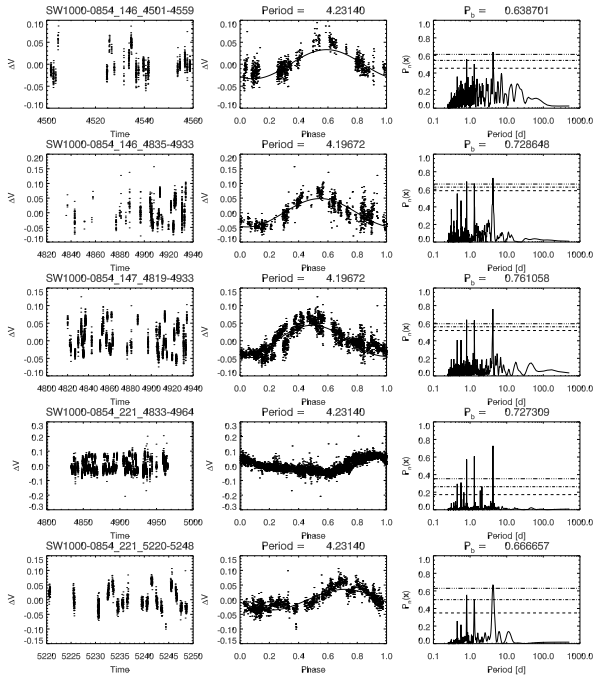

SW1130−0227

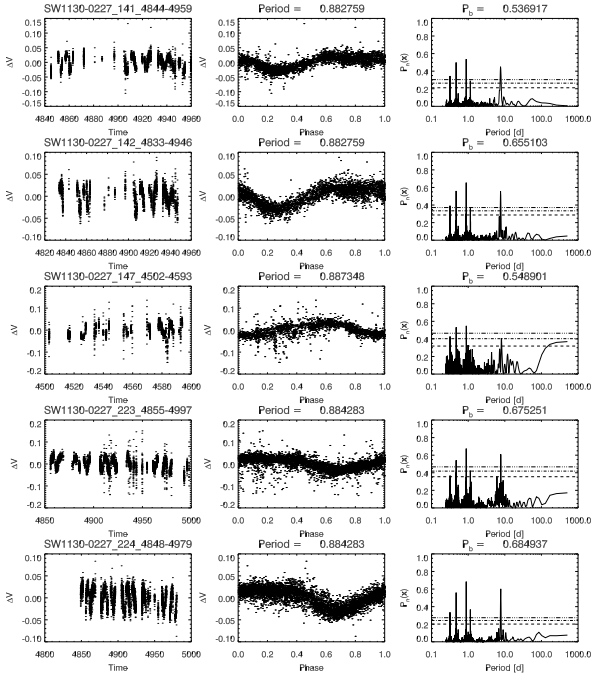

SW1055+4246

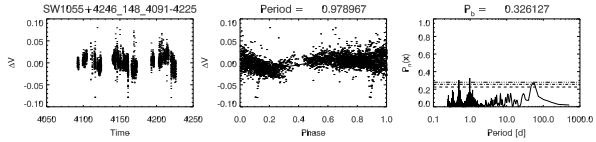

SW1059+2315

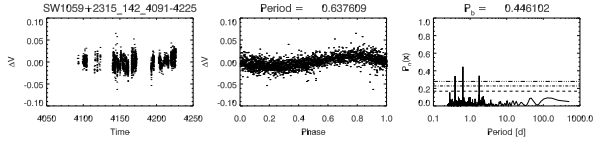

SW1133+3613

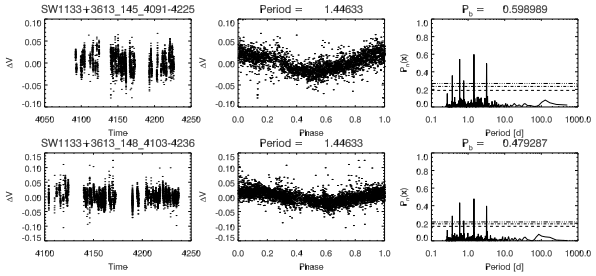

SW1208+3111

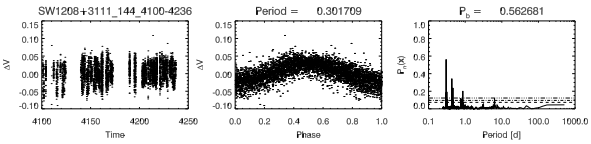

SW1146+4001

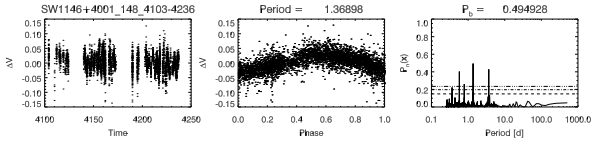

SW1221+2005

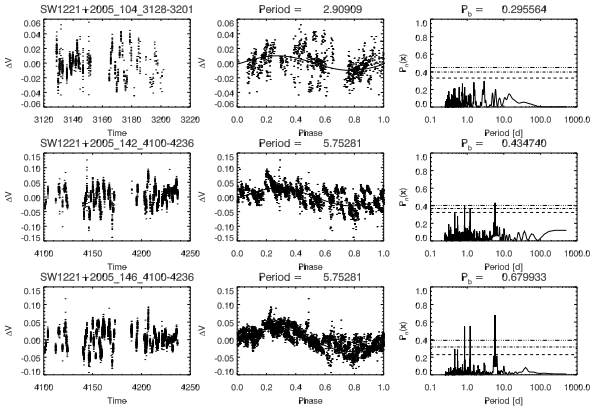

SW1148−0818

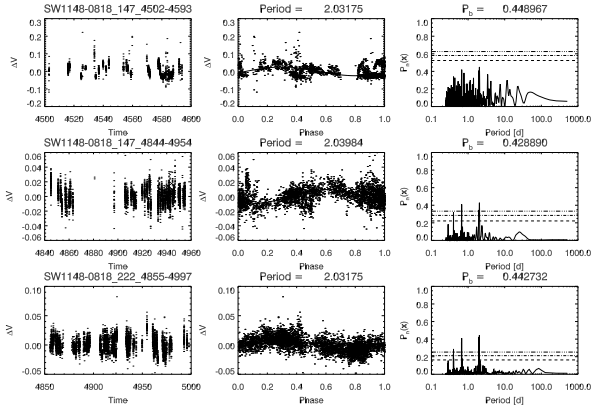

SW1237+3450

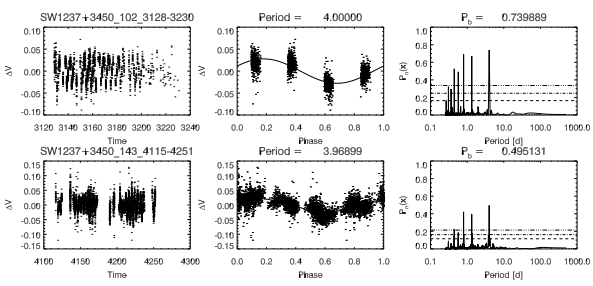

SW1251+2232

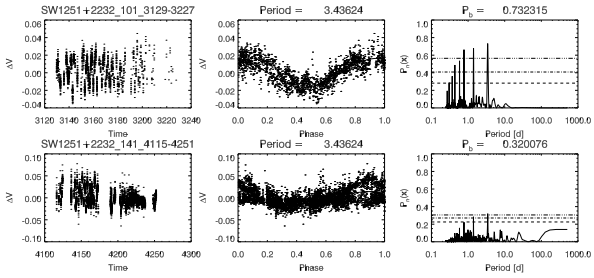

SW1328+3533

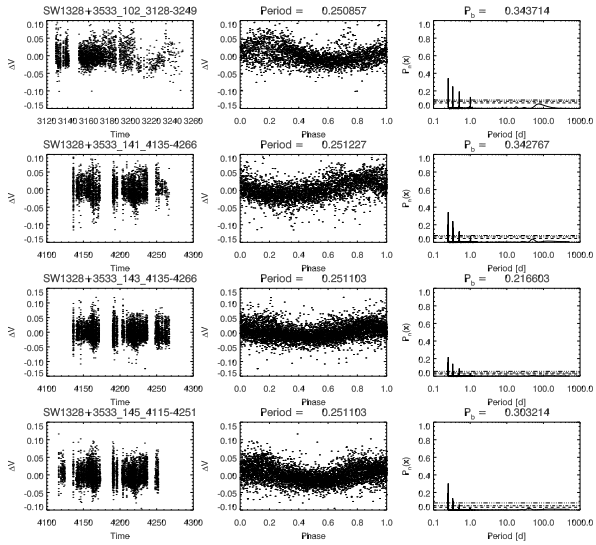

SW1251+2505

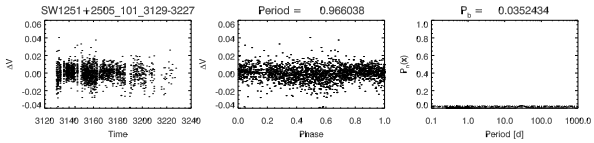

SW1321+2101

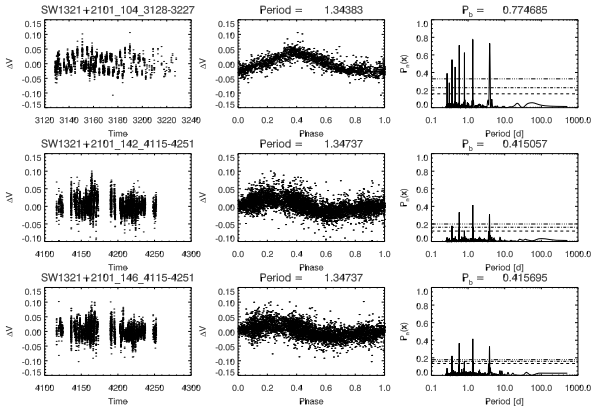

SW1329−0454

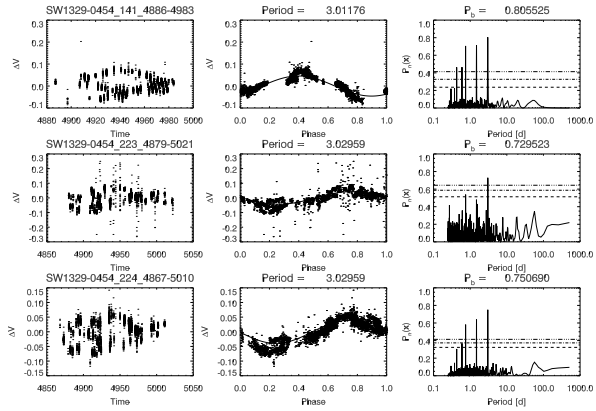

SW1327+4558

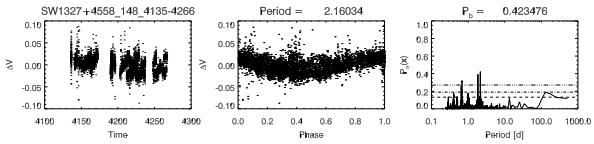

SW1333+2300

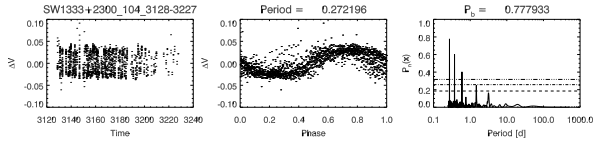

SW1343+3911

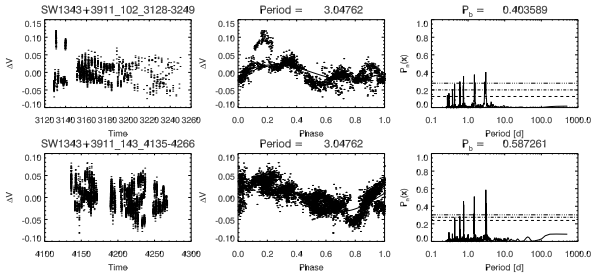

SW1420+3459

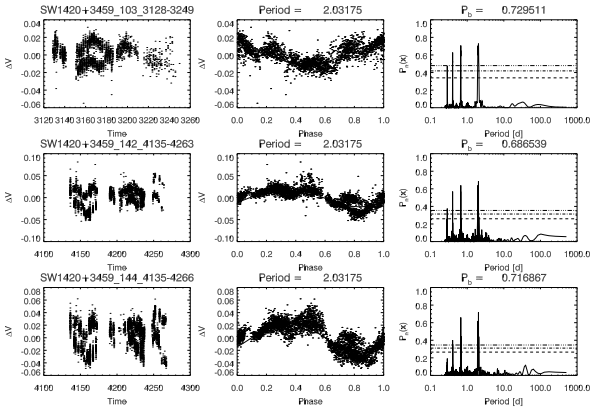

SW1419−1634

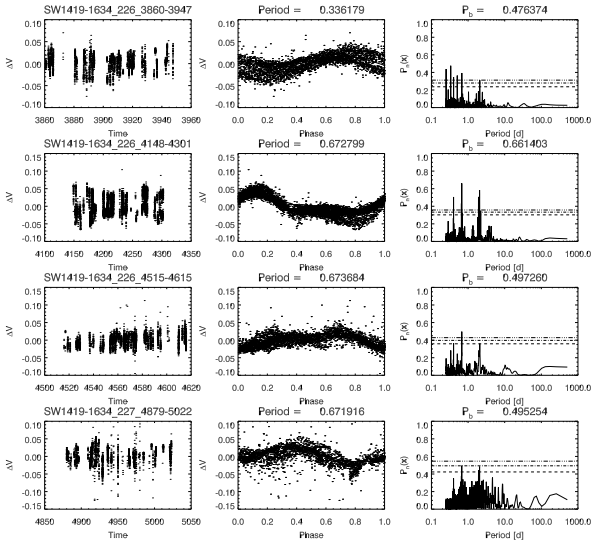

SW1429+3350

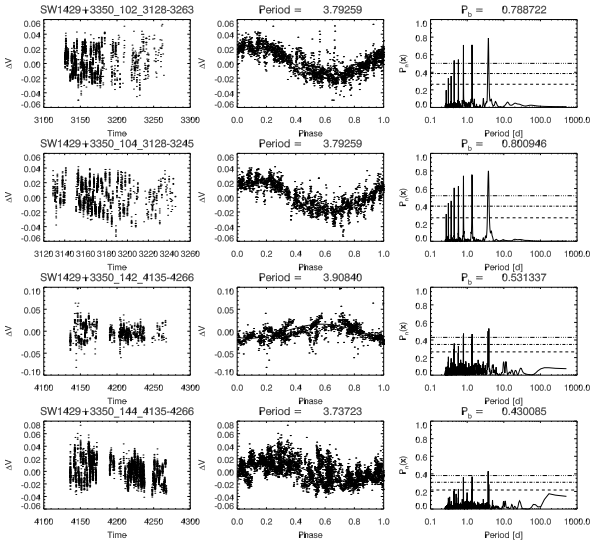

SW1437−0331

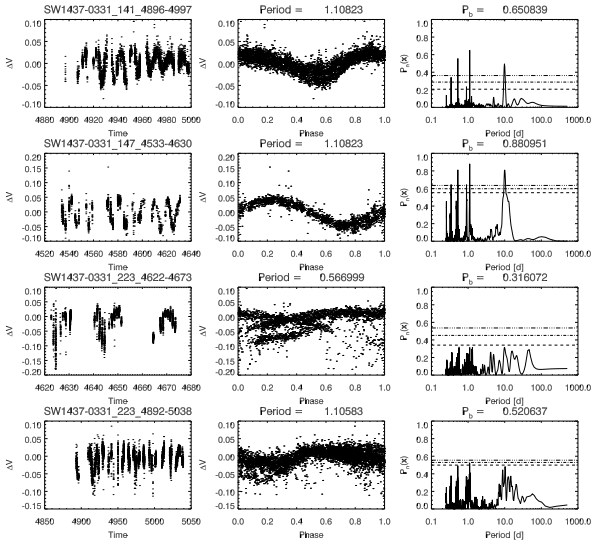

SW1502−1201

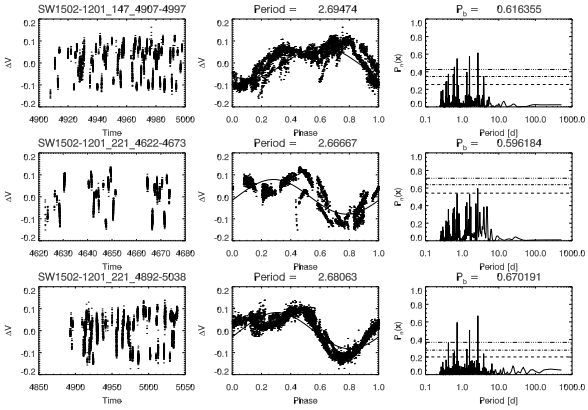

SW1445−0854

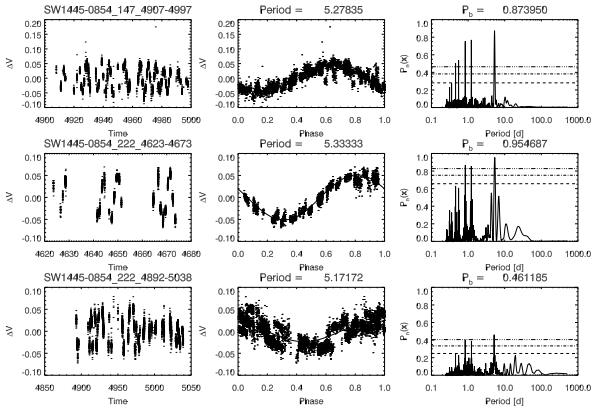

SW1528−1010

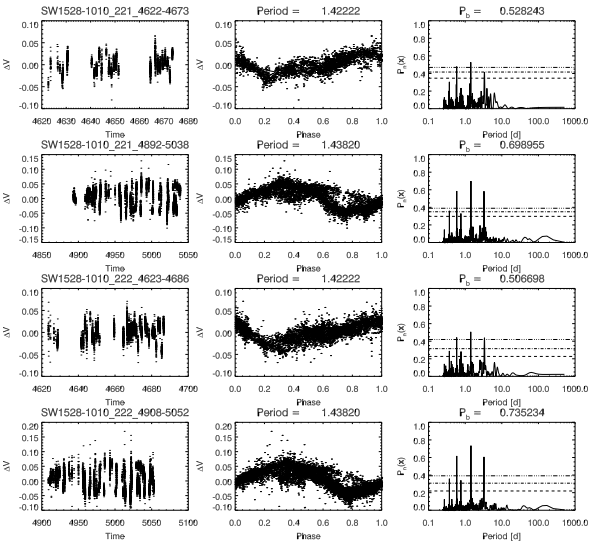

SW1531−0734

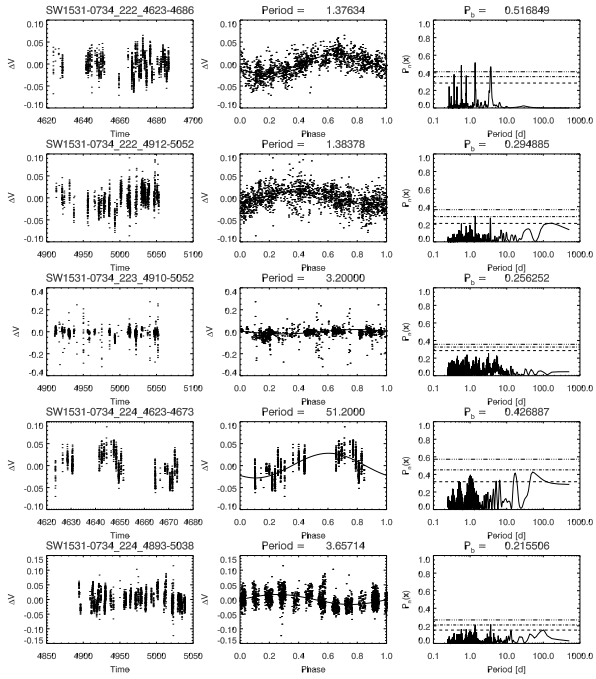

SW1607+3401

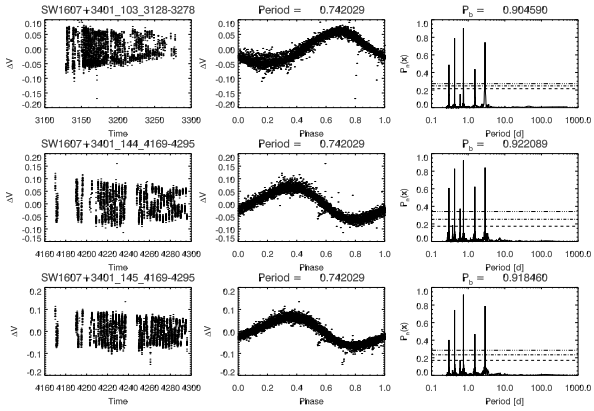

SW1548−0310

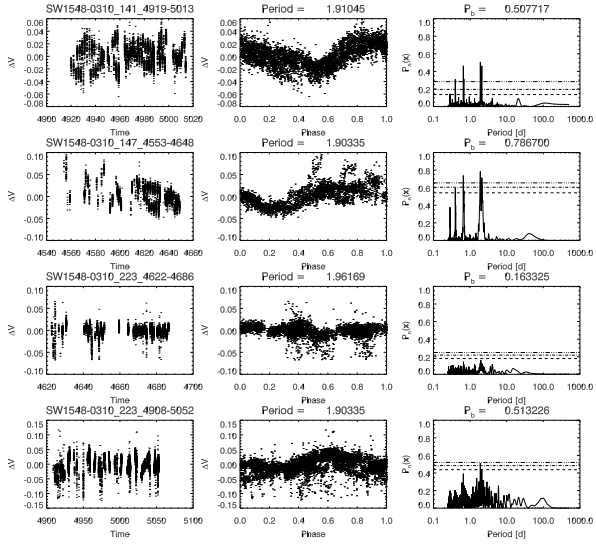

SW1622+2246

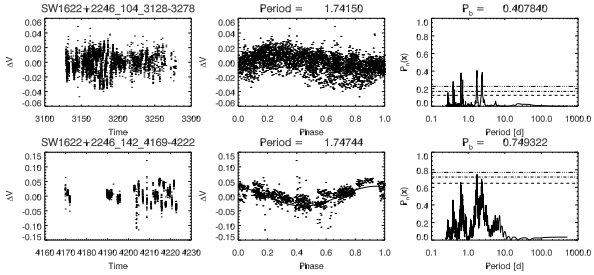

SW1626+3502

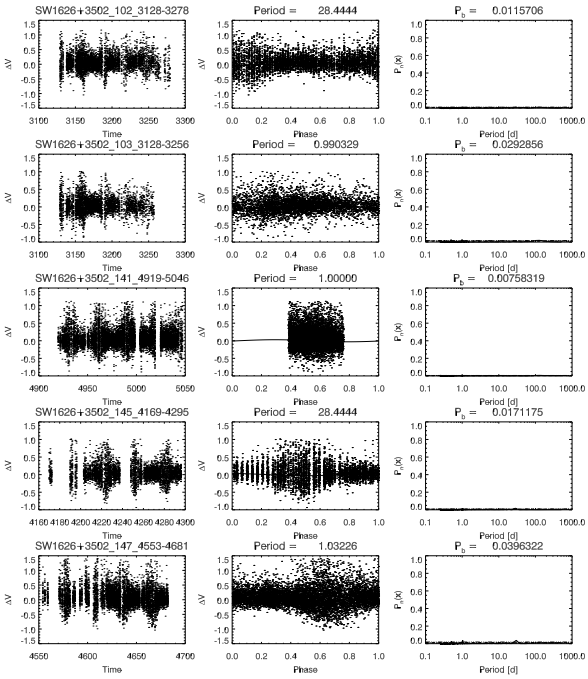

SW1626+3350

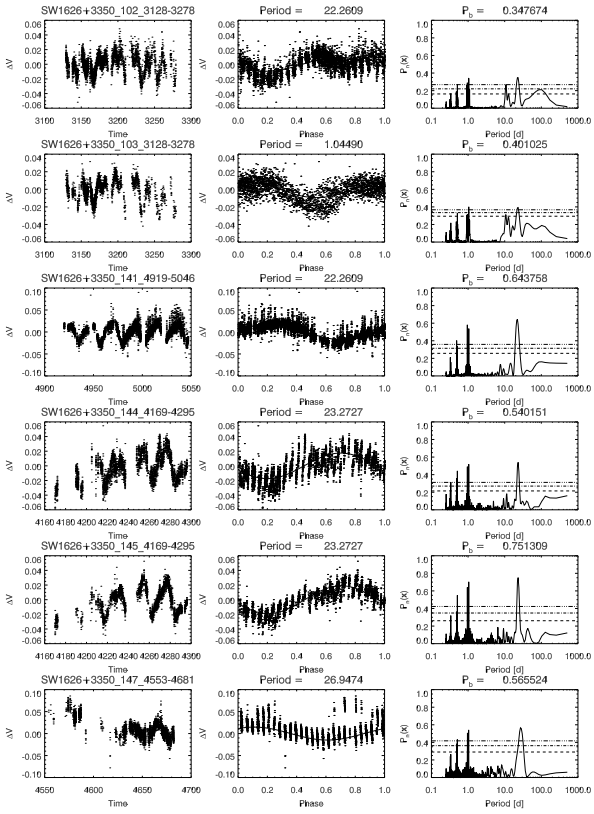

SW1637+2211

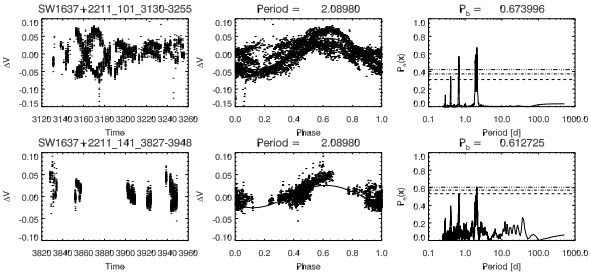

SW1637+2919

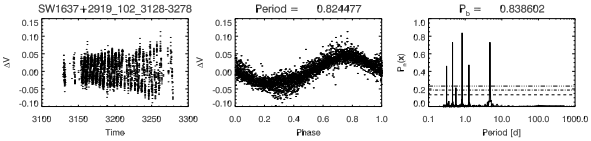

SW1649+4122

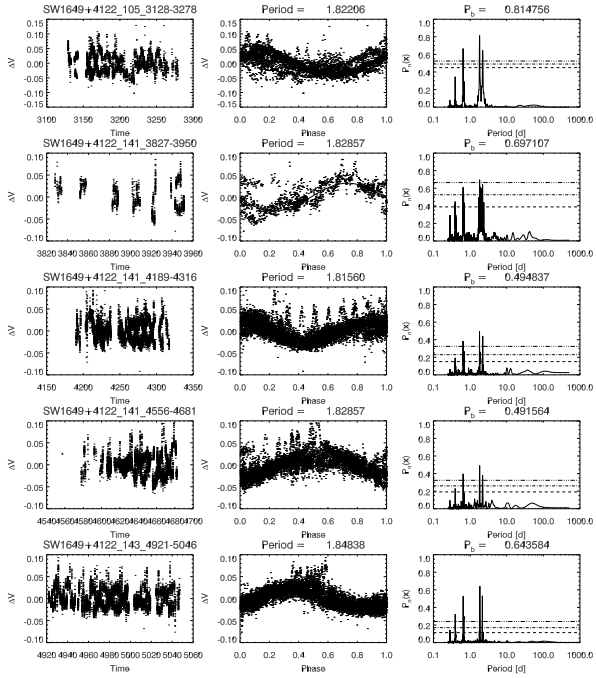

SW1659+3428

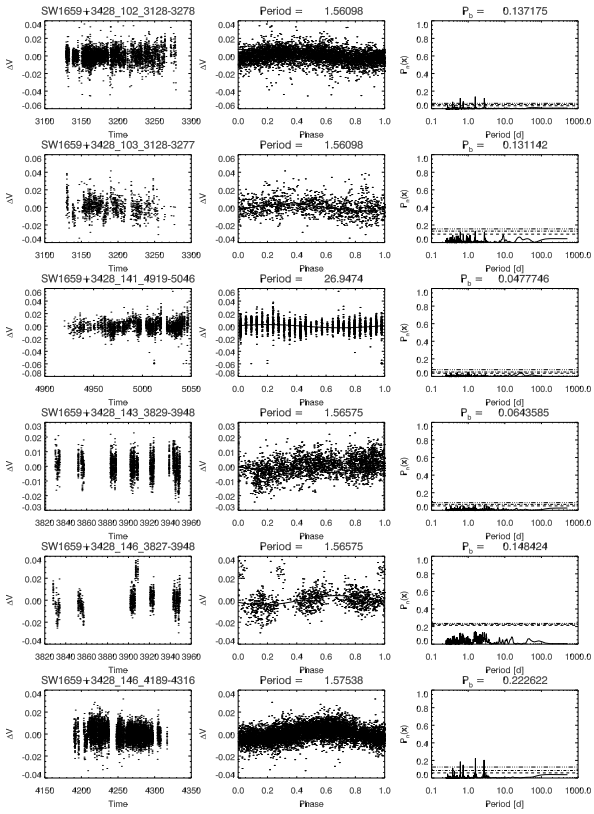

SW1659+3428 continued

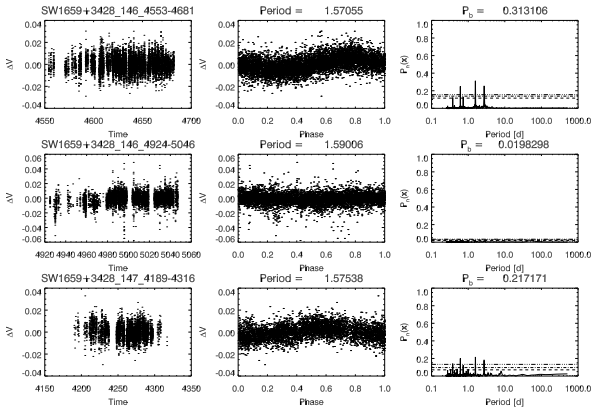

SW1703+3203

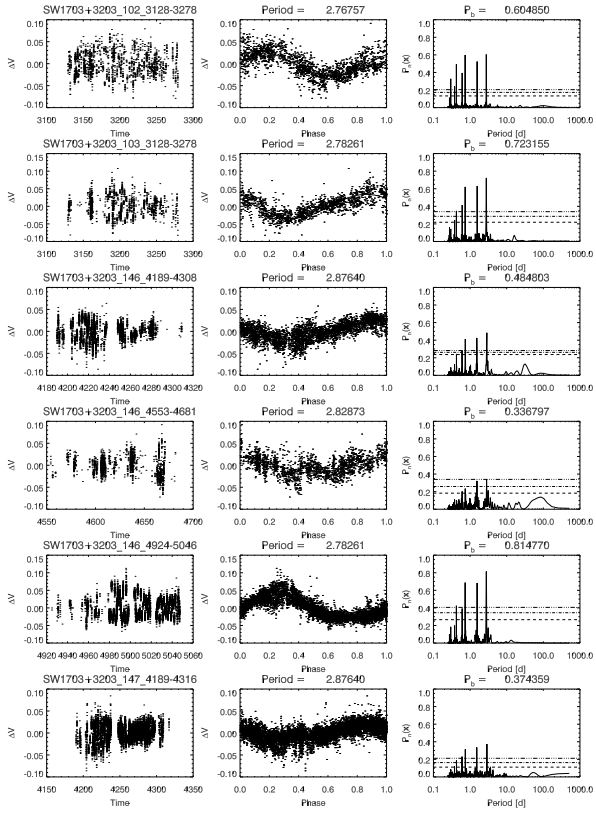

SW1704+3928

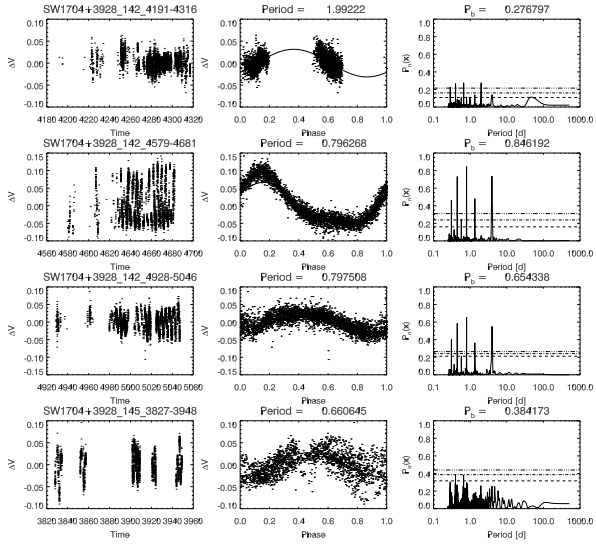

SW1703+3203 continued

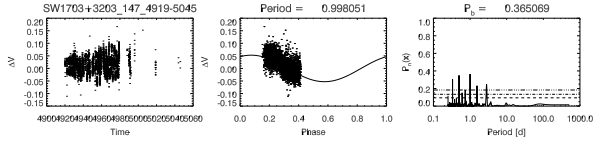

SW1713+2320

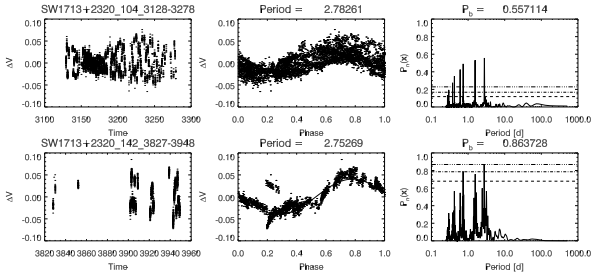

SW1724+4026

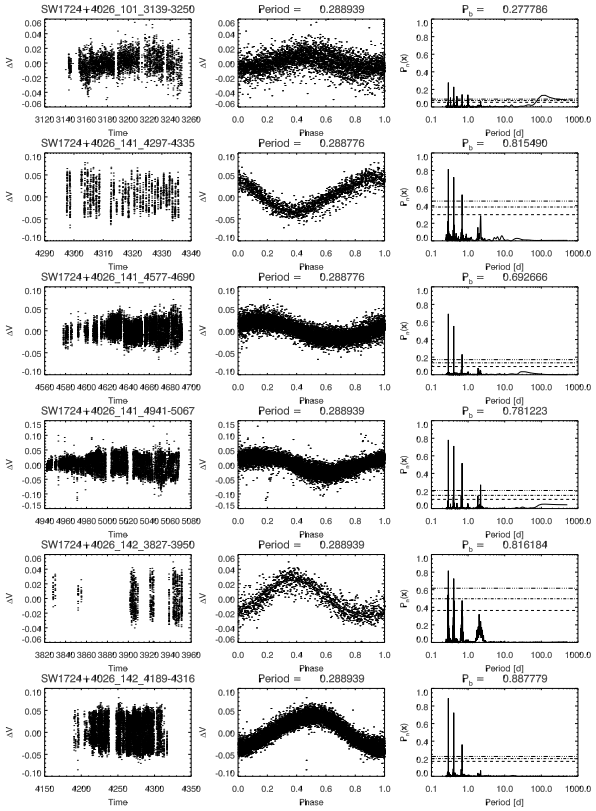

SW1724+4026 continued

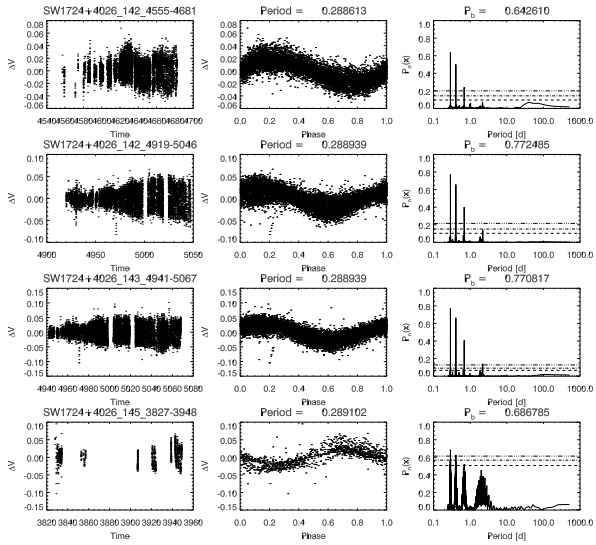

SW1744+1312

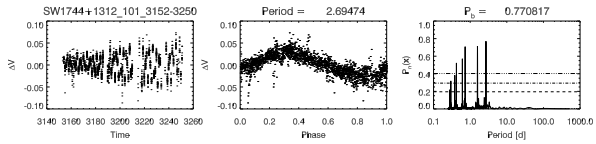

SW1747+3321

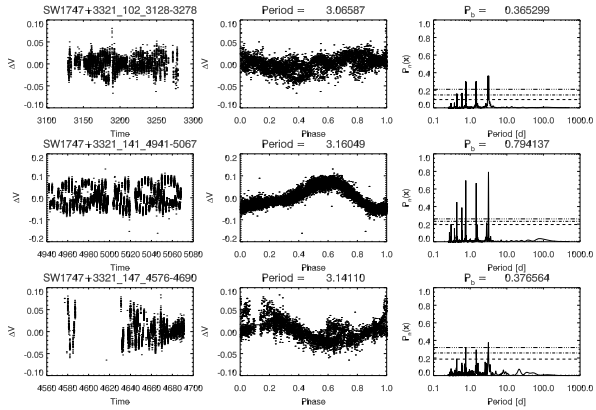

SW1749+3350

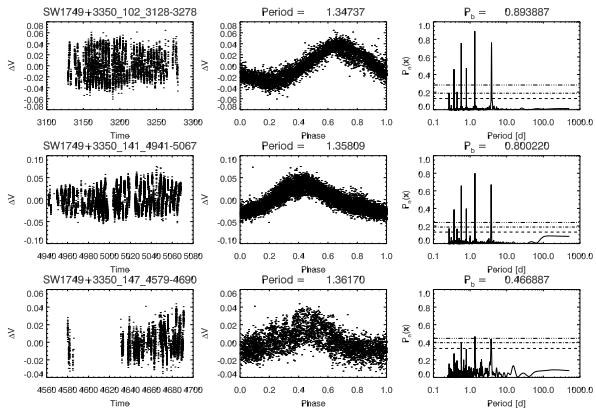

SW1752+2327

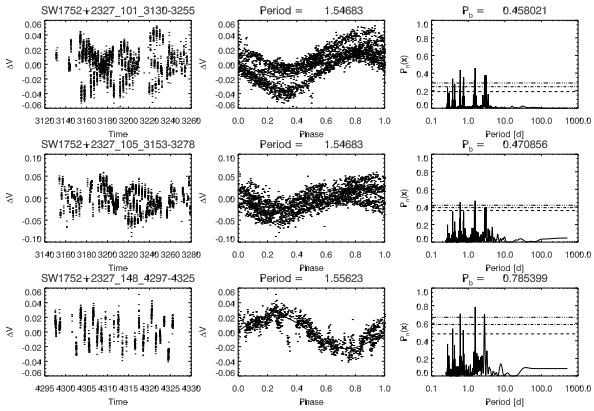

SW1751+4141

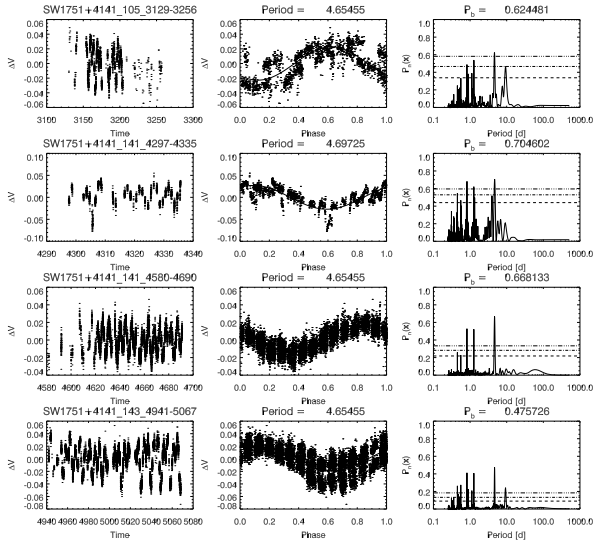

SW1757+3133

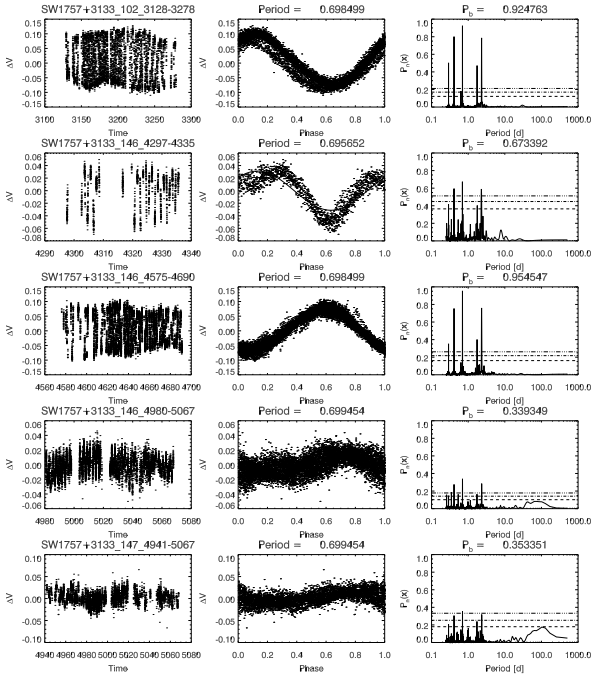

SW1757+5506

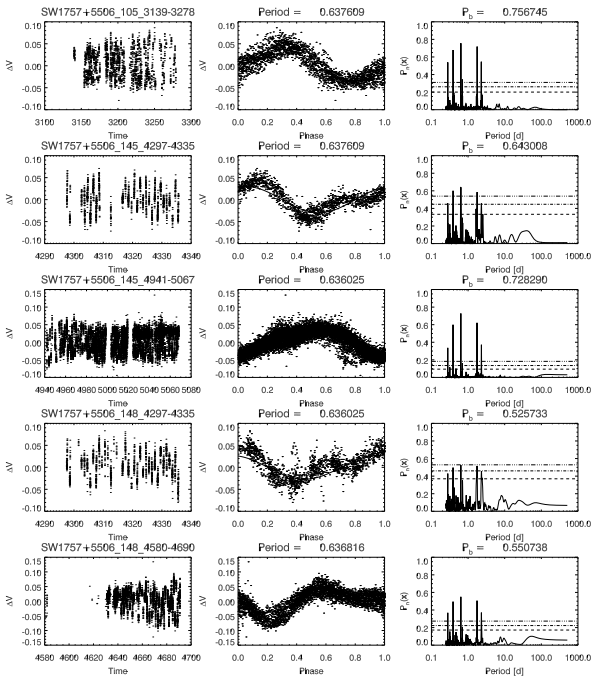

SW1800+5100

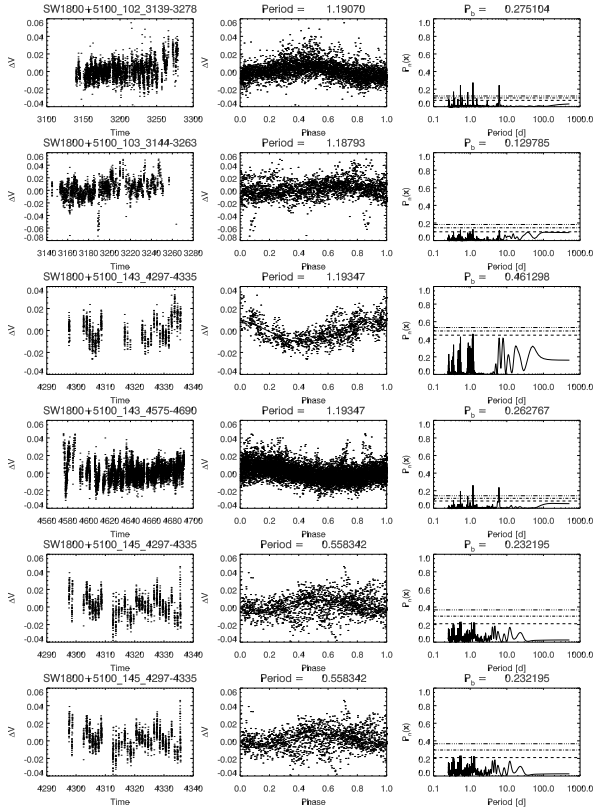

SW1758+0922

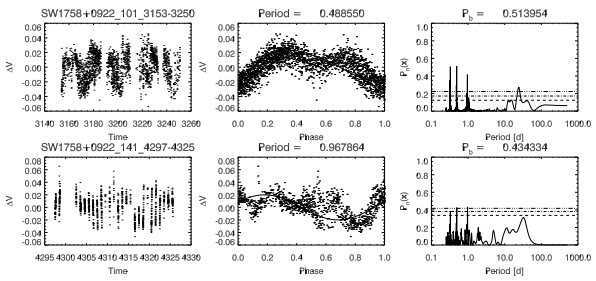

SW1800+5100 continued

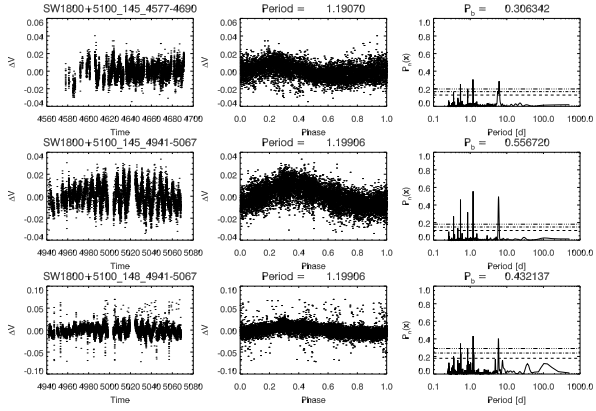

SW1812+4105

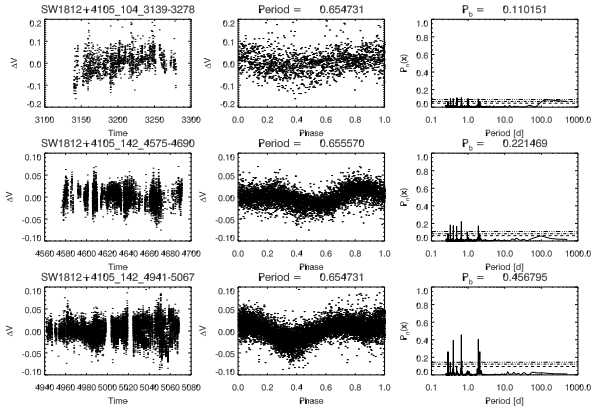

SW1815+3819

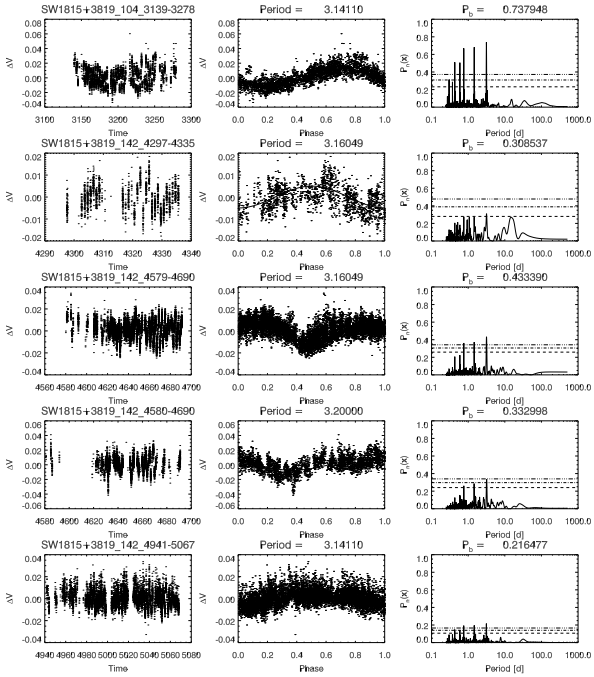

SW1815+2948

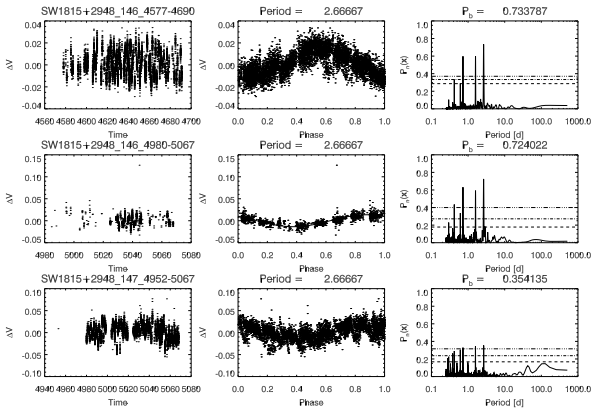

SW1830+3446

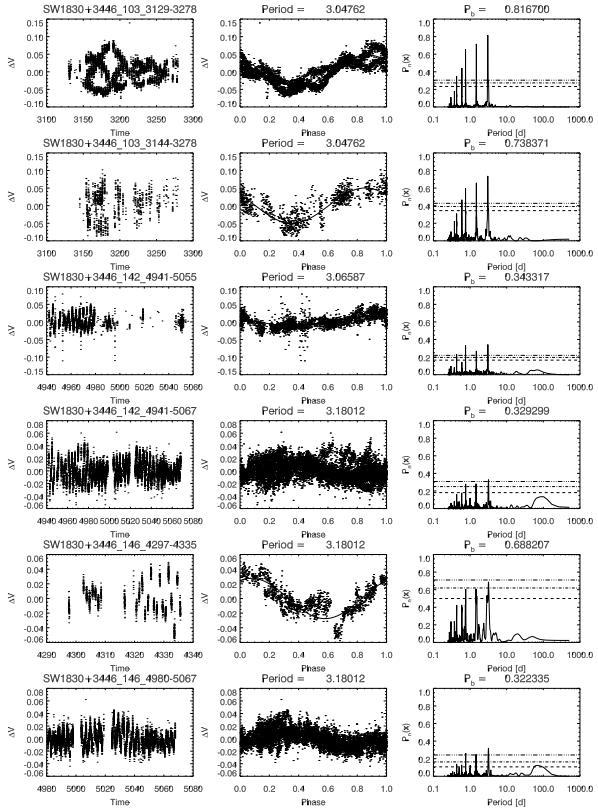

SW1831+5418

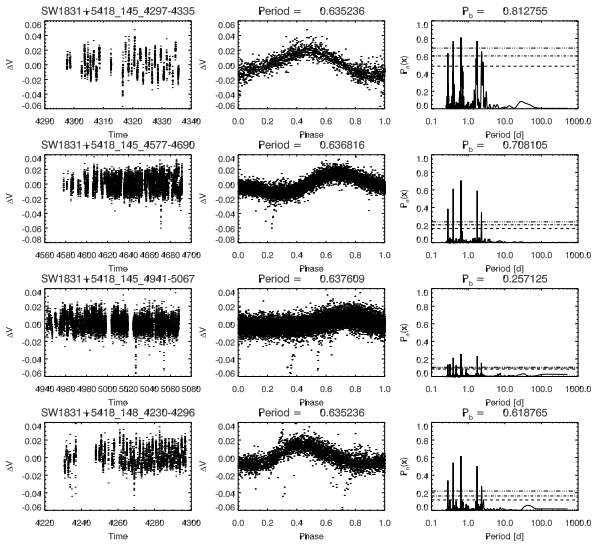

SW1913+4436

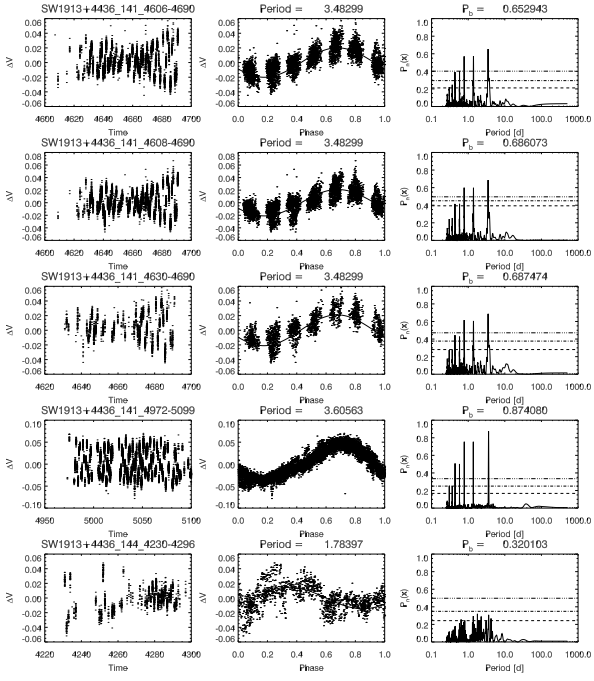

SW1830+3446 continued

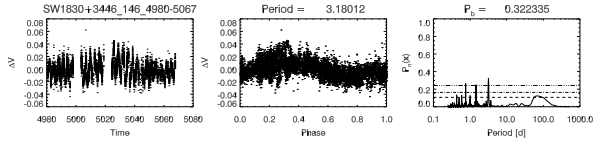

SW2028−0943

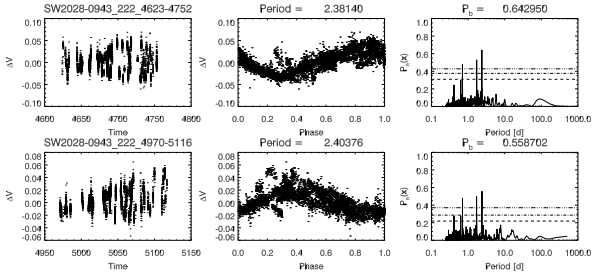

SW2044+1314

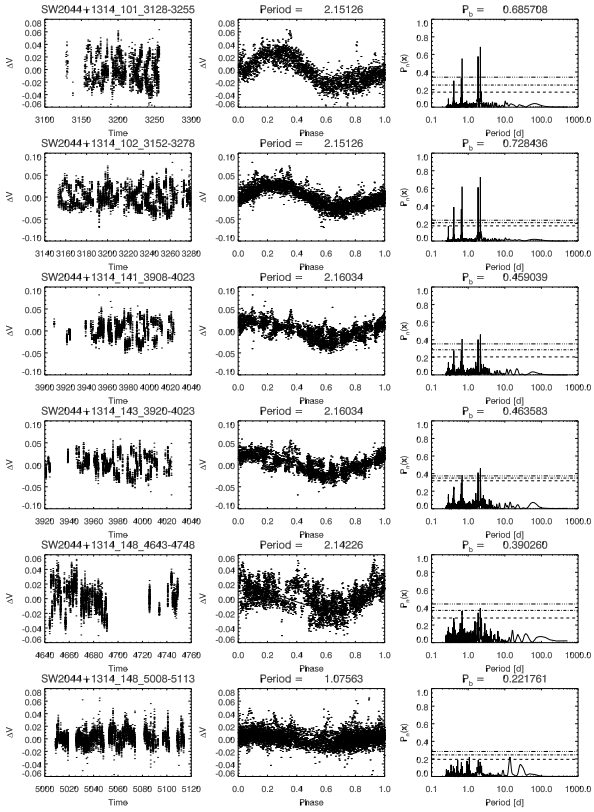

SW2028+1131

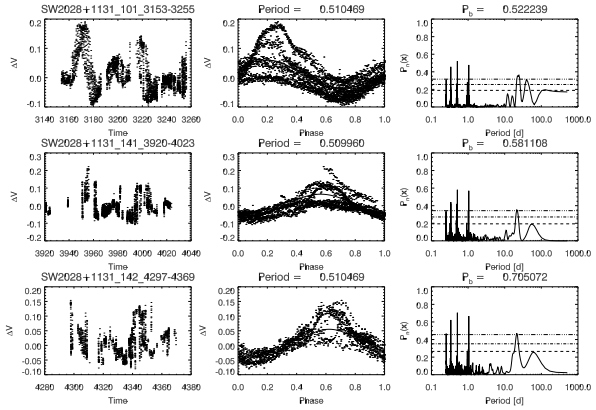

SW2048−0644

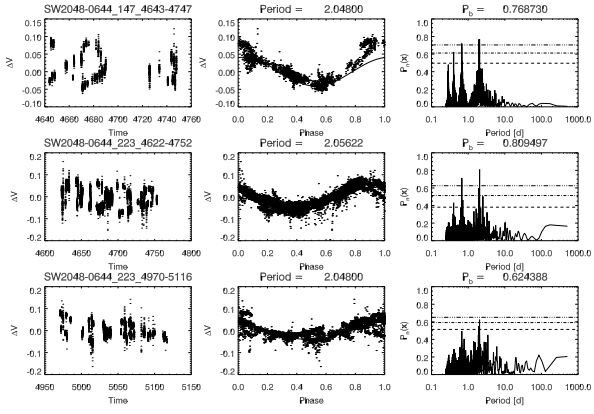

SW2107+0632

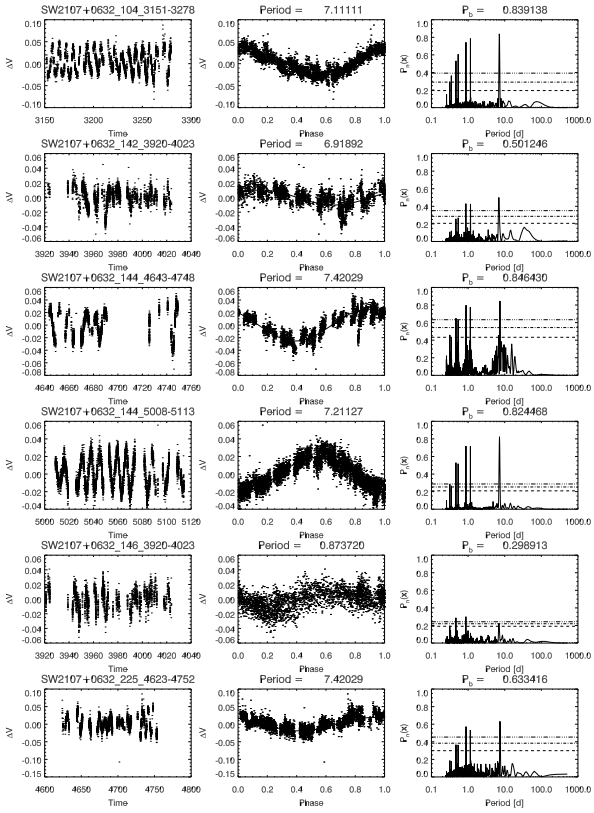

SW2107+1357

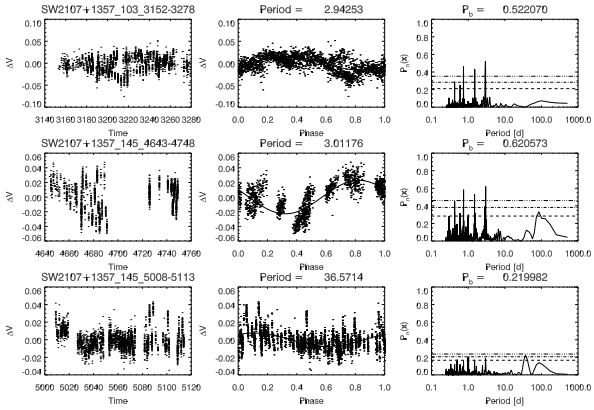

SW2121+0948

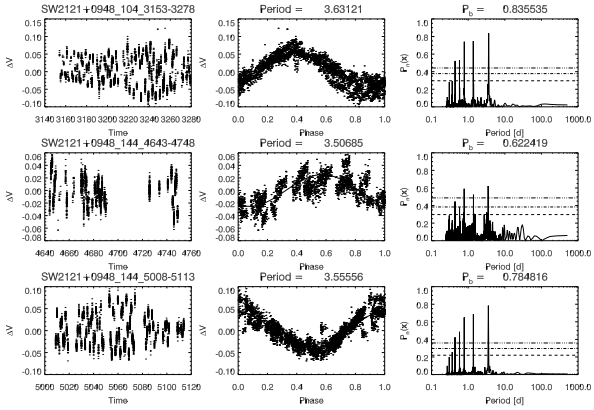

SW2107+0632 continued

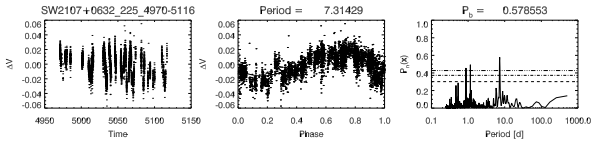

SW2148+1910

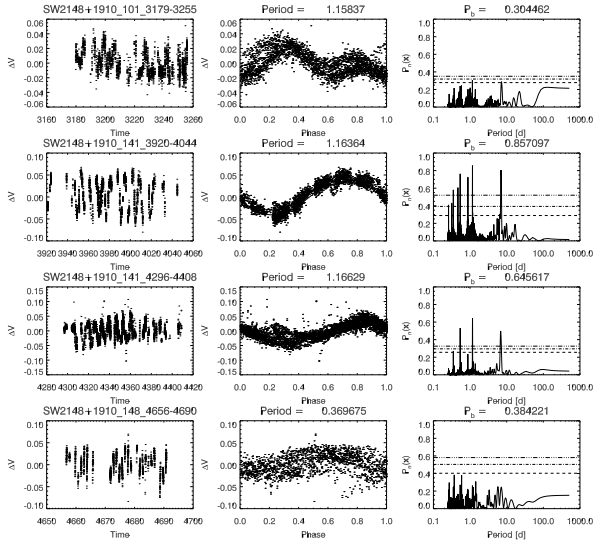

SW2205+0749

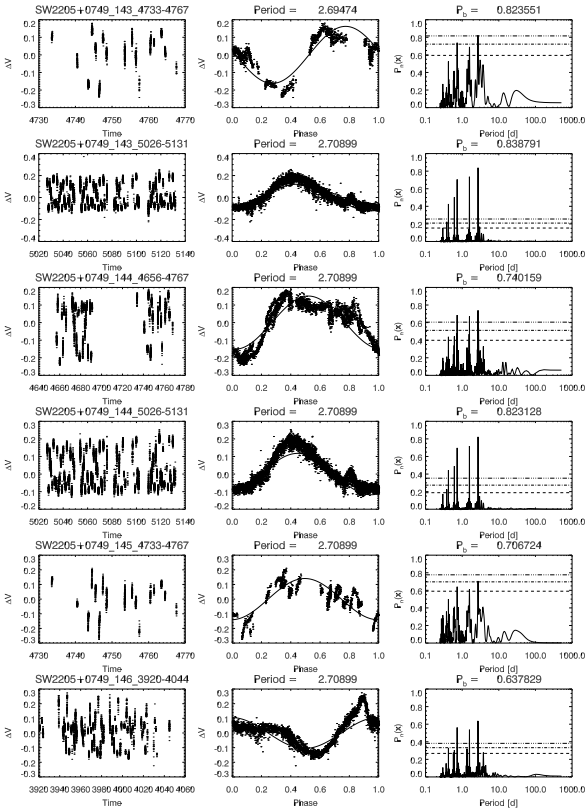

SW2205+0749 continued

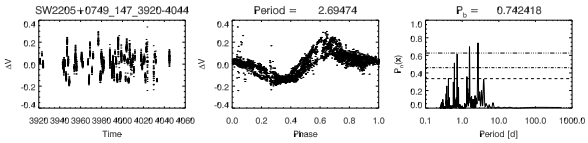

SW2222+2814

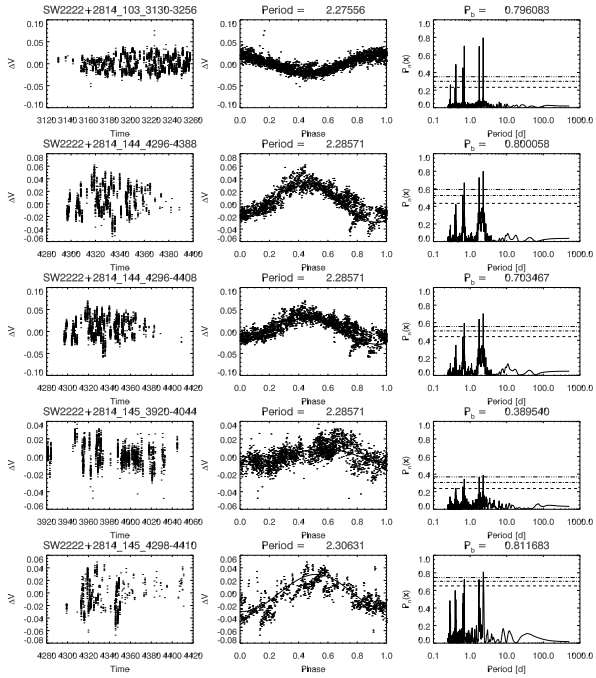

SW2310+2055

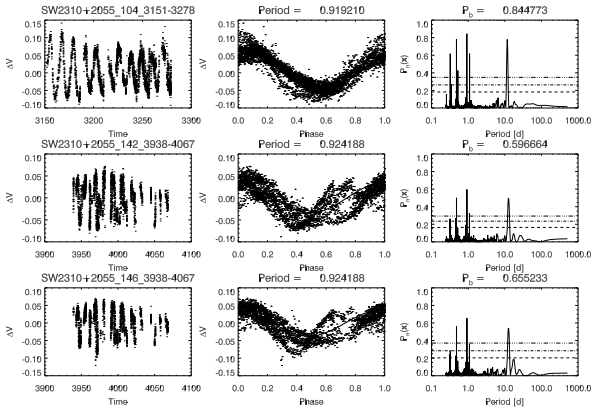

SW2244+3029

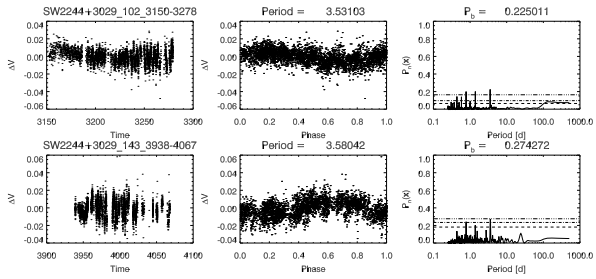

SW2312+1709

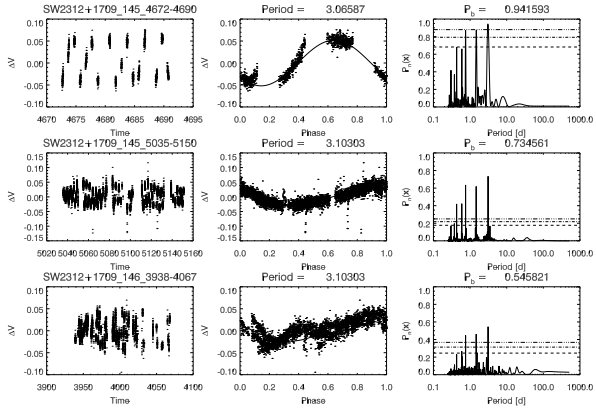

SW2320+2921

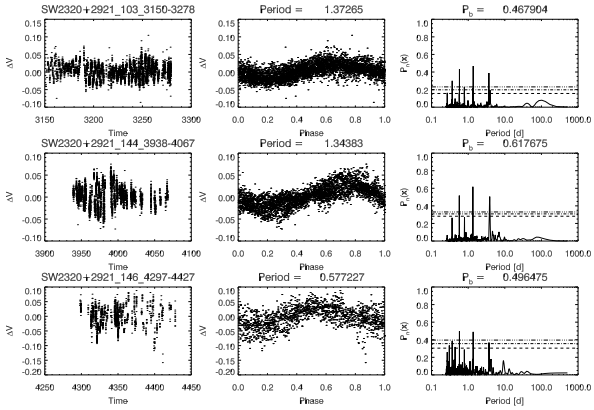

SW2317+0551

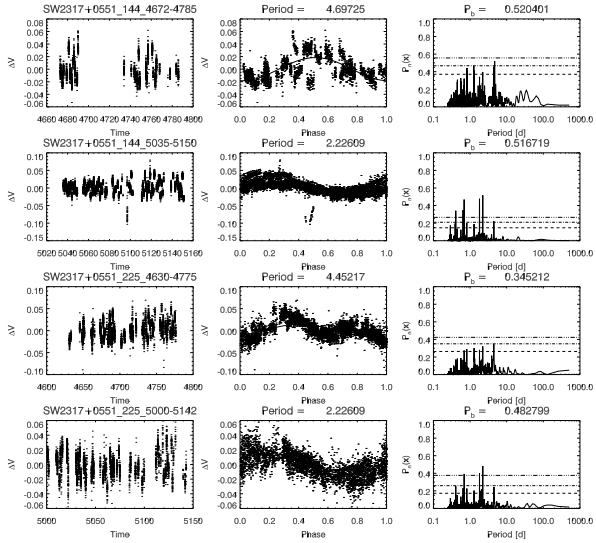

SW2339+2204

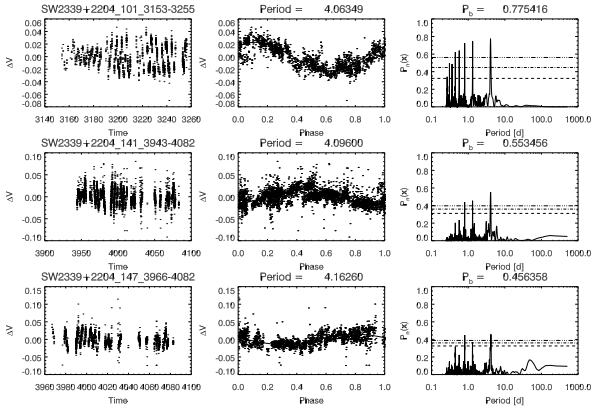

SW2340−0228

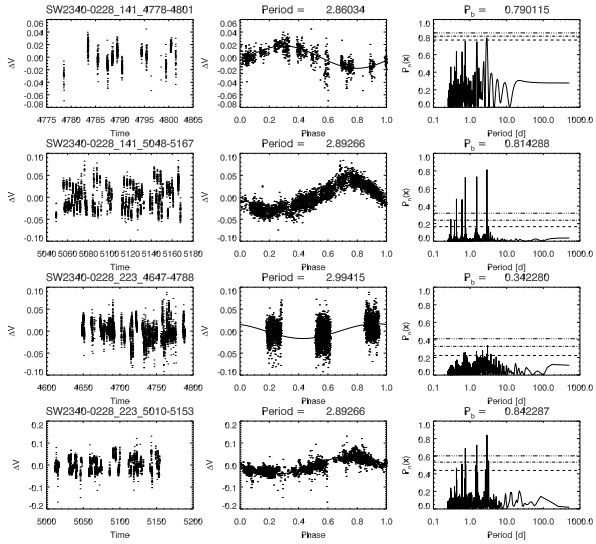

SW2357+3343